Subsonic and Intersonic Crack Growth Along Weak Planes and Bimaterial Interfaces

Thesis by

Omprakash Samudrala

In Partial Fulfillment of the Requirements

for the Degree of

Doctor of Philosophy

California Institute of Technology

Pasadena, California

2001

(Submitted May 18, 2001)

Acknowledgements

My sincere gratitude goes to my adviser Prof. Ares J. Rosakis for his guidance, encouragement and unbounded enthusiasm during this entire course of research. There were numerous instances when progress was extremely slow and I am grateful for his patience in allowing me ample time to weather the ups and downs of graduate research. Most of the ideas pursued in this work emerged out of his keen scientific intuition. I am also thankful to Prof. Y. Huang of the University of Illinois, Urbana-Champaign, who taught me many of the analytical tools used in developing the models presented in this work. I am grateful to Prof. G. Ravichandran, who made his lab facilities and equipment available generously. I am also thankful for his mentoring and helping me out with his advice time and again. I am also thankful to Prof. Knauss for his support during the initial years of my graduate study at Caltech. Thanks are also due to Prof. H. Kanamori and Prof. T. Heaton for going through my thesis painstakingly and developing an interesting discussion during my defense. I am also thankful to Prof. P. Suquet for accepting to be in my thesis defense committee at a short notice.

Thanks are also due to all my fellow students and postdocs in the solid mechanics group here, who made my long stay at the Graduate Aeronautical Laboratories memorable. In particular, I greatly enjoyed my discussions with Dr. Pradeep Guduru, Dr. Demirkan Coker and Dr. Sairam Sundaram on a wide range of topics, at times for hours together. I am also thankful to Dr. David Owen and Prof. Raman Singh for helping me out in the initial stages of learning to do experiments in the lab. Many

other friends who made life and work at Caltech interesting and exciting, include Dr. Sangwook Lee, Bibhuti Patel, Dr. Sandeep Sane, Dr. Hansuk Lee, Dr. Ben Chow, Roy Xu, Dr. Ying Huang, Javier Gonzalez, David Anderson and others. I am also indebted to Ms. Denise Thobe who was always cheerful and willing to help out with all sorts of administrative details.

The work presented in this thesis was funded by the National Science Foundation (Grant #CMS9813100 and Grant #CMS9983779) and of the Office of Naval Research (Grant #N00014-95-1-0453, Dr. Y. D. S. Rajapakse, Project Monitor). This financial support is gratefully acknowledged.

Finally, I dedicate this thesis to my mother, whose loving care, concern and strong belief in education have made me the person I am today. She is no more, but her memories and inspiration always remain with me. I am also thankful to my father and my siblings whose unwavering support through long years of my graduate study have allowed me to complete a thesis, that I am proud of.

Abstract

A combined experimental and analytical study has been conducted to investigate the phenomena of intersonic crack propagation along weak planes in homogeneous solids and dissimilar material interfaces. A single edge notch/crack oriented along a weak plane in a brittle polymer or along a polymer/metal interface was loaded in shear by impacting the specimen with a high velocity projectile fired from a gas gun. Homalite-100 or PMMA was chosen for the polymer and 6061 Aluminum or 4340 steel was chosen for the metal. The stress field information around the propagating crack tip was recorded in real time by two different optical techniques which provide complimentary information — photoelasticity and coherent gradient sensing (CGS), in conjunction with high speed photography.

Along weak planes in Homalite-100, dynamic shear cracks were observed to initiate and propagate at speeds exceeding the shear wave speed (c_s) of the polymer. The isochromatic fringe patterns reveal two distinct lines of strong stress field discontinuity (Mach waves) emanating from the crack tip. Intersonic cracks were observed to initially accelerate up to the longitudinal wave speed (c_l) of Homalite and thereafter slow down to propagate at a near constant velocity slightly above $\sqrt{2}\,c_s$. A series of short secondary opening cracks parallel to each other and at a steep angle to the weak plane ($\approx 80^o$) were also observed to initiate behind the main intersonic crack tip.

Motivated by the experimental observations, an asymptotic analysis was performed to obtain the near tip fields for an intersonically propagating steady state

mode II crack with a finite sized shear cohesive zone in front of it. The cohesive shear stress was chosen to be either a constant or to depend linearly on the magnitude of the local slip rate. Decohesion was chosen to occur when the relative slip between the two cohesive surfaces reaches a material/interface specific critical value. Unlike the case of a point sized dissipative region, it is shown that with a finite cohesive zone, the dynamic energy release rate is finite through out the intersonic regime. The influence of crack plane shear strength and of the rate parameter on the crack propagation behavior is investigated. Isochromatic fringe patterns were constructed using the cohesive crack tip fields, which compare favorably with the experimentally observed fringe patterns, and an attempt is made to extract the relevant analytical parameters. Unlike for a mode-I crack, a cohesive stress distribution that decreases with the local slip rate is found to match the experimental observations. The rate parameter was extracted by fitting the secondary crack angle observed in the experiments to that predicted by the analytical solution based on a maximum principal stress fracture criterion.

Edge notches/cracks on polymer/metal interfaces were loaded under different impact configurations and the conditions governing the attainment of intersonic crack growth along a bimaterial interface were investigated. High resolution isochromatic fringe patterns were obtained to study the nature of the crack tip fields during subsonic/intersonic transition. Careful observations of the transition of an interface crack into the intersonic regime showed the formation of crack face contact at speeds beyond c_R of the polymer. Subsequently, the contact zone is observed to expand in size, detach from the intersonic crack tip and finally vanish. The recorded isochromatic fringe patterns showed multiple Mach wave formation associated with such a scenario. Along PMMA/Al and PMMA/steel bimaterial interfaces, dynamic cracks initiating from edge notches were observed to accelerate to speeds higher than c_l of PMMA (supersonic), almost reaching c_R of aluminum. The resulting crack growth was observed to be highly transient and the gradients of in-plane normal stress components were

recorded using CGS interferometry.

Motivated by the aforementioned experimental observations, an asymptotic analysis was performed to obtain the stress and deformation fields around a steadily propagating intersonic crack on an elastic-rigid interface with a finite zone of crack face frictional sliding contact located a finite distance behind the tip. A linear frictional contact model is adopted, wherein the shear stress is proportional to the normal stress through a constant, the coefficient of dynamic friction. Isochromatic fringe patterns predicted by the near-tip fields exhibit the essential features observed during the experiments. Frictional sliding contact is shown to be possible only for velocities between c_s and $\sqrt{2}\,c_s$ of the polymer. The relevant analytical parameters were predicted by comparing the model to the experimental isochromatic fringe patterns and comments are made on the merits of the model presented.

Contents

List of Figures

List of Tables

Chapter 1

Introduction

1.1 Motivation

Many modern engineering materials like fiber/whisker/particle-reinforced polymer composites, metal-matrix composites, polycrystalline intermetallic alloys, structural ceramics and others contain interfaces joining two dissimilar materials. In addition, many engineering components like thin-film/substrate systems, laminates, multilayer capacitors, reaction-product layers, protective coatings, photovoltaic cells, soldered joints, adhesive joints, human joint replacements, piezoelectric actuators, welds and numerous others contain material interfaces. Frequently these interfaces contain flaws due to imperfect bonding, residual stresses and the like. Even otherwise, the mismatch in elastic and thermal properties across the interface leads to stress concentration and consequently becomes a favored site for flaw initiation during normal operating cycles. In cases like adhesive joints, welds and others, where the material mismatch is negligible, the joint is usually "weaker" than the base material. As such interface failure in these materials is a common occurrence, caused due to the propagation and coalescence of pre-existing or nucleated cracks along the interface. Hence an understanding of the mechanics of interface failure is essential to gauge the efficiency and reliability of such materials/components.

Interface cracks can initiate under either quasi-static or dynamic loading conditions. However, the eventual decohesion frequently proceeds in a catastrophic manner. From a practical point of view, the main interest in interface fracture is towards predicting the initiation of a pre-existing crack, however, there are numerous instances where dynamic crack propagation is of interest, especially for predicting crack arrest, for assessing and minimizing damage caused due to catastrophic failure and so on. Appropriate dynamic failure criteria are essential in obtaining accurate numerical simulations of the macroscopic response of multi-phase materials under dynamic loading. The potential applications where an understanding of dynamic crack propagation is profitable are summarized in an article by KANNINEN and O'DONOGHUE (1995).

Dynamic interfacial crack propagation is also of great importance in modeling earthquake source processes (DMOWSKA and RICE, 1986; SCHOLZ, 1990). A majority of earthquakes are caused by sudden rupturing of the earth's crust along a pre-existing fault plane (weak plane in the earth's crust), under the action of high ambient compressive and shear pre-stresses. Analysis of far-field wave forms recorded by seismic stations indicates that an earthquake rupture may be modeled as a dynamically extending shear crack along a pre-existing weak path (fault plane). Fault planes which are relatively new (with regard to geological time scales) may be considered as weak planes separating rock bodies with approximately the same elastic and thermal properties. In contrast, on more mature faults, repeated slip leading to large displacements can bring different rock bodies (elastic wave speed mismatch can be as high as 20-30% as found by tomographic inversions of seismic data) next to each other. Such is the case for plate-bounding continental and subduction zone faults along which the largest earthquakes occur. In such a case, the bimaterial nature of the fault rupture must be taken into consideration. Ruptures on shallow crustal faults are estimated to run at velocities close to the shear wave speed (c_s) of crustal rocks, although evidence has accumulated over the years of intersonic rupture speeds (speeds between c_s and

the longitudinal wave speed, c_l) at least over a portion of the faulting (ARCHULETA, 1984; OLSEN *et al.*, 1997; HERNANDEZ *et al.*, 1999; ELLSWORTH and CELEBI, 1999; BOUCHON *et al.*, 2000). Hence the dynamics of shear crack propagation is of great importance in seismology.

The theory of dynamic crack propagation is elegantly summarized by FREUND (1989) and BROBERG (1999). Most of the literature on dynamic fracture is devoted to opening cracks (mode I). Propagating mode II cracks are usually not observed in homogeneous isotropic solids, except under extreme conditions of high compressive and shear pre-stresses (MELIN, 1986; BROBERG, 1987). This is due primarily to the fact that in-plane cracks in homogeneous solids almost always propagate such that pure opening mode conditions are maintained at the tip. If the initial crack orientation does not coincide with such a symmetry plane, abrupt kinking occurs during initiation and thereafter, the crack curves smoothly onto the maximum principal plane (COTTERELL and RICE, 1980; NEMATNASSER and HORII, 1982; MELIN, 1986). However, in materials possessing "weak" surfaces and dissimilar material interfaces, mixed-mode crack propagation and in particular shear crack propagation becomes possible, as these surfaces act as preferable paths for crack growth preventing it from choosing a path that would maintain pure opening mode conditions near the tip. In fact this phenomenon becomes more pronounced under dynamic loading, as shown in this work.

For interfaces across which material mismatch is negligible or nonexistent, the theory of dynamic crack propagation in homogeneous, isotropic, linear elastic solids provides a standard frame work for obtaining the near-tip stress and deformation fields. However, if the interface is weaker than the base material, then the interface constitutive behavior must be taken into account, to make an accurate prediction of the initiation and propagation of dynamic cracks along the interface. This is done in either of two ways: One, by explicitly introducing the fracture toughness (or critical dynamic energy release rate) associated with the weak interface through a dynamic

crack initiation/propagation criterion or alternately by introducing a separate cohesive constitutive relation (that relates the traction on a cohesive surface to the local displacement, displacement rate, *etc.*) for the weak path in the solution of the initial-boundary value problem itself. The second approach is gaining in popularity because of its simplicity in application to numerical simulations of fracture. The theory of cohesive constitutive relations is summarized by NEEDLEMAN (1987; 1990a;b); ORTIZ and PANDOLFI (1999).

A fundamental question in dynamic fracture mechanics concerns the limit on attainable crack speeds. For remotely loaded mode I cracks in homogeneous, isotropic, linear elastic solids, the theoretical upper limit on the propagation speed is the Rayleigh wave speed (c_R) of the material (BARENBLATT and CHEREPANOV, 1960; BROBERG, 1960; CRAGGS, 1960). The energy flux into the crack tip vanishes at c_R and at higher speeds no analytical solution can be found with positive energy flux into the tip (BROBERG, 1989). Indeed, positive energy flux is required because crack growth involves material separation, which is an energy consuming process, and hence a necessary condition for propagation of a crack is that energy be supplied from the outer stress field to the crack tip region. Consistent with the theory, the only experimental observations of intersonic and supersonic (speeds greater than c_l) mode I crack speeds have been limited to cases where the loading is applied directly at the crack tip, thus obviating the usual mechanism of energy transfer through stress waves. WINKLER *et al.* (1970); CURRAN *et al.* (1970) reported observations of supersonic crack speeds along weak crystallographic planes in anisotropic single crystals of potassium chloride, where the crack tip was loaded by laser induced expanding plasma.

For remotely loaded mode II (in-plane shear) cracks in homogeneous, isotropic, linear elastic solids, crack speeds below c_R as well as those in the intersonic regime are permissible from similar energetic considerations (BROBERG, 1989). Hence the upper limit on the propagation speed for a remotely loaded mode II crack is c_l (BROBERG,

1996). A substantial number of analytical and numerical studies (BURRIDGE, 1973; ANDREWS, 1976; DAS and AKI, 1977; FREUND, 1979; BURRIDGE *et al.*, 1979; GEORGIADIS, 1986; BROBERG, 1989; JOHNSON, 1990; BROBERG, 1994; 1995) have explored the dynamics of shear crack propagation and the possibility of intersonic crack speeds. However, up to the present work (ROSAKIS *et al.*, 1999; 2000) there have been no supporting experimental observations in the laboratory. The only evidence, mentioned before, on the possibility of intersonic cracks is indirect, coming from the modeling of seismic records for rupture speeds during shallow crustal earthquakes. For propagating mode III (antiplane shear) cracks, the requirement of a positive energy flux into the propagating crack tip yields c_s as the limiting speed.

An in-plane crack on a dissimilar material interface generally experiences a mixed-mode deformation in the tip vicinity, even though the applied far-field loading possesses the symmetries of a pure mode. Similar to a crack in a homogeneous solid, a bimaterial interface crack also opts, if possible, to kink into one of the materials on either side and establish pure mode I conditions near the tip. However, unlike the case of a crack along a weak plane in an otherwise homogeneous solid, a bimaterial interface need not be "weaker" than both the phases to sustain propagation along the interface. If one of the phases had a higher fracture toughness than the other, an interface crack under certain far-field mode mixities might prefer to propagate along the interface itself even though it is not significantly weaker than both phases. Hence, the possibility of mixed-mode and in particular, shear dominated crack propagation is much more pronounced along a dissimilar material interface than along an interface joining two identical solids. The theory of kinking of a crack out of an interface was thoroughly explored in the articles by HE and HUTCHINSON (1989) and HE *et al.* (1991).

Dynamic crack propagation along an interface separating two dissimilar, homogeneous, isotropic, linear elastic solids has received a lot of attention only in the past decade. After a few initial analytical investigations (GOLDSHTEIN, 1966; 1967;

WILLIS, 1971; BROCK and ACHENBACH, 1973; ATKINSON, 1977) interest in the area subsided due to the lack of supporting experimental observations. In the first (to author's knowledge) systematic experimental investigation on dynamic crack propagation along a bimaterial interface, TIPPUR and ROSAKIS (1991) observed interfacial cracks along polymethylmethacrylate(PMMA)/6061 aluminum interfaces propagating at speeds close to 80% of the Rayleigh wave speed of PMMA (c_R^{PMMA}). In contrast, cracks in homogeneous PMMA rarely exceed 40-50% of c_R^{PMMA}, before branching into multiple cracks. The observation that a PMMA/Al interface can sustain much higher crack speeds spurred a renewal of interest in dynamic crack propagation along bimaterial interfaces. YANG *et al.* (1991) obtained explicit expressions for the dominant stress field around a crack running subsonically (subsonic with respect to the more compliant half) along a bimaterial interface. Based on experimental observations, LAMBROS and ROSAKIS (1995a;b) and KAVATURU and SHUKLA (1998) proposed propagation criteria for subsonic crack growth along a bimaterial interface. LAMBROS and ROSAKIS (1995a) proposed that the crack face profile remains unchanged during subsonic interfacial crack propagation, whereas KAVATURU and SHUKLA (1998) proposed that crack face displacement components increase with crack speed according to a power law. An interesting feature exhibited by both these criteria is that the dynamic fracture toughness decreases as the lower of the two Rayleigh wave speeds is approached. This behavior is opposite to that observed in homogeneous polymers and metals where dynamic fracture toughness is usually observed to increase sharply with crack speed. LIU *et al.* (1993); LAMBROS and ROSAKIS (1995c) and SINGH and SHUKLA (1996) demonstrated experimentally that under highly shear dominated conditions, bimaterial interface crack speeds can exceed c_s of the more compliant material and become intersonic (with respect to the more compliant half). Motivated by these observations, LIU *et al.* (1995); HUANG *et al.* (1996); YU and YANG (1994; 1995) derived the asymptotic near-tip fields for an intersonic crack on a bimaterial interface and showed that the essential features observed in the experimental fringe patterns are predicted by the analytical solution.

As observed experimentally and predicted analytically, the stress field distribution around an intersonic crack on a bimaterial interface differs dramatically from that around a subsonic interfacial crack. Since the crack speed has exceeded c_s of the more compliant half, all the shear waves generated by the running crack in the more compliant half are restricted to lie behind a Mach wave radiating from the crack tip. The Mach wave carries with it a strong discontinuity in stress field. Such a Mach wave was clearly seen in the isochromatic fringe patterns recorded by SINGH and SHUKLA (1996). In addition to the Mach wave radiating from the tip, they also observed a second Mach wave parallel to the first one and radiating from a point a finite distance behind the tip. LAMBROS and ROSAKIS (1995c) and SINGH and SHUKLA (1996) proposed that an intersonic crack on a bimaterial interface propagates with a finite zone of crack face frictional contact behind it, thus explaining the observation of a second Mach wave and also the finite separation distance between the two lobes of the CGS fringe pattern on either side of the intersonic crack tip. The size of the contact zone was found to be of the order of a few mm. Motivated by this observation, HUANG *et al.* (1998); WANG *et al.* (1998) obtained the near-tip fields around an intersonically propagating interfacial crack with a finite zone of crack face frictional contact behind the tip. Numerical simulations of XU and NEEDLEMAN (1996); BREITENFELD and GEUBELLE (1998); NEEDLEMAN and ROSAKIS (1999) also showed that intersonic interfacial crack propagation is accompanied by crack face contact zones and lines of stress field discontinuity. The transient mechanism governing the formation of this large-scale crack face contact zone as the interfacial crack accelerates from subsonic to intersonic speeds is rather obscure. The structure of the contact zone as well as its evolution history during the entire intersonic crack growth process are some of the issues pursued in this work.

The issue of the limiting speed for a crack on a bimaterial interface is not yet fully resolved. ATKINSON (1977) claimed that the terminal speed for a bimaterial interface crack is the lower of the Rayleigh wave speeds of the two constituents, where

as WILLIS (1973) argued that the terminal speed would be slightly greater than the lower of the two Rayleigh wave speeds. YANG *et al.* (1991) found that unlike for a homogeneous solid, the dynamic energy release rate for a bimaterial interface crack remains finite at the lower Rayleigh wave speed, even with a nonvanishing stress intensity factor. Based on this observation, they suggested that a bimaterial interface crack can exceed the lower Rayleigh wave speed. LIU *et al.* (1995) showed that for crack speeds between c_R and c_s of the more compliant half, the stress field is no longer singular, resulting in a vanishing energy flux into the tip region. Thus this particular regime is inadmissible based on energetic considerations. For intersonic crack speeds, the crack tip stress singularity exponent is less than 1/2 resulting in a vanishing energy flux into the tip (LIU *et al.*, 1995; YU and YANG, 1995; HUANG *et al.*, 1996). If the idealization of a sharp crack tip is relaxed by incorporating a Barenblatt type process zone of finite size, the energy flux to the tip region is finite, thus making intersonic crack speeds permissible. Also, YU and YANG (1995) showed that for crack speeds between the lower c_s and higher c_R there exists a finite energy flux across the interface from the stiffer half to the compliant half, which becomes unbounded as the crack speed approaches the higher Rayleigh wave speed. Based on this observation, they suggested that the higher c_R is the limiting speed for a bimaterial interface crack. However, BROBERG (1999) using a Barenblatt type process zone, showed that interfacial crack speeds higher than the c_s of the stiffer half are energetically permissible, provided they are lower than c_l of the more compliant half. The exact limiting speed appears to be dependent on the wave speed mismatch across the interface and the lack of supporting experimental observations makes it unclear. Until the present work, no observations of supersonic (with respect to the more compliant half) crack growth along a bimaterial interface have been reported. All the above results are based on steady state solutions and transient effects, along with the possibility of Stoneley waves on the interface should significantly influence the terminal speed observed.

The research work as summarized in this thesis is an attempt at addressing some of the issues raised above regarding crack propagation along weak planes in homogeneous solids and along dissimilar material interfaces. In the next section, the theory governing crack initiation, subsonic crack propagation and intersonic crack propagation along a weak plane in a homogeneous isotropic linear elastic solid under dynamic mixed-mode loading are briefly summarized. In Section 1.3, corresponding theory for a crack on a dissimilar material interface is summarized.

1.2 In-Plane Crack on a Weak Plane in a Homogeneous, Isotropic, Linear Elastic Solid

Consider a crack lying on a "weak plane" in an otherwise homogeneous, isotropic, linear elastic solid. By a "weak plane" it is understood that the fracture toughness (or fracture energy) for crack initiation and propagation along the plane is lower compared to that of the monolithic material on either side. Specifically, consider a crack in a brittle adhesive layer joining two identical brittle solids. We assume that the thickness of the adhesive layer is negligible compared to the crack length, depth of the crack (in case of plane stress) and other relevant in-plane geometrical parameters and that the mechanical properties of the adhesive layer are close to those of the adjoining solid. Under these conditions, the stress and deformation fields around the crack tip can be approximated to be the same as those around a crack in a homogeneous monolithic solid. However, the crack initiation and propagation characteristics would differ markedly, owing to the lower fracture toughness of the weak plane making it a preferred path for crack propagation. In this study, we concentrate exclusively on in-plane cracks, *i.e.*, cracks subjected to in-plane loading, around which the deformation is a combination of mode I and mode II types.

Consider a plane perpendicular to the crack edge and focus on a region in the vicinity of the crack tip (see Figure 1.1). It is well known that the structure of the near-tip fields asymptotically close to the edge of a crack in a three dimensional body

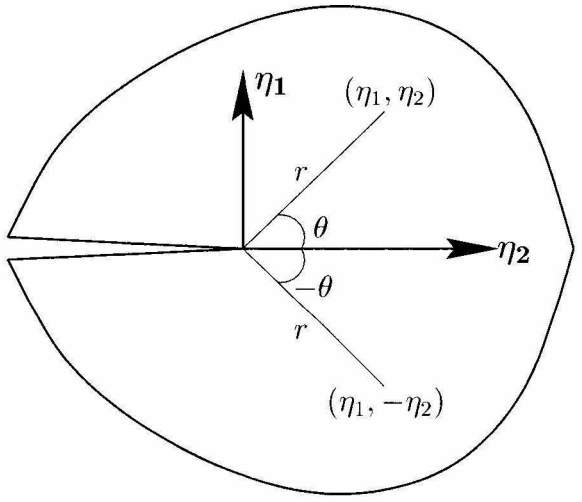

Figure 1.1: Crack in a homogeneous isotropic linear elastic solid - Tip vicinity.

is essentially two dimensional. Consider a Cartesian coordinate system (η_1, η_2) and a polar coordinate system (r, θ) centered at the crack tip as shown in Figure 1.1. Let u_α denote the components of the displacement vector and $\sigma_{\alpha\beta}$ denote the components of the stress tensor. The usual Cartesian index notation is employed, wherein repeated indices imply summation. Greek indices take the values 1 and 2 and roman indices take the values 1, 2 and 3. $\delta_{\alpha\beta}$ is the Kronecker delta, with $\delta_{\alpha\beta} = 1$ when $\alpha = \beta$ and $\delta_{\alpha\beta} = 0$ when $\alpha \neq \beta$. Also $(.)_{,\alpha} = \partial(.)/\partial\eta_\alpha$ and an overdot on any quantity represents derivative with respect to time t.

1.2.1 Stationary Crack Subjected to Dynamic Mixed-Mode Loading

The stress field around the tip of a stationary in-plane crack with traction free crack faces, in a homogeneous, isotropic, linear elastic solid, subjected to dynamic mixed-mode loading has the general form

$$\sigma_{\alpha\beta}(r, \theta, t) = \frac{K_I(t)}{\sqrt{2\pi r}} \Sigma^I_{\alpha\beta}(\theta) + \frac{K_{II}(t)}{\sqrt{2\pi r}} \Sigma^{II}_{\alpha\beta}(\theta) + T(t)\, \delta_{\alpha 1}\delta_{\beta 1}. \tag{1.1}$$

All other higher order contributions to the stress field vanish as $r \to 0$. The functions $\Sigma^I_{\alpha\beta}(\theta)$ and $\Sigma^{II}_{\alpha\beta}(\theta)$ are given in many fracture mechanics text books (KANNINEN and

POPELAR, 1985; BROBERG, 1999). They are independent of the material properties and as such they are *universal functions*. $K_I(t)$ and $K_{II}(t)$ are the mode I and mode II stress intensity factors respectively and are functions of the time varying loads and geometry. The third term, called the T-stress is a constant with respect to spatial coordinates and becomes important in dealing with issues of directional stability of a propagating crack. The relative displacement of the crack faces behind the tip, $\delta_\alpha(r < 0, t) = u_\alpha(r, \theta = \pi, t) - u_\alpha(r, \theta = -\pi, t)$ in the region dominated by the singular fields is given by

$$\delta_1(r,t) = K_{II}(t)\frac{\kappa+1}{\mu}\sqrt{\frac{r}{2\pi}}\,, \tag{1.2a}$$

$$\delta_2(r,t) = K_I(t)\frac{\kappa+1}{\mu}\sqrt{\frac{r}{2\pi}}\,, \tag{1.2b}$$

where $\kappa = 3 - 4\nu$ for plane strain and $\kappa = (3-\nu)/(1+\nu)$ for plane stress.

The relation between the dynamic energy release rate $G(t)$ (defined as the energy dissipated per unit area of incipient crack growth) for straight-ahead crack advance and the instantaneous crack tip stress intensity factors is given by

$$G(t) = \frac{K_I(t)^2 + K_{II}(t)^2}{E}\begin{cases} 1 & \text{plane stress,} \\ 1-\nu^2 & \text{plane strain.} \end{cases} \tag{1.3}$$

Now consider an incipient kinked crack of length a inclined at an angle $-\Omega$ to the crack plane (with the +ve η_1-axis). Then the stress intensity factors $K_I^t(t)$ and $K_{II}^t(t)$ at the tip of the kinked crack are given by (HUTCHINSON and SUO, 1992)

$$K_I^t(t) = c_{11}K_I(t) + c_{12}K_{II}(t) + b_1 T(t)\sqrt{a}\,, \tag{1.4a}$$

$$K_{II}^t(t) = c_{21}K_I(t) + c_{22}K_{II}(t) + b_2 T(t)\sqrt{a}\,, \tag{1.4b}$$

where the c's and b's depend on the angle Ω. Let $G_{max}^t(t)$ be the energy release rate of

the kinked crack maximized with respect to the kink angle Ω. Then a stationary crack subjected to dynamic mixed-mode loading of mixity $\psi(t) = \tan^{-1}(K_{II}(t)/K_I(t))$, initiates straight ahead without kinking, provided

$$G^t_{max}(t_o) < \Gamma(\dot{G}(t_o)) \qquad \text{and} \tag{1.5a}$$

$$G(t_o) = \Gamma_{pl}(\psi(t_o), \dot{G}(t_o))\,, \tag{1.5b}$$

where Γ is the critical mode I energy release rate (fracture energy) of the monolithic material, Γ_{pl} is the fracture energy of the weak plane and t_o is the time of crack initiation. In general, the critical energy release rates Γ and Γ_{pl} depend on the "loading rates" at the crack tip as measured by $\dot{G}$. The kinked crack would propagate in a monolithic solid and hence it would initiate in a direction that would maximize G^t and also maintain mode I conditions near the tip. In contrast, a crack initiating straight ahead along the weak plane would still propagate under mixed-mode conditions and hence Γ_{pl} is a function of the mode mixity ψ. This dependence may become more pronounced as $\psi \to \pm\pi/2$, where crack face asperity contact would come into play, leading to a substantial increase in energy dissipation. This was observed by Broberg (1987), who found that under quasi-static loading, the mode II fracture toughness, K_{IIc} for PMMA in the presence of frictional contact was about 2.5 times the mode I fracture toughness, K_{Ic} of PMMA. If the crack undergoes kinking, the stability of further propagation is governed strongly by the T-stress. In general, a +ve T-stress leads to instability in crack growth leading to further inclination of the crack away from the crack plane and a -ve T-stress is stable and might push a kinked crack, back on to the parent crack plane.

1.2.2 Mixed-Mode Subsonic Crack Tip Fields

Once a mixed-mode crack is initiated along the weak plane and its directional stability is maintained, it is possible for it to attain speeds that are a significant fraction of the elastic wave speeds in the solid, in which case the near-tip stress field is no

longer governed by (1.1). If the crack speed $v(t)$ changes sufficiently smoothly, then the near-tip stress field at any instant is dominated by the stress field around a steady-state mixed-mode crack propagating with the instantaneous speed and the instantaneous mode mixity (RICE, 1968; FREUND, 1989). The stress field near the tip of a subsonically propagating mixed-mode crack with traction free crack faces, under the action of time varying far-field loads is of the general form

$$\sigma_{\alpha\beta}(r,\theta,t) = \frac{K_I^d(t)}{\sqrt{2\pi r}}\,\Sigma_{\alpha\beta}^{Id}(\theta, v(t)) + \frac{K_{II}^d(t)}{\sqrt{2\pi r}}\,\Sigma_{\alpha\beta}^{IId}(\theta, v(t)) + T(t)\delta_{\alpha 1}\delta_{\beta 1}\,, \tag{1.6}$$

where $v(t) < c_s$ is the instantaneous crack tip speed. All the higher order terms not included in (1.6) vanish as $r \to 0$. K_I^d and K_{II}^d are the mode I and mode II subsonic stress intensity factors respectively which depend on time implicitly through time varying far-field loads $P(t)$, crack length $l(t)$ and crack speed $v(t)$. The functions $\Sigma_{\alpha\beta}^{Id}$ and $\Sigma_{\alpha\beta}^{IId}$ are given in FREUND (1989). The relative displacement of the crack faces δ_α is given by

$$\delta_1(r,t) = \frac{K_{II}^d(t)}{\mu}\,\frac{4\alpha_s(1-\alpha_s^2)}{R(v)}\,\sqrt{\frac{r}{2\pi}}\,, \tag{1.7a}$$

$$\delta_2(r,t) = \frac{K_I^d(t)}{\mu}\,\frac{4\alpha_l(1-\alpha_s^2)}{R(v)}\,\sqrt{\frac{r}{2\pi}}\,, \tag{1.7b}$$

where

$$\alpha_s = \sqrt{1-\frac{v^2}{c_s^2}}\,, \tag{1.8a}$$

$$\alpha_l = \sqrt{1-\frac{v^2}{c_l^2}} \qquad \text{and} \tag{1.8b}$$

$$R(v) = 4\alpha_l\alpha_s - (1+\alpha_s^2)^2. \tag{1.8c}$$

$R(v)$ is the Rayleigh function and one of its zeros is the Rayleigh wave speed, c_R.

The dynamic energy release rate $G(t)$ associated with a subsonically propagating

mixed-mode crack may be related to the instantaneous stress intensity factors $K_I^d(t)$ and $K_{II}^d(t)$ through

$$G(t) = \left[A_I(v(t))\frac{K_I^d(t)^2}{E} + A_{II}(v(t))\frac{K_{II}^d(t)^2}{E}\right] \begin{cases} 1 & \text{plane stress,} \\ 1-\nu^2 & \text{plane strain,} \end{cases} \tag{1.9}$$

where

$$A_I(v) = \frac{2\alpha_l(\alpha_l^2 - \alpha_s^2)}{R(v)}, \tag{1.10a}$$

$$A_{II}(v) = \frac{2\alpha_s(\alpha_l^2 - \alpha_s^2)}{R(v)}. \tag{1.10b}$$

Subsonic crack growth along a weak plane is sustained as long as a propagation criterion of the form

$$G(P(t), l(t), v(t)) = \Gamma_{pl}(\psi(t), v(t)) \tag{1.11}$$

is satisfied at each instant. In fact, the above criterion is a crack tip equation of motion, which can be solved for the crack length history $l(t)$ and crack speed history $v(t)$, provided the other parameters are known. The critical dynamic energy release rate Γ_{pl} for the weak plane is likely to be a function of the mode mixity ψ and the crack speed v. For mode I subsonic cracks in homogeneous metals & polymers, it is generally observed that the propagation toughness (analogous to critical dynamic energy release rate or fracture energy) increases many-fold with increasing crack speed, and hence crack speeds realized in such materials rarely exceed 40-50% of c_R (FINEBERG and MARDER, 1999; BROBERG, 1999). At high crack speeds, the height of the process zone (for *e.g.*, zone of micro-cracking) increases, primarily due to material inertia, resulting in higher energy dissipation (JOHNSON, 1992; RAVICHANDAR and KNAUSS, 1984). Propagating mixed-mode cracks are possible only under special circumstances, like on a weak plane, and data on the dependence of propagation toughness on mode mixity and crack speed is virtually nonexistent. For subsonic cracks on a weak plane,

e.g., on a brittle adhesive layer joining two identical brittle solids, the height of the process zone is a constant irrespective of the crack speed, being equal to the thickness of the adhesive layer. In such a case, it is unlikely that the propagation toughness would increase substantially with crack speed. For cracks on an interface between two dissimilar solids, it was found that the propagation toughness usually increases slightly after initiation and thereafter decreases monotonically with further increase in crack speed (LAMBROS and ROSAKIS, 1995a; KAVATURU and SHUKLA, 1998). It is likely that cracks on a weak plane would exhibit a similar behavior, *i.e.*, a decreasing propagation toughness with crack speed at least for mixities with a predominant shearing component.

Data on terminal speeds for propagating mode II and mixed-mode cracks is largely nonexistent. However, classical elastodynamic theories predict that the speed of a subsonic in-plane crack cannot exceed c_R of the material (FREUND, 1989; BROBERG, 1999). The subsonic - super-Rayleigh speed regime ($c_R < v < c_s$) is not energetically permissible because a solution associated with positive energy flow to the crack tip region cannot be found. Similar energetic considerations rule out intersonic crack speeds for mode I cracks. However, BROBERG (1989) showed that intersonic mode II crack growth is energetically permissible. Pure mode II conditions are difficult to attain. However, for a sharp crack tip, if the far-field mode mixity is such, as to bring the crack faces closer, then the near-tip mode mixity will be pure mode II as the crack faces are constrained against interpenetration (resulting in crack face contact where normal displacement of the crack faces is identically zero). In such a case intersonic crack speeds might be attained. However, the crack faces are strictly not traction free and classical analytical solutions must be revisited with contact boundary conditions on the crack faces. As a result, mixed-mode cracks on a weak plane, under certain far-field mode mixities may attain intersonic speeds and the upper limit on the propagation speed for such cracks is c_l.

1.2.3 Mode II Intersonic Crack Tip Fields

The near-tip stress field around a steadily propagating intersonic mode II crack with traction free crack faces has the general form (FREUND, 1979)

$$\sigma_{\alpha\beta}(\eta_1,\eta_2) = K_{II}^{*d}\left[\frac{f_{\alpha\beta}(\theta_l,v)}{r_l^q} + \frac{g_{\alpha\beta}(v)}{(-\eta_1-\hat{\alpha}_s|\eta_2|)^q}H(-\eta_1-\hat{\alpha}_s|\eta_2|)\right], \tag{1.12}$$

where the functions $f_{\alpha\beta}$ and $g_{\alpha\beta}$ are given in Appendix A, $H(.)$ is the unit step function,

$$r_l = \sqrt{\eta_1^2+\alpha_l^2\eta_2^2}, \qquad \theta_l = \tan^{-1}\left[\frac{\alpha_l\eta_2}{\eta_1}\right] \qquad \text{and} \tag{1.13}$$

the singularity exponent q associated with mode II intersonic crack tip stress field is given by

$$q = \frac{1}{\pi}\tan^{-1}\left[\frac{4\alpha_l\hat{\alpha}_s}{(1-\hat{\alpha}_s^2)^2}\right], \qquad \text{where} \tag{1.14a}$$

$$\hat{\alpha}_s = \sqrt{\frac{v^2}{c_s^2}-1}\,. \tag{1.14b}$$

The intersonic stress intensity factor K_{II}^{*d} is defined as

$$K_{II}^{*d} = \lim_{\eta_1\to 0^+}\sqrt{2\pi}\,\eta_1^q\,\sigma_{12}(\eta_1>0,\eta_2=0)\,. \tag{1.15}$$

Unlike the subsonic case, crack tip stress singularity q for an intersonic mode II crack is a function of crack speed v. It increases monotonically from 0 at c_s to 1/2 at $\sqrt{2}c_s$ and thereafter decreases monotonically to 0 at c_l. The stress field (1.12) predicts two Mach waves radiating from the crack tip along the lines $\eta_1 \pm \hat{\alpha}_s\eta_2 = 0$. Stresses are singular not only at the crack tip, but all along the Mach fronts, with the same order of singularity as that at the tip. In addition, across the Mach front, the normal stress and the normal velocity perpendicular to the front are continuous, where as the shear stress and tangential velocity suffer an infinite jump. Hence these fronts are shear

Mach waves. The relative sliding displacement on the crack faces is given by

$$\delta_1(r) = \frac{K_{II}^{*d}}{\mu\sqrt{2\pi}} \frac{2\hat{\alpha}_s(1+\hat{\alpha}_s^2)}{(1-q)R_q} r^{1-q}\,, \tag{1.16}$$

where

$$R_q = \sqrt{16\alpha_l^2\hat{\alpha}_s^2 + (1-\hat{\alpha}_s^2)^4}\,. \tag{1.17}$$

The dynamic energy release rate G associated with an intersonic mode II crack is identically zero at all intersonic speeds, except at $v = \sqrt{2}\,c_s$ where it has a finite value, given by

$$G = \frac{K_{II}^{*d^2}}{4\mu\alpha_l}\,. \tag{1.18}$$

FREUND (1979) pointed out that at this crack speed, the intersonic crack behaves "subsonic-like" and that the trailing shear Mach waves disappear. For all other intersonic speeds, energy is radiated away along the Mach waves without deposition at the tip. Hence, for intersonic mode II cracks, the idealization of the crack tip process zone to a point-size dissipative region results in a physically unrealistic situation, wherein the requirement of positive energy flux is met only at $\sqrt{2}c_s$. However, if the crack tip region is modeled to have a dissipative zone of finite size in front of the tip then ANDREWS (1976); BROBERG (1989) showed that positive energy flux to the dissipative region results at all intersonic speeds except at c_s and c_l. A dissipative zone of finite size can be incorporated readily by considering a line cohesive zone of finite length in front of the tip. The length of the cohesive zone emerges naturally from eliminating the pathological stress singularity at the crack tip. Intersonic crack growth criteria may now be cast in terms of a critical sliding displacement at the crack tip (ANDREWS, 1976; BURRIDGE *et al.*, 1979) or equivalently in terms of the energy dissipated within the cohesive zone.

1.3 In-Plane Crack on an Interface between Two Dissimilar, Homogeneous, Isotropic, Linear Elastic Solids

In the first analytical study of cracks on a bimaterial interface, WILLIAMS (1959) investigated the characteristic behavior of the stress field in the vicinity of a crack between two homogeneous, isotropic linear elastic media. He found that the stress field is singular and in addition, the various components oscillate with increasing frequency as the crack tip is approached. It was later shown that the solution also predicts unacceptable interpenetration of the crack faces. These unexpected features associated with an interfacial crack tip makes the treatment of interfacial cracks much more difficult in comparison with cracks on a weak plane between two identical solids. However, because of its practical importance, a substantial amount of research effort has gone into developing the concepts of static linear elastic interfacial crack mechanics. Some of the noteworthy contributions are those by RICE and SIH (1965); ERDOGAN (1965); ENGLAND (1965); MALYSHEV and SALGANIK (1965); COMNINOU (1977a;b); SYMINGTON (1987); DUNDURS and GAUTESEN (1988); GAUTESEN and DUNDURS (1988); COMNINOU (1990); SHIH (1991). Contributions deserving a special mention are those by RICE (1988) who gave a detailed analysis of linear elastic interfacial fracture mechanics using the method of Muskhelishvili potentials, and HUTCHINSON and SUO (1992) who solved for the interfacial crack tip stress intensity factors for a wide range of practical geometries.

Consider a crack lying on the interface between two dissimilar, homogeneous, isotropic, linear elastic solids and focus on a region in vicinity of the crack tip as shown in Figure 1.2. Consider a Cartesian coordinate system (η_1, η_2) and a polar coordinate system (r, θ) centered at the crack tip as shown in the figure. The material occupying the region $\eta_2 > 0$ is termed as material #1 and that occupying the region $\eta_2 < 0$ is termed as material #2. Let μ_α, ν_α and ρ_α be the shear modulus, Poisson's ratio and mass density of the two halves respectively. Without loss of generality, from

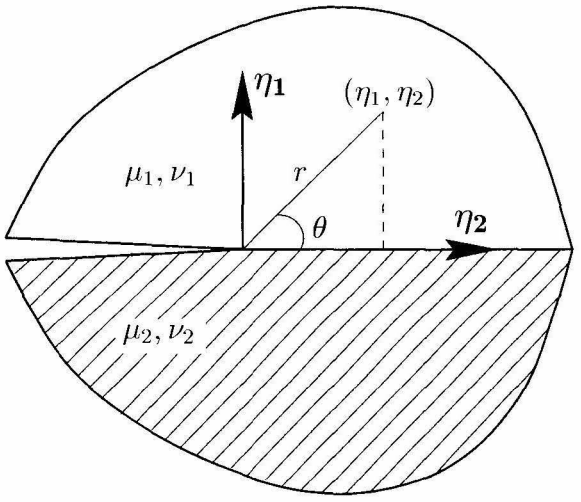

Figure 1.2: Crack on a bimaterial interface - Tip vicinity.

now on we assume that material #1 is more compliant as compared to material #2.

1.3.1 Stationary Crack Subjected to Dynamic Loading

The stress field around the tip of an in-plane crack with traction free crack faces on an interface between two homogeneous, isotropic, linear elastic solids subjected to far-field dynamic loading has the general form,

$$\sigma_{\alpha\beta}(r,\theta,t) = \frac{\mathrm{Re}\left[K(t)r^{i\epsilon}\right]}{\sqrt{2\pi r}}\Sigma^1_{\alpha\beta}(\theta;\epsilon) + \frac{\mathrm{Im}\left[K(t)r^{i\epsilon}\right]}{\sqrt{2\pi r}}\Sigma^2_{\alpha\beta}(\theta;\epsilon) + T(t)\delta_{\alpha 1}\delta_{\beta 1}\,, \qquad (1.19)$$

where $K(t) = K_1(t) + iK_2(t)$ is the complex crack tip stress intensity factor, the angular functions $\Sigma^1_{\alpha\beta}$ and $\Sigma^2_{\alpha\beta}$ are given in Rice *et al.* (1990) and ϵ, the oscillatory index is given by

$$\epsilon = \frac{1}{2\pi}\ln\left(\frac{1-\beta}{1+\beta}\right)\,. \qquad (1.20)$$

β is the second Dundurs' parameter which is a measure of the mismatch in elastic properties across the interface.

$$\beta = \frac{\mu_1(\kappa_2 - 1) - \mu_2(\kappa_1 - 1)}{\mu_1(\kappa_2 + 1) + \mu_2(\kappa_1 + 1)}\,. \qquad (1.21)$$

$T(t)$ is the T-stress which is spatially invariant in each of the constituents of the bimaterial but it may be different on either side of the interface. The traction on the interface ahead of the crack tip ($r > 0$) is given by

$$\sigma_{22} + i\sigma_{12}(r,t) = \frac{K(t)}{\sqrt{2\pi r}} r^{i\epsilon}\,, \tag{1.22}$$

and the relative displacement of the crack faces is given by

$$\delta_2(r,t) + i\delta_1(r,t) = \frac{8}{(1+2i\epsilon)\cosh(\pi\epsilon)} \frac{K(t)}{E^*} \sqrt{\frac{r}{2\pi}}\, r^{i\epsilon}\,, \qquad \text{where} \tag{1.23}$$

$$\frac{1}{E^*} = \frac{1}{2}\left(\frac{1}{E_1} + \frac{1}{E_2}\right) \qquad \text{for plane stress.} \tag{1.24}$$

As seen from (1.19), the near-tip stress field around the tip of an interfacial crack is singular as well as oscillatory (for $\beta \neq 0$). Moreover, the expression (1.23) for the crack face displacements indicates that they interpenetrate behind the tip, provided $\beta \neq 0$. Crack face interpenetration is physically impossible, and so they can only come into contact. An estimate of the contact zone size may be obtained by finding the largest r (within the range of dominance of the K-field) for which the opening gap δ_2 vanishes, *i.e.*, for which

$$\mathrm{Re}\left[K(t) r^{i\epsilon}/(1+2i\epsilon)\right] = 0\,. \tag{1.25}$$

With the existence of a crack face contact zone, the traction free boundary conditions are violated and the problem of a stationary interface crack must be revisited. Various approaches have been suggested in the literature to recast the interface crack problem in a way so that unacceptable crack face interpenetrations are eliminated. They include the introduction of a frictionless contact zone behind the tip (COMNINOU, 1977a), the recourse to finite elastostatics (KNOWLES and STERNBERG, 1983), the

adoption of smoothly varying material properties through the interface (DELALE and ERDOGAN, 1988; HUTCHINSON, 1989) and the introduction of a cohesive zone of finite size in front of the tip (ACHENBACH *et al.*, 1979; ORTIZ and BLUME, 1990). RICE (1988) introduced the concept of "small-scale" contact and showed that the predicted interpenetration of the crack faces means that the solution is unacceptable on the scale of the contact zone. However, the complex stress intensity factor does provide a proper characterizing parameter for the near-tip state in circumstances when the contact zone size is much smaller than the crack length and other relevant geometrical parameters and when it is completely embedded within the K-dominant zone at all times.

For a bimaterial interface crack, the two in-plane modes of crack tip deformation are coupled and the mode mixity ψ varies with distance away from the crack tip. Hence a reference length L is chosen, and the mode mixity $\psi(t)$ is defined using the ratio of shear and normal traction at this distance ahead of the tip.

$$\psi(t) = \tan^{-1}\left[\frac{\mathrm{Im}\{K(t)L^{i\epsilon}\}}{\mathrm{Re}\{K(t)L^{i\epsilon}\}}\right] . \tag{1.26}$$

Though not necessary, it is preferable to pick L within the zone of dominance of the K-field, otherwise the definition of ψ as the measure of mode mixity a distance L ahead of the tip is lost. If ψ_1 is the mixity associated with a reference length L_1 and ψ_2 is the mixity associated with a reference length L_2, then

$$\psi_2 = \psi_1 + \epsilon \ln(L_2/L_1) . \tag{1.27}$$

When ϵ is small, the change in ψ will be negligible even for changes of L of several orders of magnitude. RICE (1988) showed that the contact zone size is less than $L/100$ for most interfaces and most mixities, and hence small-scale contact conditions are satisfied in most cases.

The dynamic energy release rate for incipient crack advance along the interface is

given by

$$G(t) = \frac{1-\beta^2}{E^*} |K(t)|^2 . \tag{1.28}$$

Now consider an incipient crack kink of length a kinking from the interface into material #2 (below) at an angle Ω to the interface. Then the conventional mode I and mode II stress intensity factors $K_I^t(t)$ and $K_{II}^t(t)$ at the tip of the kinked crack are related to the complex stress intensity factor $K(t)$ and the mode mixity $\psi(t)$ (defined with respect to a reference length L) at the parent crack tip through

$$K_I^t(t) + iK_{II}^t(t) = c(\Omega,\alpha,\beta)K(t)a^{i\epsilon} + \bar{d}(\Omega,\alpha,\beta)\bar{K}(t)a^{-i\epsilon} + b(\Omega,\alpha,\beta)T(t)\sqrt{a}\,, \tag{1.29}$$

where $T(t)$ is the nonsingular contribution to σ_{11} in material #2 at the parent crack tip prior to kinking and the functions b, c and d are complex valued functions of the kink angle and the Dundurs' parameters α, β. β is defined above and α is given by

$$\alpha = \frac{\mu_1(\kappa_2+1) - \mu_2(\kappa_1+1)}{\mu_1(\kappa_2+1) + \mu_2(\kappa_1+1)} . \tag{1.30}$$

Let $G_{max}^t(t)$ be the energy release rate of the kinked crack maximized with respect to the kink angle Ω. Then a stationary crack on a bimaterial interface subjected to dynamic loading will initiate straight ahead without kinking, provided

$$G_{max}^t(t_o) < \Gamma(\dot{G}(t_o)) \qquad \text{and} \tag{1.31}$$

$$G(t_o) = \Gamma_{int}(\psi(t_o), \dot{G}(t_o)) , \tag{1.32}$$

where Γ is the mode I fracture energy for material #2, Γ_{int} is the fracture energy of the interface and t_o is the time of crack initiation. Γ and Γ_{int} depend on the loading rate through $\dot{G}$. Also the fracture energy of the interface Γ_{int} is a strong function of the mode mixity ψ. LIECHTI and CHAI (1991) showed that for an epoxy/glass interface, the fracture energy increases by almost eight times as the mixity changes from being opening dominated to shear dominated.

1.3.2 Subsonic Interfacial Crack Tip Fields

Similar to a subsonic crack in a homogeneous solid, if the speed $v(t)$ of a bimaterial interface crack changes sufficiently smoothly, then the near-tip stress field at any instant is dominated by the stress field around a steady-state subsonic interfacial crack propagating with the instantaneous crack speed and the instantaneous mode mixity (YANG *et al.*, 1991). The most singular term in the stress field near the tip of a subsonically ($v(t) < c_s^{(1)}$) propagating bimaterial interface crack with traction free crack faces, under the action of time varying far-field loads is of the general form

$$\sigma_{\alpha\beta}(r,\theta,t) = \frac{\mathrm{Re}\left[K^d(t)r^{i\epsilon}\right]}{\sqrt{2\pi r}}\Sigma^{1d}_{\alpha\beta}(\theta,v) + \frac{\mathrm{Im}\left[K^d(t)r^{i\epsilon}\right]}{\sqrt{2\pi r}}\Sigma^{2d}_{\alpha\beta}(\theta,v)\,, \tag{1.33}$$

where $K^d(t) = K_1^d(t) + iK_2^d(t)$ is the complex stress intensity factor, and the angular functions $\Sigma^{1d}_{\alpha\beta}$ and $\Sigma^{2d}_{\alpha\beta}$ are given in YANG *et al.* (1991). The oscillatory index ϵ is still related to β through (1.20), but now both β and ϵ are functions of the crack speed $v(t)$. The oscillatory index ϵ increases monotonically with crack speed and becomes unbounded at $c_R^{(1)}$ (YANG *et al.*, 1991). Hence it may be expected that oscillatory effects in the near-tip field would become more pronounced and that the size of the contact zone would increase drastically with crack speed, especially as the crack speed approaches $c_R^{(1)}$. However, experimental investigations of LAMBROS (1994) and SINGH (1995) on subsonic crack propagation along polymer/metal interfaces showed that the mode mixity ψ (with respect to a reference length L) also changes substantially with crack speed along with ϵ, resulting in a cumulative effect of keeping the contact zone size rather small for all but the highest sub-Rayleigh ($v(t) < c_R^{(1)}$) crack speeds. The mode mixity ψ for subsonic crack speeds is defined in the same way as in (1.26). XU and NEEDLEMAN (1996); BREITENFELD and GEUBELLE (1998) also observed in their numerical simulations that the crack face contact zone size remains very small for subsonic crack speeds and for most mixities with an opening component. The

traction on the interface ahead of the crack tip ($r > 0$) is given by

$$\sigma_{22}(r,t) + i\frac{\sigma_{12}(r,t)}{\eta} = \frac{K^d(t)}{\sqrt{2\pi r}}\, r^{i\epsilon}\,, \tag{1.34}$$

where η is the traction resolution factor, which depends on the material properties of the bimaterial constituents and the crack speed. η increases smoothly from unity for a quasi-statically growing interfacial crack and becomes unbounded as the crack speed approaches $c_s^{(1)}$. The relative displacement of the crack faces is given by

$$\delta_2 + i\eta\delta_1 = \frac{H_{22}K^d(t)r^{i\epsilon}}{(1+2i\epsilon)\cosh\pi\epsilon}\sqrt{\frac{2r}{\pi}}\,, \tag{1.35}$$

where H_{22} is a function of material properties of the bimaterial constituents and the crack speed (YANG *et al.*, 1991).

The dynamic energy release rate associated with a subsonically propagating bimaterial interface crack is given by

$$G(t) = \frac{F(v)}{4\mu_1}|K^d(t)|^2\,. \tag{1.36}$$

$F(v)$ is termed the energy factor and is a function of the material properties of the bimaterial constituents and the crack speed (YANG *et al.*, 1991). $F(v)$ increases monotonically with crack speed and a reaches a finite maximum value at $c_R^{(1)}$. Hence the dynamic energy release rate associated with a subsonic interfacial crack is finite at $c_R^{(1)}$ even with a nonvanishing stress intensity factor $K^d(t)$. Based on this observation YANG *et al.* (1991) suggested that the speed of a bimaterial interface crack may exceed $c_R^{(1)}$. Sub-Rayleigh crack growth along a bimaterial interface can be sustained, provided a propagation criterion of the form

$$G(t) = \Gamma_{int}(\psi(t), v(t))\,, \tag{1.37}$$

is satisfied at each instant. Based on the experimental observations of subsonic crack

growth along polymer/metal interfaces, LAMBROS and ROSAKIS (1995a) proposed that the interfacial crack profile remains unchanged during sub Rayleigh crack propagation, *i.e.*, the relative crack face displacements δ_1 and δ_2 an arbitrary distance r^* behind the crack tip are independent of the crack speed. Similar experiments by KAVATURU and SHUKLA (1998) led them to conclude that that ratio of δ_1/δ_2 an arbitrary distance r^* behind the crack tip remains constant, however, the individual components increase with crack speed according to a power law, *i.e.*, $(\delta_1, \delta_2) \propto (v/c_s)^n$, where n is a parameter that depends on the material properties of the bimaterial constituents. Both these observations on the relative crack face displacements result in a fracture energy $\Gamma_{int}(\psi, v)$ which decreases with crack speed v as $c_R^{(1)}$ is approached. This is contrary to the behavior of Γ in homogeneous solids where it exhibits a sharp increase with crack speed. This difference may be primarily responsible for the bimaterial interface being able to sustain much higher crack speeds as compared to a homogeneous, monolithic solid. LIU *et al.* (1995) found that for subsonic - super-Rayleigh ($c_R^{(1)} < v < c_s^{(1)}$) crack speeds, the near-tip fields are no longer singular but purely oscillatory. Hence the dynamic energy release rate during this speed regime is identically zero resulting in this speed regime being inadmissible.

1.3.3 Intersonic Interfacial Crack Tip Fields

Analytical investigation of intersonic interfacial crack tip fields was primarily motivated by the experimental observations of intersonic crack speeds along polymer/metal interfaces (LIU *et al.*, 1993; LAMBROS and ROSAKIS, 1995c; SINGH and SHUKLA, 1996). In general, the term intersonic refers to crack speeds lying between $c_s^{(1)}$ and $c_l^{(2)}$. Intersonic crack growth along a bimaterial interface is complicated by the presence of three characteristic wave speeds, $c_l^{(1)}$, $c_R^{(2)}$ and $c_s^{(2)}$ within the intersonic regime. In addition, if the shear wave speeds of the two materials across the interface do not differ markedly, then the interface can sustain Stoneley waves which trap energy along the interface. HUANG *et al.* (1996); YU and YANG (1995) obtained the near-tip fields

for a steady-state intersonic crack propagating along a bimaterial interface. The nature of the crack tip stress singularity for an intersonic interfacial crack is complicated, with the singularity exponents being real, pure imaginary or complex depending on the crack speed. The near-tip stress field has the form

$$\sigma_{\alpha\beta}(r,\theta) = \frac{K_1^{*d}}{\sqrt{2\pi}}\, r^{-p_1} \Sigma_{\alpha\beta}^{1d*}(\theta, v) + \frac{K_2^{*d}}{\sqrt{2\pi}}\, r^{-p_2} \Sigma_{\alpha\beta}^{2d*}(\theta, v)\,, \tag{1.38}$$

when the singularity exponents p_1 and p_2 are real, in which case both K_1^{*d} and K_2^{*d} are also real. In the case of complex stress indices, the near-tip stress field is of the form

$$\sigma_{\alpha\beta}(r,\theta) = \mathrm{Re}\left[\frac{K^{*d}}{\sqrt{2\pi}}\, r^{-p}\right] \Sigma_{\alpha\beta}^{1d*}(\theta, v) + \mathrm{Im}\left[\frac{K^{*d}}{\sqrt{2\pi}}\, r^{-p}\right] \Sigma_{\alpha\beta}^{2d*}(\theta, v)\,, \tag{1.39}$$

where p is the complex stress index and $K^{*d} = K_1^{*d} + iK_2^{*d}$ is the complex stress intensity factor. The angular functions $\Sigma_{\alpha\beta}^{1d*}$ and $\Sigma_{\alpha\beta}^{2d*}$ are given in YU and YANG (1995).

For the case of polymer/metal bimaterial interfaces considered in this work the wave speed mismatch across the interface is substantial in that no Stoneley waves are possible along the interface. Moreover, the wave speeds are in the order $c_s^{(1)} < c_l^{(1)} < c_R^{(2)} < c_s^{(2)} < c_l^{(2)}$. It is found that the stress singularity changes its character twice within the regime $c_s^{(1)} < v < c_l^{(1)}$ (HUANG *et al.*, 1996). In the first interval, the singularity exponents are real, in the second one the singularity exponents are complex (both singular and oscillatory) and in the third one they are again real. For polymer/metal interfaces and in the case of plane stress, it is found that the first interval extends over most of the speed regime $c_s^{(1)} < v < c_l^{(1)}$ with the second and third intervals being extremely short. In such a case, WANG *et al.* (1998) showed that a polymer/metal bimaterial interface may be approximated as a polymer/rigid interface. They showed that the near-tip stress field for an intersonic crack on a polymer/rigid interface closely approximates that near an intersonic crack on a poly-

mer/metal interface. In this study, we deal exclusively with polymer/metal interfaces in generalized plane stress configuration and for the sake of simplicity a polymer/rigid approximation is used. With the new approximation, we redefine the term intersonic to include all crack speeds lying between $c_s^{(1)}$ and $c_l^{(1)}$.

The near-tip stress field around an intersonic crack propagating on an elastic/rigid bimaterial interface has the general form (LIU *et al.*, 1995)

$$\sigma_{\alpha\beta}(r,\theta) = \frac{A_o}{r_l^q} f_{\alpha\beta}(\theta, v) + \frac{g_{\alpha\beta}(v)}{(\eta_1 + \hat{\alpha}_s\eta_2)^q} H(\eta_1 + \hat{\alpha}_s\eta_2) + \frac{h_{\alpha\beta}(v)}{(-\eta_1 - \hat{\alpha}_s\eta_2)^q} H(-\eta_1 - \hat{\alpha}_s\eta_2)\,, \tag{1.40}$$

where A_o is a measure of the near-tip stress intensity, the functions $f_{\alpha\beta}, g_{\alpha\beta}$ and $h_{\alpha\beta}$ are given in LIU *et al.* (1995), and q, the singularity exponent is given by

$$q = \frac{1}{\pi}\tan^{-1}\frac{\alpha_l\hat{\alpha}_s\{4 - (1-\hat{\alpha}_s^2)^2\}}{4\alpha_l^2\hat{\alpha}_s^2 + (1-\hat{\alpha}_s^2)^2}\,. \tag{1.41}$$

q is real and for plane stress deformation, it increases monotonically from 0 at c_s, reaches a maximum below 1/2 and thereafter decreases monotonically back to 0 at c_l. The stress field (1.40) predicts a shear Mach wave radiating from the tip along the line $\eta_1 + \hat{\alpha}_s\eta_2 = 0$. The shear Mach wave is a line of strong stress field discontinuity and the stress components are singular along the line with the same order of singularity q as that at the crack tip. The traction on the interface ahead of the crack tip is given by

$$\begin{pmatrix}\sigma_{22}(r)\\ \sigma_{12}(r)\end{pmatrix} = \frac{\mu A_o}{r^q}\frac{\alpha_l(1+\hat{\alpha}_s^2)}{1+\alpha_l^2\hat{\alpha}_s^2}\begin{pmatrix}\hat{\alpha}_s\\ 1\end{pmatrix}. \tag{1.42}$$

The relative opening displacement of the crack faces behind the tip is given by

$$\delta_2(r) = -\frac{A_o r^{1-q}}{1-q}\frac{(1-\hat{\alpha}_s^2)\alpha_l(1+\hat{\alpha}_s^2)}{4\alpha_l^2\hat{\alpha}_s^2 + (1-\hat{\alpha}_s^2)^2}\cos q\pi\,. \tag{1.43}$$

Note that δ_2 behind the crack tip changes sign at $\sqrt{2}\,c_s$. So, A_o too must change sign at $\sqrt{2}\,c_s$, otherwise crack faces would come into contact. Crack face contact

zones were observed during intersonic crack propagation along polymer/metal bimaterial interfaces (LAMBROS and ROSAKIS, 1995c; SINGH and SHUKLA, 1996). HUANG *et al.* (1998) obtained the near-tip fields for an intersonic crack propagating along an elastic/rigid interface with a finite zone of crack face frictional contact.

YU and YANG (1995); HUANG *et al.* (1996) showed that the real parts of the singularity exponents are always less than 1/2 for all crack speeds between $c_s^{(1)}$ and $c_l^{(2)}$. Hence the dynamic energy release rate for an intersonic crack on a bimaterial interface is identically zero. YU and YANG (1995) showed that energy flows from the stiffer material to the compliant material through the interface, which is then radiated away by the Mach waves without deposition at the tip. Unlike an intersonic mode II crack in a homogeneous solid (GAO *et al.*, 1999), there is no intersonic speed at which an interfacial crack becomes "radiation-free". However, if we incorporate a line cohesive zone of finite size in front of the intersonic interfacial crack tip, then positive energy flux to the tip region should result for some of the intersonic speeds.

1.4 Overview of the Thesis

In Chapter 2, the specimen preparation procedure is described in detail. The working principle governing the two optical techniques for stress analysis used in this experimental investigation — dynamic photoelasticity and coherent gradient sensing are briefly summarized. The experimental setup used for inducing dynamic crack propagation and real time recording of stress field information around the propagating crack tip using high speed photography is also described.

In Chapter 3, experimental records of isochromatic fringe patterns around a dynamically propagating crack along a weak plane joining two plates of Homalite-100 are shown. Under asymmetric impact shear loading, it is demonstrated that cracks on a weak bond line joining two identical homogeneous, isotropic, linear elastic solids can attain intersonic speeds. It is found that a shear crack on the weak plane, immediately after initiation, attains intersonic speeds, subsequently accelerating to speeds

close to c_l. As the loading pulse is cutoff, the intersonic crack decelerates and begins to propagate at a speed close to $\sqrt{2}\,c_s$. Intersonic mode II crack growth is found to be accompanied by shear Mach wave formation as well as a series of short, parallel tensile cracks (secondary cracks) at a large angle to the crack plane. The experimental observations are compared critically against the singular solution for a mode II intersonic crack (FREUND, 1979), motivating the necessity of a cohesive zone model.

In Chapter 4, subsonic and intersonic mode-II crack propagation in a homogeneous, isotropic, linear elastic solid with a rate independent Dugdale type line cohesive zone in front of it is analyzed. Explicit expressions are derived for the near-tip stress and particle velocity fields. It is shown that positive energy flux into the tip region is possible for the entire intersonic regime. A critical crack tip sliding displacement criterion is introduced and its predictions regarding crack tip stability are examined in light of the experimental observations. The influence of the shear strength of the crack plane on the near-tip fields, energy flux and stability of crack growth is investigated. An attempt is made to predict the secondary crack angle, thus motivating the necessity for a more elaborate cohesive constitutive relation. Experimentally recorded isochromatic fringe patterns are compared against those predicted by the theory.

In Chapter 5, subsonic and intersonic mode-II crack propagation in a homogeneous, isotropic, linear elastic solid with a rate dependent line cohesive zone in front of it is analyzed. A cohesive law is assumed, wherein the cohesive shear traction is either a constant or varies linearly with the local sliding rate. Complete decohesion is assumed to occur when the crack tip sliding displacement reaches a material specific critical value. Closed form expressions are obtained for the near-tip fields. Influence of the rate parameter on crack propagation behavior is investigated. The rate parameter is extracted by comparing its prediction of the secondary crack angle with that observed experimentally. It is found that the rate parameter is negative, indicating that the shear strength of the crack plane decreases with local sliding rate. The isochromatic fringe patterns predicted by the analytical solution compare very

well with those recorded during the experiments.

In Chapter 6, experimental observations of intersonic and supersonic crack propagation along bimaterial interfaces are presented. The conditions governing the transition of an interfacial crack from subsonic to intersonic speeds are examined. Asymmetric impact shear loading by a gas gun resulted in intersonic crack propagation along a Homalite/Al or Homalite/steel interface at speeds between c_s and $\sqrt{2}c_s$ of the polymer. Careful observations of the transition of an interface crack from subsonic speeds to intersonic speeds showed the formation of crack face contact at speeds beyond c_R of the polymer. Subsequently, the contact zone is observed to expand in size, shrink and collapse into the intersonic crack tip. The recorded isochromatic fringe patterns showed multiple Mach wave formation associated with such a scenario. It is found that the nature of contact zone formation as well as its size differ substantially depending on the sign of the opening component of loading. Intersonic crack growth along inclined interfaces is also briefly examined. At high impact speeds, dynamic cracks along PMMA/Al and PMMA/steel bimaterial interfaces were observed to accelerate to speeds higher than c_l of PMMA, almost reaching c_R of aluminum. The resulting crack growth was observed to be highly transient and the gradients of in-plane normal stress components were recorded using CGS interferometry.

Motivated by the aforementioned experimental observations, in Chapter 7, a higher order asymptotic analysis was performed to obtain the stress and deformation fields around a steadily propagating intersonic crack along an elastic-rigid interface with a finite zone of crack face frictional sliding contact located a finite distance behind the tip. A linear frictional contact model is adopted, wherein the shear stress is proportional to the normal stress through a constant, the coefficient of dynamic friction. Isochromatic fringe patterns predicted by the near-tip fields exhibit the essential features observed during the experiments. Frictional sliding contact is shown to be possible only for velocities between c_s and $\sqrt{2}c_s$ of the polymer. The relevant analytical parameters were predicted by comparing the model to the experimental

isochromatic fringe patterns. It is argued that frictional contact during intersonic interfacial crack propagation is more severe at a finite distance behind the tip.

Nomenclature

(η_1, η_2)	Cartesian coordinates
(r, θ)	polar coordinates
(r_l, θ_l)	relativistic coordinates
α, β	Dundurs' parameters
$\alpha_l, \alpha_s, \hat{\alpha}_s$	relativistic parameters
δ_α	relative displacement of the crack faces
$\delta_{\alpha\beta}$	Kronecker delta
ϵ	oscillatory index
η	traction resolution factor
Γ	mode I fracture energy
Γ_{int}	fracture energy of the bimaterial interface
Γ_{pl}	fracture energy of the weak plane
κ	material parameter, varies for plane stress and plane strain
$K_{II}^{\star d}$	intersonic mode II stress intensity factor
μ	shear modulus

ν	Poisson's ratio
Ω	inclination of the incipient kink
ψ	mode mixity
ρ	mass density
$\sigma_{\alpha\beta}$	components of the stress tensor
$\Sigma^{I}_{\alpha\beta}, \Sigma^{II}_{\alpha\beta}$	mode I & mode II angular functions for a stationary crack
$\Sigma^{1d}_{\alpha\beta}, \Sigma^{2d}_{\alpha\beta}$	angular functions for a subsonic bimaterial interface crack
$\Sigma^{1}_{\alpha\beta}, \Sigma^{2}_{\alpha\beta}$	angular functions for a static bimaterial interface crack
$\Sigma^{1d*}_{\alpha\beta}, \Sigma^{2d*}_{\alpha\beta}$	angular functions for an intersonic bimaterial interface crack
$\Sigma^{Id}_{\alpha\beta}, \Sigma^{IId}_{\alpha\beta}$	mode I & mode II angular functions for a subsonic crack
a	length of incipient kink
A_{o}	amplitude of the near-tip fields for an intersonic crack on an elastic/rigid interface
A_I, A_{II}	mode I & mode II subsonic energy factors
c_l	longitudinal wave speed
c_R	Rayleigh wave speed
c_s	shear wave speed
E	Young's modulus
E^*	reduced modulus for the bimaterial interface
F	energy factor for a subsonic bimaterial interface crack

G	energy release rate
G^t	energy release rate for the kinked crack
$H(.)$	unit step function
$H_{\alpha\beta}$	functions of bimaterial properties and crack speed
$K = K_1 + iK_2$	complex stress intensity factor for a static bimaterial interface crack
$K^d = K_1^d + iK_2^d$	complex stress intensity factor for a subsonic bimaterial interface crack
$K^{*d}, K_1^{*d}, K_2^{*d}$	stress intensity factors for an intersonic bimaterial interface crack
K_I, K_{II}	mode I & mode II stress intensity factors for a stationary crack
K_I^d, K_{II}^d	mode I & mode II subsonic stress intensity factors
K_I^t, K_{II}^t	mode I & mode II stress intensity factors at the tip of the kinked crack
K_{Ic}, K_{IIc}	mode I & mode II fracture toughnesses
L	reference length
l	crack length
n	bimaterial parameter governing the dependence of crack face displacements on crack speed
P	far-field load
p, p_1, p_2	singularity exponents for an intersonic bimaterial interface crack
q	intersonic crack tip stress singularity
$R(v)$	Rayleigh function

r^*	an arbitrary distance behind the interfacial crack tip
R_q	intersonic parameter (a function of crack speed)
T	T-stress
t	time
t_o	time of crack initiation
u_α	components of the displacement vector
v	crack speed

Bibliography

ACHENBACH, J. D., KEER, L. M., KHETAN, P. R., and CHEN, S. H. (**1979**), Loss of Adhesion at the Tip of an Interface Crack, *Journal of Elasticity*, **9**, pp. 397–424.

ANDREWS, D. J. (**1976**), Rupture Velocity of Plane Strain Shear Cracks, *Journal of Geophysical Research*, **81**(32), pp. 5679–5687.

ARCHULETA, R. J. (**1984**), A Faulting Model for the 1979 Imperial-Valley Earthquake, *Journal of Geophysical Research*, **89**(6), pp. 4559–4585.

ATKINSON, C. (**1977**), Dynamic Crack Problems in Dissimilar Media, in *Mechanics of Fracture - Vol. IV: Elastodynamic Problems*, edited by G. C. Sih, Noordhoff, pp. 213–248.

BARENBLATT, G. I. and CHEREPANOV, G. P. (**1960**), On the Wedging of Brittle Bodies, *Journal of Applied Mathematics and Mechanics*, **23**, pp. 993–1014.

BOUCHON, M., TOKSÖZ, N., KARABULUT, H., BOUIN, M. P., DIETRICH, M., AKTAR, M., and EDIE, M. (**2000**), Seismic Imaging of the 1999 Izmit (Turkey) Rupture Inferred from the Near-Fault Recordings, *Geophysical Research Letters*, **27**(18), pp. 3013–3016.

BREITENFELD, M. S. and GEUBELLE, P. H. (**1998**), Numerical Analysis of Dynamic Debonding under 2-D In-Plane and 3-D Loading, *International Journal of Fracture*, **93**(1-4), pp. 13–38.

BROBERG, K. B. (**1960**), The Propagation of a Brittle Crack, *Arkiv för Fysik*, **18**, pp. 159–192.

BROBERG, K. B. (**1987**), On Crack Paths, *Engineering Fracture Mechanics*, **28**(5-6), pp. 663–679.

BROBERG, K. B. (**1989**), The Near-tip Field at High Crack Velocities, *International Journal of Fracture*, **39**(1-3), pp. 1–13.

BROBERG, K. B. (**1994**), Intersonic Bilateral Slip, *Geophysical Journal International*, **119**(3), pp. 706–714.

BROBERG, K. B. (**1995**), Intersonic Mode II Crack Expansion, *Archives of Mechanics*, **47**, pp. 859–871.

BROBERG, K. B. (**1996**), How Fast Can a Crack Go?, *Materials Science*, **32**(1), pp. 80–86.

BROBERG, K. B. (**1999**), *Cracks and Fracture*, Academic Press, London.

BROCK, L. M. and ACHENBACH, J. D. (**1973**), Extension of an Interface Flaw under the Influence of Transient Waves, *International Journal of Solids and Structures*, **9**, pp. 53–67.

BURRIDGE, R. (**1973**), Admissible Speeds for Plane Strain Shear Cracks With Friction but Lacking Cohesion, *Geophysics Journal of the Royal Astronomical Society*, **35**, pp. 439–455.

BURRIDGE, R., CONN, G., and FREUND, L. B. (**1979**), The Stability of a Rapid Mode II Shear Crack with Finite Cohesive Traction, *Journal of Geophysical Research*, **85**(B5), pp. 2210–2222.

COMNINOU, M. (**1977**a), The Interface Crack, *Journal of Applied Mechanics*, **44**, pp. 631–636.

COMNINOU, M. (**1977**b), Interface Crack With Friction in the Contact Zone, *Journal of Applied Mechanics*, **44**, pp. 780–781.

COMNINOU, M. (**1990**), An Overview of Interface Cracks, *Engineering Fracture Mechanics*, **37**(1), pp. 197–208.

COTTERELL, B. and RICE, J. R. (**1980**), Slightly Curved or Kinked Cracks, *International Journal of Fracture*, **16**, pp. 155–169.

CRAGGS, J. W. (**1960**), On the Propagation of a Crack in an Elastic-Brittle Material, *Journal of the Mechanics and Physics of Solids*, **8**, pp. 66–75.

CURRAN, D. A., SHOCKEY, D. A., and WINKLER, S. (**1970**), Crack Propagation at Supersonic Velocities - II. Theoretical Model, *International Journal of Fracture Mechanics*, **6**(3), pp. 271–278.

DAS, S. and AKI, K. (**1977**), A Numerical Study of Two-Dimensional Spontaneous Rupture Propagation, *Geophysics Journal of the Royal Astronomical Society*, **50**, pp. 643–668.

DELALE, F. and ERDOGAN, F. (**1988**), On the Mechanical Modeling of the Interfacial Region in Bonded Half Planes, *Journal of Applied Mechanics*, **55**, pp. 317–324.

DMOWSKA, R. and RICE, J. R. (**1986**), Fracture Theory and its Seismological Applications, in *Continuum Theories in Solid Earth Physics*, edited by R. Teisseyre, Elsevier, Amsterdam, pp. 187–255.

DUNDURS, J. and GAUTESEN, A. K. (**1988**), An Opportunistic Analysis of the Interface Crack, *International Journal of Fracture*, **36**(2), pp. 151–159.

ELLSWORTH, W. L. and CELEBI, M. (**1999**), Near-Field Displacement Time Histories of the M 7.4 Kocaeli (Izimit), Turkey, Earthquake of August 17, 1999, in *AGU99 Fall Meeting*, San Fransisco, CA.

ENGLAND, A. H. (**1965**), A Crack Between Dissimilar Media, *Journal of Applied Mechanics*, **32**, pp. 400–402.

ERDOGAN, F. (**1965**), Stress Distribution in Bonded Dissimilar Materials with Cracks, *Journal of Applied Mechanics*, **32**, pp. 403–410.

FINEBERG, J. and MARDER, M. (**1999**), Instability in Dynamic Fracture, *Physics Reports*, **313**(1-2), pp. 2–108.

FREUND, L. B. (**1979**), The Mechanics of Dynamic Shear Crack Propagation, *Journal of Geophysical Research*, **84**(B5), pp. 2199–2209.

FREUND, L. B. (**1989**), *Dynamic Fracture Mechanics*, Cambridge University Press, Cambridge.

GAO, H., HUANG, Y., GUMBSCH, P., and ROSAKIS, A. J. (**1999**), On Radiation-Free Transonic Motion of Cracks and Dislocations, *Journal of the Mechanics and Physics of Solids*, **47**(9), pp. 1941–1961.

GAUTESEN, A. K. and DUNDURS, J. (**1988**), The Interface Crack under Combined Loading, *Journal of Applied Mechanics*, **55**(3), pp. 580–586.

GEORGIADIS, H. G. (**1986**), On the Stress Singularity in Steady-State Transonic Shear Crack Propagation, *International Journal of Fracture*, **30**(3), pp. 175–180.

GOLDSHTEIN, R. V. (**1966**), Stationary Motion of a Crack Along a Straight Bond Line Between Two Dissimilar Materials (in Russian), *Mekhanika Tverdogo Tela*, **1**(5), pp. 93–102.

GOLDSHTEIN, R. V. (**1967**), On Surface Waves in Joined Elastic Materials and Their Relation to Crack Propagation Along the Junction, *Applied Mathematics and Mechanics*, **31**(3), pp. 496–502.

He, M. Y., Bartlett, A., Evans, A. G., and Hutchinson, J. W. (**1991**), Kinking of a Crack out of an Interface - Role of Inplane Stress, *Journal of the American Ceramics Society*, **74**(4), pp. 767–771.

He, M. Y. and Hutchinson, J. W. (**1989**), Kinking of a Crack out of an Interface, *Journal of Applied Mechanics*, **56**, pp. 270–278.

Hernandez, B., Cotton, F., and Campillo, M. (**1999**), Contribution of Radar Interferometry to a Two-Step Inversion of the Kinematic Process of the 1992 Landers Earthquake, *Journal of Geophysical Research*, **104**(B6), pp. 13083–13099.

Huang, Y., Liu, C., and Rosakis, A. J. (**1996**), Transonic Crack Growth Along a Bimaterial Interface: An Investigation of the Asymptotic Structure of Near-Tip Fields, *International Journal of Solids and Structures*, **33**(18), pp. 2625–2645.

Huang, Y., Wang, W., Liu, C., and Rosakis, A. J. (**1998**), Intersonic Crack Growth in Bimaterial Interfaces: An Investigation of Crack Face Contact, *Journal of the Mechanics and Physics of Solids*, **46**(11), pp. 2233–2259.

Hutchinson, J. W. (**1989**), Mixed mode fracture mechanics of interfaces, Technical report, Harvard University.

Hutchinson, J. W. and Suo, Z. (**1992**), Mixed-Mode Cracking in Layered Materials, *Advances in Applied Mechanics*, **29**, pp. 63–191.

Johnson, E. (**1990**), On the Initiation of Unidirectional Slip, *Geophysical Journal International*, **101**(1), pp. 125–132.

Johnson, E. (**1992**), Process Region Changes for Rapidly Propagating Cracks, *International Journal of Fracture*, **55**(1), pp. 47–63.

Kanninen, M. F. and O'Donoghue, P. E. (**1995**), Research Challenges Arising from Current and Potential Applications of Dynamic Fracture Mechanics to the

Integrity of Engineering Structures, *International Journal of Solids and Structures*, **32**(17-18), pp. 2423–2445.

KANNINEN, M. F. and POPELAR, C. H. (**1985**), *Advanced Fracture Mechanics*, Oxford University Press, New York.

KAVATURU, M. and SHUKLA, A. (**1998**), Dynamic Fracture Criteria for Crack Growth Along Bimaterial Interfaces, *Journal of Applied Mechanics*, **65**(2), pp. 293–299.

KNOWLES, J. K. and STERNBERG, E. (**1983**), Large Deformations Near a Tip of an Interface-Crack Between 2 Neo-Hookean Sheets, *Journal of Elasticity*, **13**(3), pp. 257–293.

LAMBROS, J. (**1994**), *Dynamic Decohesion of Bimaterial Interfaces*, Ph.D. thesis, California Institute of Technology, Pasadena, CA, USA.

LAMBROS, J. and ROSAKIS, A. J. (**1995**a), Development of a Dynamic Decohesion Criterion for Subsonic Fracture of the Interface Between Two Dissimilar Materials, *Proceedings of the Royal Society of London*, **A451**(1943), pp. 711–736.

LAMBROS, J. and ROSAKIS, A. J. (**1995**b), Dynamic Decohesion of Bimaterials - Experimental Observations and Failure Criteria, *International Journal of Solids and Structures*, **32**(17-18), pp. 2677–2702.

LAMBROS, J. and ROSAKIS, A. J. (**1995**c), Shear Dominated Transonic Interfacial Crack Growth in a Bimaterial. 1. Experimental Observations, *Journal of the Mechanics and Physics of Solids*, **43**(2), pp. 169–188.

LIECHTI, K. M. and CHAI, Y. S. (**1991**), Biaxial Loading Experiments for Determining Interfacial Fracture Toughness, *Journal of Applied Mechanics*, **58**(3), pp. 680–687.

LIU, C., HUANG, Y., and ROSAKIS, A. J. (**1995**), Shear Dominated Transonic Interfacial Crack Growth in a Bimaterial. 2. Asymptotic Fields and Favorable Velocity Regimes, *Journal of the Mechanics and Physics of Solids*, **43**(2), pp. 189–206.

LIU, C., LAMBROS, J., and ROSAKIS, A. J. (**1993**), Highly Transient Elastodynamic Crack Growth in a Bimaterial Interface - Higher Order Asymptotic Analysis and Optical Experiments, *Journal of the Mechanics and Physics of Solids*, **41**(12), pp. 1857–1954.

MALYSHEV, B. M. and SALGANIK, R. L. (**1965**), The Strength of Adhesive Joints Using the Theory of Fracture, *International Journal of Fracture*, **1**, pp. 114–128.

MELIN, S. (**1986**), When Does a Crack Grow Under Mode II Conditions, *International Journal of Fracture*, **30**(2), pp. 103–114.

NEEDLEMAN, A. (**1987**), A Continuum Model for Void Nucleation by Inclusion Debonding, *Journal of Applied Mechanics*, **54**(3), pp. 525–531.

NEEDLEMAN, A. (**1990**a), An Analysis of Decohesion Along an Imperfect Interface, *International Journal of Fracture*, **42**(1), pp. 21–40.

NEEDLEMAN, A. (**1990**b), An Analysis of Tensile Decohesion Along an Interface, *Journal of the Mechanics and Physics of Solids*, **38**(3), pp. 289–324.

NEEDLEMAN, A. and ROSAKIS, A. J. (**1999**), The Effect of Bond Strength and Loading Rate on the Conditions Governing the Attainment of Intersonic Crack Growth Along Interfaces, *Journal of the Mechanics and Physics of Solids*, **47**(12), pp. 2411–2449.

NEMATNASSER, S. and HORII, H. (**1982**), Compression-Induced Nonplanar Crack Extension With Application to Splitting, Exfoliation, And Rockburst, *Journal of Geophysical Research*, **87**(B8), pp. 6805–6821.

OLSEN, K. B., MADARIAGA, R., and ARCHULETA, R. J. (**1997**), Three-Dimensional Dynamic Simulation of the 1992 Landers Earthquake, *Science*, **278**(5339), pp. 834–838.

ORTIZ, M. and BLUME, J. A. (**1990**), Effect of Decohesion and Sliding on Bimaterial Crack-tip Fields, *International Journal of Fracture*, **42**, pp. 117–128.

ORTIZ, M. and PANDOLFI, A. (**1999**), Finite-Deformation Irreversible Cohesive Elements for Three-Dimensional Crack-Propagation Analysis, *International Journal For Numerical Methods In Engineering*, **44**(9), pp. 1267–1282.

RAVICHANDAR, K. and KNAUSS, W. G. (**1984**), An Experimental Investigation into Dynamic Fracture. 2. Microstructural Aspects, *International Journal of Fracture*, **26**(1), pp. 65–80.

RICE, J. R. (**1968**), Mathematical Analysis in the Mechanics of Fracture, in *Fracture - Vol II*, edited by H. Liebowitz, Academic Press, pp. 191–311.

RICE, J. R. (**1988**), Elastic Fracture Mechanics Concepts for Interfacial Cracks, *Journal of Applied Mechanics*, **55**(1), pp. 98–103.

RICE, J. R. and SIH, G. C. (**1965**), Plane Problems of Cracks in Dissimilar Media, *Journal of Applied Mechanics*, **33**, pp. 418–423.

RICE, J. R., SUO, Z., and WANG, J. (**1990**), Mechanics and Thermodynamics of Brittle Interfacial Failure in Bimaterial Systems, in *Metal-Ceramic Interfaces*, edited by M. Ruhle, A. Evans, M. Ashby, and J. Hirth, Acta-Scripta Metallurgica Proceedings, Pergamon, pp. 269–294.

ROSAKIS, A. J., SAMUDRALA, O., and COKER, D. (**1999**), Cracks Faster than the Shear Wave Speed, *Science*, **284**(5418), pp. 1337–1340.

ROSAKIS, A. J., SAMUDRALA, O., and COKER, D. (**2000**), Intersonic Shear Crack Growth Along Weak Planes, *Materials Research Innovations*, **3**(4), pp. 236–243.

SCHOLZ, C. H. (**1990**), *The Mechanics of Earthquakes and Faulting*, Cambridge University Press, Cambridge.

SHIH, C. F. (**1991**), Cracks on Bimaterial Interfaces - Elasticity and Plasticity Aspects, *Materials Science and Engineering*, **A143**(1-2), pp. 77–90.

SINGH, R. P. (**1995**), *Catastrophic Failure of Bimaterial Interfaces*, Ph.D. thesis, University of Rhode-Island, Kingston, RI, USA.

SINGH, R. P. and SHUKLA, A. (**1996**), Subsonic and Intersonic Crack Growth Along a Bimaterial Interface, *Journal of Applied Mechanics*, **63**(4), pp. 919–924.

SYMINGTON, M. F. (**1987**), Eigenvalues for Interface Cracks in Linear Elasticity, *Journal of Applied Mechanics*, **54**(4), pp. 973–974.

TIPPUR, H. V. and ROSAKIS, A. J. (**1991**), Quasi-Static and Dynamic Crack Growth Along Bimaterial Interfaces - A Note on Crack-tip Field Measurements using Coherent Gradient Sensing, *Experimental Mechanics*, **31**(3), pp. 243–251.

WANG, W., HUANG, Y., ROSAKIS, A. J., and LIU, C. (**1998**), Effect of Elastic Mismatch in Intersonic Crack Propagation Along a Bimaterial Interface, *Engineering Fracture Mechanics*, **61**(5-6), pp. 471–485.

WILLIAMS, M. L. (**1959**), The Stresses Around a Fault or Crack in Dissimilar Media, *Bulletin of the Seismological Society of America*, **49**(2), pp. 199–204.

WILLIS, J. R. (**1971**), Fracture Mechanics of Interfacial Cracks, *Journal of the Mechanics and Physics of Solids*, **19**, pp. 353–368.

WILLIS, J. R. (**1973**), Self-Similar Problems in Elastodynamics, *Philosophical Transactions of the Royal Society of London*, **40**(7), pp. 1671–1681.

WINKLER, S., SHOCKEY, D. A., and CURRAN, D. A. (**1970**), Crack Propagation at Supersonic Velocities - I, *International Journal of Fracture Mechanics*, **6**(2), pp. 151–158.

Xu, X. P. and Needleman, A. (**1996**), Numerical Simulations of Dynamic Crack Growth Along an Interface, *International Journal of Fracture*, **74**(4), pp. 289–324.

Yang, W., Suo, Z., and Shih, C. F. (**1991**), Mechanics of Dynamic Debonding, *Proceedings of the Royal Society of London*, **A433**(1889), pp. 679–697.

Yu, H. H. and Yang, W. (**1994**), Mechanics of Transonic Debonding of a Bimaterial Interface - The Antiplane Shear Case, *Journal of the Mechanics and Physics of Solids*, **42**(11), pp. 1789–1802.

Yu, H. H. and Yang, W. (**1995**), Mechanics of Transonic Debonding of a Bimaterial Interface - The Inplane Case, *Journal of the Mechanics and Physics of Solids*, **43**(2), pp. 207–232.

Chapter 2

Experimental Procedures

The primary goal of the experiments is to investigate the nature of supershear dynamic crack propagation along weak planes and bimaterial interfaces. The experimental procedures used for this investigation closely parallel to those adopted by LAMBROS (1994) and SINGH (1995). Polymer/polymer adhesive joints were used to model weak planes (interfaces with no wave speed mismatch) and polymer/metal adhesive joints were chosen to model bimaterial interfaces with strong wave speed mismatch. Dynamic crack growth was induced along the bond line by impacting the specimen with a projectile fired from a high-speed gas gun. To extract stress field information around the propagating crack, two different full-field optical techniques were used — photoelasticity and coherent gradient sensing (CGS) interferometry. The resulting fringe patterns were recorded in real time using high-speed photography. Section 2.1 describes the specimen preparation procedure. The principles governing the extraction of stress field information using the optical techniques mentioned above are discussed briefly in Section 2.2. Finally, the setup and the experimental procedure are detailed in Section 2.3.

2.1 Specimen Preparation

The specimens for investigating dynamic crack growth along a weak plane were made by bonding two identical plates of polymer, either Homalite-100[1] or polymethylmethacrylate[2] (PMMA) (see Figure 2.1(**A**)). Each plate was 6″ long, 5″ wide and either 3/16″, 1/4″ or 3/8″ thick. The specimens for investigating dynamic crack growth along a dissimilar material interface were made by bonding two plates of identical dimensions, one of polymer, either Homalite or PMMA, and the other of metal, either 6061-T6 Aluminum Alloy[3] or SAE-AISI 4340 Steel[4] (see Figure 2.1(**B**)). Each half of the bimaterial specimens was 6″ long, 5″ wide and either 1/4″ or 3/8″ thick.

2.1.1 Material Properties

The polymers were chosen for their suitability to apply particular optical techniques for stress analysis. Homalite when stressed becomes optically birefringent, which permits the use of photoelasticity for stress analysis. PMMA is optically isotropic and transparent. CGS interferometry in transmission configuration is used for extracting stress field information in PMMA. Both Homalite and PMMA are brittle and exhibit a linear elastic behavior at room temperature and at the rates of loading experienced in the experiments. Metals were chosen to be the second halves of the bimaterial, since they provide a strong wave speed and stiffness mismatch across the interface, mimicking the scenario encountered in composites. The mechanical and optical properties of relevance for the specimen materials are given in Table 2.1.

[1] Commercial name for a thermosetting polyester made by Homalite Division, Brandywine Investment Group, Brookside Drive, Wilmington, Delaware, USA. It is commonly used as a display filter for CRTs and LCDs.

[2] Cast PMMA sheets were obtained from Polycast Corporation, Stamford, Connecticut, USA. PMMA is thermoplastic and the commercial version undergoes glass transition around 125° C.

[3] 6061-T6 is a designation following the Aluminum Association System, given to a solution heat treated and artificially aged aluminum alloy of the following composition: Si=0.4-0.8%, Fe=0.7%, Cu=0.15-0.4%, Mn=0.15%, Mg=0.8-1.2%, Cr=0.04-0.35%, Zn=0.25%, Ti=0.15% and rest Al.

[4] 4340 is the designation given by American Iron and Steel Institute to annealed plain carbon steel of the following composition: C=0.36-0.44%, Mn=0.6-0.9%, P=0.04%, S=0.05% and rest Fe.

Property	PMMA		Homalite-100		6061 Aluminum	4340 Steel
	Static	Dynamic	Static	Dynamic		
Young's modulus, E (GPa)	3.2	5.9	3.9	5.2	74.2	213.1
Shear modulus, μ (GPa)	1.2	2.2	1.4	1.9	27.8	82.9
Poisson's ratio, ν	0.35	0.33	0.35	0.34	0.34	0.29
Density, ρ (Kg/m^3)	1190		1230		2710	7830
Shear wave speed, c_s (m/s)	998	1363	1084	1255	3200	3254
Longitudinal wave speed (plane strain), $c_l^{pl-\epsilon}$ (m/s)	2078	2715	2256	2558	6445	5935
Longitudinal wave speed (plane stress), $c_l^{pl-\sigma}$ (m/s)	1751	2358	1901	2187	5555	5443
Rayleigh wave speed (plane strain), $c_R^{pl-\epsilon}$ (m/s)	933	1271	1014	1172	2986	3010
Rayleigh wave speed (plane stress), $c_R^{pl-\sigma}$ (m/s)	919	1253	998	1155	2943	2977
Mode-I fracture toughness, K_{Ic} (MPa$\sqrt{\text{m}}$)	1.4[5]	–	0.6[6]	–	29[7]	47[7]
Tensile strength, σ_o (MPa)	55[8]	–	35[8]	–	310[7]	1200[9]
Shear strength, τ_o (MPa)	–	–	42	–	207[7]	–
Stress-optic coefficient, c_σ (m^2/N)	-1.08 x 10^{-10}		-0.92 x 10^{-10}		–	–
Material fringe constant, F_σ (KN/m) 514.5nm	-123		22.6		–	–

Table 2.1: Material property chart.

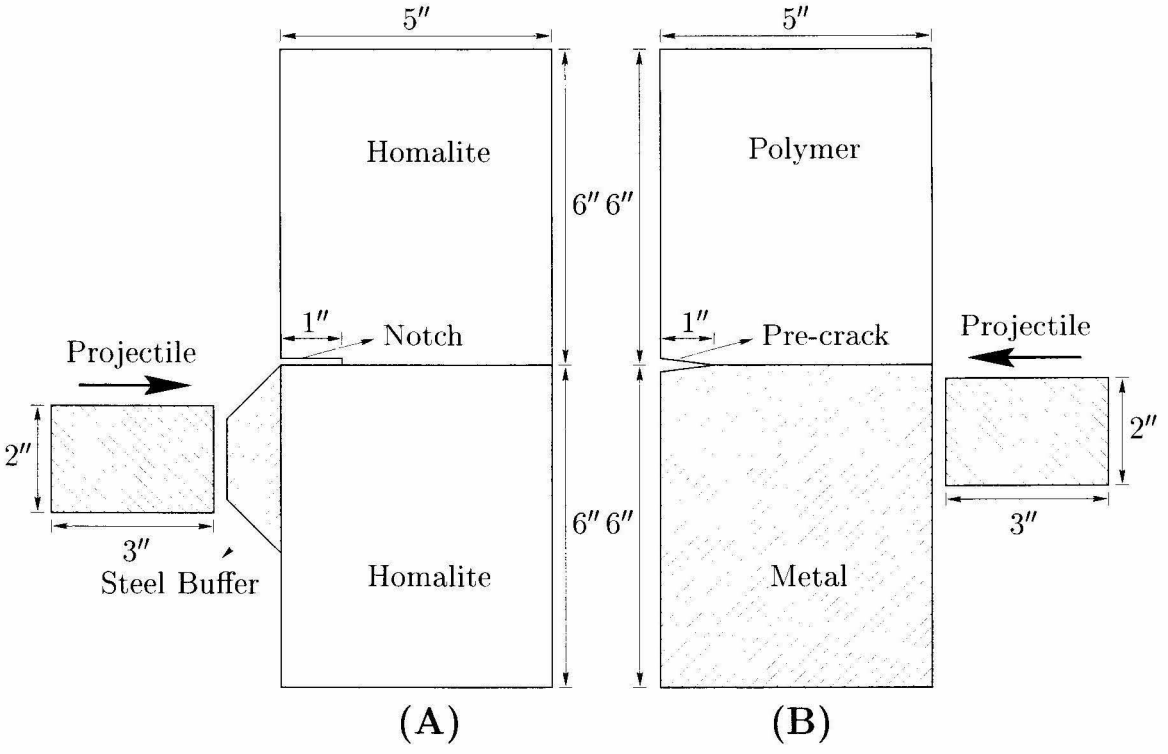

Figure 2.1: Specimen configuration. (A) Homalite/Homalite specimen, (B) Polymer/metal bimaterial specimen.

Both the polymeric materials, Homalite and PMMA exhibit rate sensitivity with regard to their elastic wave speeds & elastic moduli. The static values given in Table 2.1 correspond to a strain rate of the order 10^{-3} s^{-1}, where as the dynamic values correspond to a strain rate of the order 10^{3} s^{-1} (SINGH *et al.*, 1997). In general, the material surrounding a propagating crack experiences a wide spectrum of strain rates and in the tip vicinity the strain rates experienced by the material particles usually fall in the dynamic range. Hence for the material in the vicinity of a propagating crack tip, the dynamic values of the material properties are more relevant. The static values of E and ν for the polymers shown in Table 2.1 were taken from SINGH *et al.* (1997) and the rest of the elastic properties were calculated

[5]From TIPPUR and ROSAKIS (1991)
[6]From KOBAYASHI and MALL (1978)
[7]From ASM Handbook
[8]Average of the measured values
[9]Varies with the heat treatment

using the standard relations for a isotropic linear elastic solid. The dynamic values of the elastic wave speeds, $c_l^{pl-\epsilon}$ and c_s were measured by a pulse-echo technique using a 10 MHz transducer on an ultrasonic analyzer. The dynamic moduli and other elastic properties are calculated from these measured values. Both the metals, 6061 Aluminum and 4340 Steel do not exhibit any appreciable strain rate sensitivity. The material properties for aluminum are taken from ASM handbook and those of steel were obtained from the manufacturer.

The specimen thickness is small compared to its in-plane dimensions and it was subjected to in-plane loading. Hence generalized plane stress conditions are expected to prevail through out the specimen except for regions close to the crack tip and at distances close to the interface (in case of bimaterials). Experimental and numerical investigations have been performed, to obtain the regions of validity of the generalized plane stress assumption, around a stationary single edge crack in a homogeneous three point bend specimen subjected to dynamic loading (ROSAKIS and RAVICHANDAR, 1986; ROSAKIS, 1993; KRISHNASWAMY *et al.*, 1991) and around a stationary single edge crack along the interface in a three point bend bimaterial specimen subjected to dynamic loading (LEE and ROSAKIS, 1993). However, no detailed investigations of the three dimensional effects near a dynamically propagating crack tip in the specimens of the type mentioned above are available.

2.1.2 Bonding Procedure and Interface Characteristics

The polymer/polymer and polymer/metal adhesive joints were made by following essentially the same procedure. The polymer halves were cut from plate stock of appropriate thickness and are machined to size. The bonding surface on the polymer halves was roughened by mechanical abrasion with 220 grit sand paper. For Homalite/Homalite specimens, a rectangular notch 1″ long and 2.3 mm wide was machined on the upper half starting from the left along the bonding surface (see Figure 2.1(**A**)). For bimaterial specimens, the metal halves were blanchard ground to

the desired thickness and the bonding surfaces were surface ground to obtain a flat profile. The bonding surface on the metal halves was roughened uniformly by bead blasting with glass beads of 10-20 μm diameter. The specimen halves were cleaned thoroughly using isopropyl alcohol (for polymers) and acetone (for metals) prior to bonding.

The bonding agents were chosen carefully so that the constitutive properties of the bond are close to those of the polymer, thus avoiding the introduction of a new material. For PMMA/metal bimaterial specimens, methylmethacrylate monomer was chosen to be the adhesive with the appropriate catalyst for polymerization. For Homalite/Homalite and Homalite/metal specimens, unplasticized polyester resin was chosen as the adhesive with the appropriate hardener and accelerator. The composition of the bonding agents is shown in Table 2.2. The bonding agent was prepared by mixing the constituents in appropriate ratio by weight. It is applied uniformly to the two surfaces, which are then aligned and held under pressure in a specially designed fixture. After about 48 hrs at room temperature the curing of the bond is complete. The thickness of the bond obtained using the above procedure was about 100 μm and about 20-30 μm for the methylmethacrylate adhesive and polyester resin adhesive respectively. The bimaterial specimens have either a precut edge notch or a sharp edge precrack, 1″ long along the interface. To introduce a precrack, a thin teflon tape or machine grease was used to prevent bonding over a 1″ region starting from one end. In some of the bimaterial specimens, a blunt notch, 1″ long was machined using a band saw, starting from one end. Adequate care was taken to ensure that the notch is centered along the interface. The notch width was dictated by the width of the band saw, which was approximately 750 μm. For Homalite/Homalite specimens a mild steel plate of the same thickness as the specimen was bonded to the lower half at the impact site (see Figure 2.1(**A**)). This was done to prevent shattering of the specimen immediately after impact and to obtain a planar loading wave front.

Tippur and Rosakis (1991), Lambros (1994) and Singh (1995) performed cal-

PMMA/metal & PMMA/PMMA	Homalite/Homalite & Homalite/metal
Base - 88.5% by wt Methylmethacrylate monomer Traces of titanium dioxide (dye) Traces of acrylic synthetic resin **Catalyst** - 11.5% by wt Traces of benzoylperoxide (catalyst) Methylethylketone (solvent)	**Base** - 99.1% by wt Polyester resin **Hardener** - 0.86% by wt Methylethylketoneperoxide **Accelerator** - 0.04% by wt Cobaltoctate

Table 2.2: Composition of bonding agents.

ibration tests for bonds obtained using the above procedure. TIPPUR and ROSAKIS (1991) bonded two halves of PMMA using the methylmethacrylate monomer adhesive and following the same procedure as described above. A pre-crack was introduced along the bond and its initiation fracture toughness under mode I conditions was measured by a static three point bend test. They found that the fracture toughness of bonded PMMA specimens was over 95% of that of homogeneous PMMA. LAMBROS (1994) performed static three point bend tests on PMMA/steel edge cracked bimaterial specimens and found that under predominantly mode I conditions, the initiation toughness is still over 95% that of homogeneous PMMA. SINGH (1995) measured the tensile strength of a Homalite/Homalite tension specimen bonded using the polyester resin adhesive and found that the tensile strength of the bond was about 75% of that of Homalite.

The above calibration tests bear testimony to the strength of the bond. Additional tests were also performed to obtain the tensile strength and shear strength of PMMA/PMMA and Homalite/Homalite adhesive bonds. It was found that the strength of the bond can vary substantially depending on the relative proportions of the adhesive constituents, surface roughness, curing time and rate of loading. The shear strength of a Homalite/Homalite adhesive bond was measured using the standard Iosipescu shear test fixture and was found to be about 14 MPa (about 0.4 times

that of Homalite). The tensile strength of PMMA/PMMA bonds was found to be as low as 21 MPa. These tests show that irrespective of the bonding procedure followed, the bond line is always weaker than the monolithic material itself and hence always forms a preferred path for crack propagation. Also the tensile and shear strengths of the bonds under quasi-static loading rates may vary significantly from those at the dynamic loading rates experienced by the bond during dynamic crack propagation. In this context it might be more fruitful to investigate the tensile and shear strengths of the bond at strain rates of the order $10^3\,s^{-1}$ using a tensile Hopkinson bar and torsional Hopkinson bar, respectively. However such a line of investigation was not pursued here.

2.2 Optical Techniques

Two different optical techniques were used to record, in real time, the stress field information around a propagating crack. For Homalite/Homalite specimens and Homalite/metal specimens, dynamic photoelasticity was used, whereas for PMMA/metal bimaterial specimens, CGS interferometry was used. Both these techniques are complimentary, in the sense that the information about the stress field provided by these techniques is different. Whereas photoelasticity provides information about the local maximum in-plane shear stress, CGS interferometry provides information about the gradient (in the shearing direction) of the sum of in-plane normal stresses at the point. The working principle behind each technique is explained briefly. The theory of photoelasticity is thoroughly explored in DALLY and RILEY (1991) and CGS interferometry is explained in detail by ROSAKIS (1993).

2.2.1 Photoelasticity

Photoelasticity is a very commonly employed technique for experimental stress analysis. It makes use of the property of temporary double refraction (temporary birefringence) exhibited by many transparent noncrystalline materials. Most polymers

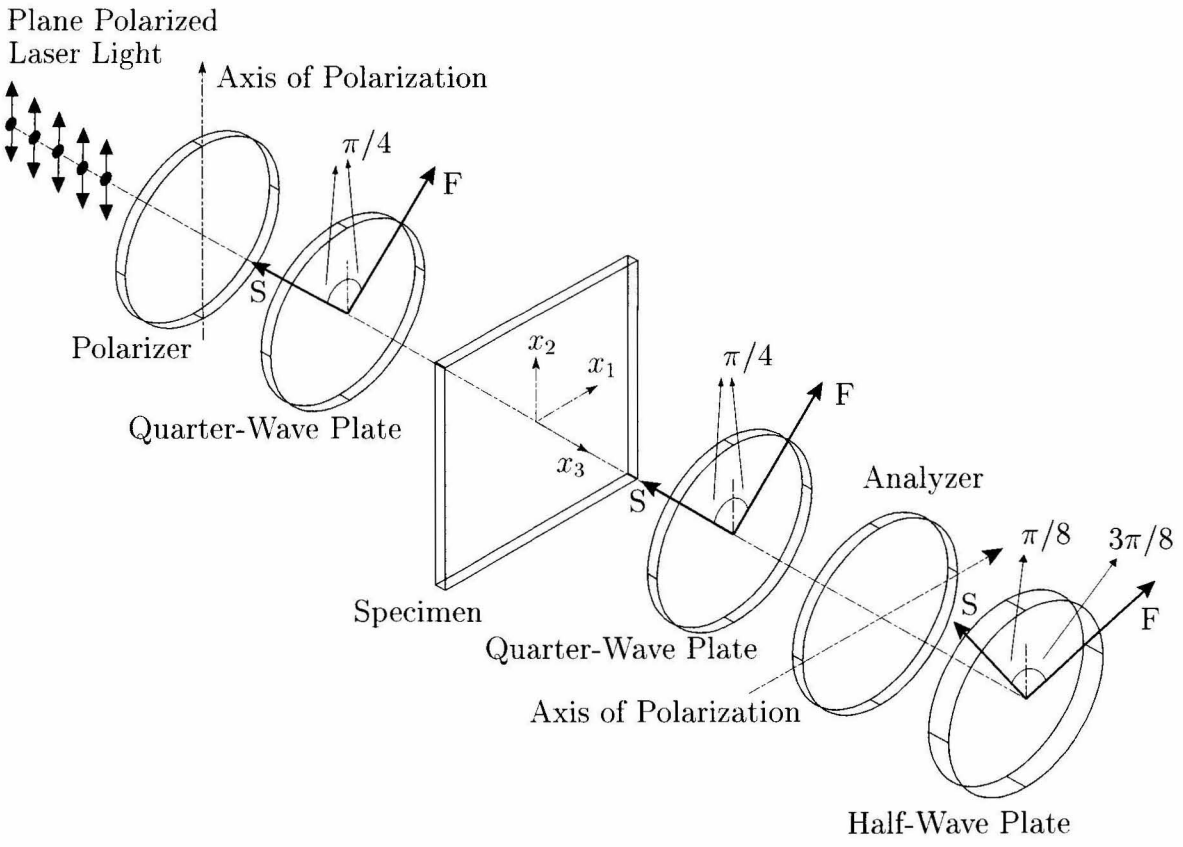

Figure 2.2: Working principle of a light field circular polariscope.

like Homalite belong to this class, which are transparent and optically isotropic under stress free conditions, however become optically anisotropic[10] when stressed. Viewing a stressed specimen made of such a material through a polariscope would result in a fringe pattern from which useful stress field information can be extracted. For our experiments, Homalite-based specimens were placed inside a circular polariscope and when loaded by projectile impact result in an isochromatic fringe pattern which is recorded in real time by a high-speed camera. The various elements constituting the circular polariscope used in our laboratory are shown in Figure 2.2.

The optical cavity of a laser emits an intense beam of plane polarized light. The laser used in our experiments emits a 100:1 vertically polarized laser beam which is

[10]refractive index varies with direction

collimated to 50 mm diameter and then transmitted through a polarizer, a quarter-wave plate, the specimen, another quarter-wave plate, analyzer, a half-wave plate and then through the camera optics on to the film track. A simple analysis is provided of the principle governing the interpretation of the recorded isochromatic fringe order at a point in terms of the local stress state. The reader is referred to DALLY and RILEY (1991) for further details. We will consider a single light ray as it travels through the optical elements and the specimen on to the film track. The first optical element is a polarizer[11] oriented with its axis of polarization in the vertical direction (x_2-axis). The magnitude of the electric field vector associated with a light ray emerging out of the polarizer may be expressed as

$$E_p = a \cos \omega t \,, \tag{2.1}$$

where a is the amplitude and ω is its angular frequency. As the light ray enters a quarter wave plate[12] the electric field vector is resolved into two components, one along its fast axis and another along its slow axis which are oriented at 45° on either side of the vertical. The magnitude of the two components are given by

$$E_f = \frac{a}{\sqrt{2}} \cos \omega t \,, \tag{2.2a}$$

$$E_s = \frac{a}{\sqrt{2}} \cos \omega t \,. \tag{2.2b}$$

On emerging from the quarter-wave plate the component along the slow axis suffers a relative phase lag of $\pi/2$. The components of the electric field vector as the light

[11] A polarizer is commonly used to produce plane polarized light. When using a laser beam as the light source it can be done away with. However, in our experiments we used circular polarizers which are laminated polarizer/quarter-wave plate combinations.

[12] A wave plate is made of a doubly refracting (birefringent) material. Plane polarized light incident on a quarter-wave plate is resolved into two components, one along its fast axis and the other along its slow axis and these components are transmitted through the plate at different velocities resulting in a relative retardation of quarter-wave length at emergence.

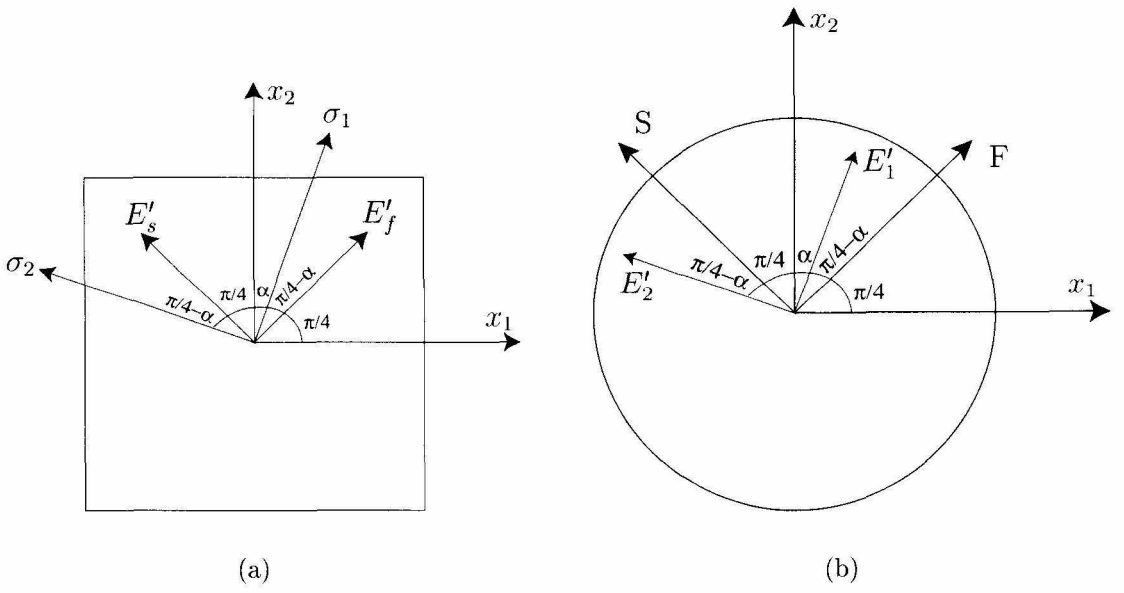

Figure 2.3: Resolution of the electric field vector. (a) Light ray entering the stressed specimen. (b) Light ray entering the second quarter-wave plate.

ray emerges out of the quarter-wave plate are given by

$$E'_f = \frac{a}{\sqrt{2}} \cos \omega t \,, \tag{2.3a}$$

$$E'_s = \frac{a}{\sqrt{2}} \cos(\omega t - \frac{\pi}{2}) = \frac{a}{\sqrt{2}} \sin \omega t \,. \tag{2.3b}$$

Thus the emerging light beam is circularly polarized[13]. The stressed specimen acts as a temporary wave plate with its fast axis oriented at an angle (say α) to the vertical (see Figure 2.3). The electric field vector on entering the specimen gets resolved into two components, the magnitudes of which are given by

$$E_1 = E'_f \cos(\frac{\pi}{4} - \alpha) + E'_s \sin(\frac{\pi}{4} - \alpha) \; = \frac{a}{\sqrt{2}} \cos(\omega t + \alpha - \frac{\pi}{4}) \,, \tag{2.4a}$$

$$E_2 = E'_s \cos(\frac{\pi}{4} - \alpha) - E'_f \sin(\frac{\pi}{4} - \alpha) \; = \frac{a}{\sqrt{2}} \sin(\omega t + \alpha - \frac{\pi}{4}) \,. \tag{2.4b}$$

[13]A light wave is said to be circularly polarized if the tip of its electric field vector traces out a circular path on a plane perpendicular to the direction of propagation.

The slower component acquires a relative retardation (phase lag) of an amount Δ during passage through the specimen. The magnitudes of the components of electric field vector upon emerging from the specimen may be expressed as

$$E_1' = \frac{a}{\sqrt{2}} \cos(\omega t + \alpha - \frac{\pi}{4}) , \tag{2.5a}$$

$$E_2' = \frac{a}{\sqrt{2}} \sin(\omega t + \alpha - \frac{\pi}{4} - \Delta) . \tag{2.5b}$$

Following the same procedure we can obtain the two components of the electric field vector after emergence from the second quarter-wave plate.

$$E_f' = \frac{a}{\sqrt{2}} \left\{ \cos(\omega t + \alpha - \frac{\pi}{4}) \cos(\frac{\pi}{4} - \alpha) - \sin(\omega t + \alpha - \frac{\pi}{4} - \Delta) \sin(\frac{\pi}{4} - \alpha) \right\} , \tag{2.6a}$$

$$E_s' = \frac{a}{\sqrt{2}} \left\{ \sin(\omega t + \alpha - \frac{\pi}{4}) \sin(\frac{\pi}{4} - \alpha) - \cos(\omega t + \alpha - \frac{\pi}{4} - \Delta) \cos(\frac{\pi}{4} - \alpha) \right\} . \tag{2.6b}$$

As the light ray emerges through the analyzer, the vertical components of E_f' and E_s' are absorbed while the horizontal components are transmitted. The magnitude of the electric field vector as it emerges through the analyzer is given by

$$E_a = \frac{1}{\sqrt{2}} (E_f' - E_s') = a \cos\frac{\Delta}{2} \cos(\omega t - \frac{\Delta}{2}) . \tag{2.7}$$

Finally, the light ray passes through a half-wave plate oriented with its fast axis at 67.5° to the vertical. In typical circular polariscope setups, a half-wave plate is not required. It is used here because of the special requirement imposed by the high-speed camera used in our experiments (Cordin model 330A). It requires that any incoming plane polarized light beam have its axis of polarization inclined at 45° to the vertical. One of the optics inside the high-speed camera is a polarizing beam splitter, which is used to split the incoming light beam into two parts one for each half of the film track. When unpolarized light is passed through a polarizing beam splitter, it is

separated into two polarized beams (with their axes of polarization perpendicular to each other) which emerge from the beam splitter in directions which are 90° apart with an accurate 1:1 split in the irradiance of the incident beam. However, when the incident beam itself is plane polarized, its axis of polarization must be oriented at an appropriate angle (which in our case is 45° to the vertical) so that the emerging beams have the same intensity and the film on both the film tracks is exposed uniformly. A half-wave plate[14] is used to rotate the axis of polarization of the light ray emerging from the analyzer from the horizontal direction to a direction at 45° to the vertical. The magnitudes of the two components of the electric field vector along the fast and slow axes of the half-wave plate on emergence are given by

$$E'_f = a\cos\frac{\Delta}{2}\cos(\omega t - \frac{\Delta}{2})\cos\frac{\pi}{8}\,, \tag{2.8a}$$

$$E'_s = -a\cos\frac{\Delta}{2}\cos(\omega t - \frac{\Delta}{2} - \pi)\sin\frac{\pi}{8} = a\cos\frac{\Delta}{2}\cos(\omega t - \frac{\Delta}{2})\sin\frac{\pi}{8}\,. \tag{2.8b}$$

Thus the light ray emerging out of the half-wave plate is plane polarized with its axis of polarization oriented at 45° to the vertical. The intensity of the light ray as it emerges out of the half-wave plate is proportional to the square of its amplitude, *i.e.*,

$$I \propto a^2\cos^2\frac{\Delta}{2}\,. \tag{2.9}$$

In an unstressed specimen ($\Delta = 0$) the image plane would be bright and hence this arrangement of the polariscope is called a light-field arrangement. (2.9) shows that extinction ($I = 0$) would occur when

$$\frac{\Delta}{2} = \left(n + \frac{1}{2}\right)\pi \quad \text{for } n = 0, 1, 2, 3, \ldots \tag{2.10}$$

The relative retardation in terms of cycles of retardation is termed as the isochromatic

[14]The two components of the electric field vector along the fast and slow axes of a half-wave plate suffer a relative retardation of one half the wave length on emergence. When the incident light ray is plane polarized, a half-wave plate merely rotates the axis of polarization of the incident beam.

fringe order N.

$$N = \frac{\Delta}{2\pi} = n + \frac{1}{2}\,. \tag{2.11}$$

Thus the bright back ground is associated with a fringe order 0, the first dark fringe is associated with a fringe order 1/2, the second dark fringe with a fringe order 3/2 and so on.

The stress-optic law can be used to relate the relative retardation (Δ) through a stressed specimen to the local stress state.

$$\Delta = \frac{2\pi hc}{\lambda}(\sigma_1 - \sigma_2)\,, \tag{2.12}$$

where, h is the specimen thickness, c is the relative stress-optic coefficient of the material and λ is the wave length of incident light. Combining (2.11) and (2.12) we have a relation between the fringe order at a point and the local in-plane principal stress components,

$$\sigma_1 - \sigma_2 = \frac{F_\sigma}{h} N\,, \tag{2.13}$$

where, $F_\sigma = \lambda/c$ is the material fringe constant associated with the wave length λ. Since $(\sigma_1 - \sigma_2) = 2\,\tau_{max}$, the isochromatic fringe order at a point is proportional to the local maximum in-plane shear stress.

The stress-optic law and consequently the material fringe constant F_σ, usually vary with the local strain rate. Modest increases in F_σ occur ($\approx 20\%$), as the loading times are decreased from static values of 10^3 s to dynamic values of 10^{-4} s (DALLY, 1978). As mentioned before, during dynamic crack propagation, the material surrounding the tip goes through a wide spectrum of strain rates, and hence presumably, the material fringe constant too, must vary from point to point. DALLY (1978) found no appreciable difference in the interpretation of stress waves generated due to explosive loading in an epoxy resin irrespective of whether static or dynamic value of the material fringe constant was used for the analysis. Because of this uncertainty and also

because we are more interested in the nature of the phenomenon observed rather than the absolute values of the field quantities, no effort is made to determine a suitable dynamic value of the fringe constant, and instead the static value was used for the interpretation of the experimentally recorded fringe patterns.

One major limitation of photoelasticity is its requirement that the specimens should exhibit the property of temporary birefringence. PMMA, for all practical purposes can be considered to be optically isotropic. Hence, an optical technique based on interference of light, lateral shearing CGS interferometer, is used for stress analysis in PMMA. The principle governing CGS interferometry is explained briefly in the next section.

2.2.2 CGS Interferometry

TIPPUR and ROSAKIS (1991) first proposed the method of Coherent Gradient Sensing (CGS) as a full-field optical technique for experimental stress analysis. ROSAKIS (1993) provided a thorough analysis of the technique and its application to fracture experiments. The method can be applied both in transmission (for transparent materials) and reflection (for opaque materials). We are interested in acquiring stress field information in transparent PMMA and hence CGS interferometry in transmission configuration is employed. A coherent, monochromatic, collimated laser beam is transmitted through the dynamically deforming specimen. After transmission through the transparent specimen, it acquires an optical path difference due to the stress induced changes in refractive index and also due to thickness changes resulting from lateral contraction/expansion (Poisson's effect). After emerging from the specimen, the laser beam loses collimation, which is then transmitted through a pair of line diffraction gratings placed a finite distance apart. The gratings perform a shearing of the incident wave front. The gratings' output intensity is transmitted through a filtering lens, which produces a diffraction spot pattern on its back focal plane. On this plane, all but one diffraction orders are blocked. The one remaining

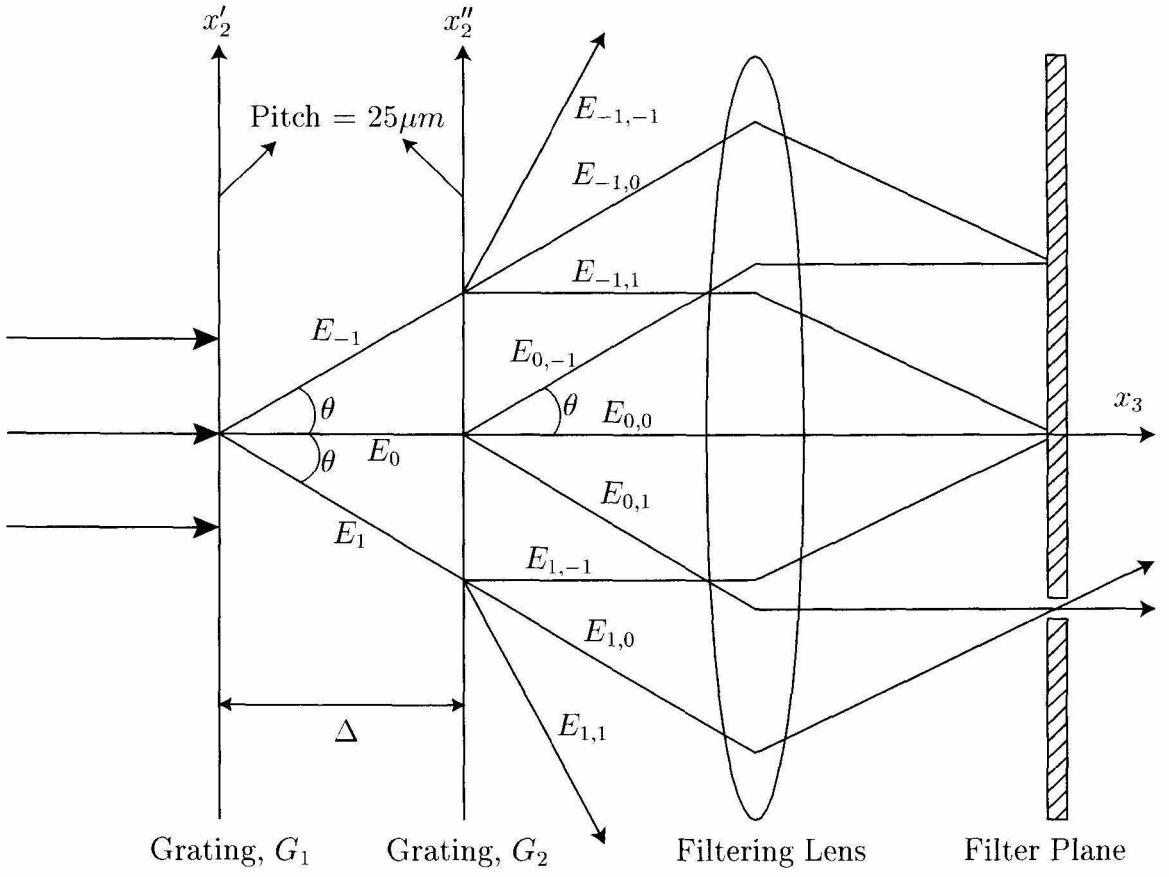

Figure 2.4: Working principle of a lateral shearing CGS interferometer.

diffraction spot (either of ± 1 orders) is imaged to produce an interference pattern. The interference fringe order at a point on the image plane can be related to the local stress state in the specimen through the stress-optic law.

The working principle of the CGS interferometer is illustrated in Figure 2.4. A simple shearing analysis usually performed for lateral shearing interferometers, will be presented here and the reader is referred to ROSAKIS (1993) for a more detailed exposition. Without loss of generality, the line gratings are assumed to have a sinusoidal transmittance. A plane wave propagating along the optical axis is transmitted through the grating G_1. We consider three diffracted wave fronts E_0, E_1, and E_{-1} emerging from G_1 as shown in Figure 2.4. The angle between the propagation direc-

tions of E_0 and $E_{\pm 1}$ is given by the diffraction equation,

$$\theta = \sin^{-1}\left(\frac{\lambda}{p}\right) \approx \frac{\lambda}{p}, \tag{2.14}$$

where λ is the wavelength of light and p is the grating pitch. For $\lambda = 514.5$ nm and $p = 25\,\mu$m, the diffraction angle is about 1.2°. The second grating G_2 will diffract each wave front emerging from G_1, and we consider three additional wavefronts associated with each incident wave front (see Figure 2.4). Each of the nine wave fronts emerging from the second grating is traveling in distinctly different directions, some of which are parallel. Wavefronts having parallel directions of propagation are combined and then brought to focus on the back focal plane of the filtering lens, forming a series of diffraction spots. A spatial filter (iris diaphragm) located in this plane blocks all diffraction orders except either +1 or -1, which is allowed through to the image plane. In Figure 2.4 only the -1 order has been allowed through.

Now consider a distorted wave front (distorted from being planar) emerging from the deforming specimen. Mathematically, this is manifested as a phase (or optical path) change $S(x_1, x_2)$ that is dependent on the local stress and deformation state in the specimen. Light rays transmitted through regions of the specimen where the deformations are small, remain nearly parallel to the optical axis after emergence. When a large portion of such a bundle of light rays nearly parallel to the optical axis, are passed through the CGS interferometer, the diffraction spots on the filtering plane will be surrounded by a small halo of light. If, as is shown in Figure 2.4, we allow the -1 spot through, then an interference pattern caused by the superposition of the two wavefronts traveling along the parallel directions $E_{0,1}$ and $E_{1,0}$ will be visible on the image plane. Thus the resulting image consists of a superposition of the original wavefront with itself, after being sheared (displaced) by an amount approximately equal to d. This shearing distance d is given by

$$d = \Delta \tan\theta \approx \Delta\theta \tag{2.15}$$

for small θ. In our experiments, the grating separation distance employed was usually between 20 and 30 mm. Hence with a diffraction angle $\theta = 1.2°$, the shearing distance was $\approx 0.4 - 0.6$ mm.

The condition for constructive interference of $E_{0,1}$ and $E_{1,0}$ on the image plane of the camera is

$$S(x_1, x_2 + d) - S(x_1, x_2) = m\lambda\,, \tag{2.16}$$

where $m = 0, \pm 1, \pm 2, \ldots$. By dividing both sides of (2.16) with d and substituting for d and θ from (2.15) and (2.14) respectively, we obtain

$$\frac{S(x_1, x_2 + d) - S(x_1, x_2)}{d} = \frac{mp}{\Delta}\,. \tag{2.17}$$

If now we let $d \to 0$, which essentially means moving the two diffraction gratings closer together (*i.e.*, $\Delta \to 0$) or increasing the grating pitch (*i.e.*, $p \to \infty$), then the condition for interference on the image plane becomes

$$\frac{\partial(S(x_1, x_2))}{\partial x_2} = \frac{mp}{\Delta}, \quad m = 0, \pm 1, \pm 2, \ldots\,. \tag{2.18}$$

For solid mechanics applications, it is desirable to relate the quantity $S(x_1, x_2)$ to the stress state in the deforming specimen. Consider a planar wavefront normally incident on an optically and mechanically isotropic, transparent plate of initial uniform thickness h and refractive index n. In our case, this would be the test specimen whose center plane lies in the (x_1, x_2) plane. When it undergoes any kind of deformation (static or dynamic), the transmitted wavefront may be expressed as $x_3 + S(x_1, x_2) = \text{const}$, where $S(x_1, x_2)$ is the optical path change acquired during transmission through the stressed specimen. As discussed in detail by ROSAKIS (1993), $S(x_1, x_2)$ is related to the deformation state in the specimen by the relation,

$$S(x_1, x_2) = 2h(n-1)\int_0^{\frac{1}{2}} \epsilon_{33}\, d(x_3/h) + 2h\int_0^{\frac{1}{2}} \delta n\, d(x_3/h)\,. \tag{2.19}$$

The first term of (2.19) represents the net optical path difference due to the plate thickness change caused by the strain component ϵ_{33}. The second term is due to the stress induced change of refractive index of the material. This change in the refractive index δn is given by the stress-optic law,

$$\delta n = D_1(\sigma_{11} + \sigma_{22} + \sigma_{33})\,, \tag{2.20}$$

where D_1 is a stress-optic coefficient and σ_{ij} are Cartesian components of the stress tensor. For isotropic, linear elastic solids, the strain component ϵ_{33} can also be related to the stress and thus

$$S(x_1, x_2) = 2hc_\sigma \int_0^{\frac{1}{2}} \left\{ (\sigma_{11} + \sigma_{22}) \left[1 - D_2 \left(\frac{\sigma_{33}}{\nu(\sigma_{11} + \sigma_{22})} \right) \right] \right\} d(x_3/h)\,, \tag{2.21}$$

where

$$c_\sigma = \left[D_1 - \frac{\nu}{E}(n-1) \right], \quad D_2 = - \left[\frac{\nu D_1 + \dfrac{\nu(n-1)}{E}}{D_1 \dfrac{\nu(n-1)}{E}} \right]. \tag{2.22}$$

E, ν and c_σ are the Young's modulus, Poisson's ratio and the stress-optic coefficient of the material respectively.

In regions where generalized plane stress is valid, $\sigma_{33} = \nu(\sigma_{11} + \sigma_{22})$. The net optical path difference thus reduces to

$$S(x_1, x_2) \approx c_\sigma h[\hat{\sigma}_{11}(x_1, x_2) + \hat{\sigma}_{22}(x_1, x_2)]\,. \tag{2.23}$$

For points where the generalized plane stress assumption is valid, the CGS patterns assume a simple interpretation in terms of two-dimensional stress field approximations. In particular the CGS fringe order can be related to the in-plane gradients of $\hat{\sigma}_{11} + \hat{\sigma}_{22}$ as

$$c_\sigma h \frac{\partial(\hat{\sigma}_{11} + \hat{\sigma}_{22})}{\partial x_2} = \frac{mp}{\Delta}, \quad m = 0, \pm 1, \pm 2, \ldots\,. \tag{2.24}$$

Note that the shearing direction chosen in Figure 2.4 is along the x_2-axis. By rotating the gratings through 90°, the shearing direction is changed to x_1, and thus information about gradients of $\hat{\sigma}_{11} + \hat{\sigma}_{22}$ along the x_1-direction may be obtained. All the experiments performed and analyzed in this work are assumed to conform to the generalized plane stress approximation and hence all stress and strain components measured are thickness averages. Therefore, for convenience, we omit the overhat on stress and strain components.

2.3 Experimental Setup

Dynamic cracks along interfaces propagate at very high speeds of the order of a kilometer per second or higher. Hence, to make an accurate observation of the evolution of stress/displacement fields around a propagating crack tip, a series of recordings of the instantaneous stress/displacement field information must be made, in an extremely short time, before the crack runs out of the field of view. Optical techniques of stress analysis in conjunction with high-speed photography satisfy this requirement and consequently have been employed widely in dynamic fracture experiments. High-speed photography of dynamic crack tip fields requires exposure times of the order of only a few nanoseconds to prevent blurring caused by the high speed of the moving object being imaged. Therefore, such a recording requires a high powered pulsed light source and a high-speed camera capable of recording a multitude of images in a very short time.

Figure 2.5 shows a typical experimental setup for dynamic photoelasticity experiments and Figure 2.6 shows a typical experimental setup for dynamic CGS interferometry. A schematic of the specimen geometries is shown in Figure 2.1 along with all the relevant dimensions. This specimen geometry is a simplified version of the one introduced by KALTHOFF (1987) for investigating crack behavior under dynamic shear loading. The specimen is loaded dynamically by impacting it with a projectile fired from a high-speed gas gun. A compressive longitudinal loading pulse results

which loads the crack/notch tip predominantly in a shearing mode. The gas gun has a $7'$ long steel barrel and fires a $3''$ long, $2''$ diameter cylindrical projectile made of hardened steel. Compressed air at 12 psi to 80 psi was used as the driving medium which resulted in projectile velocities ranging from 8m/s to 40m/s. The gas gun was calibrated and a pressure *vs* projectile velocity curve was obtained apriori.

An Innova Sabre argon-ion pulsed laser was used as the light source in our experiments. The laser was set to operate on a single wave length - 514.5 nm (blue-green light). At this wave length the continuous (CW) power output of the laser is 8 W. The laser emits an intense beam of 2 mm diameter which is 100:1 vertically polarized. An acousto-optic modulator (Bragg cell) is placed in front of the laser to produce a pulsed output. The duration of each laser pulse can be varied between 8 ns and 20 ns. Such short exposure times are required to prevent blurring and to record a sharp image on the film. During the actual experiment, the acousto-optic modulator is driven by the high-speed camera to control the timing of each laser pulse, so that it coincides with the time the camera optics are aligned to expose a particular frame on the film track. An electromechanical shutter is placed in front of the laser to prevent the light "leaking" through the Bragg cell from exposing the film. A wide gap sensor mounted on the gas gun barrel about $1'$ from the end is used to trigger the shutter open for a short duration ($\approx$ 10 ms) during the event. A strain gage bonded to the specimen at the impact site is used to trigger recording by the high-speed camera on impact. The coherent, monochromatic, plane polarized light output by the laser is collimated to a beam of 50 mm diameter. The laser beam is transmitted through the specimen placed inside a circular polariscope or a CGS interferometer and the resulting fringe pattern is recorded by a high speed camera. For bimaterial specimens, the metal half being opaque, only one half of the beam is transmitted through the specimen.

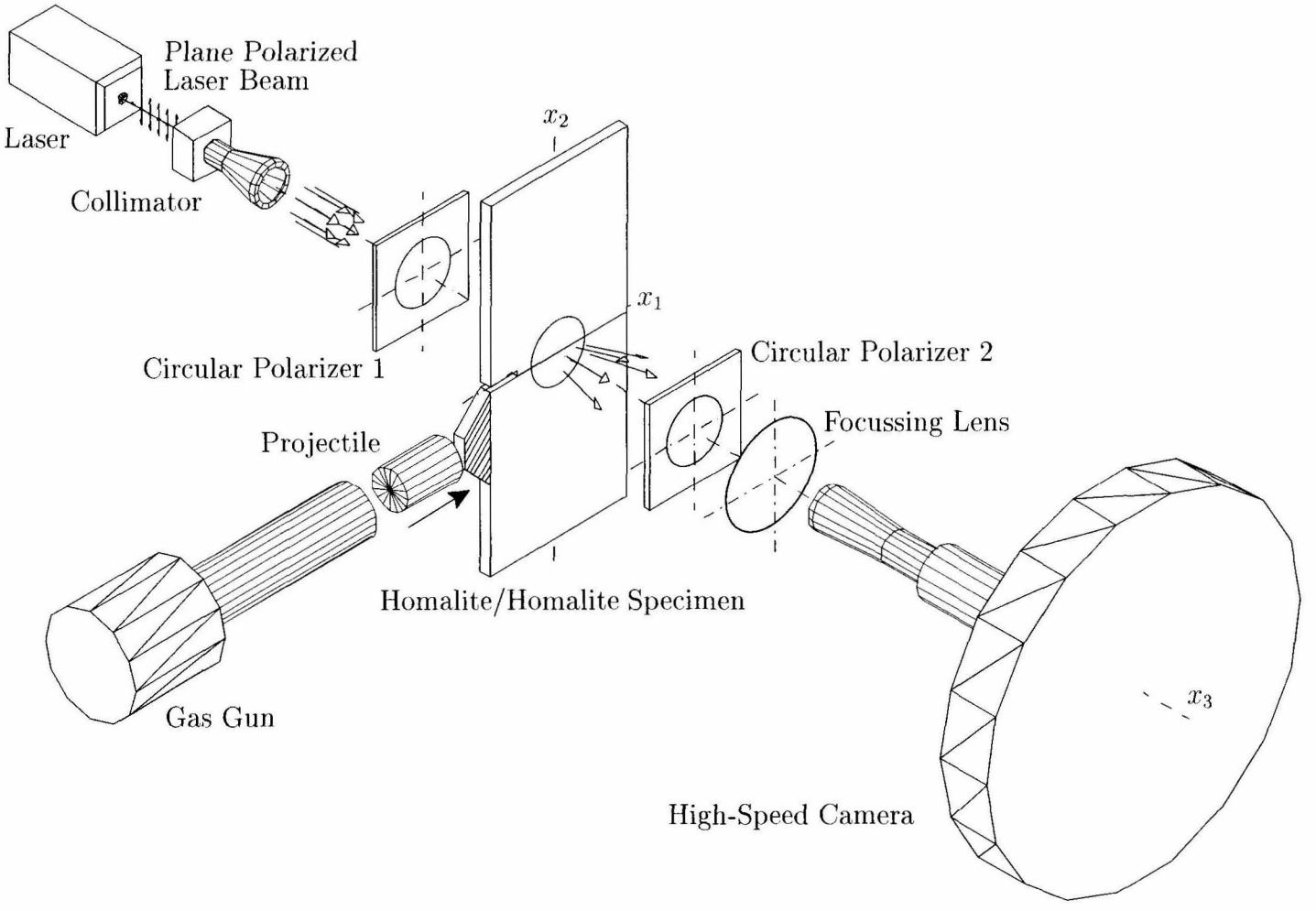

Figure 2.5: Dynamic photoelasticity setup showing a Homalite/Homalite specimen placed inside a circular polariscope and being subjected to impact shear loading by a projectile fired from a high-speed gas gun. The resulting isochromatic fringe patterns are recorded by high-speed photography.

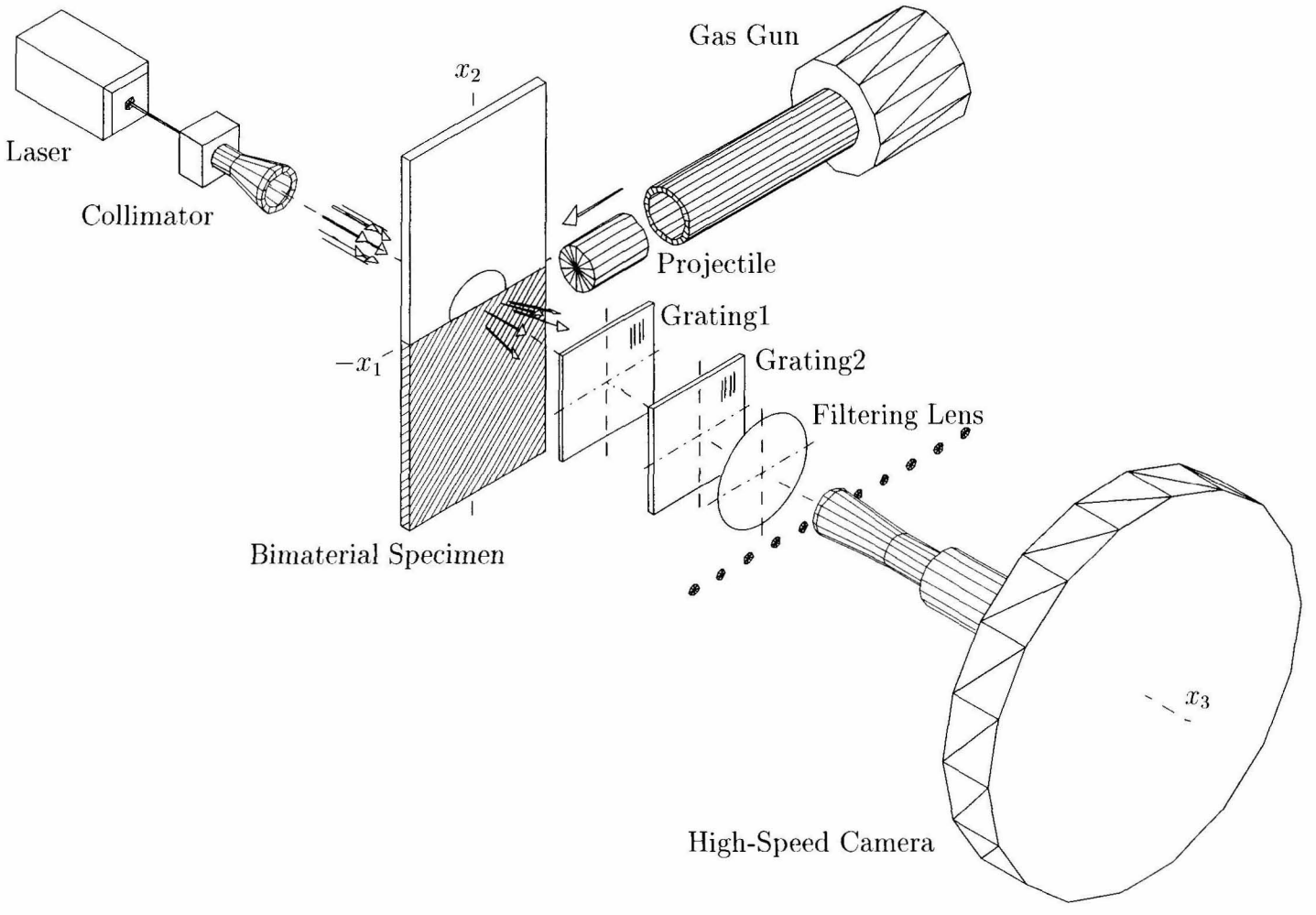

Figure 2.6: Experimental setup for dynamic CGS interferometry in transmission configuration. Figure shows a bimaterial specimen being subjected to impact shear loading by a projectile fired from a high-speed gas gun and the recording of the dynamic CGS interferograms by high-speed photography.

A Cordin model 330A rotating mirror type high-speed film camera was used to record the instantaneous fringe patterns generated by either of the two optical techniques mentioned above. The high-speed camera contains a rotating mirror which directs the image on to the film mounted on a film track surrounding it. The rotating mirror is driven by a gas turbine running on compressed helium. Individual frames are exposed sequentially by inducing the laser to produce a high-powered pulse of short duration as and when the rotating mirror is aligned to a particular frame. The high-speed camera records 80 distinct frames at framing rates of up to 2 million frames per second. A feedback signal from the turbine is fed to a 10Khz frequency counter which allows a precise monitoring of the turbine speed. Also the synchronizing signal sent by the camera to the acousto-optic modulator is simultaneously routed to a HP digital oscilloscope to obtain a record of the timings of each individual laser pulse. In this experimental work, most of the high-speed photography was performed at 720,000 frames per second, resulting in a frame every 1.4 μs. This provides a total recording time of about 112 μs. Kodak TMAX 400 or 3200 black & white film was used to record the fringe patterns. The optical system in the high-speed camera introduces an elliptical distortion to the image recorded on the film. For a circular input beam, the recorded image is an ellipse with its major axis about 15% larger in comparison with the minor axis. The developed negatives were scanned using a negative scanner and the elliptical distortion was removed from the final image digitally.

Nomenclature

(x_1, x_2, x_3)	Cartesian coordinates
α	inclination of the fast axis of the stressed specimen to the x_2-axis
Δ	phase lag of the slow component of the electric field vector through the specimen or spacing between the gratings
$\epsilon_{\alpha\beta}$	components of the strain tensor
λ	wave length of incident light
μ	shear modulus
ν	Poisson's ratio
ω	angular frequency of the electric field vector
ρ	mass density
σ_1, σ_2	in-plane principal stresses
σ_o	tensile strength
τ_o	shear strength
τ_{max}	maximum in-plane shear stress
θ	diffraction angle

a	amplitude of the electric field vector
c	relative stress-optic coefficient
c_l	longitudinal wave speed
c_R	Rayleigh wave speed
c_s	shear wave speed
c_σ	stress-optic coefficient
d	shearing distance
D_1	stress-optic coefficient
E	Young's modulus
E_1', E_2'	components of the electric field vector along the fast and slow axes respectively, emerging out of the stressed specimen
E_f', E_s'	components of the electric field vector along the fast and slow axes respectively, after emerging out of a quarter/half-wave plate
E_1, E_2	components of the electric field vector along the fast and slow axes respectively, entering the stressed specimen
E_a	magnitude of the electric field vector as it emerges out of the analyzer
E_f, E_s	components of the electric field vector along the fast and slow axes, respectively, entering the first quarter-wave plate
$E_i, E_{i,j}$	magnitudes of the electric field vectors associated with different diffraction orders after emerging from 1 and 2 gratings, respectively
E_p	magnitude of the electric field vector emerging from the polarizer

F_σ	material fringe constant
h	specimen thickness
I	intensity of the light ray as it emerges out of the half-wave plate
K_{Ic}	mode I fracture toughness
m	CGS fringe order
N	isochromatic fringe order
n	refractive index
p	grating pitch
S	optical path difference

Bibliography

DALLY, J. W. (**1978**), Dynamic Photoelastic Studies of Stress Wave Propagation, in *Modern Problems in Elastic Wave Propagation*, edited by J. Miklowitz and J. D. Achenbach, Wiley, New York, pp. 3–21.

DALLY, J. W. and RILEY, W. F. (**1991**), *Experimental Stress Analysis*, McGraw-Hill, New York.

KALTHOFF, J. F. (**1987**), Shadow Optical Analysis of Dynamic Shear Fracture, in *Proceedings of the International Conference on Photomechanics and Speckle Metrology*, SPIE Vol.814, pp. 531–538.

KOBAYASHI, A. S. and MALL, S. (**1978**), Dynamic Fracture Toughness of Homalite-100, *Experimental Mechanics*, **18**, pp. 11–18.

KRISHNASWAMY, S., ROSAKIS, A. J., and RAVICHANDRAN, G. (**1991**), On the Extent of Dominance of Asymptotic Elastodynamic Crack-Tip Fields. 2. Numerical Investigation of Three Dimensional and Transient Effects, *Journal of Applied Mechanics*, **58**(1), pp. 95–103.

LAMBROS, J. (**1994**), *Dynamic Decohesion of Bimaterial Interfaces*, Ph.D. thesis, California Institute of Technology, Pasadena, CA, USA.

LEE, Y. J. and ROSAKIS, A. J. (**1993**), Interfacial Cracks in Plates – A Three Dimensional Numerical Investigation, *International Journal of Solids and Structures*, **30**(22), pp. 3139–3158.

ROSAKIS, A. J. (**1993**), Two Optical Techniques Sensitive to Gradients of Optical Path Difference: The Method of Caustics and The Coherent Gradient Sensor (CGS), in *Experimental Techniques in Fracture*, edited by J. S. Epstein, VCH, New York, pp. 327–425.

ROSAKIS, A. J. and RAVICHANDAR, K. (**1986**), On Crack-Tip Stress State - An Experimental Evaluation of Three Dimensional Effects, *International Journal of Solids and Structures*, **22**(2), pp. 121–134.

SINGH, R. P. (**1995**), *Catastrophic Failure of Bimaterial Interfaces*, Ph.D. thesis, University of Rhode-Island, Kingston, RI, USA.

SINGH, R. P., LAMBROS, J., SHUKLA, A., and ROSAKIS, A. J. (**1997**), Investigation of the Mechanics of Intersonic Crack Propagation Along a Bimaterial Interface Using Coherent Gradient Sensing and Photoelasticity, *Proceedings of the Royal Society of London*, **A453**(1967), pp. 2649–2667.

TIPPUR, H. V. and ROSAKIS, A. J. (**1991**), Quasi-Static and Dynamic Crack Growth Along Bimaterial Interfaces - A Note on Crack-tip Field Measurements using Coherent Gradient Sensing, *Experimental Mechanics*, **31**(3), pp. 243–251.

Chapter 3

Experimental Observations

Experiments were performed in the laboratory to verify the possibility of intersonic mode II crack growth in constitutively homogeneous, isotropic, linear elastic solids. To ensure the directional stability of a propagating mode II crack, a thin layer of lower fracture toughness, compared to that of the monolithic material, was introduced along the prospective crack path. It is demonstrated that shear cracks propagating along a weak plane can attain intersonic speeds. The stress field around the propagating crack tip is recorded by a full-field optical technique in conjunction with high speed photography. The experimental observations are compared with Freund's singular solution (FREUND, 1979), motivating the necessity of a cohesive zone model.

3.1 Effect of Impact Speed

The specimen geometry and loading configuration are shown in Figure 2.1(A). To assess the nature of stress wave loading induced in the specimen after impact, a calibration test was performed. For the calibration specimens, no edge notch was machined, and the two Homalite halves were bonded all along the width of the specimen. Also, the steel buffer plate was bonded symmetrically with respect to the bond line as shown in Figure 3.1(a). The horizontal dashed line represents the weak plane joining the two Homalite halves. The specimen was subjected to impact by a cylindri-

cal steel projectile fired from a high speed gas gun. Results are shown in Figure 3.1 for an impact speed of 21.6 m/s. Under the generalized plane stress assumption, which is expected to hold through out the specimen, the stress wave fronts radiating from the impact site are as shown in Figure 3.1(a). Apart from the loading planar longitudinal wave front, unloading cylindrical wavefronts are also initiated simultaneously from the corners of the steel buffer. The specimen was placed inside a circular polariscope and the isochromatic fringe patterns resulting from the propagating stress waves in the specimen were recorded by a high speed camera. Figure 3.1(b) shows a typical recorded fringe pattern at 36.9 μs after impact. The field of view shown has a diameter of 50 mm and was centered on the bond line, 65 mm from the impact edge. A thin horizontal line seen along the diameter of the field of view is the bond line. A thick vertical dark band seen perpendicular to the bond line is the streak line which is an artifact of the camera and is seen in all the fringe patterns which were recorded by the rotating mirror type high speed camera. However, a few of the patterns shown later, which do not feature a vertical dark band, were recorded using a high speed digital camera. In Figure 3.1(b) we see a series of fringes moving into the field of view indicating that the material behind is being loaded progressively. From symmetry considerations, we can conclude that the loading induces a compressive stress normal to the impact direction in material particles close to the bond line. Each passing fringe results in an increase in compressive normal stress σ of magnitude $\approx F_\sigma/h = 4.76$ MPa. The time history of the compressive stress induced on a material particle situated at a distance of 40 mm from the impact edge (roughly at the center of the field of view) is shown in Figure 3.1(c). It can be seen that the loading pulse is of the ramp type, with a rise time of about 27 μs and a peak compressive stress around 54 MPa. The rise time corresponds roughly to the time taken for a longitudinal wave to traverse twice the length of the projectile, which is also the time for which the projectile is in contact with the steel buffer. Unloading waves are seen immediately afterwards, however, their interpretation is complicated. The dashed line showing the unloading part of the pulse is only an estimate. Due

to the dispersive nature of the material, it is likely that the rise time of the loading pulse would be slightly shorter at distances less than 40 mm from the impact edge.

The speed with which the fringes move across field of view is a measure of the wave speeds in the material. We can clearly see that the fringes are continuous across the bond line and are not affected even at distances very close to the bond. This indicates that the constitutive properties of the bond are very close to those of the material on either side. The first fringe, which would be the closest to the longitudinal wave front, propagates at a speed of 2048 m/s. This falls between the plane stress c_l determined for Homalite at two different strain rates shown in Table 2.1. From the loading pulse it can be estimated that the loading occurs at strain rates of the order 10^2 s^{-1} resulting in a c_l lower than that determined using an ultrasonic analyzer, which corresponds to higher strain rates of the order 10^3 s^{-1}. Near a propagating crack, the governing strain rates must be higher than those corresponding to the loading phase and hence we will use the higher wave speeds determined using the ultrasonic analyzer as the representative ones in analyzing crack growth. With the estimate of c_l of 2048 m/s and approximating the steel projectile and the buffer to be rigid with respect to Homalite, we can make a simple approximation for the induced compressive normal stress based on the elastodynamics of plane waves. According to this approximation, the compressive normal stress induced must be equal to $\rho c_l^{\sigma} V(1-\nu)$, which is close to the peak stress observed for the loading pulse. Here ρ is the mass density and V is the projectile impact speed.

Figure 3.2 shows the effect of projectile impact speed on crack initiation from the tip of a notch/precrack in the actual specimen. Figures 3.2(a), (b) and (c) are the isochromatic fringe patterns around the notch at various times (measured from time of impact) as indicated, for a projectile impact speed of 11 m/s. Around 50 μs after impact, a kinked crack is observed to initiate from the notch, inclined at an angle of 39° to the weak plane ahead. If we assume, that the kink angle observed follows the criterion of maximal energy dissipation (HUTCHINSON and SUO, 1992), it can

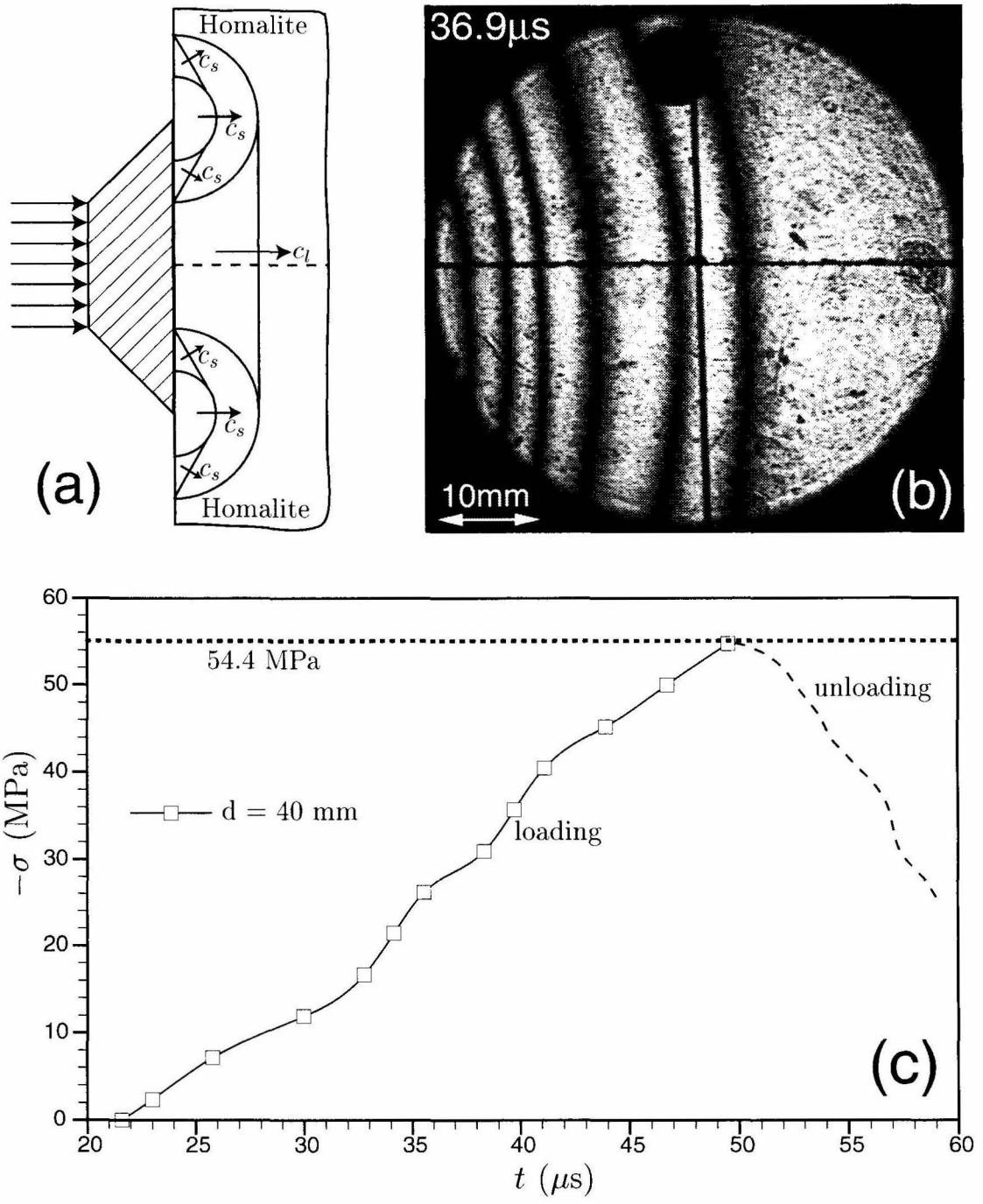

Figure 3.1: Stress wave propagation in Homalite due to projectile impact loading. Impact speed = 21.6 m/s. **(a)** Spreading of wave fronts from the impact site. **(b)** Isochromatic fringes in a field of view of 50 mm diameter centered on the bond line at a distance of 65 mm from the impact edge. **(c)** Estimated shape of the loading pulse at 40 mm from impact edge.

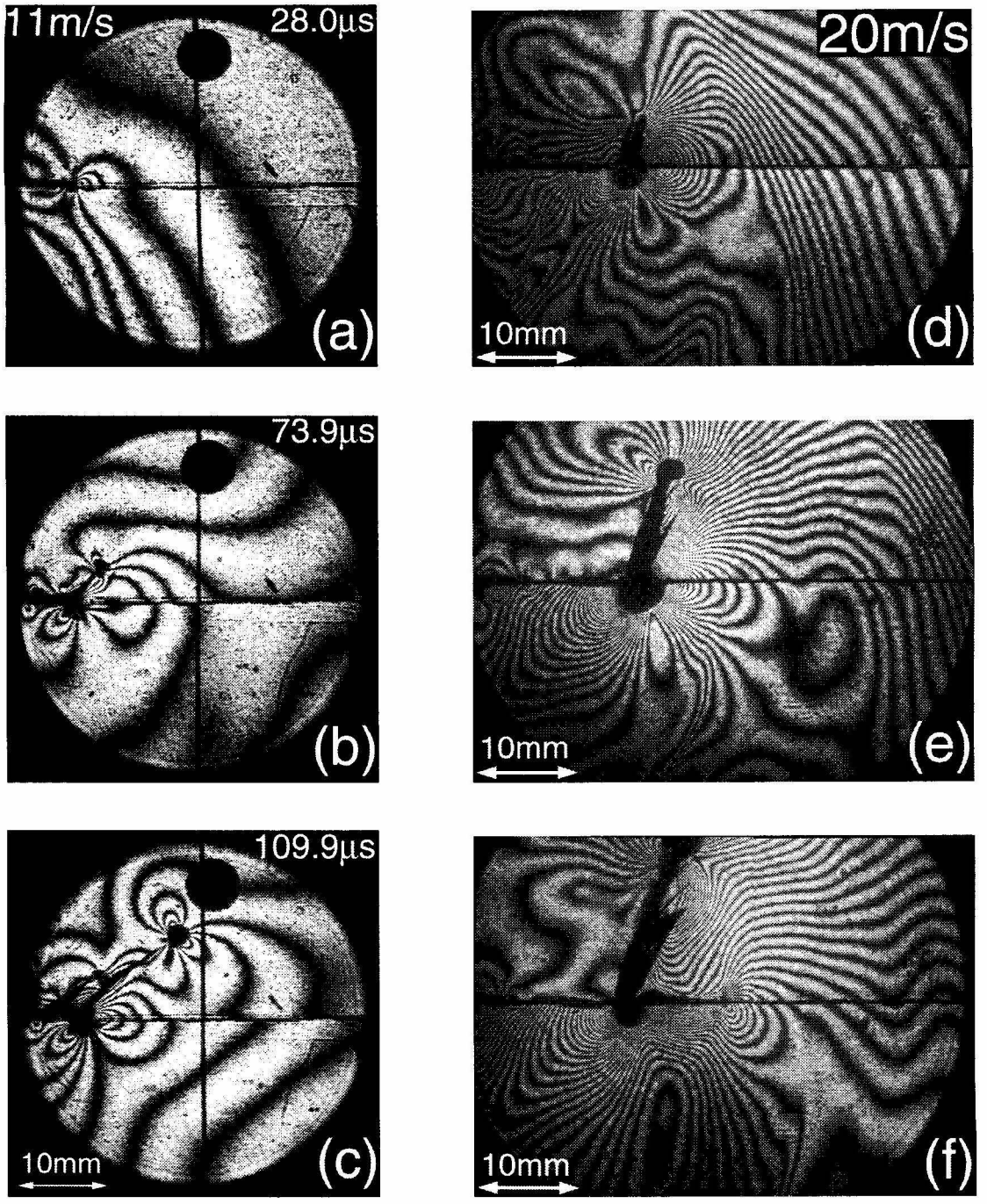

Figure 3.2: Single edge notch/crack along a weak plane in Homalite under impact shear loading. **(a-c)** Impact speed = 11 m/s. A crack initiating from the notch kinks at 39° to the weak plane. **(d-f)** Impact Speed = 20 m/s. The precrack kinks at 70° to the weak plane. In addition, a second crack is also seen propagating along the weak plane (see **f**).

be deduced that the mode mixity $\psi = \tan^{-1}(K_{II}/K_I)$ at initiation is $\approx 24^o$. Hence, at initiation, the magnitude of the mode I stress intensity factor, K_I was almost 2.25 times that of the mode II stress intensity factor, K_{II}. The opening dominated nature of the notch-tip fields can also be readily expected from the time taken for crack initiation after impact. Crack initiation occurs around 50 μs, by which time unloading waves due to the finite width of the loading pulse ($\approx$ 28 μs), reflections from the far end (with respect to the notch tip) of the buffer plate and also from the free surface to the left on the top half of the specimen, have arrived and impinged on the notch eventually changing its mode mixity to a predominantly opening mode. The kinked crack propagates with mode I symmetry at its tip, as seen from the symmetry of the two lobes oriented at 90^o to the crack plane (Figure 3.2(c)). The average speed of the kinked crack was $\approx 0.26\, c_s$. Figures 3.2(d), (e), and (f) are the isochromatic fringe patterns around the precrack in a specimen subjected to projectile impact at 20 m/s. A kinked crack is observed to initiate from the loaded precrack at an angle of 70^o to the crack plane. Again using the criterion of maximal energy dissipation, one can see that at initiation, mode mixity $\psi \approx 72^o$. Hence, at initiation, magnitude of K_{II} was almost 3.1 times that of K_I. Apart from the kinked crack, another crack can also be observed to propagate straight ahead, along the weak plane (see Figure 3.2(f)). The crack along the weak plane is likely to be shear dominated, since it initiated from a shear dominated precrack, though the isochromatic fringe pattern is complicated by the presence of the kinked crack. Also from Figure 3.2(d) and (f), we can deduce that the shear crack along the weak plane propagates at a substantially higher speed compared to the kinked crack. SCHARDIN (1959) also reported a similar phenomenon, where a crack along a preexisting scratch on a glass plate travels at a higher speed as compared to a crack in solid glass. This suggests that a higher impact speed resulting in initiation under predominantly shearing mode might result in a fast shear crack propagating ahead along the weak plane. Also, if the fracture energy of the weak plane is low compared to the monolithic material then the kinked crack might be eliminated. The substantial increase in the number

of fringes observed is a reflection of the fact that the impact speed was higher and also due to the fact that the specimen thickness in the higher impact case was $3/8''$, where as the specimen thickness in the lower impact case was $1/4''$.

The conditions governing the straight ahead initiation of a dynamically loaded stationary crack subjected to mixed mode loading may be summarized as follows. Consider a stationary crack subjected to time varying mixed mode loading of mixity $\psi(t)$. Let $G^t(\Omega, \psi(t), t)$ be the dynamic energy release rate of an incipient kink inclined at an angle Ω to the initial crack direction. $G^t(0, \psi(t), t)$ corresponds to straight ahead propagation while $G^t(\Omega^*(t), t)$ corresponds to crack growth at an angle $\Omega^*(t) = \Omega^*(\psi(t))$ that maximizes the function $G^t(\Omega, \psi(t), t)$ at each t. Given the above, a dynamically loaded stationary crack subjected to mixed mode loading of mixity $\psi(t)$, initiates straight ahead along the weak plane without kinking, provided

$$G^t_{max}(t_o) < \Gamma(\dot{G}(t_o)) \qquad \text{and} \tag{3.1a}$$

$$G(t_o) = \Gamma_{pl}(\psi(t_o), \dot{G}(t_o))\,, \tag{3.1b}$$

where G is the energy release rate for straight ahead propagation, Γ is the critical mode I energy release rate (fracture energy), Γ_{pl} is the critical energy release rate for the weak plane and t_o is the time of crack initiation. In general, the critical energy release rates Γ and Γ_{pl} depend on the "loading rates" at the crack tip as measured by $\dot{G}$. The kinked crack would propagate in a monolithic solid and hence if possible, it would initiate in a direction that would maintain mode I conditions near the tip. In contrast, a crack initiating straight ahead along the weak plane would still propagate under mixed-mode conditions and hence Γ_{pl} is a weak function of the mode mixity ψ. The dependence may become more pronounced as $\psi \to \pm\pi/2$, where crack face asperity contact would come into play, leading to a substantial increase in the energy dissipated. This was observed by BROBERG (1987), who found that the mode II fracture toughness, K_{IIc} for PMMA in the presence of frictional contact was about

2.5 times the mode I fracture toughness, K_{Ic} of PMMA. Once a straight ahead shear crack is initiated, and its directional stability is maintained, it is possible for it to achieve intersonic speeds as shown in Figure 3.3.

3.2 Intersonic Cracks on a Weak Plane

As explained in the previous section, if (3.1) is satisfied, then a stationary notch/crack subjected to mixed mode loading can initiate a crack straight ahead along the weak plane without prior kinking. In all the propagation tests, a blunt notch was used instead of a precrack as the initiation site, so as to prevent the "leaking" of the stress waves into the top half of the specimen through crack face contact (prior to initiation) and also because of its higher initiation threshold. Figure 3.3 shows a selected sequence of isochromatic fringe patterns around a shear crack initiating from a notch and propagating along the weak plane joining two Homalite plates. The time after impact as well as the crack tip speed (after initiation) are shown in each frame. Speed of the projectile at the time of impact was 26.3 m/s and the field of view of 50 mm diameter was centered on the weak plane, 20.6 mm ahead of the notch tip. In Figure 3.3(a) we can see the stress waves from the impact site arriving at the notch tip. In Figure 3.3(b) we see the stress waves diffracting around the notch tip and simultaneously observe the stress concentration building up. In Figure 3.3(c) at 26.3 μs after impact, a shear crack has just initiated from the notch tip and begins to propagate along the weak plane. LEE and FREUND (1990) derived analytically the time history of mode I and mode II stress intensity factors at the notch tip for a step loading pulse. In the problem they considered, the loading was applied above the notch, whereas in our case the loading is applied below the notch. From symmetry, this difference should merely change the sign of the mode II stress intensity factor induced at the tip. According to their results, both K_I and K_{II} at the notch tip should become negative at the time of the arrival of the longitudinal wave front from the impact site and become progressively more and more negative until the arrival

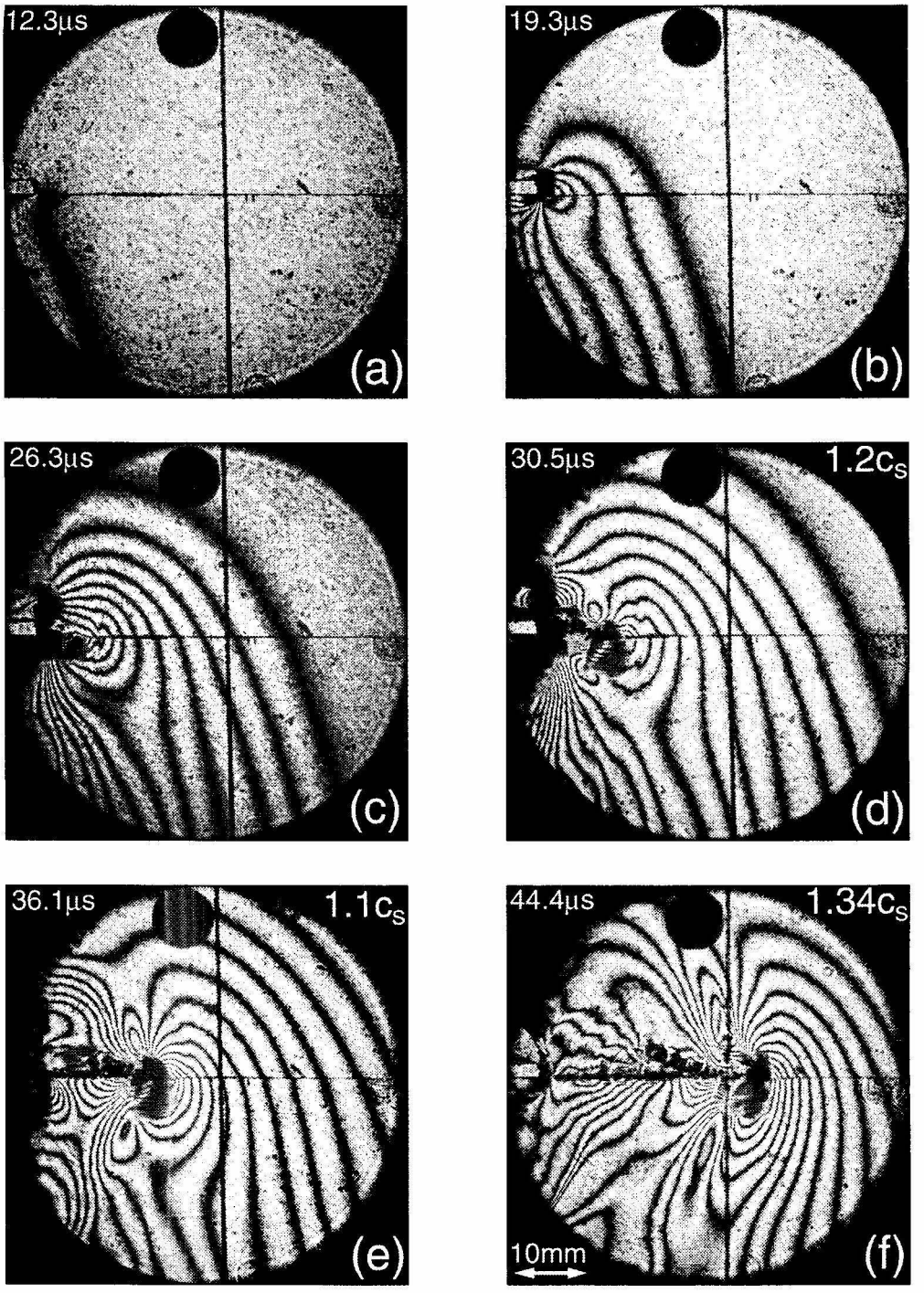

Figure 3.3: Isochromatic fringe pattern around a crack initiating from a single edge notch along a weak plane in Homalite under impact shear loading. Impact speed = 26.3 m/s. Field of view of 50 mm diameter is centered on the bond line, 20.6 mm ahead of the notch tip.

at the notch tip, of the reflected longitudinal wave front from the free boundary to the left on the upper half of the specimen, *i.e.*, until $t = 3l/c_l$, where l is the crack length. However, the magnitude of K_{II} for this entire duration was almost 2.5 times that of K_I. This result was confirmed experimentally by MASON *et al.* (1992) (where the loading pulse was likely a ramp instead of a step as in the analytical solution of LEE and FREUND (1990)), who showed that the shear dominated nature of the deformation at the notch tip extends to a much longer duration, *i.e.*, until the reflected longitudinal wave front arrives from the end of the specimen opposite to the notch. In our case, crack initiation from the notch occurs at 26.3 μs, which is equivalent to $1.3l/c_l$, and hence the notch tip deformation was predominantly shear at the time of initiation. After initiation, however, the nature of the crack tip deformation must be pure mode II. To sustain the expected negative K_I at the propagating sharp crack tip, the crack faces must come closer from their initial configuration. A negative K_I is possible at the tip of a notch, where the notch faces are separated by a finite notch width, however for a sharp crack, the crack faces are already in contact (but traction free) in their rest configuration. Hence, a sharp crack tip cannot sustain a negative K_I, and pure mode II conditions must prevail at the tip, albeit with negative normal tractions acting on the crack faces (which annul the negative K_I required at the tip due to the mixity of far-field loading). In Figure 3.3(d) we can clearly distinguish the stress concentration around the propagating crack. Note that the crack speed is already intersonic at this stage. This confirms the analytical predictions of ANDREWS (1976); FREUND (1979); BROBERG (1989), *etc.*, that intersonic mode II crack growth is energetically permissible. The next two frames shows an increased stress intensity around the propagating crack tip, and in addition, in Figure 3.3(f) we can discern a series of shadow spots all lined up at a shallow angle to the crack plane behind the crack tip. We will return to these shadow spots again in Section 3.5.

Figure 3.4 shows a selected sequence of isochromatic fringe patterns around a propagating mode II crack along the weak plane. The experimental conditions are

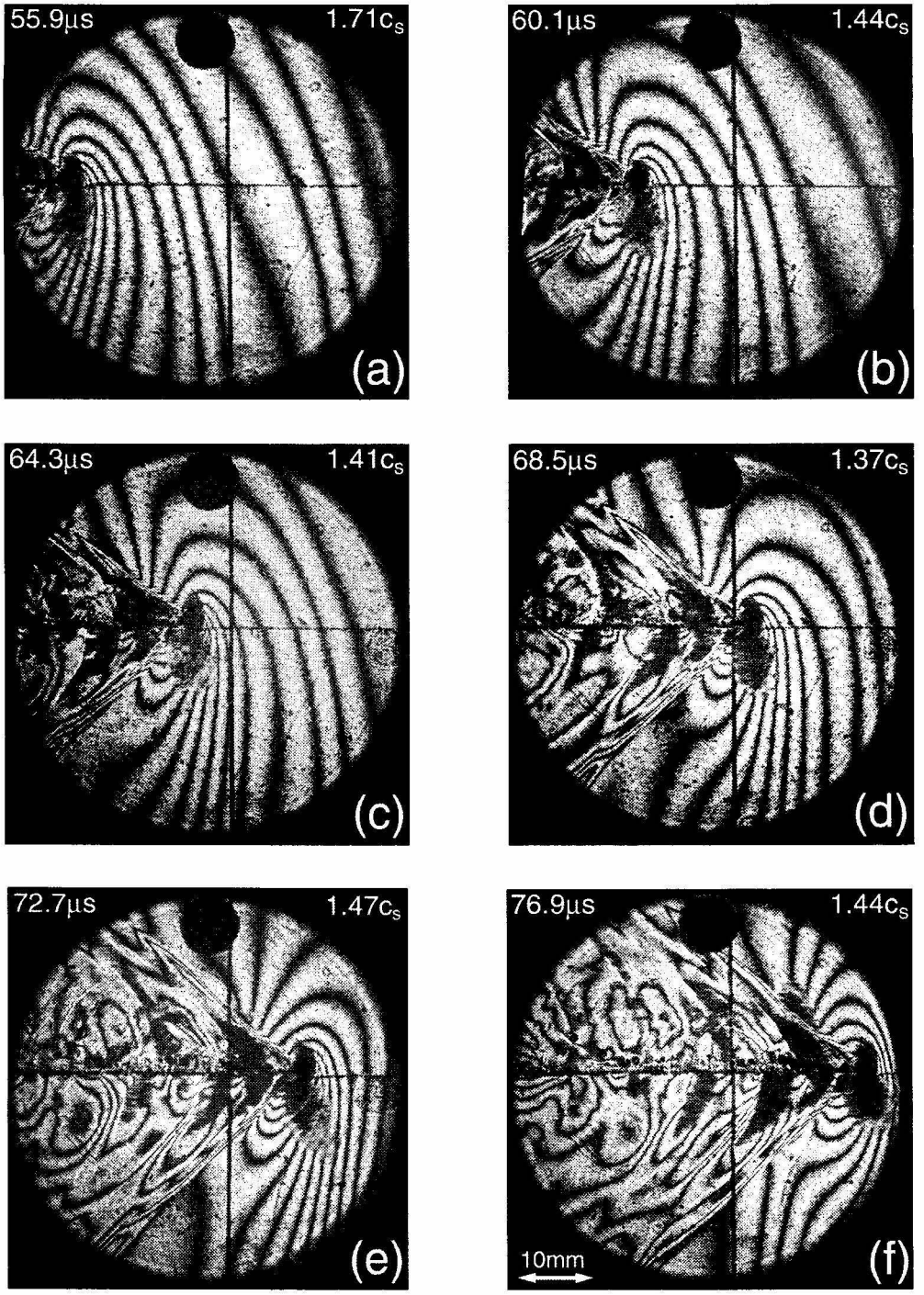

Figure 3.4: Isochromatic fringe pattern around a propagating intersonic crack along a weak plane in Homalite. Impact speed = 27.7 m/s. Field of view of 50 mm diameter is centered on the bond line, 63.1 mm ahead of the notch tip. The two Mach waves radiating from the crack tip can be clearly distinguished.

similar to the one whose results are shown in Figure 3.3. However, the field of view is located further downstream from the notch tip. Again, the time after impact as well as the crack tip speed are shown in each frame. Speed of the projectile at the time of impact was 27.7 m/s and the field of view of 50 mm diameter was centered on the weak plane, 63.1 mm ahead of the notch tip. The crack speeds in all the frames shown are in the intersonic range. In Figure 3.4(a), around 56 μs after impact, we see a crack entering the field of view around which the shape of the isochromatic fringe pattern has changed dramatically from that seen in Figure 3.3(f) (at 44.4 μs). A sequence from an experiment which captures the isochromatic patterns at intermediate times is shown later in Figure 3.12 to motivate the necessity of a cohesive zone model. In frames (**b-f**) we can clearly distinguish two lines radiating from the crack tip, across which the fringe pattern changes abruptly, indicating that the stress field suffers a discontinuity across these lines. These two lines correspond to the two traveling shear Mach waves, which limit the spread of shear waves emanating from the crack tip as it propagates along the interface at intersonic speeds. Hence, the angle ξ the Mach waves make with the crack faces can be related to the crack speed v through

$$\xi = \sin^{-1}(c_s/v)\,. \tag{3.2}$$

In the last four frames, the crack speed and the Mach angle are in close proximity, indicating that the mechanical state in the vicinity of the propagating crack tip does not change appreciably during these times. The stress intensity near a propagating crack tip is governed by the far-field loading, crack length and the crack speed. In the last four frames, crack speed hovers around $\sqrt{2}\,c_s$, and the decreasing far-field loading (note that the loading pulse lasts up to about 50 μs after impact) is counteracted by the increasing crack length, in effect keeping the stress intensity and consequently the mechanical state around the crack tip approximately the same. Hence the propagating crack may be approximated to have reached a steady state. Also, the reflected waves from the far end of the specimen would reach the propagating crack tip around 76 μs,

which is around the time of recording of Figure 3.4(f).

3.3 Crack Speed and Mach Angle Histories

Typical crack length and crack speed histories for two similar and representative experiments varying only in the position of the field of view are shown in Figure 3.5. In one of the experiments (Expt 9), the speed of the projectile at impact was 26.8 m/s and the field of view of 50 mm was centered on the bond line, 29.1 mm ahead of the notch tip. In the second experiment (Expt 15) for which data is shown, the speed of projectile at impact was 27.7 m/s and the field of view of 50 mm was centered on the bond line, 63.1 mm ahead of the notch tip. Figure 3.5(a) shows the crack length history for both the experiments. Crack length measurements immediately after initiation were complicated by the presence of the stress concentration around the notch, making it difficult to identify the exact position of the crack tip from the fringe patterns. Hence, crack length measurements were taken after the shear crack has propagated a finite distance ahead of the notch tip. Note that the crack length shown includes the initial length of notch which was about 1″. The time of impact is considered the reference point on the time scale and hence $t = 0$ μs corresponds to the time at which the projectile impacts the steel buffer. At distances far away from the initial notch and at times greater than 65 μs, the crack length seems to increase fairly linearly with time, indicating that the shear crack is propagating at a near constant speed, which was found to be close to $\sqrt{2}\,c_s$. The error in crack length measurement varies from frame to frame, ranging from ± 0.5 mm to ± 1.5 mm. The timing of each frame was measured exactly by routing the laser-camera synchronization signal to a digital oscilloscope. Hence the timing of each frame was measured accurately to within 1/100 of a μs. To determine the crack speed, a second order interpolating polynomial is obtained for every three successive points in the crack length history, which is then differentiated with time to give the crack speed for the mid-point.

The variation of the crack speed as the shear crack propagates along the weak plane

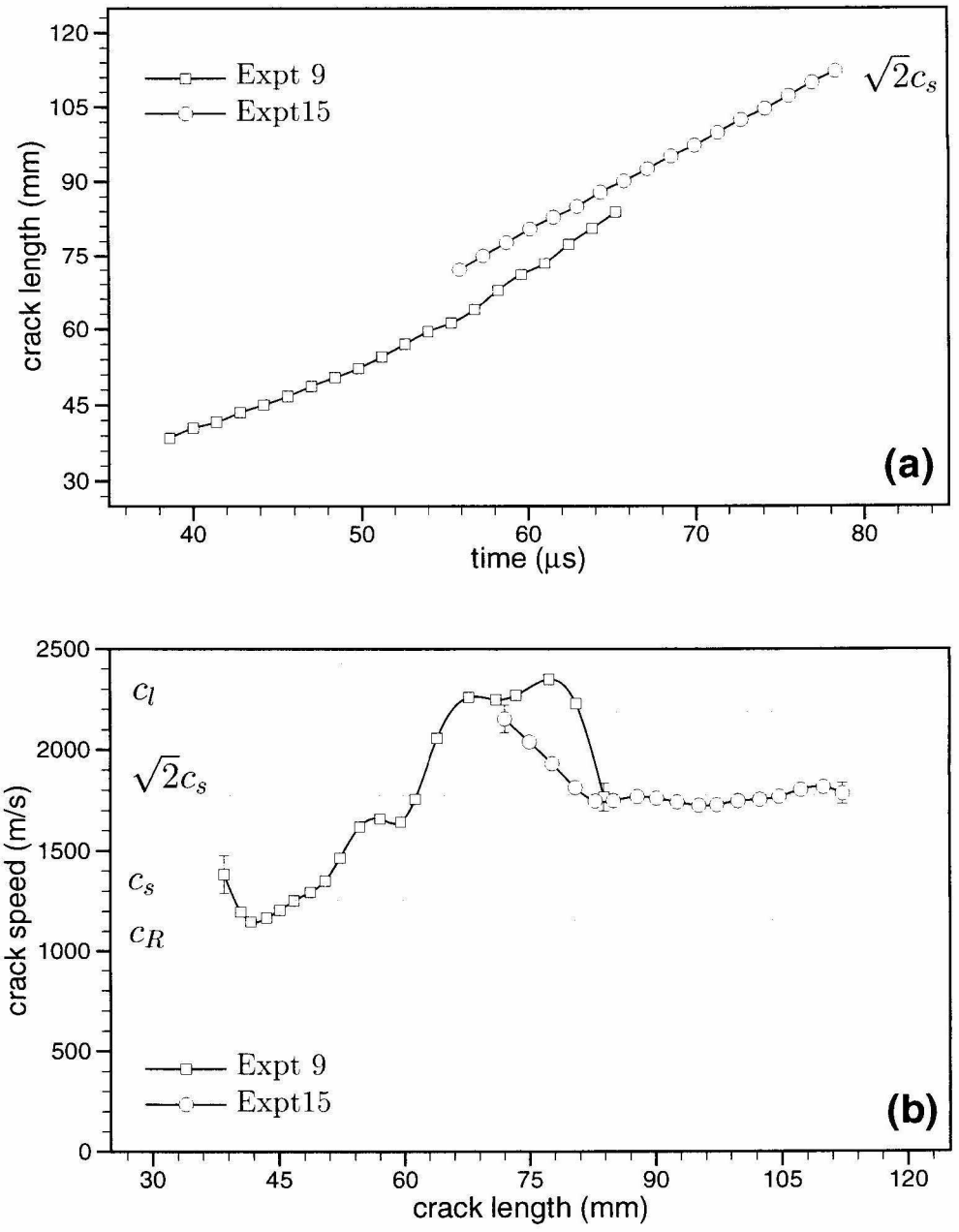

Figure 3.5: **(a)** Time history of crack length. Crack length includes length of the starter notch. **(b)** Evolution of crack speed v as the crack propagates along the weak plane. Expt 9 corresponds to an impact speed of 26.8 m/s and the field of view of 50 mm is centered on the bond line, 29.1 mm ahead of the notch tip. Expt 15 corresponds to an impact speed of 27.7 m/s and the field of view of 50 mm is centered on the bond line, 63.1 mm ahead of the notch tip.

is shown in Figure 3.5(b) for the same two experiments. From the figure, we see that the initially recorded crack tip speed is close to the shear wave speed of Homalite, beyond which it accelerates (at the order of $10^8\,\mathrm{ms}^{-2}$), thus becoming intersonic. Thereafter, it continues to accelerate up to the plane stress longitudinal wave speed of Homalite, following which it decelerates and ultimately reaches a steady state value close to $\sqrt{2}\,c_s$. With the error estimates for crack length and timing mentioned above, a simple error analysis for the crack speed determination procedure yields errors in crack speed evaluation ranging from ± 50 m/s to ± 110 m/s. The error bars are indicated on the first and last data points for both the experiments. A few of the data points indicate that the crack speed has exceeded c_l of Homalite. However, a remotely loaded crack cannot exceed c_l of the material. Possible reasons for this overshoot could be the errors in crack speed measurements or an error in choosing the representative value (not that the wave speeds of the material are dependent on strain rate) of c_l of the material itself. At long times after impact, when the loading pulse has been cut off, the crack speed remains fairly constant around $\sqrt{2}\,c_s$.

It should be recalled here that the speed regime between c_R and c_s is forbidden by theory, based on energy considerations. For this speed regime, the asymptotic singular solution predicts radiation of energy away from the crack tip (negative energy release rate), which is not possible on physical grounds. The non-singular solution predicts zero energy flux to the tip, which is also inadmissible since crack propagation requires finite energy dissipation in the tip region. Hence a crack with a smoothly varying crack speed cannot pass through this forbidden regime. According to this rationale, a crack will have to jump discontinuously from the sub-Rayleigh regime to the intersonic regime. BURRIDGE (1973) and ANDREWS (1976) proposed a mechanism by which a sub Rayleigh mode II crack may attain intersonic speeds. In probably the first study on intersonic shear cracks, BURRIDGE (1973) analyzed the problem of a mode II crack growing self-similarly from zero initial length along an interface between two identical half spaces held together by Coulomb frictional contact and subjected to preimposed

uniform normal and shear stresses. In effect, he considered the limiting case of zero cohesive energy together with a finite stress limit, or in other words a propagating stress drop. He found that for subsonic crack speeds, a positive peak in shear stress propagating along with the shear wave front appears ahead of the crack tip. This peak in shear stress is observed to increase in magnitude as the crack speed increases and he postulated that it might lead to a secondary slip zone in front of the main crack tip provided the limiting static friction is small. He argued that a shear crack on such an interface will propagate at c_R and if the limiting static friction is small, it would propagate at c_l. ANDREWS (1976) analyzed numerically, the problem of transient symmetric expansion of a mode II crack propagating along a prescribed path with a linearly slip weakening cohesive zone (IDA, 1972; PALMER and RICE, 1973), under the action of a uniform remote shear stress. Corroborating Burridge's prediction, he found that the expanding shear crack rapidly accelerates to speeds close to c_R, and if the limiting static friction is not high enough, it initiates a secondary slip zone in front of it, which coalesces with the main crack and the combination was found to propagate at speeds around $1.5\,c_s$. These analytical and numerical observations describe one possible mechanism for a subsonic shear crack to cross the forbidden speed regime between c_R and c_s. However, another possibility for generating such intersonic speeds is to bypass this forbidden regime by nucleating a crack from the initial notch that instantaneously starts to propagate at a speed above c_s. Within our experimental time resolution, the second scenario seems to be the most probable.

Motivated by these experimental observations (reported in ROSAKIS *et al.* (1999; 2000)), numerical and atomistic work has been performed recently to investigate the mechanism of intersonic crack initiation and its propagation behavior along a weak plane. NEEDLEMAN (1999) performed a finite element simulation of the intersonic shear crack growth experiments reported here, using a cohesive surface constitutive relation for the weak crack path. He found that a shear crack initiating from a precrack along the weak path either propagates at c_R or accelerates to a near con-

stant intersonic speed above $\sqrt{2}\,c_s$. When the loading pulse was cut off, he observed the crack decelerating to $\sqrt{2}\,c_s$. ABRAHAM and GAO (2000) performed an atomistic simulation of shear crack propagation along a weak interface characterized by a Lennard-Jones potential, joining two harmonic crystals. Their simulations showed that a shear dominated crack, soon after initiation accelerates to c_R and then nucleates an intersonic daughter crack that travels at c_l, in accordance with the predictions of BURRIDGE (1973) and ANDREWS (1976). When the applied strain was completely relaxed after the initiation of the daughter crack, they found shear crack propagation at $\sqrt{2}\,c_s$, similar to the behavior observed in our experiments. GEUBELLE and KUBAIR (2000) studied numerically, using a spectral boundary element scheme, the problem of transient initiation and propagation of a mixed mode in-plane crack in its own plane under the action of remote uniform mixed mode loading. Using a quasi-linear cohesive failure model, they observed that a shear dominated crack can attain intersonic speeds either by initiation of a secondary slip zone in front of the tip (the Burridge-Andrews mechanism) or simply by a rapid, but smooth acceleration through the forbidden regime. The latter case, which was also observed by JOHNSON (1990) is in contradiction with the theoretical prediction that an in-plane crack with a continuously varying speed cannot accelerate through c_R.

As mentioned in Chapter 1, estimates of rupture speeds falling in the intersonic regime have been reported in seismological literature, primarily for shallow crustal earthquakes (ARCHULETA, 1984; OLSEN *et al.*, 1997; HERNANDEZ *et al.*, 1999; ELLSWORTH and CELEBI, 1999; BOUCHON *et al.*, 2000). For the recent Izmit (Turkey) earthquake, BOUCHON *et al.* (2000) reported that the portion of rupture zone propagating towards the east attained a remarkably high average speed of 4.7 km/s. With the average shear wave speed in crustal rocks at those depths being around 3.4 to 3.5 km/s, the rupture speed was about 1.4 c_s. This is very close to $\sqrt{2}\,c_s$, the speed around which a steady state intersonic shear crack was observed to propagate in our experiments.

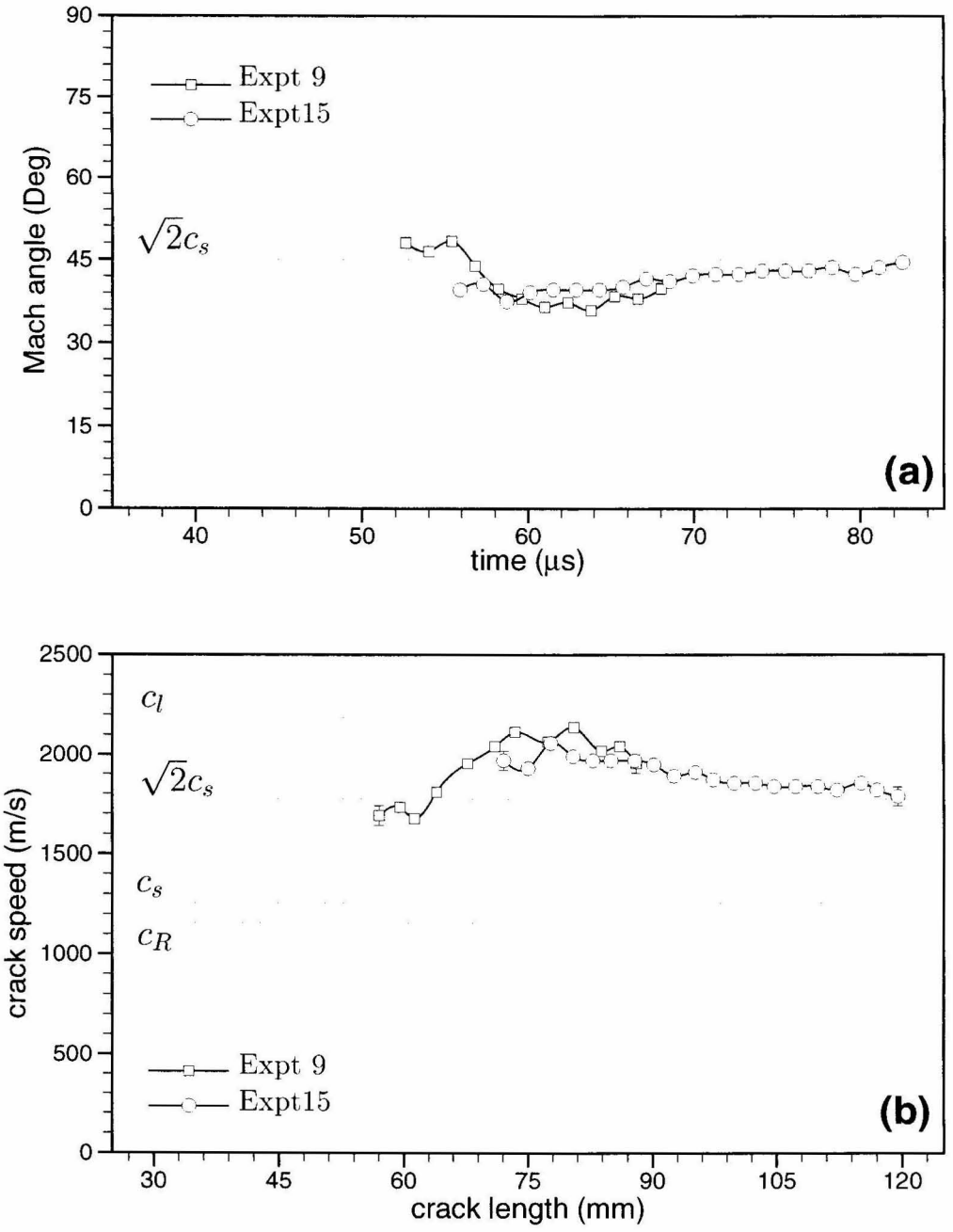

Figure 3.6: **(a)** Time history of Mach angle ξ. **(b)** Evolution of crack speed v (obtained from Mach angle), as the crack propagates along the weak plane. Expt 9 and Expt 15 are the same as in Figure 3.5.

Figure 3.6(a) shows the time history of Mach wave angle ξ for the same two experiments considered in Figure 3.5. At times close to initiation, the Mach waves are not radiated over a sufficient distance to be clearly distinguished. Hence Mach wave angle data is shown only after a substantial time has elapsed since crack initiation. The Mach wave angle under steady state conditions reaches an almost constant value around 43° to 45°. It was mentioned before that the unloading waves reflected from the far end of the specimen would reach the crack tip at $t = 76$ μs. However, from Figure 3.5(a) and Figure 3.6(a), we see that there is no discernible effect on the crack propagation behavior around this time. The high stress intensity around the intersonic crack tip coupled with the geometric attenuation and material dispersion of the loading pulse result in a rather negligible change in the mechanical state around the crack tip, due to the reflected pulse from the far end of the specimen. The crack speed data shown in Figure 3.6(b) was obtained by measuring the Mach angle and using the relation (3.2). Error in Mach angle measurements was about $\pm 1^{\circ}$, which resulted in errors in crack speed estimates of the order ± 30 m/s to ± 40 m/s. Crack speed estimates from Mach angle measurements are more accurate compared to those obtained from the crack length history due to the inherent propagation of errors in the differentiation process.

3.4 Comparison with Freund's Singular Solution

Consider a semi-infinite mode II crack propagating at a constant intersonic speed v in an otherwise unbounded homogeneous, isotropic, linear elastic solid under 2-D plane stress or plane strain conditions (see Figure 3.7(a)). (η_1, η_2) is a moving cartesian coordinate system centered at the crack tip and oriented as shown in Figure 3.7(a). (r, θ) is a moving polar coordinate system centered at the tip. The two dashed lines represent the two shear Mach waves radiated from the crack tip. They are inclined at an angle ξ to the crack faces, which is related to the crack speed v through (3.2). Freund (1979) obtained the asymptotic stress and particle velocity fields around a

steady state intersonic mode II crack, constrained to propagate along a straight line path. Note that even for transient intersonic mode II crack growth, the near tip field is dominated by the steady state solution for the instantaneous speed, provided the crack speed changes smoothly. The general form of the near tip singular stress field is given in (1.12–1.15) and the complete solution is given in Appendix A.

The stress field $\sigma_{\alpha\beta}$ at any point (η_1, η_2) in the tip vicinity is given by

$$\sigma_{11} = \frac{K_{II}^{*d}}{2\alpha_l\sqrt{2\pi}}\left[\frac{-(1+2\alpha_l^2+\hat{\alpha}_s^2)}{r_l^q}\sin q\theta_l + \frac{(1-\hat{\alpha}_s^2)\sin[\mathrm{sgn}(\eta_2)q\pi]}{(-\eta_1-\hat{\alpha}_s|\eta_2|)^q}H(-\eta_1-\hat{\alpha}_s|\eta_2|)\right], \tag{3.3a}$$

$$\sigma_{22} = \frac{K_{II}^{*d}}{2\alpha_l\sqrt{2\pi}}\left[\frac{(1-\hat{\alpha}_s^2)}{r_l^q}\sin q\theta_l - \frac{(1-\hat{\alpha}_s^2)\sin[\mathrm{sgn}(\eta_2)q\pi]}{(-\eta_1-\hat{\alpha}_s|\eta_2|)^q}H(-\eta_1-\hat{\alpha}_s|\eta_2|)\right], \tag{3.3b}$$

$$\sigma_{12} = \frac{K_{II}^{*d}}{\sqrt{2\pi}}\left[\frac{1}{r_l^q}\cos q\theta_l - \frac{\cos[\mathrm{sgn}(\eta_2)q\pi]}{(-\eta_1-\hat{\alpha}_s|\eta_2|)^q}H(-\eta_1-\hat{\alpha}_s|\eta_2|)\right], \tag{3.3c}$$

where $H(\cdot)$ is the unit step function. Further, the singularity exponent

$$q = \frac{1}{\pi}\tan^{-1}\left[\frac{4\alpha_l\hat{\alpha}_s}{(1-\hat{\alpha}_s^2)^2}\right], \tag{3.4}$$

$$\mathrm{sgn}(\eta_2) = \begin{cases} 1 & \eta_2 \geq 0\,, \\ -1 & \eta_2 < 0. \end{cases} \tag{3.5}$$

and the intersonic stress intensity factor K_{II}^{*d} is defined as

$$K_{II}^{*d} = \lim_{\eta_1\to 0^+}\sqrt{2\pi}\,\eta_1^q\,\sigma_{12}(\eta_1>0, \eta_2=0). \tag{3.6}$$

r_l, θ_l are defined in (1.13), α_l is defined in (1.8b), and $\hat{\alpha}_s$ in (1.14b).

Unlike the subsonic case, the crack tip stress singularity q for an intersonic mode II crack is a function of crack speed and its variation is plotted in Figure 3.7(b) for both plane stress and plane strain for the case of $\nu = 0.34$. It can be seen that q increases monotonically from 0 at c_s, to 1/2 at $\sqrt{2}\,c_s$, and thereafter decreases monotonically

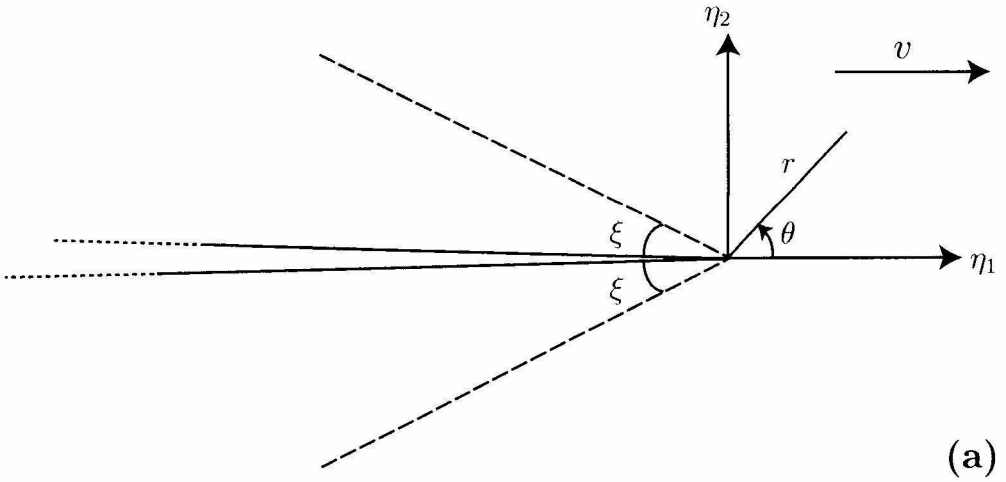

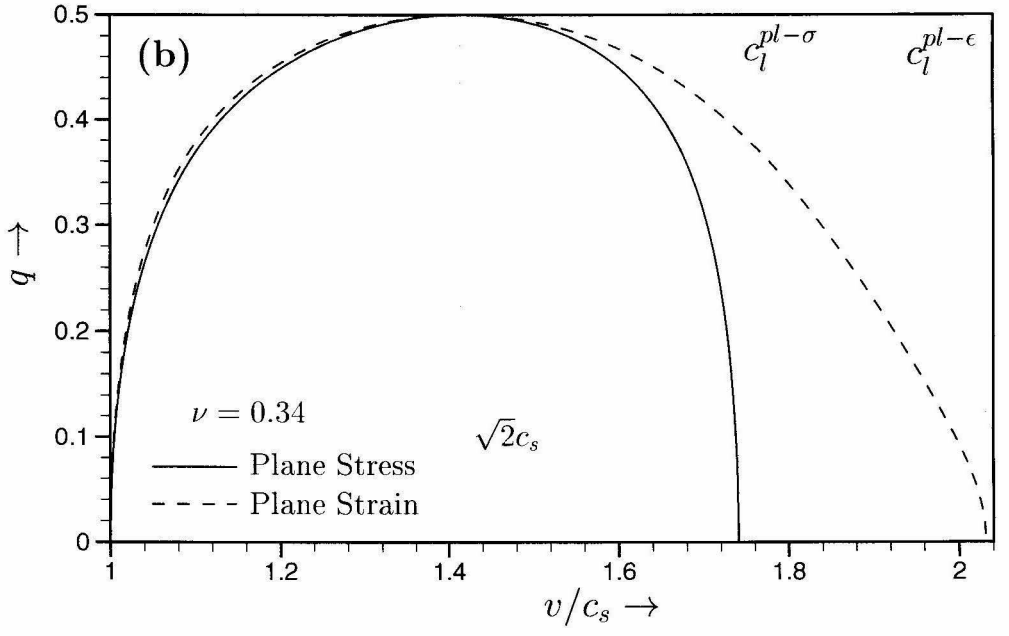

Figure 3.7: Intersonic ($c_s < v < c_l$) mode II crack in a homogeneous, isotropic, linear elastic solid. **(a)** Illustration showing the Mach waves and the crack tip coordinate system. **(b)** Crack tip stress singularity.

to 0 at c_l. Moreover, the stress field (3.3) predicts two Mach waves radiating from the crack tip. Stresses are singular not only at the crack tip, but all along the Mach fronts, with the same order of singularity as that at the tip. In addition, across the Mach front, the normal stress and normal velocity perpendicular to the front are continuous, where as the shear stress and tangential velocity suffer an infinite jump. Hence these fronts are shear Mach waves. At $v = \sqrt{2}\,c_s$, the terms in the stress field with the Heaviside step function vanish (see (3.3)), indicating that the Mach waves disappear at this intersonic speed. At this curious speed, the crack behaves "subsonic-like" with the singularity exponent associated with the near-tip stress field being equal to 1/2.

Figure 3.8 compares an isochromatic fringe pattern recorded during the experiment (Figure 3.8(a)) with that predicted by the Freund's singular solution (Figure 3.8(b)). As seen from (2.13) the isochromatic fringe order at any point may be related to the local stress state in the specimen. Within the region of dominance of the singular stress field, the isochromatic fringe order n at any point in the vicinity of an intersonic mode II crack is given by

$$n(\eta_1, \eta_2) = \frac{h}{F_\sigma} \frac{K_{II}^{*d}}{\sqrt{2\pi}} \sqrt{S_1^2 + 4S_2^2}\,, \tag{3.7}$$

where

$$S_1(\eta_1, \eta_2) = -\frac{(1+\alpha_l^2)}{\alpha_l} \frac{\sin q\theta_l}{r_l^q} + \frac{(1-\hat{\alpha}_s^2)}{\alpha_l} \frac{\sin\left[\mathrm{sgn}(\eta_2) q\pi\right]}{(-\eta_1 - \hat{\alpha}_s|\eta_2|)^q} H(-\eta_1 - \hat{\alpha}_s|\eta_2|)\,, \tag{3.8a}$$

$$S_2(\eta_1, \eta_2) = \frac{\cos q\theta_l}{r_l^q} - \frac{\cos\left[\mathrm{sgn}(\eta_2) q\pi\right]}{(-\eta_1 - \hat{\alpha}_s|\eta_2|)^q} H(-\eta_1 - \hat{\alpha}_s|\eta_2|)\,. \tag{3.8b}$$

F_σ, the material fringe constant for Homalite is given in Table 2.1 and h, the specimen thickness was 4.76 mm. The crack speed in both experimental and simulated fringe patterns was $1.47\,c_s$ and the Mach angle, $\xi \approx 43^\circ$. The intersonic stress intensity factor, K_{II}^{*d} for the simulation was chosen to be 2 MPa-m^q. A formal fit using linear least

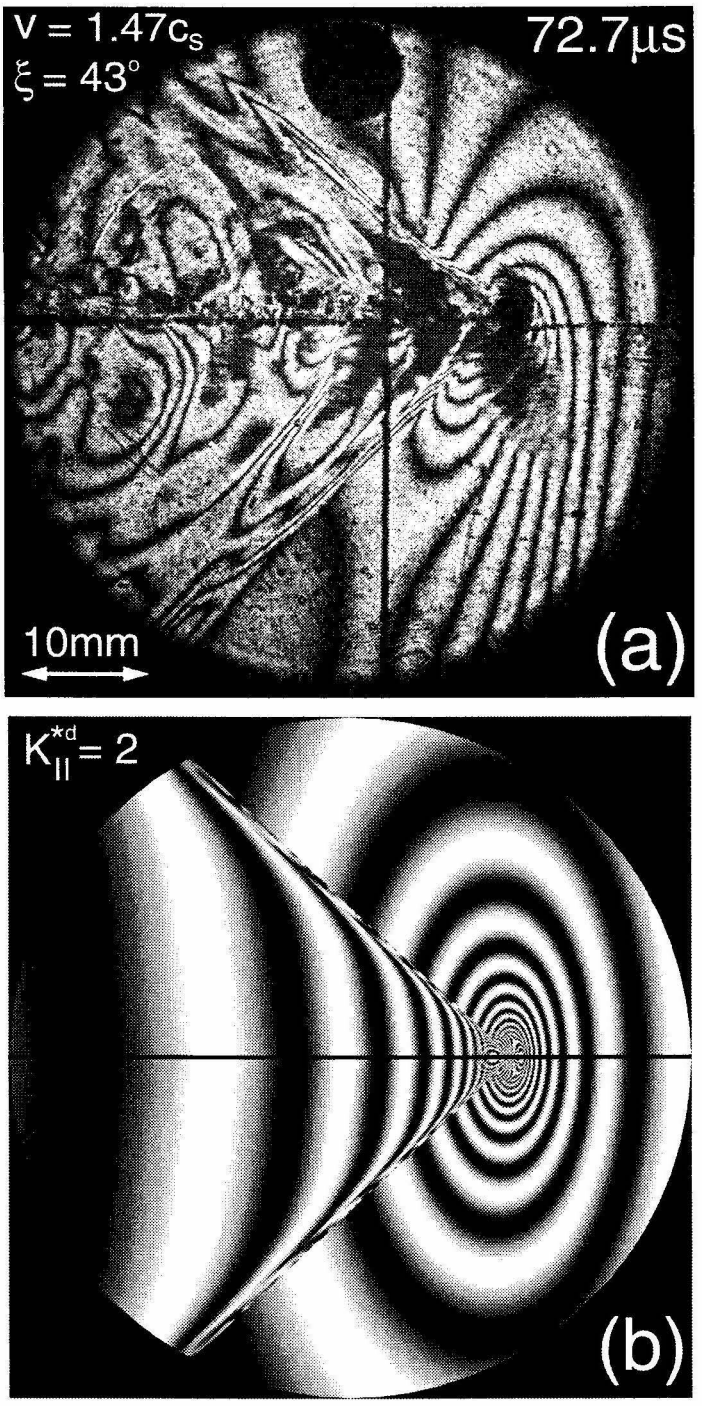

Figure 3.8: Isochromatic fringe pattern around a propagating intersonic crack along a weak plane in Homalite. **(a)** Experimental observation. **(b)** Theoretical prediction based on Freund's singular solution.

squares yielded a value for K_{II}^{*d} varying from 1.8 MPa-m^q to 2.3 MPa-m^q, depending upon the region around the tip from which the experimental data was chosen, to make the fit. There is no clear dominance of the singular field over an annular zone surrounding the tip. However, both the experimental and simulated fringe patterns are in good agreement with regard to the prediction of the two shock waves, their inclination to the crack faces, as well as the oval shape of the fringe pattern in front of the tip. However, there are clear discrepancies due to the influence of the loading waves, as well as due to crack face frictional contact and subsequent damage. Also, the transient effects, neglected in the singular solution above, should play a role in such a dynamic event.

Figure 3.9 compares a CGS fringe pattern recorded during the experiment (Figure 3.9(a)) with that predicted by the Freund's singular solution (Figure 3.9(b)). The CGS fringe pattern was taken from an experiment in which the specimen was the identical to the one shown in Figure 2.1(A), with both the halves being Homalite. However, a CGS interferometer was used to obtain the stress field information around the running crack (see Section 2.2.2). The projectile speed at impact was 25.1 m/s and the field of view of 50 mm diameter was centered 44 mm ahead of the notch tip. Following the relation (2.24) the CGS fringe order at any point may be related to the local stress state in the specimen. Within the region of dominance of the singular stress field, the CGS fringe order m at any point in the vicinity of an intersonic mode II crack is given by

$$m(\eta_1, \eta_2) = \frac{c_\sigma h \Delta}{p} \frac{K_{II}^{*d}}{\sqrt{2\pi}} \frac{q(\alpha_l^2 + \hat{\alpha}_s^2)}{\alpha_l} \frac{\sin(q+1)\theta_l}{r_l^{q+1}} . \tag{3.9}$$

The thickness h of the Homalite halves was 4.45 mm, the grating pitch p was 25.4 μm and their separation distance Δ was 32.5 mm. c_σ, the stress-optic coefficient of Homalite is given in Table 2.1. The crack speed in both experimental and simulated fringe patterns was $1.51\, c_s$ and the Mach angle $\xi \approx 51^\circ$. The intersonic stress intensity factor K_{II}^{*d} for the simulation was chosen to be 2 MPa-m^q. This value gives roughly

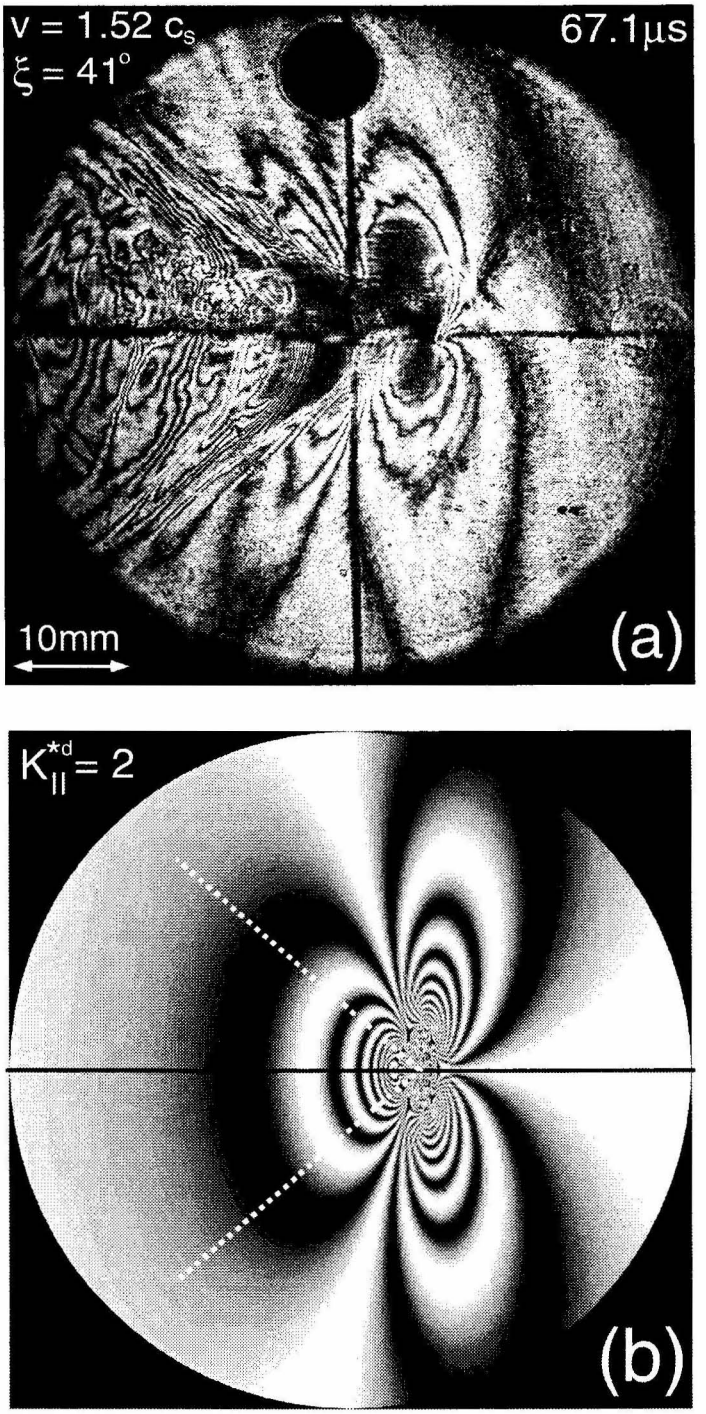

Figure 3.9: CGS fringe pattern around a propagating intersonic crack along a weak plane in Homalite. **(a)** Experimental observation. **(b)** Theoretical prediction based on Freund's singular solution. The expected position of the shear Mach waves is shown by white dashed lines.

the same fringe order, at distances far away from the crack tip, as recorded in the experiments. From (3.9) one can readily see that the simulated fringe pattern is not affected by the Mach waves present in the near tip stress field. This is reflected in Figure 3.9(b) where we see the characteristic three lobes of the CGS fringe pattern. The position of the Mach waves is indicated by the two white dashed lines. CGS fringes are contours of constant gradients of the hydrostatic component of the stress tensor. These gradients are continuous across the shear Mach fronts (see (3.9)) and hence are not expected to be recorded by the CGS interferometer. However, they are seen in the experimental fringe pattern (Figure 3.9(b)) where they are not sharp, but delineate a region behind the tip, where the fringe pattern bears no resemblance to that expected from the singular stress field. As seen in the comparison of the isochromatic fringe patterns, the stress field behind the Mach waves is strongly influenced by the damage behind the main crack front due to the initiation and propagation of secondary tensile cracks at a steep angle to the crack plane, which is discussed in detail in the next section. However, the overall shape of the CGS fringes in front of the crack tip is very similar to that predicted by the Freund's singular solution.

Homalite is not an ideal material for performing CGS interferometry with the experimental setup as shown in Figure 2.6. Due to its property of stress-induced birefringence, the optical path change is also influenced by the orientation of the axis of polarization of the incoming light rays with the principal axes associated with the local stress state. This makes the interpretation of the CGS fringes according to (3.9) only approximately correct. From (3.7), we can see that the isochromatic fringe order is singular at the crack tip with a singularity exponent q, where as the CGS fringe order (see (3.9)) is singular at the crack tip with a singularity exponent $q+1$. This results in the CGS fringes being much more concentrated (bunched up) at the tip as compared to isochromatic fringes. CGS fringes, which record information about the magnitude of stress gradient, are rather insensitive to stress waves as compared to isochromatic fringes, which record information about the magnitude of the stress

state itself. Stress waves, especially of the ramp type as shown in Figure 3.1(c) induce rather small stress gradients and hence the CGS fringe pattern as shown in Figure 3.9(a) is not influenced by the loading waves as much as the isochromatic fringe pattern shown in Figure 3.8(a). Both the equations (3.7) and (3.9) assume that the generalized plane stress approximation is valid within the field of view. However, due to the finite thickness of the specimen, 3-D effects become important at distances (a fraction of the specimen thickness) close to the crack tip as well as in some angular sectors. The exact regions where the generalized plane stress approximation is valid as well as the range of dominance of the singular solution can be determined only through a full 3-D numerical simulation of intersonic crack growth taking the actual specimen geometry into account.

3.5 Secondary Opening Cracks

Figure 3.10(b) shows a post-mortem photograph of a portion near the notch tip on the upper half of the test specimen. Figure 3.10(a) shows an illustration of the specimen with the area photographed shown as a dashed rectangle. Starting from a finite distance ahead of the notch tip along the crack path, a series of short opening cracks, parallel to each other and inclined to the main shear crack path can be observed. These secondary cracks were observed all along the main crack path on the upper half, but no such cracks were observed in the lower half of the specimen. It can be concluded that these cracks have initiated on the upper crack face, propagated a finite distance (varying from few μm to few mm) slightly off-vertical into the upper half of the specimen and subsequently got arrested. Occasionally, a few cracks have gone further. The broken specimens are carefully reassembled and the angle of inclination of the secondary cracks to the vertical (line perpendicular to the crack plane) was measured. The measurements were made on specimens from five different experiments and Figure 3.10(b) shows a variation of the secondary crack angle with frequency (# of secondary cracks inclined at the same angle). It was found that the angle of

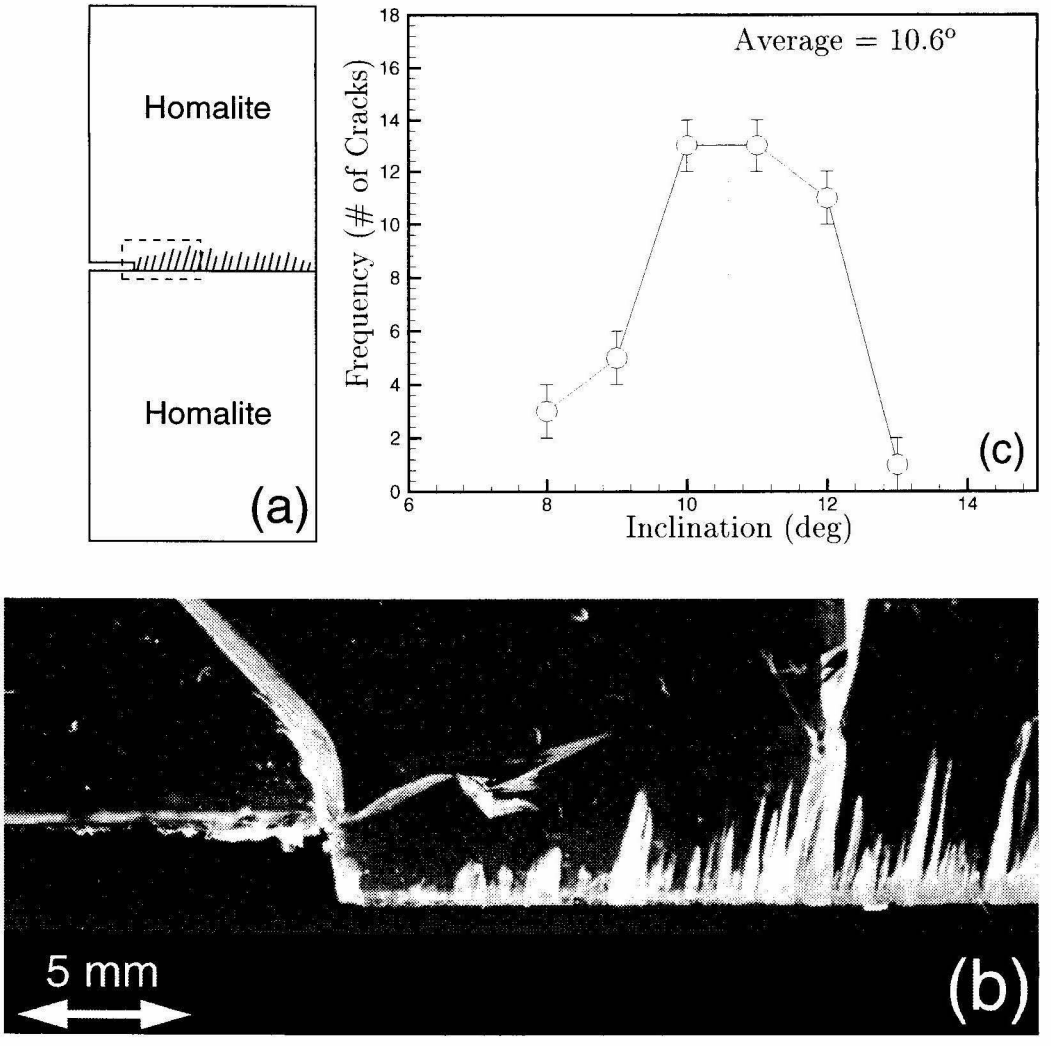

Figure 3.10: Secondary cracks formed on the tensile half of the specimen during intersonic shear crack growth. **(a)** Illustration of the specimen showing the location and orientation of the secondary tensile cracks (not to scale). **(b)** Magnified photograph of the region delineated by the dashed rectangle in the illustration in **(a)**. **(c)** Measured data on the inclination of the secondary cracks to the vertical.

inclination varies roughly from 8° to 13°, with an average of about 10.6°. Within the measurement error of ±1°, no strong correlation was found between the secondary crack angle and the main shear crack speed. The angle of inclination was found to reduce slightly towards the edge of the specimen, possibly due to the influence of the free boundary. Cracks that grew longer curved towards the vertical, but the initial orientation of all of them was almost the same. Most of the secondary cracks, especially the short ones seem to have a 3-D structure, in that they didn't extend through the specimen thickness.

The initiation, propagation and arrest of these cracks can be observed in real time. The high-speed images of the isochromatic fringe pattern around the main shear crack tip contain information about the initiation and the growth of these cracks. A typical photograph in which the phenomenon can be clearly distinguished is shown in Figure 3.11(a). A series of symmetric shadow spots, associated with strong deformation around the secondary crack tips, originate on the crack face, propagate a finite distance into the upper half of the specimen and arrest subsequently. Such a series of shadow spots surrounding these secondary cracks are also clearly distinguishable in Figure 3.3(f). The centers of all these shadow spots fall on almost a straight line inclined at about $\approx 23^{\circ}$ (α) to the crack face. From this measure, as well as the small inclination of these cracks from the vertical ($\theta^{*} \approx 11^{\circ}$) and from the speed of the main shear crack, an estimate of their propagation speed was found to be $\approx 0.6\, c_s$. The stress field surrounding the main intersonic mode II crack provides the driving force for the secondary cracks and as it passes by rapidly, the driving force diminishes and they arrest. The symmetric nature of the shadow spots reveals the tensile (mode-I) nature of these secondary cracks. If we extend the line passing through the center of the shadow spots to the crack face, we can readily see that they originate a finite, albeit a small distance behind the main crack tip. Hence, formation of these secondary cracks is not akin to the typical branching phenomenon observed in high-speed subsonic crack propagation. Nor are they akin to the *en echelon* cracks

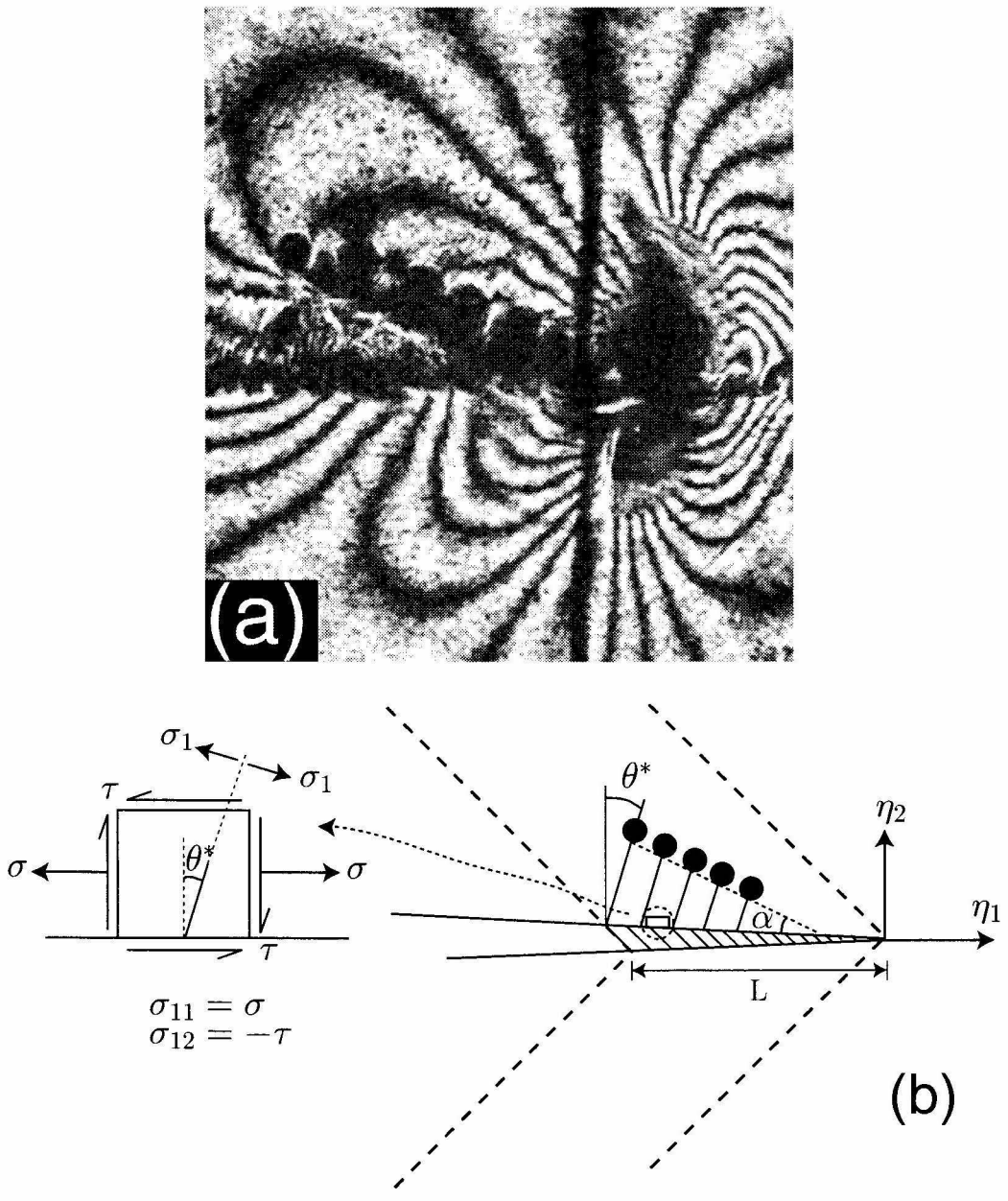

Figure 3.11: Formation of secondary tensile cracks during intersonic shear crack growth along a weak plane in Homalite. **(a)** Isochromatic fringe pattern showing the initiation and propagation of secondary cracks behind the main intersonic crack. **(b)** An illustration of the stress state on the crack face, providing an explanation for the inclination of these secondary cracks to the vertical.

formed in front of a shear crack when its kinking into a tensile crack is prevented due to overall compressive stresses. These secondary, subsonic, opening mode cracks behind the main intersonic shear crack tip cannot be explained completely based on the asymptotic solution for a traction free intersonic crack. The stress component σ_{11} (direct stress parallel to the crack faces) around the intersonic shear crack tip is tensile in the top half of the specimen, whereas it is compressive in the bottom half. This explains why the opening cracks are observed only in the tensile half of the specimen. If the cracks originated on a traction free surface, we would expect them to propagate vertically based on a maximum principal stress criterion for brittle fracture. The inclination of the secondary cracks from the vertical can only be explained in terms of a more complex state of stress at the initiation site. As mentioned before, it is likely that the crack faces are in contact and subsequently undergo frictional sliding resulting in a biaxial state of stress at the initiation site. However, most of these cracks seem to originate only a couple of mm behind the main crack tip and in the absence of overall normal compression, a simple way to include the frictional stress at the initiation site is to introduce a shear cohesive zone of finite size behind the tip. Indeed, subsequently we introduce a line cohesive zone at the intersonic crack tip to explain the inclination of these secondary cracks to the vertical. Figure 3.11(b) shows an illustration of the region near the crack tip explaining our interpretation as to the origin and directivity of the secondary tensile cracks. The main intersonic shear crack is propagating with a line cohesive zone of length L in front of it. The secondary cracks originate on the top cohesive surface, where the stress state is 2-dimensional, with a tensile direct stress σ parallel to the interface along with a local shear cohesive traction, $-\tau$. With the biaxial state of stress at the initiation site, the maximum principal tensile stress acts on a plane inclined at an angle θ^* to the vertical, thus explaining the off-vertical orientation of these cracks.

3.6 Necessity for a Cohesive Zone Model

From (3.3) we see that the intersonic stress intensity factor, K_{II}^{*d} governs the amplitude of the near tip stress field for an intersonic mode II crack. However, unlike for stationary and subsonically propagating dynamic cracks, the definition of K_{II}^{*d} (see (3.6)) varies with crack speed. As a consequence, even if K_{II}^{*d} is the same at two stages of intersonic mode II crack growth, it does not necessarily mean that the level of stress in front of the tip is the same, provided the crack speed differs. Only for cases where the intersonic mode II crack propagates at a more or less constant speed, K_{II}^{*d} may be taken as an appropriate parameter to characterize the near tip stress field. Also, the physical units of K_{II}^{*d} in SI units are MPa-m^q. This indicates that the units change with crack speed! Hence, any intersonic propagation criterion based on K_{II}^{*d} requires the intersonic mode II fracture toughness to exhibit a certain dependence on crack speed, whereas any such dependence must be entirely phenomenological. Thus, K_{II}^{*d} is not an appropriate crack tip characterizing parameter on which to base an intersonic mode II propagation criterion.

The dynamic energy release rate G for a steady state intersonic mode II crack, defined as the energy flux into the crack tip per unit crack advance per unit length along the crack front, may be expressed as (Irwin's crack closure integral)

$$G = \lim_{a \to 0} \frac{1}{2a} \int_0^a \sigma_{12}(a - r)\delta_1(r)dr \,, \tag{3.10}$$

where a is an arbitrary length scale, r is the distance behind the tip and σ_{12} and δ_1 are measured on the crack plane. Substituting the expressions for σ_{12} and δ_1 from Appendix A, we obtain

$$G = \frac{\left(K_{II}^{*d}\right)^2}{2\pi\mu} \frac{\hat{\alpha}_s(1 + \hat{\alpha}_s^2)}{(1 - q)R_q} B(2 - q, 1 - q) \lim_{a \to 0} a^{1-2q} \,, \tag{3.11}$$

where $B(x, y)$ is the standard beta function. From the above expression, we see that

the dynamic energy release rate G is zero every where in the intersonic regime except at $\sqrt{2}\,c_s$ where it has a finite value, given by

$$G = \frac{K_{II}^{*d^2}}{4\mu\alpha_l}\,. \tag{3.12}$$

A more general definition of the dynamic energy release rate G is given by FREUND (1989), which for steady state crack growth reduces to

$$G = \lim_{\Sigma\to 0} \oint_{\Sigma} \left[\sigma_{\alpha\beta} n_\beta u_{\alpha,1} - \frac{1}{2}(\sigma_{\alpha\beta}u_{\alpha,\beta} + \rho v^2 u_{\alpha,1}u_{\alpha,1})n_1\right] d\Sigma\,, \tag{3.13}$$

where Σ is a contour starting on the lower crack face and ending on the upper crack face. n_α are the coordinates of unit vector normal to the contour Σ, pointing in the outward direction and ρ is the mass density. For any contour Σ, it can be shown that $G = 0$ for all intersonic speeds, except for $v = \sqrt{2}\,c_s$, where it has a finite value given by (3.12). It will be shown in the next chapter that energy flows towards the crack tip from material upstream, which is radiated away by the Mach waves without deposition at the tip. Note that the singular Mach waves are non-dissipative. Following ABEYARATNE and KNOWLES (1990), one can show that the scalar driving traction on the singular lines $\eta_1 \pm \hat{\alpha}_s\eta_2 = 0$ vanishes. The scalar driving traction $f(\eta_1, \eta_2)$ on a singular line is expressed as

$$f(\eta_1,\eta_2) = [U(\eta_1,\eta_2)]_\delta - \frac{1}{2}\left\{\sigma_{\alpha\beta}(\eta_1+\delta,\eta_2) + \sigma_{\alpha\beta}(\eta_1-\delta,\eta_2)\right\}[\epsilon_{\alpha\beta}(\eta_1,\eta_2)]_\delta$$

where U is the strain energy density and $[\cdot]_\delta$ is the δ-jump across the shock line. This implies that there is no energy dissipation as the singular Mach waves move in the material. Energy is dissipated only at the crack tip, if possible. For intersonic mode II cracks, the idealization of the crack tip process zone to a point-size dissipative region results in a physically unrealistic situation, wherein the requirement of a positive

energy flux to the crack tip region is met only at $\sqrt{2}\,c_s$. On the contrary, the experimental observations show crack growth at all intersonic speeds. ANDREWS (1976) pointed out that for intersonic cracks, where the crack tip stress singularity is less than 1/2, a non-zero fracture energy is supported only for the case where the stress drop is not abrupt, *i.e.*, the crack tip region must have a finite extent. A comparatively simple way to eliminate this difficulty would be to incorporate a dissipative zone of finite size in front of the tip (ANDREWS, 1976; BROBERG, 1989). In such a case, they showed that positive energy flux to the dissipative zone results at all intersonic speeds except at c_s and c_l.

Another motivation to study intersonic shear cracks with a finite-sized shear cohesive zone is shown in Figure 3.12. It shows a sequence of isochromatic fringe patterns around an intersonic mode II crack along a weak plane in Homalite-100. Here the impact speed was 20.8 m/s and the field of view of 50 mm diameter, was centered on the weak plane, 38.2 mm ahead of the notch tip. Compared to the sequence shown in Figure 3.4, the impact speed here is lower and also the field of view is much closer to the initiation site. In such a case, we see that the Mach waves radiating from the tip are no longer very sharp and have structure with a finite width. The finite width of the Mach waves is not modeled by the singular solution (FREUND, 1979), which predicts line Mach waves. An intersonic mode II crack model incorporating a cohesive zone of finite extent is required to model the structure of the Mach waves as well as the crack tip process zone.

Also, as mentioned in the previous section, inclination of the secondary cracks to the vertical may be readily explained by incorporating a cohesive zone of finite size in front of the tip. A dissipative zone of finite extent can be incorporated readily by considering a line cohesive zone of finite extent in front of the tip. Such a line cohesive zone has a natural motivation from the experiments described above, where the fracture process zone is mostly confined to a thin weak layer in front of the crack tip. In the next two chapters, line cohesive zone models for intersonic mode II

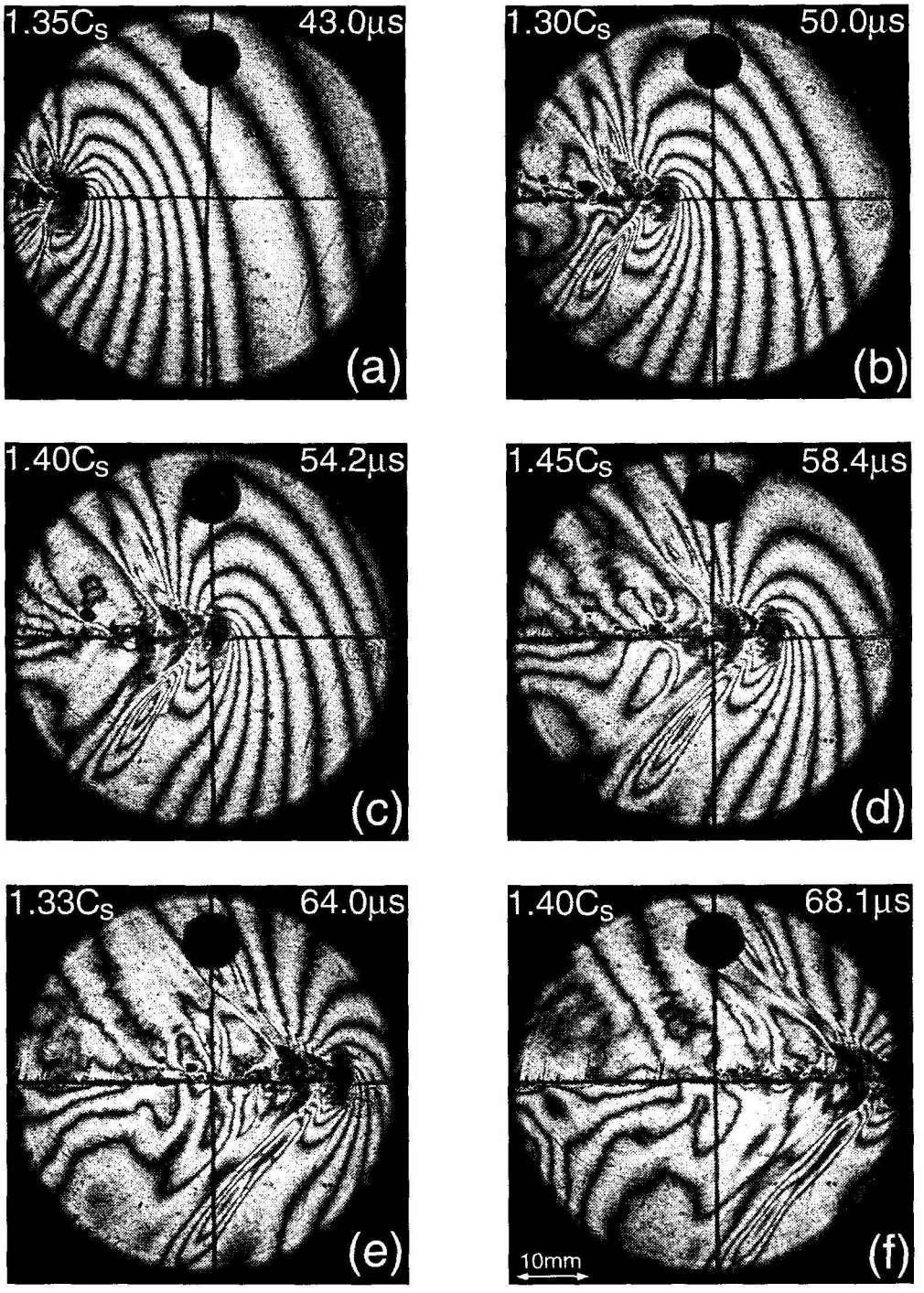

Figure 3.12: Isochromatic fringe pattern around a propagating intersonic crack along a weak plane in Homalite showing a cohesive zone of finite extent near the tip. Impact speed = 20.8 m/s. Field of view of 50 mm diameter is centered on the bond line, 38.2 mm ahead of the notch tip.

crack growth are introduced along with a propagation criterion, and their predictions regarding energy release rate, structure of Mach waves, inclination of secondary cracks to the vertical as well as stability of crack growth are critically examined.

Nomenclature

(η_1, η_2)	crack tip Cartesian coordinate system
(r, θ)	crack tip polar coordinate system
(r_l, θ_l)	relativistic coordinates
α	angle made by the line joining the secondary crack tips with the crack plane
$\alpha_l, \hat{\alpha}_s$	relativistic parameters
Δ	grating separation distance
δ_α	displacement discontinuity across the crack faces
$\epsilon_{\alpha\beta}$	cartesian components of the strain tensor
Γ	mode I fracture energy
Γ_{pl}	fracture energy associated with the weak plane
K_{II}^{*d}	intersonic stress intensity factor
μ	shear modulus
ν	Poisson's ratio
Ω	kink angle

Ω^*	kink angle that would maximize the energy release rate
ψ	mode mixity
ρ	mass density
σ	compressive normal stress induced from impact
σ_1	maximum principal tensile stress
$\sigma_{\alpha\beta}$	Cartesian components of the stress tensor
θ^*	angle of inclination of the secondary cracks to the vertical
ξ	mach angle
a	arbitrary length scale
c_σ	stress-optic coefficient
c_l	longitudinal wave speed
c_R	Rayleigh wave speed
c_s	shear wave speed
d	distance from the impact edge
f	scalar driving traction
F_σ	material fringe constant
G	energy release rate for straight ahead crack advance
G^t	dynamic energy release rate associated with the kinked crack
h	specimen thickness
$H(\cdot)$	Heaviside step function

K_I, K_{II}	mode I and mode II stress intensity factors
K_{Ic}, K_{IIc}	mode I & mode II fracture toughnesses
L	cohesive zone length
l	crack length
m	CGS fringe order
n	isochromatic fringe order
n_α	unit outward vector normal to the contour Σ
p	grating pitch
q	singularity exponent for an intersonic mode II crack
t	time after impact
t_o	time of crack initiation
U	strain energy density
V	impact speed
v	crack speed

Bibliography

ABEYARATNE, R. and KNOWLES, J. K. (**1990**), On the Driving Traction Acting on a Surface of Strain Discontinuity in a Continuum, *Journal of the Mechanics and Physics of Solids*, **38**(3), pp. 345–360.

ABRAHAM, F. F. and GAO, H. J. (**2000**), How Fast can Cracks Propagate?, *Physical Review Letters*, **84**(14), pp. 3113–3116.

ANDREWS, D. J. (**1976**), Rupture Velocity of Plane Strain Shear Cracks, *Journal of Geophysical Research*, **81**(32), pp. 5679–5687.

ARCHULETA, R. J. (**1984**), A Faulting Model for the 1979 Imperial-Valley Earthquake, *Journal of Geophysical Research*, **89**(6), pp. 4559–4585.

BOUCHON, M., TOKSÖZ, N., KARABULUT, H., BOUIN, M. P., DIETRICH, M., AKTAR, M., and EDIE, M. (**2000**), Seismic Imaging of the 1999 Izmit (Turkey) Rupture Inferred from the Near-Fault Recordings, *Geophysical Research Letters*, **27**(18), pp. 3013–3016.

BROBERG, K. B. (**1987**), On Crack Paths, *Engineering Fracture Mechanics*, **28**(5-6), pp. 663–679.

BROBERG, K. B. (**1989**), The Near-Tip Field at High Crack Velocities, *International Journal of Fracture*, **39**(1-3), pp. 1–13.

BURRIDGE, R. (**1973**), Admissible Speeds for Plane Strain Shear Cracks with Fric-

tion but Lacking Cohesion, *Geophysics Journal of the Royal Astronomical Society*, **35**, pp. 439–455.

ELLSWORTH, W. L. and CELEBI, M. (**1999**), Near-Field Displacement Time Histories of the M 7.4 Kocaeli (Izimit), Turkey, Earthquake of August 17, 1999, in *AGU99 Fall Meeting*, San Fransisco, CA.

FREUND, L. B. (**1979**), The Mechanics of Dynamic Shear Crack Propagation, *Journal of Geophysical Research*, **84**(B5), pp. 2199–2209.

FREUND, L. B. (**1989**), *Dynamic Fracture Mechanics*, Cambridge University Press, Cambridge.

GEUBELLE, P. H. and KUBAIR, D. (**2000**), Intersonic Crack Propagation in Homogeneous Media Under Shear Dominated Loading: I. Numerical Analysis, to appear in JMPS.

HERNANDEZ, B., COTTON, F., and CAMPILLO, M. (**1999**), Contribution of Radar Interferometry to a Two-Step Inversion of the Kinematic Process of the 1992 Landers Earthquake, *Journal of Geophysical Research*, **104**(B6), pp. 13083–13099.

HUTCHINSON, J. W. and SUO, Z. (**1992**), Mixed-Mode Cracking in Layered Materials, *Advances in Applied Mechanics*, **29**, pp. 63–191.

IDA, Y. (**1972**), Cohesive Force Across the Tip of a Longitudinal-Shear Crack and Griffith's Specific Surface Energy, *Journal of Geophysical Research*, **77**(20), pp. 3796–3805.

JOHNSON, E. (**1990**), On the Initiation of Unidirectional Slip, *Geophysical Journal International*, **101**(1), pp. 125–132.

LEE, Y. J. and FREUND, L. B. (**1990**), Fracture Initiation Due to Asymmetric Impact Loading of an Edge Cracked Plate, *Journal of Applied Mechanics*, **57**(1), pp. 104–111.

MASON, J. J., LAMBROS, J., and ROSAKIS, A. J. (**1992**), The Use of a Coherent Gradient Sensor in Dynamic Mixed Mode Fracture Mechanics Experiments, *Journal of the Mechanics and Physics of Solids*, **40**(3), pp. 641–661.

NEEDLEMAN, A. (**1999**), An Analysis of Intersonic Crack Growth Under Shear Loading, *Journal of Applied Mechanics*, **66**(4), pp. 847–857.

OLSEN, K. B., MADARIAGA, R., and ARCHULETA, R. J. (**1997**), Three-Dimensional Dynamic Simulation of the 1992 Landers Earthquake, *Science*, **278**(5339), pp. 834–838.

PALMER, A. C. and RICE, J. R. (**1973**), The Growth of Slip Surfaces in the Progressive Failure of Over-Consolidated Clay, *Proceedings of the Royal Society of London*, **A332**, pp. 527–548.

ROSAKIS, A. J., SAMUDRALA, O., and COKER, D. (**1999**), Cracks Faster than the Shear Wave Speed, *Science*, **284**(5418), pp. 1337–1340.

ROSAKIS, A. J., SAMUDRALA, O., and COKER, D. (**2000**), Intersonic Shear Crack Growth Along Weak Planes, *Materials Research Innovations*, **3**(4), pp. 236–243.

SCHARDIN, H. (**1959**), Velocity Effects in Fracture, in *Fracture*, edited by B. L. Averback, John Wiley, pp. 12.1–12.32.

Chapter 4

A Rate Independent Cohesive Zone Model

In the previous chapter, experimental records of intersonic mode II crack tip fields were compared with the predictions of Freund's singular solution (FREUND, 1979), thereby motivating the necessity of a cohesive zone model. In the current chapter, subsonic and intersonic mode II crack propagation with a rate independent Dugdale type cohesive zone is analyzed. Cohesive zone models for intersonic mode II crack propagation have been used in the past, primarily in numerical simulations of earthquake fault rupture (modeled as a dynamically extending shear crack). A class of cohesive zone models, the so called slip weakening models (IDA, 1972; PALMER and RICE, 1973) have been employed for this purpose. They account for the zone of strength degradation at an extending shear rupture front, caused due to nonuniform frictional sliding. ANDREWS (1976) used a finite difference technique to simulate transient symmetric expansion of a mode II crack propagating in its own plane with a slip weakening cohesive zone, under the action of a uniform remote shear stress distribution. BURRIDGE *et al.* (1979) investigated the stability of a steady state mode II semi-infinite crack with a slip weakening cohesive zone driven by a point load acting on the crack faces a finite distance behind the tip. BROBERG (1994; 1995) solved analytically the problem of a self-similar intersonic mode II crack expanding symmetrically from zero initial length under the action of remote uniform shear stress.

By assuming a Barenblatt type process zone, he computed the energy flux into the intersonic crack tip region. Slip weakening cohesive zones were also used by JOHNSON (1990) to show that steady state unidirectional mode II crack growth is possible in earthquake events.

More recent studies of intersonic crack growth using cohesive crack models were motivated by the experiments of Rosakis and coworkers on homogeneous, isotropic solids (previous chapter), on bimaterials (LAMBROS and ROSAKIS, 1995) and on transversely isotropic solids (COKER and ROSAKIS, 2000). YU and SUO (2000) developed a unified method based on analytic function theory to obtain the near tip fields for a quasi-static/subsonic/intersonic crack in a homogeneous solid or along a bimaterial interface with the constituents being either isotropic or anisotropic. They used a Dugdale type cohesive zone model and identified those crack speed regimes that result in negative cohesive zone length to be forbidden. NEEDLEMAN (1999) performed a finite element simulation of the intersonic shear crack experiments of ROSAKIS *et al.* (1999) using a cohesive surface constitutive relation for the weak crack path. He found that a shear crack initiating from a precrack along the weak path either propagates at c_R or accelerates to a near constant intersonic speed above $\sqrt{2}\,c_s$. He examined the effect of shear strength of the interface, the fracture energy and the duration of the loading pulse on the transition from a sub-Rayleigh to an intersonic speed, as well as on the terminal speed achieved. GEUBELLE and KUBAIR (2000) studied numerically, using a spectral boundary element scheme, the problem of transient initiation and propagation of a mixed mode in-plane crack in its own plane under the action of remote uniform mixed mode loading. Using a quasi-linear cohesive failure model, they observed that a shear dominated crack can attain intersonic speeds either by initiation of a secondary slip zone in front of the tip (the Burridge-Andrews mechanism) or simply by a rapid, but smooth acceleration through the forbidden regime.

The current work as summarized in this chapter, aims at adding to the substan-

tial body of knowledge on dynamic mode II crack growth. In particular, the work is motivated by the experimental observations of intersonic shear cracks in our laboratory. A Dugdale type cohesive law is assumed, wherein the cohesive shear traction is constant through out the cohesive zone. Complete decohesion is assumed to occur when the crack tip sliding displacement reaches a material specific critical value. Closed form expressions are obtained for the near tip fields. With a cohesive zone of finite size, it is found that the dynamic energy release rate is finite through out the intersonic regime. Issues concerning stability of crack growth are addressed and favorable speed regimes are identified. The influence of shear strength of the crack plane on crack propagation behavior is investigated. The isochromatic fringe patterns predicted by the analytical solution are compared with the experimental observations and comments are made on the validity of the proposed model.

4.1 Energy Flux Vector Field

At first, we complete the discussion on energy concepts for an intersonic mode II crack (see Section 3.6). Consider a mode II crack extending at a constant speed v through a 2D homogeneous, isotropic, linear elastic solid undergoing plane stress deformation (see Figure 3.7(a)). Also, consider an imaginary contour Σ starting on the lower crack face, surrounding the crack tip and ending on the upper crack face. Σ is assumed to translate along with the crack tip, and let $\vec{n} = n_\alpha e_\alpha$ be the unit outward vector normal to it at any point. The instantaneous rate of flow of energy F_e through Σ towards the crack tip is given by (FREUND, 1989)

$$F_e(\Sigma) = \int_\Sigma \left[\sigma_{\alpha\beta} \frac{\partial u_\alpha}{\partial t} + (U+T) v \delta_{1\beta} \right] n_\beta \, d\Sigma \,. \tag{4.1}$$

The first term in the integral represents the rate of work done on the material inside of Σ, by the tractions acting on Σ. The second term represents the contribution to the energy flux due to transport of material through Σ, with its associated energy density, $U+T$. U is the strain energy density field and T is the kinetic energy density

field and are given by

$$U = \tfrac{1}{2}\sigma_{\alpha\beta}u_{\alpha,\beta}\,, \tag{4.2a}$$

$$T = \tfrac{1}{2}\rho\,\dot{u}_\alpha\dot{u}_\alpha\,. \tag{4.2b}$$

Combining (4.1) and (4.2) we can express energy flux through Σ as

$$F_e(\Sigma) = \int_\Sigma \vec{P}.\vec{n}\,d\Sigma\,, \tag{4.3}$$

where $\vec{P}$ is the energy flux vector field. For a steadily propagating mode II crack, its components are given by

$$P_\gamma = -v\sigma_{\alpha\gamma}u_{\alpha,1} + \tfrac{1}{2}v\delta_{1\gamma}\left(\sigma_{\alpha\beta}u_{\alpha,\beta} + \rho v^2 u_{\alpha,1}u_{\alpha,1}\right)\,. \tag{4.4}$$

The dominant stress and particle velocity fields around a subsonically propagating mode II crack are given in FREUND (1989) and those around an intersonically propagating mode II crack are given in Appendix A.

Figures 4.1(a) and 4.1(b) show the energy flux vector field around the tip of a propagating mode II crack at two different subsonic speeds, $0.6\,c_s$ and $0.95\,c_s$ respectively. Also, Figures 4.2(a) and 4.2(b) show the energy flux vector field around the tip of a propagating mode II crack at two different intersonic speeds, $1.2\,c_s$ and $1.6\,c_s$ respectively. The crack tip in all these figures is located at the center of the field of view and the crack faces lie on a horizontal line extending to the left. The energy flux vectors are drawn on a series of 8 concentric circular contours with the crack tip at the center, and their radii ranging from 0.125 units to 1 unit with an increment of 0.125 units. The flux vectors are drawn on these circles at points whose angular coordinates range from -175° to 175° with an increment of 10°. The length of each vector shown, is a measure of the magnitude of energy flux at that point. The magnitude scale shown stands for so many units of $(K_{II}^d)^2 c_s/2\pi\mu$ in the case of subsonic

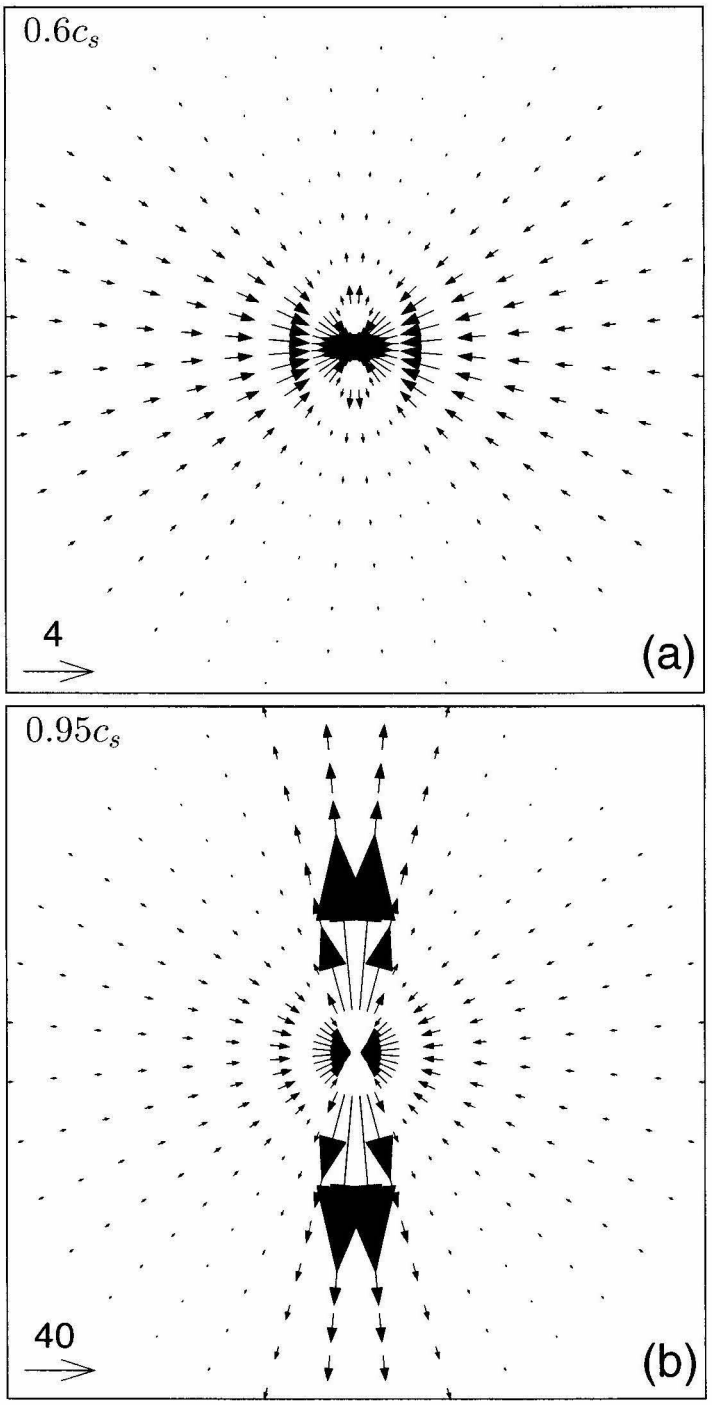

Figure 4.1: Energy flux vector field around the tip of a subsonically propagating mode II crack. **(a)** $v/c_s = 0.6$. There is a net $+ve$ energy flux into the tip. **(b)** $v/c_s = 0.95$. There is a net radiation ($-ve$ energy flux) of energy away from the tip.

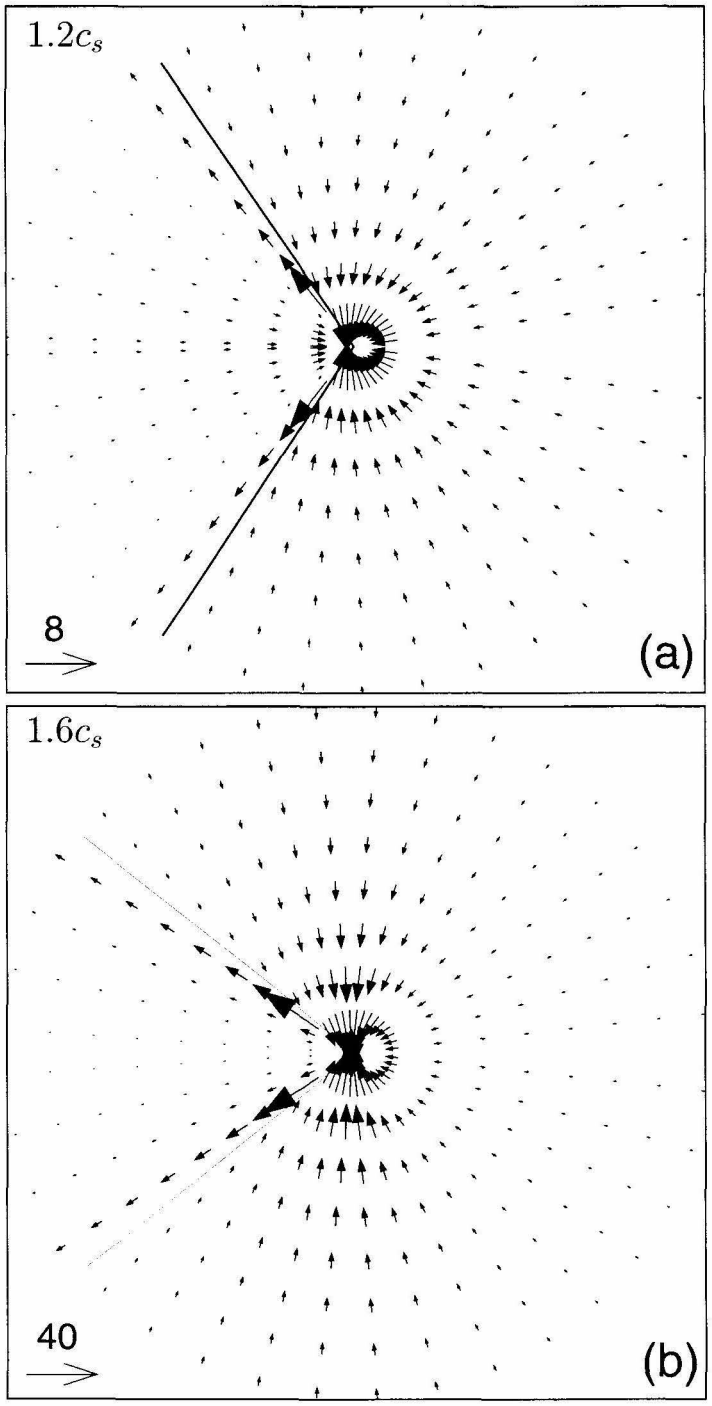

Figure 4.2: Energy flux vector field around the tip of an intersonically propagating mode II crack. **(a)** $v/c_s = 1.2$. **(b)** $v/c_s = 1.6$. In both cases the net energy flux into the crack tip is zero. Note the strong radiation of energy away from the tip along the two Mach waves.

speeds (Figure 4.1) and in the case of intersonic speeds (Figure 4.2), the magnitude scale stands for so many units of $(K_{II}^{*d})^2 c_s / 4\pi\mu D^q$. D is an arbitrary length scale chosen to be unity. From Figure 4.1(a), which is representative of sub-Rayleigh crack speeds, we can see that there is a net positive energy flux towards the tip. Hence subsonic mode II crack growth is energetically permissible for all crack speeds below c_R. From Figure 4.1(b), which is representative of subsonic - super-Rayleigh crack speeds, we can see that there is a net radiation of energy away from the crack tip. A propagating crack tip which radiates energy is physically unacceptable and hence mode II crack growth is not energetically permissible for crack speeds between c_R and c_s. From Figure 4.2, we can see that for intersonic crack speeds energy flows towards the tip from the region ahead of the two Mach waves, which is then radiated away by the Mach waves without deposition at the tip. The Mach waves are indicated by two dark lines radiating from the tip (Figure 4.2). The net energy flux into an intersonically propagating mode II crack tip is zero, except at $v = \sqrt{2}\, c_s$, where the two Mach waves disappear and the energy flux vector field appears sub-Rayleigh like. However, if we relax the idealization that the intersonic mode II crack tip is mathematically sharp and obeys the linear elastic constitutive relation all the way up to the tip, by including a process zone of finite size near the tip, we can show that mode II crack growth is energetically permissible at all intersonic speeds.

4.2 Dynamic Mode II Crack With a Dugdale Type Cohesive Zone

4.2.1 Formulation

Consider a semi-infinite mode II crack with a line cohesive zone of length L in front of the tip, propagating at a constant speed v through a homogeneous, isotropic, linear elastic medium under 2D plane strain or plane stress conditions (see Figure 4.3(a)). The crack is constrained to propagate in its own plane and the crack speed can be either subsonic or intersonic ($0 < v < c_l$). For planar deformation, the displacement field u_α with respect to a fixed coordinate system (x_1, x_2) can be expressed in terms of

two displacement potentials $\phi(x_1, x_2, t)$ and $\psi(x_1, x_2, t)$ as (Helmholtz decomposition)

$$u_\alpha(x_1, x_2, t) = \phi_{,\alpha}(x_1, x_2, t) + \epsilon_{\alpha\beta}\, \psi_{,\beta}(x_1, x_2, t)\,, \tag{4.5}$$

where $\epsilon_{\alpha\beta}$ is the 2D alternator with $\epsilon_{11} = \epsilon_{22} = 0$ and $\epsilon_{12} = -\epsilon_{21} = 1$. The equations of motion of this system (in the absence of body forces) in terms of the displacement potentials $\phi(x_1, x_2, t)$ and $\psi(x_1, x_2, t)$ are

$$\phi_{,\alpha\alpha}(x_1, x_2, t) - \frac{1}{c_l^2}\ddot{\phi}(x_1, x_2, t) = 0\,, \tag{4.6a}$$

$$\psi_{,\alpha\alpha}(x_1, x_2, t) - \frac{1}{c_s^2}\ddot{\psi}(x_1, x_2, t) = 0\,. \tag{4.6b}$$

Now, consider moving crack tip coordinates (η_1, η_2) centered at the front end of the cohesive zone, which are related to the fixed coordinates (x_1, x_2) through the Galilean transformation

$$\eta_1 = x_1 - vt\,, \qquad \eta_2 = x_2\,. \tag{4.7}$$

The equations of motion (4.6) expressed in terms of the moving crack tip coordinates (η_1, η_2) become

$$(1 - \frac{v^2}{c_l^2})\phi_{,11}(\eta_1, \eta_2, t) + \phi_{,22}(\eta_1, \eta_2, t) + \frac{\dot{v}}{c_l^2}\,\phi_{,1} + \frac{2v}{c_l^2}\,\dot{\phi}_{,1} - \frac{1}{c_l^2}\,\ddot{\phi} = 0\,, \tag{4.8a}$$

$$(1 - \frac{v^2}{c_s^2})\psi_{,11}(\eta_1, \eta_2, t) + \psi_{,22}(\eta_1, \eta_2, t) + \frac{\dot{v}}{c_s^2}\,\psi_{,1} + \frac{2v}{c_s^2}\,\dot{\psi}_{,1} - \frac{1}{c_s^2}\,\ddot{\psi} = 0\,. \tag{4.8b}$$

For steady state crack propagation, the crack tip speed is constant and moreover all the field quantities are invariant with time for an observer located at the crack tip and moving along with it. This idealization is clearly inadequate when considering the abrupt initiation or arrest of a dynamic fracture, but it is quite acceptable for describing processes for which the acceleration and deceleration phases are short compared to the total duration of the process (BROBERG, 1999). Therefore, the

equations of motion (4.8) reduce to

$$\left(1-\frac{v^2}{c_l^2}\right)\phi_{,11}(\eta_1,\eta_2)+\phi_{,22}(\eta_1,\eta_2)=0\,, \tag{4.9a}$$

$$\left(1-\frac{v^2}{c_s^2}\right)\psi_{,11}(\eta_1,\eta_2)+\psi_{,22}(\eta_1,\eta_2)=0\,. \tag{4.9b}$$

Defining relativistic quantities α_l, α_s and $\hat{\alpha}_s$ as

$$\alpha_l=\sqrt{1-\frac{v^2}{c_l^2}}\,,\qquad \alpha_s=\sqrt{1-\frac{v^2}{c_s^2}}\qquad\text{and}\qquad \hat{\alpha}_s=\sqrt{\frac{v^2}{c_s^2}-1}\,, \tag{4.10}$$

the equations of motion (4.9) reduce to

$$\phi_{,11}(\eta_1,\eta_2)+\frac{1}{\alpha_l^2}\phi_{,22}(\eta_1,\eta_2)=0 \qquad 0<v<c_l\,, \tag{4.11a}$$

$$\psi_{,11}(\eta_1,\eta_2)+\frac{1}{\alpha_s^2}\psi_{,22}(\eta_1,\eta_2)=0 \qquad 0<v<c_s\,, \tag{4.11b}$$

$$\psi_{,11}(\eta_1,\eta_2)-\frac{1}{\hat{\alpha}_s^2}\psi_{,22}(\eta_1,\eta_2)=0 \qquad c_s<v<c_l\,. \tag{4.11c}$$

Thus the motion is governed by two elliptic equations in the subsonic case, whereas for the intersonic case it is governed by an elliptic and a hyperbolic equation. The strain field and stress field components can be expressed in terms of the displacement potentials ϕ and ψ using the strain-displacement relations and the generalized Hooke's law. Henceforth, the formulations for subsonic and intersonic cases are treated separately.

4.2.2 Subsonic case, $0<v<c_s$

The most general solutions for the displacement potentials are (FREUND, 1989)

$$\phi(\eta_1,\eta_2)=\mathrm{Re}\{F(z_l)\}\,, \tag{4.12a}$$

$$\psi(\eta_1,\eta_2)=\mathrm{Im}\{G(z_s)\}\,, \tag{4.12b}$$

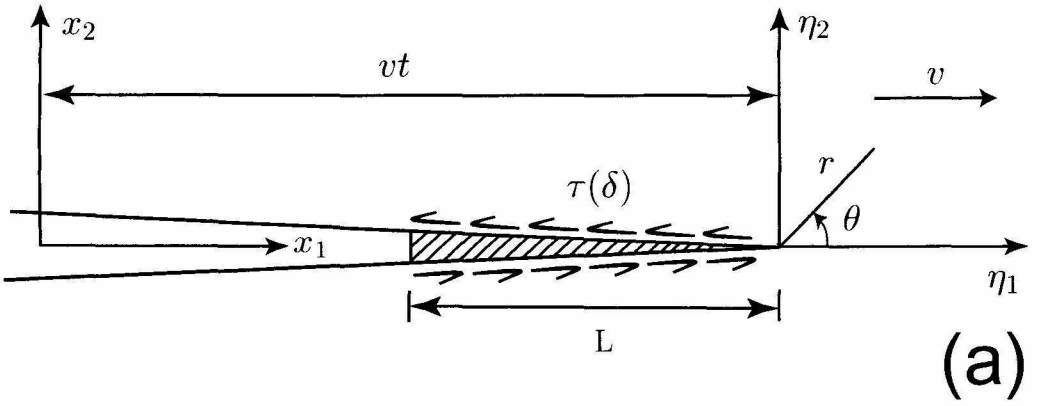

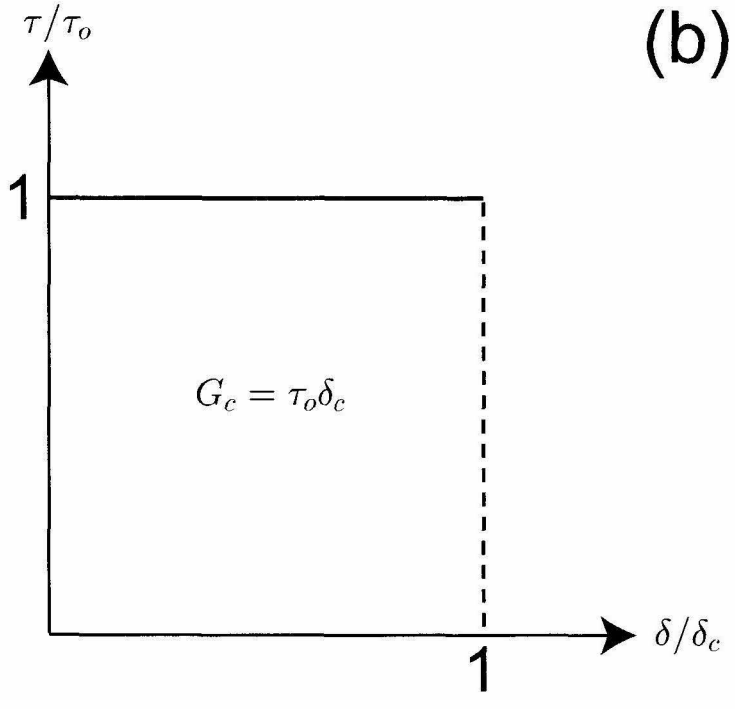

Figure 4.3: Dynamic mode II crack in a homogeneous, isotropic, linear elastic solid with a line cohesive zone of the Dugdale type. **(a)** Illustration showing the cohesive zone and the crack tip coordinate system. **(b)** Dugdale type cohesive law relating the shear traction to the local sliding displacement.

where $F(\cdot)$ is a function, analytic with respect to its argument, $z_l = \eta_1 + i\,\alpha_l\eta_2$ everywhere in the z_l-plane except on the crack faces and $G(\cdot)$ is a function, analytic with respect to its argument, $z_s = \eta_1 + i\,\alpha_s\eta_2$ everywhere in the z_s-plane except on the crack faces. The displacement field, following (4.5), is given by

$$u_1(\eta_1,\eta_2) = \mathrm{Re}\{F'(z_l) + \alpha_s G'(z_s)\}\,, \tag{4.13a}$$

$$u_2(\eta_1,\eta_2) = -\mathrm{Im}\{\alpha_l F'(z_l) + G'(z_s)\}\,, \tag{4.13b}$$

and the stress field is given by

$$\sigma_{11}(\eta_1,\eta_2) = \mu\,\mathrm{Re}\{(1+2\alpha_l^2-\alpha_s^2)F''(z_l) + 2\alpha_s G''(z_s)\}\,, \tag{4.14a}$$

$$\sigma_{22}(\eta_1,\eta_2) = \mu\,\mathrm{Re}\{-(1+\alpha_s^2)F''(z_l) - 2\alpha_s G''(z_s)\}\,, \tag{4.14b}$$

$$\sigma_{12}(\eta_1,\eta_2) = \mu\,\mathrm{Im}\{-2\alpha_l F''(z_l) - (1+\alpha_s^2)G''(z_s)\}. \tag{4.14c}$$

For a mode II crack, the displacement component u_1 is antisymmetric with respect to the crack plane, where as the component u_2 is symmetric with respect to the crack plane. Hence

$$F'^{-}(\eta_1) = -\bar{F}'^{-}(\eta_1)\,, \tag{4.15a}$$

$$G'^{-}(\eta_1) = -\bar{G}'^{-}(\eta_1)\,. \tag{4.15b}$$

The superscripts "+" and "−" stand for the limits $\eta_2 \to 0^+$ and $\eta_2 \to 0^-$ respectively. The traction boundary conditions on the cohesive surfaces and the crack faces are given by

$$\sigma_{22}^{\pm}(\eta_1) = 0 \qquad \eta_1 < 0\,, \tag{4.16a}$$

$$\sigma_{12}^{\pm}(\eta_1) = \begin{cases} \tau(\eta_1/L) & -L < \eta_1 < 0\,, \\ 0 & \eta_1 < -L\,, \end{cases} \tag{4.16b}$$

where $\tau(\eta_1/L)$ is the unknown cohesive traction distribution on the cohesive surfaces. Substituting for the stress fields from (4.14) and incorporating the mode II symmetries from (4.15), we have

$$(1+\alpha_s^2)\left\{F''^{+}(\eta_1)-F''^{-}(\eta_1)\right\}+2\alpha_s\left\{G''^{+}(\eta_1)-G''^{-}(\eta_1)\right\}=0 \qquad \eta_1<0\,, \tag{4.17}$$

$$i\mu\left[\alpha_l\left\{F''^{+}(\eta_1)+F''^{-}(\eta_1)\right\}+\frac{(1+\alpha_s^2)}{2}\left\{G''^{+}(\eta_1)+G''^{-}(\eta_1)\right\}\right] = \begin{cases}\tau\,(\eta_1/L) & -L<\eta_1<0\,,\\ 0 & \eta_1<-L\,.\end{cases} \tag{4.18}$$

The first of the two equations above implies that the function

$$P(z)=(1+\alpha_s^2)F''(z)+2\alpha_s G''(z)\,, \tag{4.19}$$

which is analytic everywhere in the $z=\eta_1+i\eta_2$ plane, except possibly along the crack line, is continuous across the crack line and it does not have any poles there. Hence $P(z)$ is an entire function. Furthermore, the vanishing of stress at remote points implies that $P(z)\to 0$ as $|z|\to 0$. Hence $P(z)$ is a bounded entire function and by Liouville's theorem $P(z)$ is a constant. In particular, $P(z)=0$ everywhere. Hence

$$G''(z)=\frac{-(1+\alpha_s^2)}{2\alpha_s}F''(z)\,. \tag{4.20}$$

Equation (4.18) becomes

$$iF''^{+}(\eta_1)-(-i)F''^{-}(\eta_1)=\begin{cases}\dfrac{4\alpha_s}{\mu R(v)}\tau(\eta_1/L) & -L<\eta_1<0\,,\\ 0 & \eta_1<-L\,,\end{cases} \tag{4.21}$$

where $R(v)=4\alpha_l\alpha_s-(1+\alpha_s^2)^2$ is the Rayleigh function. One of its zeros is the Rayleigh wave speed, c_R. Equation (4.21) is an inhomogeneous Hilbert problem. The

general solution of which is given by (MUSKHELISHVILI, 1963; GAKHOV, 1990)

$$F''(z) = \frac{A(z)}{\sqrt{z}} + \frac{1}{2\pi i}\frac{4\alpha_s}{\mu R(v)}\frac{1}{\sqrt{z}}\int_{-L}^{0}\frac{\sqrt{|\xi|}\,\tau(\xi/L)}{\xi - z}\,d\xi\,, \tag{4.22}$$

where $A(z)$ is an entire function that represents the remotely applied load. Expanding $A(z)$ about the origin in terms of a Taylor series,

$$A(z) = \sum_{n=0}^{\infty} A_n z^n\,, \tag{4.23}$$

where $A_o, A_1, A_2, \ldots, A_n, \ldots$ are complex constants. Considering only the singular terms,

$$F''(z) = \frac{A_o}{\sqrt{z}} + \frac{1}{2\pi i}\frac{4\alpha_s}{\mu R(v)}\frac{1}{\sqrt{z}}\int_{-L}^{0}\frac{\sqrt{|\xi|}\,\tau(\xi/L)}{\xi - z}\,d\xi\,. \tag{4.24}$$

Following (4.15) we can readily conclude that A_o is pure imaginary. The shear stress ahead of the crack tip is given by

$$\sigma_{12}(\eta_1 > 0, \eta_2 = 0) = \frac{i\mu R(v)}{2\alpha_s}\left\{\frac{A_o}{\sqrt{|\eta_1|}} + \frac{1}{i\pi}\frac{2\alpha_s}{\mu R(v)}\frac{1}{\sqrt{|\eta_1|}}\int_{-L}^{0}\frac{\sqrt{|\xi|}\,\tau(\xi/L)}{\xi - |\eta_1|}\,d\xi\right\}. \tag{4.25}$$

If conditions for small-scale yielding are met, that is, if the cohesive zone size L is much less than all other in-plane physical dimensions, then far ahead of the crack tip, *i.e.*, for $\eta_1 = D \gg L, \eta_2 = 0$, the solution must match the square root singular stress intensity factor field for steady subsonic crack growth.

$$\sigma_{12}(\eta_1 = D, \eta_2 = 0) \approx \frac{\mu R(v)}{2\alpha_s}\frac{iA_o}{\sqrt{D}} = \frac{K_{II}^d}{\sqrt{2\pi D}}\,. \tag{4.26}$$

$$\Rightarrow iA_o = \frac{1}{\sqrt{2\pi}}\frac{K_{II}^d}{\mu}\frac{2\alpha_s}{R(v)}\,. \tag{4.27}$$

Also, with the presence of a cohesive zone, the stresses must be bounded at its front end and the stress intensity factor here should vanish.

$$\lim_{\eta_1 \to 0^+} \sigma_{12}(\eta_1 > 0, \eta_2 = 0)\sqrt{2\pi\eta_1} = 0\,. \tag{4.28a}$$

$$\Rightarrow iA_o = \frac{1}{\mu\pi}\frac{2\alpha_s}{R(v)}\int_{-L}^{0}\frac{\tau(\xi/L)}{\sqrt{|\xi|}}\,d\xi\,. \tag{4.28b}$$

$$\Rightarrow K_{II}^d = \sqrt{\frac{2}{\pi}}\int_{-L}^{0}\frac{\tau(\xi/L)}{\sqrt{|\xi|}}\,d\xi\,. \tag{4.28c}$$

4.2.3 Intersonic case, $c_s < v < c_l$

Owing to the symmetry of the problem, we consider the solution to equations (4.11) only in the upper half plane ($\eta_2 \geq 0$). The general solutions for the displacement potentials are (FREUND, 1989)

$$\phi(\eta_1, \eta_2) = \mathrm{Re}\{F(z_l)\}\,, \tag{4.29a}$$

$$\psi(\eta_1, \eta_2) = g(\eta_1 + \hat{\alpha}_s\eta_2)\,, \tag{4.29b}$$

where F is the same function as in the subsonic case and $g(\cdot)$ is a real function of its argument. The radiation condition is employed here, *i.e.*, an intersonic crack is only capable of generating backward running shear waves. The displacement field in terms of F and g is given by

$$u_1(\eta_1, \eta_2) = \mathrm{Re}\{F'(z_l)\} + \hat{\alpha}_s\, g'(\eta_1 + \hat{\alpha}_s\eta_2)\,, \tag{4.30a}$$

$$u_2(\eta_1, \eta_2) = -\alpha_l\mathrm{Im}\{F'(z_l)\} - g'(\eta_1 + \hat{\alpha}_s\eta_2)\,. \tag{4.30b}$$

and the stress field is given by

$$\sigma_{11}(\eta_1, \eta_2) = \mu\left[(1 + 2\alpha_l^2 + \hat{\alpha}_s^2)\mathrm{Re}\{F''(z_l)\} + 2\hat{\alpha}_s g''(\eta_1 + \hat{\alpha}_s\eta_2)\right]\,, \tag{4.31a}$$

$$\sigma_{22}(\eta_1, \eta_2) = \mu\left[-(1 - \hat{\alpha}_s^2)\mathrm{Re}\{F''(z_l)\} - 2\hat{\alpha}_s g''(\eta_1 + \hat{\alpha}_s\eta_2)\right]\,, \tag{4.31b}$$

$$\sigma_{12}(\eta_1,\eta_2)=\mu\left[-2\alpha_l\mathrm{Im}\{F''(z_l)\}-(1-\hat{\alpha}_s^2)g''(\eta_1+\hat{\alpha}_s\eta_2)\right]. \tag{4.31c}$$

Owing to mode II symmetries, ahead of the crack tip we have

$$u_1(\eta_1>0,\eta_2=0)=0\,, \tag{4.32a}$$

$$\sigma_{22}(\eta_1>0,\eta_2=0)=0\,, \tag{4.32b}$$

which reduce to

$$F''^{+}(\eta_1)=-\bar{F}''^{-}(\eta_1) \qquad \eta_1>0\,, \tag{4.33a}$$

$$g''^{+}(\eta_1)=0 \qquad \eta_1>0\,. \tag{4.33b}$$

Following (4.33) we can define $\theta(z)$ (by analytic continuation), a function analytic everywhere on the complex z-plane except on the crack faces as

$$\theta(z)=\begin{cases} F''(z) & \mathrm{Im}\{z\}\geq 0\,, \\ -\bar{F}''(z) & \mathrm{Im}\{z\}<0\,. \end{cases} \tag{4.34}$$

The traction boundary conditions on the upper crack face and the cohesive surface result in

$$g''^{+}(\eta_1)=\frac{-(1-\hat{\alpha}_s^2)}{4\hat{\alpha}_s}\{F''^{+}(\eta_1)+\bar{F}''^{-}(\eta_1)\} \qquad \eta_1<0\,, \tag{4.35a}$$

$$\mu\left[-2\alpha_l\mathrm{Im}\{F''^{+}(\eta_1)\}-(1-\hat{\alpha}_s^2)g''^{+}(\eta_1)\right]=\begin{cases} \tau(\eta_1/L) & -L<\eta_1<0\,, \\ 0 & \eta_1<-L\,. \end{cases} \tag{4.35b}$$

The second of the above equations reduces to

$$\left[(1-\hat{\alpha}_s^2)^2+4i\alpha_l\hat{\alpha}_s\right]\theta^+(\eta_1)-\left[(1-\hat{\alpha}_s^2)^2-4i\alpha_l\hat{\alpha}_s\right]\theta^-(\eta_1)$$
$$=\begin{cases}[+8pt]\dfrac{4\hat{\alpha}_s}{\mu}\,\tau(\eta_1/L) & -L<\eta_1<0\,,\\ 0 & \eta_1<-L\,.\end{cases} \tag{4.36}$$

Similar to the subsonic case, the general solution for the inhomogeneous Hilbert problem in the upper half plane ($\eta_2 \geq 0$), is given by

$$\theta(z)=F''(z)=\frac{A_o}{z^q}+\frac{1}{2\pi i}\,\frac{4\hat{\alpha}_s}{\mu R_q}\,\frac{1}{z^q}\int_{-L}^{0}\frac{|\xi|^q\,\tau(\xi/L)}{\xi-z}\,d\xi\,, \tag{4.37}$$

where

$$q=\frac{1}{\pi}\tan^{-1}\left[\frac{4\alpha_l\hat{\alpha}_s}{(1-\hat{\alpha}_s^2)^2}\right], \tag{4.38a}$$

$$R_q=\sqrt{16\alpha_l^2\hat{\alpha}_s^2+(1-\hat{\alpha}_s^2)^4}\,. \tag{4.38b}$$

From mode II symmetries we can readily conclude that A_o is pure imaginary. Also,

$$g''(\eta_1+\hat{\alpha}_s\eta_2)=\begin{cases}0 & \eta_1+\hat{\alpha}_s\eta_2>0\,,\\ -\dfrac{(1-\hat{\alpha}_s^2)}{2\hat{\alpha}_s}\,\mathrm{Re}\{F''(\eta_1+\hat{\alpha}_s\eta_2)\} & \eta_1+\hat{\alpha}_s\eta_2<0\,.\end{cases} \tag{4.39}$$

The shear stress ahead of the crack tip is given by

$$\sigma_{12}(\eta_1>0,\eta_2=0)=\frac{2\mu\alpha_l i A_o}{|\eta_1|^q}+\frac{\sin q\pi}{\pi}\,\frac{1}{|\eta_1|^q}\int_{-L}^{0}\frac{|\xi|^q\tau(\xi/L)}{\xi-|\eta_1|}\,d\xi\,. \tag{4.40}$$

Far ahead of the crack tip, *i.e.*, for $\eta_1=D\gg L,\eta_2=0$, the solution must match the singular solution (3.3).

$$\sigma_{12}(\eta_1=D,\eta_2=0)\approx\frac{2\mu\alpha_l i A_o}{D^q}=\frac{K_{II}^{*d}}{\sqrt{2\pi}\,D^q}\,. \tag{4.41}$$

$$\Rightarrow iA_o = \frac{1}{\sqrt{2\pi}} \frac{K_{II}^{*d}}{2\mu\alpha_l} . \tag{4.42}$$

Also, with the presence of a cohesive zone, the stresses must be bounded at the front end and the stress intensity factor here should vanish.

$$\lim_{\eta_1 \to 0^+} \sigma_{12}(\eta_1 > 0, \eta_2 = 0)\sqrt{2\pi}\,\eta_1^q = 0 . \tag{4.43a}$$

$$\Rightarrow iA_o = \frac{1}{2\mu\alpha_l} \frac{\sin q\pi}{\pi} \int_{-L}^{0} \frac{\tau(\xi/L)}{|\xi|^{1-q}}\, d\xi . \tag{4.43b}$$

$$\Rightarrow K_{II}^{*d} = \sin q\pi \sqrt{\frac{2}{\pi}} \int_{-L}^{0} \frac{\tau(\xi/L)}{|\xi|^{1-q}}\, d\xi . \tag{4.43c}$$

4.2.4 Cohesive Law

In linear elastic fracture mechanics, it is assumed that the tip of a crack is mathematically sharp and that the material obeys a linear elastic constitutive relation all the way up to the tip. This assumption results in an unphysical situation wherein stresses at the crack tip become unbounded. This is clearly an artifact of the mathematical idealization, since no real material can actually support such high stresses. The usual rationalization for admitting such a singular stress distribution, the strength of which is measured by the stress intensity factor, is based on the concept of small-scale yielding. Under small-scale yielding conditions, the stress intensity factor may be considered to be a one parameter measure of the amplitude of the stress which is being applied to the material in the crack tip region. The stress intensity factor approach circumvents consideration of how the material in the crack tip region actually responds to the applied stress.

In reality, the maximum stress in the vicinity of a crack tip is determined by the intrinsic strength (or cohesive strength) of the material. Stress in the crack vicinity increases continuously as the crack tip is approached, ultimately reaching the cohesive strength of the material, when it begins to unravel, eventually leading to complete separation at the physical crack tip. Line cohesive zone models offer a simple mecha-

nism by which the physical process of decohesion may be modeled. Such line cohesive zone models were introduced for tensile cracks by BARENBLATT (1962) to represent molecular cohesion during brittle fracture and by DUGDALE (1960) to represent approximately, effects of plastic yielding in ductile materials. The linear elastic constitutive relation for the bulk material is not valid within the cohesive zone and a separate cohesive constitutive relation is chosen (based on phenomenological/atomistic considerations) to represent the break down processes occurring here. For a line cohesive zone, the cohesive constitutive relation is expected to relate the cohesive traction at any point in the cohesive zone to the local displacement discontinuity, its derivatives with respect to time and other "local state" variables. If the interatomic force is its main origin, the dependence of the cohesive traction on the displacement discontinuity would be the most important. However, for shear cracks propagating along weak planes (see Chapter 3), the cohesive stress can originate either due to bonding or due to nonuniform frictional sliding. Hence, the cohesive constitutive relation is likely to be rate dependent. However, in this chapter a rate independent model is analyzed and the effects of rate dependence are considered in the next chapter. The line cohesive zone model has a natural motivation for the experiments described in Chapter 3, where the fracture process zone was mostly confined to a thin weak layer (bond line) in front of the crack tip.

To summarize, in order to deal with crack motion in cases where the zone of strength degradation is not confined to the immediate vicinity of the crack tip, as well as to obtain an interpretation of the fracture energy Γ (primarily for intersonic speeds), we employ a line cohesive zone model. Section 3.6 details the necessity of a cohesive zone model in studying intersonic shear cracks and in interpreting the experimental observations described in Chapter 3. The line cohesive zone model is analyzed by making the crack longer by an amount L, the cohesive zone size. The cohesive stresses act in this zone so as to restrain crack face sliding. When the zone L of strength degradation is small compared to overall crack size, then Rice's

boundary layer formulation for small-scale yielding can be applied, with the crack surface regarded as semi-infinite, the body as infinite, and the remote stress field given by the characteristic elastic singular field.

For the present analysis, we choose a cohesive constitutive relation of the Dugdale type, according to which the cohesive shear traction at any point within the cohesive zone is a constant, being equal to the shear strength τ_o of the material (see Figure 4.3(b)), *i.e.*,

$$\tau(\frac{\eta_1}{L}) = \tau_o \qquad -L < \eta_1 < 0\,. \tag{4.44}$$

A more realistic rate dependent model is motivated and analyzed in the next chapter. As mentioned before, the crack speed regime $c_R < v < c_s$ is inadmissible for running mode II cracks from energetic considerations and henceforth we restrict ourselves to sub-Rayleigh ($0 \leq v < c_R$) and intersonic regimes only.

4.2.5 Cohesive Zone Length

Incorporating the cohesive traction distribution from (4.44) into (4.28c) and (4.43c) we can obtain the length of the cohesive zone in terms of the dynamic stress intensity factor (K_{II}^d or K_{II}^{*d}) , shear cohesive strength of the crack plane (τ_o), and the crack speed (v). Since the definition of stress intensity factor varies from sub-Rayleigh to intersonic speeds, we choose σ_{12}^D as a measure of the amplitude of far-field applied loading. σ_{12}^D is the shear stress on the crack plane a distance $D \gg L$ ahead of the crack tip, where the usual singular solution for the case of a mathematically sharp crack with no cohesive zone is expected to apply. σ_{12}^D is related to the subsonic and intersonic stress intensity factors as

$$\sigma_{12}^D = \sigma_{12}(\eta_1 = D, \eta_2 = 0) = \begin{cases} \dfrac{K_{II}^d}{\sqrt{2\pi D}} & 0 \leq v < c_R\,, \\ \dfrac{K_{II}^{*d}}{\sqrt{2\pi}\, D^q} & c_s < v < c_l\,. \end{cases} \tag{4.45}$$

The normalized cohesive zone length L/L_o in terms of σ_{12}^D, τ_o and v is given by

$$\frac{L}{L_o} = \begin{cases} 1 & 0 \leq v < c_R\,, \\ \dfrac{4}{\pi^2}\left(\dfrac{q\pi}{\sin q\pi}\right)^{1/q}\left(\dfrac{\sigma_{12}^D}{\tau_o}\right)^{1/q-2} & c_s < v < c_l\,. \end{cases} \tag{4.46}$$

The normalizing parameter L_o is the length of the cohesive zone associated with a quasi-statically growing crack with the same far-field applied loading σ_{12}^D and the same cohesive strength of the crack plane τ_o. It is given by

$$L_o = \frac{\pi^2}{4}\left(\frac{\sigma_{12}^D}{\tau_o}\right)^2 D\,. \tag{4.47}$$

Hence (4.46) represents the variation of cohesive zone length with crack speed under a constant σ_{12}^D/τ_o.

Figure 4.4 shows the variation of L/L_o with crack speed for different values of σ_{12}^D/τ_o. Here, as well as in all subsequent plots, plane stress deformation conditions are assumed and ν is taken to be 0.34 (Poisson's ratio of Homalite). Under a constant far-field load (σ_{12}^D = constant), the different curves indicate the influence of the shear strength of the crack plane, τ_o. For sub-Rayleigh crack speeds, the cohesive zone length is independent of v under a constant far-field applied load, where as, it is a strong function of v in the intersonic case. In the intersonic case, L increases monotonically from 0 at $v = c_s$ to its quasi-static value at $\sqrt{2}\,c_s$ and thereafter decreases monotonically to 0 at c_l. This behavior is a direct reflection of the behavior of crack tip stress singularity in the case of a point sized process zone. For the subsonic case, the singularity exponent is a constant (= 1/2) and hence the cohesive zone length remains constant at its quasi-static value. In the intersonic case, the dependence of L/L_o on v is similar to the dependence of the singularity exponent q on v. As $\tau_o \to \infty$ the material is linear elastic all the way up to the crack tip, which is equivalent to the singular case with no cohesive zone. Then L/L_o is zero every where

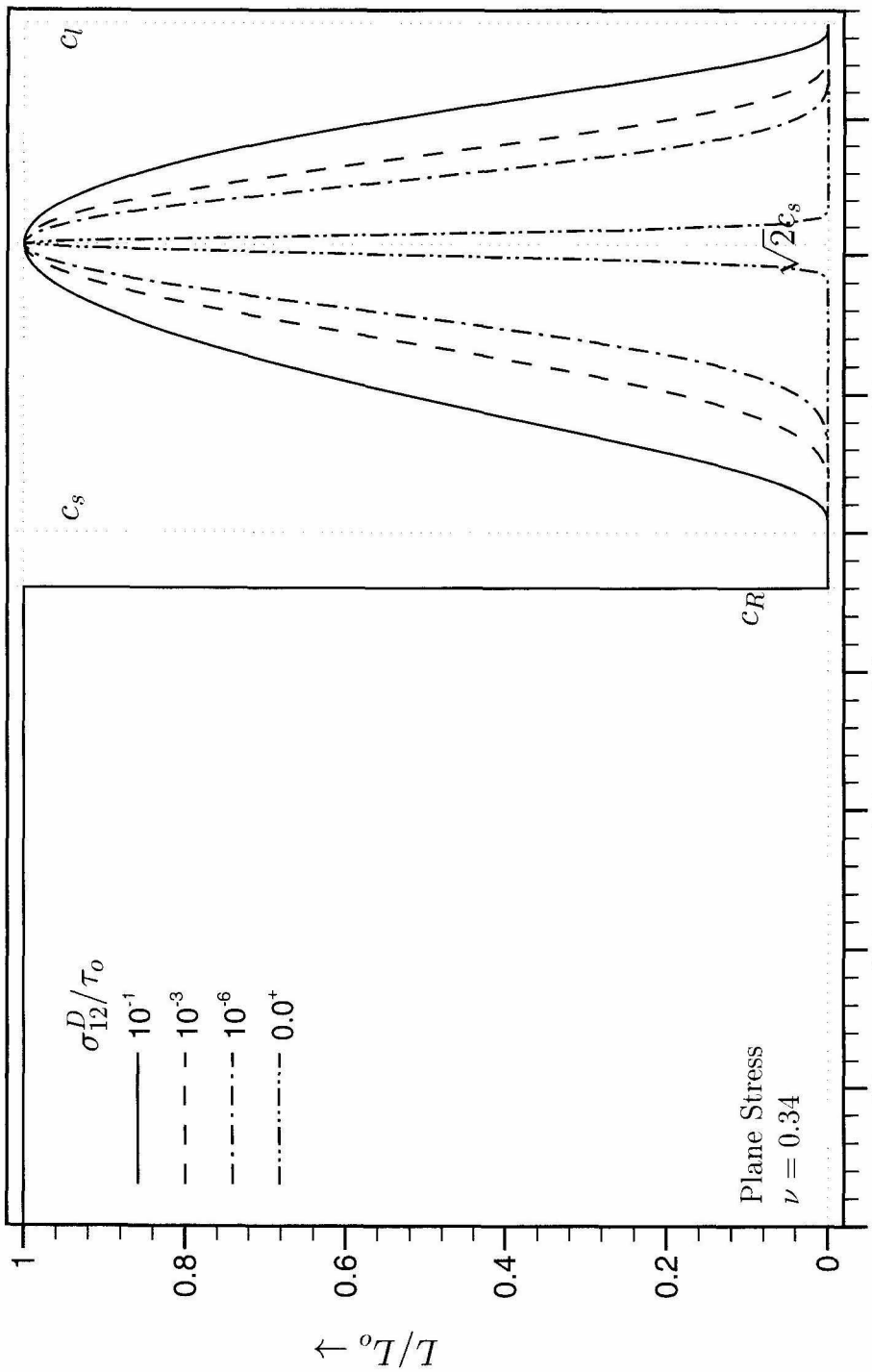

Figure 4.4: Dynamically propagating mode II crack with a Dugdale type cohesive zone — Dependence of the cohesive zone length on crack tip speed v, plotted for different values of σ_{12}^D/τ_o.

in the intersonic regime, except at $\sqrt{2}\,c_s$, where it attains its quasi-static value. Also as may be expected, lower the shear strength of the crack plane, higher the cohesive zone length in the intersonic regime, except at $\sqrt{2}\,c_s$.

4.2.6 Near-Tip Stress Field

With the assumed cohesive shear traction (4.44) one can compute the functions F'', G'' and g'' and thus obtain the dominant near-tip stress field from (4.14) and (4.31). The near-tip stress field is given in Appendix B for sub-Rayleigh crack speeds and in Appendix C for intersonic crack speeds. The shear stress component σ_{12} on the crack plane ($\eta_2 \to 0^+$) is given by

$$\frac{\sigma_{12}(\eta_1/L > 0)}{\tau_o} = \begin{cases} \dfrac{2}{\pi}\left(\dfrac{\eta_1}{L}\right)^{-1/2}\left[1 - \dfrac{1}{2}\displaystyle\int_0^1 \frac{\sqrt{\xi}}{\xi + \eta_1/L}\,d\xi\right] & 0 \le v < c_R\,, \\ \dfrac{\sin q\pi}{q\pi}\left(\dfrac{\eta_1}{L}\right)^{-q}\left[1 - q\displaystyle\int_0^1 \frac{\xi^q}{\xi + \eta_1/L}\,d\xi\right] & c_s < v < c_l\,. \end{cases} \tag{4.48}$$

$\sigma_{12} = \tau_o$ within the cohesive zone ($-L < \eta_1 < 0, \eta_2 \to 0^+$) and vanishes on the crack faces. The variation of σ_{12} on the crack plane is plotted in Figure 4.5(a) for different subRayleigh crack speeds and is plotted in Figure 4.6(a) for different intersonic speeds. As seen, σ_{12} is bounded all along the crack plane. Its variation is independent of crack speed in the sub-Rayleigh regime, where as in the intersonic regime it is dependent on crack speed.

For a propagating mode I crack with a Dugdale type cohesive zone, all the stress components are bounded in the tip region. However, for a crack propagating under mode II conditions, the stress component σ_{11} is unbounded at the physical crack tip ($\eta_1 = -L, \eta_2 = 0$), with a logarithmic singularity (weaker than 1/2). The stress

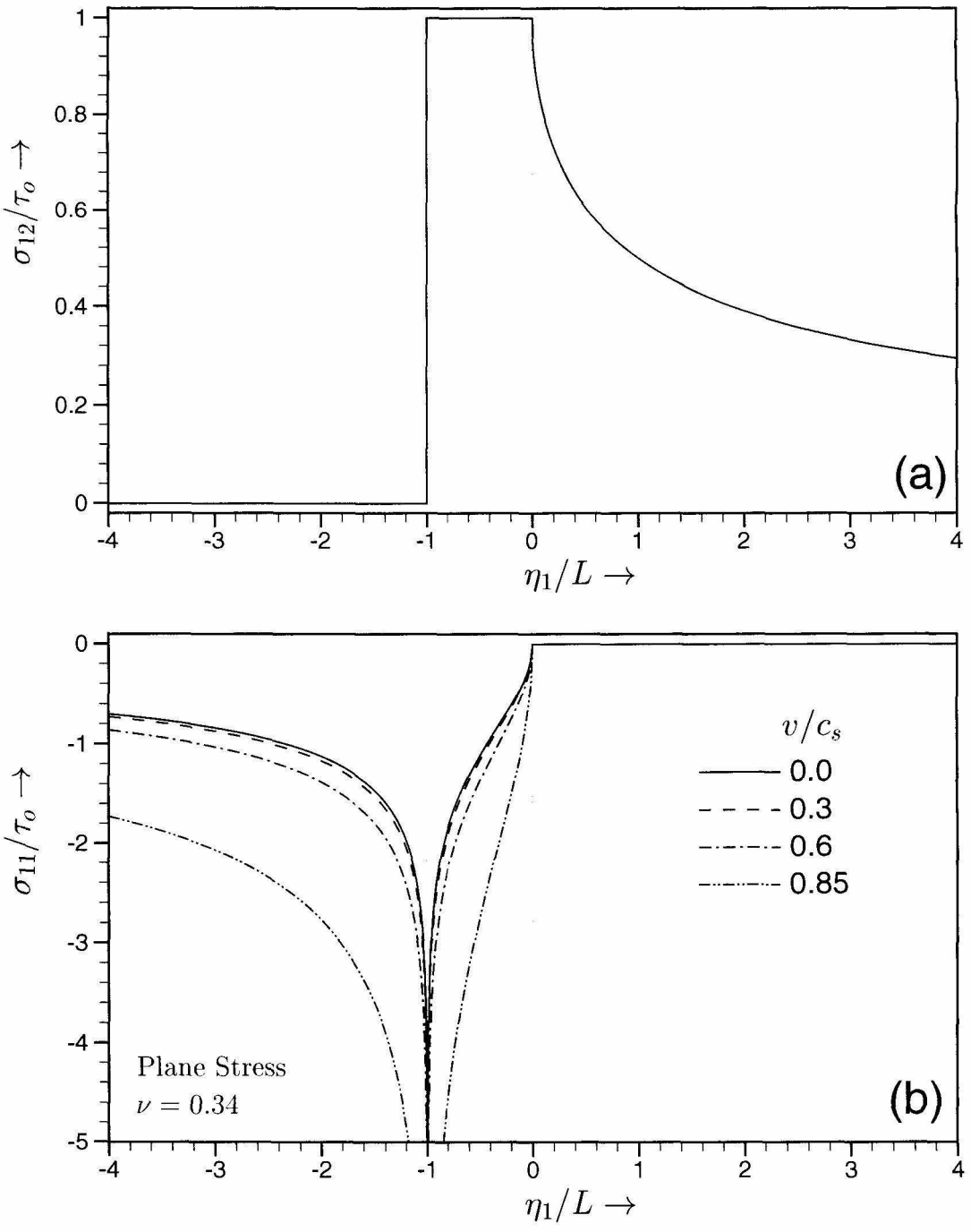

Figure 4.5: Subsonically propagating mode II crack with a Dugdale type cohesive zone. **(a)** Stress component σ_{12} on the crack plane. **(b)** Stress component σ_{11} on the crack plane.

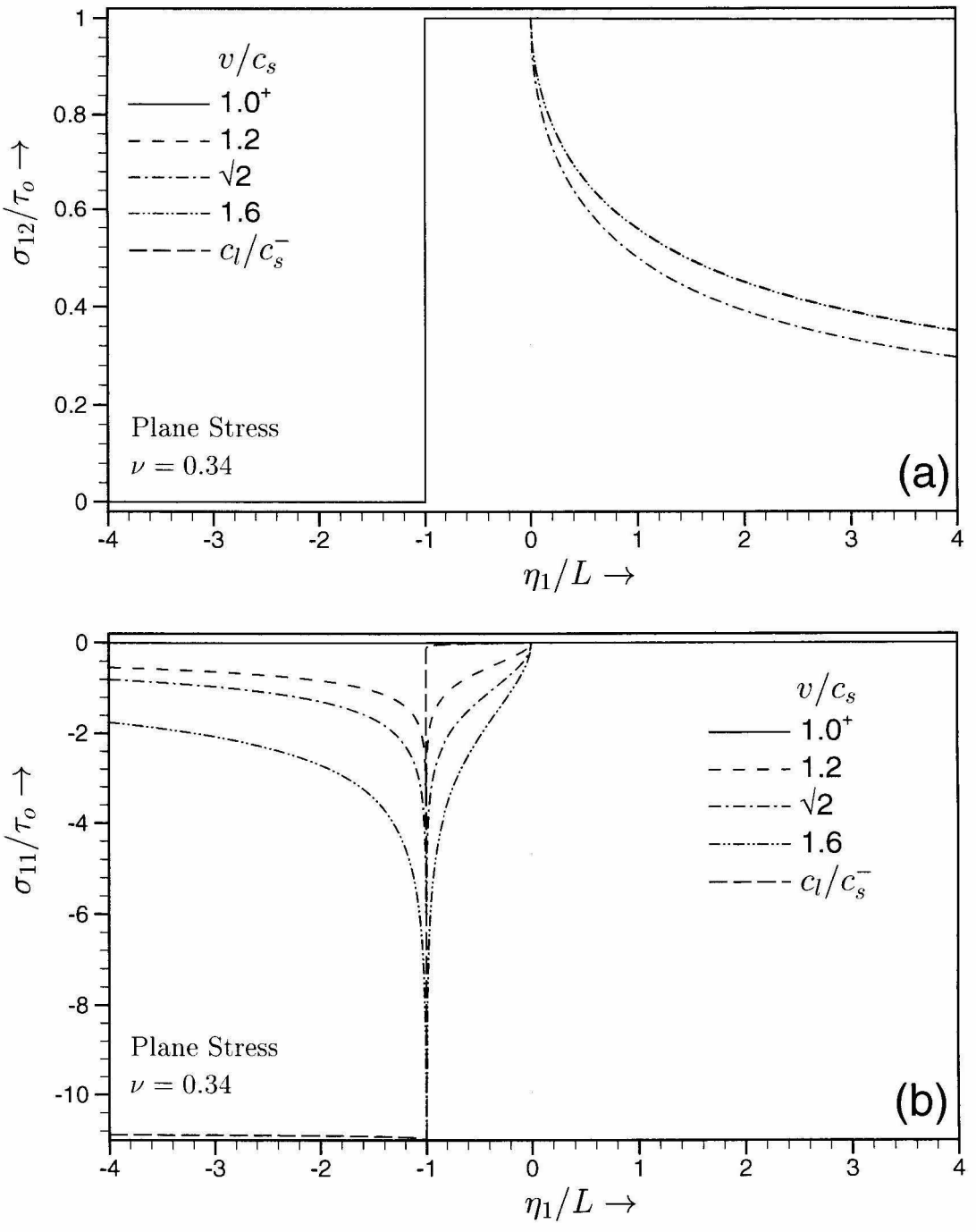

Figure 4.6: Intersonically propagating mode II crack with a Dugdale type cohesive zone. **(a)** Stress component σ_{12} on the crack plane. **(b)** Stress component σ_{11} on the crack plane.

component σ_{11} on the crack plane ($\eta_2 \to 0^+$) is given by

$$\sigma_{11} = \begin{cases} -\dfrac{1}{\pi}\dfrac{4\alpha_s(\alpha_l^2-\alpha_s^2)}{R(v)} \ln\left[\dfrac{1+\sqrt{-\eta_1/L}}{1-\sqrt{-\eta_1/L}}\right] & -1 < \dfrac{\eta_1}{L} \le 0\,, \\ -\dfrac{1}{\pi}\dfrac{4\alpha_s(\alpha_l^2-\alpha_s^2)}{R(v)} \ln\left[\dfrac{\sqrt{-\eta_1/L}+1}{\sqrt{-\eta_1/L}-1}\right] & \dfrac{\eta_1}{L} < -1\,, \end{cases} \tag{4.49}$$

for $0 \le v < c_R$ and

$$\sigma_{11} = \frac{(\alpha_l^2+\hat{\alpha}_s^2)}{\alpha_l}\left[\sin q\pi \cos q\pi - \frac{\sin^2 q\pi}{q\pi}\left(-\frac{\eta_1}{L}\right)^{-q}\left\{1 - q\,\mathrm{pv}\int_0^1 \frac{\xi^q}{\xi+\eta_1/L}\,d\xi\right\}\right]$$
$$-1 < \frac{\eta_1}{L} \le 0\,, \tag{4.50a}$$

$$\sigma_{11} = -\frac{(\alpha_l^2+\hat{\alpha}_s^2)}{\alpha_l}\frac{\sin^2 q\pi}{q\pi}\left(-\frac{\eta_1}{L}\right)^{-q}\left[1 - q\int_0^1 \frac{\xi^q}{\xi+\eta_1/L}\,d\xi\right]$$
$$\frac{\eta_1}{L} < -1\,, \tag{4.50b}$$

for $c_s < v < c_l$. Also, $\sigma_{11}(\eta_1/L > 0) = 0$ for both sub-Rayleigh and intersonic crack speeds. Figure 4.5(b) shows the variation of the stress component σ_{11} along the crack plane for different sub-Rayleigh crack speeds and Figure 4.6(b) shows the variation of σ_{11} along the crack plane for different intersonic crack speeds. As seen from the figure, σ_{11} is compressive and is singular at the physical crack tip. It must be noted here, that the nature of loading in our experiments (as described in Chapter 3) is such, that the dynamic mode II stress intensity factor associated with the propagating crack is negative. This results in σ_{11} to be positive in the upper half plane ($\eta_2 > 0$) and negative in the lower half. However, the analytical solution derived in this chapter follows the conventional approach by assuming the far-field dynamic stress intensity factor (and thus σ_{12}^D) to be positive, resulting in σ_{11} being compressive in the upper half plane.

4.2.7 Particle Velocity Field

For steady crack growth, the particle velocity field is related to displacement gradients through

$$\dot{u}_\alpha(\eta_1, \eta_2) = -v \frac{\partial u_\alpha}{\partial \eta_1}(\eta_1, \eta_2)\,. \tag{4.51}$$

Following (4.13) and (4.30) we have

$$\dot{u}_1(\eta_1, \eta_2) = -v\,\mathrm{Re}\{F''(z_l) + \alpha_s G''(z_s)\}\,, \tag{4.52a}$$

$$\dot{u}_2(\eta_1, \eta_2) = v\,\mathrm{Im}\{\alpha_l F''(z_l) + G''(z_s)\}\,, \tag{4.52b}$$

for $0 \leq v < c_R$ and

$$\dot{u}_1(\eta_1, \eta_2) = -v\,[\mathrm{Re}\{F''(z_l)\} + \hat{\alpha}_s g''(\eta_1 + \hat{\alpha}_s \eta_2)]\,, \tag{4.53a}$$

$$\dot{u}_2(\eta_1, \eta_2) = v\,[\alpha_l \mathrm{Im}\{F''(z_l)\} + g''(\eta_1 + \hat{\alpha}_s \eta_2)]\,. \tag{4.53b}$$

for $c_s < v < c_l$. With the assumed cohesive shear traction (4.44) one can compute the functions F'', G'' and g'' and thus obtain the dominant near tip particle velocity field from (4.52) and (4.53). The particle velocity field is given in Appendix B for sub-Rayleigh crack speeds and in Appendix C for intersonic crack speeds.

Figure 4.7(a) shows the sliding rate (or slip rate), $\dot{\delta}_1 = \dot{u}_1^+ - \dot{u}_1^-$ on the crack plane ($\eta_2 \to 0^+$) for various sub-Rayleigh speeds. Similarly Figure 4.8(a) shows the variation of $\dot{\delta}_1$ on the crack plane for various intersonic speeds. The parameter μ/τ_o was chosen to be 136, which is equal to the ratio of shear modulus of Homalite (1.9 GPa) and the shear strength of the Homalite/Homalite bond ($\approx$14 MPa). For

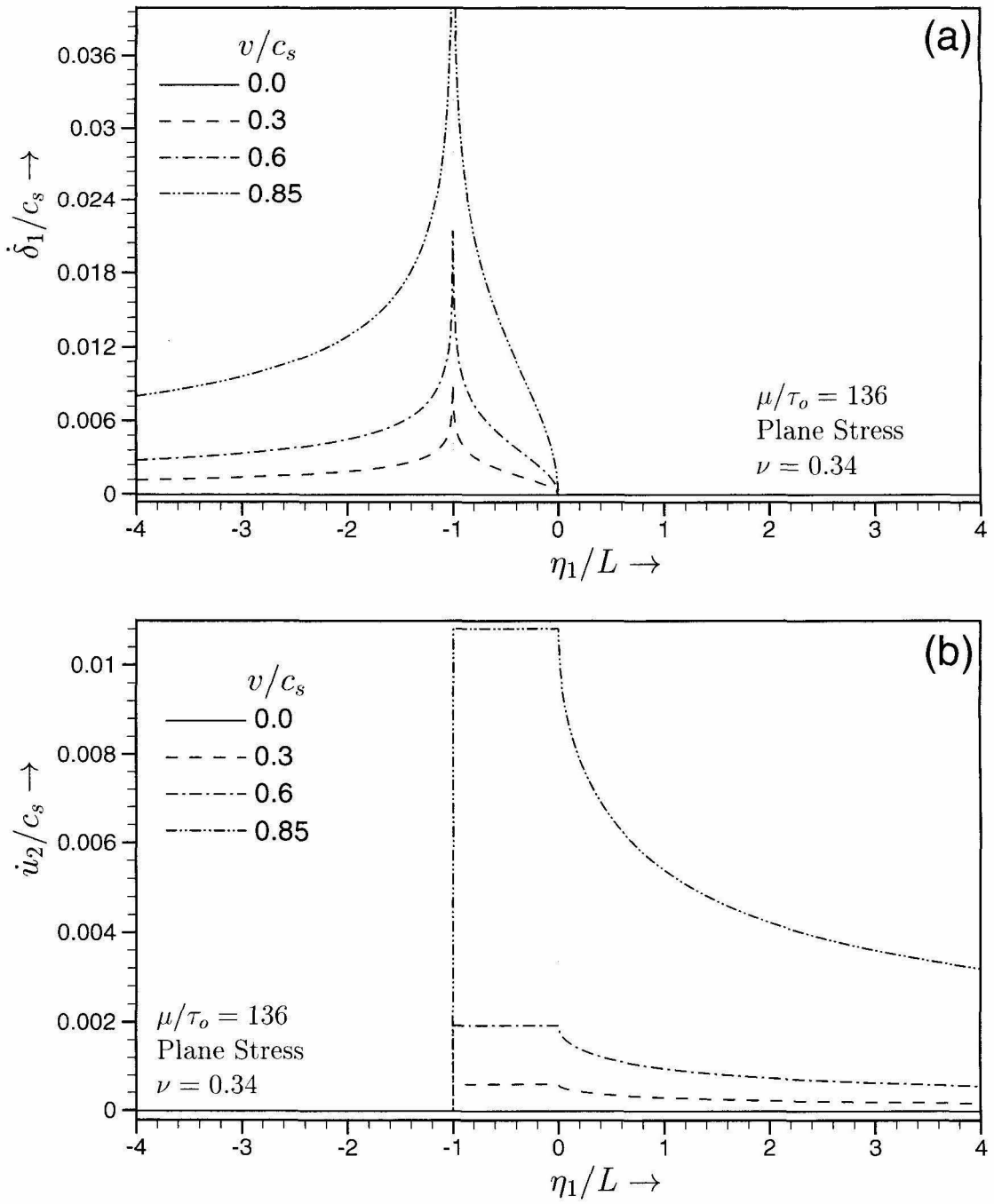

Figure 4.7: Subsonically propagating mode II crack with a Dugdale type cohesive zone. **(a)** Relative sliding rate $\dot{\delta}_1$ on the crack plane. **(b)** Particle velocity component $\dot{u}_2$ on the crack plane.

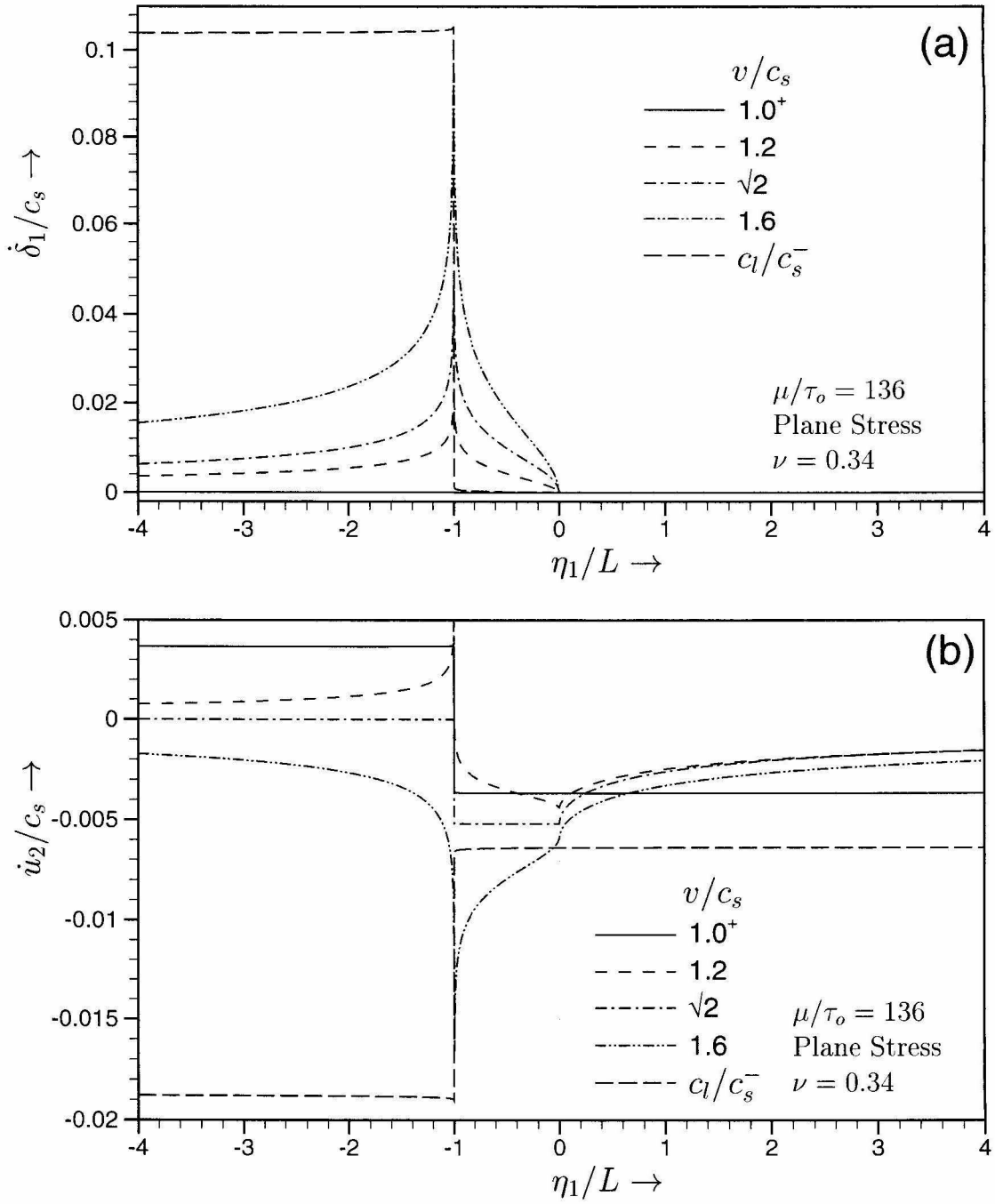

Figure 4.8: Intersonically propagating mode II crack with a Dugdale type cohesive zone. **(a)** Relative sliding rate $\dot{\delta}_1$ on the crack plane. **(b)** Particle velocity component $\dot{u}_2$ on the crack plane.

$0 \le v < c_R$,

$$\frac{\dot{\delta}_1}{c_s} = \begin{cases} \dfrac{2}{\pi}\dfrac{\tau_o}{\mu}\dfrac{\alpha_s(1-\alpha_s^2)}{R(v)}\dfrac{v}{c_s}\ln\left[\dfrac{1+\sqrt{-\eta_1/L}}{1-\sqrt{-\eta_1/L}}\right] & -1 < \dfrac{\eta_1}{L} < 0\,, \\ \dfrac{2}{\pi}\dfrac{\tau_o}{\mu}\dfrac{\alpha_s(1-\alpha_s^2)}{R(v)}\dfrac{v}{c_s}\ln\left[\dfrac{\sqrt{-\eta_1/L}+1}{\sqrt{-\eta_1/L}-1}\right] & \dfrac{\eta_1}{L} < -1\,, \end{cases} \tag{4.54}$$

and for $c_s < v < c_l$,

$$\frac{\dot{\delta}_1}{c_s} = \frac{2\tau_o}{\mu}\frac{\hat{\alpha}_s(1+\hat{\alpha}_s^2)}{R_q}\frac{v}{c_s}\left[-\cos q\pi + \frac{\sin q\pi}{q\pi}\frac{1}{(-\eta_1/L)^q}\left\{1 - q\,\mathrm{pv}\int_0^1 \frac{\zeta^q}{\zeta+\eta_1/L}\,d\zeta\right\}\right]$$
$$-1 < \frac{\eta_1}{L} < 0\,, \tag{4.55a}$$

$$\frac{\dot{\delta}_1}{c_s} = \frac{2\tau_o}{\mu}\frac{\hat{\alpha}_s(1+\hat{\alpha}_s^2)}{R_q}\frac{v}{c_s}\frac{\sin q\pi}{q\pi}\frac{1}{(-\eta_1/L)^q}\left\{1 - q\int_0^1 \frac{\zeta^q}{\zeta+\eta_1/L}\,d\zeta\right\}$$
$$\frac{\eta_1}{L} < -1\,. \tag{4.55b}$$

Note that $\dot{\delta}_1(\eta_1 > 0, \eta_2 \to 0) = 0$. $\dot{\delta}_1$ is unbounded at the physical crack tip with a logarithmic singularity. However, through most of the cohesive zone, $\dot{\delta}$ is within $\approx 2\%$ of c_s for sub-Rayleigh speeds and is within $\approx 4\%$ of c_s for intersonic speeds. 2-4% of c_s corresponds to sliding rates of a few m/s.

The variation of the particle velocity component $\dot{u}_2$ along the crack plane is shown in Figure 4.7(b) for various sub-Rayleigh crack speeds and in Figure 4.8(b) for various intersonic crack speeds. For $0 \le v < c_R$,

$$\frac{\dot{u}_2}{c_s} = \begin{cases} \dfrac{2}{\pi}\dfrac{\tau_o}{\mu}\dfrac{1+\alpha_s^2-2\alpha_l\alpha_s}{R(v)}\dfrac{v}{c_s}\tan^{-1}\left(\dfrac{1}{\sqrt{\eta_1/L}}\right) & \dfrac{\eta_1}{L} > 0\,, \\ \dfrac{\tau_o}{\mu}\dfrac{1+\alpha_s^2-2\alpha_l\alpha_s}{R(v)}\dfrac{v}{c_s} & -1 < \dfrac{\eta_1}{L} < 0\,, \\ 0 & \dfrac{\eta_1}{L} < -1\,, \end{cases} \tag{4.56}$$

and for $c_s < v < c_l$,

$$\frac{\dot{u}_2}{c_s} = -\frac{v}{2c_s}\frac{\tau_o}{\mu}\frac{\sin q\pi}{q\pi}\frac{1}{(\eta_1/L)^q}\left[1 - q\int_0^1 \frac{\xi^q}{\xi + \eta_1/L}\,d\xi\right] \qquad \frac{\eta_1}{L} > 0\,, \tag{4.57a}$$

$$\frac{\dot{u}_2}{c_s} = -\frac{v}{2c_s}\frac{\tau_o}{\mu}\left[\left\{1 + \frac{(1-\hat{\alpha}_s^4)}{R_q}\cos q\pi\right\} - \frac{\sin q\pi}{q\pi}\frac{(1-\hat{\alpha}_s^4)}{R_q}\frac{1}{(-\eta_1/L)^q}\left\{1 - q\,\mathrm{pv}\int_0^1 \frac{\xi^q}{\xi + \eta_1/L}\,d\xi\right\}\right] \qquad -1 < \frac{\eta_1}{L} < 0\,, \tag{4.57b}$$

$$\frac{\dot{u}_2}{c_s} = \frac{v}{2c_s}\frac{\tau_o}{\mu}\frac{\sin q\pi}{q\pi}\frac{(1-\hat{\alpha}_s^4)}{R_q}\frac{1}{(-\eta_1/L)^q}\left\{1 - q\int_0^1 \frac{\xi^q}{\xi + \eta_1/L}\,d\xi\right\} \qquad \frac{\eta_1}{L} < -1\,. \tag{4.57c}$$

Note that $\dot{u}_2$ is bounded all along the crack plane.

4.2.8 Dynamic Energy Release Rate

The dynamic energy release rate G, defined as the rate of flow of mechanical energy into the crack tip region per unit crack advance per unit thickness along the crack front, is given by (FREUND, 1989)

$$G = \lim_{\Sigma\to 0}\left\{\frac{1}{v}\oint_\Sigma \left[\sigma_{\alpha\beta}n_\beta\dot{u}_\alpha + \frac{1}{2}(\sigma_{\alpha\beta}u_{\alpha,\beta} + \rho\dot{u}_\alpha\dot{u}_\alpha)vn_1\right]d\Sigma\right\}\,, \tag{4.58}$$

where Σ is a contour starting on the lower crack face, surrounding the crack tip and ending on the upper crack face. n_α are the components of the unit outward vector normal to the contour Σ at any point on it. In the presence of a line cohesive zone, the crack tip region is not a single point but has a finite size. Shrinking the contour Σ on to the boundaries of the cohesive zone and making use of mode II symmetries and the steady state approximation, we obtain

$$G = 2\int_0^{-L} \sigma_{12}(\eta_1, \eta_2 \to 0^+)\, u_{1,1}(\eta_1, \eta_2 \to 0^+)\, d\eta_1 \tag{4.59}$$

With the assumed cohesive shear traction (4.44), the dynamic energy release rate G reduces to

$$G = \tau_o \delta_t \tag{4.60}$$

where $\delta_t = u_1(\eta_1 = -L, \eta_2 \to 0^+) - u_1(\eta_1 = -L, \eta_2 \to 0^-)$ is the crack tip sliding displacement (relative slip at the physical crack tip). The crack tip sliding displacement δ_t can be obtained by integrating the displacement gradient $u_{1,1}$ along the cohesive surfaces from the front end of the cohesive zone to the physical crack tip. It is given by

$$\frac{\delta_t}{L} = \begin{cases} \dfrac{4}{\pi}\dfrac{\tau_o}{\mu}\dfrac{\alpha_s(1-\alpha_s^2)}{R(v)} & 0 \le v < c_R\,, \\[2ex] \dfrac{2\sin q\pi}{(1-q)\pi}\dfrac{\tau_o}{\mu}\dfrac{\hat{\alpha}_s(1+\hat{\alpha}_s^2)}{R_q} & c_s < v < c_l\,, \end{cases} \tag{4.61}$$

and thus from (4.60) the normalized dynamic energy release rate is given by

$$\frac{G}{G_o} = \begin{cases} \dfrac{2\alpha_s(\alpha_l^2-\alpha_s^2)}{R(v)} & 0 \le v < c_R\,, \\[2ex] \dfrac{4}{\pi^2}\dfrac{\hat{\alpha}_s(\alpha_l^2+\hat{\alpha}_s^2)}{R_q}\dfrac{\sin q\pi}{1-q}\left(\dfrac{q\pi}{\sin q\pi}\right)^{1/q}\left(\dfrac{\sigma_{12}^D}{\tau_o}\right)^{1/q-2} & c_s < v < c_l\,, \end{cases} \tag{4.62}$$

where G_o is the energy release rate associated with a quasi-statically propagating crack with the same far-field applied load σ_{12}^D and the same cohesive strength of the crack plane τ_o. It is given by

$$G_o = \frac{\pi(\kappa+1)}{4}\frac{{\sigma_{12}^D}^2 D}{\mu}\,. \tag{4.63}$$

Hence (4.62) represents the variation of dynamic energy release rate with crack speed under a constant σ_{12}^D/τ_o.

Figure 4.9 shows the variation of the G/G_o with crack speed for different values of σ_{12}^D/τ_o. For steady sub-Rayleigh crack growth G is path independent and hence the process zone characteristics need not be taken into account as long as an annular

region around the crack tip exists, where the square root singular fields are dominant. As seen from Figure 4.9, G is independent of σ_{12}^D/τ_o for sub-Rayleigh crack speeds. However, for intersonic speeds, G is dependent on the size and characteristics of the process zone. It depends on the extent of the process region as $(L/D)^{1-2q}$, where L is the cohesive zone and D is the distance at which the Freund's singular solution dominates. As seen from Figure 4.9, the dynamic energy release rate G is finite through out the intersonic regime except for crack speeds close to c_s and c_l. In contrast, with a point sized process zone, G is zero everywhere in the intersonic regime except at $v = \sqrt{2}\, c_s$. Hence, based on the requirement of a positive energy flux, the entire intersonic regime is admissible for mode II crack growth in the presence of a process zone of finite size. At a fixed far-field load σ_{12}^D, the dynamic energy release rate for intersonic speeds depends strongly on the shear strength of the fracture plane τ_o. As $\tau_o \to \infty$, the singular solution with no cohesive zone is recovered and once again there exists only one intersonic speed $v = \sqrt{2}\, c_s$, at which the dynamic energy release rate is finite. With a lower shear strength, more of the intersonic regime becomes admissible, the energy flux into the crack tip increases and also the energy flux attains its peak at a speed higher than $\sqrt{2}\, c_s$. At $v = \sqrt{2}\, c_s$, an intersonic crack behaves "subsonic-like", *i.e.*, the explicit dependence on τ_o disappears and G attains a constant value equal to $2G_o/\sqrt{(1+\kappa)(3-\kappa)}$.

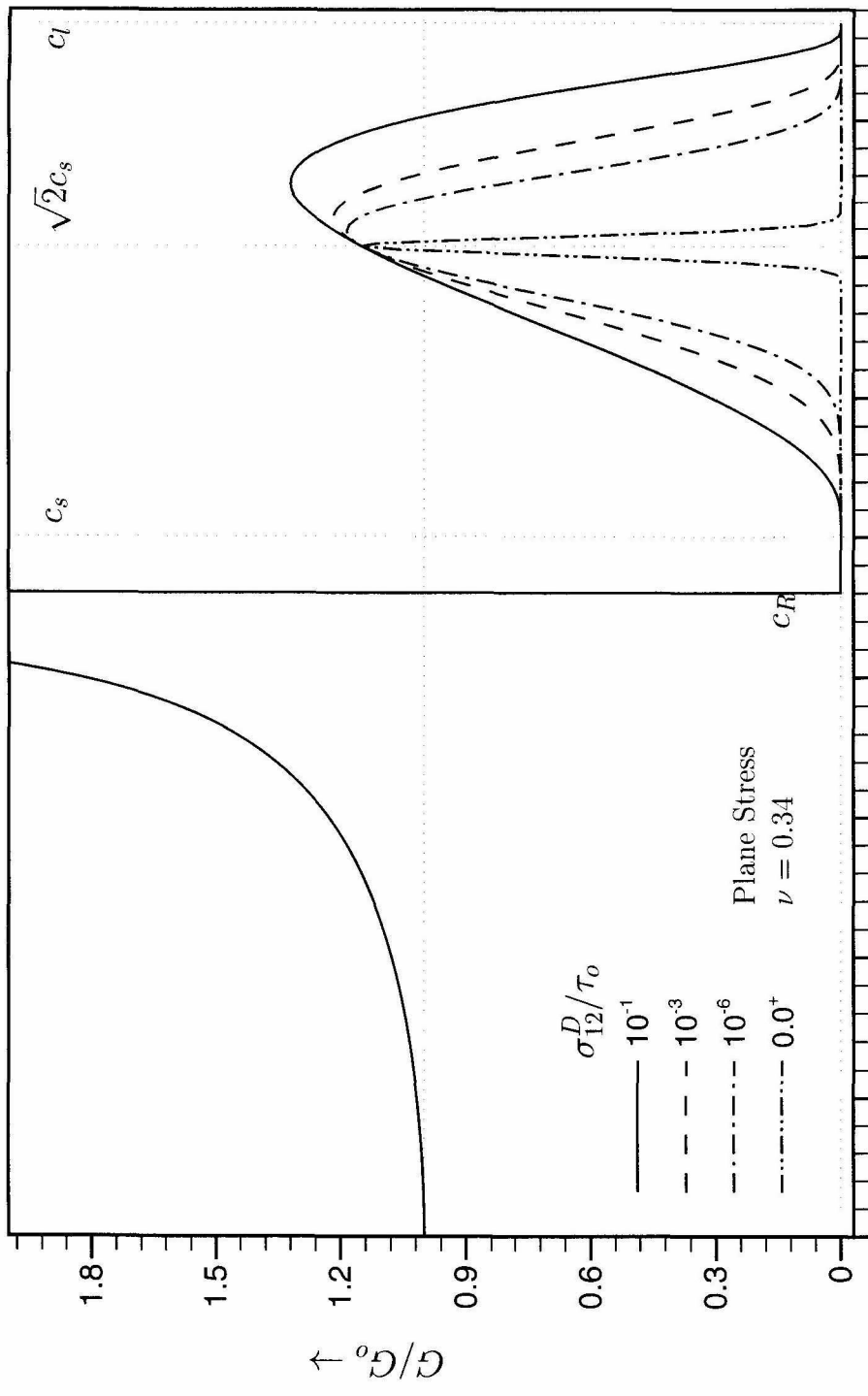

Figure 4.9: Dynamically propagating mode II crack with a Dugdale type cohesive zone — Dependence of the dynamic energy release rate on crack tip speed v, plotted for different values of σ_{12}^D/τ_o.

4.2.9 Displacement Field on the Crack Faces

The displacement field on the crack faces is obtained by integrating the displacement gradients along the cohesive surfaces and the crack faces.

$$u_\alpha(-L < \eta_1 < 0, \eta_2 \to 0^+) = \int_0^{\eta_1} u_{\alpha,1}(-L < \eta_1' < 0, \eta_2 \to 0^+) d\eta_1' \,, \tag{4.64a}$$

$$u_\alpha(\eta_1 < -L, \eta_2 \to 0^+) = u_\alpha(\eta_1 = -L) + \int_{-L}^{\eta_1} u_{\alpha,1}(\eta_1' < -L, \eta_2 \to 0^+) d\eta_1' \,. \tag{4.64b}$$

Note that $u_{1,1}$ is singular at the physical crack tip and hence the integration is done separately over the cohesive surface and the crack face. With a Dugdale type cohesive zone, the sliding displacement discontinuity across the cohesive zone and the crack faces ($\eta_1 < 0$) is given by

$$\frac{\delta_1}{L} = \frac{4}{\pi}\frac{\tau_o}{\mu}\frac{\alpha_s(1-\alpha_s^2)}{R(v)}\left[\sqrt{\frac{-\eta_1}{L}} + \frac{1}{2}\left(1+\frac{\eta_1}{L}\right)\int_0^{-L/\eta_1}\frac{d\xi}{\sqrt{\xi}(\xi-1)}\right], \tag{4.65}$$

for $0 \le v < c_R$. Within the cohesive zone ($-L < \eta_1 < 0$), the integral in the above expression must be interpreted in the Cauchy principal value sense. For $c_s < v < c_l$,

$$\frac{\delta_1}{L}(-1 < \frac{\eta_1}{L} < 0) = \frac{2\tau_o}{\mu}\frac{\hat{\alpha}_s(1+\hat{\alpha}_s^2)}{R_q}\frac{\sin q\pi}{\pi}\left[\left(1+\frac{\eta_1}{L}\right)\frac{\pi}{\tan q\pi} + \frac{1}{1-q}\left(\frac{-\eta_1}{L}\right)^{1-q} + (1+\frac{\eta_1}{L})\,\mathrm{pv}\int_0^{-L/\eta_1}\frac{\zeta^{q-1}}{\zeta-1}d\zeta\right], \tag{4.66a}$$

$$\frac{\delta_1}{L}(\frac{\eta_1}{L} < -1) = \frac{2\tau_o}{\mu}\frac{\hat{\alpha}_s(1+\hat{\alpha}_s^2)}{R_q}\frac{\sin q\pi}{\pi}\left[\frac{1}{q}\left(\frac{-\eta_1}{L}\right)^{-q}\left\{\frac{1}{1-q}\left(\frac{-\eta_1}{L}\right)-1\right\} + (1+\frac{\eta_1}{L})\int_0^{-L/\eta_1}\frac{\zeta^q}{\zeta-1}d\zeta\right]. \tag{4.66b}$$

The variation of sliding displacement discontinuity along the crack faces and the

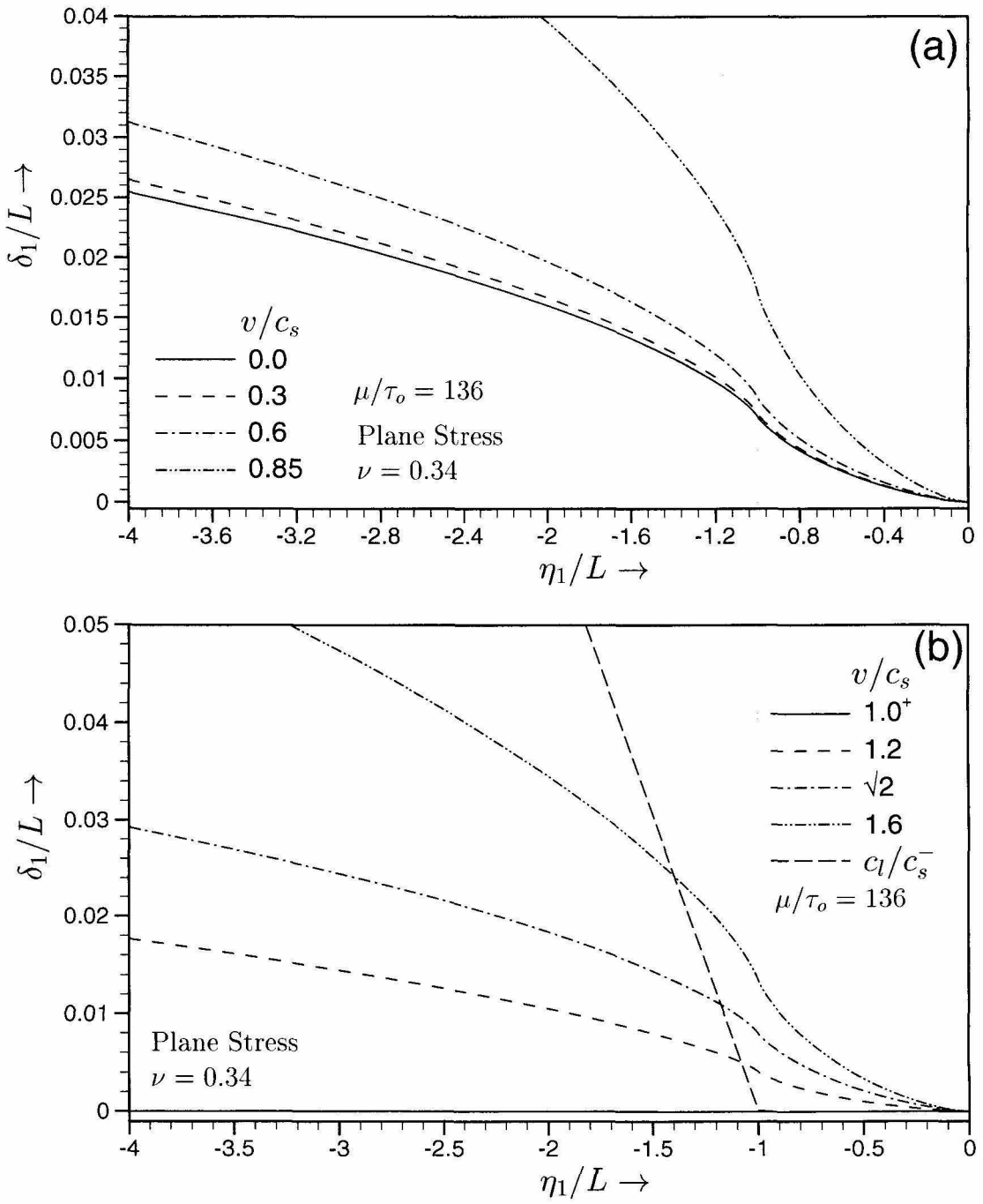

Figure 4.10: Dynamically propagating mode II crack with a Dugdale type cohesive zone — Relative sliding displacement δ_1 on the crack plane. **(a)** Sub-Rayleigh speeds. **(b)** Intersonic speeds.

cohesive zone is shown in Figure 4.10(a) for various sub-Rayleigh crack speeds and in Figure 4.10(b) for various intersonic crack speeds. The parameter μ/τ_o was chosen to be 136, which represents the ratio of shear modulus of Homalite and the shear strength of the Homalite/Homalite bond. As seen from the figure, sliding begins smoothly at the front end of the cohesive zone. The crack tip sliding displacement (δ_1 at $\eta_1 = -L$) is found to be less than 2% of the cohesive zone length for both sub-Rayleigh and intersonic crack speeds, except at speeds close to c_R. The displacement component u_2 on the crack faces and the cohesive surfaces is given in the Appendix B for sub-Rayleigh crack speeds and is given in Appendix C for intersonic crack speeds.

It was mentioned before that the cohesive constitutive relation for a line cohesive zone relates the traction on a cohesive surface to the local displacement discontinuity, displacement rate and other variables representing the past history of deformation. However, as seen from the formulation above, cohesive crack problems featuring cohesive laws that relate the traction to position within the cohesive zone ($\tau - \eta_1$) are more amenable to analytical solution techniques. Crack problems with realistic Cohesive constitutive laws (that relate the traction to local displacement discontinuity), are difficult to solve analytically for closed form solutions and often require recourse to numerical methods. For this reason, a number of researchers in the past have used "$\tau - \eta_1$" cohesive laws to obtain analytical solutions to various cohesive crack problems (BARENBLATT, 1962; GOODIER, 1968; BROBERG, 1994; 1995). The justification in using such a cohesive law lies in the fact that if an appropriate "$\tau - \eta_1$" law is chosen, an eventual "$\tau - \delta$" relation can be obtained after solving the problem analytically, which is very close to the actual phenomenological/atomistic cohesive constitutive relation of the material. However, when dealing with propagating crack solutions, the eventual "$\tau - \delta$" relation obtained must also be independent of crack speed. For example, consider a steadily propagating dynamic mode II crack with a line cohesive zone, and a cohesive traction that decays linearly with distance from its

front end.

$$\tau(-1 < \frac{\eta_1}{L} < 0) = \tau_o \left(1 + \frac{\eta_1}{L}\right) . \tag{4.67}$$

Solving the governing equations for the near tip fields using the cohesive traction distribution above, results in a "$\tau - \delta$" relation as shown in Figure 4.11(a) for sub-Rayleigh crack speeds and as shown in Figure 4.11(b) for intersonic crack speeds. Here δ_c is the critical crack tip sliding displacement. For sub-Rayleigh crack speeds, the "shear traction vs sliding displacement" relation is nearly linear, and is independent of crack speed. Hence the use of a "$\tau - \eta_1$" cohesive law is physically acceptable. For intersonic crack speeds, the "shear traction vs sliding displacement" relation is dependent on crack speed and is physically unacceptable. Hence "$\tau - \eta_1$" cohesive laws cannot be used for intersonic cohesive crack solutions. The fracture energy Γ, which is the area under the "$\tau - \delta$" curve is given by

$$\Gamma = \begin{cases} \dfrac{4}{9}\tau_o\delta_c & 0 \leq v < c_R \,, \\ \\ \dfrac{3}{3(2-q)}\tau_o\delta_c & c_s < v < c_l \,. \end{cases} \tag{4.68}$$

However, the Dugdale type cohesive law assumed in this chapter results in a constant "$\tau - \delta$" relation which is independent of crack speed for both sub-Rayleigh and intersonic crack speeds.

4.2.10 Secondary Tensile Cracks

It was mentioned in the previous chapter, that the experimentally observed intersonic mode II cracks were accompanied by a series of short opening cracks, parallel to each other and inclined at a steep angle to the main shear crack path. These cracks were observed only in the top half of the specimen and their angle of inclination θ^* with the η_2-axis varied roughly from 8^o to 13^o, with an average of about 10.6^o. θ^* was roughly the same through out the crack path and no strong correlation was found between this

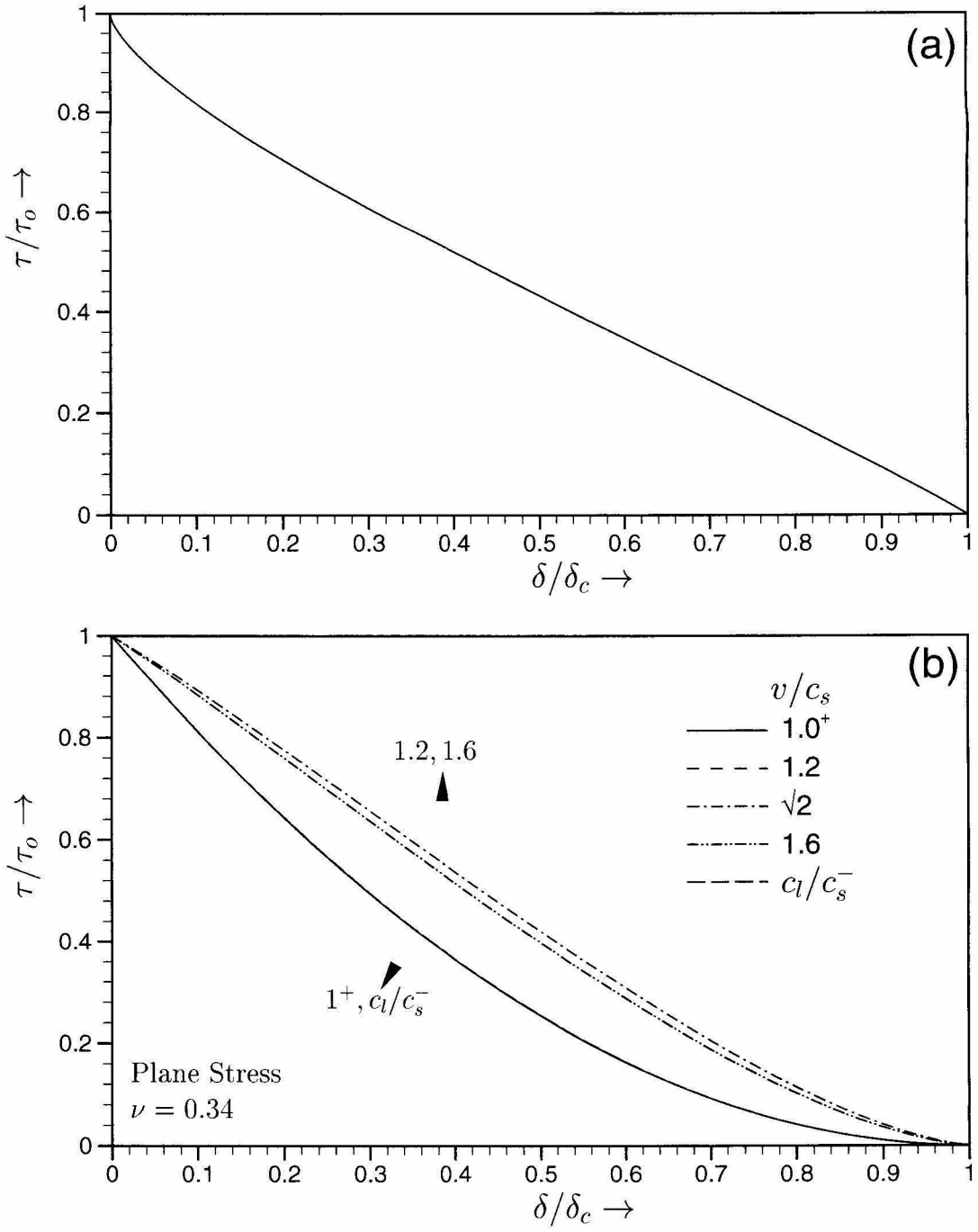

Figure 4.11: $\tau - \delta$ relation obtained for a dynamically propagating mode II crack with a cohesive zone characterized by a cohesive stress distribution that varies linearly with distance from the crack tip. **(a)** Sub-Rayleigh speeds. **(b)** Intersonic speeds.

angle and the main shear crack speed (v). It was found that these secondary opening cracks originated a finite but small distance ($\approx 1-2$ mm) behind the main intersonic shear crack tip. It was also argued that, if these cracks originated on a traction free crack face, they would have propagated vertically, and to explain their inclination to the vertical, a more complex 2-D state of stress must exist at the initiation site. Here, we will make an attempt to see if these cracks could originate from the upper cohesive surface and if so, their relative orientation from the vertical and whether the predictions based on the current intersonic cohesive crack model match with the experimental observations.

It was mentioned before that the mode II stress intensity factor at the tip of experimentally observed intersonic mode II cracks was negative. Hence, to be consistent with the experimental observations, we change the sign of the remote shear load (σ_{12}^{D}) in the present model, which results in a change in the sign of cohesive shear tractions as well. For $c_s < v < c_l$, the stress state at every point on the upper cohesive surface ($-L < \eta_1 < 0, \eta_2 \to 0^+$) is such that the shear stress component σ_{12} is -ve and the direct stress component σ_{11} is +ve (tensile). Note that $\sigma_{22} = 0$ on the upper cohesive surface. A simple Mohr's circle analysis yields the result that the maximum principal stress at every point on the upper cohesive surface is invariably tensile. Moreover, the minimum principal tensile stress is invariably compressive. The maximum principal tensile stress at any point on the upper cohesive surface is given by

$$\sigma_1(-L < \eta_1 < 0, \eta_2 \to 0^+) = \frac{\sigma_{11}}{2} + \sqrt{\left(\frac{\sigma_{11}}{2}\right)^2 + \sigma_{12}^2}\,, \tag{4.69}$$

and the angle of inclination of the principal plane (its normal) with the horizontal (see Fig 3.11(b)) at any point on the upper cohesive surface is given by

$$\theta^*(-L < \eta_1 < 0, \eta_2 \to 0^+) = \frac{1}{2}\tan^{-1}\left(\frac{-2\sigma_{12}}{\sigma_{11}}\right)\,. \tag{4.70}$$

For a steadily propagating intersonic mode II crack, $\sigma_{12}(-L < \eta_1 < 0, \eta_2 \to 0^+) = -\tau_o$

and σ_{11} on the upper cohesive surface is given in (4.50) with the opposite sign. Thus σ_1 on the upper cohesive surface may be obtained following (4.69). The principal angle θ^* for $-L < \eta_1 < 0, \eta_2 \to 0^+$ is given by

$$\theta^* = \frac{1}{2}\tan^{-1}\left[\frac{-2\alpha_l}{(\alpha_l^2+\hat{\alpha}_s^2)}\frac{q\pi}{\sin^2 q\pi}\left\{\frac{q\pi}{\tan q\pi} - \left(\frac{-\eta_1}{L}\right)^{-q}\left\{1 - q\,\mathrm{pv}\int_0^1 \frac{\zeta^q}{\zeta+\eta_1/L}d\zeta\right\}\right\}^{-1}\right]. \tag{4.71}$$

Figure 4.12(a) shows the variation of the maximum principal tensile stress σ_1 along the upper cohesive surface for different intersonic speeds. As seen, σ_1 increases monotonically from zero at the mathematical crack tip ($\eta_1 = 0$) and becomes unbounded at the physical crack tip ($\eta_1 = -L$). If we assume that Homalite obeys the maximum principal stress criterion for brittle fracture, then a tensile crack would initiate at a point $\eta_1 = -L^*$ on the upper cohesive surface, where

$$\sigma_1(\eta_1 = -L^*, \eta_2 \to 0^+) = \sigma_u^H\,. \tag{4.72}$$

σ_u^H is the ultimate tensile strength of Homalite, which is $\approx$ 35 MPa (see Table 2.1). Since σ_1 on the upper cohesive surface always attains a value higher than σ_u^H, a secondary tensile crack is initiated at all intersonic speeds except at c_s and c_l. Consider a material particle on the crack plane ahead of the approaching intersonic mode II crack tip, which would eventually end up on the upper crack face. As the front end of the cohesive zone passes through this particle, the maximum principal tensile stress acting on it increases monotonically from zero and when it reaches σ_u^H at $\eta_1 = -L^*$, a tensile crack is initiated on the principal plane. From Figure 4.12(a), we can see that L^* is a strong function of crack speed and depending on it, the tensile crack would initiate at different relative positions on the upper cohesive surface. For example, the tensile crack would initiate at $L^* = 0.48L$ for $v = 1.6c_s$ and at $L^* = 0.8L$ for $v = \sqrt{2}\,c_s$. Figure 4.12(b) shows the variation of θ^*, the angle of inclination of the principal plane (see Fig 3.11(b)) along the upper cohesive surface. Having determined

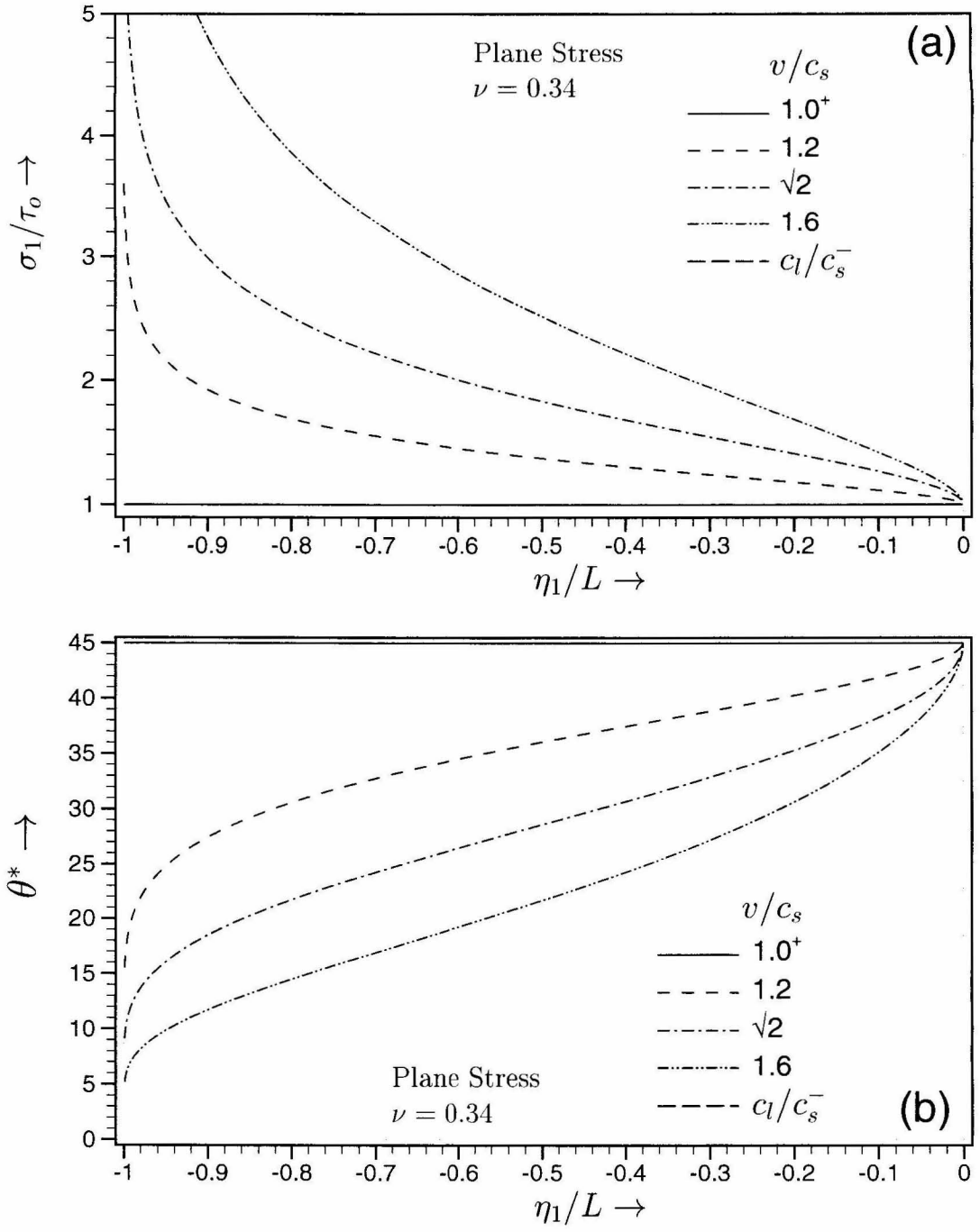

Figure 4.12: Dynamically propagating mode II crack with a Dugdale type cohesive zone. **(a)** Maximum principal tensile stress σ_1 on the upper cohesive surface. **(b)** Inclination θ^* of the principal plane to the vertical.

the position along the upper cohesive surface where a tensile crack is likely to initiate, we can also determine the angle θ^* made by this tensile crack with the vertical from Figure 4.12(b). Remarkably, for all intersonic speeds, the angle θ^* is identical, being equal to $\approx 21.8^o$. This is partially in agreement with the experimental observations, where the angle of inclination of the secondary tensile cracks was almost the same and no strong correlation was found between θ^* and v. However, the angle of inclination of 21.8^o is almost twice that observed in the experiments. A major reason for this discrepancy may lie in the simple Dugdale type cohesive constitutive relation adopted in the current model. As mentioned before, phenomenological considerations indicate that the cohesive failure process in our experimental specimens is likely to be rate dependent. In the next chapter, we will introduce a rate dependent cohesive model and study its predictions on the secondary tensile cracks to see if such a model is indeed more appropriate.

4.2.11 Stress Jump Across Mach Waves

As seen before, intersonic mode II crack propagation is accompanied by strong Mach wave radiation from the crack tip region. Across these Mach waves, stress and particle velocity fields suffer a jump. Consider a Mach wave oriented at an angle ξ to the crack face (see Figure 3.7(a)). The crack speed v is then equal to $c_s/\sin\xi$. The normal stress perpendicular to the Mach wave σ_n and the tangential shear stress along the Mach wave σ_t are given by

$$\sigma_n = \vec{e_n}.\tilde{\sigma}\vec{e_n} = \sigma_{11}\sin^2\xi + \sigma_{22}\cos^2\xi + \sigma_{12}\sin 2\xi \tag{4.73a}$$

$$\sigma_t = \vec{e_n}.\tilde{\sigma}\vec{e_t} = (\sigma_{22} - \sigma_{11})\sin\xi\cos\xi - \sigma_{12}\cos 2\xi\,, \tag{4.73b}$$

where $(\sin\xi, \cos\xi)$ are the components of the unit vector $\vec{e_n}$ normal to the Mach wave and $(-\cos\xi, \sin\xi)$ are the components of the unit vector $\vec{e_t}$ tangential to the Mach wave in the $\eta_1 - \eta_2$ plane.

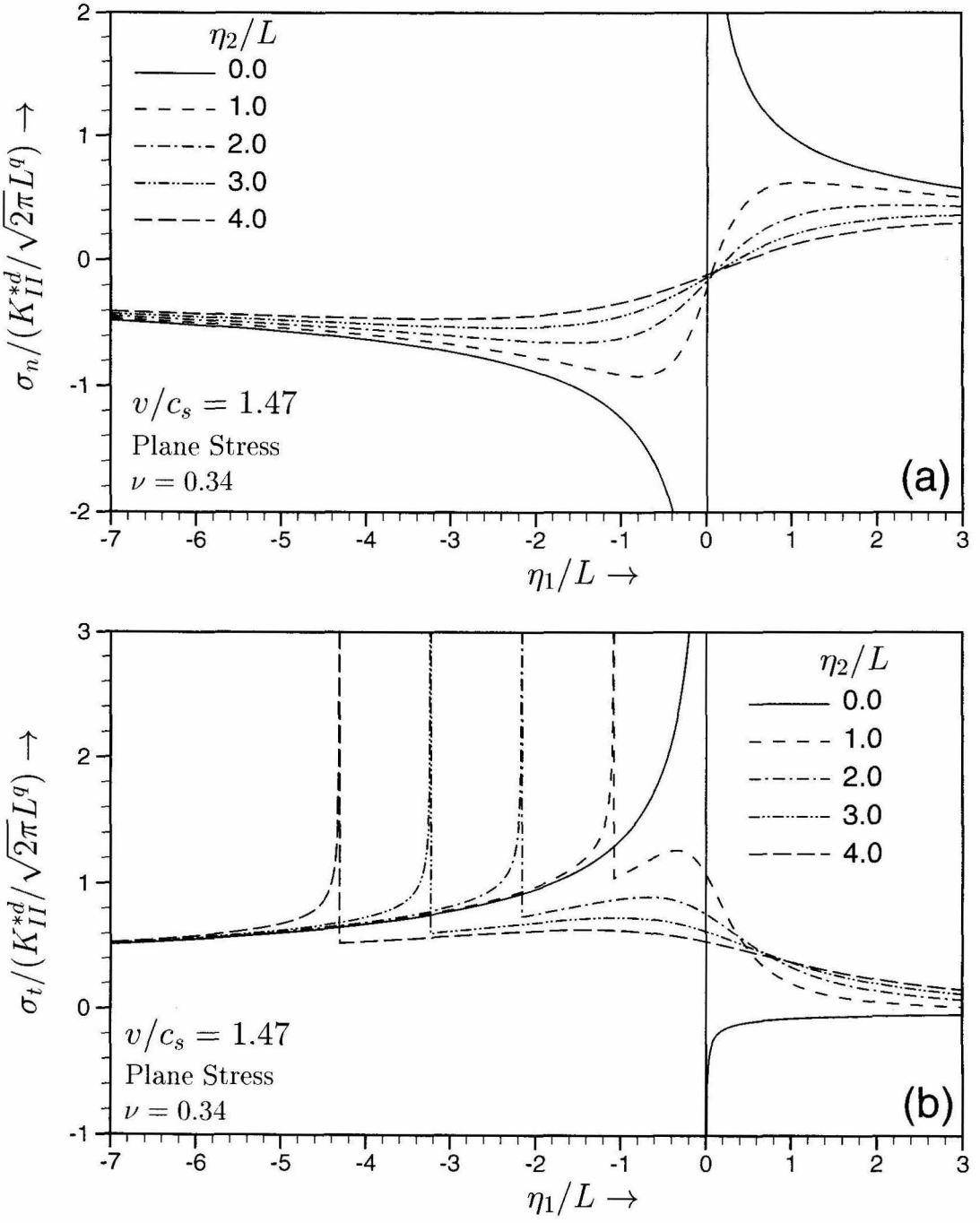

Figure 4.13: Dynamically propagating mode II crack without a cohesive zone — Stress jump across the Mach waves. **(a)** Normal stress σ_n at different heights above the crack plane. **(b)** Tangential stress σ_t at different heights above the crack plane.

Consider a steadily propagating intersonic mode II crack with a mathematically sharp crack tip (no cohesive zone) at a speed $v = 1.47c_s$. Such a crack radiates two Mach waves from its tip, one into the upper half plane and the other into the lower half plane, both inclined at an angle $\xi = 42.9^o$ to the crack faces. The near-tip stress field is given by the Freund's singular solution (see Appendix A). Thus σ_n and σ_t can be obtained from (4.73). Figure 4.13(a) shows the variation of normal stress σ_n along a horizontal line ($-7L < \eta_1 < 3L$), with the different curves representing different heights ($\eta_2 = 0, L, 2L, 3L, 4L$) above the crack plane. Here L is an arbitrary length scale chosen to be unity. From the figure, we can see that at any height above the crack plane, the normal stress σ_n doesn't suffer a jump across the Mach wave and is continuous across it. In the same way, one can show that the velocity component normal to the Mach wave is also continuous across it. Figure 4.13(b) shows the variation of tangential stress σ_t along a horizontal line ($-7L < \eta_1 < 3L$), with the different curves representing different heights ($\eta_2 = 0, L, 2L, 3L, 4L$) above the crack plane. From the figure, we can see that at any height above the crack plane, the tangential stress σ_t suffers an infinite jump across the Mach wave. $\sigma_t \to \infty$ as the Mach wave is approached in the +ve η_1 direction, whereas it attains a finite value as the Mach wave is approached in the -ve η_1 direction. In the same way, one can show that the velocity component tangential to the Mach wave suffers an infinite jump across it. Thus across the Mach wave, the normal stress and normal velocity component are continuous, whereas the tangential shear stress and the tangential velocity component suffer infinite jumps. This is true for all intersonic speeds and hence these Mach waves are shear Mach waves.

Now, consider a steadily propagating intersonic mode II crack with a Dugdale type line cohesive zone in front of the tip at a speed $v = 1.47c_s$. Such a crack radiates two Mach waves into both the upper and lower half planes, one emitted from the front end of the cohesive zone and the other from the physical crack tip, all of them inclined at an angle $\xi = 42.9^o$ to the crack faces. The near tip stress field is

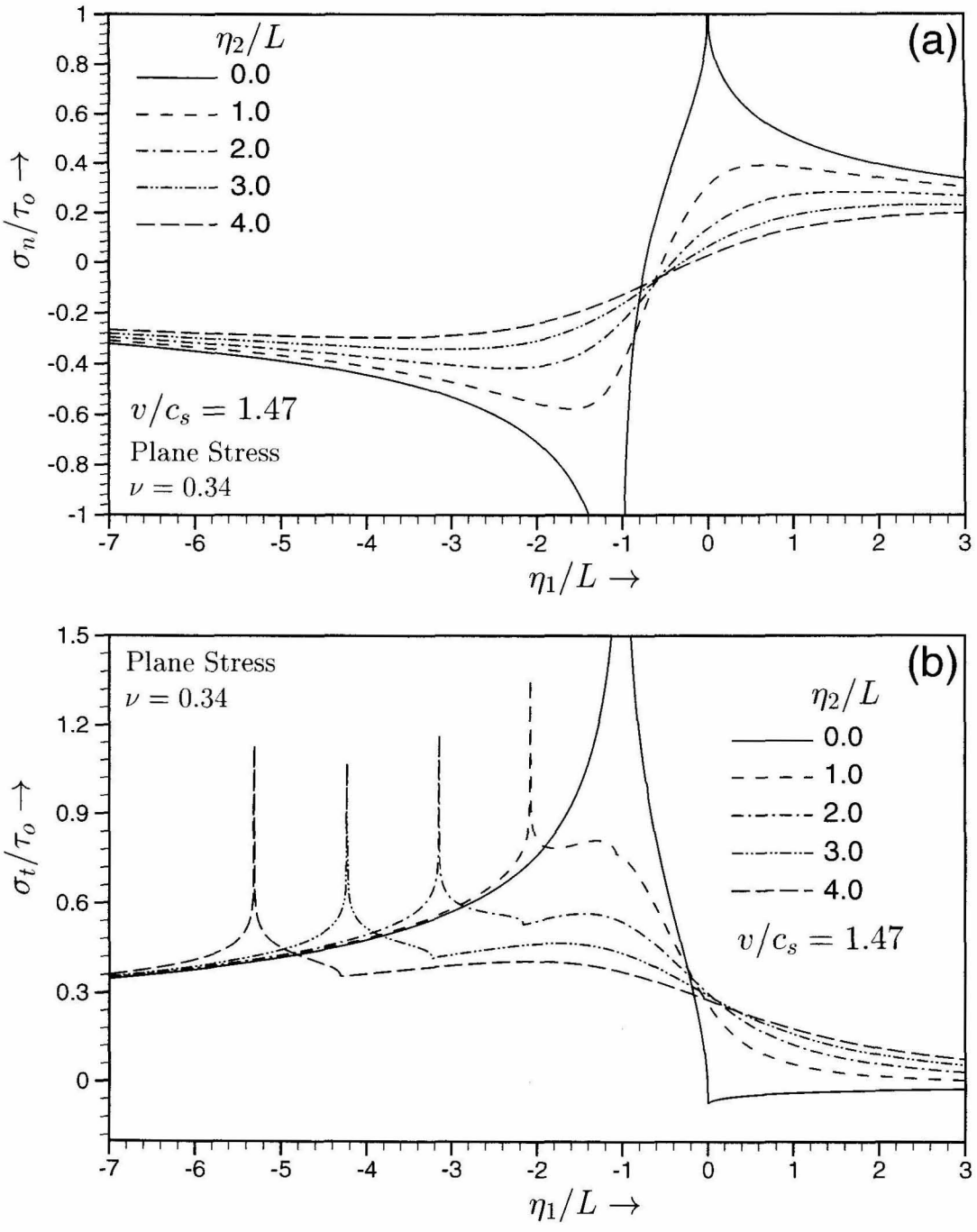

Figure 4.14: Dynamically propagating mode II crack with a Dugdale type cohesive zone — Stress jump across the Mach waves. **(a)** Normal stress σ_n at different heights above the crack plane. **(b)** Tangential stress σ_t at different heights above the crack plane.

given in Appendix C. Thus σ_n and σ_t can be obtained from (4.73). Figure 4.14(a) shows the variation of normal stress σ_n and Figure 4.14(b) shows the variation of tangential stress σ_t along a horizontal line ($-7L < \eta_1 < 3L$), with the different curves representing different heights ($\eta_2 = 0, L, 2L, 3L, 4L$) above the crack plane. Here L is the length of the cohesive zone. From Figure 4.14(a), we can see that at any height above the crack plane, the normal stress σ_n doesn't suffer a jump across either of the Mach waves and is continuous across them. However, the tangential stress σ_t is continuous at the Mach wave emanating from the front end of the cohesive zone, but becomes unbounded at the Mach wave emanating from the physical crack tip (see Figure 4.14(b)). Unbounded stress along a Mach wave is unphysical and it is desirable to modify the cohesive constitutive relation to eliminate this singularity.

4.3 Critical Crack Tip Sliding Displacement Criterion

Now we implement the second part of our cohesive law, *i.e.*, we introduce a propagation criterion, which states that sustained dynamic mode II crack propagation occurs under a constant crack tip sliding displacement. (see Figure 4.3(b)).

$$\delta_t = u_1(\eta_1 = -L, \eta_2 \to 0^+) - u_1(\eta_1 = -L, \eta_2 \to 0^-) = \delta_c \,. \tag{4.74}$$

δ_c is the critical crack tip sliding displacement, a material specific parameter. In our case, it is based on the properties of the Homalite/Homalite bond and should depend strongly on the conditions at the surface of sliding — the nature of bonded surfaces, asperity contacts, whether deformation at asperity contacts occurs by brittle cracking, plastic flow, or, at elevated temperature by melting etc. Such a propagation criterion, which is concerned only with the local state in the vicinity of the crack tip, is more convenient (as compared to a non-local criterion like the Griffith's criterion) for modeling the actual physical mechanism of crack growth as well as for application to practical problems using numerical techniques. Also, unlike in the subsonic case, for an intersonic crack, the process zone characteristics need to be known to determine

the energy flux to the tip region and hence the advantage of employing a small-scale yielding type approach is lost. The propagation criterion (4.74) is equivalent to the constant critical G criterion (independent of crack speed), since the critical G is equal to the area under the curve of cohesive stress vs sliding displacement.

Consider a steadily propagating dynamic mode II crack with a Dugdale type cohesive zone in front of the tip. The crack speed is either subsonic or intersonic ($0 < v < c_l$). For a shear strength of the crack plane τ_o and a far-field load σ_{12}^D, the crack tip sliding displacement δ_t is given by

$$\delta_t/\delta_t^o = \begin{cases} \dfrac{2\alpha_s(\alpha_l^2 - \alpha_s^2)}{R(v)} & 0 \le v < c_R\,, \\ \dfrac{4}{\pi^2}\dfrac{\hat{\alpha}_s(\alpha_l^2 + \hat{\alpha}_s^2)}{R_q}\dfrac{\sin q\pi}{1-q}\left(\dfrac{q\pi}{\sin q\pi}\right)^{1/q}\left(\dfrac{\sigma_{12}^D}{\tau_o}\right)^{1/q-2} & c_s < v < c_l\,, \end{cases} \tag{4.75}$$

where δ_t^o is the crack tip sliding displacement associated with a quasi-statically growing mode II crack under the same far-field loading σ_{12}^D and shear strength of the crack plane τ_o.

$$\delta_t^o = \frac{\pi(\kappa+1)}{4}\frac{\tau_o}{\mu}\left(\frac{\sigma_{12}^D}{\tau_o}\right)^2 D\,. \tag{4.76}$$

The critical crack tip sliding displacement criterion (4.74) states that $\delta_t = \delta_t^o = \delta_c$. Hence (4.75) gives a relationship between the critical values (required to satisfy the criterion) of σ_{12}^D, v, and τ_o.

4.3.1 Stability of Crack Growth

Figure 4.15 shows the variation with crack speed of the critical far-field load $(\sigma_{12}^D)_{dyn}^c$ (required to satisfy the critical crack tip sliding displacement criterion (4.74)) from its quasi-static value $(\sigma_{12}^D)_o^c$ for both sub-Rayleigh and intersonic crack speeds. The

ratio $(\sigma_{12}^D)_{dyn}^c/(\sigma_{12}^D)_o^c$ is given by

$$\frac{(\sigma_{12}^D)_{dyn}^c}{(\sigma_{12}^D)_o^c} = \begin{cases} \sqrt{\left[\dfrac{R(v)}{2\alpha_s(\alpha_l^2-\alpha_s^2)}\right]} & 0 \le v < c_R\,, \\ \left(\dfrac{\mu\delta_c}{D\tau_o}\right)^{q-1/2} \sqrt{\left[\dfrac{\pi}{2}\dfrac{(1+\hat{\alpha}_s^2)}{(\alpha_l^2+\hat{\alpha}_s^2)}\right]} \left(\dfrac{\sin q\pi}{q\pi}\right) \left[\dfrac{2\pi\alpha_l(1-q)}{(1+\hat{\alpha}_s^2)\sin^2 q\pi}\right]^q & c_s < v < c_l\,, \end{cases} \tag{4.77}$$

where the critical far-field load required for quasi-static crack propagation, $(\sigma_{12}^D)_o^c$ is given by

$$(\sigma_{12}^D)_o^c = \tau_o\sqrt{\frac{4}{(\kappa+1)\pi}\frac{\mu\delta_c}{D\tau_o}} \tag{4.78}$$

As seen from Figure 4.15, for a sub-Rayleigh crack, the far-field load required to sustain a small acceleration in crack speed is lower compared to its previous value. This situation may be interpreted as an instability and it can be expected that a subsonic mode II crack would accelerate rapidly to c_R. This explains the reason for nonobservation of any subsonic crack speeds for mode II shear cracks propagating along a weak plane in Homalite (see Figure 3.5(b)). Even if the shear crack initiating from the notch initially propagated at sub-Rayleigh speeds, it would immediately accelerate to c_R and beyond.

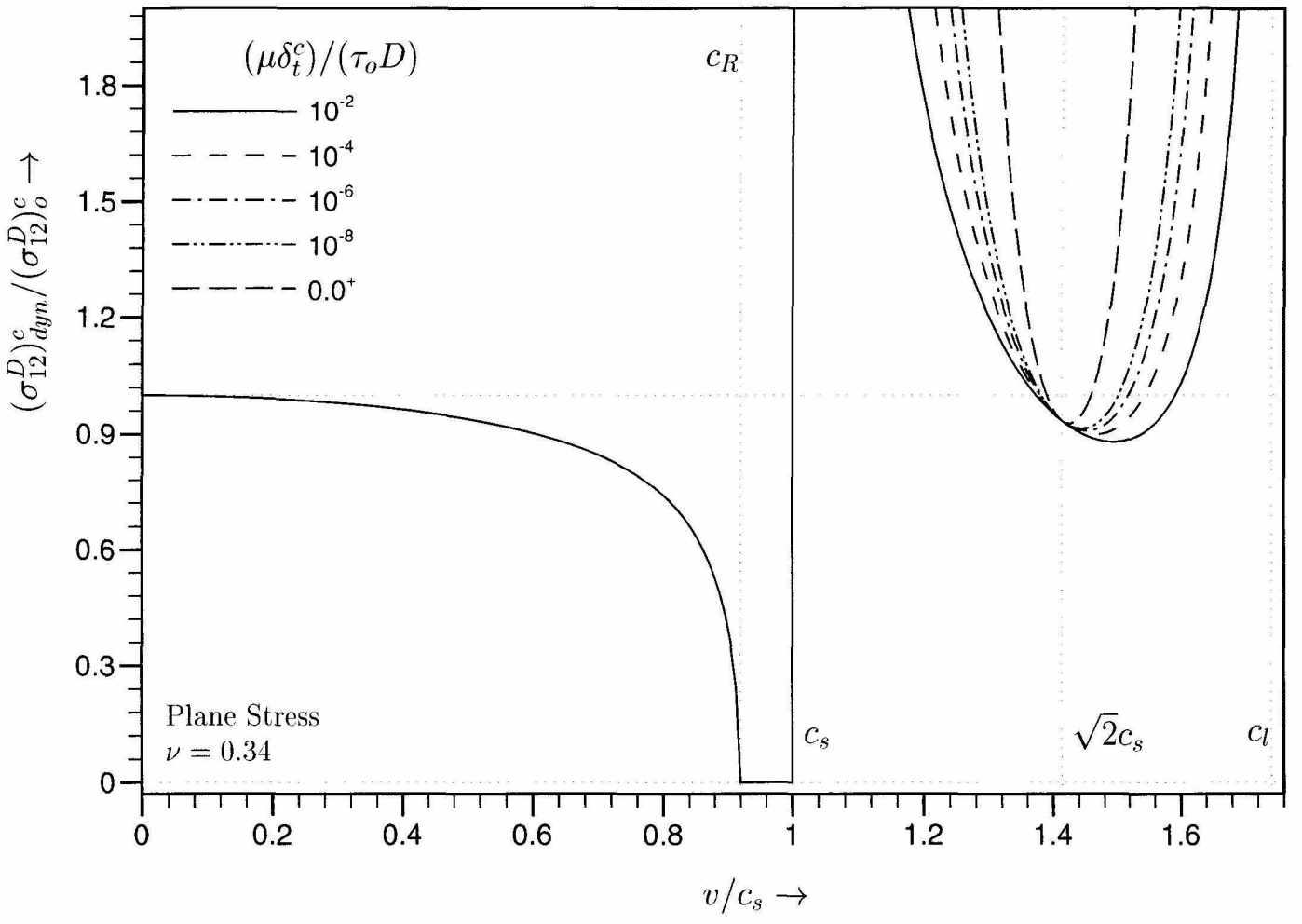

Figure 4.15: Dynamically propagating mode II crack with a Dugdale type cohesive zone — Stability of crack growth. Dependence of the critical far-field load (required during sustained dynamic crack growth) on crack tip speed v, plotted for different values of the interface strength parameter $(\mu\delta_t^c)/(\tau_o D)$.

By the same interpretation, for an intersonic crack, there is an initially unstable speed regime followed by a stable speed regime. The critical far-field load $(\sigma_{12}^D)_{dyn}^c/(\sigma_{12}^D)_o^c$ is also a function of a material parameter $(\mu\delta_c)/(\tau_o D)$ in the intersonic regime. μ and δ_c are material constants and D is an arbitrary distance ahead of the crack tip at which the singular solution (with no cohesive zone) dominates. Hence the parameter $(\mu\delta_c)/(\tau_o D)$ may be interpreted as a measure of shear strength of the fracture plane and different curves in Figure 4.15 indicate the stability characteristics for different fracture plane strengths. It is seen that the entire speed regime $c_s < v < \sqrt{2}\,c_s$ is unstable and the speed at which intersonic crack propagation becomes stable depends on the shear strength of the fracture plane. For $\tau_o \to 0$, *i.e.*, for the case of vanishing shear strength of the fracture plane, almost the entire intersonic regime becomes unstable, indicating that a mode II crack on a weak plane of vanishing strength should propagate at speeds close to c_l. On the other hand, for $\tau_o \to \infty$, the singular solution with no cohesive zone is recovered and the onset of stability occurs at $v = \sqrt{2}\,c_s$. Similar observations that the speed regime $\sqrt{2}\,c_s < v < c_l$ is stable for intersonic mode II crack growth were made by BURRIDGE *et al.* (1979); FREUND (1979). For more realistic values of the parameter $(\mu\delta_c)/(\tau_o D) \approx 10^{-2} - 10^{-3}$, the critical load required to sustain intersonic crack propagation is a minimum between $\sqrt{2}\,c_s$ and 1.5. This explains the observed experimental behavior of crack speed, where the intersonic mode II crack was found to accelerate to speeds close to c_l and then as the loading pulse was cut off, settled down to a stable propagation speed close to $\sqrt{2}\,c_s$. Such a crack speed behavior was also observed by NEEDLEMAN (1999) in his numerical simulations of mode II crack growth along a weak plane.

Here, it must be understood that stability results obtained for a steadily moving semi-infinite crack may be significantly different from those for cracks with more realistic geometries. For example, stability results obtained for a steadily moving semi-infinite crack may be significantly different from those for an expanding finite crack, because one mechanism tending to produce instability in a spreading finite

crack, namely, the increase in crack length, is lacking in the case of a steadily moving semi-infinite crack. Thus, if a certain velocity regime is found to unstable for a steadily moving semi-infinite crack, then there is even more reason to suppose that such a regime would also be unstable for an expanding finite crack in a pre-stressed medium. This is probably the reason why BROBERG (1994; 1995) found that for a symmetrically expanding mode II crack under uniform remote shear loading, the entire intersonic regime is unstable and that such a crack would accelerate all the way up to c_l. BURRIDGE *et al.* (1979) also argued that instability is more pronounced in the case of finite cracks undergoing transient crack growth. If a particular speed regime is found to be unstable for a moving steady state semi-infinite crack, then the possibility that it would also be unstable for an expanding finite crack is much more.

4.3.2 Critical Cohesive Zone Length

Figure 4.16 shows the variation with crack speed, of the critical cohesive zone length L^c_{dyn}/L^c_o required for sustained dynamic mode II crack growth.

$$L^c_{dyn}/L^c_o = \begin{cases} \dfrac{R(v)}{2\alpha_s(\alpha_l^2 - \alpha_s^2)} & 0 \le v < c_R\,, \\ \dfrac{(1-q)R_q}{\hat{\alpha}_s(\alpha_l^2 + \hat{\alpha}_s^2)} \dfrac{1}{\sin q\pi} & c_s < v < c_l\,. \end{cases} \tag{4.79}$$

where, the critical cohesive zone length for quasi-static crack propagation,

$$L^c_o = \frac{\pi(\kappa+1)}{16}\left(\frac{\mu\delta_c}{\tau_o}\right). \tag{4.80}$$

The critical cohesive zone size for sub-Rayleigh speeds, was found to decrease monotonically as the crack accelerates to c_R. ANDREWS (1976) in a numerical simulation of a symmetrically expanding mode II crack under the action of remote uniform shear stresses found that the cohesive zone size decreases continuously with crack speed in the sub-Rayleigh regime attaining its minimum value at c_R.

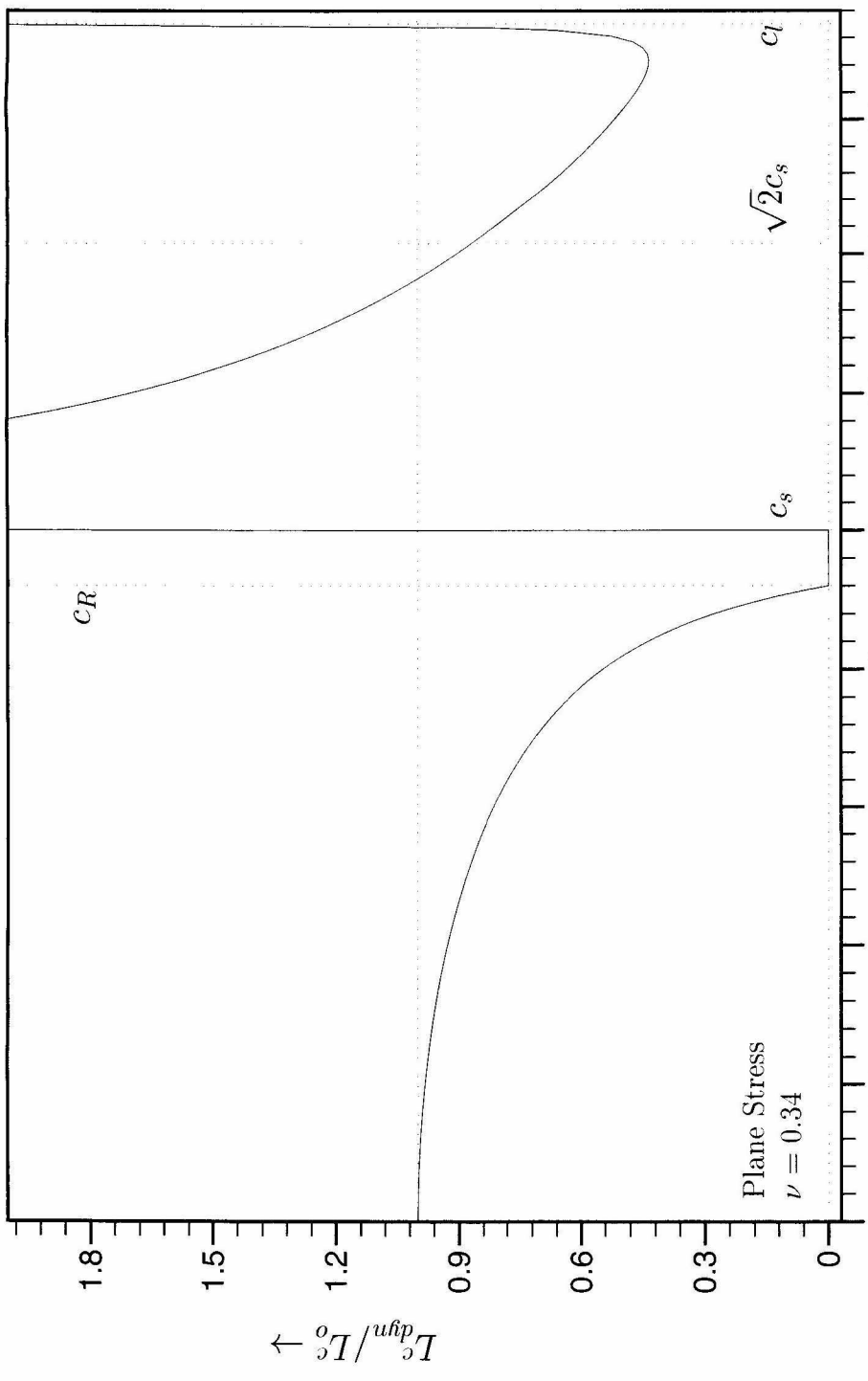

Figure 4.16: Dynamically propagating mode II crack with a Dugdale type cohesive zone — Variation of critical cohesive zone length (required during sustained dynamic crack growth) with crack speed v.

Such a behavior was also observed in the numerical simulations of GEUBELLE and KUBAIR (2000). In the intersonic case, the cohesive zone size is always finite and positive. Such an observation was used by YU and SUO (2000) to justify the admissibility of mode II intersonic crack growth.

4.4 Isochromatic Fringe Pattern

The near tip stress field for a steadily propagating dynamic mode II crack with a Dugdale type cohesive zone in front of the tip, is given in Appendix B for sub-Rayleigh crack speeds and in Appendix C for intersonic crack speeds. From this field, we can construct isochromatic fringe patterns and compare them with experimentally recorded isochromatic patterns so as to check the validity of the assumed cohesive crack model. Under generalized plane stress assumption and within the region of dominance of the near tip field, the isochromatic fringe order n at any point is given by

$$n(\eta_1, \eta_2) = \frac{h}{F_\sigma}\sqrt{(\sigma_{11} - \sigma_{22})^2 + 4\sigma_{12}^2}\,, \tag{4.81}$$

where h is the specimen thickness and F_σ is the material fringe constant. F_σ for Homalite is given in Table 2.1 and the specimen thickness h was chosen to be 4.76 mm (same as in experiment). μ for Homalite is also given in Table 2.1 and the shear strength of the fracture plane was taken to be $\approx$ 14 MPa. The mode II crack is assumed to obey the critical crack tip sliding displacement criterion. However, no data is available for δ_c, and hence an indirect estimate for δ_c was obtained by placing a restriction that the cohesive zone size must lie between 1 to 5 mm over the entire intersonic regime. Such a restriction is motivated by the experimentally recorded isochromatic fringe patterns (see Figure 3.12), where the cohesive zone size is always within these limits. A reasonable estimate of δ_c that would satisfy this restriction was found to be $\approx$ 21 μm. Keeping all these parameters constant isochromatic fringe patterns are constructed for different sub-Rayleigh and intersonic crack speeds.

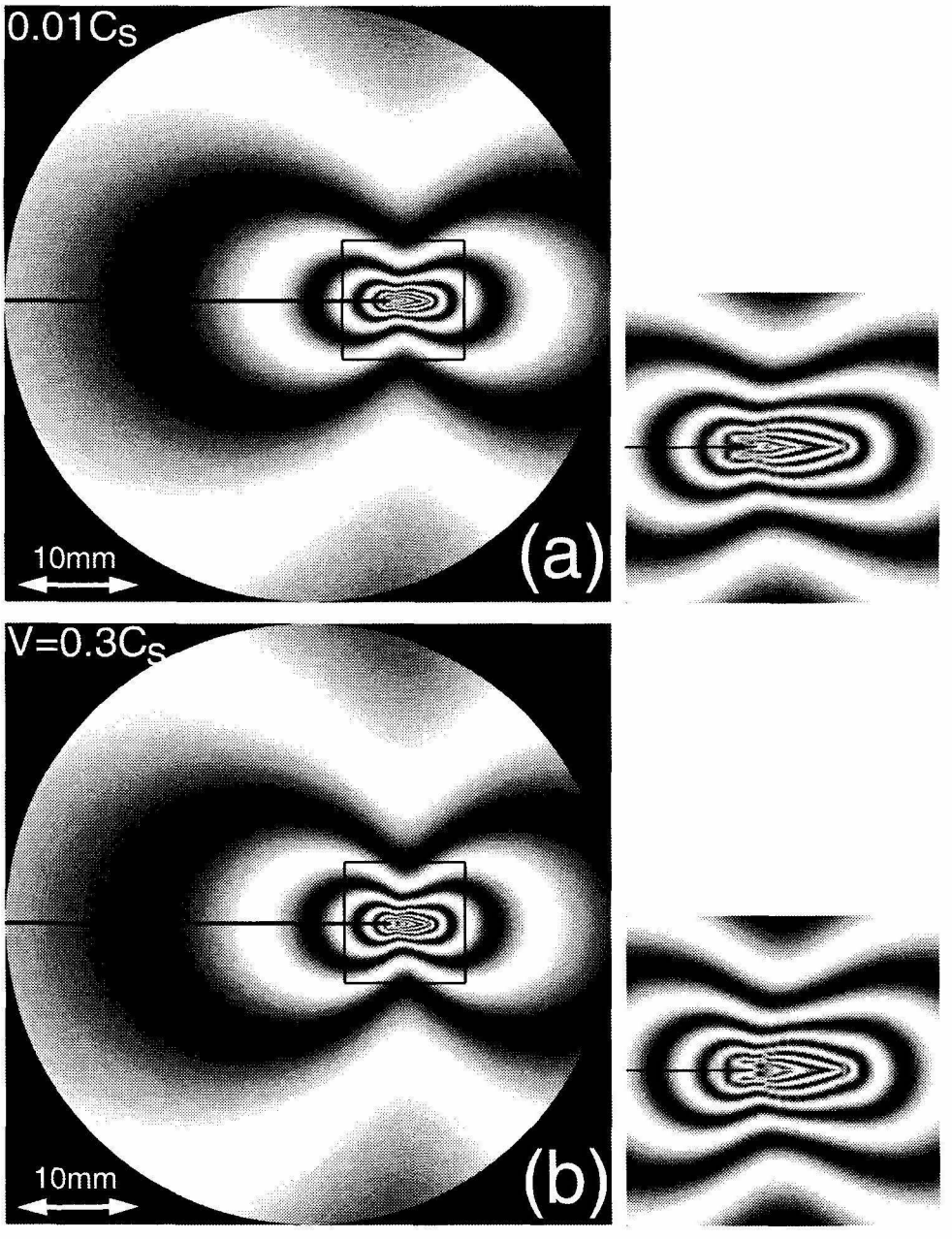

Figure 4.17: Isochromatic fringe pattern around a propagating subsonic mode II crack with a Dugdale type cohesive zone. The propagating crack obeys a critical crack tip sliding displacement criterion with $\delta_c \approx 21$ μm and $\mu/\tau_o = 136$. A magnified view of the region around the crack tip (enclosed in the black rectangle) is shown on the right. **(a)** $v/c_s = 0.01$ & $L^c_{dyn} = 3$ mm. **(b)** $v/c_s = 0.3$ & $L^c_{dyn} = 2.9$ mm.

Figure 4.17 and Figure 4.18 show the theoretically predicted isochromatic fringe patterns around a subsonically propagating mode II crack with a Dugdale type line cohesive zone in front of it. The patterns are constructed for four different subsonic speeds - $0.01\,c_s$, $0.3\,c_s$, $0.6\,c_s$ and $0.85\,c_s$. Similarly, Figure 4.19 and Figure 4.20 show the theoretically predicted isochromatic fringe patterns around an intersonically propagating mode II crack with a Dugdale type line cohesive zone in front of it. The patterns are constructed for four different intersonic speeds - $1.2\,c_s$, $\sqrt{2}\,c_s$, $1.47\,c_s$ and $1.65\,c_s$. In each case the cohesive zone length was determined from (4.79) and (4.80). The field of view shown in all these patterns has a diameter of 50 mm and the front end of the cohesive zone is located on the horizontal diameter about 35 mm from the left edge of the field of view. A horizontal dark line is drawn to indicate the position of the crack faces. A magnified view of the region close to the tip (identified by a rectangle of size 10 mm $\times$ 10 mm) is shown as an inset to the right of each pattern.

From Figure 4.17(a) and Figure 4.17(b) we can see that for moderate crack speeds, the isochromatic fringe pattern doesn't change appreciably from its quasi-static configuration. However, as the crack speed approaches c_R, the isochromatic fringe pattern changes dramatically (see Figure 4.18(a) and Figure 4.18(b)) from a two-lobe pattern to a three-lobe pattern. Note that the far-field load σ_{12}^D (or K_{II}^d) decreases monotonically as the crack speed approaches c_R (see Figure 4.15), however, the stress intensity at the tip as measured by the density of fringes here increases, simply from the effect of increased crack speed. Also, the cohesive zone length decreases continuously with increasing crack speed (see Figure 4.16). For high subsonic speeds, the cohesive zone lengths are small relative to the size of the field of view size (50 mm) and the isochromatic fringe pattern doesn't differ markedly from that for a singular solution with no cohesive zone.

For the intersonic case, dramatic changes in fringe pattern may be observed with increased crack speed. For $v = 1.2c_s$ (Figure 4.19(a)), the cohesive zone size is large ($\approx$ 5.1 mm) and the fringe pattern is distinctly different in the three regions

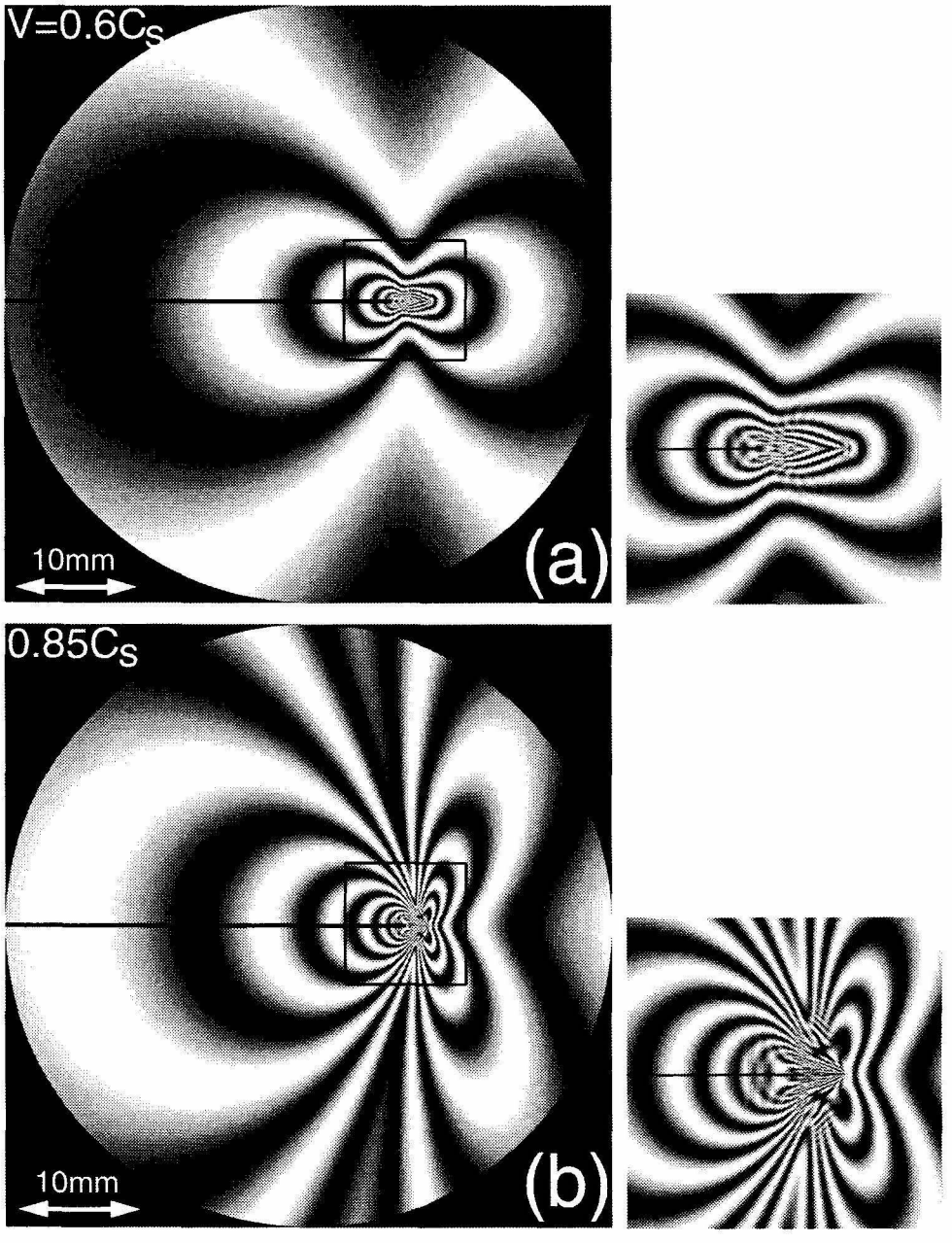

Figure 4.18: Isochromatic fringe pattern around a propagating subsonic mode II crack with a Dugdale type cohesive zone. The propagating crack obeys a critical crack tip sliding displacement criterion with $\delta_c \approx 21\mu m$ and $\mu/\tau_o = 136$. A magnified view of the region around the crack tip (enclosed in the black rectangle) is shown on the right. **(a)** $v/c_s = 0.6$ & $L^c_{dyn} = 2.45mm$. **(b)** $v/c_s = 0.85$ & $L^c_{dyn} = 1.22mm$.

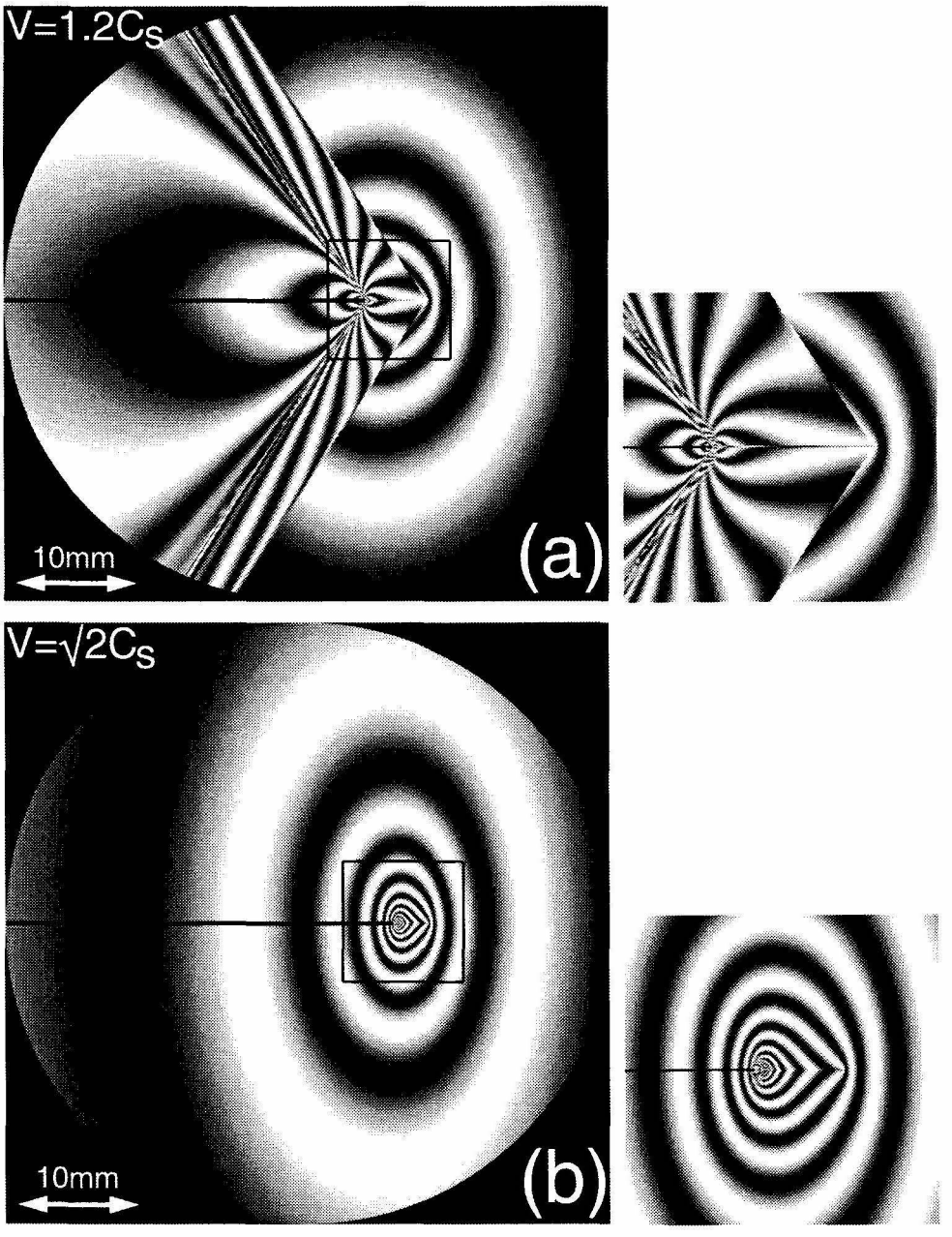

Figure 4.19: Isochromatic fringe pattern around a propagating intersonic mode II crack with a Dugdale type cohesive zone. The propagating crack obeys a critical crack tip sliding displacement criterion with $\delta_c \approx 21\ \mu m$ and $\mu/\tau_o = 136$. A magnified view of the region around the crack tip (enclosed in the black rectangle) is shown on the right. **(a)** $v/c_s = 1.2$ & $L^c_{dyn} = 5.1$ mm. **(b)** $v/c_s = \sqrt{2}$ & $L^c_{dyn} = 2.61$ mm.

— ahead of the Mach waves, within the Mach waves, and behind the Mach waves. For $v = \sqrt{2}\, c_s$ (Figure 4.19(b)), the Mach waves disappear. This is an artifact of the steady state approximation, and certainly no such phenomenon can be observed in the experiments where the crack speed keeps varying continuously. Figure 4.20(a) shows the isochromatic fringe pattern for a crack speed of 1.47 c_s, which may be compared against the experimental patterns shown in Figure 3.8(a) and Figure 3.12. We see that the presence of a cohesive zone gives a finite width to the Mach waves emanating from the tip region. We see that both the experimental and analytically predicted patterns are similar in the region ahead of the tip. However, as mentioned in Section 3.4, there are clear discrepancies due to the influence of the loading waves and damage behind the tip, which are not accounted for in the current model. Also, the fringe pattern within the finite width of the Mach waves, seems to be qualitatively similar. The range of dominance of the current solution seems to be of the order of about 20 mm. However, at later times (see Figure 3.4), where approximate steady state conditions prevail, the range of dominance is higher. As the crack speed approaches c_l (see Figure 4.20(b)) the influence of the crack tip fields is not felt much farther from the tip resulting in fringes being squeezed back wards. The cohesive zone length and consequently the width of the Mach waves decreases with increase in crack speed (see Figure 4.16).

As seen in this chapter, the rate independent cohesive crack model introduced for intersonic mode II crack growth eliminates some of the pathologies associated with the Freund's singular solution. It results in a dynamic energy release rate which is finite at all intersonic speeds, explaining the experimental observation of shear cracks at all intersonic speeds. It also yields a structure to the Mach waves emanating from the crack tip region, as seen in the experimentally recorded patterns. It also explains why the secondary tensile cracks are all parallel to each other. However, the current model does suffer a few serious drawbacks. The Dugdale type cohesive constitutive relation adopted has limited physical basis and was merely chosen for its

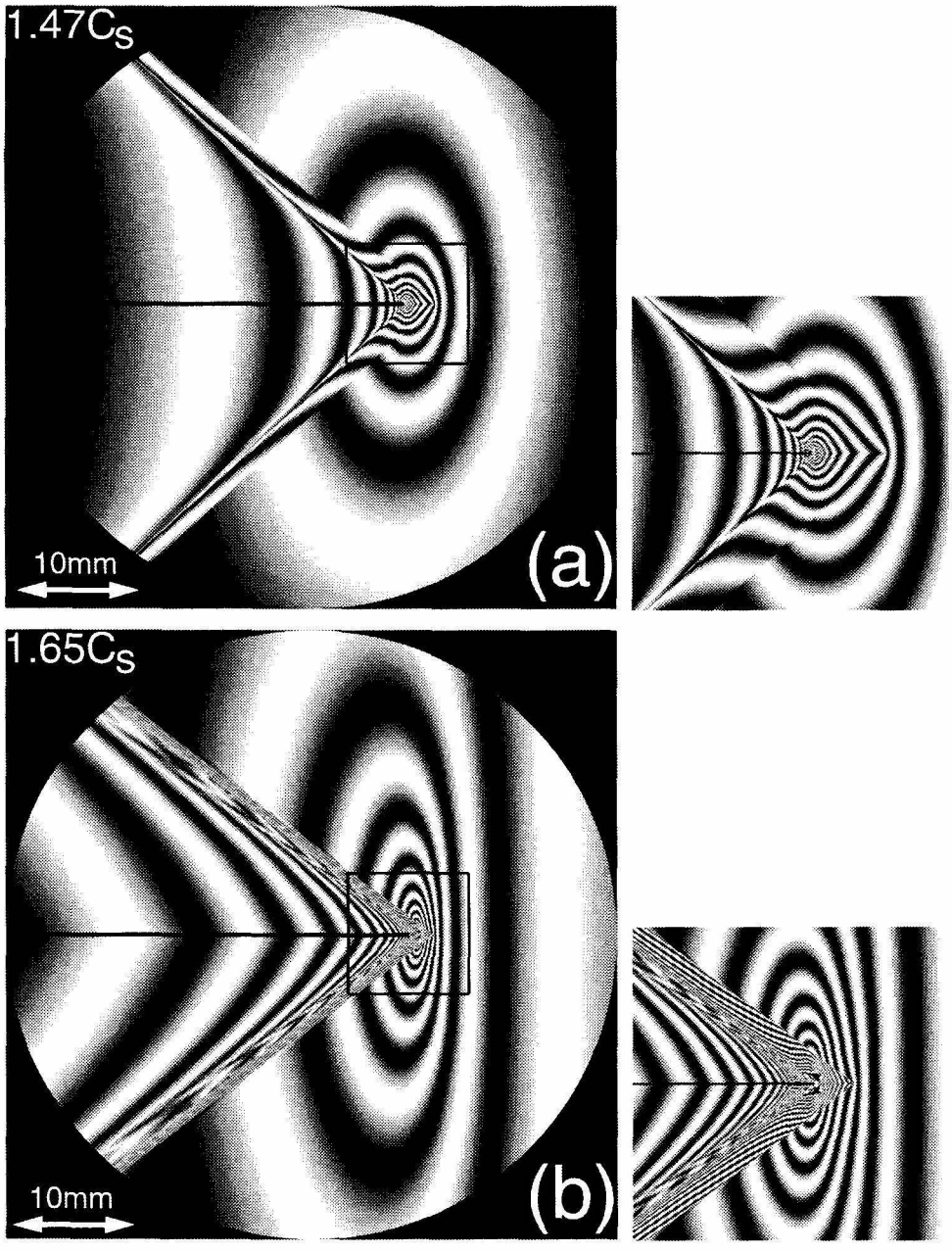

Figure 4.20: Isochromatic fringe pattern around a propagating intersonic mode II crack with a Dugdale type cohesive zone. The propagating crack obeys a critical crack tip sliding displacement criterion with $\delta_c \approx 21\mu m$ and $\mu/\tau_o = 136$. A magnified view of the region around the crack tip (enclosed in the black rectangle) is shown on the right. **(a)** $v/c_s = 1.47$ & $L^c_{dyn} = 2.24$ mm. **(b)** $v/c_s = 1.65$ & $L^c_{dyn} = 1.37$ mm.

simplicity in obtaining an analytical closed form solution. It still predicts unbounded stresses along the Mach waves, which is unphysical and is clearly not observed in the experiments. Also, the angle it predicts for the secondary tensile cracks is almost twice that observed in the experiments. A rate dependent cohesive crack model is introduced in the next chapter to address these limitations.

Nomenclature

(η_1, η_2)	Cartesian coordinates w.r.t the moving (mathematical) crack tip
$(\sigma_{12}^D)_o^c$	critical far-field load for quasi-static mode II crack growth
$(\sigma_{12}^D)_{dyn}^c$	critical far-field load for dynamic mode II crack growth
(r, θ)	polar coordinates
(x_1, x_2)	fixed Cartesian coordinates
$\alpha_l, \alpha_s, \hat{\alpha}_s$	relativistic parameters
δ, δ_1	shear displacement discontinuity
δ_c	critical crack tip sliding displacement
δ_t	crack tip sliding displacement
δ_t^o	crack tip sliding displacement for a quasi-statically growing mode II crack
$\delta_{\alpha\beta}$	Kronecker delta
$\epsilon_{\alpha\beta}$	2D alternator
Γ	fracture energy
κ	material parameter - varies for plane stress and plane strain

K_{II}^{d}	subsonic mode II stress intensity factor
K_{II}^{*d}	intersonic mode II stress intensity factor
μ	shear modulus
ν	Poisson's ratio
ϕ	longitudinal potential
ψ	shear potential
ρ	mass density
σ_{12}^{D}	shear stress a distance $D \gg L$ ahead of the crack tip
σ_1	maximum principal tensile stress
σ_n	normal stress perpendicular to the Mach wave
σ_t	tangential shear stress along the Mach wave
σ_u^H	ultimate tensile strength of Homalite
$\sigma_{\alpha\beta}$	Cartesian components of the stress tensor
τ	cohesive stress distribution
τ_o	shear cohesive strength of the material
$\theta(z)$	an analytic function of $z = \eta_1 + i\eta_2$
θ^*	angle of inclination of the principal plane with the vertical
$\vec{e_n}$	unit vector normal to the Mach wave
$\vec{e_t}$	unit vector tangential to the Mach wave
$\vec{n} = n_\alpha e_\alpha$	unit outward vector normal to Σ

$\vec{P} = P_\gamma e_\gamma$	energy flux vector field
A_o	amplitude of the near tip field
c_l	longitudinal wave speed
c_R	Rayleigh wave speed
c_s	shear wave speed
e_α	unit vectors along the Cartesian coordinate axes
F	analytic function of $z_l = \eta_1 + i\,\alpha_l \eta_2$
F_σ	material fringe constant
F_e	energy flux through Σ
G	analytic function of $z_s = \eta_1 + i\,\alpha_s \eta_2$
G	dynamic energy release rate
g	a real function of $\eta_1 + \hat{\alpha}_s \eta_2$
G_c	critical dynamic energy release rate
G_o	energy release rate for a quasi-statically growing mode II crack
h	specimen thickness
L	cohesive zone length
L^*	initiation site for the secondary tensile crack
L_o	cohesive zone length for a quasi-statically growing crack
L_o^c	critical cohesive zone length for quasi-static mode II crack growth
L_{dyn}^c	critical cohesive zone length for dynamic mode II crack growth

n	isochromatic fringe order
P	analytic function of $z = \eta_1 + i\,\eta_2$
q	singularity exponent for an intersonic mode II crack
$R(v)$	Rayleigh function
R_q	intersonic parameter
T	kinetic energy density field
t	time
U	strain energy density field
u_α	components of the displacement vector
v	crack speed

Bibliography

ANDREWS, D. J. (**1976**), Rupture Velocity of Plane Strain Shear Cracks, *Journal of Geophysical Research*, **81**(32), pp. 5679–5687.

BARENBLATT, G. I. (**1962**), The Mathematical Theory of Equilibrium Cracks in Brittle Fracture, *Advances in Applied Mechanics*, **7**, pp. 55–129.

BROBERG, K. B. (**1994**), Intersonic Bilateral Slip, *Geophysical Journal International*, **119**(3), pp. 706–714.

BROBERG, K. B. (**1995**), Intersonic Mode II Crack Expansion, *Archives of Mechanics*, **47**, pp. 859–871.

BROBERG, K. B. (**1999**), *Cracks and Fracture*, Academic Press, London.

BURRIDGE, R., CONN, G., and FREUND, L. B. (**1979**), The Stability of a Rapid Mode II Shear Crack with Finite Cohesive Traction, *Journal of Geophysical Research*, **85**(B5), pp. 2210–2222.

COKER, D. and ROSAKIS, A. J. (**2000**), Experimental Observations of Intersonic Crack Growth in Asymmetrically Loaded Unidirectional Composite Plates, to appear in Philosophical Magazine.

DUGDALE, D. S. (**1960**), Yielding of Steel Sheets Containing Slits, *Journal of the Mechanics and Physics of Solids*, **8**, pp. 100–104.

FREUND, L. B. (**1979**), The Mechanics of Dynamic Shear Crack Propagation, *Journal of Geophysical Research*, **84**(B5), pp. 2199–2209.

FREUND, L. B. (**1989**), *Dynamic Fracture Mechanics*, Cambridge University Press, Cambridge.

GAKHOV, F. D. (**1990**), *Boundary Value Problems*, Dover, New York.

GEUBELLE, P. H. and KUBAIR, D. (**2000**), Intersonic Crack Propagation in Homogeneous Media Under Shear Dominated Loading: I. Numerical Analysis, to appear in JMPS.

GOODIER, J. N. (**1968**), Mathematical Theory of Equilibrium Cracks, in *Fracture - Vol II*, edited by H. Liebowitz, Academic Press, pp. 1–66.

IDA, Y. (**1972**), Cohesive Force Across the Tip of a Longitudinal-Shear Crack and Griffith's Specific Surface Energy, *Journal of Geophysical Research*, **77**(20), pp. 3796–3805.

JOHNSON, E. (**1990**), On the Initiation of Unidirectional Slip, *Geophysical Journal International*, **101**(1), pp. 125–132.

LAMBROS, J. and ROSAKIS, A. J. (**1995**), Shear Dominated Transonic Interfacial Crack Growth in a Bimaterial. 1. Experimental Observations, *Journal of the Mechanics and Physics of Solids*, **43**(2), pp. 169–188.

MUSKHELISHVILI, N. I. (**1963**), *Some Basic Problems of the Mathematical Theory of Elasticity*, Noordhoff, Groningen, Holland.

NEEDLEMAN, A. (**1999**), An Analysis of Intersonic Crack Growth Under Shear Loading, *Journal of Applied Mechanics*, **66**(4), pp. 847–857.

PALMER, A. C. and RICE, J. R. (**1973**), The Growth of Slip Surfaces in the Progressive Failure of Over-Consolidated Clay, *Proceedings of the Royal Society of London*, **A332**, pp. 527–548.

ROSAKIS, A. J., SAMUDRALA, O., and COKER, D. (**1999**), Cracks Faster than the Shear Wave Speed, *Science*, **284**(5418), pp. 1337–1340.

YU, H. H. and SUO, Z. (**2000**), Intersonic Crack Growth On an Interface, *Proceedings of the Royal Society of London*, **A456**(1993), pp. 223–246.

Chapter 5

A Rate Dependent Cohesive Zone Model

5.1 Motivation

In Sections 3.6 and 4.2.4, the necessity of a cohesive crack model for analytical investigations of intersonic mode II crack propagation was emphasized. Subsequently, a Dugdale type line cohesive zone model for dynamic mode II crack propagation was introduced (in the previous chapter), and its predictions were critically examined in light of the experimental observations described in Chapter 3. This particular cohesive zone model was introduced by DUGDALE (1960) to simulate line plastic zones observed in thin sheets made of a ductile steel. As mentioned apriori, the Dugdale model has limited physical basis in representing the breakdown processes occurring near a dynamic shear crack tip in our laboratory specimens. The laboratory specimens used in our experiments were made of Homalite-100, a strongly rate dependent material (see Table 2.1). The intersonic shear cracks observed in our laboratory propagated along the weak interface joining two thin Homalite sheets. The bonding agent used for joining the two Homalite halves was based on polyester resin, which after curing becomes highly brittle and attains a similar chemical composition as that of Homalite-100. The crack tip process zone, in which the mechanisms leading to decohesion occur, was confined to the thin bond layer whose thickness was of the order of

10-30 μm. The process of interface decohesion is likely to be rate dependent, in light of the bonding agent used. Consider a material particle on the crack plane in front of the approaching crack tip. As the crack tip nears, the shear stress acting on this material particle increases rapidly, resulting in a substantial increase in its cohesive shear strength. Hence, it is desirable to have a cohesive law modeling the fracture process zone that takes rate effects into account. If we use a line cohesive zone model for the fracture process zone, rate effects may be incorporated by introducing a cohesive constitutive relation that relates the traction on the cohesive surfaces to the local sliding rate (slip rate). Data on the dependence of cohesive shear strength on sliding rate, at the rates experienced in our experiments is rather obscure. Also, due to the brittle nature of interface decohesion, the extent of any such process zone is likely to be extremely small.

It was argued in Section 3.2 that intersonic mode II crack growth in our laboratory specimens is accompanied by a far-field negative mode I dynamic stress intensity factor (-ve K_I^d). This results in crack face contact, with large negative normal tractions acting on the crack faces at distances close to the tip. Hence, in the vicinity of the tip, one might expect the crack faces to undergo nonuniform frictional sliding. Based on experimental data, RUINA (1983); RICE and RUINA (1983) proposed that the sliding friction, apart from being linearly proportional to the normal traction, is also a nonlinear function of slip rate and a number of internal variables that describe the local "state" of the sliding surfaces. The slip rates at distances close to the tip are very large (of the order of few m/s). In general, the frictional resistance exhibits a long term decrease with increasing slip rate. It may be noted that, constitutive data on the "state" dependent part of the friction law is not yet available for any material[1], while the dependence on slip rate is known mostly for rates of the order of 1 mm/sec (KILGORE *et al.*, 1993). To author's knowledge, only a single experimental study exists, on the sliding of a hard steel and a titanium alloy on tungsten carbide

[1]However, it is believed that the dependence on "state" is equivalent to a functional dependence of frictional stress on prior slip rates (history dependence).

(PRAKASH and CLIFTON, 1992; 1993), which deals with dynamic friction at slip rates of the order 2-30 m/s. However, it is generally accepted that steady state frictional stress decreases with increasing slip rate, even at very high slip rates (of the order of a few m/s). A rate dependent line cohesive zone may also be used to model the finite zone in the vicinity of the crack tip, where nonuniform frictional sliding occurs. Here the cohesive constitutive relation represents a friction law, relating the frictional resistance (cohesive shear traction) to the local slip rate. Under the assumption of steady crack propagation, the dependence of sliding friction on local "state" may be neglected. However, unlike the case of rate dependent crack plane shear strength, nonuniform frictional sliding results in decreasing cohesive shear traction with increasing slip rate (velocity weakening).

In modeling our experiments using a line cohesive zone in the tip vicinity, we should identify apriori, the mechanism that is dominant at the dynamic shear crack tip — rate dependent crack plane shear strength or nonuniform frictional sliding. The primary difference between these two mechanisms is the effect of sliding rate on the cohesive shear traction; rate dependence of crack plane shear strength increases the cohesive shear traction with sliding rate, whereas nonuniform frictional sliding results in a decrease in cohesive shear traction with sliding rate. From the experimental observations, it is unclear as to which one of the two mechanisms dominates. A unified approach is presented in this chapter to model either of these two phenomena, with a cohesive law containing a rate parameter, the sign of which determines which one of these mechanisms dominates. Consequently, in this chapter, subsonic and intersonic mode II crack propagation with a rate dependent line cohesive zone is analyzed. A rate dependent cohesive law is assumed, wherein the cohesive shear traction varies linearly with the local sliding rate. The rate of variation is governed by a material/specimen dependent parameter. Complete decohesion is assumed to occur when the crack tip sliding displacement reaches a material specific critical value (a characteristic break down slip). The governing equations are solved using

a standard technique in analytic function theory and the nature of the predicted near-tip fields is examined. With a cohesive zone of finite size, it is found that the dynamic energy release rate is finite through out the intersonic regime. Crack tip stability issues are addressed and favorable speed regimes are identified. The influence of shear strength of the crack plane and the rate parameter on crack propagation behavior is also investigated. From the inclination of the secondary tensile cracks and other experimental observations, it is argued that the dominant rate dependent mechanism operating at the dynamic shear crack tip is nonuniform frictional sliding. The isochromatic fringe patterns predicted by the analytical solution are compared against those recorded experimentally and estimates are obtained of the fracture energy, rate parameter, extent of the cohesive zone as well as the characteristic break down slip.

5.2 Propagating Mode II Cracks With a Rate Dependent Cohesive Zone

5.2.1 Formulation

Consider a mode II crack with a line cohesive zone of length L, propagating at a constant speed v through a homogeneous, isotropic, linear elastic medium under 2D plane strain or plane stress conditions. Attention is focussed on the crack tip vicinity (see Figure 5.1(a)). The crack is constrained to propagate in its own plane and the crack speed can be either subsonic or intersonic ($0 < v < c_l$). The governing equations of motion are solved in the same way as in the previous chapter, to obtain the near tip fields (see Sections 4.2.1 to 4.2.3). The boundary conditions are identical to those used in Chapter 4, except for the unknown cohesive traction distribution, $\tau(-L < \eta_1 < 0)$. With a rate dependent line cohesive zone, the cohesive shear traction depends on *local* sliding rate, $\dot{\delta}_1(\eta_1 < 0) = \dot{u}_1(\eta_1 < 0, \eta_2 \to 0^+) - \dot{u}_1(\eta_1 < 0, \eta_2 \to 0^-)$.

For steady crack growth, sliding rate within the cohesive zone may be expressed

in terms of the local displacement gradient.

$$\dot{\delta}_1(-L < \eta_1 < 0) = -2\, v\, u_{1,1}(-L < \eta_1 < 0, \eta_2 \to 0^+)\,. \tag{5.1}$$

The η_1-gradient of the sliding displacement u_1 along the upper cohesive surface $(-L < \eta_1 < 0, \eta_2 \to 0^+)$ may be expressed in terms of the unknown cohesive traction distribution as (see Sections 4.2.2 and 4.2.3)

$$u_{1,1} = -\frac{v^2}{c_s^2}\,\frac{\alpha_s}{R(v)}\,\frac{\sqrt{|\eta_1|}}{\mu\pi}\ \mathrm{pv}\int_{-L}^{0} \frac{\tau(\xi/L)}{\sqrt{|\xi|}(\xi + |\eta_1|)}\,d\xi\,, \tag{5.2}$$

for $0 \le v < c_R$ and

$$u_{1,1} = \frac{(1+\hat{\alpha}_s^2)\sin^2 q\pi}{4\pi\mu\alpha_l}\left\{\frac{\pi\tau(\eta_1/L)}{\tan q\pi} - |\eta_1|^{1-q}\ \mathrm{pv}\int_{-L}^{0}\frac{\tau(\xi/L)}{|\xi|^{1-q}(\xi+|\eta_1|)}\,d\xi\right\}, \tag{5.3}$$

for $c_s < v < c_l$. For steady crack growth, (5.2) and (5.3) represent the relation between the rate of sliding within the cohesive zone to the cohesive shear traction resisting the sliding.

5.2.2 A Rate Dependent Cohesive Law

Rate dependent cohesive constitutive relations, which relate the traction on a cohesive surface to the local displacement rate, have been used in the past for modeling elastic-viscoplastic material behavior (Glennie, 1971a;b; Freund and Lee, 1990). Glennie (1971a) analyzed the problem of a uniformly moving semi-infinite mode I crack in plane strain, with a rate dependent cohesive zone in front of it. He used a strip yield zone, with the yield stress linearly dependent on strain rate to model thin plastic zones ahead of running mode I cracks in sheets of mildsteel. Employing a critical crack tip opening displacement criterion, he argued that the increased re-

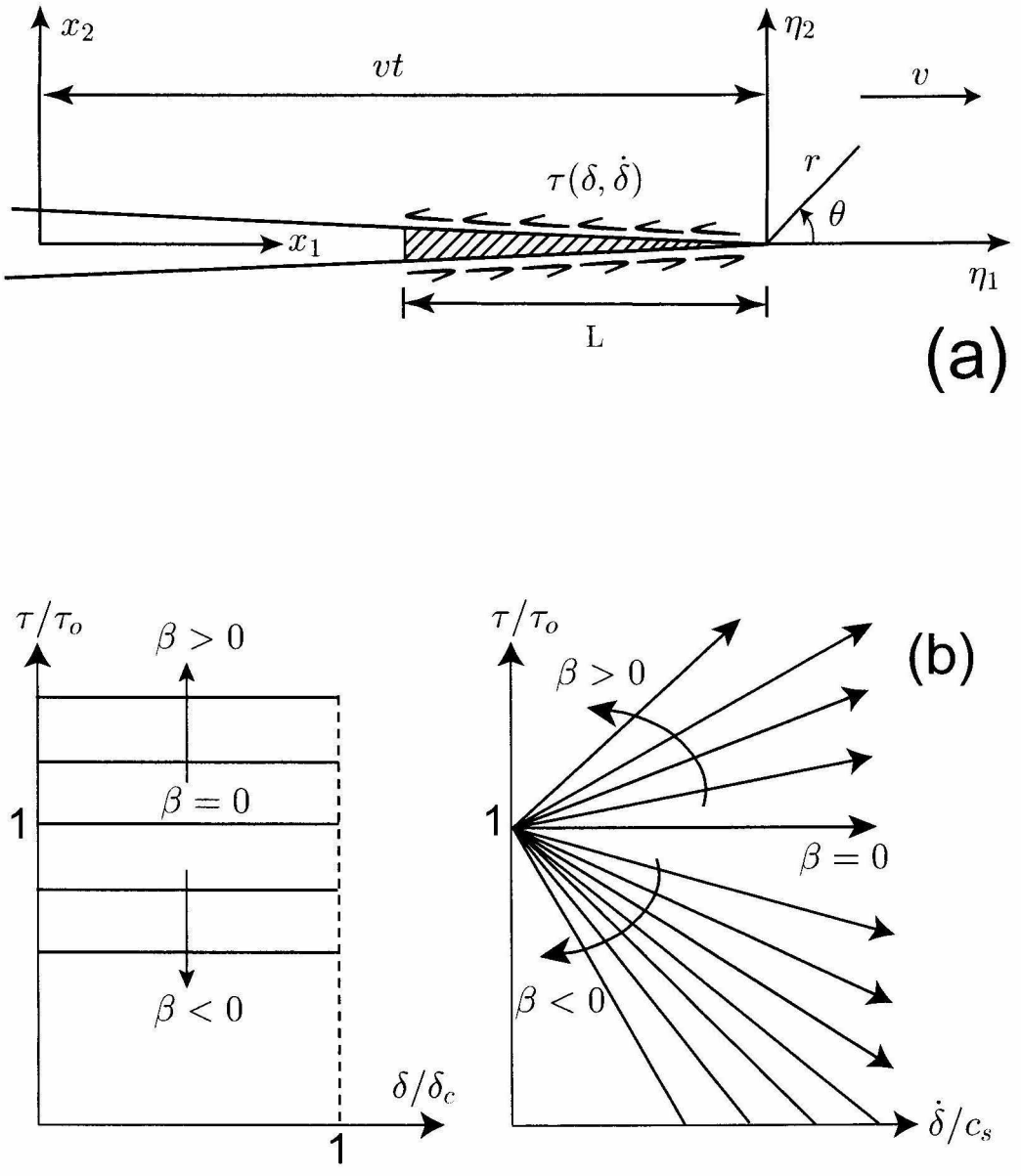

Figure 5.1: Dynamic mode II crack in a homogeneous, isotropic, linear elastic solid with a rate dependent line cohesive zone. **(a)** Illustration showing the cohesive zone and the crack tip coordinate system. **(b)** Rate dependent cohesive law relating the shear traction to the local sliding displacement and the local sliding rate.

sistance to plastic flow at high crack speeds can explain the relatively low terminal speeds observed for running mode I cracks. FREUND and LEE (1990) analyzed the same problem, and to model the failure mode transition observed in some ferritic steels, introduced two different fracture criteria, one for ductile fracture based on a critical crack tip opening displacement and another for brittle fracture based on a critical stress in front of the tip. They investigated the dependence of the far-field applied stress intensity factor, crack speed and a rate parameter on the failure mode selection.

The rate dependent cohesive law used by GLENNIE (1971a;b) and FREUND and LEE (1990) is adapted here for modeling the rate dependent fracture process zone (or the finite zone of nonuniform frictional sliding) in the vicinity of a dynamic shear crack propagating along a weak plane. The cohesive constitutive relation, that relates the cohesive shear traction at any point within the cohesive zone to the local sliding rate was chosen to be of the form (see Figure 5.1(b)),

$$\tau(\frac{\eta_1}{L}) = \tau_o \left[1 + \beta C \frac{|\dot{\delta}(\eta_1/L)|}{c_s} \right] \qquad -1 < \frac{\eta_1}{L} < 0\,, \tag{5.4}$$

where τ_o is the cohesive shear strength of the material under quasi-static sliding, β is a rate parameter and C is a dimensionless parameter, to be chosen appropriately such that β has the order of unity. Note that $\delta = \delta_1$ for pure mode II crack growth. Choosing C to be positive, a positive β results in an increasing shear cohesive traction with increasing sliding rate. Hence, the cohesive constitutive relation above, in conjunction with the condition $\beta > 0$ models a rate dependent fracture process zone of finite extent in front of the physical crack tip. Alternately, $\beta < 0$ results in a decreasing shear cohesive traction with increasing sliding rate. Hence, the cohesive constitutive relation above, in conjunction with the condition $\beta < 0$ models a finite zone of nonuniform frictional sliding behind the physical crack tip (velocity weakening). With $\beta < 0$, the shear cohesive strength decreases from τ_o at the front end of

the cohesive zone and vanishes at its rear end, where the sliding rate has a magnitude $c_s/(C|\beta|)$. For the sake of clarity, from now on we call the front end of the cohesive zone as mathematical crack tip and the rear end as physical crack tip, irrespective of which mechanism operates in the cohesive zone.

In reality, the cohesive shear traction (representing frictional resistance) must also be proportional to the normal compressive traction acting on the sliding surfaces. If we assume that the dependence is akin to a Coulomb friction law (at each slip rate), then the magnitude of frictional resistance is linearly proportional to the normal compressive traction, the constant of proportionality λ_f being equal to the coefficient of sliding friction (which depends on $\dot{\delta}$). In our laboratory specimens, the normal compressive traction on the crack faces arises from the requirement that the expected far field -ve K_I^d cannot be sustained at the tip of a propagating sharp crack. The normal compressive traction on the crack faces is expected to decay rapidly away from the tip and it is not entirely unreasonable to expect that a distribution equivalent to $-\tau(\eta_1/L)/\lambda_f$ acting over an extent L behind the physical crack tip can annul the expected far-field -ve K_I^d, resulting in pure mode II conditions at the tip of the propagating sharp crack. Moreover, the initiation of secondary opening cracks and the resulting damage of the crack surfaces (see Section 3.5) is likely to restrict the compressive normal traction resulting from the propagating sharp crack tip fields to distances very close to the tip (of the order of few mm). Hence, the extent of nonuniform frictional sliding is likely to be much smaller than the extent over which the singular field dominates.

To obtain an estimate of the "average" sliding rate within the cohesive zone, consider a point along the crack line, a fixed distance ahead of the tip. As the crack traverses through this point at an intersonic speed, the material particles on either side of this point undergo a net relative sliding displacement, $\delta_t = u_1(\eta_1 = -L, \eta_2 \to 0^+) - u_1(\eta_1 = -L, \eta_2 \to 0^-)$ within a time L/v. Hence an "average" sliding rate within the cohesive zone is given by $\dot{\delta}_{ave} = v\delta_t/L$. Typically v is of the order of a

km/sec (for an intersonic crack), δ_t is of the order of a few μm and L is of the order of a few mm (for our laboratory specimens). Hence the average sliding rate should be typically of the order of a few m/s. If we interpret τ_o to be the shear strength of the material under quasi-static loading conditions, then for a quasi-statically growing mode II crack under small-scale yielding, we have

$$L = \frac{\pi}{8}\left(\frac{K_{II}}{\tau_o}\right)^2 \qquad \text{and} \qquad \delta_t = \frac{\kappa+1}{8}\frac{K_{II}^2}{\mu\tau_o}\,. \tag{5.5}$$

Hence the "average" sliding rate within the cohesive zone for a quasi-statically growing crack at a speed $v \to 0$ would be

$$\dot{\delta}_{ave} = \frac{\kappa+1}{\pi}\frac{\tau_o}{\mu}\,v\,. \tag{5.6}$$

For intersonic crack speeds in our laboratory specimens, the above expression for $\dot{\delta}_{ave}$ also yields values of the order of few m/s. Hence the dimensionless parameter C should be of the order μ/τ_o and the rate dependent cohesive law is chosen to be

$$\tau(\frac{\eta_1}{L}) = \tau_o\left[1+\beta\frac{\mu}{2\tau_o}\frac{|\dot{\delta}(\eta_1/L)|}{c_s}\right] \qquad -1 < \frac{\eta_1}{L} < 0\,. \tag{5.7}$$

The relative sliding displacement δ (or δ_1) at the mathematical crack tip ($\eta_1 = \eta_2 = 0$) is zero and if we reasonably assume that back slipping is not permissible then it should increase monotonically as the physical crack tip ($\eta_1 = -L, \eta_2 = 0$) is approached. Hence $\dot{\delta}(\eta_1/L) = -2\,v\,u_{1,1}(\eta_1/L, \eta_2 \to 0^+)$ must be nonnegative over the entire cohesive zone. We discuss the consequences of this "physical restriction" in the next section.

Using the constitutive assumption on the response within the cohesive zone as given in (5.7), a singular integral equation for the unknown cohesive traction distribution is obtained as follows. Substituting for $u_{1,1}$ from (5.2) and (5.3) into (5.7) and

noting the relationship between $\dot{\delta}_1$ and $u_{1,1}$ from (5.1), we obtain

$$f(\eta_1) - \left\{\beta\frac{v^3}{c_s^3}\frac{\alpha_s}{R(v)}\right\}\frac{1}{\pi}\,\mathrm{pv}\int_{-L}^{0}\frac{f(\xi)}{(\xi+|\eta_1|)}\,d\xi = \frac{1}{\sqrt{|\eta_1|}} \qquad 0 \le v < c_s\,, \tag{5.8a}$$

$$\hat{f}(\eta_1)\left\{1+\beta\frac{v^3}{c_s^3}\frac{\hat{\alpha}_s}{R_q}\cos q\pi\right\} - \left\{\beta\frac{v^3}{c_s^3}\frac{\hat{\alpha}_s}{R_q}\sin q\pi\right\}\frac{1}{\pi}\,\mathrm{pv}\int_{-L}^{0}\frac{\hat{f}(\xi)}{(\xi+|\eta_1|)}\,d\xi = \frac{1}{|\eta_1|^{1-q}} \qquad c_s < v < c_l\,, \tag{5.8b}$$

where

$$f(\eta_1) = \frac{\tau(\eta_1/L)}{\tau_o\sqrt{|\eta_1|}} \qquad 0 \le v < c_s\,, \tag{5.9a}$$

$$\hat{f}(\eta_1) = \frac{\tau(\eta_1/L)}{\tau_o|\eta_1|^{1-q}} \qquad c_s < v < c_l\,. \tag{5.9b}$$

(5.8) is a pair of singular integral equations of the Cauchy type, the solutions to which subject to the boundary conditions,

$$\tau(\frac{\eta_1}{L}\to 0^-)\to\tau_o\,, \qquad \sqrt{1+\frac{\eta_1}{L}}\;\tau(\eta_1/L\to -1^+)\to 0 \qquad 0\le v<c_s\,, \tag{5.10a}$$

$$\tau(\frac{\eta_1}{L}\to 0^-)\to\tau_o\,, \qquad \left(1+\frac{\eta_1}{L}\right)^q\tau(\eta_1/L\to -1^+)\to 0 \qquad c_s<v<c_l\,, \tag{5.10b}$$

give the unknown cohesive traction distributions, $\tau(-1<\eta_1/L<0)$ for the subsonic and intersonic cases respectively. The boundary conditions (5.10) ensure that the singularity exponent at the physical crack tip is smaller than that in the case of a no cohesive zone. The solution procedure is given in Appendix F.

5.3 Solution

The shear traction distribution within the cohesive zone is given by (see Appendix F)

$$\frac{\tau(-1<\eta_1/L\le 0)}{\tau_o}=\begin{cases}1+\dfrac{\sin\gamma\pi}{\pi}\dfrac{(-\eta_1/L)^{\gamma+1/2}}{(1+\eta_1/L)^{\gamma}}\displaystyle\int_0^1\frac{(1-s)^{\gamma}}{\sqrt{s}(1+s\,\eta_1/L)}\,ds & 0\le v<c_R\,,\\[2ex] 1+\dfrac{\sin\lambda\pi}{\pi}\dfrac{(-\eta_1/L)^{1-q+\lambda}}{(1+\eta_1/L)^{\lambda}}\displaystyle\int_0^1\frac{(1-s)^{\lambda}}{s^{q}(1+s\,\eta_1/L)}\,ds & c_s<v<c_l\,,\end{cases} \tag{5.11}$$

where

$$\gamma=\frac{1}{\pi}\tan^{-1}\left\{\beta\frac{v^3}{c_s^3}\frac{\alpha_s}{R(v)}\right\} \qquad 0\le v<c_R\,, \tag{5.12}$$

$$\lambda=\frac{1}{\pi}\tan^{-1}\left\{\frac{\beta\dfrac{v^3}{c_s^3}\dfrac{\hat{\alpha}_s}{R_q}\sin q\pi}{1+\beta\dfrac{v^3}{c_s^3}\dfrac{\hat{\alpha}_s}{R_q}\cos q\pi}\right\} \qquad c_s<v<c_l\,, \tag{5.13}$$

and the integrals in (5.11) converge for $-1\le\eta_1/L\le 0$. As mentioned before, the crack speed regime $c_R<v<c_s$ is inadmissible for running mode II cracks from energetic considerations and henceforth we restrict ourselves to sub-Rayleigh ($0\le v<c_R$) and intersonic regimes only.

If the cohesive shear traction arises due to nonuniform frictional sliding ($\beta<0$), then by taking the limit, $\eta_1\to -L$ in (5.11), we can readily conclude that τ/τ_o vanishes at the physical crack tip. In fact, it is shown later that τ decreases monotonically from τ_o at $\eta_1=0$ and vanishes at the physical crack tip ($\eta_1\to -L$), for both sub-Rayleigh and intersonic crack speeds with $\beta<0$. Moreover, frictional sliding requires that the cohesive shear traction (frictional resistance) must always oppose the relative sliding between the cohesive surfaces. Hence, the relative slip between the cohesive surfaces must always be positive (no back slipping) and the slip rate $\dot{\delta}_1$ must be non-negative as well, over the entire cohesive zone. Hence, the solution (5.11) is

admissible, provided

$$\frac{\dot{\delta}_1}{c_s}(-L < \eta_1 < 0) \geq 0\,. \tag{5.14}$$

Combining (5.11) and (5.7), an expression for the slip rate in terms of the crack speed v and the rate parameter β can be obtained. For $-L < \eta_1 < 0$,

$$\frac{\dot{\delta}_1}{c_s} = \begin{cases} \dfrac{2}{\beta}\dfrac{\tau_o}{\mu}\dfrac{\sin\gamma\pi}{\pi}\dfrac{(-\eta_1/L)^{\gamma+1/2}}{(1+\eta_1/L)^{\gamma}}\displaystyle\int_0^1 \frac{(1-s)^{\gamma}}{\sqrt{s}(1+s\,\eta_1/L)}\,ds & 0 \leq v < c_R\,, \\ \dfrac{2}{\beta}\dfrac{\tau_o}{\mu}\dfrac{\sin\lambda\pi}{\pi}\dfrac{(-\eta_1/L)^{1-q+\lambda}}{(1+\eta_1/L)^{\lambda}}\displaystyle\int_0^1 \frac{(1-s)^{\lambda}}{s^q(1+s\,\eta_1/L)}\,ds & c_s < v < c_l\,. \end{cases} \tag{5.15}$$

From the above expressions for $\dot{\delta}_1$, we can conclude that for velocity weakening cohesive zones ($\beta < 0$), the required condition (5.14) is satisfied for all $0 \leq v < c_R$, but for intersonic crack speeds, it is satisfied only over a portion of the $\beta - v/c_s$ space. For $\beta < 0$ and $c_s < v < c_l$, (5.14) is satisfied if

$$1 + \beta\frac{v^3}{c_s^3}\frac{\hat{\alpha}_s}{R_q}\cos q\pi > 0\,. \tag{5.16}$$

An alternate way of arriving at the same condition above, is by imposing a physical restriction that energy must be dissipated and not generated over any part of the velocity weakening cohesive zone, *i.e.*,

$$\frac{1}{v}\int_{\eta^*}^{\eta^*+d\eta^*} \tau(\eta_1)\dot{\delta}_1(\eta_1)d\eta_1 \geq 0\,, \tag{5.17}$$

for every η^* such that $-L < \eta^* < 0$. Since $\tau(-L < \eta_1 < 0) \geq 0$ (according to (5.11)) everywhere in the cohesive zone, the above condition implies that $\dot{\delta}_1$ is nonnegative over the entire cohesive zone. For the sub-Rayleigh speed regime this condition is satisfied for all $\beta \leq 0$. However, for intersonic crack speeds, such a condition is satisfied only if (5.16) is met.

Figure 5.2 shows a curve in the $\beta - v/c_s$ space that delineates the region of validity of the solution (5.11) for an intersonic mode II crack with a velocity weakening cohe-

sive zone. Moderate values of β up to -5 are chosen. The energetic requirement (5.16) is satisfied for most of the intersonic regime, except for crack speeds close to c_l. For plane stress and with $\nu = 0.34$ (conditions of our laboratory experiments), there exists a small range, $-0.149 < \beta \leq 0$, where the solution (5.11) is valid over the entire intersonic regime. With decreasing β, the solution becomes invalid over more and more of the intersonic regime, and as $\beta \to -\infty$, at only one intersonic speed equal to $\sqrt{2}\,c_s$, is (5.17) satisfied. This can be readily expected, since the solution (5.11) at $v = \sqrt{2}\,c_s$ behaves "subsonic-like". As mentioned before, the unknown rate parameter β is expected to be of the order 'unity' and hence in the intersonic regime, the velocity weakening cohesive zone model presented here is likely to be inadmissible over a small speed regime close to c_l. Similar to this figure, rest of the figures in this Chapter are all plotted for 2-D plane stress and for $\nu = 0.34$ (Poisson's ratio of Homalite-100) so as to be able to compare directly with the experimental observations described in Chapter 3.

Figure 5.3(a) shows the variation of the γ with crack speed (sub-Rayleigh) for different chosen values of the rate parameter β. Figure 5.3(b) is a similar plot of λ for intersonic crack speeds. From (5.11) one can see that γ and λ are the singularity exponents associated with the shear stress at the physical crack tip. For a rate strengthening cohesive zone ($\beta > 0$), τ is singular at the physical crack tip, except for the trivial case with $\beta = 0$ (rate independent Dugdale type cohesive zone for which both γ and λ are identically zero). For the case where the material is linear elastic all the way to the crack tip (no cohesive zone), the singularity exponent for a sub-Rayleigh crack is 1/2. With a rate dependent cohesive zone, the singularity exponent γ is always less than 1/2 and more over it is a function of crack speed. As $v \to c_R$, $\gamma \to 1/2$, *i.e.*, as $v \to c_R$, the usual square root singular solution is recovered for any positive value of the rate parameter β. For intersonic crack speeds, with no cohesive zone, the singularity exponent is given by q, with its peak value of 1/2 attained at $v = \sqrt{2}\,c_s$ (see Figure 3.7(b)). With a rate strengthening cohesive zone

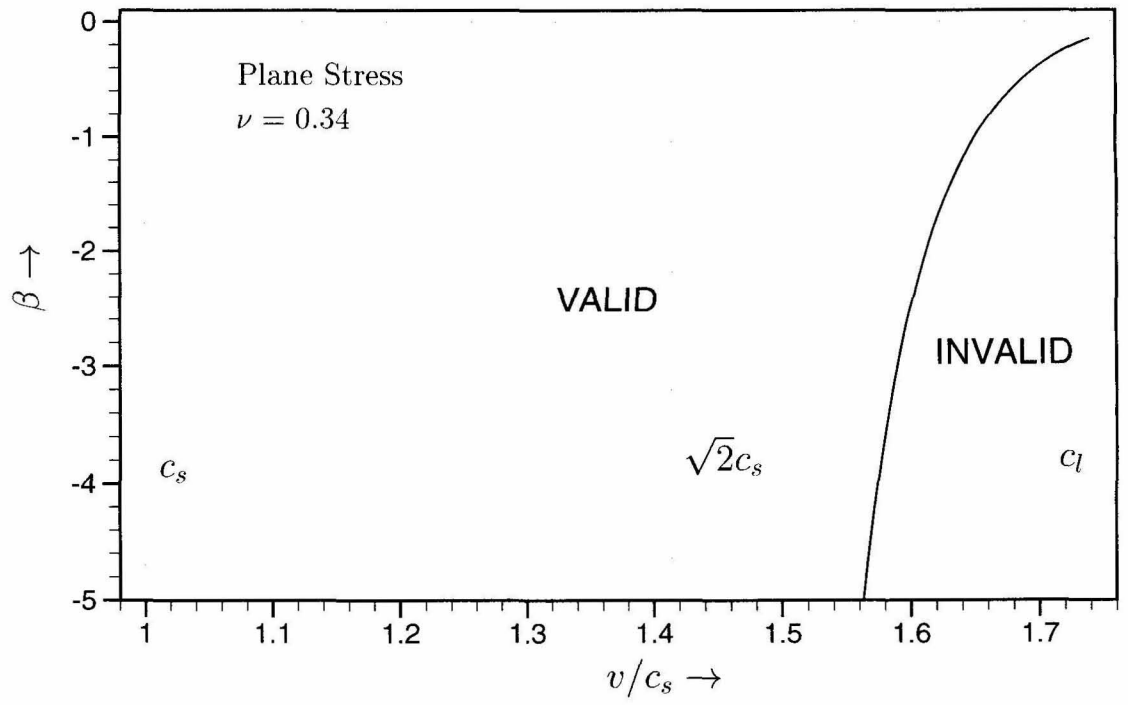

Figure 5.2: Region of validity of the velocity weakening solution in the $\beta - v/c_s$ space. Note for $-0.141228 < \beta < 0$, the velocity weakening solution is valid for the entire sub-Rayleigh as well as the intersonic regime. For $\beta < -0.141228$, a small velocity regime close to c_l becomes inadmissible.

($\beta > 0$), the singularity exponent λ is always less than q, is a function of crack speed and its peak value is attained at a speed higher than $\sqrt{2}\,c_s$. As the influence of rate sensitivity becomes greater with other factors held fixed, the strength of the crack edge singularity increases and the fraction of the yield zone over which the singular solution dominates becomes greater. However, for a velocity weakening cohesive zone ($\beta < 0$), shear stress vanishes at the physical crack tip and γ and λ are the indices measuring the rate of decay of τ as the physical crack tip is approached. Lower the value of β (for $\beta < 0$), faster the decay of cohesive shear stress within the cohesive zone.

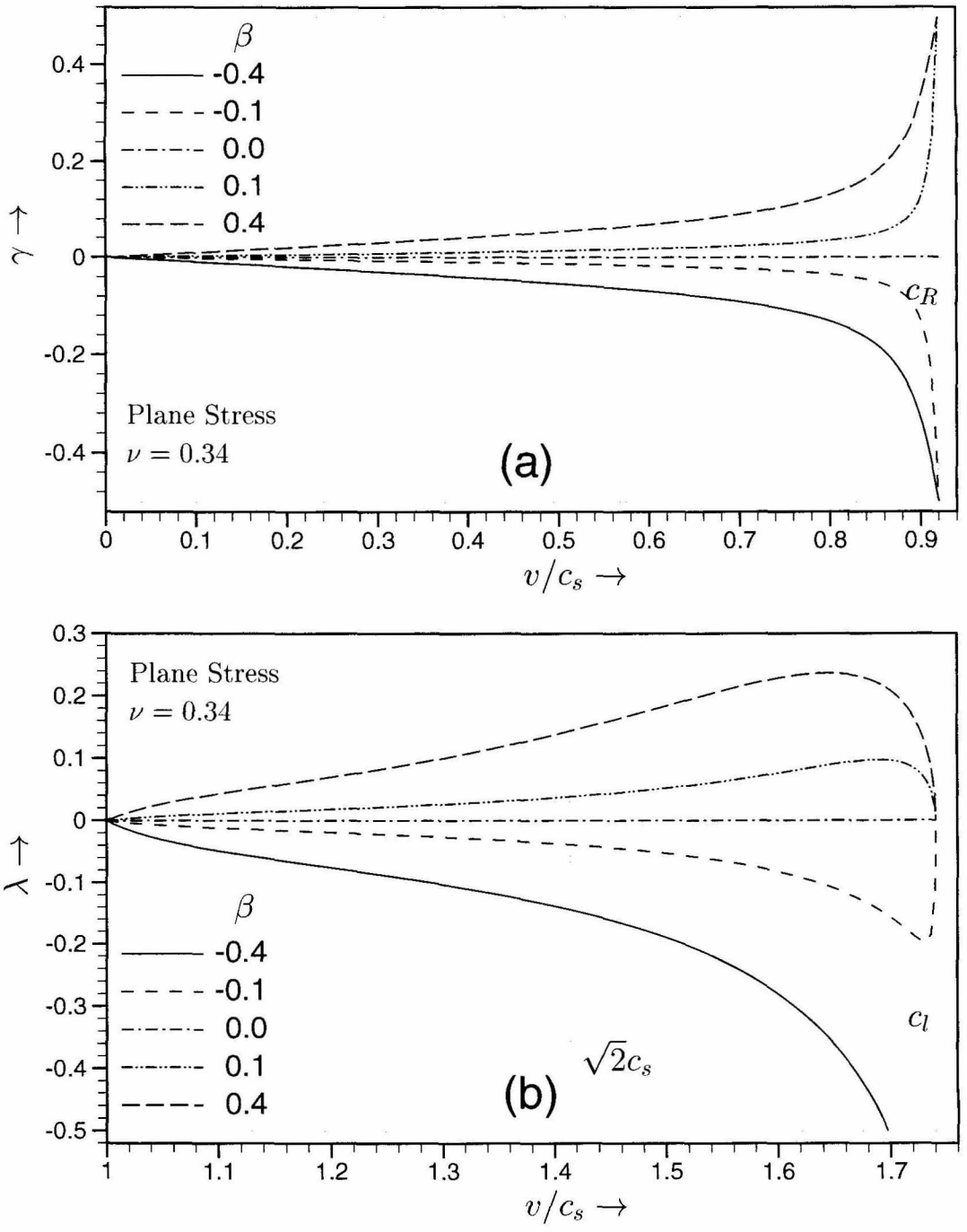

Figure 5.3: Dynamically propagating mode II crack with a rate dependent cohesive zone — Crack tip stress singularity. **(a)** For subsonic speeds at different values of the rate parameter β. **(b)** For intersonic speeds at different values of the rate parameter β.

5.3.1 Near-Tip Stress Field

With the known cohesive shear traction (5.11), one can compute F'', G'' and g'' and thus obtain the dominant near-tip stress field (see Sections 4.2.2 and 4.2.3). The stress field is given in Appendix D for sub-Rayleigh crack speeds and in Appendix E for intersonic crack speeds. For sub-Rayleigh mode II cracks with a rate dependent cohesive zone, σ_{12} on the crack plane ($\eta_2 \to 0^+$), ahead of the mathematical crack tip, is given by

$$\frac{\sigma_{12}}{\tau_o}(\eta_1/L > 0) = \frac{1}{\pi}\sqrt{\frac{\eta_1}{L}}\left[\int_0^1 \frac{d\xi}{\sqrt{\xi}(\xi + \eta_1/L)} + \int_0^1 \frac{ds}{\sqrt{s}(1 + s\,\eta_1/L)} - \left(\frac{\eta_1/L}{1 + \eta_1/L}\right)^{\gamma} \int_0^1 \frac{(1-s)^{\gamma}}{\sqrt{s}(1 + s\,\eta_1/L)}\,ds\right]. \tag{5.18}$$

The shear stress component σ_{12} on the upper cohesive surface is given in (5.11) and it vanishes on the crack faces. σ_{12} on the crack plane is plotted in Figure 5.4(a) for different values of the rate parameter β at a representative subsonic speed, $v = 0.6\,c_s$. As seen, σ_{12} vanishes at the physical crack tip for $\beta < 0$, but is singular there for $\beta > 0$ with a singularity exponent, $\gamma < 1/2$. Far ahead of the tip $\eta_1 \gg L$, the square-root singular solution for a sharp crack is recovered. Figure 5.4(b) shows the crack plane distribution of σ_{12} for various subsonic speeds at a fixed value of $\beta = -0.4$[2]. It can be seen that an increase in the crack speed results in a faster decay of the cohesive shear stress within the velocity weakening cohesive zone.

For intersonic mode II cracks with a rate dependent cohesive zone, σ_{12} on the

[2]Later on, it will be shown that $\beta = -0.4$ for our laboratory specimens (at slip rates of a few m/s) by comparing the model predictions with experimental observations.

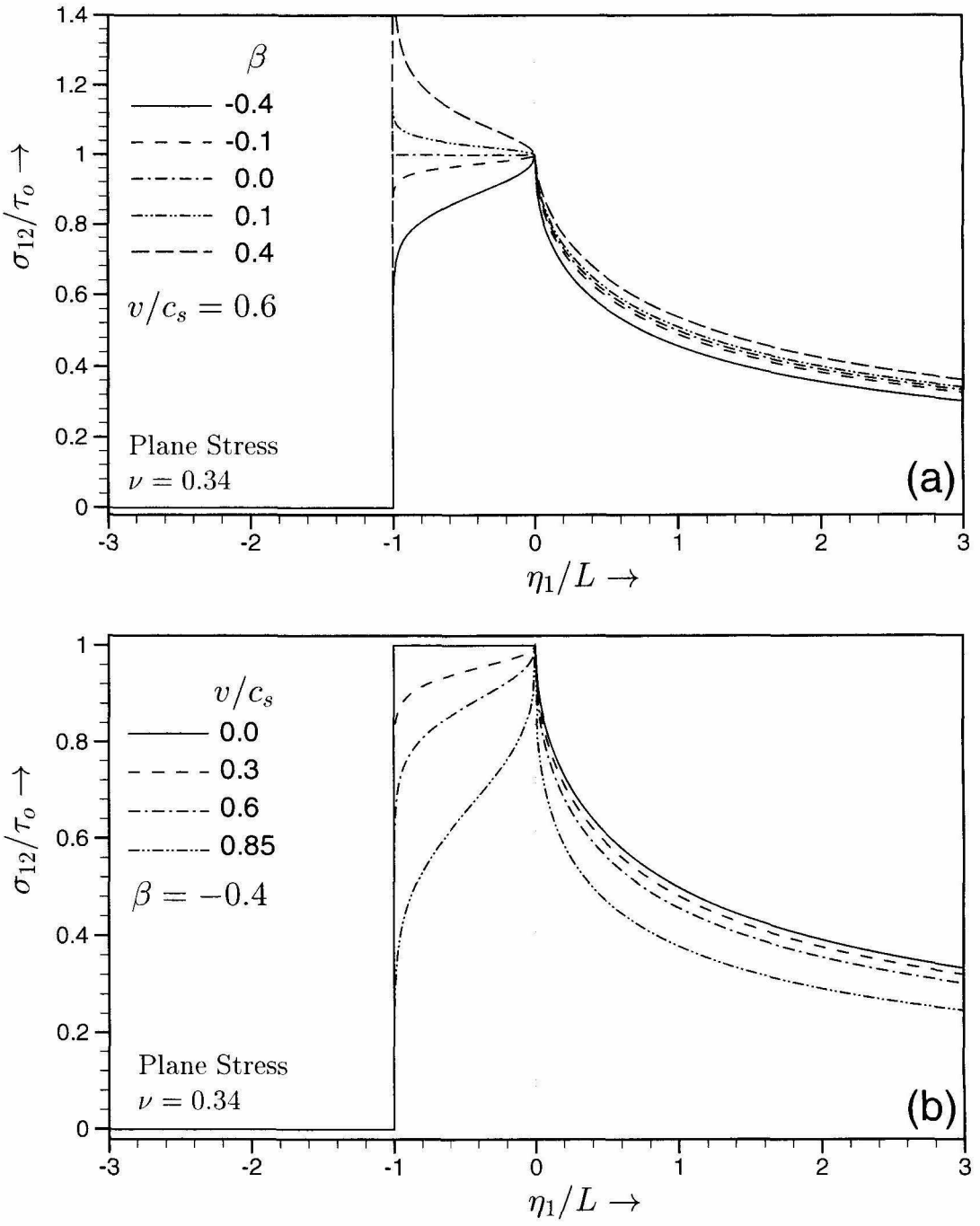

Figure 5.4: Subsonically propagating mode II crack with a rate dependent cohesive zone. **(a)** Stress component σ_{12} on the crack plane for $v/c_s = 0.6$ and for different values of the rate parameter β. **(b)** Stress component σ_{12} on the crack plane for $\beta = -0.4$ and for different values of crack tip speed v.

crack plane ($\eta_2 \to 0^+$), ahead of the mathematical crack tip is given by

$$\frac{\sigma_{12}}{\tau_o}(\eta_1/L > 0) = \frac{\sin q\pi}{\pi}\left(\frac{\eta_1}{L}\right)^{1-q}\left\{\int_0^1 \frac{d\xi}{\xi^{1-q}(\xi+\eta_1/L)} + \int_0^1 \frac{ds}{s^q(1+s\,\eta_1/L)} - \left(\frac{\eta_1/L}{1+\eta_1/L}\right)^{\lambda}\int_0^1 \frac{(1-s)^{\lambda}}{s^q(1+s\,\eta_1/L)}\,ds\right\}. \tag{5.19}$$

σ_{12} within the cohesive zone is given in (5.11) and it vanishes on the crack faces. The influence of the rate parameter β on crack plane shear stress distribution is shown in Figure 5.5(a) for a fixed intersonic speed, $v = 1.47\,c_s$[3]. Similar to the subsonic case, σ_{12} vanishes at the physical crack tip for $\beta < 0$, but is singular there for $\beta > 0$. The singularity exponent $\lambda(< 1/2)$ increases with increasing +ve β. As $\beta \to \infty$, the distribution becomes the same as in the case of a singular solution with no cohesive zone. Again, Figure 5.5(b) shows the crack plane distribution of σ_{12} for various intersonic speeds at a fixed value of $\beta = -0.4$.

As seen in the previous chapter, for a propagating mode II crack with a Dugdale type cohesive zone ($\beta = 0$), the stress component σ_{11} is unbounded at the physical crack tip, with a singularity less than 1/2 for sub-Rayleigh crack speeds and less than q for intersonic crack speeds. This undesirable artifact is due to the particular cohesive law used. For dynamic mode II cracks with a rate dependent cohesive zone, σ_{11} is singular at the physical crack tip for $\beta > 0$ and is finite and nonsingular at the physical crack tip for $\beta < 0$. Figure 5.6(a) shows the effect of rate sensitivity on the distribution of σ_{11} on the crack plane for an intersonic speed of $1.47\,c_s$. As seen from the figure, σ_{11} is compressive and singular at the physical crack tip for $\beta > 0$ and attains a finite value there for $\beta < 0$. Figure 5.6(b) shows the variation of the stress component σ_{11} on the crack plane for different intersonic crack speeds at a fixed value

[3]Later on, we will compare the isochromatic fringe pattern predicted by the model with the experimentally recorded pattern at this particular intersonic speed.

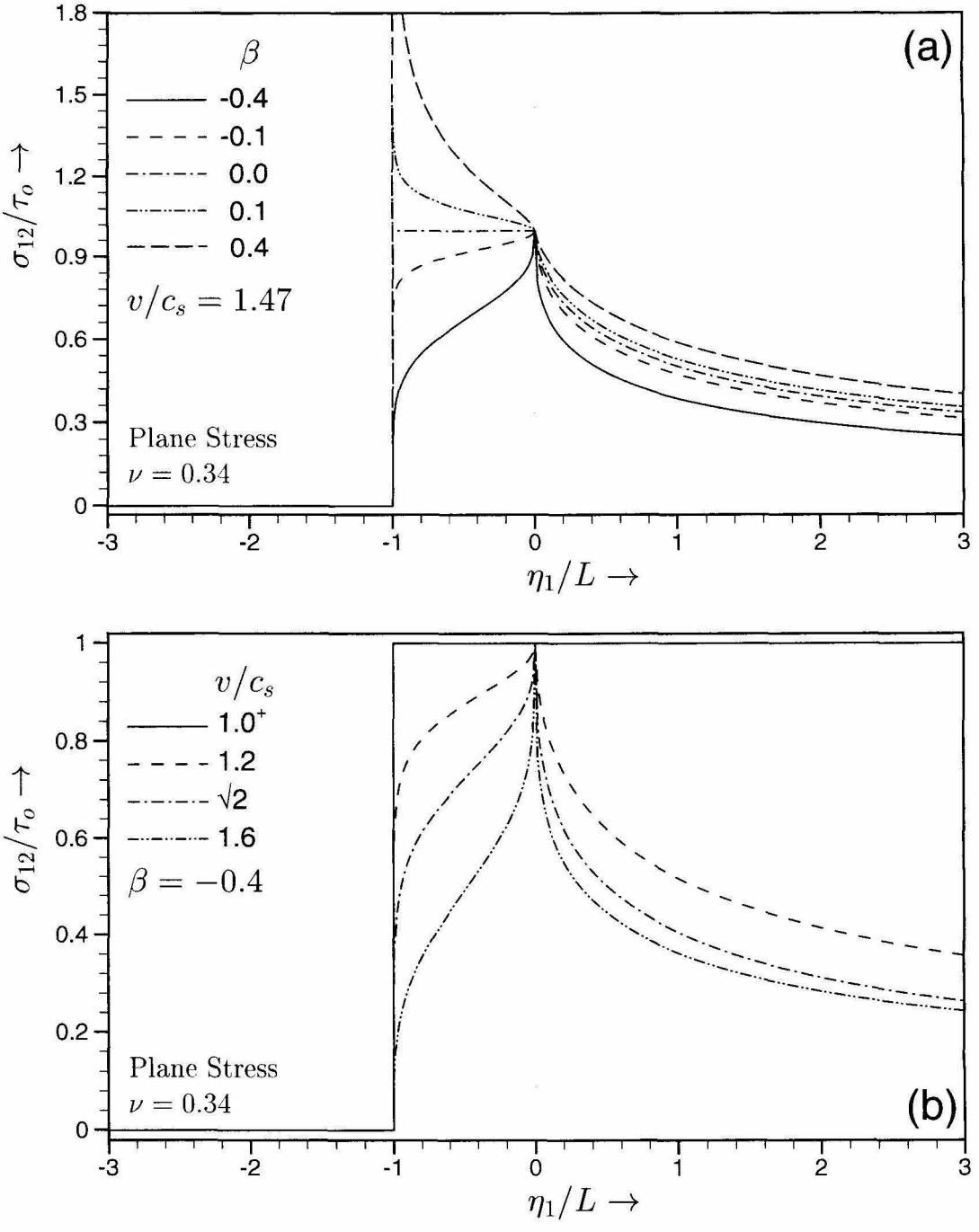

Figure 5.5: Intersonically propagating mode II crack with a rate dependent cohesive zone. **(a)** Stress component σ_{12} on the crack plane for $v/c_s = 1.47$ and for different values of the rate parameter β. **(b)** Stress component σ_{12} on the crack plane for $\beta = -0.4$ and for different values of crack tip speed v.

of $\beta = -0.4$. On the crack plane ($\eta_2 \to 0^+$),

$$\frac{\sigma_{11}}{\tau_o}(-1 < \frac{\eta_1}{L} < 0) = \frac{(\alpha_l^2 + \hat{\alpha}_s^2)}{\alpha_l} \frac{\sin^2 q\pi}{\pi} \left[\frac{\pi}{\tan q\pi} + \left(\frac{-\eta_1}{L} \right)^{1-q} \left\{ \text{pv} \int_0^1 \frac{d\xi}{\xi^{1-q}(\xi + \eta_1/L)} + \int_0^1 \frac{ds}{s^q(1 + s\,\eta_1/L)} \right\} + \sin \lambda\pi \frac{(-\eta_1/L)^{1-q+\lambda}}{(1 + \eta_1/L)^\lambda} \left\{ \frac{1}{\tan q\pi} - \frac{1}{\tan \lambda\pi} \right\} \int_0^1 \frac{(1-s)^\lambda}{s^q(1 + s\,\eta_1/L)} ds \right], \tag{5.20a}$$

$$\frac{\sigma_{11}}{\tau_o}(\frac{\eta_1}{L} < -1) = \frac{(\alpha_l^2 + \hat{\alpha}_s^2)}{\alpha_l} \frac{\sin^2 q\pi}{\pi} \left(\frac{-\eta_1}{L} \right)^{1-q} \left[\int_0^1 \frac{d\xi}{\xi^{1-q}(\xi + \eta_1/L)} \int_0^1 \frac{ds}{s^q(1 + s\,\eta_1/L)} - \left(\frac{\eta_1/L}{1 + \eta_1/L} \right)^\lambda \int_0^1 \frac{(1-s)^\lambda}{s^q(1 + s\,\eta_1/L)} ds \right], \tag{5.20b}$$

for $c_s < v < c_l$. Also, $\sigma_{11}(\eta_1/L > 0) = 0$. It must be noted here, that the nature of loading in our experiments (as described in Chapter 3) is such, that the dynamic mode II stress intensity factor associated with the propagating crack is negative. This results in σ_{11} to be positive in the upper half plane ($\eta_2 > 0$) and negative in the lower half. However, the analytical solution derived in this chapter follows the conventional approach by assuming the far-field dynamic stress intensity factor (and thus σ_{12}^D) to be positive, resulting in σ_{11} being compressive in the upper half plane.

5.3.2 Cohesive Zone Length

The cohesive zone length L is determined by imposing a physical requirement that the stress intensity at the front end of the cohesive zone should vanish. As in the case of a Dugdale type cohesive zone, we incorporate the cohesive traction distribution from (5.11) into (4.28c) and (4.43c) and thus obtain the cohesive zone length in terms of the dynamic stress intensity factor (K_{II}^d or K_{II}^{*d}), shear cohesive strength of the crack plane (τ_o), crack speed (v) and the rate parameter (β). Since the definition of stress intensity factor varies from sub-Rayleigh to intersonic speeds, we again choose

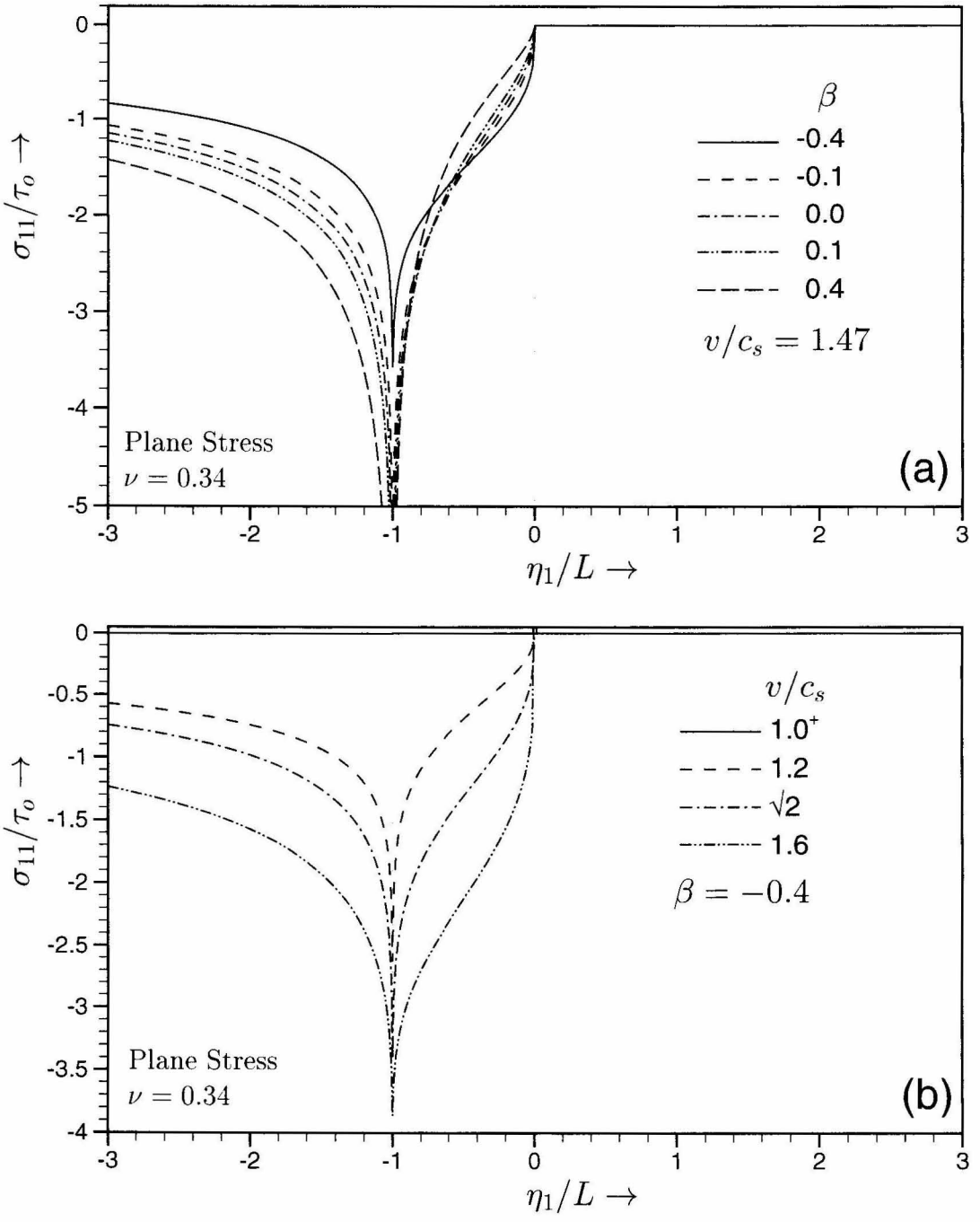

Figure 5.6: Intersonically propagating mode II crack with a rate dependent cohesive zone. **(a)** Stress component σ_{11} on the crack plane for $v/c_s = 1.47$ and for different values of the rate parameter β. **(b)** Stress component σ_{11} on the crack plane for $\beta = -0.4$ and for different values of crack tip speed v.

σ_{12}^D as a measure of the amplitude of far-field applied loading. σ_{12}^D is related to the subsonic and intersonic stress intensity factors as given in (4.45). The normalized cohesive zone length L/L_o in terms of σ_{12}^D, τ_o, v and β is given by

$$\frac{L}{L_o} = \begin{cases} \dfrac{1}{\pi}\left[\dfrac{\Gamma(\gamma+1/2)}{\Gamma(\gamma+1)}\right]^2 & 0 \le v < c_R\,, \\ \dfrac{4}{\pi^2}\left(\dfrac{q\pi}{\sin q\pi}\right)^{1/q}\left(\dfrac{\sigma_{12}^D}{\tau_o}\right)^{1/q-2}\left[\dfrac{\Gamma(\lambda-q+1)}{\Gamma(1-q)\Gamma(1+\lambda)}\right]^{1/q} & c_s < v < c_l\,, \end{cases} \tag{5.21}$$

where $\Gamma(\cdot)$ is the standard Euler Gamma function. The normalizing parameter L_o is the length of the cohesive zone associated with a quasi-statically growing crack with the same far-field applied loading σ_{12}^D and the same cohesive strength of the crack plane τ_o. It is given by

$$L_o = \frac{\pi^2}{4}\left(\frac{\sigma_{12}^D}{\tau_o}\right)^2 D\,. \tag{5.22}$$

Hence under a constant σ_{12}^D/τ_o, (5.21) represents the dependence of cohesive zone length on v and β.

Figure 5.7 shows the influence of the rate parameter β on the variation of the normalized cohesive zone length with crack speed for a fixed value of $\sigma_{12}^D/\tau_o = 0.1$. As seen from the figure, in the sub-Rayleigh regime, L/L_o is a constant for $\beta = 0$ and for any positive value of β, it decreases monotonically to a constant value of $4/\pi^2$ as $v \to c_R$. As $v \to c_R$, $\gamma \to 1/2$ and the stress field in front of the physical crack tip, becomes identical to that predicted by a singular solution with no cohesive zone. Hence one might expect the cohesive zone length to vanish as $v \to c_R$. However, the cohesive zone length is nonzero as $v \to c_R$, being equal to the distance ahead of the tip at which $\sigma_{12} = \tau_o$. The stress distribution both within the cohesive zone and outside becomes identical to that of the singular solution without a cohesive zone. In the intersonic regime for $\beta > 0$, the cohesive zone length decreases with increasing rate sensitivity and also the peak shifts to a speed below $\sqrt{2}\,c_s$ with increasing β.

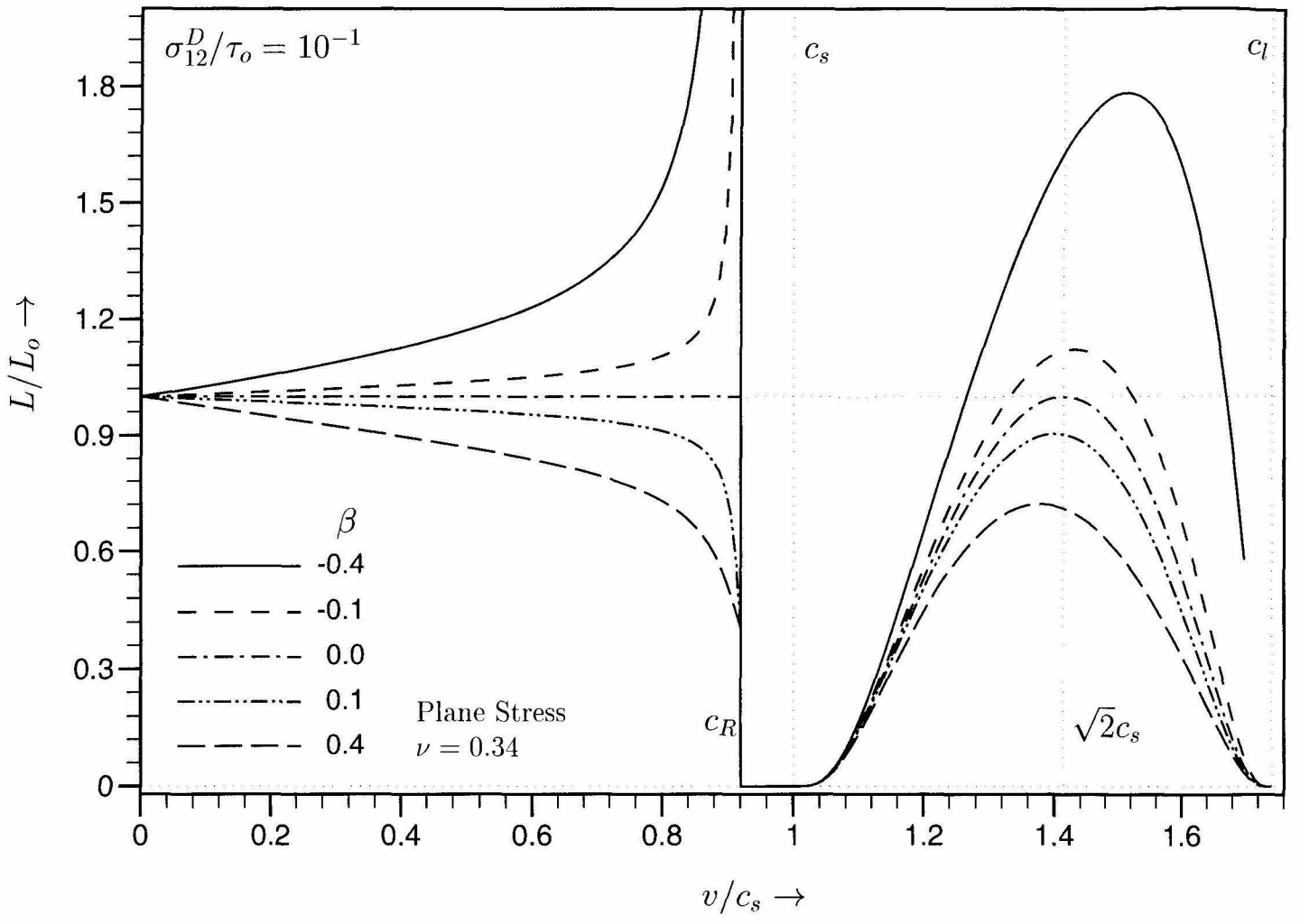

Figure 5.7: Dynamically propagating mode II crack with a rate dependent cohesive zone — Dependence of the cohesive zone length on crack tip speed v, plotted for for $\sigma_{12}^D/\tau_o = 10^{-1}$ and for different values of the rate parameter β.

For velocity weakening ($\beta < 0$), L/L_o increases with crack speed and becomes unbounded as $v \to c_R$ ($\gamma \to -1/2$). Also as expected, smaller β results in an increase in cohesive zone length and in the intersonic regime, the peak shifts to a speed higher than $\sqrt{2}\,c_s$. The dependence of L/L_o on the shear strength of the crack plane, at any β is similar to the case of $\beta = 0$, which was discussed in Section 4.2.5.

5.3.3 Sliding Rate Within the Cohesive Zone

The sliding rate (or slip rate) distribution $\dot{\delta}_1$ within the cohesive zone is given in (5.15) for both sub-Rayleigh and intersonic crack speeds. From (5.15) we see that the slip rate at any point in the cohesive zone is directly proportional to the shear strength (at quasi-static sliding) of the crack plane τ_o. The slip rate distribution is also dependent on v and β in a complicated way. We examine the dependence of slip rate distribution within the cohesive zone on v and β at a constant value of μ/τ_o, chosen to be 136, which is equal to the ratio of shear modulus of Homalite (1.9 GPa) and the shear strength of the Homalite/Homalite bond ($\approx$14 MPa). Figure 5.8(a) shows the influence of the rate parameter on $\dot{\delta}_1$ within the cohesive zone for a representative sub-Rayleigh speed, $v = 0.6c_s$. On the other hand, Figure 5.8(b) shows the variation of $\dot{\delta}_1$ within the cohesive zone for various sub-Rayleigh speeds and at a constant value of $\beta = -0.4$. $\dot{\delta}_1$ increases monotonically from $\eta_1 = 0$ and becomes unbounded at the physical crack tip for all $\beta \geq 0$. However, for $\beta < 0$, $\dot{\delta}_1$ attains a finite, bounded maximum at the physical crack tip. This is the slip rate at which the cohesive shear strength vanishes in the velocity weakening model. It can be clearly discerned from Figure 5.8 that distribution of $\dot{\delta}_1$ in the cohesive zone exhibits a rather weak dependence on β, where as the dependence on v is very strong. As $v \to c_R$, $\dot{\delta}_1$ becomes unbounded through out the cohesive zone.

Similarly Figure 5.9(a) shows the influence of β on the variation of $\dot{\delta}_1$ within the cohesive zone for a chosen intersonic speed, $v = 1.47\,c_s$ and Figure 5.9(b) shows the variation of $\dot{\delta}_1$ within the cohesive zone for various intersonic speeds at a particular

value of $\beta = -0.4$. Similar to the sub-Rayleigh case, for $\beta > 0$, $\dot{\delta}_1$ is singular at the physical crack tip, whereas if the cohesive zone is velocity weakening ($\beta < 0$), $\dot{\delta}_1$ is nonsingular and attains a finite maximum at the physical crack tip. Effect of β on $\dot{\delta}_1$ is rather small, though a bit more pronounced than in the sub-Rayleigh case. $\dot{\delta}_1 = 0$, everywhere in the cohesive zone for $v \to c_s, c_l$, but $\dot{\delta}_1$ is strongly influenced by v at all other intersonic speeds. It may be noted that through most of the cohesive zone, $\dot{\delta}_1$ is within $\approx 2\%$ of c_s for sub-Rayleigh speeds and is within $\approx 4\%$ of c_s for intersonic speeds. 2-4% of c_s corresponds to sliding rates of a few m/s, consistent with our expectation while choosing the cohesive law. Note that these slip rates are comparable to those observed in earthquake ruptures (HEATON, 1990).

5.3.4 Crack Tip Sliding Displacement

The shear displacement discontinuity at the physical crack tip or the crack tip sliding displacement, δ_t is readily obtained by integrating the displacement gradient $u_{1,1}$ within the cohesive zone (see (5.2), (5.3) and (5.11)).

$$\delta_t = 2\int_0^{-L} u_{1,1}(\eta_1, \eta_2 \to 0^+)\, d\eta_1 \,. \tag{5.23}$$

δ_t is a directly proportional to τ_o and the dependence on v and β is given by

$$\frac{\delta_t}{\delta_t^o} = \frac{2\gamma}{\beta}\frac{(\alpha_l^2 - \alpha_s^2)}{(v^3/c_s^3)}\left[\frac{\Gamma(\gamma + 1/2)}{\Gamma(\gamma+1)}\right]^2 \qquad 0 \le v < c_R \,, \tag{5.24a}$$

$$\frac{\delta_t}{\delta_t^o} = \frac{4\lambda}{\pi\beta(1-q)}\frac{(\alpha_l^2 + \hat{\alpha}_s^2)}{(v^3/c_s^3)}\left(\frac{q\pi}{\sin q\pi}\right)^{1/q}\left(\frac{\sigma_{12}^D}{\tau_o}\right)^{1/q-2}\left[\frac{\Gamma(\lambda - q + 1)}{\Gamma(1-q)\Gamma(1+\lambda)}\right]^{1/q}$$
$$c_s < v < c_l \,, \tag{5.24b}$$

where δ_t^o is the crack tip sliding displacement associated with a quasi-statically growing mode II crack under the same σ_{12}^D and τ_o.

$$\delta_t^o = \frac{\pi(\kappa+1)}{4}\frac{\tau_o}{\mu}\left(\frac{\sigma_{12}^D}{\tau_o}\right)^2 D \,. \tag{5.25}$$

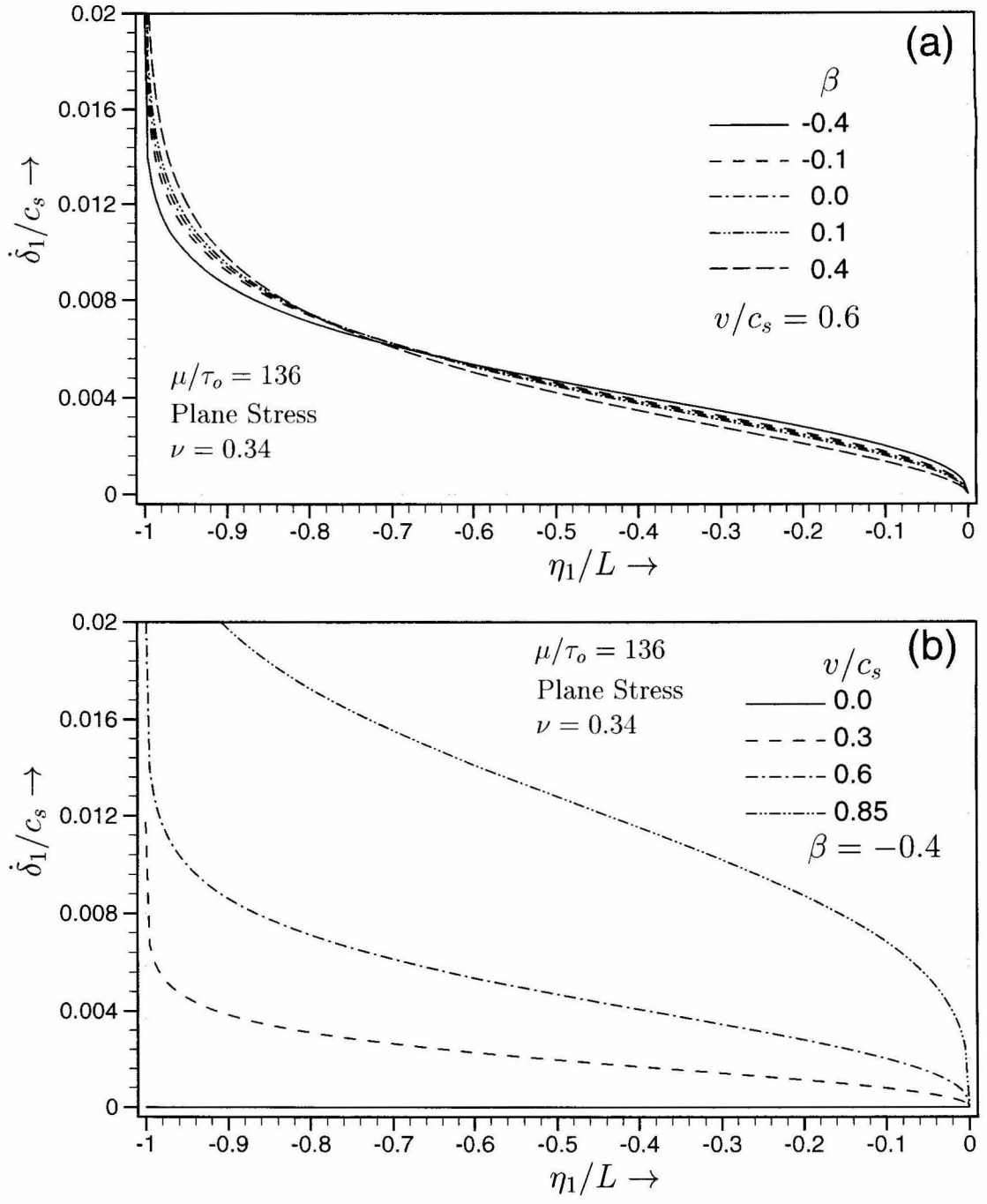

Figure 5.8: Subsonically propagating mode II crack with a rate dependent cohesive zone. **(a)** Relative sliding rate $\dot{\delta}_1$ on the crack plane for $v/c_s = 0.6$ and for different values of the rate parameter β. **(b)** Relative sliding rate $\dot{\delta}_1$ on the crack plane for $\beta = -0.4$ and for different values of the crack tip speed v.

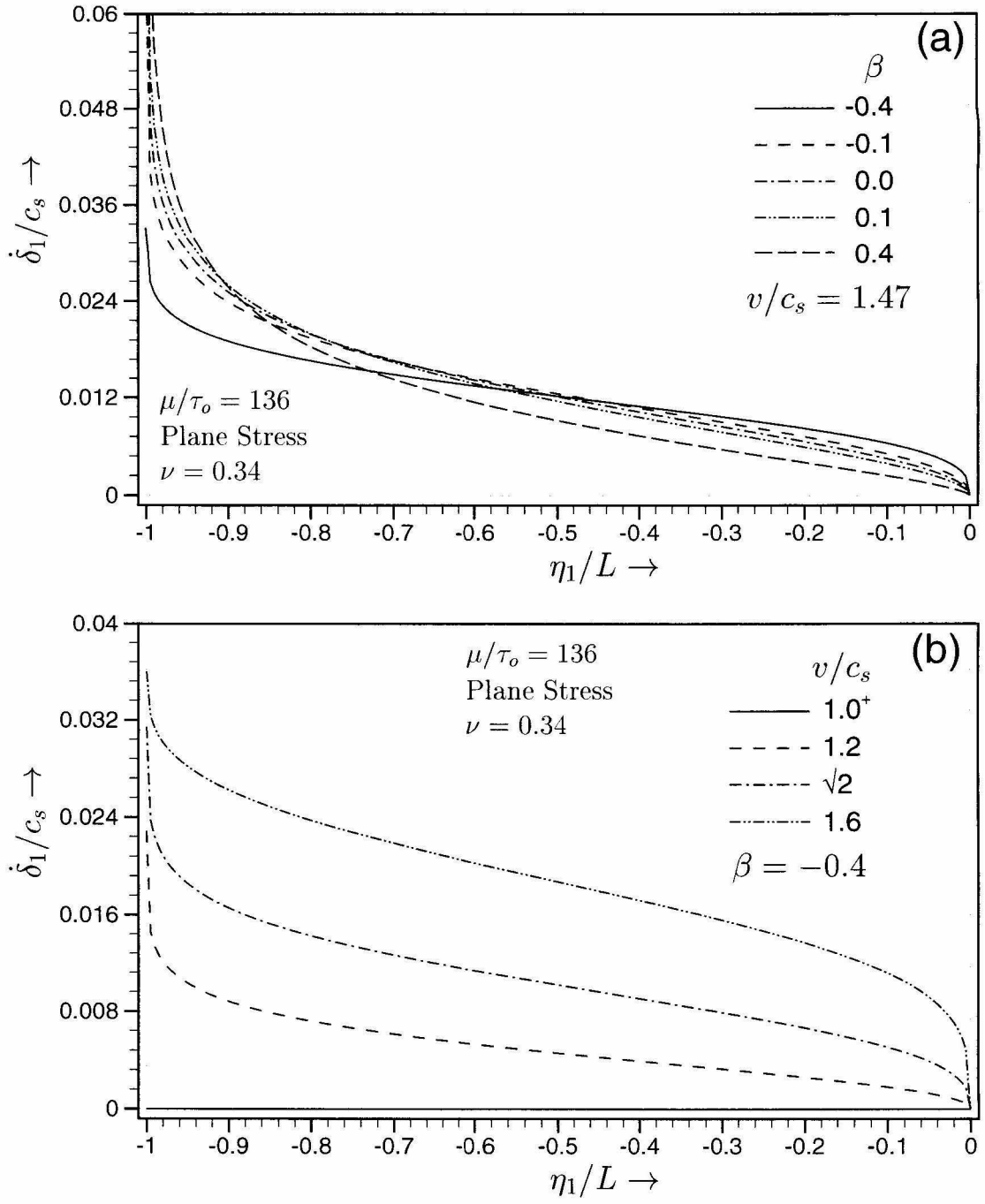

Figure 5.9: Intersonically propagating mode II crack with a rate dependent cohesive zone. **(a)** Relative sliding rate $\dot{\delta}_1$ on the crack plane for $v/c_s = 1.47$ and for different values of the rate parameter β. **(b)** Relative sliding rate $\dot{\delta}_1$ on the crack plane for $\beta = -0.4$ and for different values of the crack tip speed v.

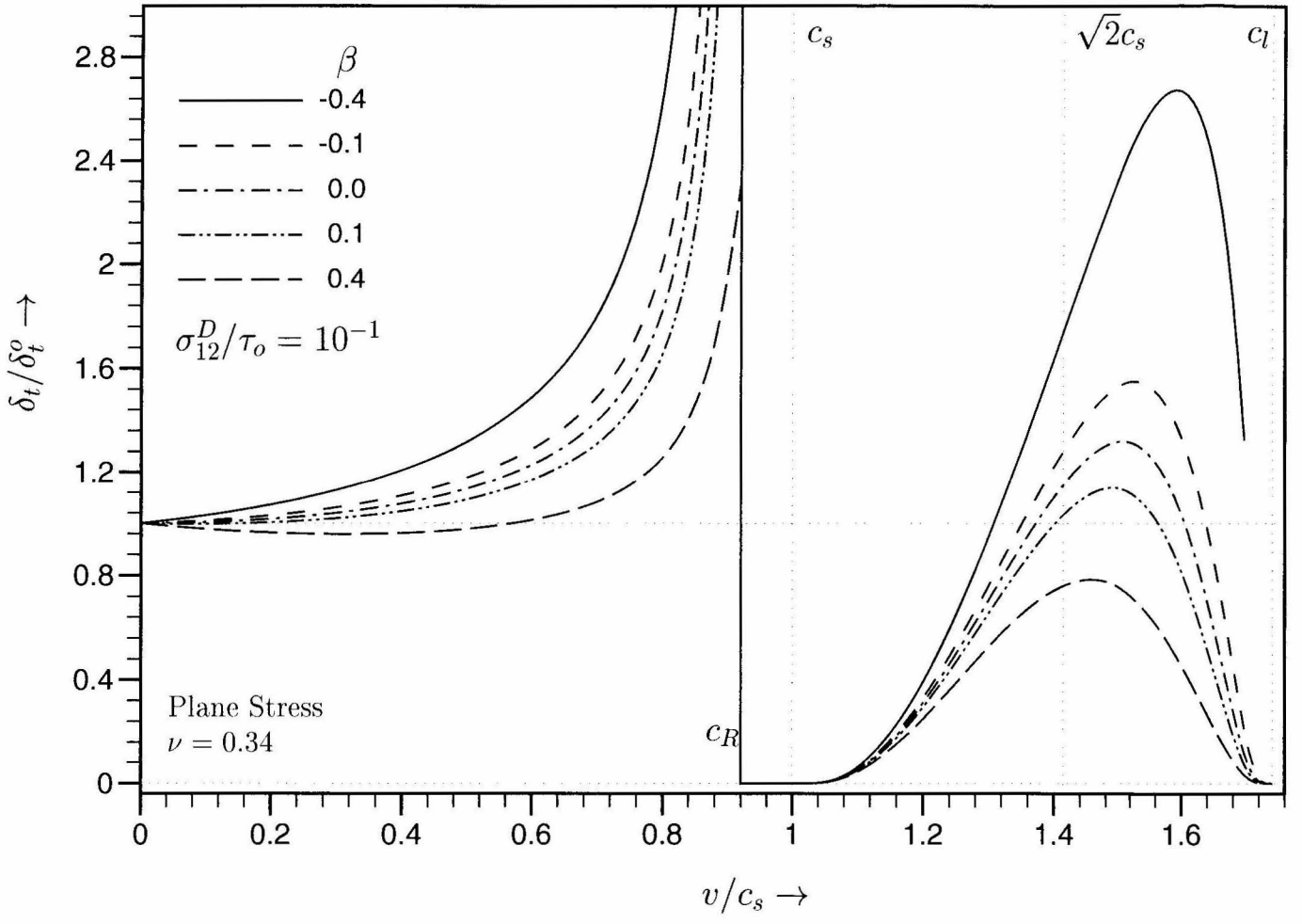

Figure 5.10: Dynamically propagating mode II crack with a rate dependent cohesive zone — Dependence of the crack tip sliding displacement on crack tip speed v, plotted for $\sigma_{12}^D/\tau_o = 10^{-1}$ and for different values of the rate parameter β.

Figure 5.10 shows the variation of δ_t/δ_t^o with crack speed for different β at a constant value of $\sigma_{12}^D/\tau_o = 0.1$. For subsonic speeds, δ_t/δ_t^o becomes unbounded as $v \to c_R$ for all $\beta \leq 0$. For $\beta > 0$, it shows an initial decrease and an eventual increase as $v \to c_R$ where it attains a finite value equal to $2(1+\nu)c_s/(\pi\beta c_R)$ (for plane stress). For intersonic speeds, δ_t increases from zero at c_s, reaches a finite maximum at a speed beyond $\sqrt{2}\,c_s$, and thereafter vanishes again at c_l. Note that for $\beta = -0.4$, the curve is abruptly cut off at a speed less than c_l, as the current solution is no longer valid in this regime. Later on, we will introduce a propagation criterion based on the attainment of a material/specimen specific critical crack tip sliding displacement to predict the behavior of a dynamically propagating mode II shear crack with a rate dependent cohesive zone.

5.3.5 Dynamic Energy Release Rate

The dynamic energy release rate G, defined as energy flux into the cohesive zone per unit crack advance per unit thickness along the crack front, may be expressed as (see Section 4.2.8)

$$G = 2\int_0^{-L} \sigma_{12}(\eta_1, \eta_2 \to 0^+)\, u_{1,1}(\eta_1, \eta_2 \to 0^+)\, d\eta_1 \,. \tag{5.26}$$

For a steadily propagating mode II crack with a rate dependent cohesive zone, the shear traction acting on the upper cohesive surface is given in (5.11) and the displacement gradient $u_{1,1}$ here is given in (5.2) and (5.3). Hence, we obtain

$$\frac{G}{G_o} = \frac{1}{\beta}\frac{(\alpha_l^2 - \alpha_s^2)}{v^3/c_s^3}\left[\frac{\Gamma(\gamma+1/2)}{\Gamma(1+\gamma)}\right]^2 g(\gamma) \qquad 0 \leq v < c_R\,, \tag{5.27a}$$

$$\frac{G}{G_o} = \frac{4}{\pi}\frac{1}{\beta}\frac{(\alpha_l^2 + \hat{\alpha}_s^2)}{v^3/c_s^3}\left(\frac{q\pi}{\sin q\pi}\right)^{1/q}\left(\frac{\sigma_{12}^D}{\tau_o}\right)^{1/q-2}\left[\frac{\Gamma(\lambda-q+1)}{\Gamma(1-q)\Gamma(1+\lambda)}\right]^{1/q} g^*(\lambda, q)$$
$$c_s < v < c_l\,, \tag{5.27b}$$

where

$$g(\gamma) = 2\gamma + \frac{\sin^2 \gamma\pi}{\pi^2} \int_0^1 \frac{\xi^{2\gamma+1}}{(1-\xi)^{2\gamma}} \left[\int_0^1 \frac{(1-s)^\gamma}{\sqrt{s}\,(1-s\,\xi)}\, ds \right]^2 d\xi \qquad 0 \le v < c_R\,, \tag{5.28a}$$

$$g^*(\lambda, q) = \frac{\lambda}{1-q} + \frac{\sin^2 \lambda\pi}{\pi^2} \int_0^1 \frac{\xi^{2-2q+2\lambda}}{(1-\xi)^{2\lambda}} \left[\int_0^1 \frac{(1-s)^\lambda}{s^q\,(1-s\,\xi)}\, ds \right]^2 d\xi \qquad c_s < v < c_l\,. \tag{5.28b}$$

and G_o is the energy release rate associated with a quasi-statically propagating crack with the same σ_{12}^D/τ_o. Hence G/G_o represents the dependence of the dynamic energy release rate on v and β. G_o is given by

$$G_o = \frac{\pi(\kappa+1)}{4} \frac{{\sigma_{12}^D}^2 D}{\mu}. \tag{5.29}$$

For steady sub-Rayleigh crack growth, G is independent of the process zone characteristics and hence it is also equal to that in the case of a point sized process zone. Thus $G/G_o = 2\alpha_s(\alpha_l^2 - \alpha_s^2)/R(v)$ and hence, for sub-Rayleigh crack speeds, it is independent of β. This is reflected in the Figure 5.11 which shows the variation of G/G_o with crack speed for different β at a constant value of $\sigma_{12}^D/\tau_o = 0.1$. However, for intersonic speeds, G is dependent on the size and characteristics of the process zone. As seen from Figure 5.11, the dynamic energy release rate G is finite through out the intersonic regime except for crack speeds close to c_s and c_l. Hence, based on the requirement of a positive energy flux, the entire intersonic regime is admissible for mode II crack growth. The variation of G/G_o for intersonic speeds depends strongly on the shear strength of the fracture plane τ_o (see Section 4.2.8). However, as seen from the figure, the influence of β is rather small.

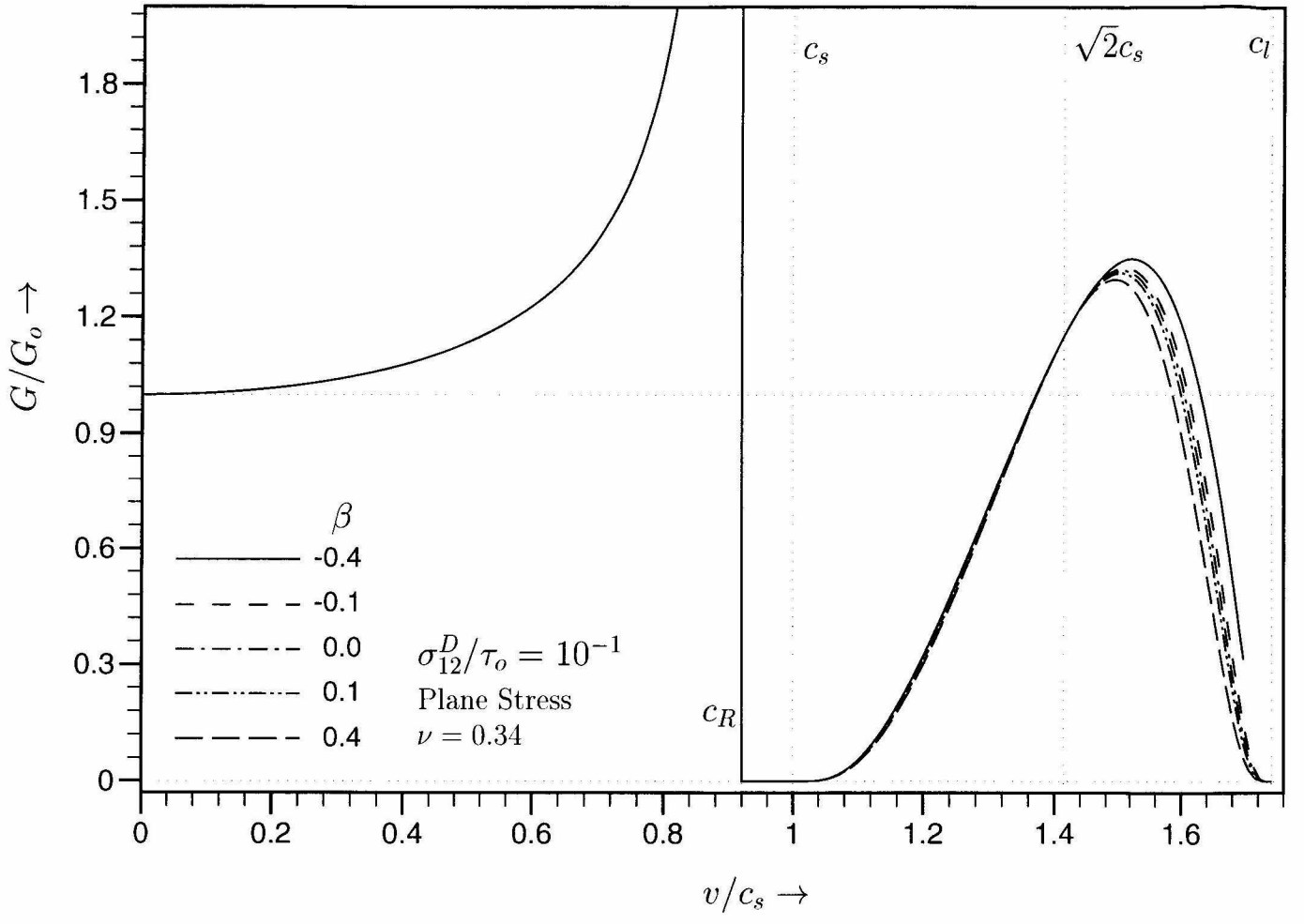

Figure 5.11: Dynamically propagating mode II crack with a rate dependent cohesive zone — Dependence of the dynamic energy release rate on crack tip speed v, plotted for $\sigma_{12}^D/\tau_o = 10^{-1}$ and for different values of the rate parameter β.

5.4 Critical Crack Tip Sliding Displacement Criterion

Now, we implement the second part of our cohesive law, *i.e.*, we introduce a propagation criterion for dynamic mode II crack growth, which states that sustained dynamic mode II crack growth at any sub-Rayleigh or intersonic speed, occurs under a constant crack tip sliding displacement (see Figure 5.1(b)).

$$\delta_t = u_1(\eta_1 = -L, \eta_2 \to 0^+) - u_1(\eta_1 = -L, \eta_2 \to 0^-) = \delta_t^c \,. \tag{5.30}$$

This is the same propagation criterion which was used in the previous chapter for propagating mode II cracks with a Dugdale type cohesive zone and the merits of employing a propagating criterion of this type were discussed there. However, with a rate dependent cohesive zone, the critical crack tip sliding displacement criterion and the constant critical G criterion are no longer equivalent. The crack tip sliding displacement δ_t for a dynamically propagating mode II crack with a rate dependent cohesive zone was given in (5.24). The critical crack tip sliding displacement criterion (5.30) states that $\delta_t = \delta_t^o = \delta_t^c$. Hence (5.24) gives a relationship between the critical values (required to satisfy the criterion) of σ_{12}^D, v, β and δ_t^c, provided τ_o is known.

5.4.1 Stability of Crack Growth

Figure 5.12 shows the variation with crack speed of the critical far-field load $(\sigma_{12}^D)_{dyn}^c$ (required to satisfy the critical crack tip sliding displacement criterion (5.30)) from its quasi-static value $(\sigma_{12}^D)_o^c$ for both sub-Rayleigh and intersonic crack speeds. The ratio $(\sigma_{12}^D)_{dyn}^c/(\sigma_{12}^D)_o^c$ is given by

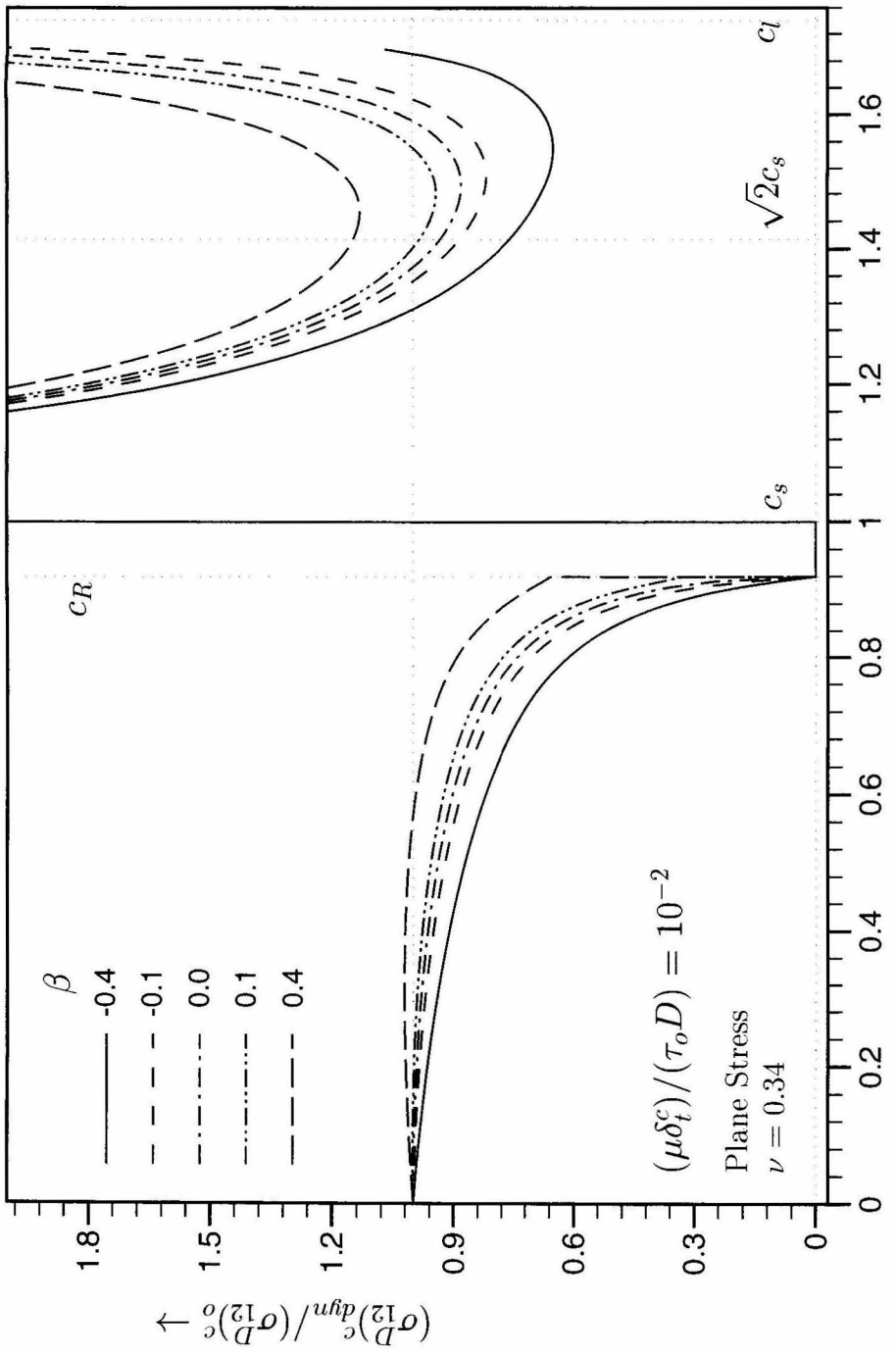

Figure 5.12: Dynamically propagating mode II crack with a rate dependent cohesive zone — Stability of crack growth. Dependence of the critical far-field load (required to sustain dynamic crack growth) on crack tip speed v, plotted for $(\mu\delta_t^c)/(\tau_o D) = 10^{-2}$ and for different values of the rate parameter β.

$$\frac{(\sigma_{12}^D)_{dyn}^c}{(\sigma_{12}^D)_o^c} = \sqrt{\left[\frac{1}{2}\frac{\beta}{\gamma}\frac{v^3/c_s^3}{\alpha_l^2-\alpha_s^2}\right]}\frac{\Gamma(\gamma+1)}{\Gamma(\gamma+1/2)} \qquad 0 \le v < c_R\,, \tag{5.31a}$$

$$\frac{(\sigma_{12}^D)_{dyn}^c}{(\sigma_{12}^D)_o^c} = \left(\frac{\mu\delta_t^c}{D\tau_o}\right)^{q-1/2}\left[\frac{\beta}{2\lambda}\frac{v}{c_s}(1-q)\right]^q\sqrt{\left[\frac{\pi}{2}\frac{1+\hat{\alpha}_s^2}{\alpha_l^2+\hat{\alpha}_s^2}\right]}\left(\frac{\sin q\pi}{q\pi}\right)\frac{\Gamma(1-q)\Gamma(1+\lambda)}{\Gamma(\lambda-q+1)}$$
$$c_s < v < c_l\,, \tag{5.31b}$$

where the critical far-field load required for quasi-static crack propagation, $(\sigma_{12}^D)_o^c$ is given by

$$(\sigma_{12}^D)_o^c = \tau_o\sqrt{\frac{4}{(\kappa+1)\pi}\frac{\mu\delta_t^c}{D\tau_o}} \tag{5.32}$$

As seen from Figure 5.12, for a sub-Rayleigh crack, the far-field load required to sustain a small acceleration in crack speed is lower compared to its previous value, provided $\beta \le 0$. This situation may be interpreted as an instability and it can be expected that a sub-Rayleigh mode II crack with a velocity weakening cohesive zone would accelerate rapidly to c_R. This is probably the reason why no subsonic mode II crack growth was observed along weak planes in our laboratory specimens (see Figure 3.5(b)). Even if the shear crack initiating from the notch initially propagated at sub-Rayleigh speeds, it would immediately accelerate to c_R and beyond. However, for $\beta > 0$, there exists a finite sub-Rayleigh speed regime, starting from $v = 0$ up to a threshold speed, in which crack growth is stable, beyond which it would accelerate unstably to c_R. As $v \to c_R$, $(\sigma_{12}^D)_{dyn}^c/(\sigma_{12}^D)_o^c$ attains a finite value equal to $\sqrt{\beta c_R\pi/(2c_s(1+\nu))}$ for $\beta > 0$, where as it vanishes for $\beta \le 0$. By the same interpretation, for an intersonic crack, there is an initially unstable speed regime followed by a stable speed regime. The critical far-field load $(\sigma_{12}^D)_{dyn}^c/(\sigma_{12}^D)_o^c$ is also a function of a material parameter $(\mu\delta_t^c)/(\tau_o D)$ in the intersonic regime. μ and δ_t^c are material constants and D is an arbitrary distance ahead of the crack tip at which the singular solution with no cohesive zone dominates. Hence the parameter $(\mu\delta_t^c)/(\tau_o D)$ may be interpreted as a

measure of shear strength of the fracture plane. In Figure 5.12, was kept constant at 10^{-2}, whereas Figure 5.13 shows the variation of $(\sigma_{12}^D)_{dyn}^c/(\sigma_{12}^D)_o^c$ for different values of $(\mu\delta_t^c)/(\tau_o D)$ at a constant $\beta = -0.4$. It is seen that the entire speed regime $c_s < v < \sqrt{2}\,c_s$ is unstable and the speed at which intersonic crack propagation becomes stable depends on the shear strength of the fracture plane τ_o and the rate parameter β. For realistic values of the parameter $(\mu\delta_t^c)/(\tau_o D) \approx 10^{-2} - 10^{-3}$ and for values of β shown, the critical load required to sustain intersonic crack propagation is a minimum between $\sqrt{2}\,c_s$ and 1.55. This probably explains the observed experimental behavior of crack speed, where the intersonic mode II crack was found to accelerate to speeds close to c_l and then as the loading pulse was cut off, settled down to a stable propagation speed slightly above $\sqrt{2}\,c_s$ (see Figure 3.6(b)). Similar to the Dugdale type cohesive zone discussed in the previous chapter, the onset of stability for an intersonic mode II crack with a rate dependent cohesive zone depends strongly on τ_o. Decreasing τ_o moves the speed at which intersonic crack growth becomes stable closer to c_l, and in the limiting case of $\tau_o \to 0$, an intersonic mode II crack is expected to accelerate all the way up to c_l. Stability results for growing cracks based on steady state crack solutions are of limited significance. Section 4.3.1 discusses briefly the scenarios under which they may be profitably employed.

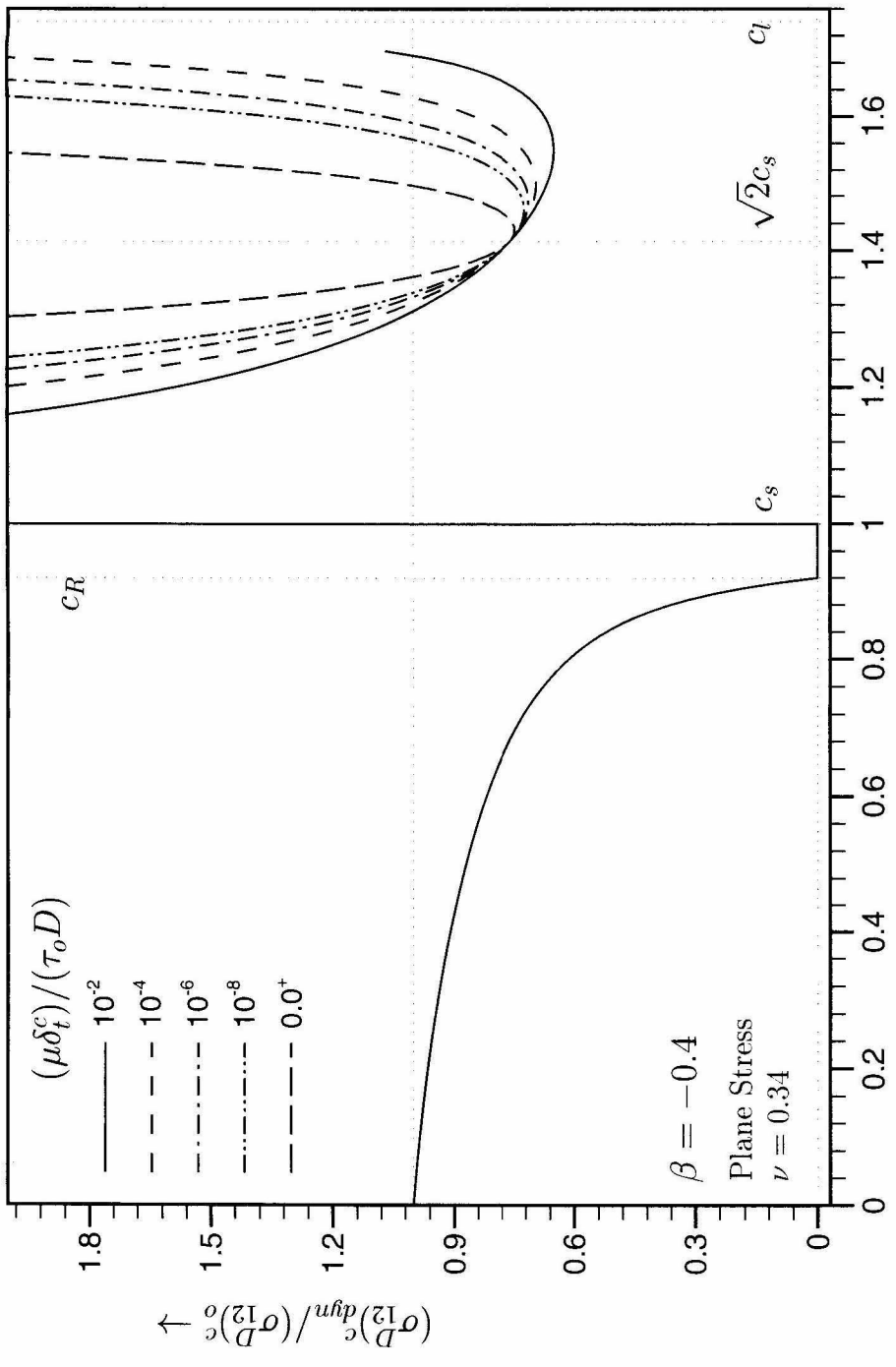

Figure 5.13: Dynamically propagating mode II crack with a rate dependent cohesive zone — Stability of crack growth. Dependence of the critical far-field load (required to sustain dynamic crack growth) on crack tip speed v, plotted for $\beta = -0.4$ and for different values of the interface strength parameter $(\mu\delta_t^c)/(\tau_o D)$.

5.4.2 Critical Cohesive Zone Length

The critical cohesive zone length or the cohesive zone size required for sustained mode II crack growth according to the propagation criterion (5.30) is given by

$$\frac{L^c_{dyn}}{L^c_o} = \begin{cases} \dfrac{1}{2\pi}\dfrac{\beta}{\gamma}\dfrac{v}{c_s}\dfrac{1-\alpha_s^2}{\alpha_l^2-\alpha_s^2} & 0 \le v < c_R\,, \\ \dfrac{1-q}{\pi}\dfrac{\beta}{\lambda}\dfrac{v}{c_s}\dfrac{1+\hat{\alpha}_s^2}{\alpha_l^2+\hat{\alpha}_s^2} & c_s < v < c_l\,, \end{cases} \tag{5.33}$$

where, the critical cohesive zone length for quasi-static mode II crack propagation L^c_o is given by,

$$L^c_o = \frac{\pi}{\kappa+1}\frac{\mu\delta^c_t}{\tau_o}\,. \tag{5.34}$$

Hence, at any sub-Rayleigh or intersonic crack speed, the critical cohesive zone length is directly proportional to the critical crack tip sliding displacement δ^c_t and is inversely proportional to the crack plane shear strength τ_o. Figure 5.14 shows the variation of the critical cohesive zone length L^c_{dyn}/L^c_o with crack speed for different values of the rate parameter β. The critical cohesive zone size for sub-Rayleigh speeds, was found to decrease monotonically up to c_R. It vanishes at c_R in the case of a rate independent cohesive zone, whereas it attains a finite value equal to $2|\beta|c_R/(\pi(1+\nu)c_s)$ at c_R for any +ve or -ve β. ANDREWS (1976) in a numerical simulation of a symmetrically expanding mode II crack under the action of remote uniform shear stresses found that the cohesive zone size decreases continuously with crack speed in the sub-Rayleigh regime attaining its minimum value at c_R. Such a behavior was also observed in the numerical simulations of GEUBELLE and KUBAIR (2000). For intersonic speeds, the critical cohesive zone size is unbounded at c_s and c_l, but remains finite and positive over the rest of the intersonic regime. Such an observation was used by YU and SUO (2000) to justify the admissibility of mode II intersonic crack growth. The critical cohesive zone length is found to be rather insensitive to the rate parameter β.

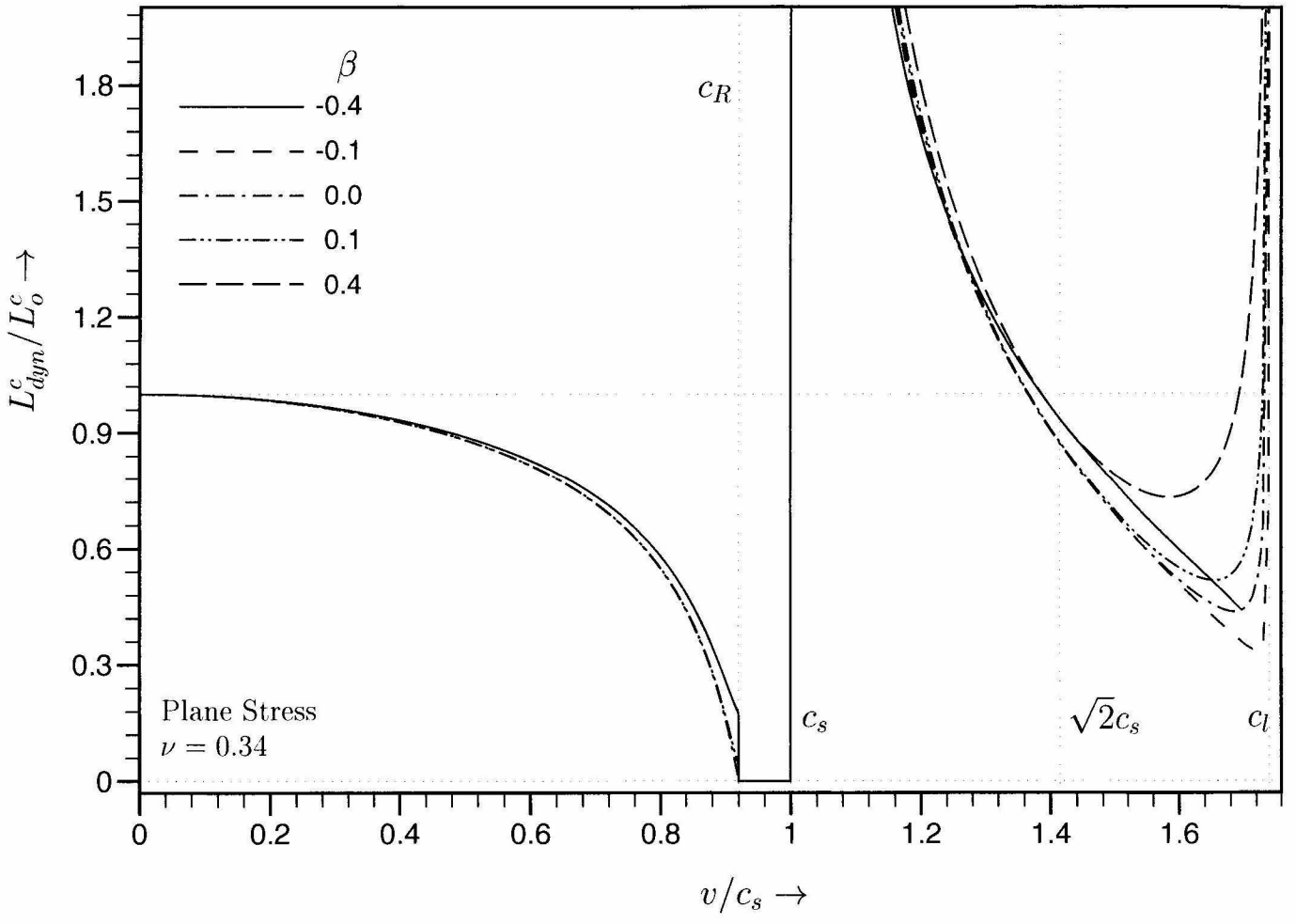

Figure 5.14: Dynamically propagating mode II crack with a rate dependent cohesive zone — Variation of the critical cohesive zone length (required to sustain dynamic crack growth) with crack tip speed v, plotted for different values of the rate parameter β.

5.4.3 Critical Dynamic Energy Release Rate

If the propagation of dynamic mode II cracks (with a rate dependent cohesive zone) is governed by the critical crack tip sliding displacement criterion given in (5.30), then the critical dynamic energy release rate (rate dependent fracture energy) is given by

$$\frac{G^c_{dyn}}{G^c_o} = \begin{cases} \dfrac{g(\gamma)}{2\gamma} = \dfrac{\beta}{\gamma}\dfrac{v^3}{c_s^3}\dfrac{\alpha_s}{R(v)}\left[\dfrac{\Gamma(\gamma+1)}{\Gamma(\gamma+1/2)}\right]^2 & 0 \le v < c_R\,, \\ \dfrac{1-q}{\lambda}\, g^*(\lambda, q) & c_s < v < c_l\,, \end{cases} \tag{5.35}$$

where G^c_o, the critical energy release rate for quasi-static crack propagation is given by

$$G^c_o = \tau_o \delta^c_t\,. \tag{5.36}$$

Hence the material/specimen dependent "fracture energy vs crack speed" curve is strongly influenced by the rate parameter β, whereas any variations in the crack plane shear strength τ_o or the critical crack tip sliding displacement δ^c_t merely shift the curve along the "energy" axis.

Figure 5.15 shows the variation of the dissipated fracture energy (required for sustained mode II crack growth) with crack speed for different values of the rate parameter β. For sub-Rayleigh crack speeds, it is found that a rate strengthening cohesive zone ($\beta > 0$) dissipates more energy with increasing crack speed, a velocity weakening cohesive zone ($\beta < 0$) dissipates less energy with increasing crack speed and a rate independent cohesive zone ($\beta = 0$) dissipates the same amount of energy irrespective of crack speed. As $v \to c_R$, the energy dissipated in the cohesive zone becomes unbounded for $\beta > 0$, whereas it vanishes for $\beta < 0$. This indicates that sustained mode II crack growth at high sub-Rayleigh crack speeds is more likely with a velocity weakening cohesive zone. Fracture energy required for sustained mode II crack growth at c_s and c_l is the same as that for a quasi-static mode II crack.

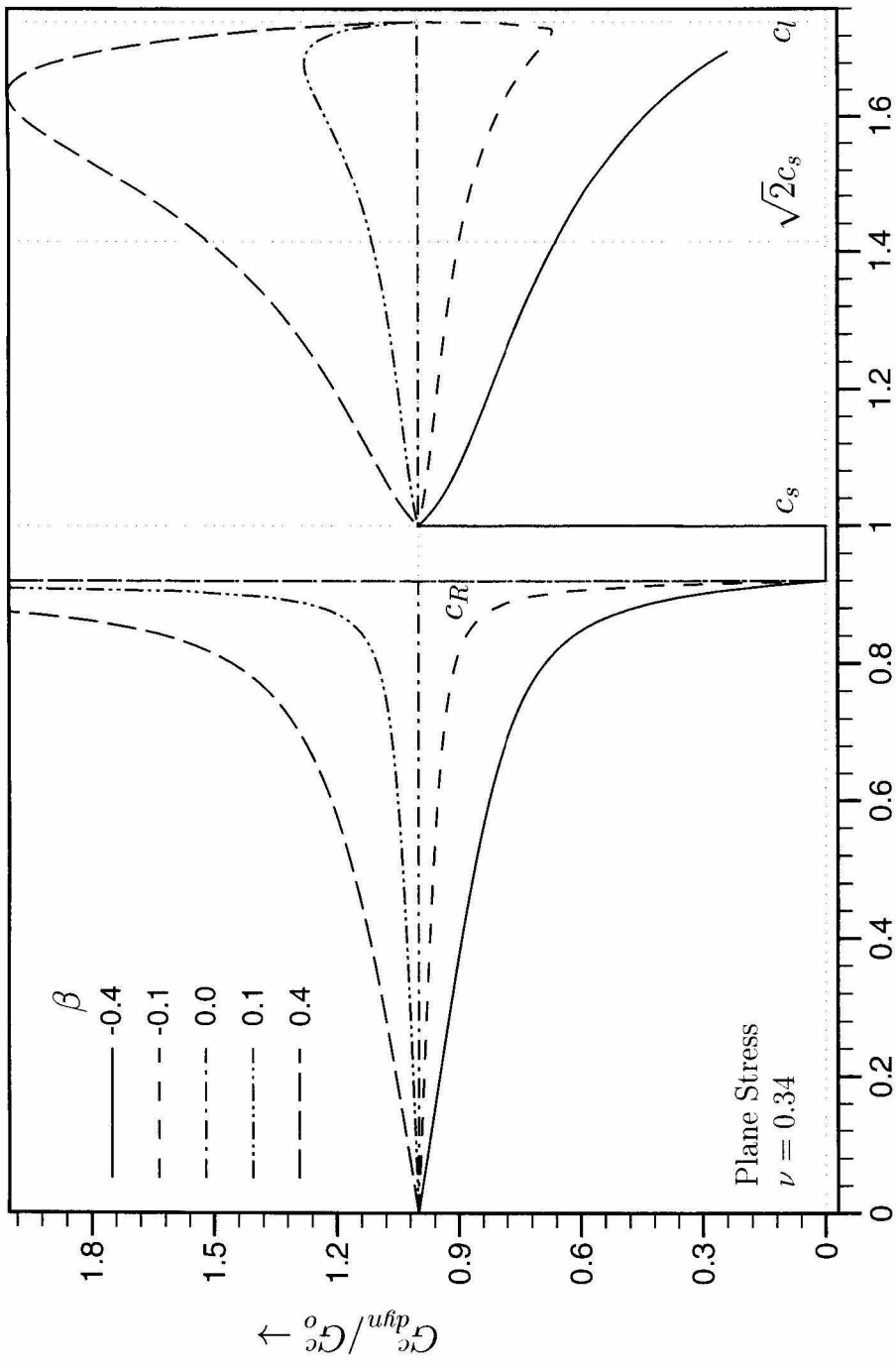

Figure 5.15: Dynamically propagating mode II crack with a rate dependent cohesive zone — Variation of the critical dynamic energy release rate (required to sustain dynamic crack growth) with crack tip speed v, plotted for different values of the rate parameter β.

However, for all other intersonic speeds, the energy dissipated is higher for $\beta > 0$, is lower for $\beta < 0$ and remains unchanged for $\beta = 0$. The importance of the curious speed of $\sqrt{2}\,c_s$ (vis-a-vis energy dissipated in the tip region) with regard to the Freund's singular crack model, disappears here, indicating that it is merely a mathematical abstraction due to the particular crack model employed.

5.5 Secondary Tensile Cracks

Intersonic mode II crack growth in our laboratory specimens was found to induce tensile cracking on the upper crack face. Remarkably, these secondary tensile cracks were all found to be almost parallel to each other and their angle of inclination was found to be $\approx 10.6^{\circ}$ with the normal to the crack plane. Experimental evidence of these cracks was discussed in detail in Section 3.5 and a possible scenario leading to their initiation, growth and arrest was presented there. In the previous Chapter (see Section 4.2.10), an attempt was made at predicting their initiation and their orientation relative to the crack plane using a Dugdale type cohesive zone model in conjunction with the maximum principal tensile stress criterion for brittle fracture. The model predictions were in partial agreement with the experimental observations; the orientation of the secondary cracks was predicted to be the same irrespective of the intersonic crack speed, however, the angle of inclination predicted was almost twice that observed experimentally. Here, we will use the current rate dependent cohesive zone model, again in conjunction with the maximum principal tensile stress criterion for brittle fracture to see whether its any better and if so, extract some of the unknown model parameters for our laboratory specimens.

The maximum principal tensile stress σ_1 at any point on the upper cohesive surface is given by (4.69) and the angle of inclination θ^* of the principal plane (its normal) with the horizontal (η_1-axis) is given by (4.70). For a steadily propagating intersonic mode II crack with a rate dependent cohesive zone, $\sigma_{12}(-L < \eta_1 < 0, \eta_2 \to 0^+) = -\tau(\eta_1/L)$, which is given in (5.11) and σ_{11} on the upper cohesive surface is given

in (5.20) with the opposite sign. Thus σ_1 and θ^* on the upper cohesive surface may be obtained. Figure 5.16(a) shows the variation of the maximum principal tensile stress σ_1 along the upper cohesive surface for different intersonic speeds, at a fixed value of the rate parameter β chosen to be -0.4. Similar to the case of $\beta = 0$ (see Figure 4.12(a)), σ_1 increases monotonically from zero at the mathematical crack tip and attains a finite maximum as the physical crack tip is approached ($\eta_1 \to -L$). This variation is similar for other permissible values of $\beta < 0$. For $\beta > 0$, the variation is similar, however, σ_1 becomes unbounded as the physical crack tip is approached. If we assume that Homalite obeys the maximum principal stress criterion for brittle fracture, then a tensile crack would initiate at a point $\eta_1 = -L^*$ on the upper cohesive surface, where

$$\sigma_1(\eta_1 = -L^*, \eta_2 \to 0^+) = \sigma_u^H \,. \tag{5.37}$$

σ_u^H is the ultimate tensile strength of Homalite, which is $\approx$ 35 MPa (see Table 2.1). For β of the order of unity, σ_1 in some region of the upper cohesive surface attains a value higher than σ_u^H for all intersonic speeds and hence a secondary tensile crack is always initiated. The position, $\eta_1 = -L^*$, where a tensile crack is initiated on the is a strong function of crack speed and β. For example, for $\beta = -0.4$, the tensile crack would initiate at $L^* = 0.95L$ for $v = \sqrt{2}\, c_s$. Figure 5.16(b) shows the variation of θ^*, the angle of inclination of the principal plane (see Fig 3.11(b)) along the upper cohesive surface. Having determined the position along the upper cohesive surface where a tensile crack is likely to initiate, we can also determine the angle θ^* made by this tensile crack with the vertical from Figure 5.16(b). Figure 5.16(b) shows the variation of θ^* along the upper cohesive surface for different intersonic speeds at a fixed value of $\beta = -0.4$. From the figure, we see that if the tensile crack initiated at a point close to the mathematical crack tip, it would be inclined at 45° to the vertical and if it initiated at the physical crack tip, it would be almost vertical. For $\beta = -0.4$ and $v = \sqrt{2}\, c_s$, the angle of inclination $\theta^* \approx 11.2°$. For all intersonic speeds, the angle θ^* is identical, being equal to $\approx 21.8°$ for $\beta = 0$, as seen in the

previous chapter. However, for $\beta > 0$, θ^* is always greater than 21.8^o, whereas for $\beta < 0$, it is always less than 21.8^o. Since the experimental observations show that $\theta^* \approx 10.6^o$, we can reasonably conclude that for our laboratory specimens $\beta < 0$ at slip rates of the order of few m/s (order of slip rates during intersonic crack growth in our specimens). Hence the cohesive zone is velocity weakening and the predominant mechanism operating near a dynamic shear crack tip is nonuniform frictional sliding.

To determine the numerical value of β a plot if made of θ^* *vs* β for different intersonic speeds, as shown in Figure 5.17. As seen, decreasing β reduces the angle of inclination of the secondary cracks and the experimentally observed angle of $\approx 11^o$ is achieved at $\beta \approx -0.4$ for $v = \sqrt{2}\, c_s$. However, at this β, the angle of inclination varies with the intersonic speed, from about 8^o to 13^o. This variation is close to the variation in measured angle of inclination of the secondary tensile cracks. Hence, $\beta = -0.4$ is a reasonable estimate for the velocity weakening parameter in the zone of nonuniform frictional sliding near an intersonically propagating mode II shear crack.

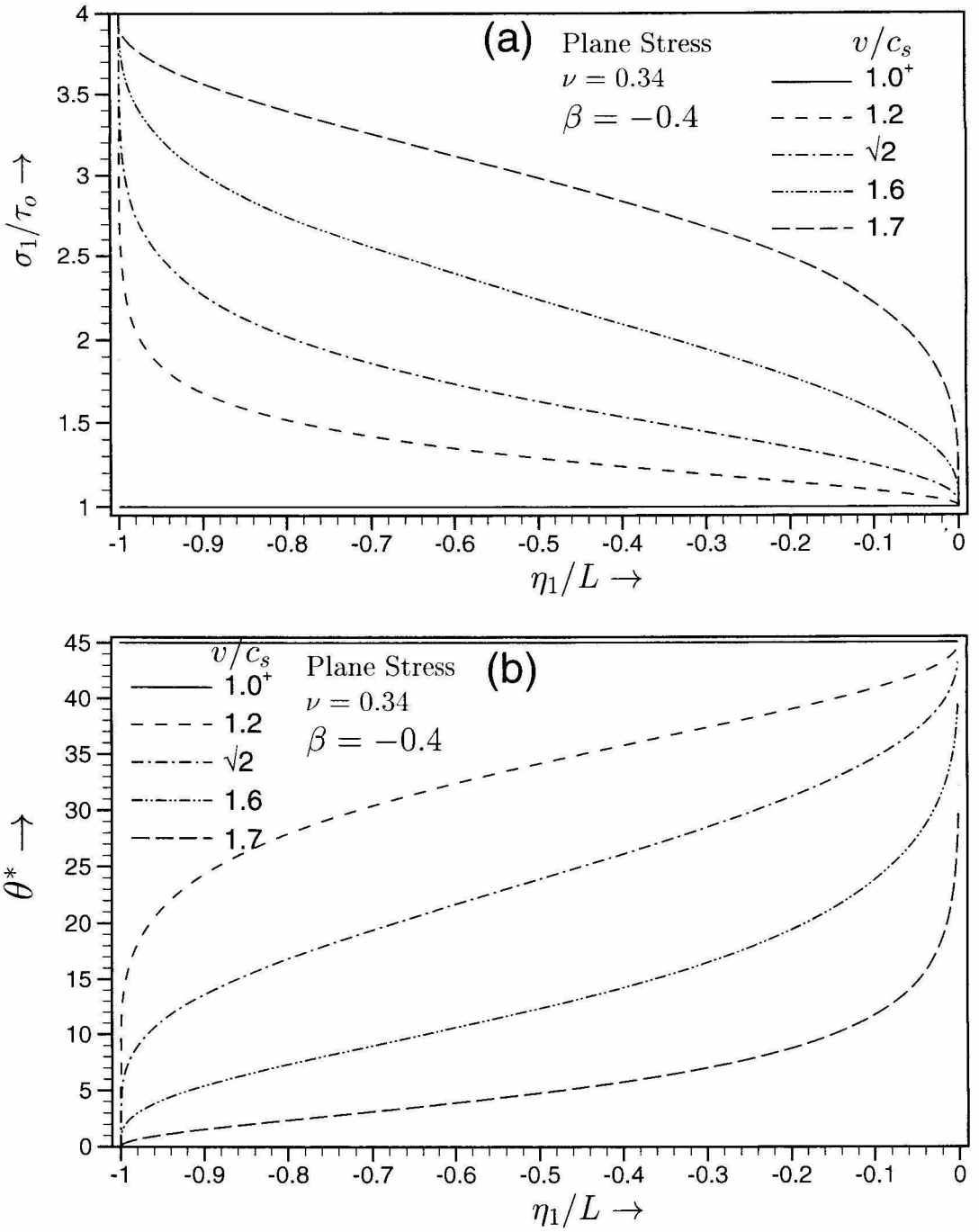

Figure 5.16: Dynamically propagating mode II crack with a velocity weakening cohesive zone. **(a)** Maximum principal tensile stress σ_1 on the upper cohesive surface for $\beta = -0.4$. **(b)** Inclination θ^* of the principal plane to the vertical for $\beta = -0.4$.

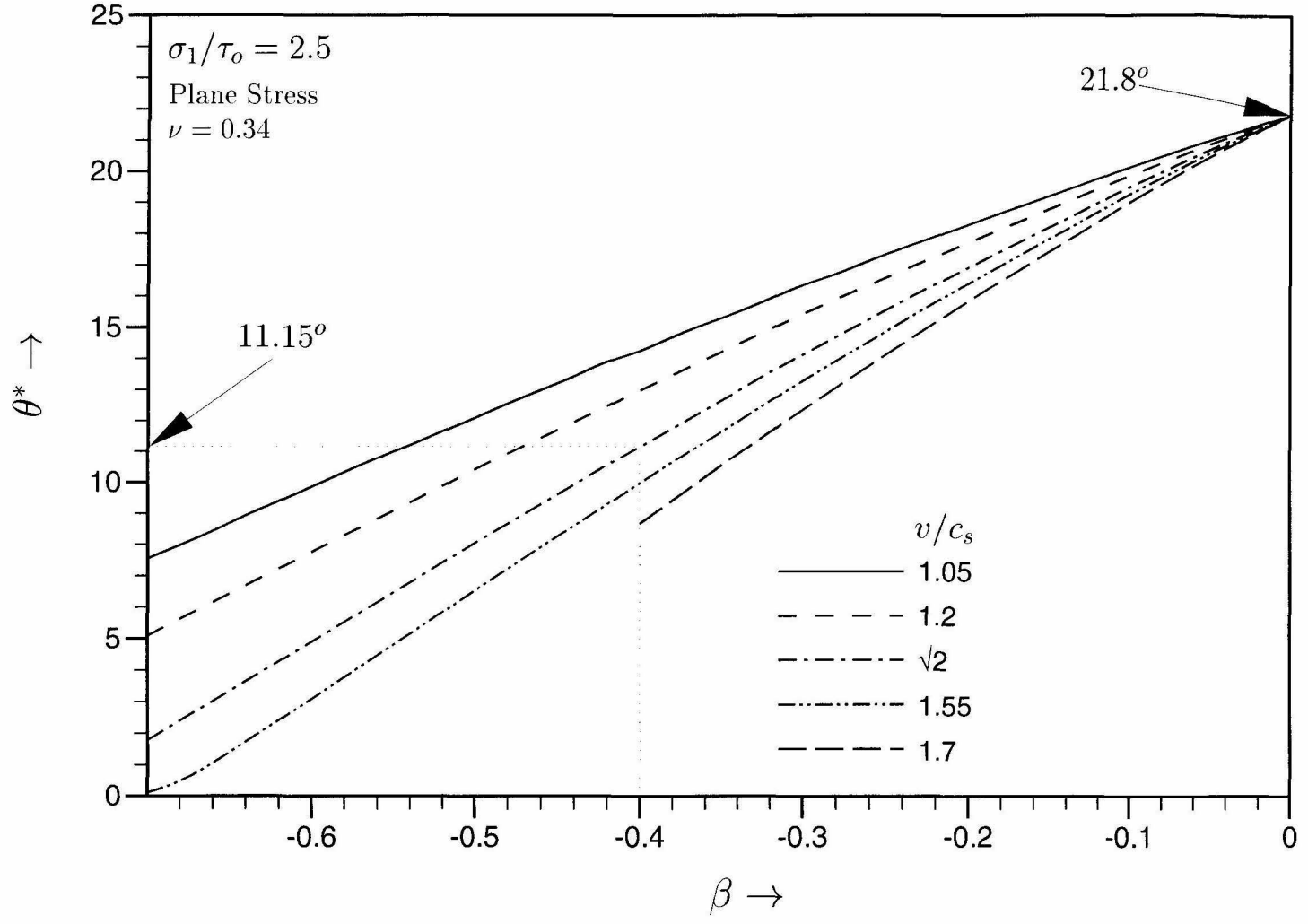

Figure 5.17: Dynamically propagating mode II crack with a rate dependent cohesive zone — Predicted inclination of the secondary tensile cracks with the vertical, as a function of the rate parameter β.

5.6 Isochromatic Fringe Patterns

Figure 5.18 and Figure 5.19 show the theoretically predicted isochromatic fringe pattern around a subsonically propagating mode II crack and around an intersonically propagating mode II crack respectively. The crack propagates with a line cohesive zone in front of the tip and also obeys the critical crack tip sliding displacement criterion. The subsonic crack was chosen to be propagating at $0.85c_s$, where as the intersonic crack was assumed to be propagating at $1.47c_s$. In Figure 5.18(a) and Figure 5.19(a) the cohesive law was assumed to be rate strengthening ($\beta = 0.4$), whereas in Figure 5.18(c) and Figure 5.19(c), the cohesive law was assumed to be velocity weakening ($\beta = -0.4$). In both cases, the ratio of shear modulus to the shear strength of the weak plane (μ/τ_o) was chosen to be 136, approximating the case of Homalite/Homalite bonded specimen used in the experiments. The critical crack tip sliding displacement was chosen to be 21 μm. This ensures that the critical cohesive zone length determined from (5.21) would lie between 2-3 mm (for intersonic speeds close to $\sqrt{2}\,c_s$), which is approximately the width of the Mach wave seen in Figure 3.12.

The field of view shown in Figure 5.18 and Figure 5.19 has a 50 mm diameter and the front end of the cohesive zone is located on the horizontal diameter about 35 mm from the left edge of the field of view. The isochromatic fringe order n at any point (η_1, η_2) is given by

$$n(\eta_1, \eta_2) = \frac{h}{F}\sqrt{(\sigma_{11} - \sigma_{22})^2 + 4\sigma_{12}^2}\,, \tag{5.38}$$

where the stress components $\sigma_{\alpha\beta}$ for the four cases are given in Appendices D & E. The cohesive zone length in the subsonic case ($v = 0.85\,c_s$) was found to be 1.36 mm for both $\beta = 0.4$ and $\beta = -0.4$, where as in the intersonic case ($v = 1.47\,c_s$) it was found to be 2.5 mm for $\beta = 0.4$ and 2.46 mm for $\beta = -0.4$. For high subsonic speeds, the cohesive zone lengths are small relative to the field of view size of 50 mm and the shape of the isochromatic fringe pattern doesn't differ markedly

irrespective of whether the cohesive zone is rate strengthening or velocity weakening. However, the number of fringes within the field of view are increased substantially in the rate strengthening case (+ve β), indicating that the stress fields are amplified with an increase in rate sensitivity. For the intersonic case, we see that the presence of a cohesive zone gives a finite width to the Mach waves emanating from the tip region. Again, the shape of the fringe patterns is similar, however, the stress fields are amplified with increasing rate sensitivity resulting in an increase in the number of fringes within the field of view.

Figure 5.20 compares an experimentally recorded isochromatic fringe pattern with that predicted by the velocity weakening cohesive zone model with $\beta = -0.4$. The crack tip speed in both cases was $1.45\, c_s$. A best fit shows that the intensity of the far-field applied loads, $K_{II}^{*d} \approx 1.04$ MPa-m^{q}. We see that the patterns are similar in a small region close to the crack tip. Also, the fringe pattern within the finite width of the Mach waves, seems to be qualitatively similar. The range of dominance of the current solution seems to be of the order of about 20 mm. However, the steady state nature of the current solution cannot capture the features like finite length of the Mach waves, transient effects due to changing crack speed, loading waves still present in the tip vicinity etc. Also, the distortion of the near tip fields due to secondary tensile cracks behind the tip is not captured by the current model. However, the model eliminates many pathologies associated with the Freund's singular solution. It eliminates the unphysical singular stresses at the tip as well as along the Mach waves, allows for finite energy flux into the tip at all intersonic speeds, gives finite width and structure to the Mach waves, provides information regarding the processes occurring in the nonlinear zone surrounding the tip and finally also predicts the orientation of the secondary tensile cracks and the reason for they being almost parallel to each other.

Owing to the importance of the mechanics of dynamic shear crack growth in modeling earthquake source processes, a few comments are in order regarding shear

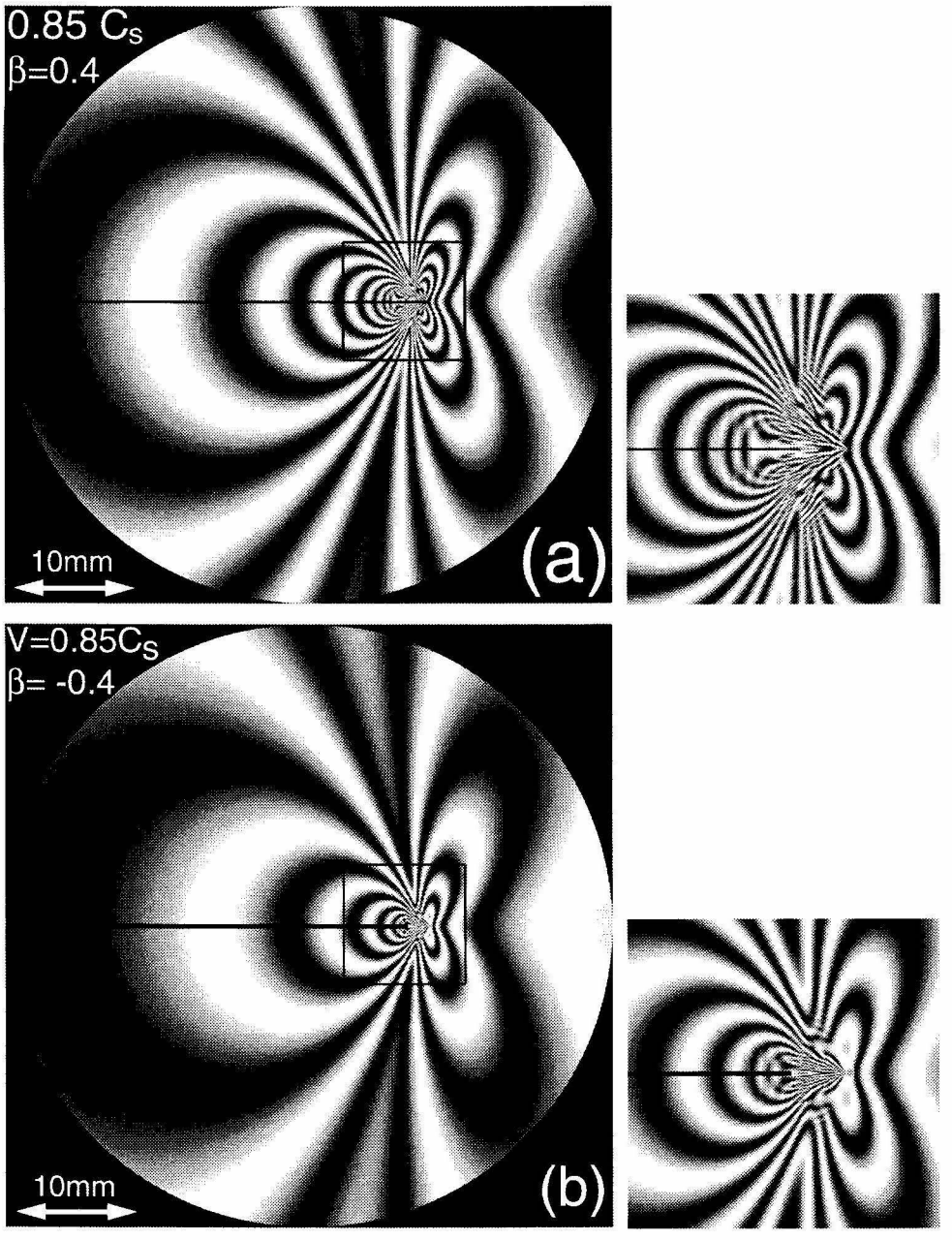

Figure 5.18: Isochromatic fringe pattern around a propagating subsonic mode II crack with a rate dependent cohesive zone. The propagating crack obeys a critical crack tip sliding displacement criterion with $\delta_t^c \approx 21\,\mu$m and $\mu/\tau_o = 136$. Also $v/c_s = 0.85$ and $L_{dyn}^c = 1.36$ mm. A magnified view of the region around the crack tip (enclosed in the black rectangle) is shown on the right.**(a)** $\beta = 0.4$. **(b)** $\beta = -0.4$.

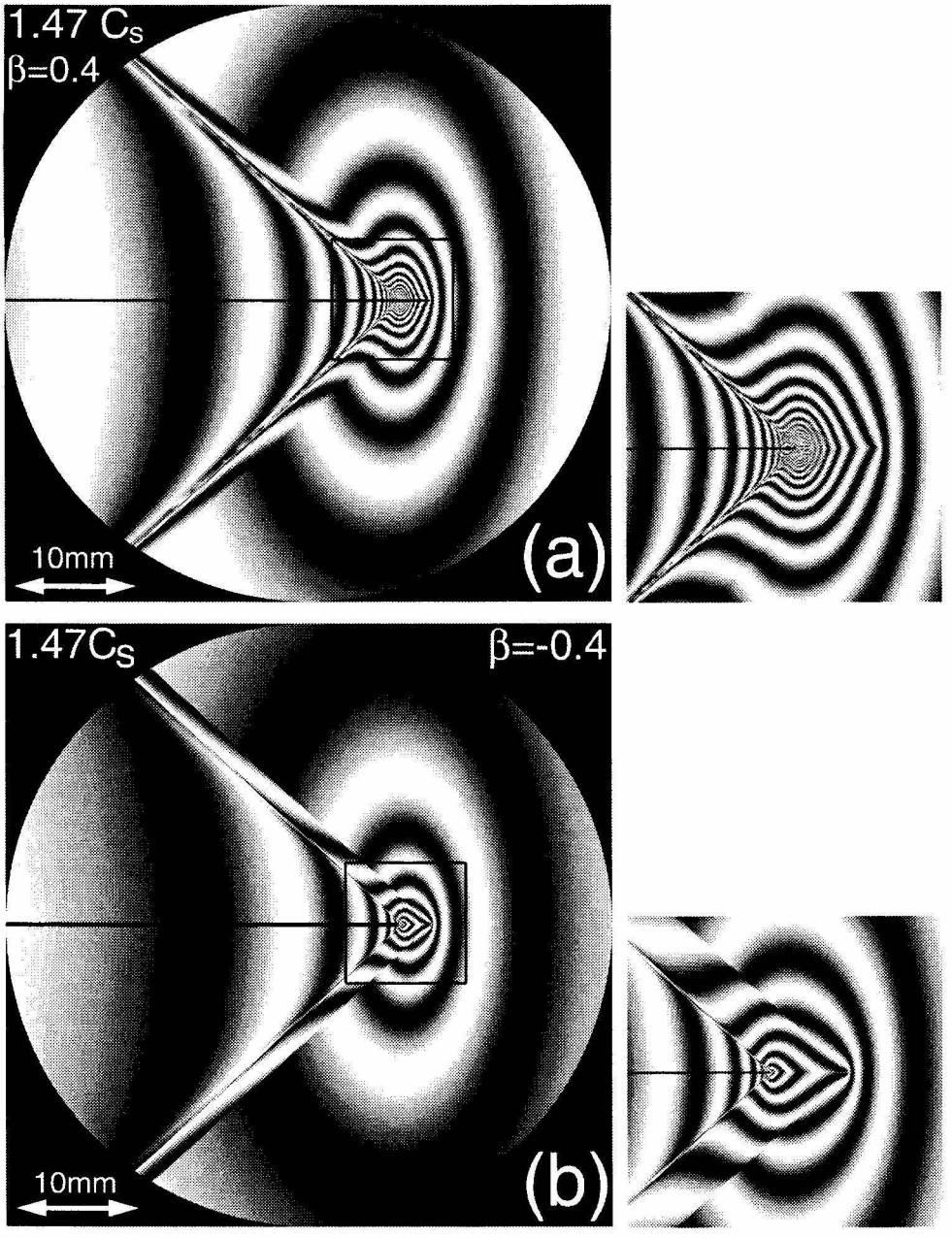

Figure 5.19: Isochromatic fringe pattern around a propagating intersonic mode II crack with a rate dependent cohesive zone. The propagating crack obeys a critical crack tip sliding displacement criterion with $\delta_t^c \approx 21\,\mu$m and $\mu/\tau_o = 136$. Also $v/c_s = 1.47$. A magnified view of the region around the crack tip (enclosed in the black rectangle) is shown on the right. **(a)** $\beta = 0.4$ & $L^c_{dyn} = 2.5$ mm. **(b)** $\beta = -0.4$ & $L^c_{dyn} = 2.46$ mm.

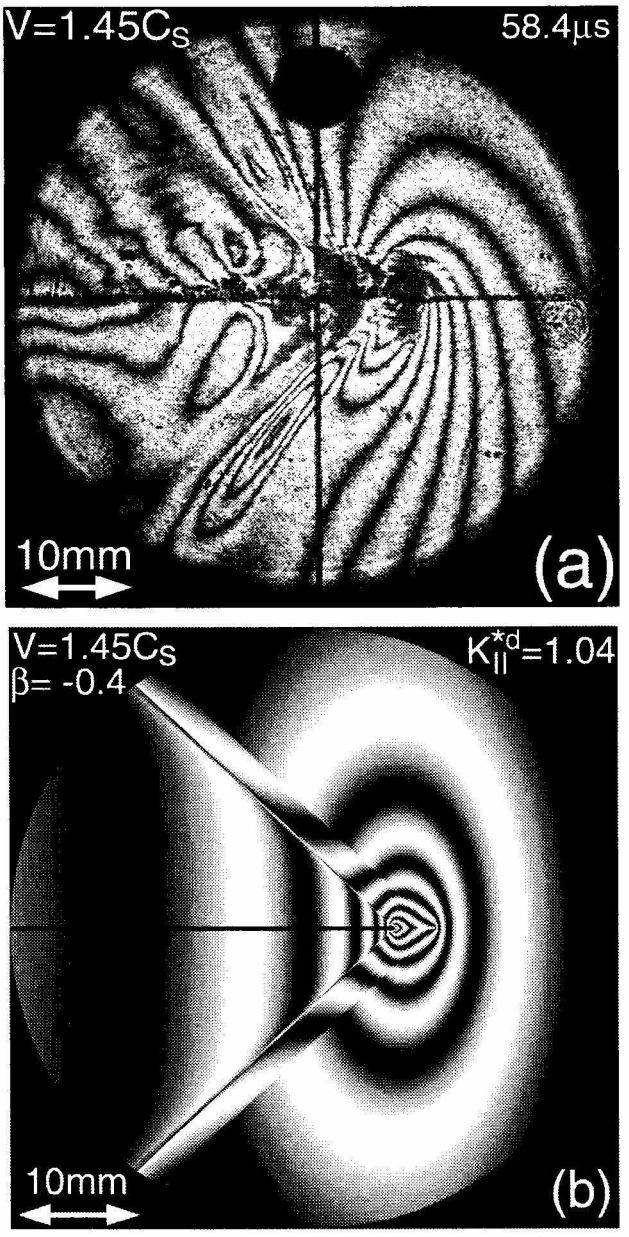

Figure 5.20: Isochromatic fringe pattern around a propagating intersonic crack along a weak plane in Homalite-100. **(a)** Experimental observation of the isochromatic fringe pattern around the crack tip with the crack tip speed $v/c_s \approx 1.5$. Note the finite width of the Mach waves. **(b)** Theoretical prediction based on the rate dependent cohesive zone model with $\beta = -0.4$. The propagating crack is assumed to obey a critical crack tip sliding displacement criterion with $\delta_t^c \approx 21\mu$m and $\mu/\tau_o = 136$. Also $v/c_s = 1.47$ & $L_{dyn}^c = 2.46$ mm.

rupture propagation on homogeneous velocity weakening faults. In a pioneering work, HEATON (1990) studied seismic records of several earthquakes, and found that the duration of slip at any point on the rupture plane was an order of magnitude smaller than the total duration of rupture propagation. If the rupture propagation was akin to that of a shear crack, both these durations must be of the same order. He concluded that the rupture propagation during earthquakes is more like a self-healing slip pulse rather than an expanding shear crack. He explained that dynamic velocity weakening friction acting on the fault surfaces causes the fault to heal itself shortly after the passage of the rupture front thus propagating in a self-healing slip pulse like manner. The particle velocity diminishes rapidly as we move away from the physical crack tip along the crack faces. If the sliding friction acting on the crack faces is velocity weakening, frictional resistance increases substantially, a finite distance behind the physical crack tip, the crack faces lock and a self-healing slip pulse results. Such self-healing slip pulses are unlikely to occur with the current configuration of our laboratory experiments, as a key ingredient, the far-field uniform compressive normal stress is absent in our experimental setup. However, crustal faults a few km beneath the earth's surface are always acted upon by large hydrostatic compressive stresses. The conditions governing the propagation of an earthquake rupture as a self-healing pulse instead of as a dynamic crack were carefully examined by a number of researchers. Apart from dynamic velocity weakening friction, presence of heterogeneities on the fault plane as well as differing elastic properties across the fault plane were also found to result in the propagation of an earthquake rupture as a self-healing pulse (BEN-ZION, 2000).

On a homogeneous fault (containing rocks with similar elastic properties on either side of the rupture plane), sliding friction acts over the entire crack faces. PERRIN *et al.* (1995) showed that self-healing slip pulse solutions do not exist for pure velocity weakening friction laws, *i.e.*, for laws of the type considered in this chapter. They showed that sliding surfaces which follow both rate and state dependent friction

laws allowing for restrengthening under stationary contact can sustain self-healing slip pulses. However, rate of velocity weakening β is a major parameter governing the transition of a initiated shear rupture into a self-healing pulse (ZHENG and RICE, 1998). With $\beta = -0.4$, their analysis predicts that shallow earthquake ruptures would indeed propagate as self-healing pulses. Hence, it is plausible that in the presence of a far-field compressive normal stress acting on the weak plane, self-healing pulses may be obtained even in our laboratory specimens.

Nomenclature

(η_1, η_2)	Cartesian coordinates w.r.t the moving crack tip
$(\sigma_{12}^D)_o^c$	critical far-field load for quasi-static mode II crack growth
$(\sigma_{12}^D)_{dyn}^c$	critical far-field load for dynamic mode II crack growth
(r, θ)	polar coordinates
(x_1, x_2)	fixed Cartesian coordinates
$\alpha_l, \alpha_s, \hat{\alpha}_s$	relativistic parameters
β	rate parameter
δ, δ_1	shear displacement discontinuity
δ_c	critical crack tip sliding displacement
δ_t	crack tip sliding displacement
δ_t^o	crack tip sliding displacement for a quasi-statically growing mode II crack
γ	crack tip stress singularity exponent for sub-Rayleigh mode II cracks with a rate dependent cohesive zone
κ	material parameter - varies for plane stress and plane strain
K_{II}	mode II stress intensity factor for a quasistatically growing crack

K_{II}^{d}	subsonic mode II stress intensity factor
K_{II}^{*d}	intersonic mode II stress intensity factor
λ	crack tip stress singularity exponent for intersonic mode II cracks with a rate dependent cohesive zone
λ_f	coefficient of sliding friction
μ	shear modulus
ν	Poisson's ratio
σ_{12}^{D}	shear stress a distance $D \gg L$ ahead of the crack tip
σ_{u}^{H}	ultimate tensile strength of Homalite
$\sigma_{\alpha\beta}$	Cartesian components of the stress tensor
τ	cohesive traction distribution
τ_o	cohesive shear strength of the material at zero sliding rate
c_l	longitudinal wave speed
c_R	Rayleigh wave speed
c_s	shear wave speed
F	analytic function of $z_l = \eta_1 + i\,\alpha_l \eta_2$
G	analytic function of $z_s = \eta_1 + i\,\alpha_s \eta_2$
g	a real function of $\eta_1 + \hat{\alpha}_s \eta_2$
G_o	energy release rate for a quasi-statically growing mode II crack
G_o^c	critical energy release rate for a quasi-statically propagating crack

G^c_{dyn}	critical dynamic energy release rate
K^d_I, K^d_{II}	mode I & mode II subsonic stress intensity factors
L	cohesive zone length
L^*	initiation site for the secondary tensile crack
L_o	cohesive zone length for a quasi-statically growing crack
L^c_o	critical cohesive zone length for quasi-static mode II crack growth
L^c_{dyn}	critical cohesive zone length
q	singularity exponent for an intersonic mode II crack
$R(v)$	Rayleigh function
R_q	intersonic parameter
t	time
u_α	components of the displacement vector
v	crack speed

Bibliography

ANDREWS, D. J. (**1976**), Rupture Velocity of Plane Strain Shear Cracks, *Journal of Geophysical Research*, **81**(32), pp. 5679–5687.

BEN-ZION, Y. (**2000**), Dynamic Rupture in Recent Models of Earthquake Faults, submitted.

DUGDALE, D. S. (**1960**), Yielding of Steel Sheets Containing Slits, *Journal of the Mechanics and Physics of Solids*, **8**, pp. 100–104.

FREUND, L. B. and LEE, Y. J. (**1990**), Observations on High Strain Rate Crack Growth Based on a Strip Yield Model, *International Journal of Fracture*, **42**(3), pp. 261–276.

GEUBELLE, P. H. and KUBAIR, D. (**2000**), Intersonic Crack Propagation in Homogeneous Media Under Shear Dominated Loading: I. Numerical Analysis, to appear in JMPS.

GLENNIE, E. B. (**1971**a), A Strain-Rate Dependent Crack Model, *Journal of the Mechanics and Physics of Solids*, **19**, pp. 255-272.

GLENNIE, E. B. (**1971**b), The Unsteady Motion of a Rate-Dependent Crack Model, *Journal of the Mechanics and Physics of Solids*, **19**, pp. 329–338.

HEATON, T. H. (**1990**), Evidence For and Implications of Self-Healing Pulses of Slip in Earthquake Rupture, *Physics of the Earth and Planetary Interiors*, **64**(1), pp. 1–20.

KILGORE, B. D., BLANPIED, M. L., and DIETERICH, J. H. (**1993**), Velocity Dependent Friction of Granite Over a Wide Range of Conditions, *Geophysical Research Letters*, **20**(10), pp. 903–906.

PERRIN, G., RICE, J. R., and ZHENG, G. (**1995**), Self-Healing Slip Pulse on a Frictional Surface, *Journal of the Mechanics and Physics of Solids*, **43**(9), pp. 1461–1495.

PRAKASH, V. and CLIFTON, R. J. (**1992**), Pressure-Shear Plate Impact Measurement of Dynamic Friction for High Speed Machining Applications, in *Proceedings of VII International Congress on Experimental Mechanics*, SEM, pp. 568–596.

PRAKASH, V. and CLIFTON, R. J. (**1993**), Time Resolved Dynamic Friction Measurements in Pressure Shear, in *Experimental Techniques in the Dynamics of Deformable Solids*, ASME - Applied Mechanics Div., New York, pp. 33–48.

RICE, J. R. and RUINA, A. L. (**1983**), Stability of Steady Frictional Slipping, *Journal of Applied Mechanics*, **50**(2), pp. 343–349.

RUINA, A. (**1983**), Slip Instability and State Variable Friction Laws, *Journal of Geophysical Research*, **88**(B12), pp. 10359–10370.

YU, H. H. and SUO, Z. (**2000**), Intersonic Crack Growth on an Interface, *Proceedings of the Royal Society of London*, **A456**(1993), pp. 223–246.

ZHENG, G. and RICE, J. R. (**1998**), Conditions Under Which Velocity-Weakening Friction Allows a Self-Healing Versus a Cracklike Mode of Rupture, *Bulletin of the Seismological Society of America*, **88**(6), pp. 1466–1483.

Chapter 6

Experimental Observations

In Chapter 1, a brief overview of dynamic crack growth along bimaterial interfaces was presented. Existing literature on this subject was briefly summarized and the relevant analytical concepts were introduced (see Section 1.3). The number of experimental investigations on this subject are few and are relatively recent. One of the interesting experimental observations referred to in Chapter 1 deals with evidence of intersonic crack growth along a bimaterial interface. In this thesis, a bimaterial interface crack is termed subsonic, intersonic or supersonic provided, its speed is lower than c_s, is between c_s and c_l and is higher than c_l respectively, of the more compliant of the two constituents. Similar to intersonic mode II cracks along weak planes in homogeneous solids, intersonic bimaterial cracks result in near-tip fields and propagation characteristics that are dramatically different as compared to their subsonic counterparts. In the current chapter, our experimental observations on intersonic interfacial crack growth are detailed, and in the next chapter, we provide an intersonic crack model to explain our experimental results, with the ultimate aim towards resolving some of the underlying issues which are as yet unclear.

6.1 Intersonic Cracks on a Bimaterial Interface

The first experimental evidence of intersonic interfacial cracks in a bimaterial, ever recorded in the laboratory was reported independently by two sets of researchers (LIU *et al.*, 1993; SINGH and SHUKLA, 1996b). LIU *et al.* (1993); LAMBROS and ROSAKIS (1995b) observed an intersonic crack propagating along a PMMA/steel interface and recorded the stress field information around the propagating crack tip using CGS interferometry, whereas SINGH and SHUKLA (1996b) observed an intersonic crack propagating along a Homalite/aluminum interface and recorded the stress field information around the propagating crack tip using dynamic photoelasticity. Both these results were compared and reviewed in SINGH *et al.* (1997). Crack tip speeds of the order $\approx 1.2\, c_s$ were observed, where c_s and all other wave speeds hence forth, are understood to be those of the more compliant solid (polymer). In addition, based on experimental observations, it was conjectured that a finite zone of crack face contact was traveling behind the intersonic crack tip. The size of the contact zone was found to be of the order of a few mm, and hence it is unlike the "small-scale" contact zone behind a subsonic interface crack, which arises due to the oscillatory nature of the near-tip fields and is typically less than a μm long. Also, as one might expect, the tip of an intersonic interfacial crack radiates out a shear Mach wave which was observed in the experimentally recorded isochromatic fringes of SINGH and SHUKLA (1996b). In addition, a second Mach wave was also observed to be radiated from the trailing edge of the contact zone. The crack speeds observed were still subsonic with respect to the metal, and hence no Mach waves were radiated into the metal half. As mentioned in Chapter 2, CGS interferometry is insensitive to shear Mach waves and hence they were not observed in LIU *et al.* (1993). Shear Mach waves carry discontinuities in tangential components of stress and particle velocities and hence, as was observed, the isochromatic fringe pattern across them changed abruptly.

In our experiments, the conditions governing the acceleration of a bimaterial inter-

face crack to intersonic speeds are examined, with particular attention being focused on recording the subsonic/intersonic transition and evolution of the finite crack face contact zone. The effect of different loading configurations and specimen geometries on the attainment of intersonic crack speeds and on the propagation behavior of the interfacial crack is investigated. Four different material combinations were used in our bimaterial experiments — Homalite/Al, Homalite/steel, PMMA/Al and PMMA/steel. The essential details regarding specimen preparation and the experimental procedure were summarized in Chapter 2. An edge precrack or a blunt notch oriented along the bimaterial interface was loaded by a projectile fired from a high speed gas gun. The stress field around the crack, as it initiates and propagates along the bimaterial interface was recorded by dynamic photoelasticity or CGS interferometry in conjunction with high speed photography. The duration of a typical experiment of a gas gun loaded bimaterial plate was about 50 to 60 μs from impact until the crack ran out of the field of view. The specimens were subjected to three different impact loading configurations as shown in Figure 6.1. The bimaterial specimen was subjected to in-plane loading and the three different loading configurations **(A)**, **(B)** and **(C)** essentially resulted in widely varying "mixities" at initiation. Impacting the specimen on the Homalite half on the side opposite the precrack/notch, resulted in cracks initiating from the impact site much earlier compared to the initiation of the edge crack on the opposite side. Hence this particular loading configuration was not pursued. The loading configuration **(A)** always resulted in a crack initiating from the edge precrack/notch at a steep angle to the interface and propagating into the polymer half. The other two loading configurations **(B)** and **(C)** resulted in interfacial crack propagation at intersonic speeds. However, the nature of the near-tip fields and propagation characteristics in either of these two cases were different, as explained later.

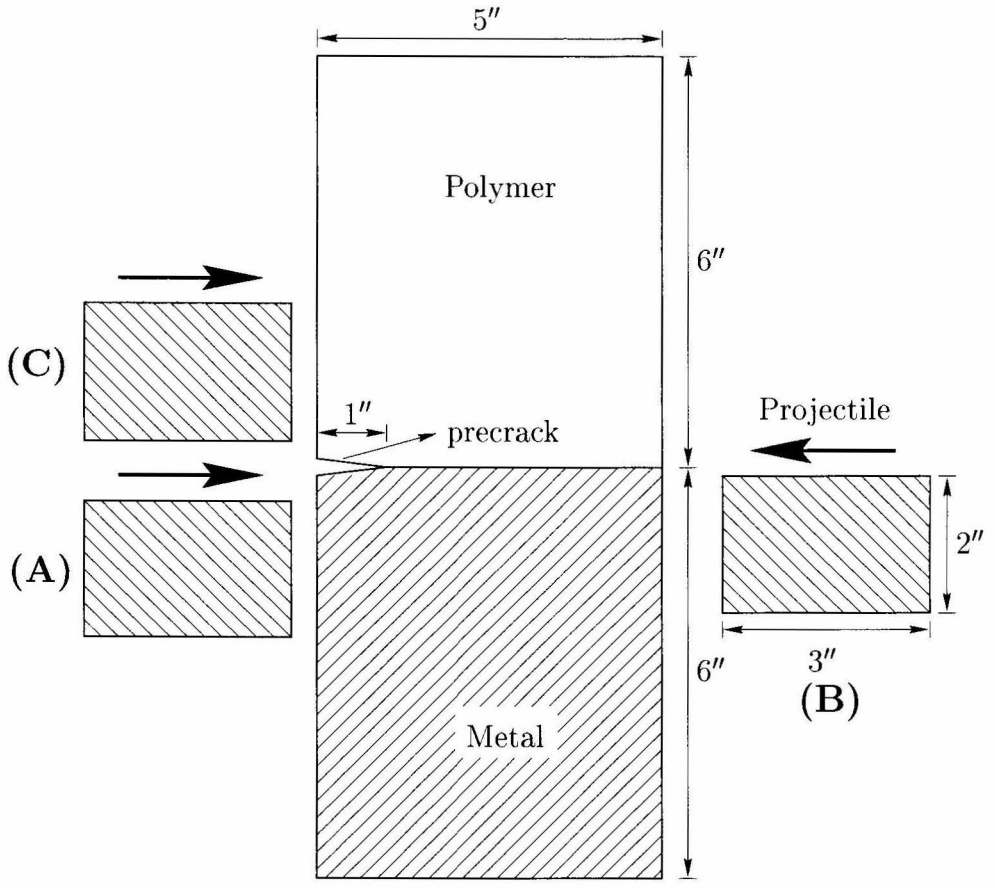

Figure 6.1: Bimaterial specimen with a precrack subjected to impact shear loading. **(A),(B)** & **(C)** show the three different impact configurations tested.

6.1.1 Kinking of a Crack From a Bimaterial Interface

Loading an edge precrack/notch on a bimaterial interface under loading configuration **(A)** (see Figure 6.1) always resulted in the initiation of a kinked crack (from the edge pre-crack/notch tip) at a steep angle to the interface and propagating into the polymer half. Specimens were loaded by impacting with cylindrical steel projectiles at speeds ranging from 10 m/s to 35 m/s, and in all these cases, a kinked crack propagating into the polymer half resulted. Figure 6.2 shows a selected sequence of four isochromatic fringe patterns depicting such an event. An edge precrack along a Homalite/Al interface was loaded by projectile impact, which resulted in the initiation and propagation of a kinked crack, inclined at an angle of $\approx 70^{\circ}$ to the interface ahead. The projectile impact speed was 25.9 m/s and the semicircular field of view of diameter 50 mm was centered on the interface, 21.6 mm ahead of the pre-crack tip. The time elapsed from impact is shown on each frame. Figure 6.2(a) shows the pre-crack being loaded by stress waves from the impact site, Figure 6.2(b) shows the initiation of the kinked crack and in Figure 6.2(c) and Figure 6.2(d) we can see the kinked crack propagating into the Homalite half at a low subsonic speed of $0.4\,c_s$. The theory governing the kinking of a dynamically loaded crack on a bimaterial interface was discussed briefly in Section 1.3.1. For a more detailed discussion, the reader is referred to HUTCHINSON and SUO (1992); HE and HUTCHINSON (1989a;b); HE *et al.* (1991). It is quite likely that under certain combinations of interface fracture toughness, intensity of applied load and the load phase angle, the pre-crack might initiate and propagate along the interface. However in our specimens, for the range of projectile impact speeds mentioned above and with a loading configuration **(A)**, a kinked crack propagating into the polymer half always resulted. The competition between crack advance within the interface and kinking out of the interface depends on the relative toughness of the interface to that of the adjoining material. The bimaterial interface toughness is not a single material parameter, but rather it is a strong function of the near-tip mode mixity ψ (associated with a reference length L) (LIECHTI and CHAI, 1991; XU and

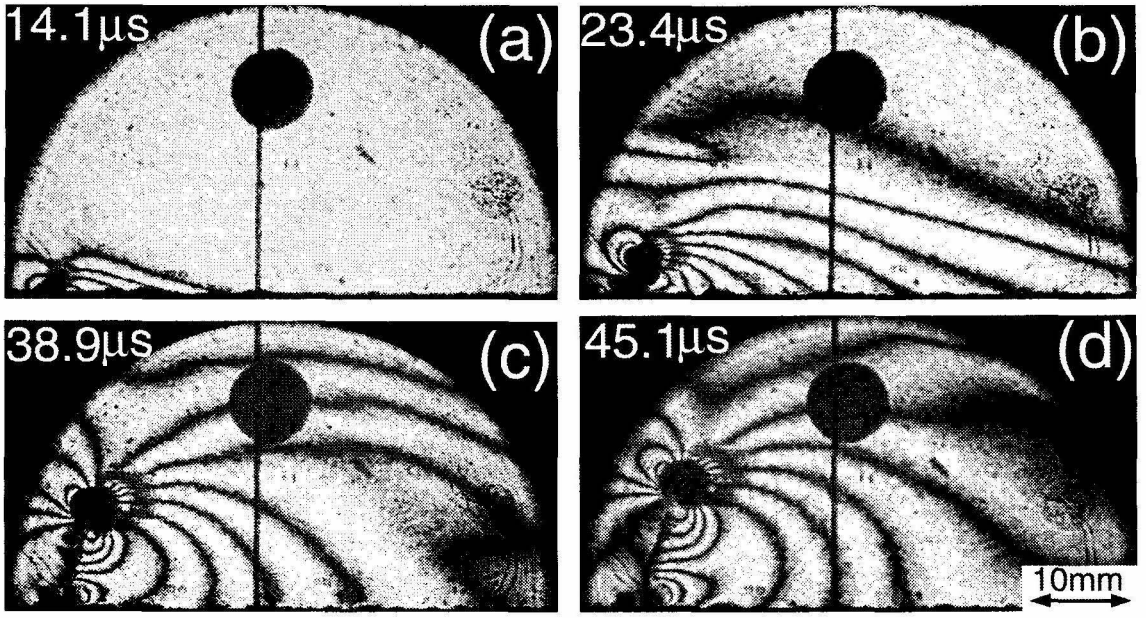

Figure 6.2: Kinking of a crack from a Homalite/aluminum interface. A kinked crack at 69.8° to the interface resulted from impacting a bimaterial specimen on the metal half, on the same side as the starter crack. Impact speed of the projectile, $V = 25.9$ m/s and the semicircular field of view of 50 mm diameter was centered on the interface 21.6 mm ahead of the crack tip.

TIPPUR, 1995), apart from being a function of loading rate (under dynamic loading only). This could possibly explain why interface crack growth was obtained under this loading configuration along a weak plane between two Homalite halves, but not on a polymer/metal interface.

6.1.2 Initiation and Propagation of Intersonic Cracks along a Bimaterial Interface under Loading Configuration **(B)**

Loading an edge pre-crack/notch on a bimaterial interface under loading configuration **(B)** always resulted in the initiation and propagation of an interface crack at intersonic speeds. Figure 6.3 shows a selected sequence of 8 isochromatic fringe patterns depicting the initiation of a precrack on a Homalite/aluminum interface and propagating along it. The time elapsed from impact and the crack tip speed (after

initiation) are shown in each frame. Speed of projectile V at impact was 9.6 m/s and the roughly semicircular field of view of 50 mm diameter was centered on the interface, 19.5 mm ahead of the pre-crack tip. In Figure 6.3(a) and Figure 6.3(b) we see the transmission of loading waves from the metal half into the polymer half through the interface and in Figure 6.3(c) we can see that the pre-crack has just initiated. From Figure 6.3(d) and Figure 6.3(e) we see that the initiated crack quickly accelerates to speeds beyond c_R of the polymer with in $7 - 8$ μs after initiation. Crack speed acceleration during this phase is as high as $10^8 - 10^9$ m/s^2. From Figure 6.3(f), Figure 6.3(g) and Figure 6.3(h) we can see that the propagating interface crack attains intersonic speeds, even though it propagates at a speed only slightly above c_s. The size of the isochromatic fringe pattern increases, reflecting the increase in magnitude of the crack tip fields due to the increase in crack length.

To observe the interface crack behavior as it propagated further away from the initial pre-crack tip, in a subsequent experiment which was performed under nominally identical conditions, the field of view of 50 mm diameter was moved further down stream along the interface. Figure 6.4 shows a selected sequence of 8 isochromatic fringe patterns around an intersonic interfacial crack propagating along a Homalite/Al interface. Again the time elapsed from impact and crack speed are shown in each frame. In this experiment, speed of projectile at impact was 9.9 m/s and the field of view of 50 mm diameter was centered on the interface, 37 mm ahead of the initial pre-crack tip. We see that once the interface crack accelerates quickly to intersonic speeds, it continues to propagate at an almost constant speed varying between c_s and $1.2\,c_s$. However, the nature of the isochromatic fringe pattern around the propagating intersonic crack tip is observed to undergo very dramatic changes. We see from Figure 6.4(b) that the crack tip region is no longer a sharp point, but more diffused as noticed from the fact that the two lobes of the isochromatic fringe pattern around the tip are separated by a finite distance. In Figure 6.4(e) and Figure 6.4(f) we can see sharp lines radiating from the crack tip region into the polymer half. These are the

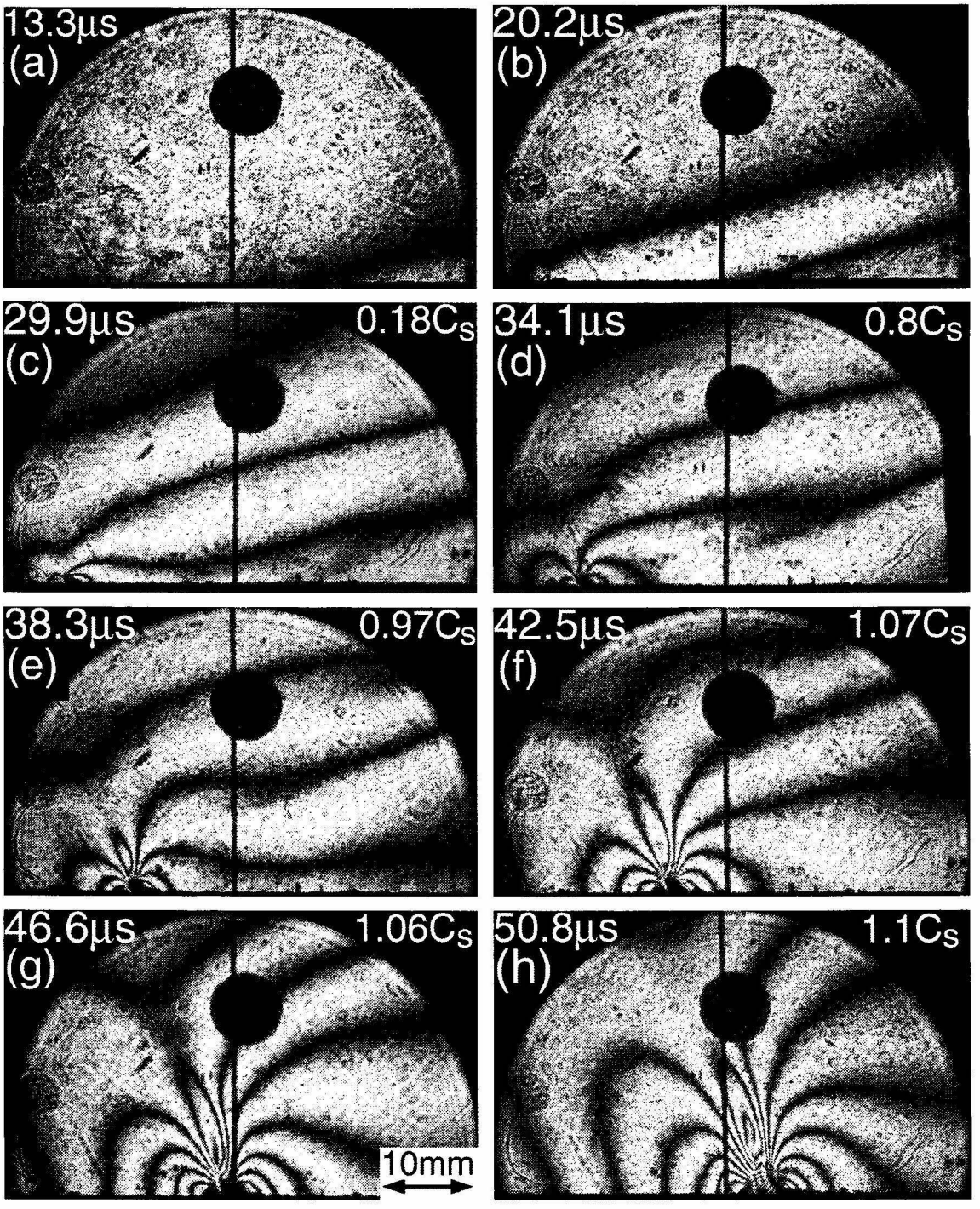

Figure 6.3: Initiation and acceleration to intersonic speeds of a crack on Homalite/aluminum interface under impact shear loading. Impact speed, V = 9.6 m/s. The semicircular field of view of 50 mm diameter is centered on the interface 19.5 mm ahead of the initial pre-crack tip.

traveling Mach waves which delineate the extent of propagation of shear disturbances emanating from the tip region. Across these Mach waves the isochromatic fringe pattern changes abruptly. The angle ξ, the Mach waves make with the crack faces can be related to the crack speed v through

$$\xi = \sin^{-1}(c_s/v)\,. \tag{6.1}$$

More than one traveling Mach waves are clearly seen and such an observation prompted SINGH and SHUKLA (1996b) to conjecture that an intersonic crack tip propagates with a finite zone of crack face contact behind it. Also in Figure 6.4(h) we can see a secondary disturbance trailing the propagating intersonic crack tip, which is later shown to be traveling at c_R of the polymer. The increased length of the propagating interface crack results in an increased magnitude of stress concentration around the propagating crack tip as indicated by the increased size of the isochromatic fringes around the tip.

Typical crack length and crack speed histories for two similar and representative experiments varying only in the position of the field of view are shown in Figure 6.5. In Expt04 and Expt24, the projectile speed at impact was ≈ 9.6 m/s and the field of view included the initial pre-crack tip. In Expt18 and Expt19, the projectile speed at impact was ≈ 9.9 m/s and the field of view was located further downstream from the initial pre-crack tip. Figure 6.5(a) shows the crack length history for all four experiments. Crack length includes the length of the pre-crack which was $\approx 1''$. Error made in measuring the crack length from recorded isochromatic fringe patterns was of the order of ± 0.5 to ± 1.0 mm. Error bars are shown on a few data points at the beginning and the end of the data set, however, since they are smaller than the symbol size, they are not clearly visible. The time of impact is considered to be the reference point on the time scale and hence $t = 0$ μs corresponds to the time at which the projectile impacts the specimen. After a few μs from the time of initiation, the crack length seems to increase almost linearly with time, indicating that the crack

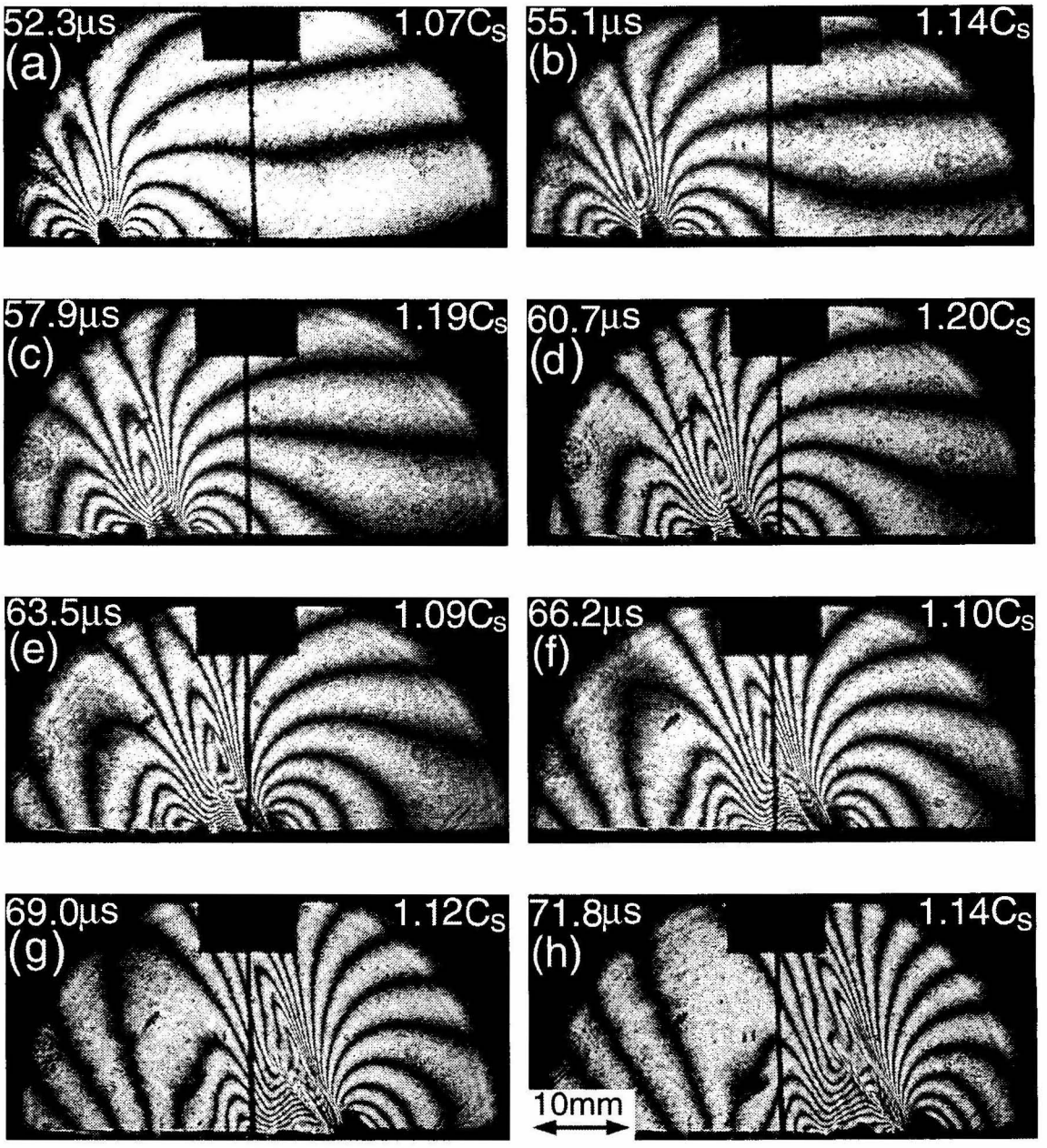

Figure 6.4: Isochromatic fringe pattern around an intersonic crack propagating along a Homalite/aluminum interface. Impact speed, $V = 9.9$ m/s. The semi-circular field of view of 50 mm diameter is centered on the interface 37 mm ahead of the initial pre-crack tip. Multiple Mach waves emanating from the crack tip region are clearly visible.

is propagating at nearly the same speed. To determine the crack speed, a second order interpolating polynomial was obtained for every three successive points in the crack length history, which is then differentiated with time to give the crack speed for the mid-point. The crack speed history as the interface crack propagates along the Homalite/Al interface is shown in Figure 6.5(b) for the same four experiments. From the figure, we see that the interface crack immediately after initiation, accelerates rapidly to speeds higher than c_R of the polymer. In three of the experiments (except Expt04) it is seen that the interface crack becomes intersonic, but seems to propagate at a relatively constant speed oscillating between c_s and $1.3\,c_s$. Error in measuring crack speed varied from ± 50 to ± 120 m/s. Error bars are shown on a few points at the beginning and the end of the data set.

Figure 6.6 shows a selected set of four isochromatic fringe patterns drawn from two experiments performed under similar conditions. Figure 6.6(a) and Figure 6.6(b) were taken from Expt04 and Figure 6.6(c) and Figure 6.6(d) were taken from Expt18. Both these experiments were performed under nominally identical conditions and differences, if any, were discussed in the previous paragraph. The interfacial crack moves from left to right, with the instantaneous crack tip speed and the time elapsed from impact being noted in the top right-hand corner of each frame. These recorded patterns show the dramatic change in the isochromatic fringes, *i.e.*, the nature of the stress field, around the crack tip as it accelerates from subsonic speeds to intersonic speeds. It is apparent that fundamental changes in the fringe patterns occur with increasing velocity. Whereas in the first two images where the crack speeds are $0.82\,c_s$ and $0.90\,c_s$, respectively, the fringes converge smoothly to the interface forming well defined lobes. The fringes in the latter two images, where the crack speed is intersonic, become increasingly compressed and more complex, featuring two distinct shear shock waves emanating from the crack tip and possibly from an end of a well formed contact zone. In the intersonic patterns, we can also clearly distinguish a Rayleigh disturbance trailing behind the crack tip.

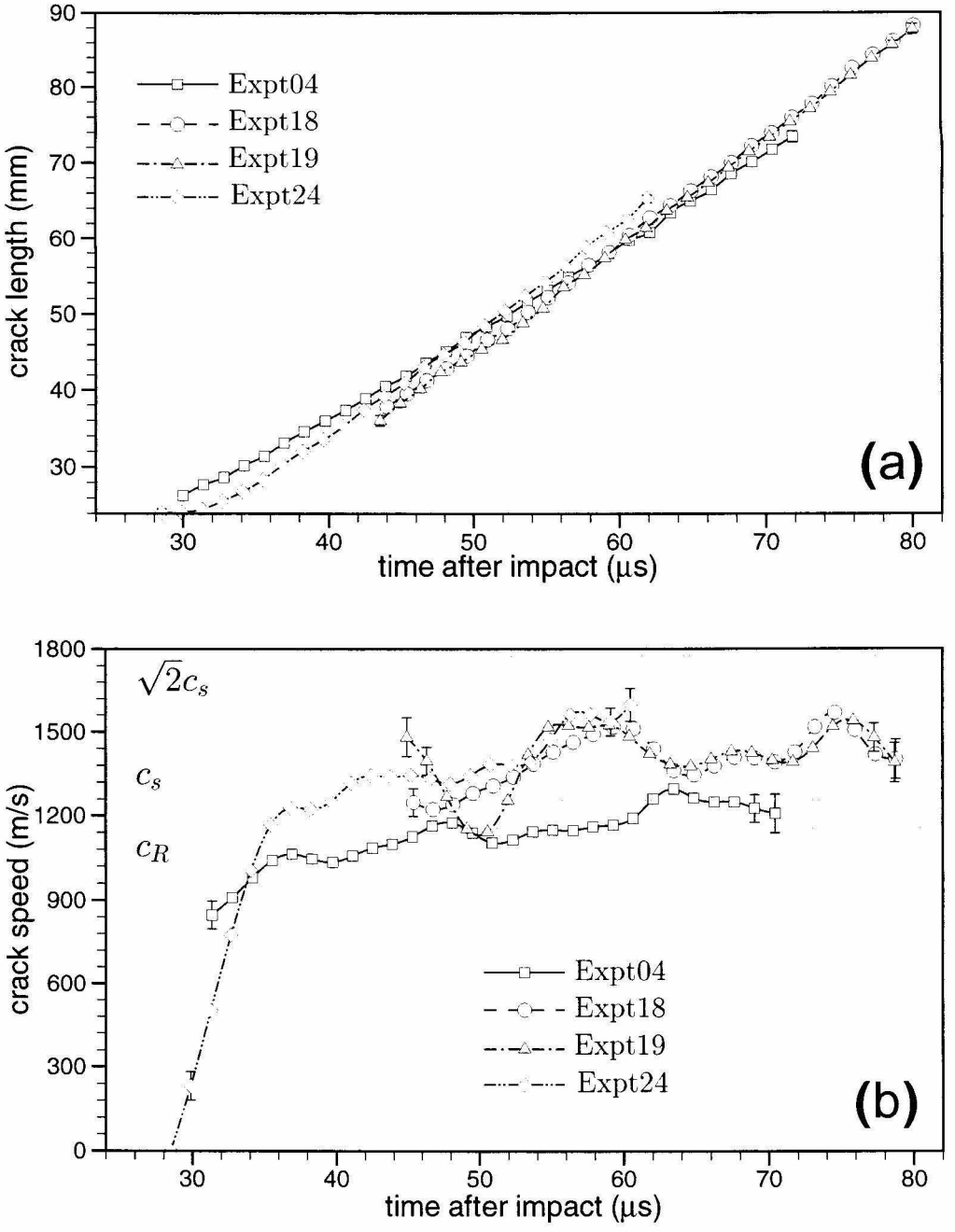

Figure 6.5: **(a)** Time history of crack length. Crack length includes length of the starter notch. **(b)** Evolution of crack speed v. Expt04 and Expt24 correspond to an impact speed of 9.6 m/s, whereas Expt18 and Expt19 correspond to an impact speed of 9.9 m/s. All the experiments were performed on Homalite/aluminum bimaterial specimens and specimen thickness was $3/16''$ in Expt24 and $1/4''$ in the other three.

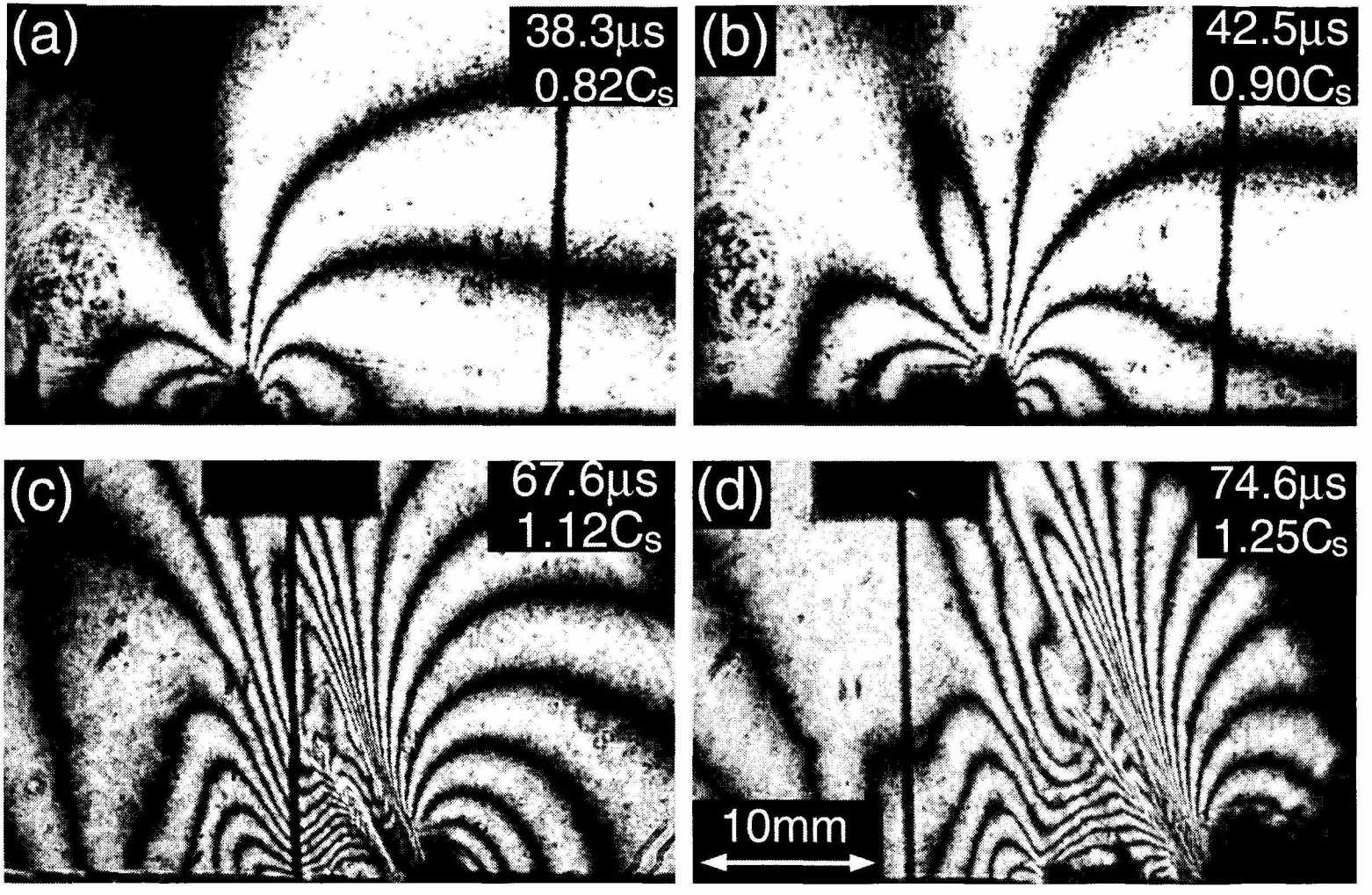

Figure 6.6: Comparison of the isochromatic fringe patterns around subsonic and intersonic cracks on a Homalite/aluminum interface. Note the strong Mach wave radiation from the intersonic crack tips.

6.1.3 Subsonic/Intersonic Transition of a Bimaterial Interface Crack

As mentioned before, the main thrust of the current experimental investigation is to understand the subsonic/intersonic transition of an interfacial crack. To carefully monitor the changes in the stress field in the crack tip region, a magnified view of the isochromatic fringe pattern near the crack tip is shown at different intervals as it undergoes this transition. All the six magnified views shown in Figure 6.7 were borrowed from the experimental records of Expt18 and the crack speed history for this experiment was shown in Figure 6.5(b). In all the six views shown, the crack speed is super-Rayleigh (above c_R) and oscillates between c_s and $1.35\,c_s$. No strong correlation was observed between a particular change in the near-tip stress field and the crack speed, indicating that this subsonic/intersonic transition is a highly dynamic event, where parameters other than crack speed come into play. In Figure 6.7(a), we can identify the crack tip to be located at a point along the interface where the smooth and round fringes in the front converge on to the interface. Note that the interfacial crack is moving from left to right. A substantial distance behind this point we see an almost vertical Mach wave radiating into the polymer half, across which the isochromatic fringe pattern changes abruptly. We see that such a separation of the front and back lobes of the isochromatic fringe pattern is the first characteristic feature of the subsonic/intersonic transition. If the interfacial crack were propagating at subsonic speeds, both the front and back lobes would meet at a single point, the crack tip (SINGH and SHUKLA, 1996a). The presence of the near vertical Mach wave can be understood as follows. A moving interfacial crack may be considered to be a moving traction distribution on the polymer surface. It was shown by FREUND (1973) that such a traction distribution, as it accelerates through the Rayleigh wave speed of the medium, results in a singularity in surface displacements as well as stresses, which trail the moving load and travel at c_R of the medium. He also showed that this singularity is one-sided, indicating that the stress field on either side of this traveling singularity is not necessarily the same. We believe that such features are indicated

by the presence of the vertical Mach wave, on either side of which the nature of stress field is different (isochromatic fringe pattern is different) and moreover seems to indicate that the stress field is singular only behind the vertical Mach wave. It may be fairly conjectured that behind the vertical Mach wave, crack faces are traction free, however, it is as yet unclear whether the crack faces in front of this Mach wave are in contact or traction free. Also, near-tip solutions for a steady subsonic - super-Rayleigh crack show that the stress fields in front of the tip are no longer singular but pure oscillatory. However, it is doubtful whether such a steady solution is valid during the transition phase, which likely to be highly transient.

In Figure 6.7(b) we see a zone of finite width growing from where the vertical Mach wave was observed before. Because of the higher concentration of isochromatic fringes here, it may be safely conjectured that this zone is a zone of high stresses, most likely due to compressive normal stresses resulting from crack face contact. Hence this zone is likely a crack face contact zone where frictional sliding takes place and ahead of it is a zone of stress field relaxation or what we euphemistically term as a "traction free zone". This conjecture is different from that put forward by LAMBROS and ROSAKIS (1995b); SINGH and SHUKLA (1996b) where it was argued that the crack face contact zone originates right behind the intersonic crack tip. This kind of a detached contact zone is also observed in many other physical phenomena. SCHALLAMACH (1971) in his sliding experiments between rubbers and hard materials, found that displacement along the interface occurs sometimes as macroscopically uniform frictional sliding and sometimes as narrow propagating waves of detachment. The current phenomenon under investigation, where the very compliant polymer is sliding over hard metal at very high slip rates of the order of few m/s, is similar to the one observed by Schallamach. ADAMS (1998) pointed out that if an elastic body is slid against a rigid substrate, dynamic instabilities may occur similar to Schallamach waves, especially in cases where the friction coefficient and Poisson's ratio are quite large. Similar features were also observed in the wrinkle like slip pulse propagation

between two dissimilar material interfaces at high slip rates by ANDREWS and BEN-ZION (1997). Detached contact zones were also observed in numerical simulations of BREITENFELD and GEUBELLE (1998) and NEEDLEMAN and ROSAKIS (1999). At the original position of the vertical Mach wave, we now have a weak Mach wave across which the fringes merely change their slope. Hence Figure 6.7(b) shows a triple Mach wave structure, one emanating from the crack tip and the other two emanating from the front and rear ends of the contact zone.

At later times we see that the size of the contact zone diminishes, with the weak Mach wave moving towards the one emanating from the front end of the contact zone (Figure 6.7(c)). In Figure 6.7(d), we find that the contact zone almost vanishes as the Rayleigh singularity trails further behind the intersonic crack tip. Here the contact appears to be almost infinitesimal from the fact that the distance between the second and the third Mach waves is almost negligible. As the Rayleigh singularity trails further behind, we find that the size of the "traction-free zone" diminishes (see Figure 6.7(e)) and eventually vanishes completely (see Figure 6.7(f)). The fact that the infinitesimal contact zone catches up with the crack tip can also be seen from the relatively steep inclination of the second Mach wave. Eventually, we find that the intersonic crack emerges traction free in Figure 6.7(f) where the Rayleigh singularity is trailing a sufficient distance behind the intersonic crack tip.

However, these features of the subsonic/intersonic transition of an interfacial crack do not appear to be universal. In another experiment, Expt19, which was also discussed before, and is nominally identical to Expt18, the essential end feature where the intersonic crack emerges traction free is not observed. Figure 6.8 shows a sequence of six magnified views of the crack tip region as the interface crack in Expt19 undergoes the subsonic/intersonic transition. The initial features like the formation of point contact (see Figure 6.8(a)), growth of contact region (see Figure 6.8(b)), diminishing of the contact zone to infinitesimal size (Figure 6.8(c) to Figure 6.8(e)) were all observed, as in Expt18. However, unlike in the case of Expt18, even as the

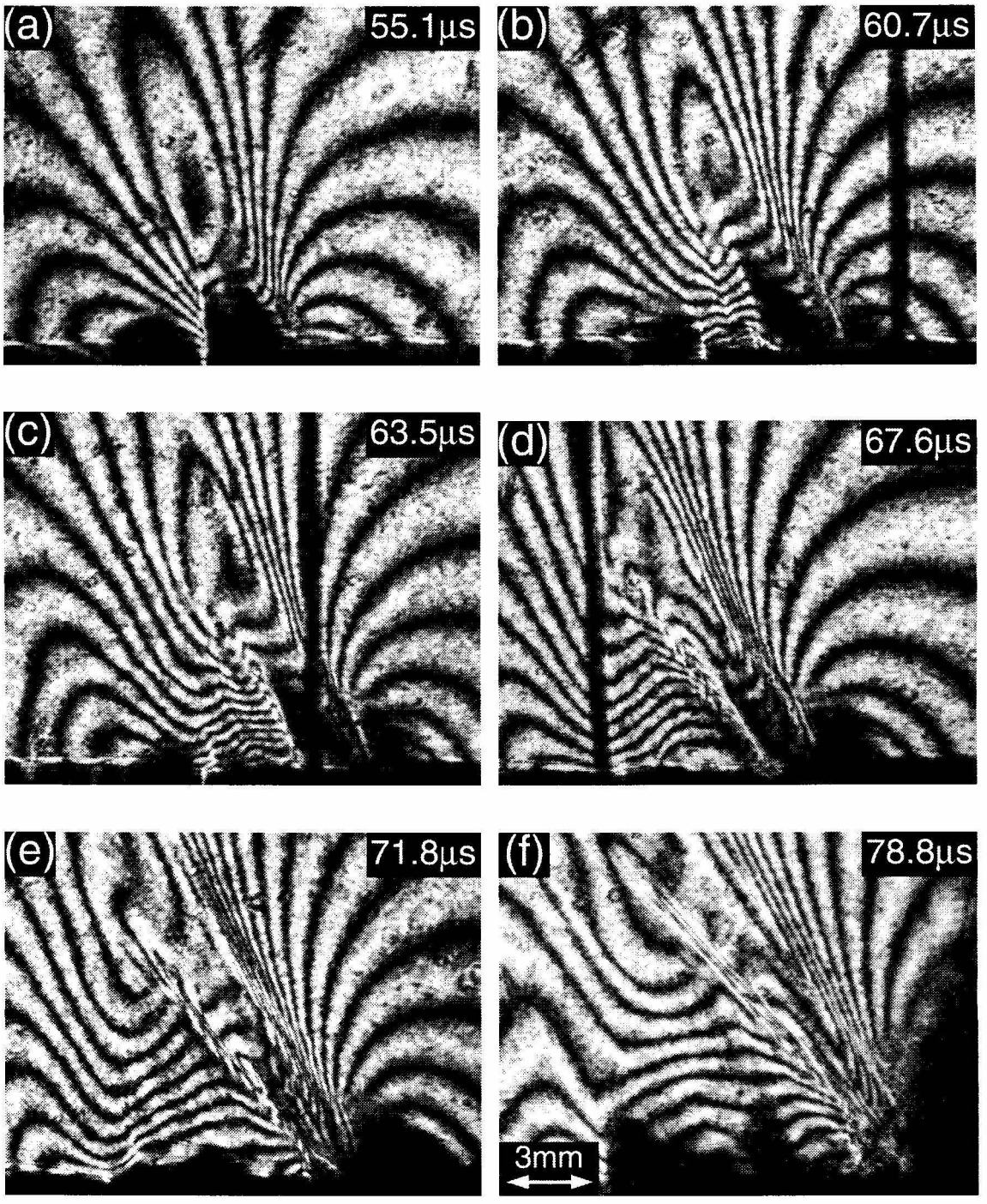

Figure 6.7: Crack face contact and multiple mach wave formation during intersonic crack growth along a Homalite/aluminum interface (Expt18). A magnified view of the area around the crack tip is shown. Impact speed, $V = 9.9$ m/s.

Rayleigh singularity trails sufficient distance away from the intersonic crack tip, the infinitesimal contact zone seems to remain at a constant distance behind the intersonic crack tip, as indicated by the two parallel Mach waves emanating from these two features (see Figure 6.8(f)). Within our experimental field of view, no emergence of a traction free intersonic crack was observed, as was the case in Expt18.

The same orderly change in the nature of the isochromatic fringe pattern in the crack tip region, as was observed in Expt18, was found to be highly repeatable and was observed in at least five other similar experiments. However, even without any substantial differences as to the specimen dimensions, properties of the interface and the loading conditions, in a particular experiment (Expt19), the change in the nature of the isochromatic fringe pattern during subsonic/intersonic transition was found to be slightly different. Hence the subsonic/intersonic transition examined above does appear to depend on additional parameters apart from the mere fact that the crack speed accelerates through the Rayleigh and shear wave speeds. As observed by Schallamach in his experiments, it might depend substantially on the interface characteristics. Also the essential features of the subsonic/intersonic transition are not functions of the crack speed and hence it is a highly transient and dynamic event. To study the effect of interface mismatch on subsonic/intersonic transition, we now examine the event in a different bimaterial system.

Figure 6.9 and Figure 6.10 show a set of four enlarged views of the isochromatic fringe pattern at different times around the tip of an intersonic crack propagating on a Homalite/steel interface. The dimension of the rectangular field of view is $\approx 20 \times 15$ mm. The projectile impact speed was $V = 9.7$ m/s, which is very close to V for Expt18 and Expt19, the results of which were discussed before. These records were made using a high speed digital camera with a much smaller optical path length as compared to the high speed film camera described in Chapter 2. However, the high speed digital camera records a mere 8 frames during the dynamic event and hence parameters like time after impact and crack speed cannot be estimated accurately for

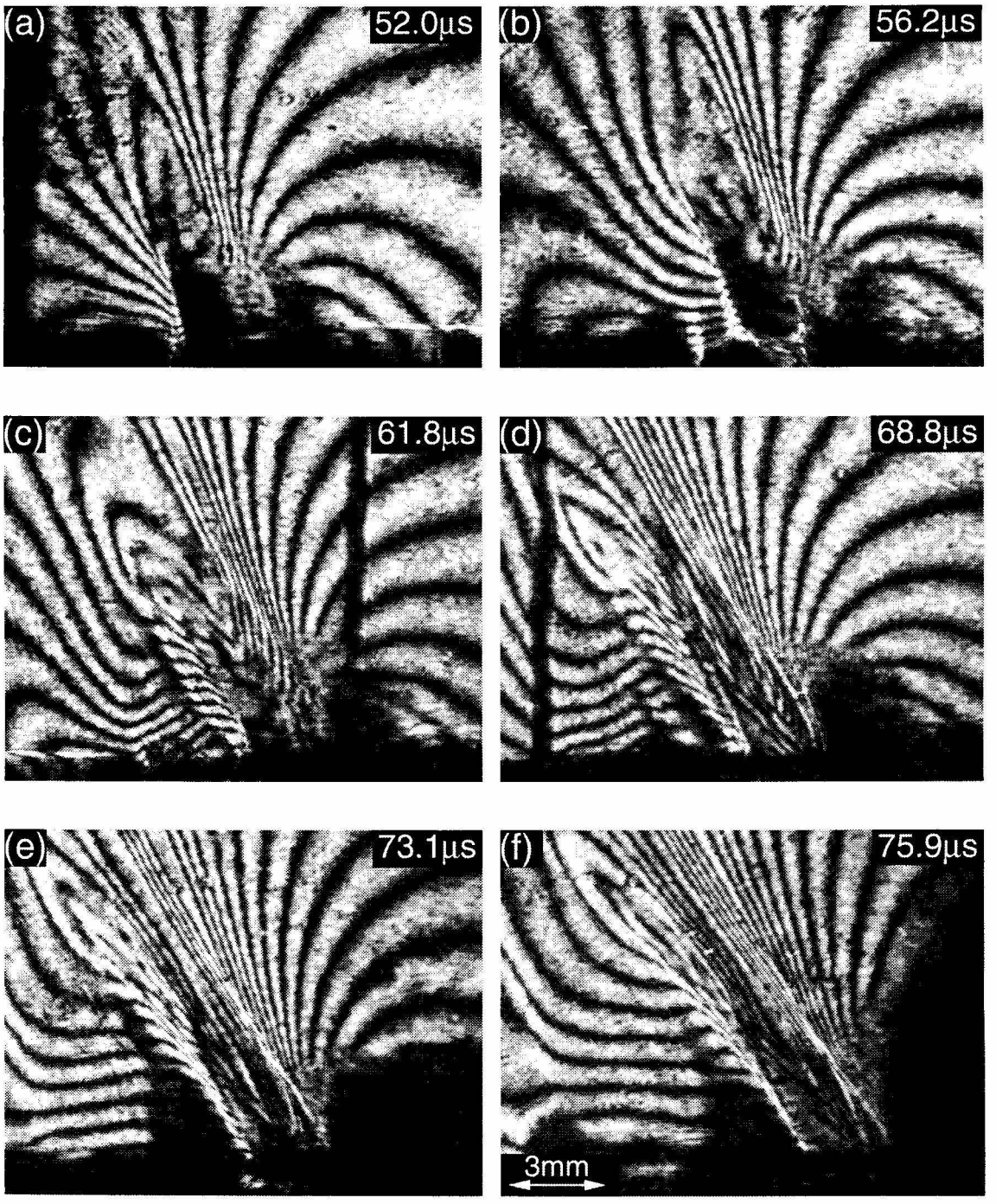

Figure 6.8: Crack face contact and multiple Mach wave formation during intersonic crack growth along a Homalite/aluminum interface (Expt19). A magnified view of the area around the crack tip is shown. Impact speed, $V = 9.9$ m/s.

each frame. However, for intersonic crack growth, the inclination of the Mach angle ξ emanating from the crack tip uniquely identifies the crack tip speed. (see (6.1)). Crack tip speed thus obtained is shown on each of the four frames in Figure 6.9 and Figure 6.10. Also, an area around the crack tip bounded by the rectangle drawn is shown as an inset to the top right of each frame. Except for Figure 6.9(a), where the inset shown is magnified, rest of the insets are the same size as the bounded rectangles.

In Figure 6.9(a), we can see that the interface crack has just attained intersonic speed, from the fact that the Mach waves emanating from the crack tip region have radiated only a short distance into the polymer. From the inset of this frame, we can clearly see the Mach wave emanating from the crack tip ahead of which the fringes are smooth and rounded and behind which the fringes close to the interface are almost parallel to it. However, this behavior of the isochromatic fringes behind the crack tip changes abruptly within a short distance of 2 mm, where yet another Mach wave seems to be emitted from the broken interface. We interpret this zone between the two Mach waves as a traction free zone, where there is a relative sliding of the polymer and metal surfaces with an accompanied relaxation of the normal compressive stress, after the interface is broken by the moving intersonic crack tip. Behind the second Mach wave, we can identify yet another region, approximately 2 mm long where we conjecture that the crack faces are under strong normal compressive stress and sliding with frictional contact takes place here. As the interface crack propagates further, we can clearly distinguish the three Mach waves emanating from the crack tip region as they have radiated over a sufficient distance into the polymer half (see Figure 6.9(b)). The two zones — traction free zone behind the crack tip (or zone of low normal compression) and the crack face frictional contact zone can be clearly identified. All the three Mach waves seen are inclined at almost the same angle of $\approx 59^{\circ}$, showing that these features are moving at about the same speed. However, as compared to Figure 6.9(a), the length of the frictional contact zone has increased substantially to

about 3.8 mm. Such a growth of contact region as the intersonic crack propagates further along the interface was also seen in Figure 6.7 and Figure 6.8.

Two more frames showing the isochromatic fringe pattern around the crack tip at later times are shown in Figure 6.10(a) and Figure 6.10(b). The three Mach waves and the two distinct zones in the crack tip region — traction free zone and the frictional contact zone are very clearly identifiable in these figures. Figure 6.10(a) is similar to Figure 6.9(b) with length of the traction free zone being approximately equal to 2 mm and the length of the frictional contact zone being approximately equal to 3.8 mm. The two Mach waves emanating from the crack tip and the front end of the contact zone are almost parallel inclined at an angle of $\approx 55^{o}$ to the interface, whereas that emanating from the trailing end of the contact zone is inclined slightly steeper at almost 60^{o} to the interface. This steeper inclination of the Mach wave emanating from the trailing end of the frictional contact zone seems to indicate that the contact zone might reduce in size, which is exactly what is seen in Figure 6.10(b). Here the contact zone seems to diminish in size and eventually vanish to a single point. However, the length of the traction free zone has remained almost the same, indicating that intersonic crack growth along the Homalite/steel interface seems to propagate further with a finite sized traction free zone and a point sized contact behind the tip. This observation is akin to that found for intersonic crack growth along a Homalite/aluminum interface in Figure 6.8, *i.e.*, for Expt19. The Rayleigh singularity is trailing sufficiently far behind the crack tip and can be clearly identified in Figure 6.10(b), as the point where the fringes bend in a V-shape almost 13 mm behind the crack tip. By this time, *i.e.*, with a sufficient separation between the intersonic crack tip and the trailing Rayleigh singularity, the intersonic crack was found to emerge with traction free crack faces in most experiments (see Figure 6.7). However, as seen in Figure 6.8 and Figure 6.10, it may not always be the case and the intersonic interfacial crack seems to propagate ahead with still a finite sized traction free zone and a infinitesimal contact zone behind the tip. Owing to the limited size

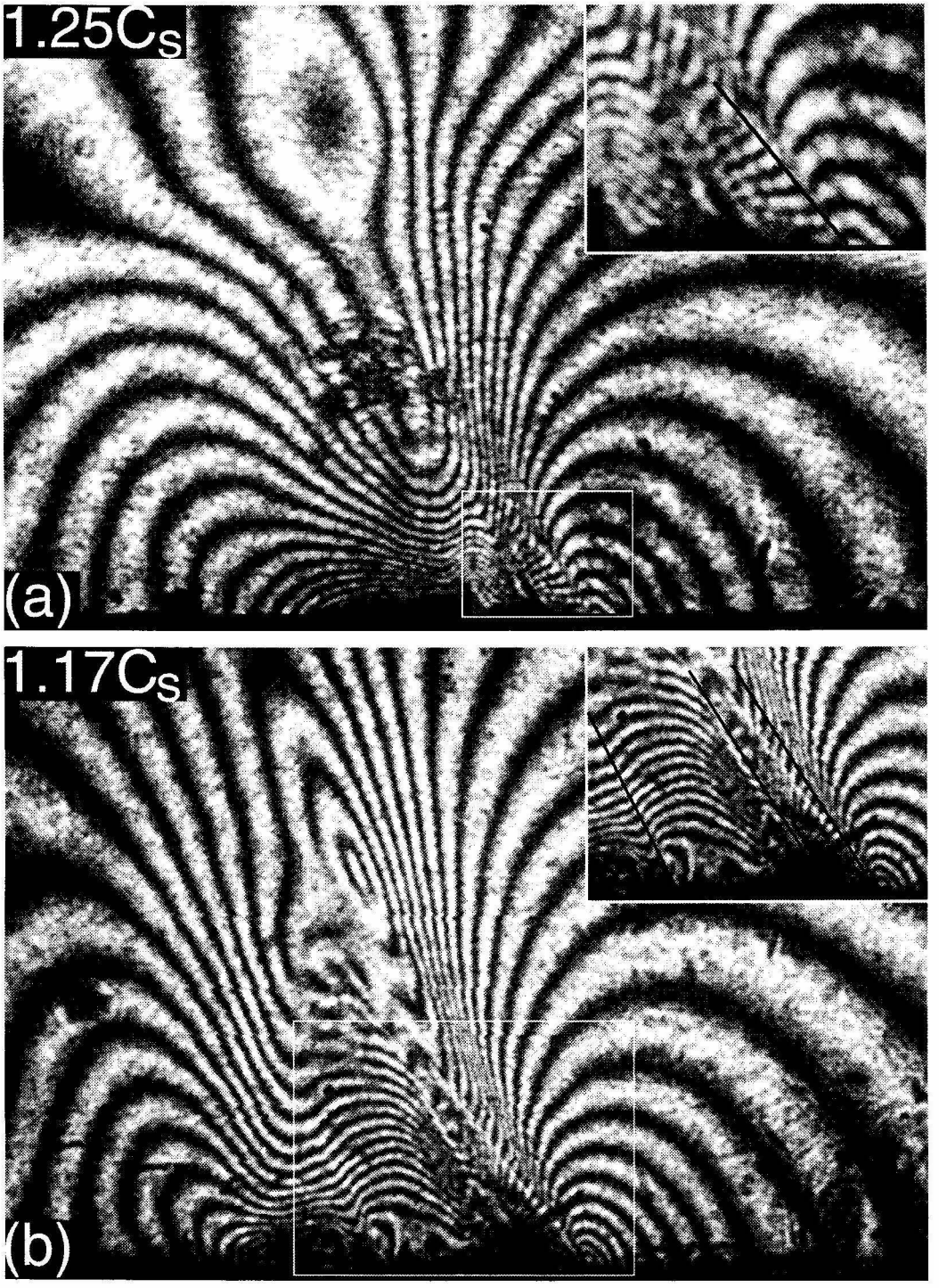

Figure 6.9: Isochromatic fringe pattern around an intersonic crack on a Homalite/steel interface - I. Three Mach waves can be seen clearly in **(b)** indicated by the three black lines (inset). Impact speed, $V = 9.7$ m/s.

of the field of view and limited extent of the interface, further events could not be captured to see if there is indeed a universal character. It is very much desirable to focus future experiments on intersonic crack growth along a bimaterial interface to resolve this ambiguity, as far as the subsonic/intersonic transition event is concerned. If indeed different phenomena are possible, it would be desirable to find out the relevant parameters that govern the emergence of one phenomenon over the other.

We discussed the subsonic/intersonic transition event quite extensively above, carefully examining the crack tip region during the transition in three different experiments, two of which involved a Homalite/Al interface and one of which involved a Homalite/steel interface. All these experiments were performed under nominally identical conditions — similar specimen dimensions and preparation methods, same projectile impact speeds, same initial crack lengths, *etc.* We identified that the features observed during the transition event are similar, however, the question whether the intersonic interfacial crack eventually emerges traction free or not was not completely resolved. Most of the experimental results point to the former case, though a certain number of experiments point to the latter. More study is required to resolve the issue. However, the general features associated with the subsonic/intersonic transition of an interfacial crack on a polymer/metal interface are laid out in an illustration shown in Figure 6.11. It shows our conjecture of the different events happening during the transition and they are described in five sketches of the crack faces ((A) to (E)) in Figure 6.11. The origin of the crack tip coordinates (η_1, η_2) indicates the location of the crack tip. In (A), the crack is propagating subsonically and the crack faces are essentially traction free. In (B) as the crack exceeds c_R of the polymer, a one sided singularity in the stress field is generated as indicated by the almost vertical Mach wave emanating from the point where the interfacial crack exceeded c_R. The crack face of the polymer half appears to be still in contact with the metal half here, under strong normal compression undergoing frictional sliding. The inclined Mach wave emanating from the crack tip indicates that it is moving at intersonic speeds and

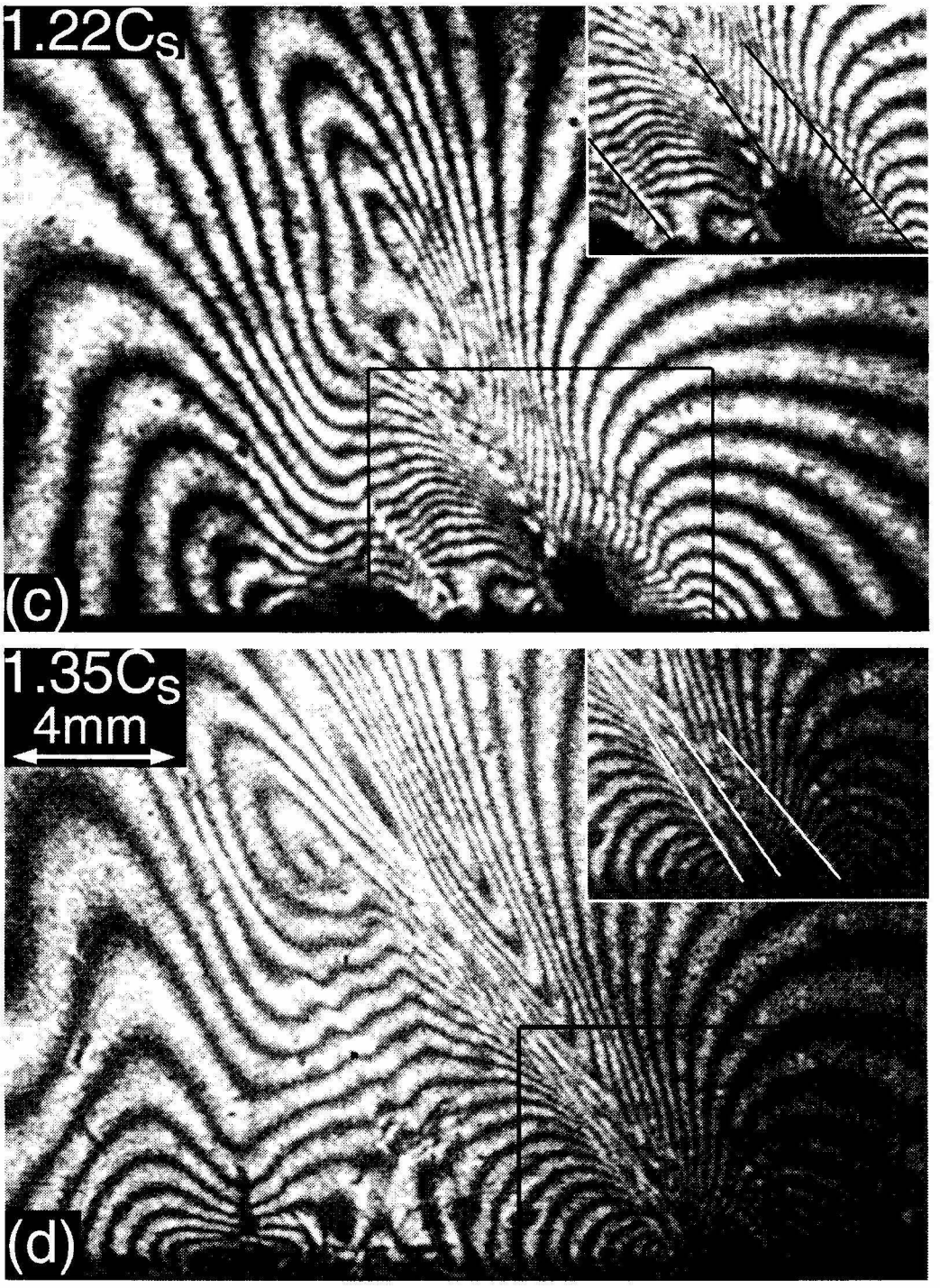

Figure 6.10: Isochromatic fringe pattern around an intersonic crack on a Homalite/steel interface - II. **(c)** shows the three Mach wave structure and **(d)** shows the fringe pattern unaffected by the Rayleigh singularity.

away from the Rayleigh singularity. In between these two points, we conjecture that the crack faces are traction free or at least under a relaxed normal compression. (C) shows that as the intersonic interfacial crack moves further away from the Rayleigh singularity, the size of the contact zone grows and the three Mach waves emanating from the crack tip, the front and trailing ends of the contact zone are almost parallel to each other indicating that they are all moving at the same speed (see Figure 6.9(b) and Figure 6.10(a)). At still later times, as the intersonic crack tip moves further away from the Rayleigh singularity, the contact zone size diminishes, as shown in (D) with only two Mach waves emanating, one from the crack tip and the other from the infinitesimal-sized contact zone. In some experiments, this event was found to go on until the crack tip ran out of the field of view. However, in most experiments it was found that as the Rayleigh singularity trails sufficiently far from the tip, the contact zone moves rapidly into the crack tip, vanishes and the crack faces were found to emerge traction free as shown in (E).

Figure 6.12 shows an enlarged view of the sketch (C) of Figure 6.11. Here the intersonic bimaterial interface crack is propagating with a finite traction free zone behind the tip, followed by a finite zone of crack face frictional contact. The location of the Rayleigh singularity is also shown. The lengths of the traction free zone and the frictional contact zones are termed l_1 and l_2 respectively. Also, the inclination to the interface, of the Mach waves emanating from the crack tip and the front end of the contact zone are termed α and β respectively. The sketch essentially introduces the nomenclature adopted from now onwards and in the next two figures the variation of some of these parameters as the intersonic crack propagates along the bimaterial interface is shown.

6.1.4 Mach Angles and Zone Lengths

Figure 6.13(a) shows the variation of the Mach wave angles α and β (see Figure 6.12) with time as the intersonic crack propagates along the bimaterial interface. Experi-

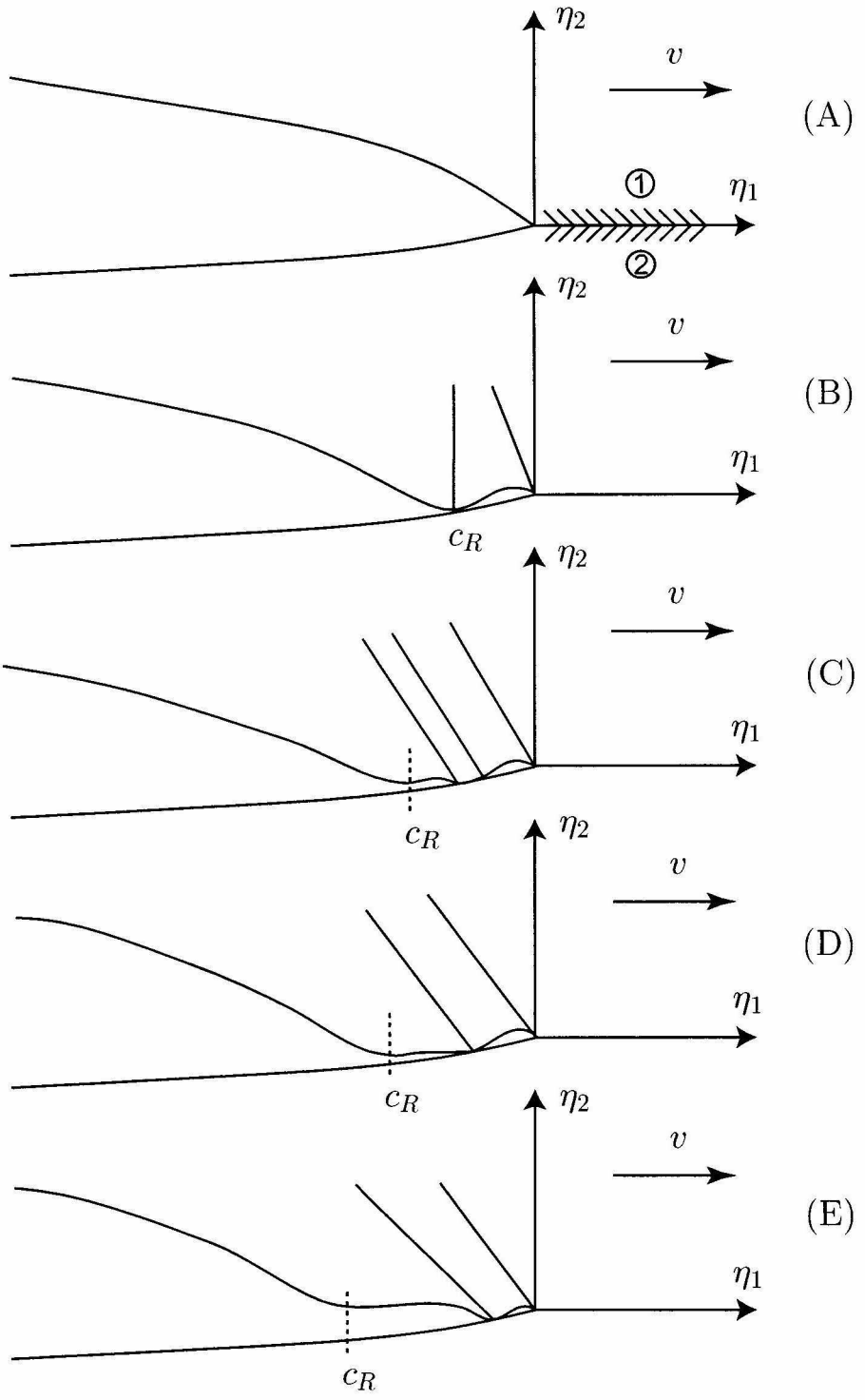

Figure 6.11: An illustration summarizing empirical interpretations regarding the formation of crack face traction free and contact zones during acceleration of an interfacial crack from subsonic to intersonic speeds.

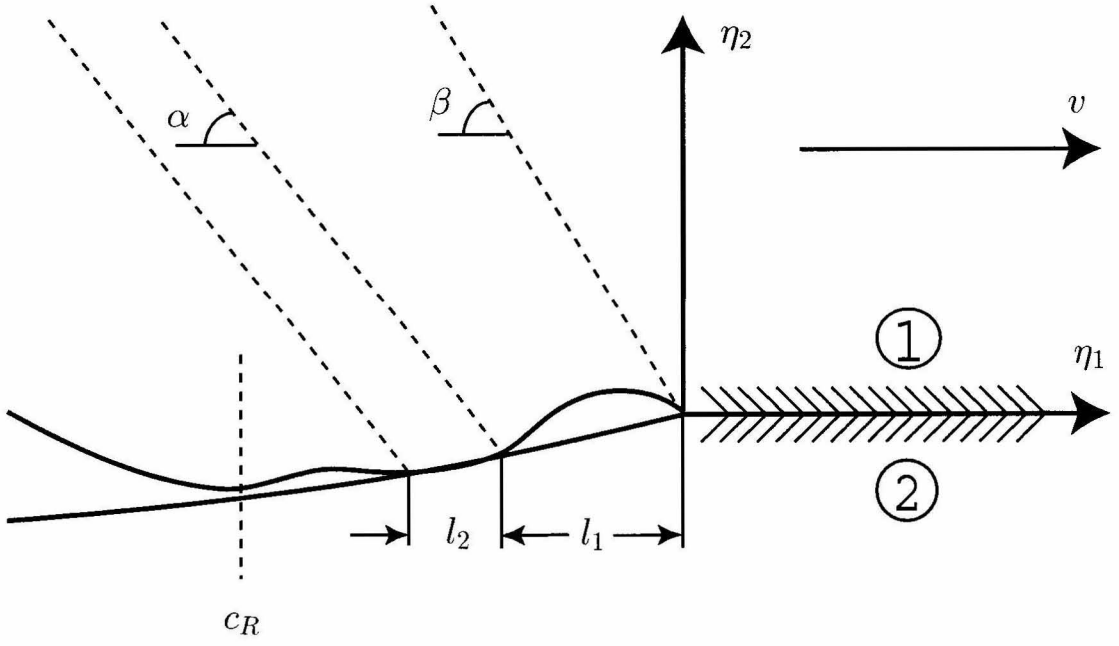

Figure 6.12: An illustration showing the various parameters associated with an intersonic bimaterial interface crack with finite crack face traction free and frictional contact zones.

mental records of isochromatic fringe patterns from two experiments — Expt18 and Expt19 (the same experiments discussed before), which were performed under nominally identical conditions, were analyzed to obtain the time history of the Mach wave angles, α and β. As seen from Figure 6.13(a), β for Expt18 and both α and β for Expt19 range between 60° and 70°. However, α for Expt18 starts initially around 80° and falls almost to around 50° by the time crack exceeds the field of view. These observations can be interpreted easily as follows. In Expt18, it was found that the Mach wave emanating from the front of the contact zone was almost vertical in the beginning, which eventually catches up with the crack tip by the time the crack runs out of the field of view. Hence the inclination of the Mach wave emanating from the contact zone becomes smaller and smaller indicating that it is catching up with the intersonic crack tip. However, in the case of Expt18, the two Mach waves from the crack tip and the front end of the contact zone were always parallel as can be seen in figure 6.13(a).

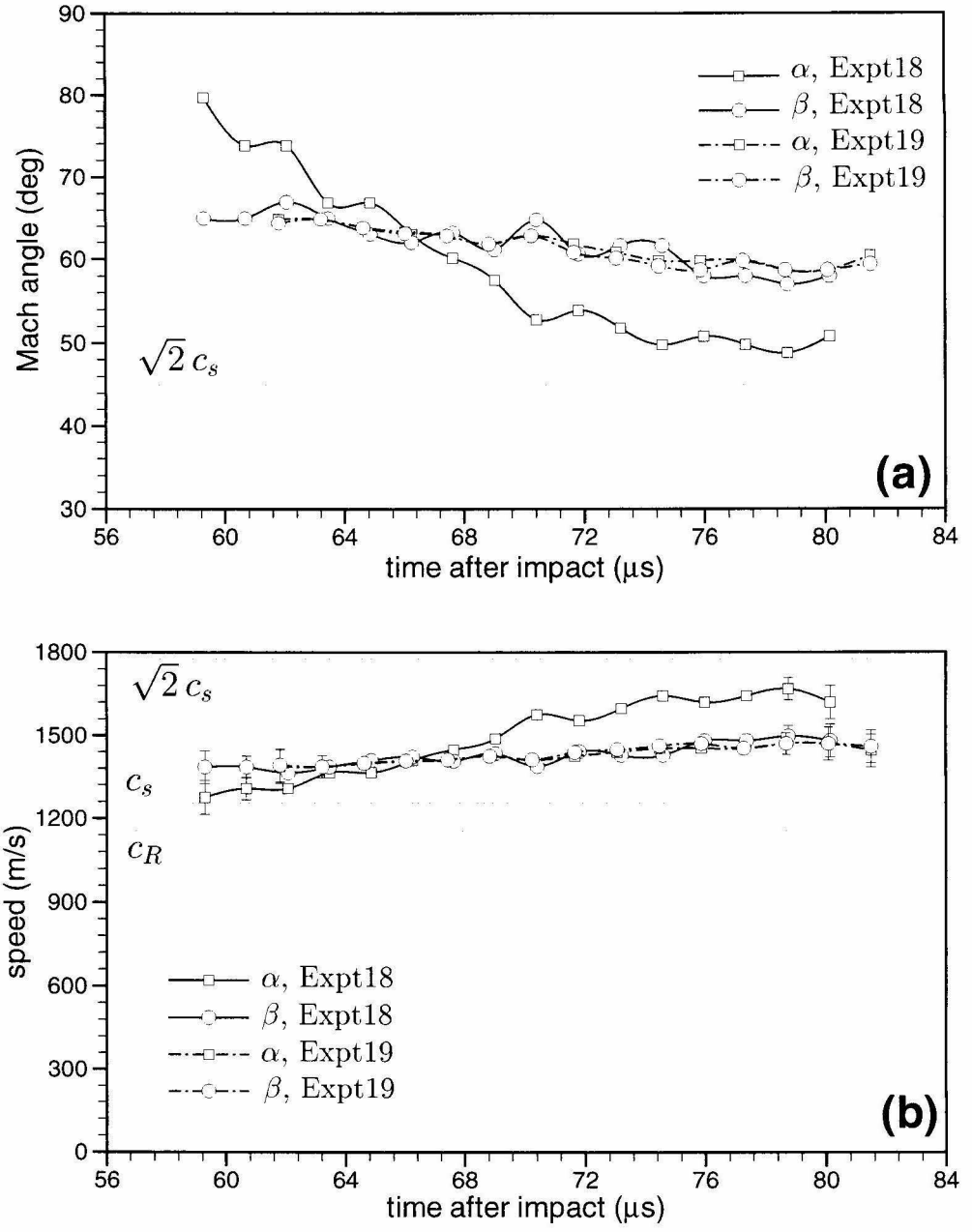

Figure 6.13: **(a)** Time history of Mach angle. β is the inclination of the Mach wave emanating from the crack tip and α is the inclination of the Mach wave emanating from the front end of the contact zone. **(b)** Speed from Mach angle histories above. Expt18 and Expt19 are the same as those in Figure 6.5.

Figure 6.13(b) shows the variation of crack speed with time as obtained from the Mach angle history given in Figure 6.13(a) and by using (6.1). It can be seen that the crack tip in Expt18 is traveling at a near constant speed increasing only slightly from around $1.05\,c_s$ to $1.25\,c_s$. In Expt19, both the crack tip as well as the front end of the contact zone move at the same speed ranging between the same limits above. Hence the observation that in Expt19, where the detached contact zone was always found at the same distance behind the crack tip. However, in Expt18, where the detached contact zone accelerates, catches up with the crack tip and vanishes, the crack speed associated with the front end of the contact zone was found to increase substantially and eventually exceed that of the crack tip. However,it may be noted that in all cases the intersonic crack speed is well below $\sqrt{2}\,c_s$, the importance of which is discussed in the next chapter.

Figure 6.14(a) shows the variation of the length of the traction free zone (l_1) and the frictional contact zone (l_2) for the same two experiments — Expt18 and Expt19. In Expt18, it was found that the contact zone starts point sized, grows to a finite size and eventually reduces back to infinitesimal size. Similar behavior was also found in Expt18. This is in agreement with the illustration of our conjecture regarding subsonic/intersonic transition shown in Figure 6.11. However, the length of the traction free zone (l_1) in Expt18 after being constant for a while, eventually shows a decrease essentially agreeing with the earlier observation that the intersonic crack eventually emerges traction free. However, in Expt19, no such traction free crack emerges and hence the length of the traction free zone was found to be almost constant as the intersonic crack travels through the field of view. Also, l_1 was found to be utmost of the order of 3 mm and l_2 was found to be utmost of the order of 2 mm. Hence these zones are finite sized, unlike in the case of subsonic interfacial crack growth, where the crack face contact zone remains infinitesimally small, except for speeds very close to c_R.

Figure 6.14(b) shows the variation of the speed of the Rayleigh singularity with

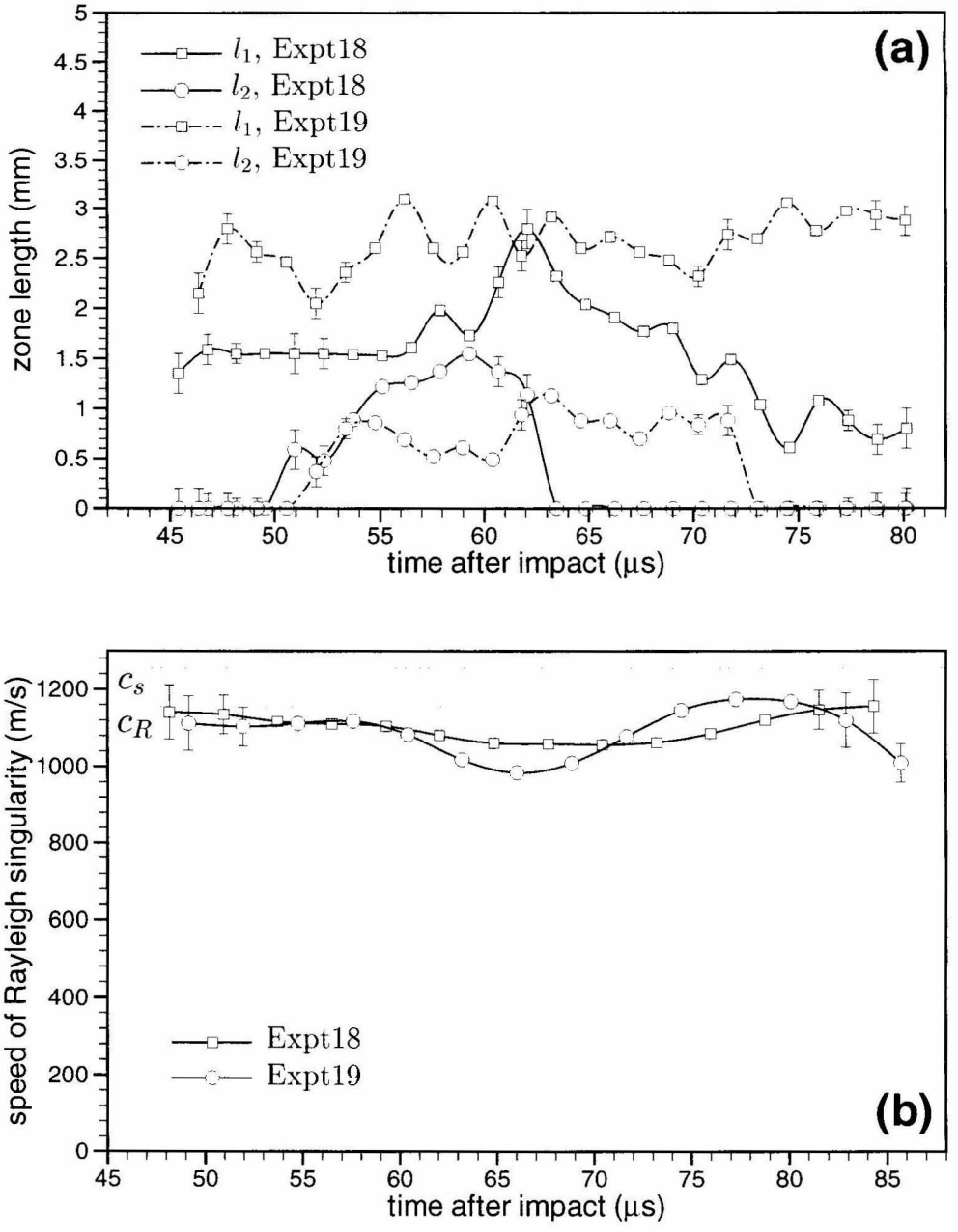

Figure 6.14: Intersonic crack growth along a Homalite/aluminum interface. **(a)** Time history of crack face traction free and frictional contact zone lengths. **(b)** Speed of Rayleigh singularity. Expt18 and Expt19 are the same as those in Figure 6.5.

time. Data is taken from the same two experiments — Expt18 and Expt19. Data essentially agrees with our assumption as to the feature in the isochromatic fringe pattern identifying the Rayleigh singularity, as it is found to propagate at a constant speed through out the field of view, very close to c_R of Homalite. The presence of this Rayleigh singularity close to the intersonic crack tip is the prime reason for the evolution of the multiple features observed during the subsonic/intersonic transition of a bimaterial interface crack.

6.1.5 Elongated Bimaterial Specimens and CGS Interferograms of Intersonic Interfacial Crack Tip Fields

Further experiments on intersonic crack growth along a polymer/metal interface were performed with a different specimen geometry to ascertain the effect of finiteness of the specimen dimensions on the propagation behavior of the intersonic crack. An elongated specimen geometry shown in Figure 6.15 was adopted and specimens with PMMA and steel as the two constituents were prepared following essentially the same procedure as given in Chapter 2. Because of the smaller height of the specimen compared to the specimen geometry shown in Figure 6.1, reflected waves from the free surface impinge back onto the propagating crack tip possibly resulting in an alteration of the propagation behavior of the intersonic interfacial crack. Since PMMA is not birefringent, CGS interferometry was used to record the stress field information around the propagating crack tip.

Figure 6.16 shows a sequence of eight selected CGS interferograms around the tip of an intersonic crack propagating on a PMMA/steel interface. The specimen was impacted by a cylindrical steel projectile at a speed, V = 19.2 m/s, and the semicircular field of view of 50 mm diameter was centered on the interface a distance of 15mm ahead of the pre-crack tip. As seen from Figure 6.16(a), the interfacial crack almost immediately after initiation attains intersonic speeds. For subsonic interfacial crack propagation, the CGS fringe pattern consists of two smooth and round lobes

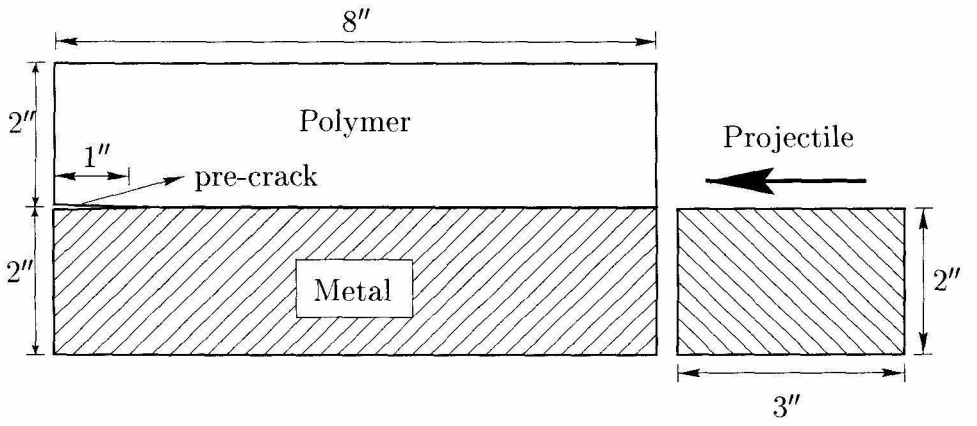

Figure 6.15: Elongated bimaterial specimen with a pre-crack subjected to impact shear loading.

which converge to a single point on the interface, the crack tip. As the interfacial crack attains intersonic speeds, the front lobe is no longer smooth and round, but develops a kink, where the fringes suddenly dip towards the interface (see Figure 6.16(b) to Figure 6.16(d)). This feature is caused by the fact that the point where the two lobes meet is no longer the actual crack tip, but is merely the location of the Rayleigh singularity. The intersonic crack tip has slid forward and the Mach wave radiating from here produces a increased stress gradient, which is reflected as an increase in the fringe order along this line, which eventually manifests itself as a sudden bending of the CGS fringes towards the interface. Note that CGS interferometry is insensitive to shear Mach waves and hence they are not seen explicitly. Thus, while analyzing CGS interferograms for the speed of an intersonic interfacial crack, one has to be very careful in identifying the location of the crack tip. Eventually, as the Rayleigh singularity trails sufficiently far from the crack tip, the crack tip stress singularity takes over, as identified by the fact that the kink in the front lobe eventually dips to the interface. It may be noted here, that the CGS interferometry suffers from severe light loss problems at the two diffraction gratings resulting in larger dark spots near locations of stress concentration. Also due to the finite height of the specimen, reflected waves from the top surface, continuously interfere with the crack tip fields resulting in fringes that have a very jagged structure. Because of the dark spots

associated with the CGS interferograms as well due to the fact that shear Mach waves are absent here, it is extremely difficult to identify the rich features associated with subsonic/intersonic transition which were observed in the isochromatic fringe patterns.

Crack length and crack speed histories for two similar and representative experiments varying in the position of the field of view and projectile impact speed are shown in Figure 6.17. In Expt31, the projectile speed at impact was $\approx$ 19.2 m/s, and in Expt32, the projectile impact speed was $\approx$ 14.5 m/s. Both these experiments involve elongated PMMA/steel specimens and stress field information around the propagating crack tip was recorded using CGS interferometry. The field of view in Expt32 was located further downstream from the initial pre-crack tip. Figure 6.17(a) shows the crack length history for both these experiments. Crack length includes the length of the precrack which was $\approx 1''$. Again, the time of impact is considered to be the reference point on the time scale and hence $t = 0$ μs corresponds to the time at which the projectile impacts the specimen. As soon as the crack enters the field of view, in both the experiments, the crack length seems to increase fairly linearly with time with only occasional deviations, indicating that the crack is propagating at nearly the same speed. To determine the crack speed, a second order interpolating polynomial was obtained for every three successive points in the crack length history, which is then differentiated with time to give the crack speed for the midpoint. The crack speed history as the interface crack propagates along the PMMA/steel interface is shown in Figure 6.17(b) for the same two experiments. From the figure, we see that the interface crack propagates at a speed close to c_s as soon as it enters the field of view, but eventually accelerates to higher intersonic speeds. However, it was always found that the crack speed remains below $\sqrt{2}\,c_s$. Note that the projectile impact speed V in both the experiments shown in Figure 6.17 is substantially higher than that seen in Figure 6.5(b), and hence the observed higher crack speeds. Also the finite height of the specimen with resulting in wave reflections towards the crack tip might

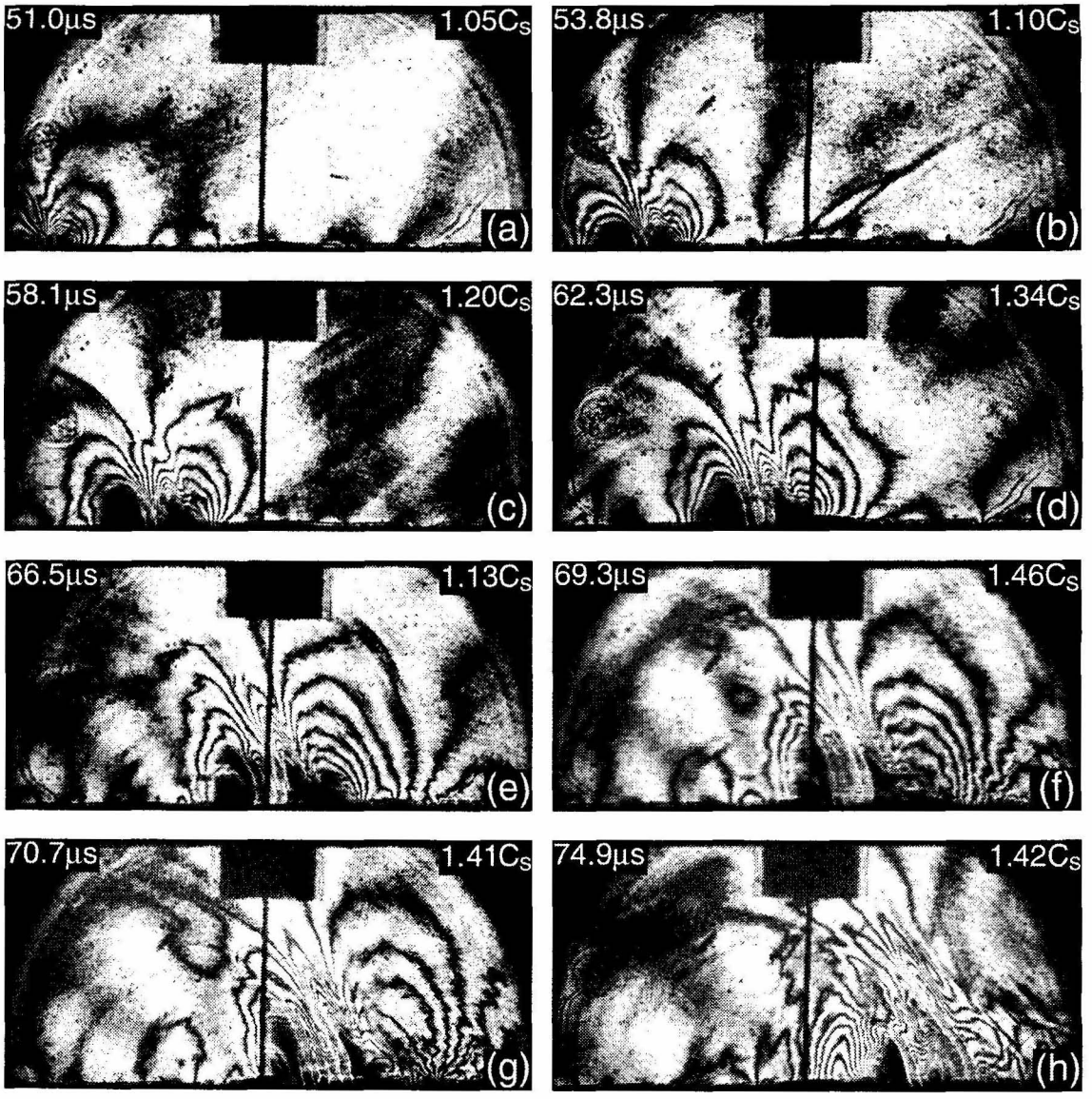

Figure 6.16: CGS fringe pattern around an intersonic crack propagating along a PMMA/Steel interface loaded under impact configuration **(b)**. Impact speed, $V = 19.2$ m/s. The semicircular field of view of 50 mm diameter is centered on the interface 15 mm ahead of the initial pre-crack tip.

be responsible for the increased fluctuations in crack speed. Error in measuring crack speed varied from ± 50 to ± 160 m/s. Error bars are shown on a few points at the beginning and the end of the data set.

6.1.6 Effect of Impact Speed on the Attainment of Intersonic Crack Speeds on a Bimaterial Interface

To determine the effect of impact speed on the attainment of intersonic crack speeds on a bimaterial interface, data is drawn from several experiments which were performed under nominally identical conditions, except for the impact speed. All these experiments involve PMMA/steel bimaterial specimens with an edge pre-crack and their dimensions are the same as those given in Figure 2.1 and were prepared following the procedures described in Chapter 2. All the specimens were loaded by impact, either by a cylindrical steel projectile fired from a high speed gas gun or by a drop weight tower. The loading configuration **(B)**, defined in Figure 6.1. Figure 6.18 shows the variation of interfacial crack speed with time for five such experiments, in two of which the bimaterial specimens were loaded at low impact speeds, 3 m/s and 4 m/s respectively using a drop weight tower and in the rest three the specimens were loaded at high impact speeds, 17 m/s, 20 m/s and 28 m/s respectively. Crack speed data was obtained from crack length history by the same procedure mentioned previously. As seen from the figure, for an impact speed of 3 m/s, the crack initiates at almost 90 μs after impact accelerates slowly and always remains subsonic. At a slightly higher impact speed of 4 m/s, the pre-crack is observed to initiate earlier, around 60 μs after impact, accelerates faster, but still remains subsonic. However, in all the gas gun loaded experiments involving high impact speeds, the pre-crack seems to initiate almost at the same time, around 30 μs after impact, then accelerates rapidly through the c_R and c_s of the polymer and becomes intersonic. It oscillates between c_s and $\sqrt{2}\,c_s$ for a while and remains within this range for an impact speed of 17 m/s. For higher impact speeds at 20 m/s and 28 m/s the intersonic crack is

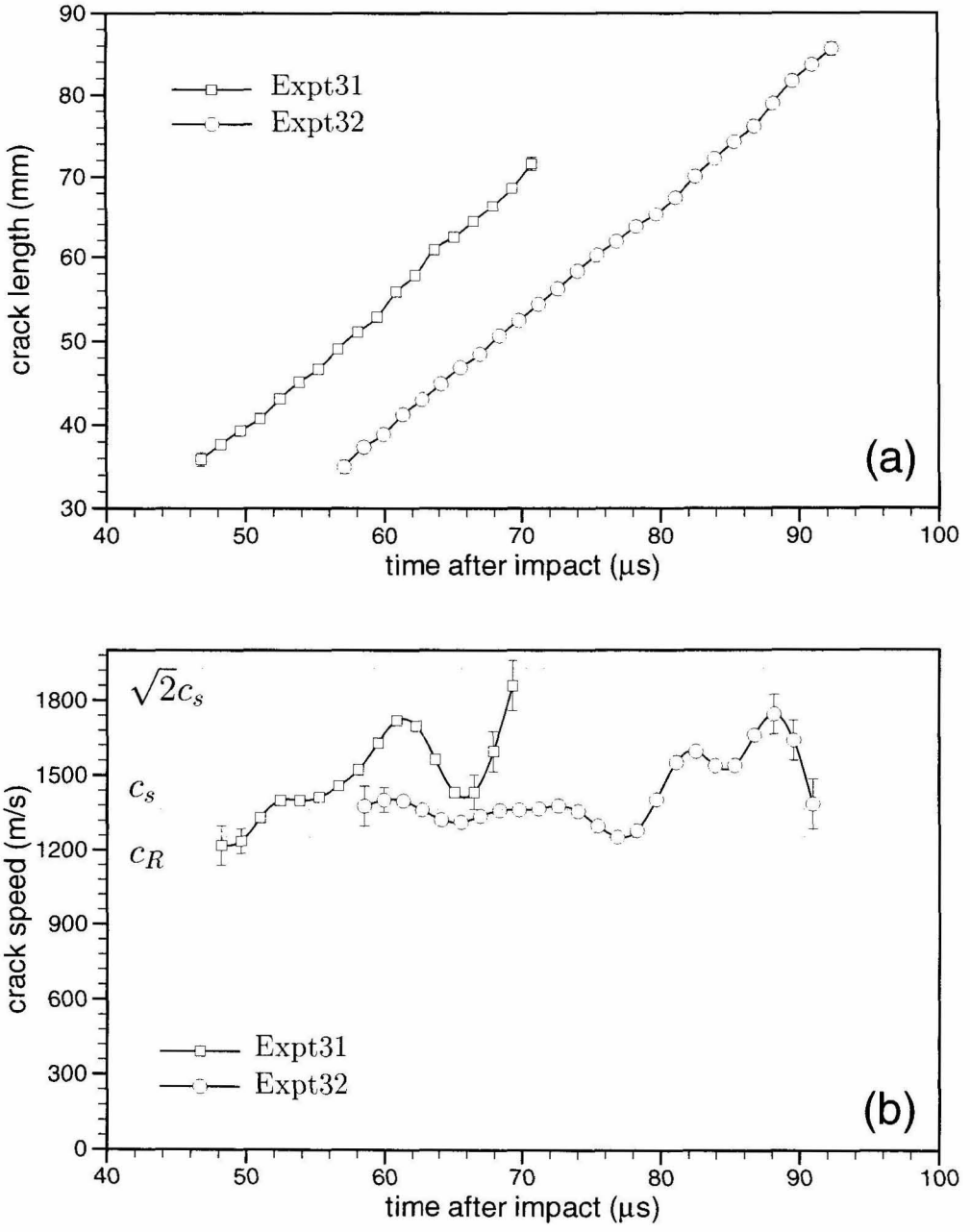

Figure 6.17: Intersonic crack growth along a PMMA/steel interface. **(a)** Time history of crack length. Crack length includes length of the pre-crack. **(b)** Evolution of crack speed v. In Expt31, projectile impact speed, $V = 19.2$ m/s and in Expt32, $V = 14.5$ m/s.

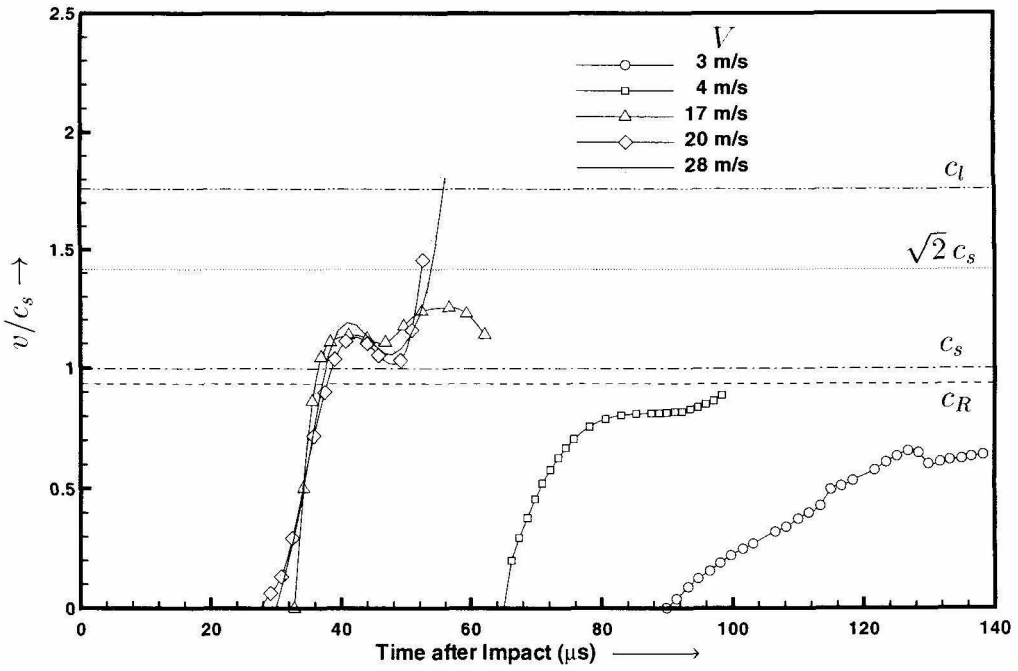

Figure 6.18: Crack growth along a PMMA/steel interface — Effect of impact speed on crack speed history. At an impact speed higher than a threshold value, the interface crack attains intersonic speeds. V is the projectile impact speed and v is the interface crack speed.

suddenly found to accelerate yet again to speeds above $\sqrt{2}\,c_s$ of the polymer and in the last case, almost seems to exceed c_l of the polymer and thus becoming supersonic with respect to it. However, it is interesting to note that in all the experiments where the crack has attained intersonic speeds, the pre-crack seems to initiate at 30 μs after impact. To understand this intriguing phenomenon, we look at the various features associated with the wave propagation from the impact site.

Figure 6.19 shows roughly the features associated with the wave propagation from the impact site. The primary longitudinal wave emanating from the impact site traverses through the metal half and reflects from the opposite free end and impinges back on the crack tip and loads it in intense shear around 30 μs after impact. Note that the loading history at the initial crack tip is primarily due to waves traveling in the metal half. The experimentally measured initiation time of 30 μs (see Figure 6.18)

after impact correlates very well with the time it takes a dilatational wave in steel to travel the height of the specimen, reflect off the bottom surface and reach the initial crack tip. Hence in all high speed impact experiments, at initiation the pre-crack is under highly shear dominated conditions. This conclusion is also supported by LAMBROS and ROSAKIS (1995a) who showed that subsonic crack growth achieved through gas gun experiments is predominantly shear dominated. The initiated shear crack under such circumstances is always found to attain intersonic speeds. In low impact speed (< 5 m/s) experiments, the stress field around the crack tip at 30 μs (when the dilatational wave in steel arrives at the crack tip after rebounding from the bottom surface) is shear dominated, but did not have high enough magnitude to initiate the crack. Hence it waits until the unloading wave from the lower right hand corner of the steel side reached the crack tip, some 70-80 μs after impact & loads the tip in an opening mode. Now, a lower magnitude of the stress field is enough to initiate the crack. In such a case, it was found that the interfacial crack always remains subsonic. Hence, it appears that one of the conditions under which a loaded pre-crack becomes intersonic is if it is loaded under intense shear.

6.1.7 Intersonic Crack Growth on a Bimaterial Interface under Loading Configuration (C)

It was mentioned apriori, that under loading configuration **(C)**, the edge precrack on a bimaterial interface initiated and propagated at intersonic speeds along the interface. Figure 6.20 shows a sequence of 8 isochromatic fringe patterns depicting such an event. Here an edge precrack, 1″ long, on a Homalite/aluminum interface was loaded by projectile impact under loading configuration **(C)**. The projectile impact speed, V was 20.7 m/s and the semicircular field of view of 50 mm diameter was centered on the interface 45 mm ahead of the initial precrack tip. Again, we see that the interface crack attains intersonic speeds almost immediately after initiation. However, the shape of the fringe pattern around the intersonic interfacial crack tip,

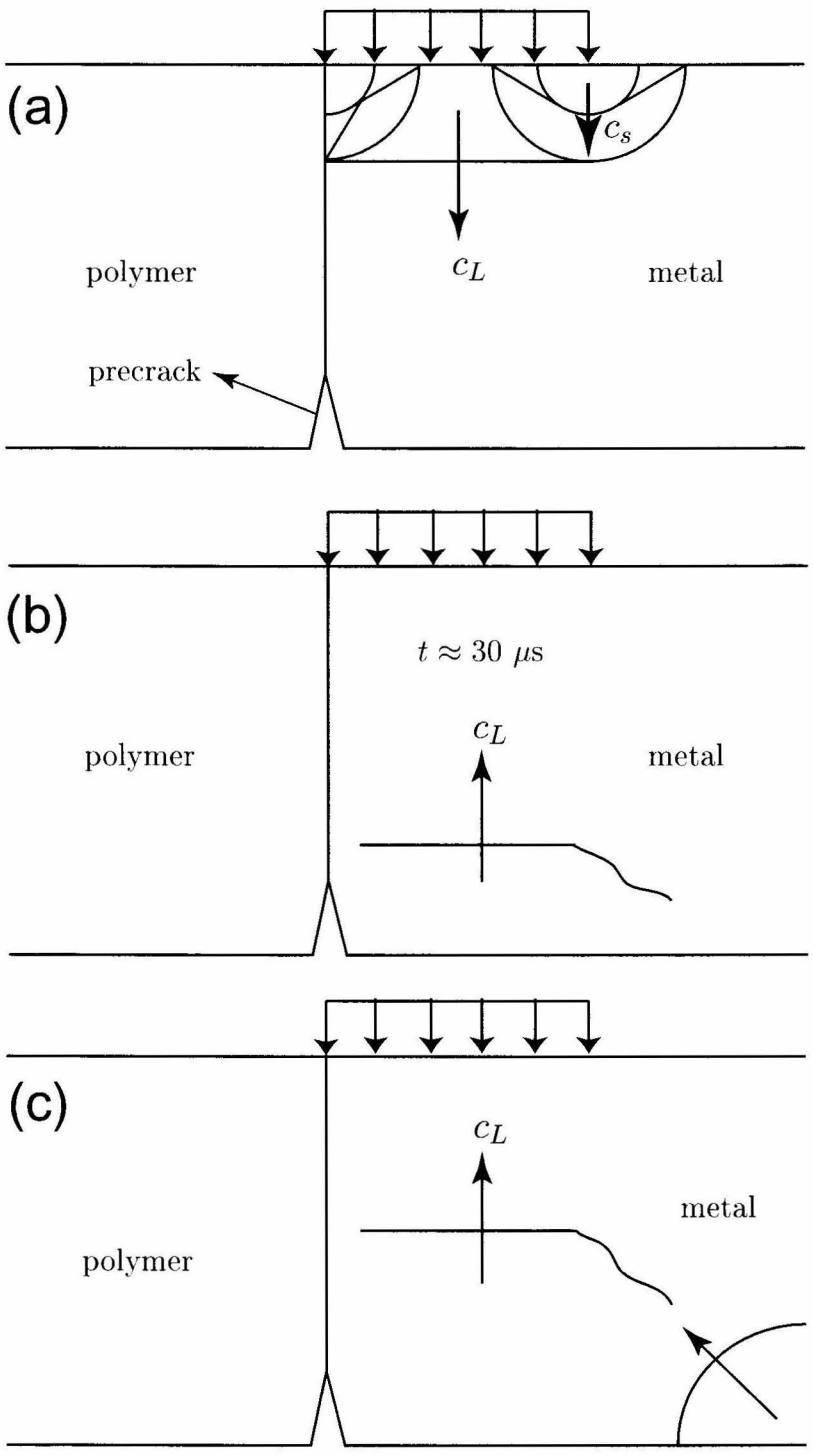

Figure 6.19: An illustration showing roughly the propagation of loading waves in the metal half of the bimaterial specimen after impact. Interfacial cracks that attain intersonic speeds are highly shear dominated at initiation.

differs substantially from that achieved under loading configuration **(B)**. The fringe pattern appears lot more squeezed horizontally and the crack tip fields appear to be dominant over a shorter region, both in front and behind the propagating crack tip. This difference in the shape of the isochromatic fringe pattern (and thus the near-tip stress field) around the intersonic interfacial crack tip achieved from two different loading configurations **(B)** and **(C)** can be explained on two counts. First, with the loading configuration **(C)**, the interfacial crack initiates and propagates with the initial loading pulse itself, which is still very strong (not enough time for geometric attenuation) as seen from the number of fringes due to the loading pulse in front of the crack tip. Also the stress induced due to the loading pulse substantially affects the crack tip stress field (primarily with regard to the direct stress parallel to the interface), thus resulting in the squeezing of the fringe pattern both in front and behind the crack tip. Second, the nature of loading is such that the precrack tip is subjected to a strong shearing component, but a compressive opening component. This results in crack face contact, and the entire rupture occurs primarily in shear. This is unlike the scenario from loading configuration **(B)** where the loading is such as to open up the crack as it propagates, rather than tending it to close. Hence, in that case we saw the intersonic crack propagate with a finite traction free zone behind the tip and any crack face frictional contact was primarily due to the presence of Rayleigh singularity. However, in the loading configuration **(C)**, the crack face frictional contact is aided not only by the presence of a Rayleigh singularity, but also due to the nature of loading itself. Hence, with this loading configuration, the crack face frictional contact zone starts right at the intersonic crack tip. Also, since the frictional contact zone starts right at the crack tip, the Mach wave radiated from the crack tip is no longer sharp, as was in the case of loading configuration **(B)**, but is more diffuse and spread out over a finite width. As the intersonic crack propagates along the interface, no dramatic changes in the isochromatic fringe pattern near the crack tip are visible, indicating that the intersonic crack propagates with a finite crack frictional contact zone behind it, throughout the field of view. Also, from

Figure 6.20(h) we can see the Rayleigh singularity separated a finite distance from the intersonic crack tip, and we see a series of fringes parallel to the interface joining these two features. These fringes are similar to those observed in the isochromatic fringe patterns obtained with loading configuration **(B)** within the frictional contact zone. Hence the essential features of the subsonic/intersonic transition of an interface crack is strongly dependent on the "mixity" of the applied dynamic loading.

Typical crack length and crack speed histories obtained from two different experiments, both involving interfacial crack initiation and propagation from an edge precrack loaded under configuration **(C)** are shown in Figure 6.21. In Expt40, the specimen thickness was $3/16''$, whereas in Expt42, the specimen thickness was $1/4''$. However, the projectile impact speed V in both experiments was the same at ≈ 20.7 m/s. As seen from Figure 6.20(a), the crack length of the interfacial crack increases almost linearly with time as it propagates through the entire field of view. Again, crack length includes the length of the precrack which was $\approx 1''$. Figure 6.20(a) gives the crack speed history obtained by successive three point parabolic fit to the length history and its differentiation to give the crack speed for the mid point. The crack speed history, thus obtained, is shown in Figure 6.20(b) for both these experiments. It can be seen that the crack speed remains fairly constant, oscillating between c_s and $1.3\,c_s$. Thus it appears that specimen thickness doesn't play much of a role in the propagation behavior of the interface crack. Also the propagation behavior was similar to that obtained with loading configuration **(B)**, though at almost half the impact speed as was used in these experiments. However, this near constant speed interfacial crack growth between c_s and $1.3\,c_s$ appears to be some kind of a universal feature for certain ranges of interface strengths and intensities of applied load. As such, it may be reflected in the nature of the intersonic interfacial crack tip fields.

Figure 6.22 compares two isochromatic fringe patterns around an intersonic crack propagating along a Homalite/aluminum interface at approximately the same crack speed, but differing in the loading configuration leading to the initiation of these

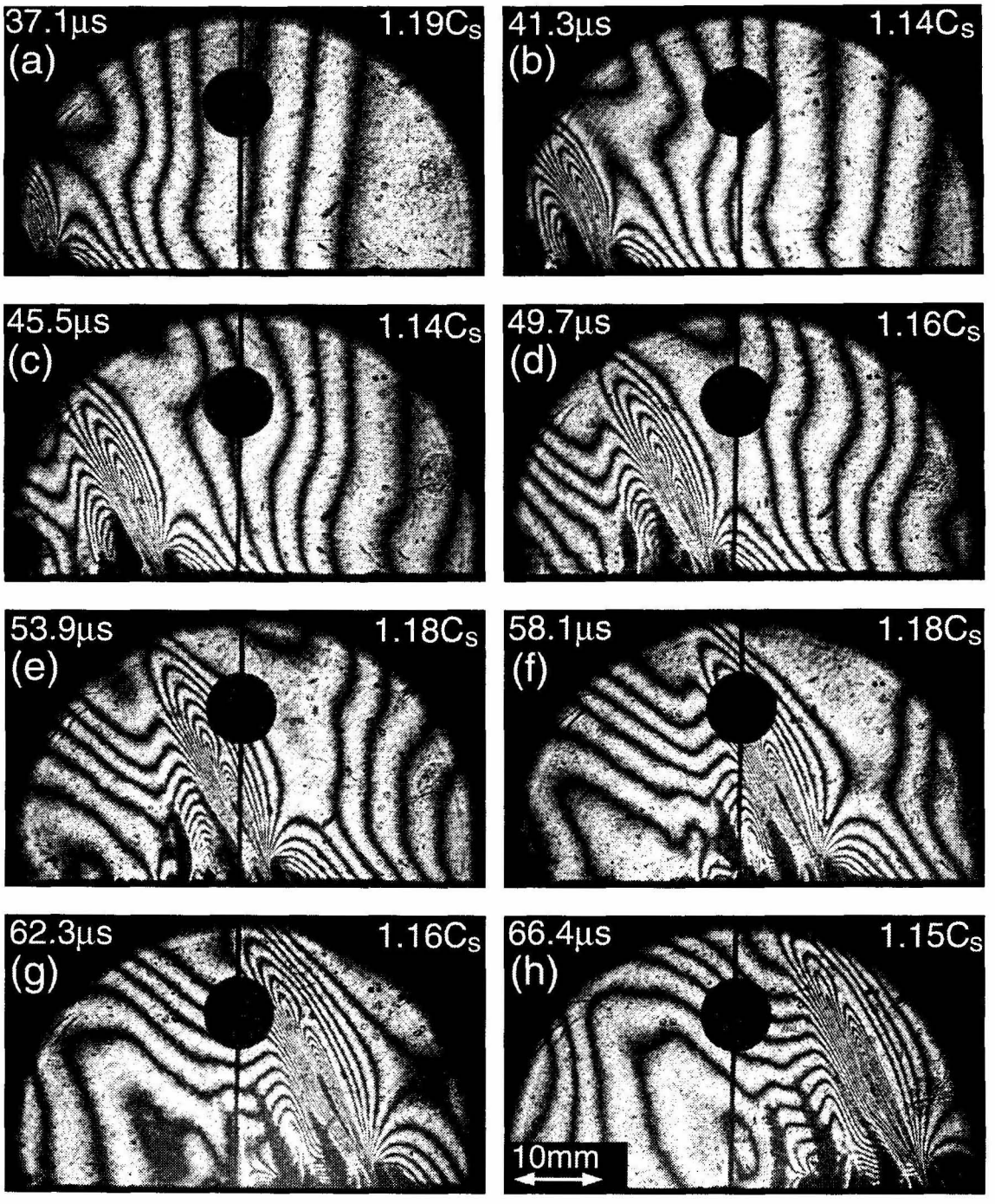

Figure 6.20: Isochromatic fringe pattern around an intersonic crack propagating along a Homalite/aluminum interface loaded under impact configuration **(c)**. Projectile impact speed, $V = 20.7$ m/s. The semicircular field of view of 50 mm diameter is centered on the interface 45 mm ahead of the initial precrack tip.

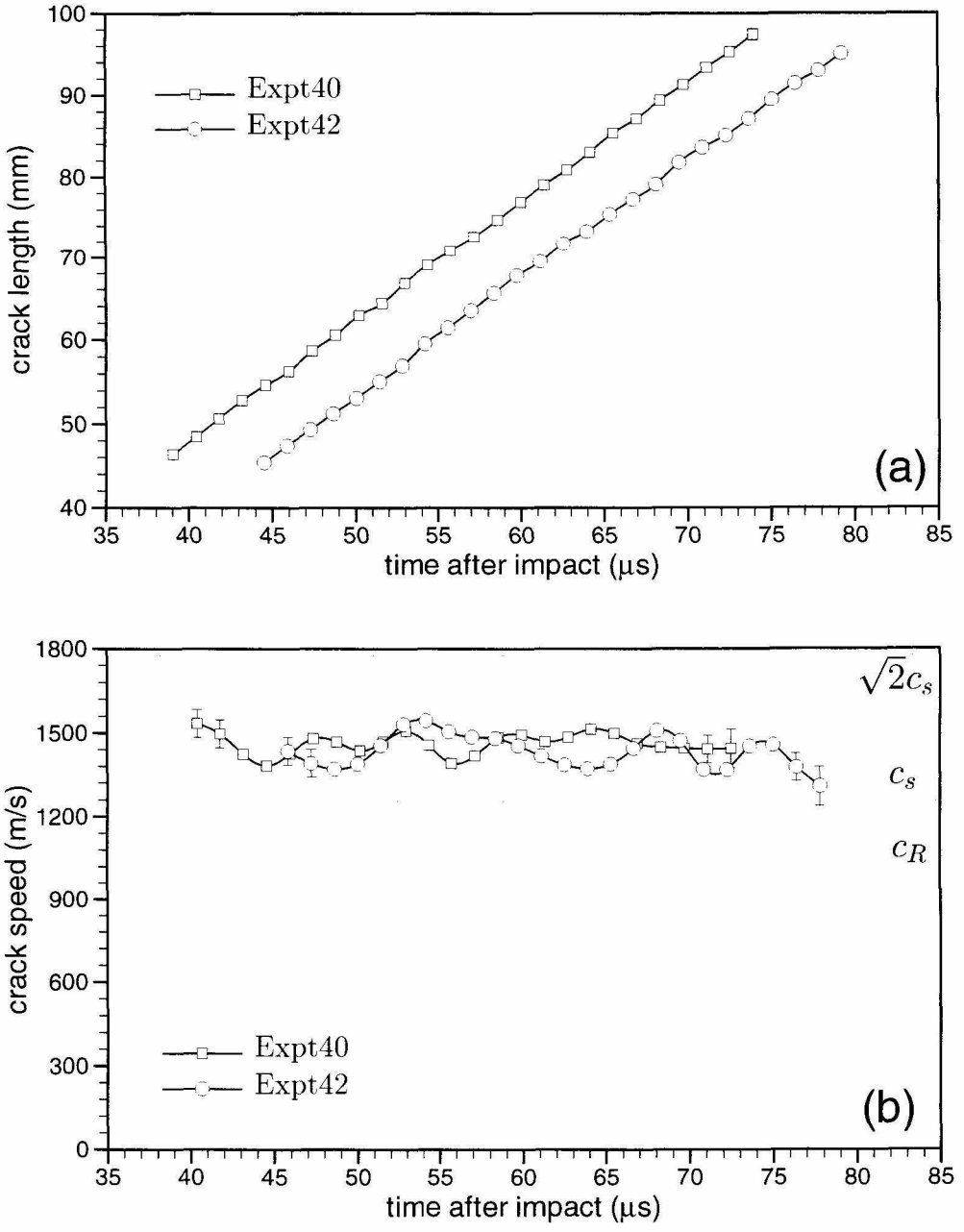

Figure 6.21: Intersonic crack growth along a Homalite/aluminum interface loaded under impact configuration **(C)**. **(a)** Time history of crack length. Crack length includes length of the precrack. **(b)** Evolution of crack speed v. In both Expt40 and Expt42 the projectile impact speed, $V = 20.7$ m/s. However, specimen thickness in Expt40 was $3/16''$ and in Expt42 it was $1/4''$.

cracks. In Figure 6.22(a), the interfacial crack was initiated from an edge precrack under loading configuration **(B)**, where as in figure 6.22(b), the interfacial crack was initiated from an edge precrack under loading configuration **(C)**. The fringe pattern around the crack tip in both these cases shows a marked contrast. In Figure 6.22(a), we have an intersonic crack with smooth and rounded fringes in front of the crack tip, a sharp Mach wave radiating from the tip and a second Mach wave, again very sharp radiating from the interface ≈ 2 mm behind the crack tip. As was conjectured before, the crack here is propagating with a finite traction free zone behind the tip followed by an infinitesimal frictional contact zone. The Rayleigh singularity trailing behind is also clearly distinguishable. In Figure 6.22(b) we see an intersonic crack around which the fringe pattern has been compressed severely in the direction parallel to the interface, with both the front lobe and the back lobe being shortened. However, the fringe pattern is elongated along the direction perpendicular to the interface. This distortion is probably due to the stress field induced by the loading pulse propagating through the Homalite. In Figure 6.22(a), the loading waves are transmitted into the Homalite half indirectly through the interface and hence the crack tip fields are not so affected by the stresses induced by the loading pulse. Also in figure 6.22(b) we conjecture that the crack face frictional contact zone starts right at the crack tip and extends all the way up to the trailing Rayleigh singularity, as indicated by the numerous fringes parallel to the interface. This also results in the Mach wave emanating from the crack tip in not being very sharp.

6.1.8 Intersonic Crack Growth on Inclined Interfaces

To study the effect of an inclined interface on the intersonic crack propagation behavior, a few experiments were performed with the type of specimens as illustrated in figure 6.23. Here the interface is inclined at an angle ω to the horizontal (direction of loading). Two different ω, 15° and 30° were considered. Again, an edge precrack of $1''$ length was loaded by impacting the specimen with a cylindrical steel projectile under

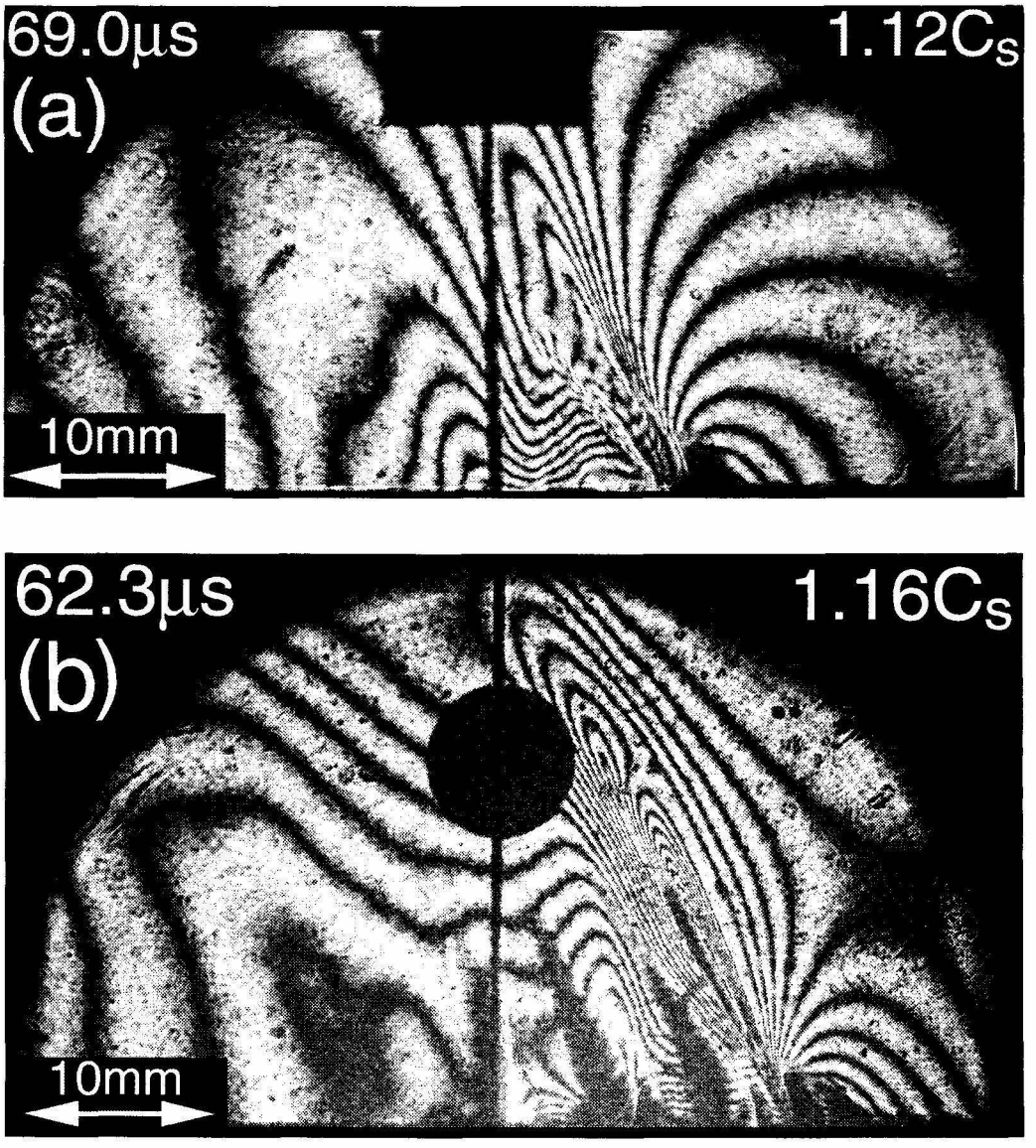

Figure 6.22: Intersonic crack growth on a Homalite/aluminum interface. **(a)** Isochromatic fringe pattern resulting from loading configuration **(B)**. **(b)** Isochromatic fringe pattern resulting from loading configuration **(C)**.

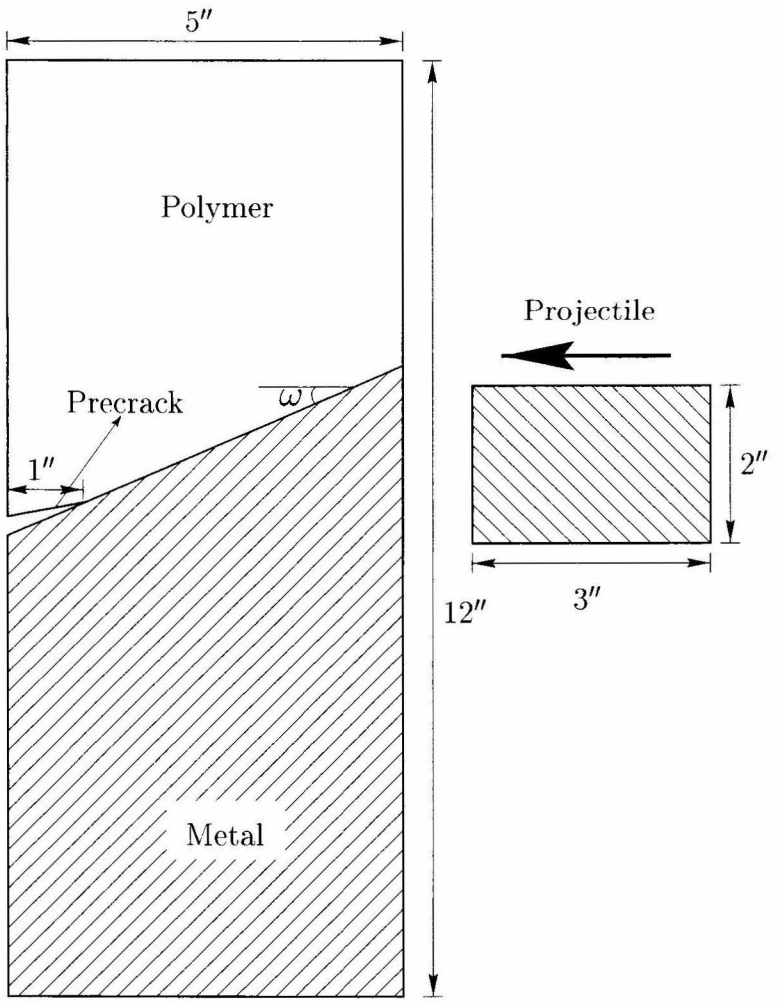

Figure 6.23: Bimaterial specimen with an inclined interface containing an edge precrack subjected to projectile impact loading. Two different angles of inclination, $\omega = 15^{\circ}, 30^{\circ}$ were considered.

loading configuration **(B)**. PMMA was chosen to be the polymer half and aluminum was chosen to be the metal half and hence CGS interferometry was used for mapping the stress field information around the propagating crack tip. Specimen thickness was $3/8''$.

Figure 6.24 shows a sequence of six CGS interferograms around the propagating interfacial crack tip on a PMMA/aluminum interface inclined at $\omega = 15^{\circ}$ with the horizontal. Projectile impact speed V was 18 m/s and the field of view of 50 mm

diameter was centered on the interface 35 mm from the initial precrack tip. We see the interfacial crack propagates at intersonic speeds, only slightly above c_s. Again the features observed in the CGS interferograms during subsonic/intersonic transition in Figure 6.16 are all visible here – the bending of the fringes in the front lobe towards the interface, caused by the sliding of the interfacial crack tip ahead of the Rayleigh singularity and its eventual meeting with the interface, clearly identifying the location of the intersonic crack tip. Again, as mentioned before, CGS interferometry suffers from light loss problems due to the increased number of optical elements at which the light gets deflected, resulting in dark spots surrounding zones of intense deformation and hence the fringes very close to the crack tip are not very clearly visible.

Crack length and crack speed histories obtained from two experiments involving intersonic interfacial crack growth along PMMA/aluminum interfaces, one inclined at $\omega = 15^{\circ}$ and another inclined at $\omega = 30^{\circ}$, under loading configuration **(B)** is shown in Figure 6.25. Both these experiments were performed under similar conditions with the same projectile impact speed, $V = 20$ m/s, and they differ only in the inclination ω of the interface. From figure 6.25(a), we see that the crack length increases almost linearly in both these experiments, though their slopes differ slightly indicating that the interface crack on a $\omega = 15^{\circ}$ interface propagates slightly faster than the one on a $\omega = 30^{\circ}$ interface. The same is reflected in the crack speed history shown in figure 6.25(b), where we see the interface crack on a $\omega = 15^{\circ}$ interface was definitely propagating at intersonic speeds ranging from c_s to $1.3\,c_s$, whereas the interface crack on a $\omega = 30^{\circ}$ interface, the crack propagates at speeds that appear to be merely super-Rayleigh, though occasionally it becomes intersonic. This behavior of the crack speed history shows that an interface crack on an inclined interface, though can achieve intersonic speeds, has its speed depressed as it has to climb a steeper and steeper slope and it is definitely possible at a sufficiently high ω, the interface crack might be merely subsonic. The effect of the inclination of the interface to the direction of loading, on the interface crack propagation behavior is a very interesting topic and

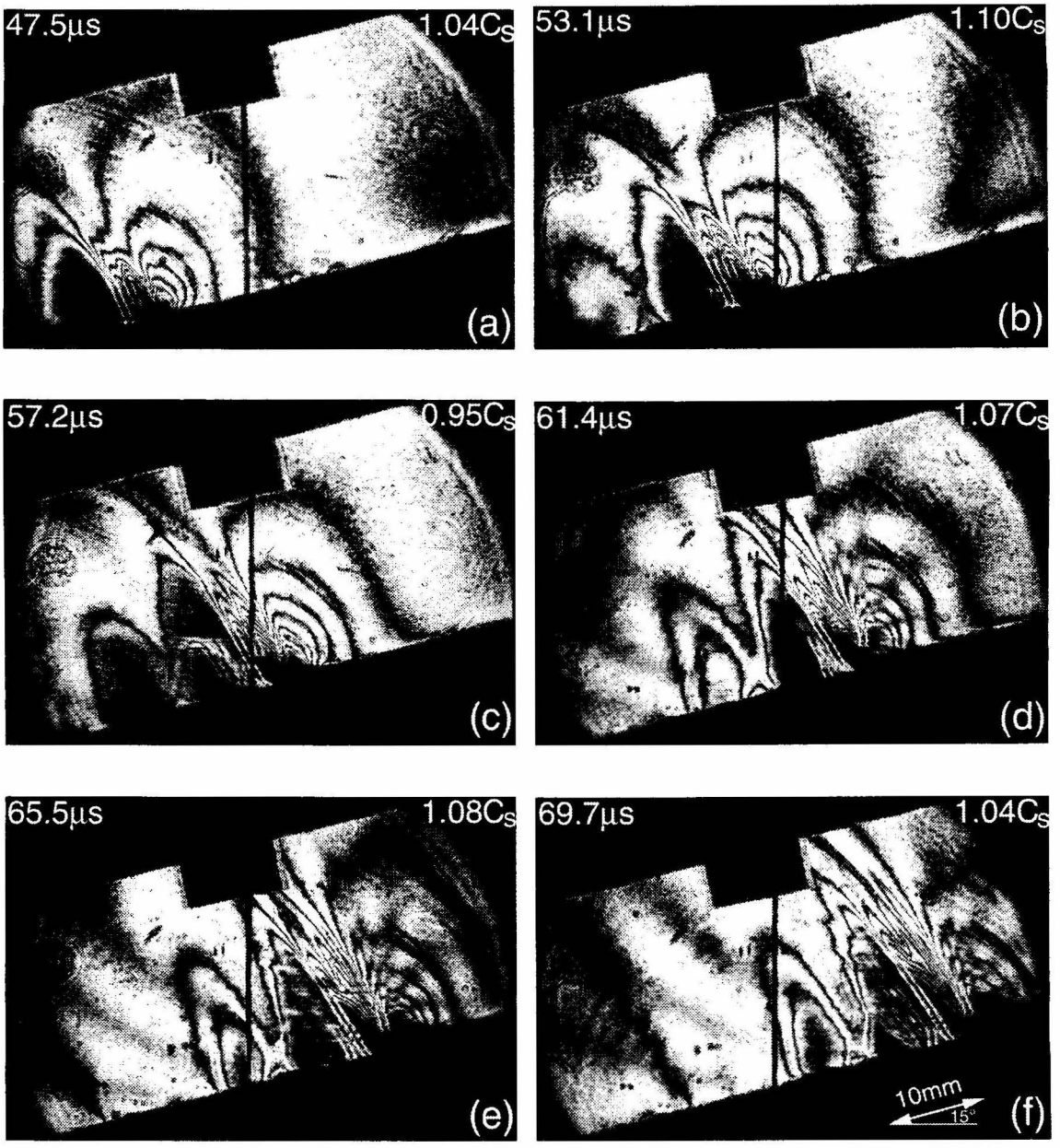

Figure 6.24: CGS fringe pattern around an intersonic crack propagating along a PMMA/Al interface, inclined at $\omega = 15^{\circ}$ to the horizontal. Projectile impact speed, $V = 18$ m/s. The field of view of 50 mm diameter is centered on the interface 35 mm ahead of the initial precrack tip.

must be studied further, as in many real situations the stress wave loading on an interface is more likely to be inclined at an angle.

6.2 Supersonic Crack Growth Along Bimaterial Interfaces

Even though most of the interfacial cracks under various loading configurations and specimen geometries discussed here were found to propagate at a speed less than $\sqrt{2}\,c_s$ of the more compliant solid, it is certainly possible to achieve higher interfacial crack speeds, if the crack were initiated from a pre-notch instead of a precrack or if the impact speed were high enough or if the interface bond strength were low enough. Experiments were conducted on PMMA/Al and PMMA/steel bimaterial systems with an initial edge pre-notch which was loaded by projectile impact at relatively high impact speeds of 18.6 m/s. Otherwise, these experiments employed the same specimen geometry as in Figure 6.1 and the edge pre-notch was loaded under load configuration **(B)**. In such cases, the interfacial crack initiating from the pre-notch was found to propagate at speeds greater than $\sqrt{2}\,c_s$ of the polymer. Figure 6.26 shows a selected sequence of 6 CGS fringe patterns from such an experiment conducted on a PMMA/Al bimaterial specimen. Figure 6.26(d) shows that at around 47 μs after impact, the interfacial crack suddenly accelerates to speeds beyond $\sqrt{2}\,c_s$ of PMMA. Figure 6.26(e) and Figure 6.26(f) show that the crack continues to accelerate, exceeding even the longitudinal wave speed of PMMA. The CGS interferograms become very complicated, and the dark spots around the crack tip region obscure a clear observation as to whether a longitudinal Mach wave is being radiated from the crack tip. In any case, it is unlikely that such a Mach wave would have radiated over a sufficient distance to be clearly visible within our narrow window of observation.

The crack tip speed history for the experiment discussed in the previous paragraph as well for another experiment involving the initiation of an interface crack from an edge pre-notch on a PMMA/steel interface again under loading configuration **(B)** is shown in Figure 6.27. In both these experiments, the projectile impact speed was

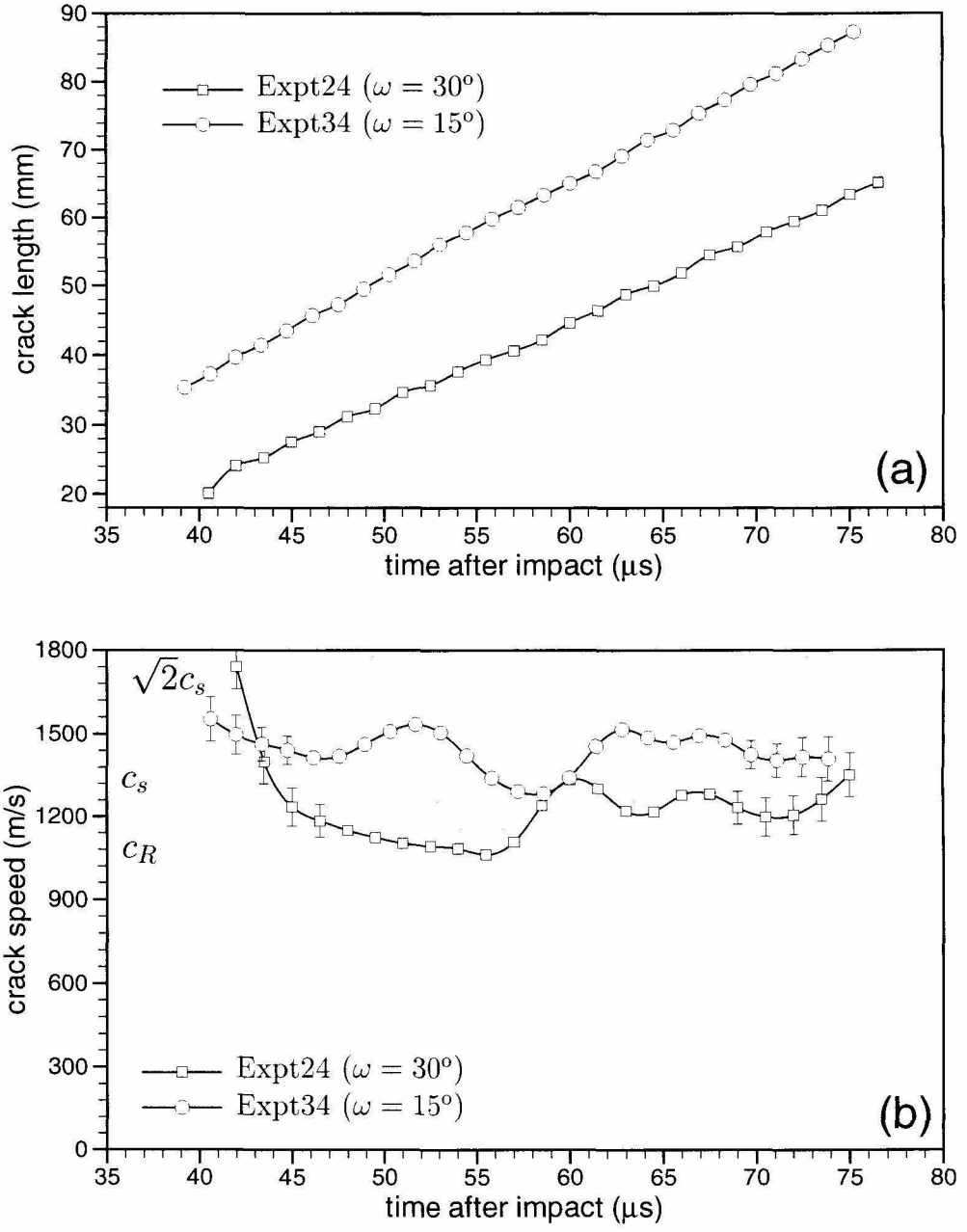

Figure 6.25: Intersonic crack growth on a PMMA/Al interface inclined at an angle ω to the horizontal. **(a)** Time history of crack length. Crack length includes length of the precrack. **(b)** Evolution of crack speed v. In both Expt24 and Expt34 the projectile impact speed, $V = 18$ m/s. However, the angle of inclination of the interface ω was 30^o in Expt24, whereas it was 15^o in Expt34.

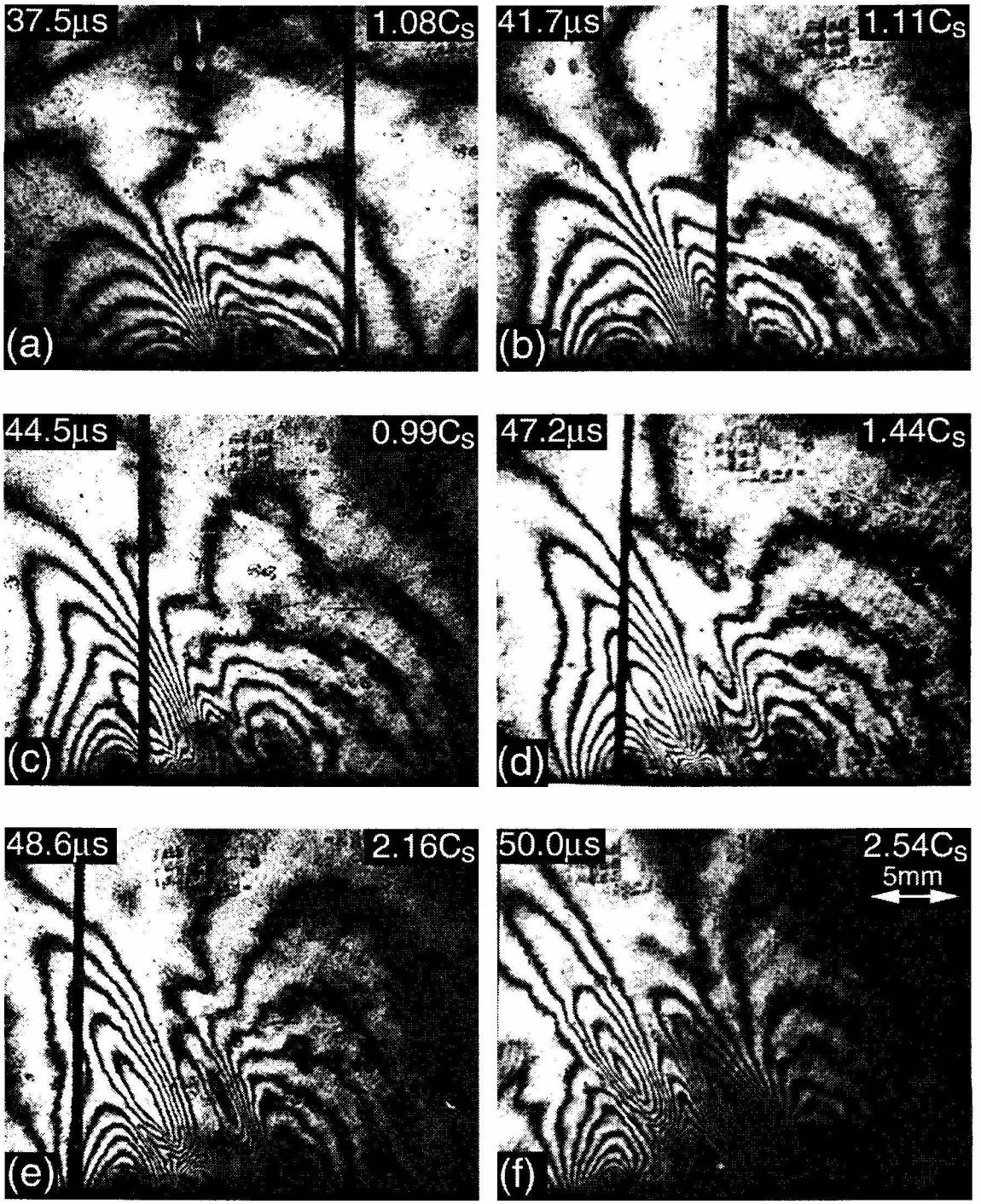

Figure 6.26: CGS fringe pattern around an interfacial crack tip propagating along a PMMA/Aluminum interface. The crack after remaining intersonic for a while, suddenly accelerates to speeds that are supersonic with respect to PMMA. Impact speed, $V = 18.6$ m/s.

≈ 18.6 m/s. It is found that the crack propagates for a while between c_s and $\sqrt{2}\,c_s$ of PMMA, before accelerating further in a rapid and highly unstable fashion. Terminal crack tip speeds in these cases have exceeded the longitudinal wave speed of aluminum, thus becoming supersonic with respect to it. To the author's knowledge this is the first observation of supersonic crack growth along a bimaterial interface. Note that the terminal crack speed on the PMMA/aluminum interface has even approached the c_R of the metal (aluminum). Such high interfacial crack tip speeds were also observed by WU and GUPTA (2000) who found that microcracks along the interface of niobium-sapphire thin film structures when loaded by laser generated stress pulses, propagated at speeds up to c_R of Sapphire (stiffer medium). In the current study, the issue of supersonic crack growth along a bimaterial interface was not dealt with in detail and further careful studies are needed to elucidate the transition events and the structure of the near-tip fields. Moreover, the terminal speed attainable for a crack on a bimaterial interface is no closer to being yet resolved.

The primary goal of the experiments discussed in this chapter was to carefully study the intersonic speed regime of crack growth along a bimaterial interface. An attempt was made to give clear physical arguments as to the nature of subsonic/intersonic transition. Also, the effect of differing specimen geometry, loading configurations, different bimaterial systems, inclination of the interface to the loading direction and the initiation site being a pre-notch or precrack on the subsonic/intersonic transition and the crack propagation behavior was investigated. To explain some of the features related to the subsonic/intersonic transition and intersonic crack growth behavior an asymptotic analytical model is developed in the next chapter to obtain the near-tip fields around an intersonic crack on an elastic/rigid interface with a detached contact zone.

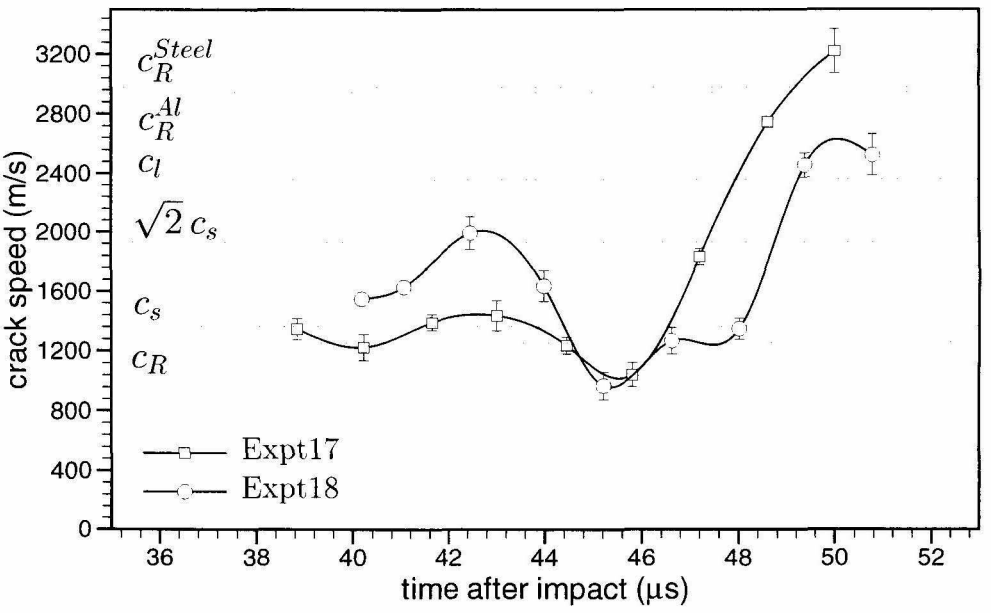

Figure 6.27: Supersonic crack growth along a PMMA/metal interface — Time history of crack speed. Expt17 involves a PMMA/Al interface and Expt18 involves a PMMA/steel interface. In both experiments, projectile impact speed was 18.6 m/s and the propagating interface crack initiated from a starter notch.

Nomenclature

(η_1, η_2)	Cartesian coordinates centered at the crack tip
α	inclination of the Mach wave emanating from the front end of the contact zone
β	inclination of the Mach wave emanating from the crack tip
ω	inclination of the interface to the horizontal
ψ	mode mixity
ξ	Mach wave angle
c_l	longitudinal wave speed
c_R	Rayleigh wave speed
c_s	shear wave speed
L	reference length
l_1	length of the traction free zone behind the crack tip
l_2	length of the crack face contact zone behind the tip
V	projectile impact speed
v	crack speed

Bibliography

ADAMS, G. G. (**1998**), Dynamic Instabilities in the Sliding of Two-Layered Elastic Half-Spaces, *Journal of Tribology*, **120**(2), pp. 289–295.

ANDREWS, D. J. and BEN-ZION, Y. (**1997**), Wrinkle-like Slip Pulse on a Fault Between Different Materials, *Journal of Geophysical Research*, **102**(B1), pp. 553–571.

BREITENFELD, M. S. and GEUBELLE, P. H. (**1998**), Numerical Analysis of Dynamic Debonding under 2-D In-Plane and 3-D Loading, *International Journal of Fracture*, **93**(1-4), pp. 13–38.

FREUND, L. B. (**1973**), The Response of an Elastic Solid to Nonuniformly Moving Surface Loads, *Journal of Applied Mechanics*, **40**, pp. 699–704.

HE, M. Y., BARTLETT, A., EVANS, A. G., and HUTCHINSON, J. W. (**1991**), Kinking of a Crack out of an Interface – Role of Inplane Stress, *Journal of the American Ceramics Society*, **74**(4), pp. 767–771.

HE, M. Y. and HUTCHINSON, J. W. (**1989**a), Crack Deflection at an Interface Between Dissimilar Elastic-Materials, *International Journal of Solids and Structures*, **25**(9), pp. 1053–1067.

HE, M. Y. and HUTCHINSON, J. W. (**1989**b), Kinking of a Crack out of an Interface, *Journal of Applied Mechanics*, **56**, pp. 270–278.

HUTCHINSON, J. W. and SUO, Z. (**1992**), Mixed-Mode Cracking in Layered Materials, *Advances in Applied Mechanics*, **29**, pp. 63–191.

LAMBROS, J. and ROSAKIS, A. J. (**1995**a), Development of a Dynamic Decohesion Criterion for Subsonic Fracture of the Interface Between Two Dissimilar Materials, *Proceedings of the Royal Society of London*, **A451**(1943), pp. 711–736.

LAMBROS, J. and ROSAKIS, A. J. (**1995**b), Shear Dominated Transonic Interfacial Crack Growth in a Bimaterial. 1. Experimental Observations, *Journal of the Mechanics and Physics of Solids*, **43**(2), pp. 169–188.

LIECHTI, K. M. and CHAI, Y. S. (**1991**), Biaxial Loading Experiments for Determining Interfacial Fracture Toughness, *Journal of Applied Mechanics*, **58**(3), pp. 680–687.

LIU, C., LAMBROS, J., and ROSAKIS, A. J. (**1993**), Highly Transient Elastodynamic Crack Growth in a Bimaterial Interface - Higher Order Asymptotic Analysis and Optical Experiments, *Journal of the Mechanics and Physics of Solids*, **41**(12), pp. 1857–1954.

NEEDLEMAN, A. and ROSAKIS, A. J. (**1999**), The Effect of Bond Strength and Loading Rate on the Conditions Governing the Attainment of Intersonic Crack Growth Along Interfaces, *Journal of the Mechanics and Physics of Solids*, **47**(12), pp. 2411–2449.

SCHALLAMACH, A. (**1971**), How Does Rubber Slide?, *Wear*, **17**, pp. 301–312.

SINGH, R. P., LAMBROS, J., SHUKLA, A., and ROSAKIS, A. J. (**1997**), Investigation of the Mechanics of Intersonic Crack Propagation Along a Bimaterial Interface Using Coherent Gradient Sensing and Photoelasticity, *Proceedings of the Royal Society of London*, **A453**(1967), pp. 2649–2667.

SINGH, R. P. and SHUKLA, A. (**1996**a), Characterization of Isochromatic Fringe Patterns for a Dynamically Propagating Interface Crack, *International Journal of Fracture*, **76**(4), pp. 293–310.

SINGH, R. P. and SHUKLA, A. (**1996**b), Subsonic and Intersonic Crack Growth Along a Bimaterial Interface, *Journal of Applied Mechanics*, **63**(4), pp. 919–924.

WU, J. X. and GUPTA, V. (**2000**), Observations of Transonic Crack Velocity at a Metal/Ceramic Interface, *Journal of the Mechanics and Physics of Solids*, **48**(3), pp. 609–619.

XU, L. M. and TIPPUR, H. V. (**1995**), Fracture Parameters for Interfacial Cracks - An Experimental-Finite Element Study of Crack-Tip Fields and Crack Initiation Toughness, *International Journal of Fracture*, **71**(4), pp. 345–363.

Chapter 7

A Crack Face Traction Free Zone and Frictional Contact Model

In the last chapter, it was argued based on experimental evidence that under certain loading configurations (like **(B)** of Fig. 6.1), *i.e.*, under certain initiation "mixities", intersonic crack growth along a bimaterial interface is accompanied by the presence of a finite traction free zone (opening) behind the tip followed by a finite zone of crack face frictional contact. This is unlike the scenario that was put forth by LAMBROS and ROSAKIS (1995); SINGH and SHUKLA (1996), where it was conjectured that the finite zone of crack face frictional contact begins right from the crack tip (under the same loading configuration **(B)**). With much higher resolution isochromatic fringe patterns around the propagating intersonic crack tip obtained in our experiments, we have shown that this may not the case and that the crack face frictional contact zone appears to be detached from the intersonic crack tip. Moreover, strong physical arguments were presented in the last chapter as to the possibility of such a detached contact zone behind the tip and some numerical evidence from literature was also presented, where such detached contact zones were observed. However, it must be mentioned that experimental evidence strongly indicates that such occurrences depend to a large extent on the loading configuration and may even be transient phenomena associated with the subsonic/intersonic transition of the interface crack

speed.

In the current chapter, an attempt is made at developing a asymptotic analytical model which can account for intersonic interfacial crack growth with a finite traction free zone behind the tip followed by a crack face frictional contact zone. At first, it is shown that the bimaterial systems investigated in our experiments (polymer/metal systems) can be approximated closely by a corresponding polymer/rigid bimaterial system, in analyzing intersonic crack growth along the interface. Yet another approximation is made that the intersonic crack tip fields are stationary with respect to an observer moving with the crack tip (steady-state). The governing equations of elastodynamics are solved with the appropriate boundary conditions and the dominant near-tip fields are obtained in closed form. The analytical results are compared against experimental observations and comments are made on the merits of the model. Owing to the twin assumptions employed, that of a mathematically sharp crack tip and the elastic/rigid approximation, issues related to energy transfer across the interface and fracture energy cannot be tackled by the current model. Finally, it is shown that the bimaterial systems considered in our experiments cannot sustain interfacial waves - both Stoneley waves on a perfectly bonded interface as well as generalized Rayleigh waves on a non-bonded interface under frictional contact. A brief summary of the past analytical solutions to intersonic crack growth problems along a bimaterial interface was presented in Chapter 1 (Section 1.3.3).

7.1 Elastic/Rigid Approximation

For a stationary or subsonic crack on a bimaterial interface, the mismatch in elastic properties along the interface, affects the spatial distribution of the near tip fields only through a single parameter, the second Dundurs' parameter, β, which is a function of the material properties of both the materials as well as the crack tip speed (see (1.19) and (1.33)) (HUTCHINSON and SUO, 1992; YANG *et al.*, 1991). However, once the interfacial crack attains intersonic speeds, there doesn't appear to be any such

single parameter which takes into account the effect, mismatch in elastic properties across the interface has on the spatial distribution of the near-tip fields. Hence we justify the elastic/rigid approximation in our mathematical model, by showing that the traction distribution along the interface ahead of the intersonic crack tip, for the polymer/metal bimaterial systems used in our experiments, differs very little from that on a corresponding polymer/rigid interface.

YU and YANG (1995); HUANG *et al.* (1996) obtained the dominant near-tip fields for a steady state intersonic crack propagating along a bimaterial interface. They showed that the traction on the interface ahead of the tip has a universal distribution governed by a single parameter, the crack tip stress singularity, q. The crack tip stress singularity for an intersonic interfacial crack can be real, complex or pure imaginary depending on the material properties of the two bimaterial halves and the crack speed. The general form of the traction distribution ahead of the tip can be deduced from (1.38) and (1.39). To show that the traction distribution ahead of an intersonic crack tip on a polymer/metal bimaterial (used in our experiments) interface is very close to that ahead of an intersonic crack tip on a corresponding polymer/rigid bimaterial interface, we compare the variation of the dominant crack tip stress singularity q (in the intersonic regime) for both these systems. With regard to (1.38) and (1.39) q is the greater of p_1 and p_2 when they are real, q is the real part of p_1 when they are complex conjugates and $q = 0$ when they are pure imaginary. Note that the intersonic regime with a polymer/rigid bimaterial interface is defined to lie between c_s and c_l of the polymer. Within this regime, the dominant crack tip stress singularity for an intersonic crack on a polymer/metal bimaterial interface is either real or complex and that on a polymer/rigid bimaterial interface is always real.

Figure 7.1 compares the variation of q with crack speed v for an interface crack propagating at intersonic speeds along a polymer/metal interface with that for one propagating on a corresponding polymer/rigid interface. Figure 7.1(a) compares q for intersonic crack growth on a PMMA/steel interface with that on a PMMA/rigid in-

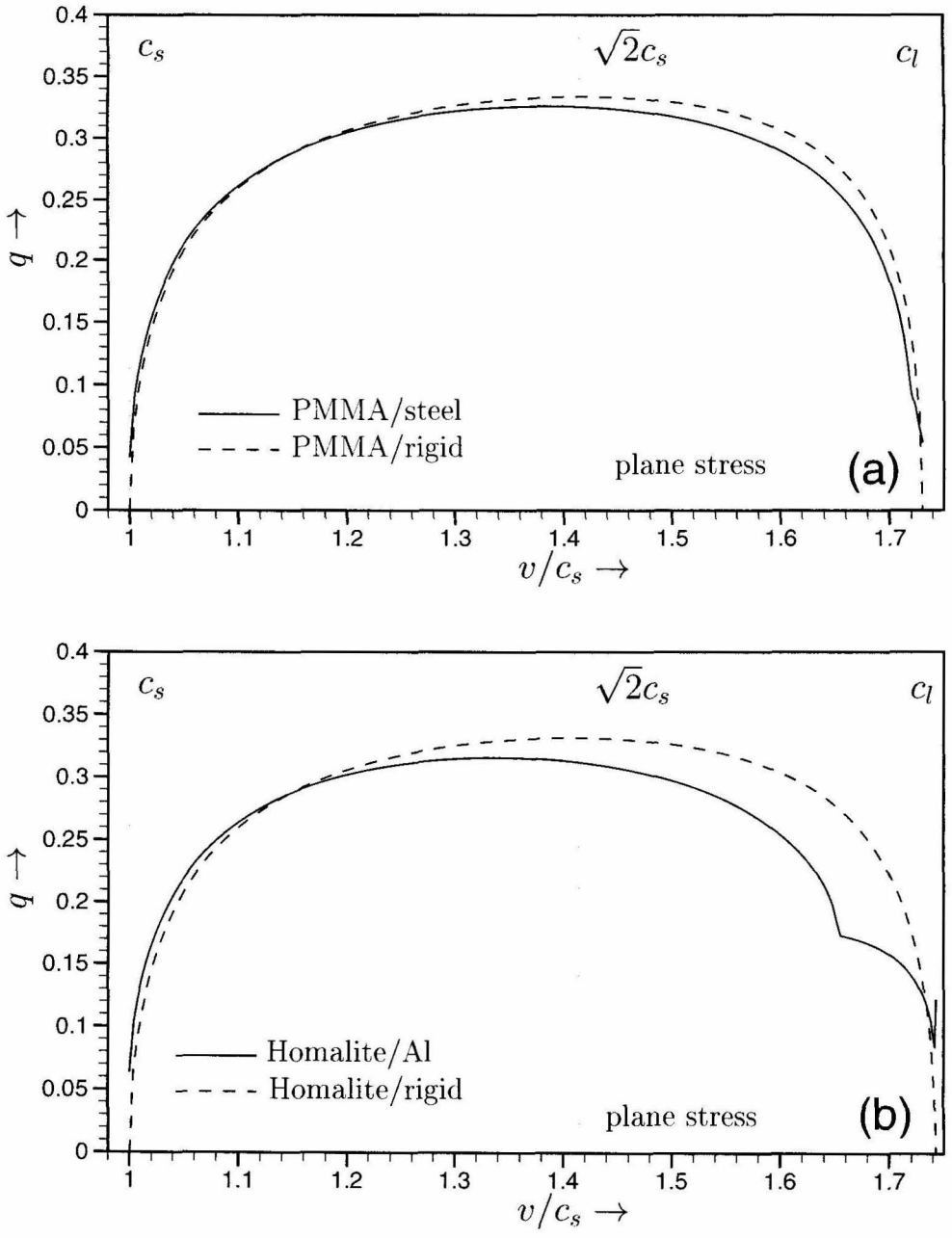

Figure 7.1: Dominant crack tip stress singularity q associated with an intersonically propagating crack on a bimaterial interface. **(a)** Comparison of q for PMMA/steel and PMMA/rigid bimaterials. **(b)** Comparison of q for Homalite/Al and Homalite/rigid bimaterials. For complex q, only the real part is shown.

terface. As seen, the singularity exponent q for a PMMA/steel interface deviates very little (< 0.02) from that of a PMMA/rigid interface, except at speeds very close to c_s and c_l. Figure 7.1(b) compares q for intersonic crack growth on a Homalite/aluminum interface with that on a Homalite/rigid interface. Again, the singularity exponent q for both these interfaces is very close for intersonic speeds less than $\sqrt{2}\,c_s$, except at speeds close to c_s. Beyond $\sqrt{2}\,c_s$, q starts to differ substantially and the polymer/rigid approximation may not account accurately for the near-tip fields in the polymer half. Note that the crack tip stress singularity for intersonic crack growth on a polymer/metal interface changes its character twice within the intersonic regime from real to complex and then back to real. Hence the observed kinks in the variation of q. From Figure 7.1 we can conclude that approximating polymer/metal interfaces with the corresponding polymer/rigid interface should provide accurate results for the near-tip fields in the polymer, certainly for speeds lower than $\sqrt{2}\,c_s$ and beyond that the approximation must be used with caution.

7.2 Intersonic Crack Growth on a Elastic/Rigid Interface with a Detached Contact Zone

Consider a semiinfinite crack propagating at a constant speed v on a perfectly bonded interface between a homogeneous, isotropic linear elastic medium and a rigid substrate under 2D plane strain or plane stress conditions (see Figure 7.2). The crack is constrained to propagate along the interface and the crack speed is intersonic with respect to the elastic medium ($c_s < v < c_l$). The crack faces behind the tip are traction free over a finite length l_1, followed by a frictional contact zone which is either semiinfinite extending over the rest of the crack faces (see Figure 7.2(a)) or is of a finite length l_2, followed again by traction free crack faces. For planar deformation, the displacement field u_α at any point in the elastic solid, with respect to a fixed coordinate system (x_1, x_2) can be expressed in terms of two displacement potentials $\phi(x_1, x_2, t)$ and $\psi(x_1, x_2, t)$ as given in (4.5) (Helmholtz decomposition). The equations of motion

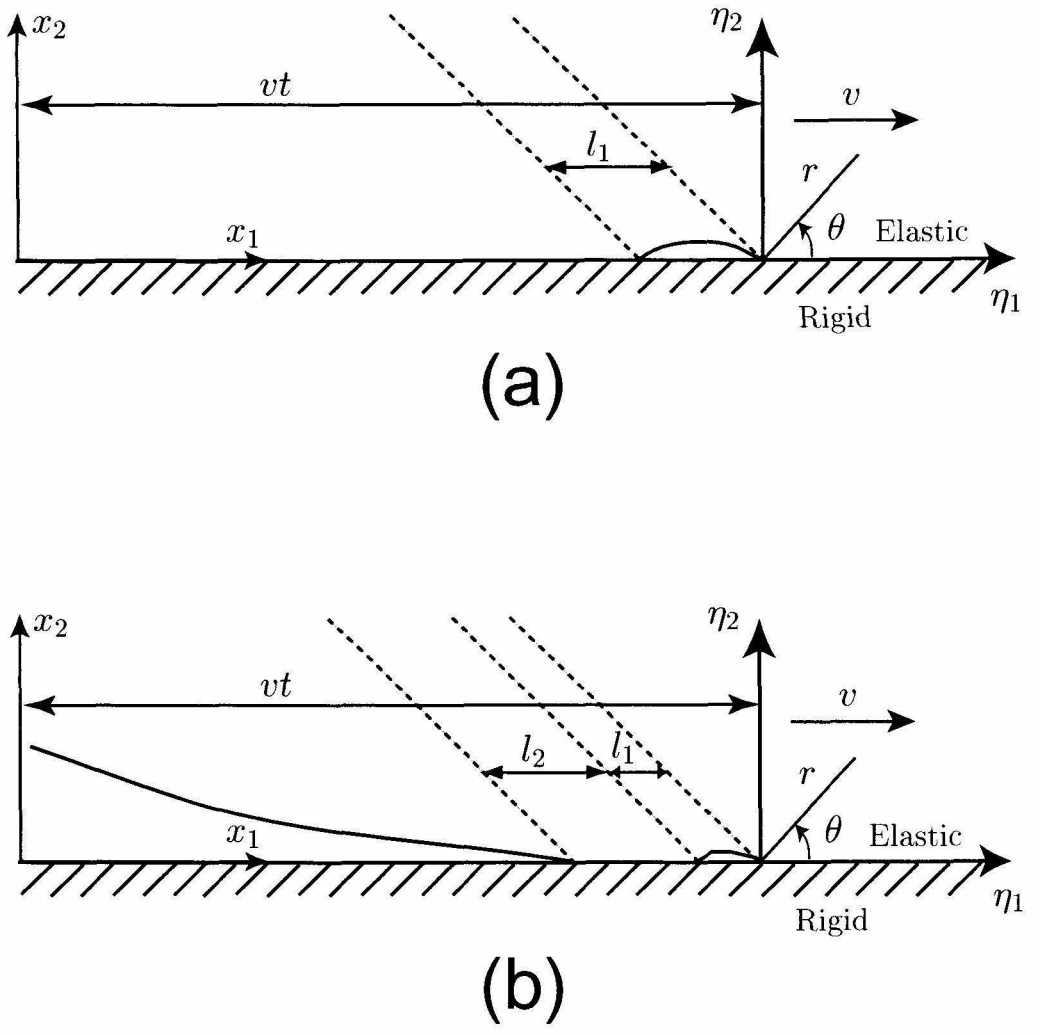

Figure 7.2: Intersonic crack on an elastic/rigid interface. **(a)** Crack model with a finite traction free zone and semiinfinite crack face frictional contact behind the tip. **(b)** Crack model with a finite traction free zone and a finite frictional contact zone behind the tip.

of this system (in the absence of body forces) in terms of the displacement potentials $\phi(x_1, x_2, t)$ and $\psi(x_1, x_2, t)$ are given in (4.6).

Now, consider moving crack tip coordinates (η_1, η_2) centered at the front end of the crack tip (see Figure 7.2), which are related to the fixed coordinates (x_1, x_2) through the Galilean transformation given in (4.7). Expressing (4.7) in terms of the crack tip coordinates and making use of the steady state approximation, the equations of motion reduce to

$$\phi_{,11}(\eta_1, \eta_2) + \frac{1}{\alpha_l^2}\phi_{,22}(\eta_1, \eta_2) = 0 \qquad 0 < v < c_l\,, \tag{7.1a}$$

$$\psi_{,11}(\eta_1, \eta_2) - \frac{1}{\hat{\alpha}_s^2}\psi_{,22}(\eta_1, \eta_2) = 0 \qquad c_s < v < c_l\,. \tag{7.1b}$$

The relativistic quantities α_l and $\hat{\alpha}_s$ are defined in (4.10). Thus the motion is governed by an elliptic and a hyperbolic equation. The strain field and stress field components can be expressed in terms of the displacement potentials ϕ and ψ using the strain-displacement relations and the generalized Hooke's law.

The general solutions for the displacement potentials in the elastic medium ($\eta_2 \geq 0$) are given by (FREUND, 1989)

$$\phi(\eta_1, \eta_2) = \mathrm{Re}\{F(z_l)\}\,, \tag{7.2a}$$

$$\psi(\eta_1, \eta_2) = g(\eta_1 + \hat{\alpha}_s\eta_2)\,, \tag{7.2b}$$

where $F(\cdot)$ is a function, analytic with respect to its argument, $z_l = \eta_1 + i\,\alpha_l\eta_2$ everywhere in the upper half plane except on the crack faces and $g(\cdot)$ is a real function of its argument. The radiation condition is employed here, *i.e.*, an intersonic crack is only capable of generating backward running shear waves. The displacement field and the stress field in terms of F and g reduce to (4.30) and (4.31) respectively.

Along the interface, the displacement field should vanish, *i.e.*,

$$u_1(\eta_1 > 0, \eta_2 = 0) = 0\,, \tag{7.3a}$$

$$u_2(\eta_1 > 0, \eta_2 = 0) = 0\,, \tag{7.3b}$$

which reduce to

$$F'^{+}(\eta_1) + \bar{F}'^{-}(\eta_1) + 2\hat{\alpha}_s g'(\eta_1) = 0 \qquad \eta_1 > 0\,, \tag{7.4a}$$

$$\alpha_l \left[F'^{+}(\eta_1) - \bar{F}'^{-}(\eta_1)\right] + 2ig'(\eta_1) = 0 \qquad \eta_1 > 0\,, \tag{7.4b}$$

where the superscripts "+" and "−" stand for the limits $\eta_2 \to 0^+$ and $\eta_2 \to 0^-$ respectively. Eliminating $g'(\eta_1)$ from (7.4) we obtain

$$F'^{+}(\eta_1) - \frac{\alpha_l\hat{\alpha}_s + i}{\alpha_l\hat{\alpha}_s - i}\,\bar{F}'^{-}(\eta_1) = 0 \qquad \eta_1 > 0\,. \tag{7.5}$$

In the traction free zone, *i.e.*, for $-l_1 < \eta_1 < 0$, $\eta_2 \to 0^+$,

$$\sigma_{22}(\eta_1, 0^+) = 0\,, \tag{7.6a}$$

$$\sigma_{12}(\eta_1, 0^+) = 0\,, \tag{7.6b}$$

which reduce to

$$(1 - \hat{\alpha}_s^2)\left[F''^{+}(\eta_1) + \bar{F}''^{-}(\eta_1)\right] + 4\hat{\alpha}_s g''(\eta_1) = 0 \qquad -l_1 < \eta_1 < 0\,, \tag{7.7a}$$

$$\alpha_l \left[F''^{+}(\eta_1) - \bar{F}''^{-}(\eta_1)\right] + i(1 - \hat{\alpha}_s^2) g''(\eta_1) = 0 \qquad -l_1 < \eta_1 < 0\,. \tag{7.7b}$$

Eliminating $g''(\eta_1)$ from the above equations,

$$F''^{+}(\eta_1) - \frac{4\alpha_l\hat{\alpha}_s + i(1 - \hat{\alpha}_s^2)^2}{4\alpha_l\hat{\alpha}_s - i(1 - \hat{\alpha}_s^2)^2}\bar{F}''^{-}(\eta_1) = 0 \qquad -l_1 < \eta_1 < 0\,. \tag{7.8}$$

In the frictional contact zone, the shear and normal stress components are related through the coulomb friction law. Here, we adopt a simple Coulomb friction law for analytical simplicity, though as seen in Chapter 5, a velocity weakening friction law would be more desirable as the slip rates within the frictional contact zone are very high of the order of a few m/s.

$$\sigma_{12} = \lambda\sigma_{22} \qquad -l_2 < \eta_1 < -l_1,\ \eta_2 \to 0^+\,, \tag{7.9}$$

where the friction coefficient λ is a constant. Also, in the contact zone, the normal displacement component u_2 on the face of the elastic half should vanish, *i.e.*,

$$u_2(-l_2 < \eta_1 < -l_1, \eta_2 \to 0^+) = 0\,. \tag{7.10}$$

Equations (7.9) and (7.10) reduce to (for $-l_2 < \eta_1 < -l_1$)

$$\left[\frac{-i\alpha_l - \lambda(1-\hat{\alpha}_s^2)/2}{(1-\hat{\alpha}_s^2) - 2\lambda\hat{\alpha}_s}\right] F''^{+}(\eta_1) + \left[\frac{i\alpha_l - \lambda(1-\hat{\alpha}_s^2)/2}{(1-\hat{\alpha}_s^2) - 2\lambda\hat{\alpha}_s}\right] \bar{F}''^{-}(\eta_1) + g''(\eta_1) = 0\,, \tag{7.11a}$$

$$\alpha_l \left[F''^{+}(\eta_1) - \bar{F}''^{-}(\eta_1)\right] + 2ig''(\eta_1) = 0\,. \tag{7.11b}$$

Eliminating $g''(\eta_1)$ from the above equations,

$$F''^{+}(\eta_1) - \frac{\alpha_l(1+\hat{\alpha}_s^2) + \lambda\left[2\alpha_l\hat{\alpha}_s + i(1-\hat{\alpha}_s^2)\right]}{\alpha_l(1+\hat{\alpha}_s^2) + \lambda\left[2\alpha_l\hat{\alpha}_s - i(1-\hat{\alpha}_s^2)\right]} \bar{F}''^{-}(\eta_1) = 0 \qquad -l_2 < \eta_1 < -l_1\,. \tag{7.12}$$

In the case of semiinfinite contact, (7.12) is valid through out the semiinfinite frictional contact zone ($l_2 \to \infty$).

For the case of finite-sized contact zone, the crack faces ($\eta_1 < -(l_1 + l_2), \eta_2 \to 0^+$) are traction free, and Equation (7.8) is valid here too. The solution procedure for the governing equations (7.1) with the boundary conditions (7.5), (7.8) and (7.12) along

with traction free boundary conditions on the crack faces (for finite contact model) closely follows that adopted in HUANG *et al.* (1998). The solution procedure involves the introduction of a new function $\theta(z)$, $z = \eta_1 + i\eta_2$ by analytic continuation as follows.

$$\theta(z) = \begin{cases} (\alpha_l \hat{\alpha}_s - i) F'(z) & \eta_2 > 0\,, \\ \\ (\alpha_l \hat{\alpha}_s + i) \bar{F}'(z) & \eta_2 < 0\,. \end{cases} \tag{7.13}$$

$\theta(z)$ is analytic everywhere except on the broken faces of the interface (traction free as well as contact faces). In terms of $\theta(z)$ the traction free boundary condition (7.8) reduces to

$$\theta'^{+}(\eta_1) - \exp^{-2i\beta(v)}\, \theta'^{-}(\eta_1) = 0 \qquad -l_1 < \eta_1 < 0\,, \tag{7.14}$$

where

$$\beta(v) = \tan^{-1}\left\{ \frac{\alpha_l \hat{\alpha}_s \left[4 - (1 - \hat{\alpha}_s^2)^2\right]}{4\alpha_l^2 \hat{\alpha}_s^2 + (1 - \hat{\alpha}_s^2)^2} \right\}. \tag{7.15}$$

In the case of a finite frictional contact zone (Figure 7.2(b)) (7.14) and (7.15) are also valid for $\eta_1 < -(l_1 + l_2)$.

The frictional contact boundary condition (7.12) in terms of $\theta(z)$ reduces to

$$\theta'^{+}(\eta_1) - \exp^{-2i\gamma(v,\lambda)}\, \theta'^{-}(\eta_1) = 0 \qquad -l_2 < \eta_1 < -l_1\,, \tag{7.16}$$

where

$$\gamma(v, \lambda) = \tan^{-1}\left\{ \frac{\alpha_l (1 + \hat{\alpha}_s^2)(1 + \lambda \hat{\alpha}_s)}{\alpha_l^2 \hat{\alpha}_s (1 + \hat{\alpha}_s^2) + \lambda (1 - \hat{\alpha}_s^2 + 2\alpha_l^2 \hat{\alpha}_s^2)} \right\}. \tag{7.17}$$

Equations (7.15) and (7.17) constitute a Riemann-Hilbert problem, the solution of which is given by

$$\theta'(z) = \frac{A(z)}{z^{q_1}(z + l_1)^{q_2}}\,, \tag{7.18}$$

in the case of semiinfinite crack face frictional contact (Figure 7.2(a)) and

$$\theta'(z) = \frac{A(z)}{z^{q_1}(z + l_1)^{q_2}(z + l_1 + l_2)^{q_3}}\,, \tag{7.19}$$

in the case of a finite crack face frictional contact zone (Figure 7.2(b)), where

$$q_1 = \frac{1}{\pi}\tan^{-1}\left\{\frac{\alpha_l\hat{\alpha}_s\,[4-(1-\hat{\alpha}_s^2)^2]}{4\alpha_l^2\hat{\alpha}_s^2+(1-\hat{\alpha}_s^2)^2}\right\}, \tag{7.20a}$$

$$q_2 = \frac{1}{\pi}\tan^{-1}\left\{\frac{\alpha_l(1+\hat{\alpha}_s^2)(1+\lambda\hat{\alpha}_s)}{\alpha_l^2\hat{\alpha}_s(1+\hat{\alpha}_s^2)+\lambda(1-\hat{\alpha}_s^2+2\alpha_l^2\hat{\alpha}_s^2)}\right\} \quad \text{and} \tag{7.20b}$$

$$q_3 = -q_2\,. \tag{7.20c}$$

$A(z)$ is an arbitrary entire function which may be expanded in terms of a Taylor series about the origin.

$$A(z) = \sum_{n=0}^{\infty} A_n z^n\,, \tag{7.21}$$

where all the coefficients A_n $(n = 0, 1, 2, ...)$ are real. Hence

$$F''(z) = \sum_{n=0}^{\infty}\left\{\frac{1}{\alpha_l\hat{\alpha}_s - i}\,\frac{A_n}{z^{q_1-n}(z+l_1)^{q_2}}\right\}, \tag{7.22}$$

for the case of semiinfinite crack face contact (Figure 7.2(a)) and

$$F''(z) = \sum_{n=0}^{\infty}\left\{\frac{1}{\alpha_l\hat{\alpha}_s - i}\,\frac{A_n}{z^{q_1-n}(z+l_1)^{q_2}(z+l_1+l_2)^{q_3}}\right\}, \tag{7.23}$$

for the case of a finite crack face frictional contact zone (Figure 7.2(a)) and the real function g can be expressed in terms of F (for the case of finite sized frictional contact zone) as

$$g'(\eta_1) = -\alpha_l \mathrm{Im}\,\{F'(\eta_1)\} \qquad \eta_1 > 0 \quad \text{or} \quad -l_2 < \eta_1 < -l_1\,, \tag{7.24a}$$

$$g''(\eta_1) = -\frac{(1-\hat{\alpha}_s^2)}{2\hat{\alpha}_s}\mathrm{Re}\,\{F''(\eta_1)\} \qquad -l_1 < \eta_1 < 0 \quad \text{or} \quad \eta_1 < -(l_1+l_2)\,. \tag{7.24b}$$

In the case of a semiinfinite contact zone, the equations may be interpreted appropriately. The stress field around the crack tip can now be obtained using (4.31) and the particle velocity field can be obtained by differentiating (4.30) and their expressions are given in Appendix G.

7.3 Discussion

From the expressions for the near-tip stress field given in Appendix G, we can clearly identify that q_1, q_2 and q_3 are the singularity exponents associated with the near-tip stress field as one approaches the crack tip, the front end of the contact zone and the trailing end of the contact zone respectively. As one approaches the crack tip infinitesimally close, then the finite length of the traction free zone appears semiinfinite and hence q_1 is the same crack tip singularity exponent as that associated with a semiinfinite traction free intersonic crack propagating on an elastic/rigid interface. It is a function only of the crack tip speed and the material properties (Poisson's ratio, ν) and is independent of the friction coefficient λ. With a semiinfinite crack face contact zone, as one moves a distance $r \gg l_1$ away from the crack tip, the traction free zone behind the crack tip appears infinitesimal sized and hence $q_1 + q_2$ must be the same as the crack tip stress singularity associated with that of an intersonic crack propagating along an elastic/rigid interface with semiinfinite crack face frictional contact (HUANG *et al.*, 1998). With a finite sized detached contact zone, as one moves a distance $r \gg l_1 + l_2$ away from the crack tip, the traction free zone and the frictional contact zone appear infinitesimal sized and hence $q_1 + q_2 + q_3$ must be the same as the crack tip stress singularity associated with that of a traction free intersonic crack propagating along an elastic/rigid interface, which is equal to q_1. Hence $q_2 + q_3 = 0$ or $q_3 = -q_2$, as seen in (7.20).

Figure 7.3 shows the variation of the crack tip stress singularity q_1 with intersonic crack speed for three different elastic/rigid interfaces, with the elastic solid having Poisson's ratio, ν equal to 0.25, 0.33 or 0.40. Plane stress conditions are assumed here. We see that q_1 increases monotonically from 0 at c_s, reaches a maximum less than 1/2 and then decreases monotonically to 0 at c_l. Note that for $\nu = 0.40$, the corresponding c_l lies beyond the limits of the crack speed axis. Hence the crack tip stress singularity for an intersonic crack on an elastic/rigid interface is less than that

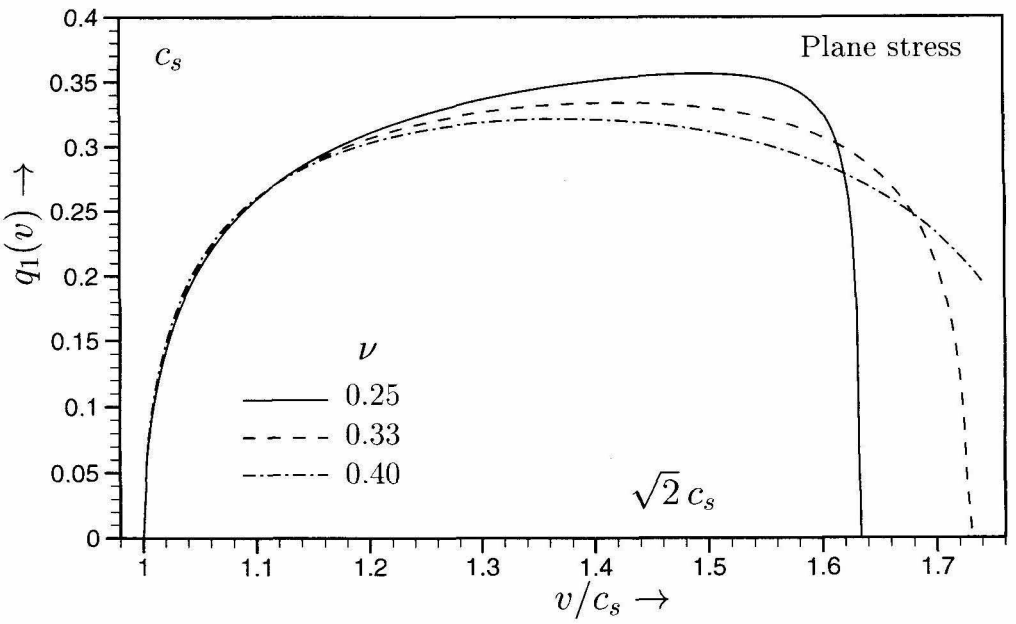

Figure 7.3: Intersonic crack on an elastic/rigid interface with a detached contact zone. Variation of crack tip stress singularity exponent with crack speed.

of of a subsonic crack on the same interface.

Figure 7.4 shows the variation of singularity exponent q_2 with crack speed for different values of the friction coefficient λ. Realistic values of $|\lambda| < 1$ were chosen and interface considered was Homalite/rigid undergoing plane stress deformation. From Figure 7.4(a) we can see that q_2 is maximum at c_s, then decreases monotonically to a minimum less than 0 (for $\lambda > 0$) and then increases back to 0 at $\sqrt{2}\,c_s$. This behavior of the singularity exponent shows that the Mach wave emanating from the front end of the contact zone changes its character as the crack accelerates through the intersonic regime. When q_2 is positive then the tangential stress and tangential particle velocity across the Mach wave suffers an infinite jump and when negative, the same quantities suffer a finite jump. Since $q_3 = -q_2$, the singularity exponent associated with the trailing end of the contact zone is negative for speeds close to c_s. This may have been reflected in the isochromatic fringe pattern as a line across which the fringes merely change their slope, as was observed in Figure 6.7(b). Also, both

the Mach waves emanating from the front end and the trailing end of the contact zone were observed to change their character as the interface crack accelerates through the intersonic regime. However, any such features reflected in the current model must be treated with caution, as the current model uses a strong assumption of steady state which, as was argued in the previous chapter may not be valid during the subsonic/intersonic transition, which is a highly transient event and moreover, the current model cannot capture features like the Rayleigh singularity observed in the experimental patterns. The variation of q_2 with crack speed for $v > \sqrt{2}\,c_s$ is shown in Figure 7.4(b) for various admissible λ. Again, depending on λ, q_2 may or may not under go a positive/negative transition. However, in our experiments we never observed an interfacial crack to propagate steadily at speeds greater than $\sqrt{2}\,c_s$ for any length of time (see Chapter 6). Since $q_3 = -q_2$, the behavior of the singularity exponent at the trailing end of the contact zone can be readily interpreted from Figure 7.4.

The solution obtained here must satisfy some additional constraints to be a physically acceptable model. Firstly, it must satisfy the law of friction, that the shear traction (frictional stress) must oppose the relative sliding between the contact face and the rigid substrate, or in other words energy must be dissipated and not generated during frictional sliding. The particle velocity component $\dot{u}_1$ on the contact face $(-(l_1 + l_2) < \eta_1 < -l_1,\ \eta_2 \to 0^+)$ is given by

$$\dot{u}_1 = -v \sum_{n=0}^{\infty} \frac{A_n \sin(q_1 + q_2 - n)\pi}{|\eta_1|^{q_1 - n} |\eta_1 + l_1|^{q_2} |\eta_1 + l_1 + l_2|^{q_3}}\,, \tag{7.25}$$

and the shear traction on the contact face is given by

$$-\sigma_{12} = -\frac{\mu\alpha_l(1 + \hat{\alpha}_s^2)}{1 + \alpha_l^2 \hat{\alpha}_s^2} \sum_{n=0}^{\infty} \frac{A_n \left[\cos(q_1 + q_2 - n)\pi - \alpha_l \hat{\alpha}_s \sin(q_1 + q_2 - n)\pi\right]}{|\eta_1|^{q_1 - n} |\eta_1 + l_1|^{q_2} |\eta_1 + l_1 + l_2|^{q_3}}\,. \tag{7.26}$$

The shear traction on the contact face must relative sliding between the contact face

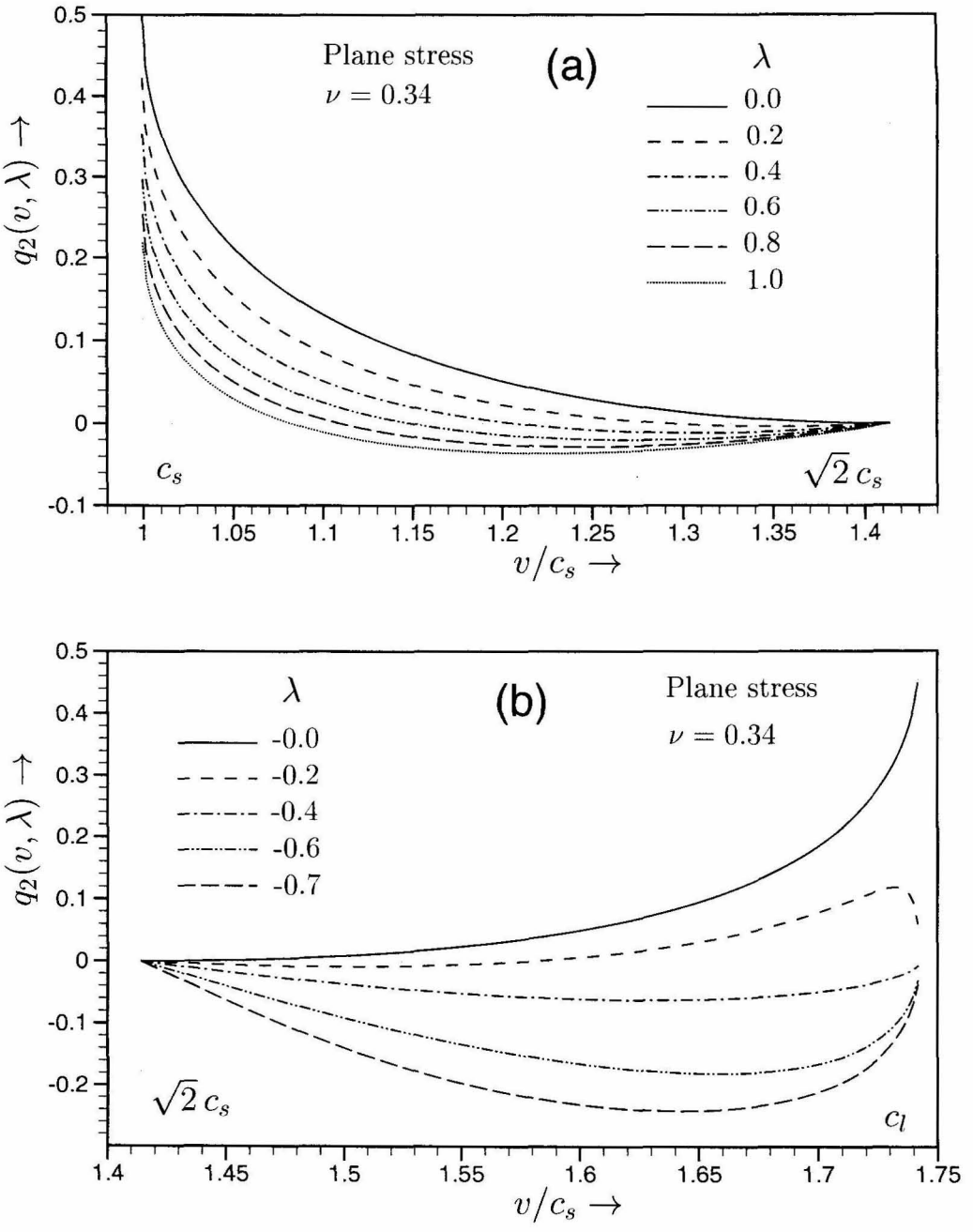

Figure 7.4: Intersonic crack on an elastic/rigid interface with a detached contact zone. Variation of the stress singularity exponent at the front end of the contact zone with crack speed. **(a)** $v < \sqrt{2}\,c_s$. **(b)** $v > \sqrt{2}\,c_s$.

and the rigid substrate, *i.e.*,

$$-\sigma_{12}\dot{u}_1 < 0 \qquad -(l_1 + l_2) < \eta_1 < -l_1,\ \eta_2 \to 0^+ . \tag{7.27}$$

Considering only the dominant first term, the above condition reduces to

$$\lambda(1 + \lambda\hat{\alpha}_s)(1 - \hat{\alpha}_s^2) > 0 , \tag{7.28}$$

which has the solution

$$\lambda > 0 \quad \text{or} \quad \lambda < -\frac{1}{\hat{\alpha}_s} \qquad c_s < v < \sqrt{2}\, c_s , \tag{7.29a}$$

$$-\frac{1}{\hat{\alpha}_s} < \lambda < 0 \qquad \sqrt{2}\, c_s < v < c_l . \tag{7.29b}$$

Figure 7.5 shows the admissible values of λ *i.e.*, those that satisfy the condition (7.29) as a function of the intersonic crack speed v. For most realistic situations, and certainly in the case of our bimaterial specimens, the coefficient of friction λ is likely to be less than 1, *i.e.*, $|\lambda| < 1$. Hence from Figure 7.5 we see that numerically, λ must be positive for $c_s < v < \sqrt{2}\, c_s$ and must be negative (greater than -0.8 for Homalite/rigid) for $v > \sqrt{2}\, c_s$. From the Coulomb friction law, $\sigma_{12} = \lambda\sigma_{22}$, we can see that numerically negative λ merely implies that the direction of the shear is reversed in the frictional contact zone.

Secondly, the model must ensure that the normal stress acting on the contact face is compressive, otherwise no frictional sliding can occur. From the expressions for the stress field shown in Appendix G, it can be readily deduced that the sign of σ_{22} within the frictional contact zone depends on the sign of the unknown amplitude parameters $A_o, A_1, \ldots..$ If we consider only the dominant term, it can be shown that A_o must change its sign at as v passes through $\sqrt{2}\, c_s$. If A_o represents the amplitude of the far-field applied loading, then it is unlikely that it will change sign as the crack speed

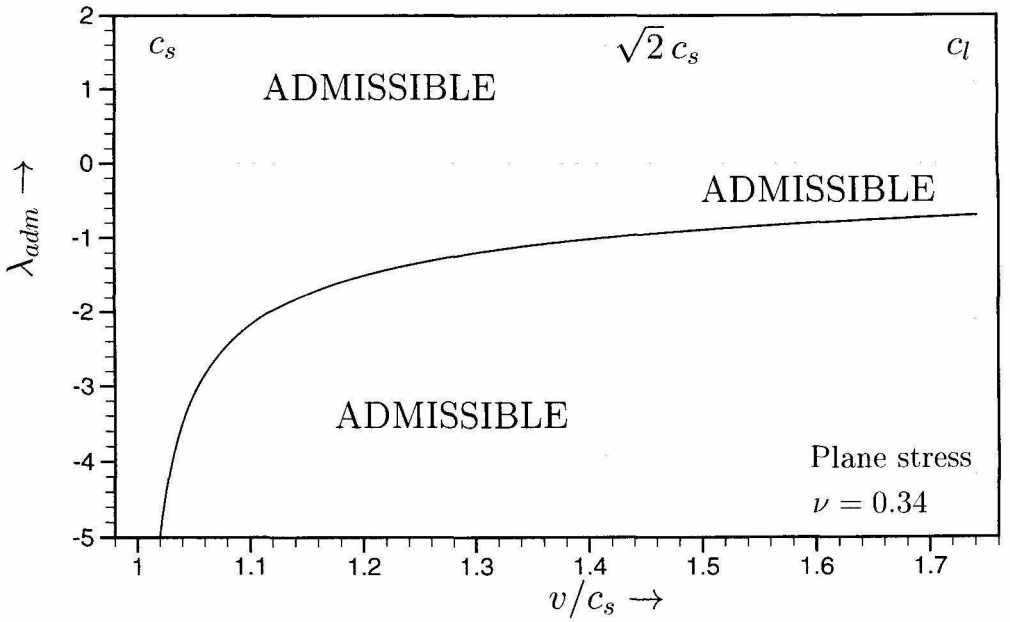

Figure 7.5: Intersonic crack on an elastic/rigid interface. Admissible values of the friction coefficient λ.

suddenly accelerates or decelerates through $\sqrt{2}\,c_s$. Hence, the intersonic crack with the frictional contact zone is likely to stay in one part of the intersonic regime ($c_s < v < \sqrt{2}\,c_s$) or the other ($\sqrt{2}\,c_s < v < c_l$). This is consistent with the observations made in Chapter 6 where the intersonic crack on a wide variety of bimaterial interfaces under different loading configurations always tended to propagate at speeds between c_s and $\sqrt{2}\,c_s$. However, the crack can accelerate through $\sqrt{2}\,c_s$ if the sign of the amplitude of far-field load changes like when the crack tip is suddenly loaded or unloaded by an incoming stress wave.

Thirdly and most importantly, the model must satisfy all the boundary conditions exactly. The boundary conditions (7.12) which the governing equations of motion (7.1) had to satisfy within the frictional contact zone were of the mixed type - a traction boundary condition in the η_1 direction ($\sigma_{12} = \lambda\sigma_{22}$) and a displacement boundary condition in the η_2 direction ($u_2 = 0$). Unfortunately, the solution procedure adopted here is such that mixed boundary conditions cannot be dealt with easily. Hence, the displacement boundary condition ($u_2 = 0$) was relaxed and a ve-

locity boundary condition ($\dot{u}_2 = 0$) was eventually imposed and used in obtaining the solution. Consequently, the solution obtained above does not rigorously satisfy the requirement that the crack faces must be in contact in the frictional contact zone, but only that the crack face normal displacement is identical everywhere. Here, note that for steady crack growth, $\dot{u}_2 = -v u_{2,1}$. Hence, for the obtained asymptotic solution to satisfy the displacement boundary condition within the frictional contact zone, an additional restriction must be imposed on the solution that $u_2(\eta_1 = -l_1, \eta_2 \to 0^+) = 0$ to ensure that the normal displacement u_2 vanishes identically everywhere in the frictional contact zone. This restriction on the solution results in a relation between the unknown parameters A_n, $(n = 0, 1, 2, ...)$. Such use of higher order terms to satisfy "far-field" (far from the crack tip) boundary conditions is very much acceptable, as these become significant at a sufficient distance away from the tip. However, the number of higher order terms that must be taken into account can only be determined by comparing with experimental results. Even with an additional relation between the parameters A_n, $(n = 0, 1, 2, ...)$, it can be shown that some of the observations made above, like the admissible values of λ and the change in the sign of A_o at $\sqrt{2}\, c_s$ are still valid.

The procedure to fit the experimentally recorded isochromatic fringe patterns to the current model and thus extracting the relevant model parameters is extremely complex. First of all, it is a highly non-linear fit and to ensure that the displacement boundary condition is satisfied rigorously within the frictional contact zone, at each iteration of the fit, the relation between the parameters A_n must be recomputed as well. Moreover, the fit is unlikely to be exact as the model suffers from the very strong steady state assumption, where as the experimentally recorded isochromatic fringe patterns exhibit the triple Mach wave structure associated with the presence of a finite sized traction free zone and a finite sized frictional contact zone during the subsonic/intersonic transition event and associated with it are present non-steady features like the Rayleigh singularity. Hence, it was decided to merely compare an

experimentally recorded isochromatic fringe pattern with that predicted by the analytical model for some realistic values of the model parameters. Note that the isochromatic fringe order n at any point (η_1, η_2) is given by

$$n(\eta_1, \eta_2) = \frac{h}{F}\sqrt{(\sigma_{11} - \sigma_{22})^2 + 4\sigma_{12}^2}\,, \tag{7.30}$$

where the stress components $\sigma_{\alpha\beta}$ are given in Appendix G, h is the specimen thickness and F is the material fringe constant of Homalite, which is given in Table 2.1.

Figure 7.6 compares a representative isochromatic fringe pattern recorded during the experiment where we conjectured the presence of a traction free zone as well as a detached frictional contact zone behind the tip (Figure 7.6(a)) with that predicted by the analytical model for some reasonable values of the model parameters (Figure 7.6(b)). The crack speed, $v = 1.15\,c_s$, the length of the traction free zone, $l_1 = 1.663$ mm and the length of the frictional contact zone $l_2 = 0.5$ mm were chosen from the experimental record. Three terms in the series expansion for the stress field were chosen with $A_o = 1.6 \times 10^{-3}$, $A_1 = 6.4 \times 10^{-3}$ and $A_2 = 1.28 \times 10^{-2}$ and λ was chosen to 0.8. The resultant analytically predicted isochromatic fringe pattern shows a strong resemblance to that observed in the experiment at distances close to the crack tip. The analytical model captured the well rounded fringes in front of the crack tip. It also captured the triple Mach wave structure, one radiating from the crack tip and the other two radiating from the front and rear ends of the frictional contact zone. Also, across the third Mach wave the isochromatic fringes merely change their slope and no stress jump can be observed as in the experimental pattern (q_3 is negative here). Finally, the experimental pattern is strongly affected by the presence of the Rayleigh singularity behind the tip which is not captured by the steady state analytical model. Also, in the experimental pattern shown, the crack has just turned intersonic and hence the triple Mach wave structure hasn't radiated far from the interface. On the contrary the analytical model is a steady state model and hence the Mach structure has radiated all the way to ∞.

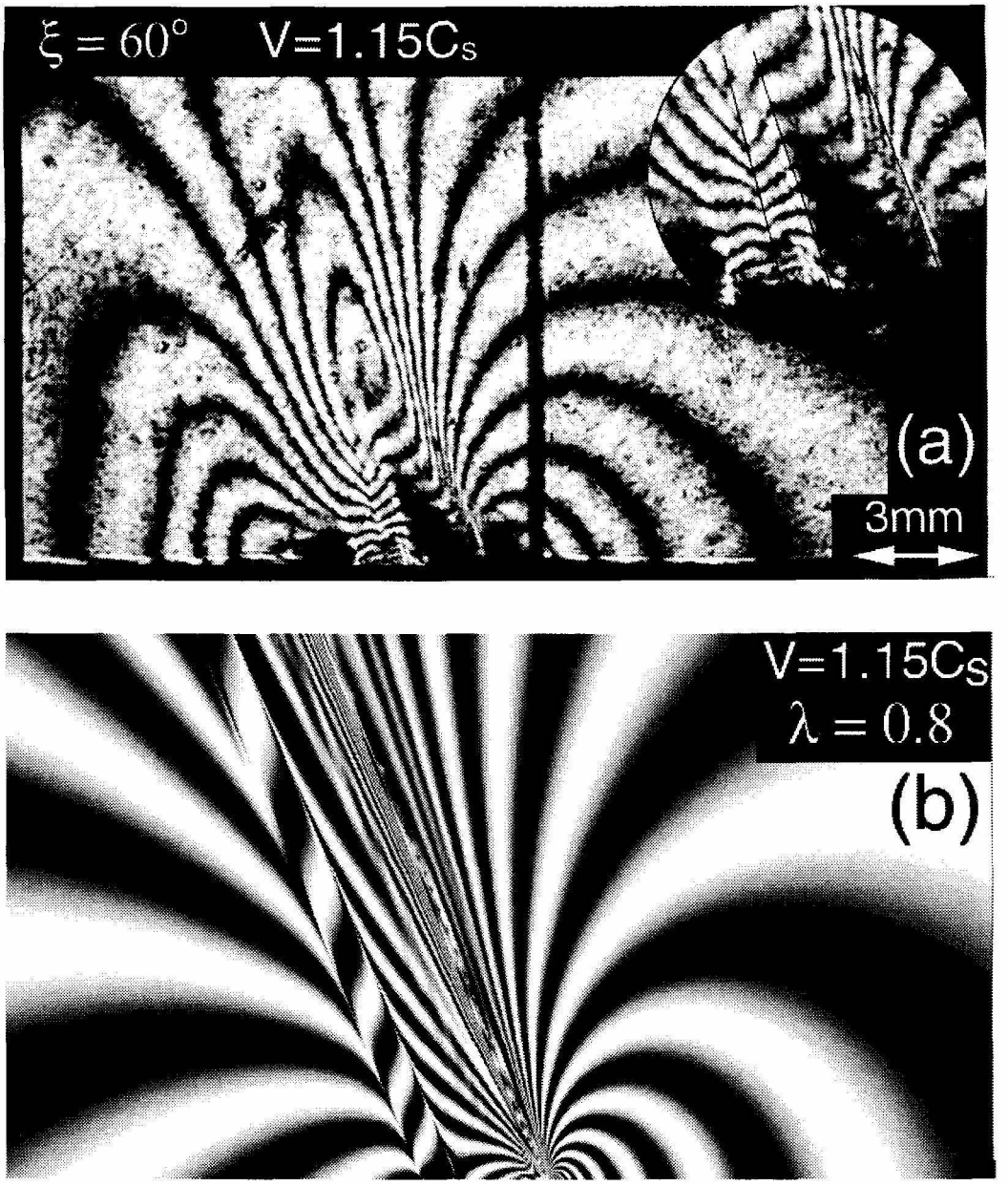

Figure 7.6: Intersonic crack on an elastic/rigid interface with a detached contact zone — Isochromatic fringe pattern. **(a)** Experimentally recorded pattern. **(b)** Analytically predicted pattern.

7.4 Interfacial Waves

Crack propagation at an interface between two dissimilar solids is complicated by the possibility that a dissimilar material interface can act as a conduit for trapping energy. If an interface can sustain interfacial waves, then energy is trapped along the interface and the overall G required from the far-field loading to dynamically debond the interface is substantially reduced, thus promoting interfacial decohesion XU and NEEDLEMAN (1996). If the interface is perfectly bonded and the material properties jump sharply across it, then such an interface can possibly sustain Stoneley waves (ERINGEN and SUHUBI, 1975). Similarly, if the two dissimilar solids are under sliding contact with Coulomb friction acting on the sliding surfaces, then such an interface can sustain Generalized Rayleigh waves (WEERTMAN, 1980; ADAMS, 1995). If the surfaces are traction free, either of them can sustain Rayleigh waves. At first, we will study the possibility of a perfectly bonded polymer/metal interface to sustain Stoneley waves, and show that such waves are not possible. We will also show that sliding polymer/metal surfaces with Coulomb friction acting on the sliding surfaces cannot sustain Generalized Rayleigh waves.

No attempt will be made here to explain the theory behind examining a particular interface for its ability to sustain Stoneley waves, and the reader is referred to ERINGEN and SUHUBI (1975) for the mathematical details. It was shown by many researchers that the velocity of Stoneley waves at the interface between two solid media falls between the velocity of Rayleigh waves and that of shear waves in the slower medium. Figure 7.7 shows the variation of the determinant of the Stoneley matrix (Δ_{SM}) with speed for speeds lying between c_R and c_s of the more compliant medium. Here it must be understood that the speed at which Δ_{SM} vanishes is the speed at which Stoneley waves propagate and thus such an interface can sustain them. Figure 7.7 shows the variation of Δ_{SM} with v/c_s^1, where c_s^1 is the shear wave speed of the more compliant medium for six different bimaterial interfaces. It can be clearly seen

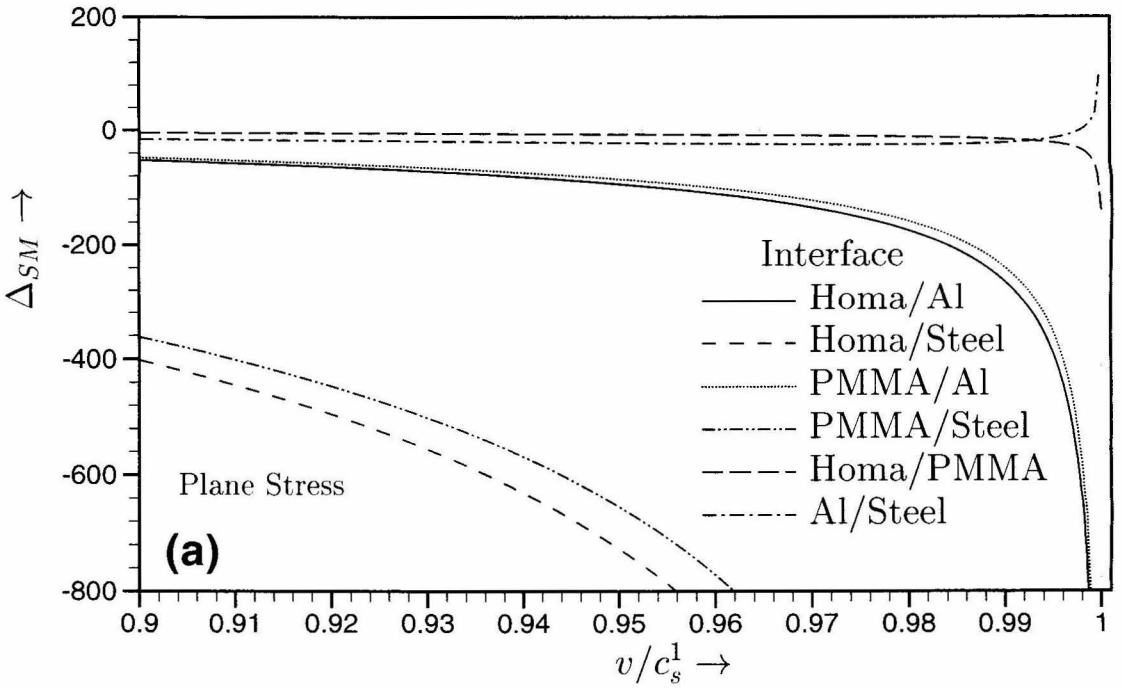

Figure 7.7: Possibility of Stoneley waves on six different material interfaces. Stoneley waves can be sustained only if the shear wave speed of both constituents is nearly the same. Stoneley waves can be sustained only on an aluminum/steel interface ($c_{Stoneley}^{Al/Steel} = 0.999\, c_s^{Al}$).

that Δ_{SM} never vanishes for any of the interfaces with strong wave speed mismatch across them, *i.e.*, all polymer/metal interfaces. It is found that, of the six bimaterial systems considered, Stoneley waves are sustainable only on an aluminum/steel interface and on such an interface Stoneley waves propagate almost at the shear wave speed of aluminum.

To examine the ability of a given dissimilar material interface, which is not bonded but is under contact and undergoes Coulomb frictional sliding, to sustain generalized Rayleigh waves, we follow closely the procedure given in WEERTMAN (1980). Again the theory is not delved into and the reader is referred to this work for further reference. It has been shown by numerous researchers that generalized Rayleigh waves on a nonbonded interface, where relative sliding occurs under Coulomb frictional contact, propagate at a speed lying between c_R and c_s of the more compliant medium.

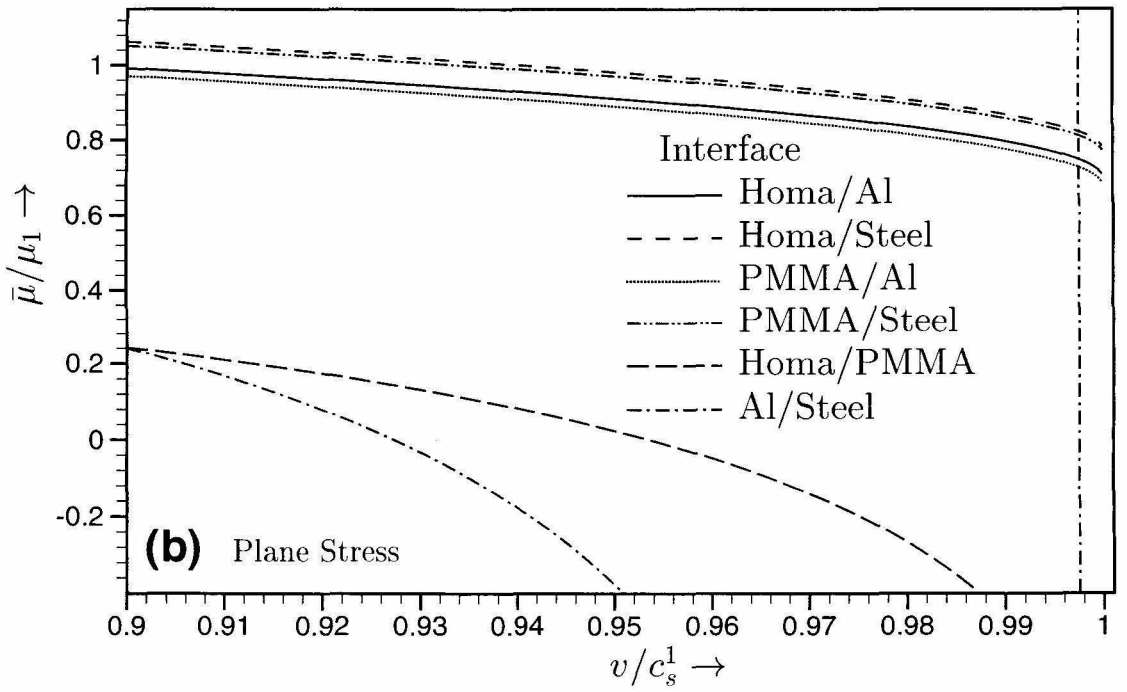

Figure 7.8: Possibility of generalized Rayleigh waves on six different material interfaces under contact. Generalized Rayleigh waves can be sustained only if the shear wave speed of both constituents is nearly the same. Generalized Rayleigh waves can be sustained only on Homalite/PMMA ($c_{GR}^{Homa/PMMA} = 0.954\, c_s^{Homa}$) and aluminum/steel interfaces ($c_{GR}^{Al/Steel} = 0.927\, c_s^{Al}$).

Figure 7.8 shows the variation of the parameter, $\bar{\mu}/\mu_1$ (see WEERTMAN (1980) for explanation) with speed for speeds lying between c_R and c_s of the more compliant medium. Here it must be understood that the speed at which $\bar{\mu}/\mu_1$ vanishes is the speed at which generalized Rayleigh waves propagate and thus such an interface can sustain them. Figure 7.8 shows the variation of $\bar{\mu}/\mu_1$ with v/c_s^1, where c_s^1 is the shear wave speed of the more compliant medium for six different bimaterial interfaces. It can be clearly seen that $\bar{\mu}/\mu_1$ never vanishes for any of the interfaces with strong wave speed mismatch across them, *i.e.*, all polymer/metal interfaces. It is found that, of the six bimaterial systems considered, generalized Rayleigh waves are sustainable only on aluminum/steel and Homalite/PMMA interfaces.

Nomenclature

(η_1, η_2)	Cartesian coordinates w.r.t the moving crack tip
(r, θ)	polar coordinates
(x_1, x_2)	fixed cartesian coordinates
$\alpha_l, \hat{\alpha}_s$	relativistic parameters
$\bar{\mu}/\mu_1$	parameter associated with generalized Rayleigh waves
β	second Dundurs' parameter
Δ_{SM}	determinant of the Stoneley matrix
λ	friction coefficient
ϕ	longitudinal potential
ψ	shear potential
A_n	unknown amplitude parameters
c_l	longitudinal wave speed
c_R	Rayleigh wave speed
c_s	shear wave speed
F	analytic function of $z_l = \eta_1 + i\,\alpha_l \eta_2$

F	material fringe constant
G	dynamic energy release rate
g	a real function of $\eta_1 + \hat{\alpha}_s \eta_2$
h	specimen thickness
l_1	length of traction free zone
l_2	length of frictional contact zone behind the tip
n	isochromatic fringe order
q	crack tip stress singularity associated with an intersonic bimaterial interface crack
q_1	stress singularity exponent associated with the crack tip
q_2	stress singularity exponent associated with the front end of the contact zone
q_3	stress singularity exponent associated with the trailing end of the contact zone
t	time
u_α	components of the displacement vector
v	crack tip speed

Bibliography

ADAMS, G. G. (**1995**), Self-Excited Oscillations of Two Elastic Half-Spaces Sliding With a Constant Coefficient of Friction, *Journal of Applied Mechanics*, **62**(4), pp. 867–872.

ERINGEN, A. C. and SUHUBI, E. S. (**1975**), *Elastodynamics-II*, Academic Press, New York.

FREUND, L. B. (**1989**), *Dynamic Fracture Mechanics*, Cambridge University Press, Cambridge.

HUANG, Y., LIU, C., and ROSAKIS, A. J. (**1996**), Transonic Crack Growth Along a Bimaterial Interface: An Investigation of the Asymptotic Structure of Near-Tip Fields, *International Journal of Solids and Structures*, **33**(18), pp. 2625–2645.

HUANG, Y., WANG, W., LIU, C., and ROSAKIS, A. J. (**1998**), Intersonic Crack Growth in Bimaterial Interfaces: An Investigation of Crack Face Contact, *Journal of the Mechanics and Physics of Solids*, **46**(11), pp. 2233–2259.

HUTCHINSON, J. W. and SUO, Z. (**1992**), Mixed-Mode Cracking in Layered Materials, *Advances in Applied Mechanics*, **29**, pp. 63–191.

LAMBROS, J. and ROSAKIS, A. J. (**1995**), Shear Dominated Transonic Interfacial Crack Growth in a Bimaterial. 1. Experimental Observations, *Journal of the Mechanics and Physics of Solids*, **43**(2), pp. 169–188.

SINGH, R. P. and SHUKLA, A. (**1996**), Subsonic and Intersonic Crack Growth Along a Bimaterial Interface, *Journal of Applied Mechanics*, **63**(4), pp. 919–924.

WEERTMAN, J. (**1980**), Unstable Slippage Across a Fault that Separates Elastic Media of Different Elastic Constants, *Journal of Geophysical Research*, **85**(B3), pp. 1455–1461.

XU, X. P. and NEEDLEMAN, A. (**1996**), Numerical Simulations of Dynamic Crack Growth Along an Interface, *International Journal of Fracture*, **74**(4), pp. 289–324.

YANG, W., SUO, Z., and SHIH, C. F. (**1991**), Mechanics of Dynamic Debonding, *Proceedings of the Royal Society of London*, **A433**(1889), pp. 679–697.

YU, H. H. and YANG, W. (**1995**), Mechanics of Transonic Debonding of a Bimaterial Interface - The Inplane Case, *Journal of the Mechanics and Physics of Solids*, **43**(2), pp. 207–232.

Appendices

Appendix A

Singular Near-Tip Fields For an Intersonically Propagating Mode II Crack

The singular stress field around the tip of an intersonic mode II crack, steadily propagating through a homogeneous, isotropic, linear elastic solid under 2-D plane stress or plane strain conditions, is as follows:

$$\sigma_{11} = \frac{K_{II}^{*d}}{2\alpha_l\sqrt{2\pi}}\left[\frac{-(1+2\alpha_l^2+\hat{\alpha}_s^2)}{r_l^q}\sin q\theta_l + \frac{(1-\hat{\alpha}_s^2)\sin[\,\mathrm{sgn}(\eta_2)\,q\pi]}{(-\eta_1-\hat{\alpha}_s|\eta_2|)^q}\,H(-\eta_1-\hat{\alpha}_s|\eta_2|)\right], \tag{A.1a}$$

$$\sigma_{22} = \frac{K_{II}^{*d}}{2\alpha_l\sqrt{2\pi}}\left[\frac{(1-\hat{\alpha}_s^2)}{r_l^q}\sin q\theta_l - \frac{(1-\hat{\alpha}_s^2)\sin[\,\mathrm{sgn}(\eta_2)\,q\pi]}{(-\eta_1-\hat{\alpha}_s|\eta_2|)^q}\,H(-\eta_1-\hat{\alpha}_s|\eta_2|)\right], \tag{A.1b}$$

$$\sigma_{12} = \frac{K_{II}^{*d}}{\sqrt{2\pi}}\left[\frac{1}{r_l^q}\cos q\theta_l - \frac{\cos[\,\mathrm{sgn}(\eta_2)\,q\pi]}{(-\eta_1-\hat{\alpha}_s|\eta_2|)^q}\,H(-\eta_1-\hat{\alpha}_s|\eta_2|)\right], \tag{A.1c}$$

where (η_1, η_2) is a coordinate system centered at the moving crack tip with the η_1-axis on the crack plane perpendicular to the crack front and the η_2-axis perpendicular to the crack plane. $H(\cdot)$ is the unit step function. Further,

$$r_l = \sqrt{\eta_1^2+\alpha_l^2\eta_2^2}\,, \qquad \theta_l = \tan^{-1}\left[\frac{\alpha_l\eta_2}{\eta_1}\right], \tag{A.2a}$$

$$\alpha_l = \sqrt{1 - \frac{v^2}{c_l^2}}\,, \qquad \hat{\alpha}_s = \sqrt{\frac{v^2}{c_s^2} - 1}\,, \tag{A.2b}$$

$$q = \frac{1}{\pi} \tan^{-1}\left[\frac{4\alpha_l \hat{\alpha}_s}{(1-\hat{\alpha}_s^2)^2}\right], \tag{A.3}$$

$$\mathrm{sgn}(\eta_2) = \begin{cases} 1 & \eta_2 \geq 0\,, \\ -1 & \eta_2 < 0\,, \end{cases} \tag{A.4}$$

and the intersonic stress intensity factor K_{II}^{*d} is defined as

$$K_{II}^{*d} = \lim_{\eta_1 \to 0^+} \sqrt{2\pi}\, \eta_1^q\, \sigma_{12}(\eta_1 > 0, \eta_2 = 0). \tag{A.5}$$

The particle velocity field around the intersonic mode II crack tip (in the upper half plane $\eta_2 > 0$) is given by

$$\dot{u}_1 = \frac{v K_{II}^{*d}}{4\mu\alpha_l\sqrt{2\pi}} \left[\frac{2\sin q\theta_l}{r_l^q} - \frac{(1-\hat{\alpha}_s^2)\sin q\pi}{(-\eta_1 - \hat{\alpha}_s\eta_2)^q}\, H(-\eta_1 - \hat{\alpha}_s\eta_2)\right], \tag{A.6a}$$

$$\dot{u}_2 = \frac{v K_{II}^{*d}}{4\mu\alpha_l\sqrt{2\pi}} \left[\frac{-2\alpha_l\cos q\theta_l}{r_l^q} + \frac{(1-\hat{\alpha}_s^2)\sin q\pi}{\hat{\alpha}_s(-\eta_1 - \hat{\alpha}_s\eta_2)^q}\, H(-\eta_1 - \hat{\alpha}_s\eta_2)\right], \tag{A.6b}$$

where v is the crack speed and μ is the shear modulus of the material. The particle velocity field in the lower half plane ($\eta_2 < 0$) can be obtained by invoking the symmetries associated with mode II deformation.

The displacement field on the upper crack face ($\eta_1 < 0, \eta_2 \to 0^+$) is given by

$$u_1 = \frac{K_{II}^{*d}}{\mu\sqrt{2\pi}} \frac{\hat{\alpha}_s(1+\hat{\alpha}_s^2)}{(1-q)R_q} (-\eta_1)^{1-q}\,, \tag{A.7a}$$

$$u_2 = \frac{K_{II}^{*d}}{\mu\sqrt{2\pi}} \frac{1-\hat{\alpha}_s^4}{2(1-q)R_q} (-\eta_1)^{1-q}\,, \tag{A.7b}$$

where $R_q = \sqrt{16\alpha_l^2\hat{\alpha}_s^2 + (1-\hat{\alpha}_s^2)^4}$. Again, the displacement field on the lower crack face ($\eta_1 < 0, \eta_2 \to 0^-$) can be obtained by invoking mode II symmetries.

Appendix B

SubRayleigh Mode II Crack With a Dugdale Type Cohesive Zone

The dominant near tip stress field (in the upper half plane $\eta_2 > 0$) around the tip of a subRayleigh mode II crack with a Dugdale type cohesive zone, steadily propagating through a homogeneous, isotropic, linear elastic solid under 2-D plane stress or plane strain conditions, is as follows:

$$\frac{\sigma_{11}}{\tau_o} = \frac{4\alpha_s}{\pi R(v)}\left[\frac{(1+2\alpha_l^2-\alpha_s^2)}{\sqrt{r_l/L}}\left\{-\sin\left(\frac{\theta_l}{2}\right)+\frac{1}{2}\int_0^1 \frac{\sqrt{\zeta}\left[\zeta\sin(\frac{\theta_l}{2})+\left(\frac{r_l}{L}\right)\sin(\frac{3\theta_l}{2})\right]}{\zeta^2+\left(\frac{r_l}{L}\right)^2+2\zeta\left(\frac{r_l}{L}\right)\cos\theta_l}\,d\zeta\right\}\right.$$
$$\left.-\frac{(1+\alpha_s^2)}{\sqrt{r_s/L}}\left\{-\sin\left(\frac{\theta_s}{2}\right)+\frac{1}{2}\int_0^1 \frac{\sqrt{\zeta}\left[\zeta\sin(\frac{\theta_s}{2})+\left(\frac{r_s}{L}\right)\sin(\frac{3\theta_s}{2})\right]}{\zeta^2+\left(\frac{r_s}{L}\right)^2+2\zeta\left(\frac{r_s}{L}\right)\cos\theta_s}\,d\zeta\right\}\right], \quad \text{(B.1a)}$$

$$\frac{\sigma_{22}}{\tau_o} = \frac{4\alpha_s(1+\alpha_s^2)}{\pi R(v)}\left[\frac{-1}{\sqrt{r_l/L}}\left\{-\sin\left(\frac{\theta_l}{2}\right)+\frac{1}{2}\int_0^1 \frac{\sqrt{\zeta}\left[\zeta\sin(\frac{\theta_l}{2})+\left(\frac{r_l}{L}\right)\sin(\frac{3\theta_l}{2})\right]}{\zeta^2+\left(\frac{r_l}{L}\right)^2+2\zeta\left(\frac{r_l}{L}\right)\cos\theta_l}\,d\zeta\right\}\right.$$
$$\left.+\frac{1}{\sqrt{r_s/L}}\left\{-\sin\left(\frac{\theta_s}{2}\right)+\frac{1}{2}\int_0^1 \frac{\sqrt{\zeta}\left[\zeta\sin(\frac{\theta_s}{2})+\left(\frac{r_s}{L}\right)\sin(\frac{3\theta_s}{2})\right]}{\zeta^2+\left(\frac{r_s}{L}\right)^2+2\zeta\left(\frac{r_s}{L}\right)\cos\theta_s}\,d\zeta\right\}\right], \quad \text{(B.1b)}$$

$$\frac{\sigma_{12}}{\tau_o} = \frac{2}{\pi R(v)}\left[\frac{-4\alpha_l\alpha_s}{\sqrt{r_l/L}}\left\{-\cos\left(\frac{\theta_l}{2}\right)+\frac{1}{2}\int_0^1 \frac{\sqrt{\zeta}\left[\zeta\cos(\frac{\theta_l}{2})+\left(\frac{r_l}{L}\right)\cos(\frac{3\theta_l}{2})\right]}{\zeta^2+\left(\frac{r_l}{L}\right)^2+2\zeta\left(\frac{r_l}{L}\right)\cos\theta_l}\,d\zeta\right\}\right.$$
$$\left.+\frac{(1+\alpha_s^2)^2}{\sqrt{r_s/L}}\left\{-\cos\left(\frac{\theta_s}{2}\right)+\frac{1}{2}\int_0^1 \frac{\sqrt{\zeta}\left[\zeta\cos(\frac{\theta_s}{2})+\left(\frac{r_s}{L}\right)\cos(\frac{3\theta_s}{2})\right]}{\zeta^2+\left(\frac{r_s}{L}\right)^2+2\zeta\left(\frac{r_s}{L}\right)\cos\theta_s}\,d\zeta\right\}\right], \quad \text{(B.1c)}$$

where (η_1, η_2) is a coordinate system centered at the moving crack tip with the η_1-axis on the crack plane perpendicular to the crack front and the η_2-axis perpendicular to the crack plane. Further,

$$r_s = \sqrt{\eta_1^2 + \alpha_s^2 \eta_2^2}\,, \qquad \theta_s = \tan^{-1}\left[\frac{\alpha_s \eta_2}{\eta_1}\right], \tag{B.2a}$$

$$r_l = \sqrt{\eta_1^2 + \alpha_l^2 \eta_2^2}\,, \qquad \theta_l = \tan^{-1}\left[\frac{\alpha_l \eta_2}{\eta_1}\right], \tag{B.2b}$$

$$\alpha_l = \sqrt{1 - \frac{v^2}{c_l^2}}\,, \qquad \alpha_s = \sqrt{1 - \frac{v^2}{c_s^2}}\,, \tag{B.2c}$$

$$R(v) = 4\alpha_l \alpha_s - (1 + \alpha_s^2)^2\,. \tag{B.2d}$$

τ_o is the cohesive shear strength of the material and L is the cohesive zone length. The integrals in (B.1) become singular of the Cauchy type for $(\theta_l, \theta_s \to +\pi, 0 < r_s, r_l < L)$. The limiting values of these integrals in such cases must be interpreted appropriately using the Plemelj formulae. The limiting values of the stress components for $0 < r_s, r_l < 1$ and $\theta_s, \theta_l \to +\pi$ are given by

$$\frac{\sigma_{11}}{\tau_o}(-1 < \frac{\eta_1}{L} < 0,\ \eta_2 \to 0^+) = \frac{4\alpha_s}{\pi R(v)} \frac{-2(\alpha_l^2 - \alpha_s^2)}{\sqrt{-\eta_1/L}} \left[1 - \frac{1}{2}\,\mathrm{pv}\int_0^1 \frac{\sqrt{\zeta}}{\zeta + \eta_1/L} d\zeta\right], \tag{B.3a}$$

$$\frac{\sigma_{22}}{\tau_o}(-1 < \frac{\eta_1}{L} < 0,\ \eta_2 \to 0^+) = 0\,, \tag{B.3b}$$

$$\frac{\sigma_{12}}{\tau_o}(-1 < \frac{\eta_1}{L} < 0,\ \eta_2 \to 0^+) = 1\,. \tag{B.3c}$$

The stress field in the lower half plane ($\eta_2 < 0$) can be obtained by invoking the symmetries associated with mode II deformation.

The particle velocity field in the upper half plane ($\eta_2 > 0$) is given by

$$\dot{u}_1 = v \frac{\tau_o}{\mu} \frac{2\alpha_s}{\pi R(v)} \left[\frac{-2}{\sqrt{r_l/L}} \left\{ -\sin\left(\frac{\theta_l}{2}\right) + \frac{1}{2}\int_0^1 \frac{\sqrt{\zeta}\left[\zeta \sin(\frac{\theta_l}{2}) + \left(\frac{r_l}{L}\right)\sin(\frac{3\theta_l}{2})\right]}{\zeta^2 + \left(\frac{r_l}{L}\right)^2 + 2\zeta\left(\frac{r_l}{L}\right)\cos\theta_l} d\zeta \right\}\right.$$

$$+\frac{(1+\alpha_s^2)}{\sqrt{r_s/L}}\left\{-\sin\left(\frac{\theta_s}{2}\right)+\frac{1}{2}\int_0^1\frac{\sqrt{\zeta}\left[\zeta\sin(\frac{\theta_s}{2})+\left(\frac{r_s}{L}\right)\sin(\frac{3\theta_s}{2})\right]}{\zeta^2+\left(\frac{r_s}{L}\right)^2+2\zeta\left(\frac{r_s}{L}\right)\cos\theta_s}\,d\zeta\right\}\Bigg], \tag{B.4a}$$

$$\dot{u}_2 = v\frac{\tau_o}{\mu}\frac{2}{\pi R(v)}\Bigg[\frac{2\alpha_l\alpha_s}{\sqrt{r_l/L}}\left\{-\cos\left(\frac{\theta_l}{2}\right)+\frac{1}{2}\int_0^1\frac{\sqrt{\zeta}\left[\zeta\cos(\frac{\theta_l}{2})+\left(\frac{r_l}{L}\right)\cos(\frac{3\theta_l}{2})\right]}{\zeta^2+\left(\frac{r_l}{L}\right)^2+2\zeta\left(\frac{r_l}{L}\right)\cos\theta_l}\,d\zeta\right\}$$

$$-\frac{(1+\alpha_s^2)}{\sqrt{r_s/L}}\left\{-\cos\left(\frac{\theta_s}{2}\right)+\frac{1}{2}\int_0^1\frac{\sqrt{\zeta}\left[\zeta\cos(\frac{\theta_s}{2})+\left(\frac{r_s}{L}\right)\cos(\frac{3\theta_s}{2})\right]}{\zeta^2+\left(\frac{r_s}{L}\right)^2+2\zeta\left(\frac{r_s}{L}\right)\cos\theta_s}\,d\zeta\right\}\Bigg], \tag{B.4b}$$

where v is the crack speed and μ is the shear modulus of the material. The particle velocity field in the lower half plane ($\eta_2 < 0$) can be obtained from mode II symmetries.

The displacement field on the upper crack face ($\eta_1 < 0, \eta_2 \to 0^+$) is given by

$$\frac{u_1}{L} = \frac{\tau_o}{\mu}\frac{2\alpha_s(1-\alpha_s^2)}{\pi R(v)}\left\{\sqrt{\frac{-\eta_1}{L}}+\frac{1}{2}\left(1+\frac{\eta_1}{L}\right)\int_0^{-L/\eta_1}\frac{d\zeta}{\sqrt{\zeta}(\zeta-1)}\right\}, \tag{B.5a}$$

$$\frac{u_2}{L} = \frac{\tau_o}{\mu}\frac{1+\alpha_s^2-2\alpha_l\alpha_s}{R(v)}\begin{cases}\dfrac{-\eta_1}{L} & -L<\eta_1<0\,,\\ 1 & \eta_1<-L\,.\end{cases} \tag{B.5b}$$

On the cohesive surface ($-L < \eta_1 < 0$), the integral in the expression for u_1 must be interpreted as its Cauchy principal value. Again, the displacement field on the lower crack face ($\eta_1 < 0, \eta_2 \to 0^-$) can be obtained by invoking mode II symmetries.

Appendix C

Intersonic Mode II Crack With a Dugdale Type Cohesive Zone

The dominant near tip stress field (in the upper half plane $\eta_2 > 0$) around the tip of an intersonic mode II crack with a Dugdale type cohesive zone, steadily propagating through a homogeneous, isotropic, linear elastic solid under 2-D plane stress or plane strain conditions, is as follows:

$$\frac{\sigma_{11}}{\tau_o} = \frac{\sin q\pi}{q\pi}\left[\frac{(1+2\alpha_l^2+\hat{\alpha}_s^2)}{2\alpha_l}\frac{1}{\left(\frac{r_l}{L}\right)^q}\left\{-\sin q\theta_l + q\int_0^1 \frac{\zeta^q\left[\zeta\sin q\theta_l + \left(\frac{r_l}{L}\right)\sin(q+1)\theta_l\right]}{\zeta^2+\left(\frac{r_l}{L}\right)^2+2\zeta\left(\frac{r_l}{L}\right)\cos\theta_l}\,d\zeta\right\}\right.$$
$$\left. - \frac{(1-\hat{\alpha}_s^2)}{2\alpha_l}\frac{\sin q\pi}{\left(\frac{-\eta_1-\hat{\alpha}_s\eta_2}{L}\right)^q}\left\{-1 + q\,\mathrm{pv}\int_0^1 \frac{\zeta^q}{\zeta+\left(\frac{\eta_1+\hat{\alpha}_s\eta_2}{L}\right)}\,d\zeta\right\}H(-\eta_1-\hat{\alpha}_s\eta_2)\right], \tag{C.1a}$$

$$\frac{\sigma_{22}}{\tau_o} = \frac{\sin q\pi}{q\pi}\left[\frac{-(1-\hat{\alpha}_s^2)}{2\alpha_l}\frac{1}{\left(\frac{r_l}{L}\right)^q}\left\{-\sin q\theta_l + q\int_0^1 \frac{\zeta^q\left[\zeta\sin q\theta_l + \left(\frac{r_l}{L}\right)\sin(q+1)\theta_l\right]}{\zeta^2+\left(\frac{r_l}{L}\right)^2+2\zeta\left(\frac{r_l}{L}\right)\cos\theta_l}\,d\zeta\right\}\right.$$
$$\left. + \frac{(1-\hat{\alpha}_s^2)}{2\alpha_l}\frac{\sin q\pi}{\left(\frac{-\eta_1-\hat{\alpha}_s\eta_2}{L}\right)^q}\left\{-1 + q\,\mathrm{pv}\int_0^1 \frac{\zeta^q}{\zeta+\left(\frac{\eta_1+\hat{\alpha}_s\eta_2}{L}\right)}\,d\zeta\right\}H(-\eta_1-\hat{\alpha}_s\eta_2)\right], \tag{C.1b}$$

$$\frac{\sigma_{12}}{\tau_o} = \frac{\sin q\pi}{q\pi}\left[\frac{-1}{\left(\frac{r_l}{L}\right)^q}\left\{-\cos q\theta_l + q\int_0^1 \frac{\zeta^q\left[\zeta\cos q\theta_l + \left(\frac{r_l}{L}\right)\cos(q+1)\theta_l\right]}{\zeta^2+\left(\frac{r_l}{L}\right)^2+2\zeta\left(\frac{r_l}{L}\right)\cos\theta_l}\,d\zeta\right\}\right.$$

$$+\frac{\cos q\pi}{\left(\frac{-\eta_1-\hat{\alpha}_s\eta_2}{L}\right)^q}\left\{-1+q\,\mathrm{pv}\int_0^1\frac{\zeta^q}{\zeta+\left(\frac{\eta_1+\hat{\alpha}_s\eta_2}{L}\right)}\,d\zeta\right\}H(-\eta_1-\hat{\alpha}_s\eta_2)\Bigg]\,, \tag{C.1c}$$

where (η_1, η_2) is a coordinate system centered at the moving crack tip with the η_1-axis on the crack plane perpendicular to the crack front and the η_2-axis perpendicular to the crack plane. $H(\cdot)$ is the unit step function. Further,

$$r_l = \sqrt{\eta_1^2+\alpha_l^2\eta_2^2}\,, \qquad \theta_l = \tan^{-1}\left[\frac{\alpha_l\eta_2}{\eta_1}\right], \tag{C.2a}$$

$$\alpha_l = \sqrt{1-\frac{v^2}{c_l^2}}\,, \qquad \hat{\alpha}_s = \sqrt{\frac{v^2}{c_s^2}-1}\,, \tag{C.2b}$$

$$q = \frac{1}{\pi}\tan^{-1}\left[\frac{4\alpha_l\hat{\alpha}_s}{(1-\hat{\alpha}_s^2)^2}\right]. \tag{C.3}$$

τ_o is the shear strength of the crack plane and L is the cohesive zone length. The integrals in the first term of the expressions in (C.1) become singular of the Cauchy type for ($\theta_l \to +\pi$, $0 < r_l < L$). The limiting values of these integrals in such cases must be interpreted appropriately using the Plemelj formulae. The limiting values of the stress components for $0 < r_l < 1$ and $\theta_l \to +\pi$ are given by

$$\frac{\sigma_{11}}{\tau_o}(-1<\frac{\eta_1}{L}<0,\ \eta_2\to 0^+) = \frac{\alpha_l^2+\hat{\alpha}_s^2}{\alpha_l}\frac{\sin^2 q\pi}{q\pi}\left[\frac{q\pi}{\tan q\pi}\right.$$
$$\left.-\left(\frac{-\eta_1}{L}\right)^{-q}\left\{1-q\,\mathrm{pv}\int_0^1\frac{\sqrt{\zeta}}{\zeta+\eta_1/L}d\zeta\right\}\right], \tag{C.4a}$$

$$\frac{\sigma_{22}}{\tau_o}(-1<\frac{\eta_1}{L}<0,\ \eta_2\to 0^+) = 0\,, \tag{C.4b}$$

$$\frac{\sigma_{12}}{\tau_o}(-1<\frac{\eta_1}{L}<0,\ \eta_2\to 0^+) = 1\,. \tag{C.4c}$$

The stress field in the lower half plane ($\eta_2 < 0$) can be obtained by invoking the symmetries associated with mode II deformation.

The particle velocity field in the upper half plane ($\eta_2 > 0$) is given by

$$\dot{u}_1 = v\frac{\tau_o}{\mu}\frac{\sin q\pi}{q\pi}\left[\frac{-1}{2\alpha_l}\frac{1}{\left(\frac{r_l}{L}\right)^q}\left\{-\sin q\theta_l + q\int_0^1 \frac{\zeta^q\left[\zeta\sin q\theta_l + \left(\frac{r_l}{L}\right)\sin(q+1)\theta_l\right]}{\zeta^2 + \left(\frac{r_l}{L}\right)^2 + 2\zeta\left(\frac{r_l}{L}\right)\cos\theta_l}\,d\zeta\right\}\right.$$
$$\left. + \frac{\hat{\alpha}_s(1-\hat{\alpha}_s^2)}{R_q}\frac{1}{\left(\frac{-\eta_1-\hat{\alpha}_s\eta_2}{L}\right)^q}\left\{-1 + q\,\mathrm{pv}\int_0^1 \frac{\zeta^q}{\zeta + \left(\frac{\eta_1+\hat{\alpha}_s\eta_2}{L}\right)}\,d\zeta\right\}H(-\eta_1 - \hat{\alpha}_s\eta_2)\right], \tag{C.5a}$$

$$\dot{u}_2 = v\frac{\tau_o}{\mu}\frac{\sin q\pi}{q\pi}\left[\frac{1}{2\left(\frac{r_l}{L}\right)^q}\left\{-\cos q\theta_l + q\int_0^1 \frac{\zeta^q\left[\zeta\cos q\theta_l + \left(\frac{r_l}{L}\right)\cos(q+1)\theta_l\right]}{\zeta^2 + \left(\frac{r_l}{L}\right)^2 + 2\zeta\left(\frac{r_l}{L}\right)\cos\theta_l}\,d\zeta\right\}\right.$$
$$\left. - \frac{(1-\hat{\alpha}_s^2)}{R_q}\frac{1}{\left(\frac{-\eta_1-\hat{\alpha}_s\eta_2}{L}\right)^q}\left\{-1 + q\,\mathrm{pv}\int_0^1 \frac{\zeta^q}{\zeta + \left(\frac{\eta_1+\hat{\alpha}_s\eta_2}{L}\right)}\,d\zeta\right\}H(-\eta_1 - \hat{\alpha}_s\eta_2)\right], \tag{C.5b}$$

where v is the crack speed and μ is the shear modulus of the material and $R_q = \sqrt{16\alpha_l^2\hat{\alpha}_s^2 + (1-\hat{\alpha}_s^2)^4}$. The particle velocity field in the lower half plane ($\eta_2 < 0$) can be obtained from mode II symmetries.

The displacement field on the upper crack face ($\eta_1 < 0, \eta_2 \to 0^+$) is given by

$$\frac{u_1}{L}(-1 < \frac{\eta_1}{L} < 0) = \frac{\tau_o}{\mu}\frac{\hat{\alpha}_s(1+\hat{\alpha}_s^2)}{R_q}\frac{\sin q\pi}{\pi}\left[\left(1+\frac{\eta_1}{L}\right)\frac{\pi}{\tan q\pi} + \frac{1}{1-q}\left(\frac{-\eta_1}{L}\right)^{1-q}\right.$$
$$\left. + (1+\frac{\eta_1}{L})\,\mathrm{pv}\int_0^{-L/\eta_1}\frac{\zeta^{q-1}}{\zeta-1}d\zeta\right], \tag{C.6a}$$

$$\frac{u_1}{L}(\frac{\eta_1}{L} < -1) = \frac{\tau_o}{\mu}\frac{\hat{\alpha}_s(1+\hat{\alpha}_s^2)}{R_q}\frac{\sin q\pi}{\pi}\left[\frac{1}{q}\left(\frac{-\eta_1}{L}\right)^{-q}\left\{\frac{1}{1-q}\left(\frac{-\eta_1}{L}\right) - 1\right\}\right.$$
$$\left. + (1+\frac{\eta_1}{L})\int_0^{-L/\eta_1}\frac{\zeta^q}{\zeta-1}d\zeta\right], \tag{C.6b}$$

$$\frac{u_2}{L}(-1 < \frac{\eta_1}{L} < 0) = \frac{\tau_o}{2\mu}\left[\frac{\eta_1}{L} + \frac{(1-\hat{\alpha}_s^4)}{R_q}\left\{\left(1+\frac{\eta_1}{L}\right)\cos q\pi + \frac{\sin q\pi}{\pi}\left(\frac{1}{1-q}\left(\frac{-\eta_1}{L}\right)^{1-q}\right.\right.\right.$$

$$+\left(1+\frac{\eta_1}{L}\right)\ \mathrm{pv}\int_0^{-L/\eta_1}\frac{\zeta^{q-1}}{\zeta-1}d\zeta\Bigg)\Bigg\}\Bigg], \tag{C.7a}$$

$$\frac{u_2}{L}(\frac{\eta_1}{L}<-1)=\frac{\tau_o}{2\mu}\Bigg[-1+\frac{(1-\hat{\alpha}_s^4)}{R_q}\,\frac{\sin q\pi}{\pi}\Bigg\{\frac{1}{q}\left(\frac{-\eta_1}{L}\right)^{-q}\left(\frac{1}{1-q}\left(\frac{-\eta_1}{L}\right)-1\right)$$

$$+\left(1+\frac{\eta_1}{L}\right)\int_0^{-L/\eta_1}\frac{\zeta^q}{\zeta-1}d\zeta\Bigg\}\Bigg]. \tag{C.7b}$$

Again, the displacement field on the lower crack face ($\eta_1 < 0, \eta_2 \to 0^-$) can be obtained by invoking mode II symmetries.

Appendix D

SubRayleigh Mode II Crack With a Rate Dependent Cohesive Zone

The dominant near tip stress field (in the upper half plane $\eta_2 > 0$) around the tip of a subRayleigh mode II crack with a rate dependent cohesive zone, steadily propagating through a homogeneous, isotropic, linear elastic solid under 2-D plane stress or plane strain conditions, is as follows:

$$\begin{aligned}\frac{\sigma_{11}}{\tau_o} = \frac{2\alpha_s}{\pi R(v)}\Bigg[&(1+2\alpha_l^2-\alpha_s^2)\sqrt{\frac{r_l}{L}}\sin\left(\frac{\theta_l}{2}\right)\Bigg\{\int_0^1 \frac{[\zeta-(\frac{r_l}{L})]}{\sqrt{\zeta}\,[\zeta^2+(\frac{r_l}{L})^2+2\zeta\,(\frac{r_l}{L})\cos\theta_l]}\,d\zeta \\ &+\frac{\sin\gamma\pi}{\pi}\int_0^1\left(\frac{\zeta}{1-\zeta}\right)^{\gamma}\frac{[\zeta-(\frac{r_l}{L})]}{[\zeta^2+(\frac{r_l}{L})^2+2\zeta\,(\frac{r_l}{L})\cos\theta_l]}\int_0^1\frac{(1-s)^{\gamma}}{\sqrt{s}\,(1-s\,\zeta)}\,ds\,d\zeta\Bigg\} \\ &-(1+\alpha_s^2)\sqrt{\frac{r_s}{L}}\sin\left(\frac{\theta_s}{2}\right)\Bigg\{\int_0^1 \frac{[\zeta-(\frac{r_s}{L})]}{\sqrt{\zeta}\,[\zeta^2+(\frac{r_s}{L})^2+2\zeta\,(\frac{r_s}{L})\cos\theta_s]}\,d\zeta \\ &+\frac{\sin\gamma\pi}{\pi}\int_0^1\left(\frac{\zeta}{1-\zeta}\right)^{\gamma}\frac{[\zeta-(\frac{r_s}{L})]}{[\zeta^2+(\frac{r_s}{L})^2+2\zeta\,(\frac{r_s}{L})\cos\theta_s]}\int_0^1\frac{(1-s)^{\gamma}}{\sqrt{s}\,(1-s\,\zeta)}\,ds\,d\zeta\Bigg\}\Bigg],\end{aligned} \tag{D.1a}$$

$$\frac{\sigma_{22}}{\tau_o} = \frac{2\alpha_s}{\pi R(v)}\Bigg[-(1+\alpha_s^2)\sqrt{\frac{r_l}{L}}\sin\left(\frac{\theta_l}{2}\right)\Bigg\{\int_0^1 \frac{[\zeta - (\frac{r_l}{L})]}{\sqrt{\zeta}\,[\zeta^2 + (\frac{r_l}{L})^2 + 2\zeta\,(\frac{r_l}{L})\cos\theta_l]}\,d\zeta$$
$$+ \frac{\sin\gamma\pi}{\pi}\int_0^1 \left(\frac{\zeta}{1-\zeta}\right)^\gamma \frac{[\zeta - (\frac{r_l}{L})]}{[\zeta^2 + (\frac{r_l}{L})^2 + 2\zeta\,(\frac{r_l}{L})\cos\theta_l]}\int_0^1 \frac{(1-s)^\gamma}{\sqrt{s}\,(1-s\,\zeta)}\,ds\,d\zeta\Bigg\}$$
$$+ (1+\alpha_s^2)\sqrt{\frac{r_s}{L}}\sin\left(\frac{\theta_s}{2}\right)\Bigg\{\int_0^1 \frac{[\zeta - (\frac{r_s}{L})]}{\sqrt{\zeta}\,[\zeta^2 + (\frac{r_s}{L})^2 + 2\zeta\,(\frac{r_s}{L})\cos\theta_s]}\,d\zeta$$
$$+ \frac{\sin\gamma\pi}{\pi}\int_0^1 \left(\frac{\zeta}{1-\zeta}\right)^\gamma \frac{[\zeta - (\frac{r_s}{L})]}{[\zeta^2 + (\frac{r_s}{L})^2 + 2\zeta\,(\frac{r_s}{L})\cos\theta_s]}\int_0^1 \frac{(1-s)^\gamma}{\sqrt{s}\,(1-s\,\zeta)}\,ds\,d\zeta\Bigg\}\Bigg]\,, \tag{D.1b}$$

$$\frac{\sigma_{12}}{\tau_o} = \frac{1}{\pi R(v)}\Bigg[4\alpha_l\alpha_s\sqrt{\frac{r_l}{L}}\cos\left(\frac{\theta_l}{2}\right)\Bigg\{\int_0^1 \frac{[\zeta + (\frac{r_l}{L})]}{\sqrt{\zeta}\,[\zeta^2 + (\frac{r_l}{L})^2 + 2\zeta\,(\frac{r_l}{L})\cos\theta_l]}\,d\zeta$$
$$+ \frac{\sin\gamma\pi}{\pi}\int_0^1 \left(\frac{\zeta}{1-\zeta}\right)^\gamma \frac{[\zeta + (\frac{r_l}{L})]}{[\zeta^2 + (\frac{r_l}{L})^2 + 2\zeta\,(\frac{r_l}{L})\cos\theta_l]}\int_0^1 \frac{(1-s)^\gamma}{\sqrt{s}\,(1-s\,\zeta)}\,ds\,d\zeta\Bigg\}$$
$$- (1+\alpha_s^2)^2\sqrt{\frac{r_s}{L}}\cos\left(\frac{\theta_s}{2}\right)\Bigg\{\int_0^1 \frac{[\zeta + (\frac{r_s}{L})]}{\sqrt{\zeta}\,[\zeta^2 + (\frac{r_s}{L})^2 + 2\zeta\,(\frac{r_s}{L})\cos\theta_s]}\,d\zeta$$
$$+ \frac{\sin\gamma\pi}{\pi}\int_0^1 \left(\frac{\zeta}{1-\zeta}\right)^\gamma \frac{[\zeta + (\frac{r_s}{L})]}{[\zeta^2 + (\frac{r_s}{L})^2 + 2\zeta\,(\frac{r_s}{L})\cos\theta_s]}\int_0^1 \frac{(1-s)^\gamma}{\sqrt{s}\,(1-s\,\zeta)}\,ds\,d\zeta\Bigg\}\Bigg]\,, \tag{D.1c}$$

where (η_1, η_2) is a coordinate system centered at the moving crack tip with the η_1-axis on the crack plane perpendicular to the crack front and the η_2-axis perpendicular to the crack plane. Further,

$$r_s = \sqrt{\eta_1^2 + \alpha_s^2\eta_2^2}\,, \qquad \theta_s = \tan^{-1}\left[\frac{\alpha_s\eta_2}{\eta_1}\right], \tag{D.2a}$$

$$r_l = \sqrt{\eta_1^2 + \alpha_l^2\eta_2^2}\,, \qquad \theta_l = \tan^{-1}\left[\frac{\alpha_l\eta_2}{\eta_1}\right], \tag{D.2b}$$

$$\alpha_l = \sqrt{1 - \frac{v^2}{c_l^2}}\,, \qquad \alpha_s = \sqrt{1 - \frac{v^2}{c_s^2}}\,, \tag{D.2c}$$

$$R(v) = 4\alpha_l\alpha_s - (1+\alpha_s^2)^2\,, \tag{D.2d}$$

$$\gamma = \frac{1}{\pi}\tan^{-1}\left[\beta\frac{v^3}{c_s^3}\frac{\alpha_s}{R(v)}\right]. \tag{D.2e}$$

τ_o is the cohesive shear strength of the material and L is the cohesive zone length. The integrals in (D.1) become singular of the Cauchy type for $(\theta_l, \theta_s \to +\pi, 0 < r_s, r_l < L)$. The limiting values of these integrals in such cases must be interpreted appropriately using the Plemelj formulae. The limiting values of the stress components for $0 < r_s, r_l < 1$ and $\theta_s, \theta_l \to +\pi$ are given by

$$\frac{\sigma_{11}}{\tau_o}(-1 < \frac{\eta_1}{L} < 0,\ \eta_2 \to 0^+) = \frac{1}{\pi}\frac{4\alpha_s(\alpha_l^2 - \alpha_s^2)}{R(v)}\sqrt{-\frac{\eta_1}{L}}\left\{ \mathrm{pv}\int_0^1 \frac{d\zeta}{\sqrt{\zeta}(\zeta + \eta_1/L)} + \int_0^1 \frac{ds}{\sqrt{s}(1 + s\,\eta_1/L)} - \cos\gamma\pi \left(\frac{-\eta_1/L}{1 + \eta_1/L}\right)^{\gamma} \int_0^1 \frac{(1-s)^{\gamma}}{\sqrt{s}(1 + s\,\eta_1/L)} ds \right\}, \tag{D.3a}$$

$$\frac{\sigma_{22}}{\tau_o}(-1 < \frac{\eta_1}{L} < 0,\ \eta_2 \to 0^+) = 0\,, \tag{D.3b}$$

$$\frac{\sigma_{12}}{\tau_o}(-1 < \frac{\eta_1}{L} < 0,\ \eta_2 \to 0^+) = 1 + \frac{\sin\gamma\pi}{\pi}\frac{(-\eta_1/L)^{\gamma+1/2}}{(1 + \eta_1/L)^{\gamma}} \int_0^1 \frac{(1-s)^{\gamma}}{\sqrt{s}(1 + s\,\eta_1/L)} ds\,. \tag{D.3c}$$

The stress field in the lower half plane ($\eta_2 < 0$) can be obtained by invoking the symmetries associated with mode II deformation.

Appendix E

Intersonic Mode II Crack With a Rate Dependent Cohesive Zone

The dominant near tip stress field (in the upper half plane $\eta_2 > 0$) around the tip of an intersonic mode II crack with a rate dependent cohesive zone, steadily propagating through a homogeneous, isotropic, linear elastic solid under 2-D plane stress or plane strain conditions, is as follows:

$$\begin{aligned}\frac{\sigma_{11}}{\tau_o} = \frac{\sin q\pi}{2\pi\alpha_l}\Bigg[&(1+2\alpha_l^2+\hat{\alpha}_s^2)\left(\frac{r_l}{L}\right)^{1-q}\Bigg\{\int_0^1 \frac{[\zeta\sin(1-q)\theta_l - \left(\frac{r_l}{L}\right)\sin q\theta_l]}{\zeta^{1-q}[\zeta^2+\left(\frac{r_l}{L}\right)^2+2\zeta\left(\frac{r_l}{L}\right)\cos\theta_l]}d\zeta \\ &+ \frac{\sin\lambda\pi}{\pi}\int_0^1\left(\frac{\zeta}{1-\zeta}\right)^{\lambda}\frac{[\zeta\sin(1-q)\theta_l - \left(\frac{r_l}{L}\right)\sin q\theta_l]}{[\zeta^2+\left(\frac{r_l}{L}\right)^2+2\zeta\left(\frac{r_l}{L}\right)\cos\theta_l]}\int_0^1\frac{(1-s)^{\lambda}}{s^q(1-s\,\zeta)}ds\,d\zeta\Bigg\} \\ &- (1-\hat{\alpha}_s^2)\sin q\pi\,\xi^{1-q}\Bigg\{\int_0^1\frac{d\zeta}{\zeta^{1-q}(\zeta-\xi)}+\int_0^1\frac{ds}{s^q(1-s\,\xi)} \\ &- Q(\xi,\lambda)\int_0^1\frac{(1-s)^{\lambda}}{s^q(1-s\,\xi)}ds\Bigg\}H(\xi)\Bigg],\end{aligned} \tag{E.1a}$$

$$\frac{\sigma_{22}}{\tau_o} = \frac{\sin q\pi}{2\pi\alpha_l}\Bigg[-(1-\hat{\alpha}_s^2)\left(\frac{r_l}{L}\right)^{1-q}\Bigg\{\int_0^1 \frac{[\zeta\sin(1-q)\theta_l - \left(\frac{r_l}{L}\right)\sin q\theta_l]}{\zeta^{1-q}[\zeta^2+\left(\frac{r_l}{L}\right)^2+2\zeta\left(\frac{r_l}{L}\right)\cos\theta_l]}d\zeta$$
$$+\frac{\sin\lambda\pi}{\pi}\int_0^1\left(\frac{\zeta}{1-\zeta}\right)^{\lambda}\frac{[\zeta\sin(1-q)\theta_l-\left(\frac{r_l}{L}\right)\sin q\theta_l]}{[\zeta^2+\left(\frac{r_l}{L}\right)^2+2\zeta\left(\frac{r_l}{L}\right)\cos\theta_l]}\int_0^1\frac{(1-s)^{\lambda}}{s^q(1-s\,\zeta)}ds\,d\zeta\Bigg\}$$
$$+(1-\hat{\alpha}_s^2)\sin q\pi\,\xi^{1-q}\Bigg\{\int_0^1\frac{d\zeta}{\zeta^{1-q}(\zeta-\xi)}+\int_0^1\frac{ds}{s^q(1-s\,\xi)}$$
$$-Q(\xi,\lambda)\int_0^1\frac{(1-s)^{\lambda}}{s^q(1-s\,\xi)}ds\Bigg\}H(\xi)\Bigg], \tag{E.1b}$$

$$\frac{\sigma_{12}}{\tau_o} = \frac{\sin q\pi}{\pi}\Bigg[\left(\frac{r_l}{L}\right)^{1-q}\Bigg\{\int_0^1 \frac{[\zeta\cos(1-q)\theta_l + \left(\frac{r_l}{L}\right)\cos q\theta_l]}{\zeta^{1-q}[\zeta^2+\left(\frac{r_l}{L}\right)^2+2\zeta\left(\frac{r_l}{L}\right)\cos\theta_l]}d\zeta$$
$$+\frac{\sin\lambda\pi}{\pi}\int_0^1\left(\frac{\zeta}{1-\zeta}\right)^{\lambda}\frac{[\zeta\cos(1-q)\theta_l+\left(\frac{r_l}{L}\right)\cos q\theta_l]}{[\zeta^2+\left(\frac{r_l}{L}\right)^2+2\zeta\left(\frac{r_l}{L}\right)\cos\theta_l]}\int_0^1\frac{(1-s)^{\lambda}}{s^q(1-s\,\zeta)}ds\,d\zeta\Bigg\}$$
$$+\cos q\pi\,\xi^{1-q}\Bigg\{\int_0^1\frac{d\zeta}{\zeta^{1-q}(\zeta-\xi)}+\int_0^1\frac{ds}{s^q(1-s\,\xi)}$$
$$-Q(\xi,\lambda)\int_0^1\frac{(1-s)^{\lambda}}{s^q(1-s\,\xi)}ds\Bigg\}H(\xi)\Bigg], \tag{E.1c}$$

where (η_1, η_2) is a coordinate system centered at the moving crack tip with the η_1-axis on the crack plane perpendicular to the crack front and the η_2-axis perpendicular to the crack plane. $H(\cdot)$ is the unit step function. Further,

$$r_l = \sqrt{\eta_1^2+\alpha_l^2\eta_2^2}\,, \qquad \theta_l = \tan^{-1}\left[\frac{\alpha_l\eta_2}{\eta_1}\right], \tag{E.2a}$$

$$\alpha_l = \sqrt{1-\frac{v^2}{c_l^2}}\,, \qquad \hat{\alpha}_s = \sqrt{\frac{v^2}{c_s^2}-1}\,, \tag{E.2b}$$

$$q = \frac{1}{\pi}\tan^{-1}\left[\frac{4\alpha_l\hat{\alpha}_s}{(1-\hat{\alpha}_s^2)^2}\right], \tag{E.3}$$

$$\lambda = \frac{1}{\pi}\tan^{-1}\left[\frac{\beta\frac{v^3}{c_s^3}\frac{\hat{\alpha}_s}{R_q}\sin q\pi}{1+\beta\frac{v^3}{c_s^3}\frac{\hat{\alpha}_s}{R_q}\cos q\pi}\right], \tag{E.4}$$

$$R_q = \sqrt{16\alpha_l^2\hat{\alpha}_s^2+(1-\hat{\alpha}_s^2)^2}\,, \tag{E.5}$$

$$\xi = \frac{-\eta_1 - \hat{\alpha}_s \eta_2}{L} \qquad \text{and} \tag{E.6}$$

$$Q(\xi, \lambda) = \begin{cases} \cos \pi\lambda \left(\dfrac{\xi}{1-\xi} \right)^{\lambda} & \xi < 1\,, \\ \left(\dfrac{-\xi}{1-\xi} \right)^{\lambda} & \xi > 1\,. \end{cases} \tag{E.7}$$

τ_o is the shear strength of the crack plane and L is the cohesive zone length. For $0 < \xi < 1$, *i.e.*, for $-L < \eta_1 + \hat{\alpha}_s \eta_2 < 0$, the integral

$$\int_0^1 \frac{d\zeta}{\zeta^{1-q}(\zeta - \xi)}\,, \tag{E.8}$$

becomes singular and hence must be evaluated in the Cauchy principal value sense. Also, the integrals containing the factor $[\zeta^2 + (r_l/L)^2 + 2\zeta(r_l/L)\cos\theta_l]$ in the denominator of the integrand, become singular of the Cauchy type for $\theta_l \to +\pi$ and $0 < (r_l/L) < 1$. The limiting values of these integrals in such cases must be interpreted appropriately using the Plemelj formulae. The limiting values of the stress components for $0 < (r_l/L) < 1$ and $\theta_l \to +\pi$ are given by

$$\begin{aligned} \frac{\sigma_{11}}{\tau_o} = \frac{\alpha_l^2 + \hat{\alpha}_s^2}{\alpha_l} \frac{\sin^2 q\pi}{\pi} \Bigg[& \frac{\pi}{\tan q\pi} + \left(\frac{-\eta_1}{L} \right)^{1-q} \Bigg\{ \mathrm{pv} \int_0^1 \frac{d\zeta}{\zeta^{1-q}(\zeta + \eta_1/L)} \\ & + \int_0^1 \frac{ds}{s^q(1 + s\,\eta_1/L)} \Bigg\} + \sin\lambda\pi \frac{(-\eta_1/L)^{1-q+\lambda}}{(1+\eta_1/L)^{\lambda}} \Bigg\{ \frac{1}{\tan q\pi} \\ & - \frac{1}{\tan\lambda\pi} \Bigg\} \int_0^1 \frac{(1-s)^{\lambda}}{s^q(1 + s\,\eta_1/L)} ds \Bigg]\,, \end{aligned} \tag{E.9a}$$

$$\frac{\sigma_{22}}{\tau_o} = 0\,, \tag{E.9b}$$

$$\frac{\sigma_{12}}{\tau_o} = 1 + \frac{\sin\lambda\pi}{\pi} \frac{(-\eta_1/L)^{1-q+\lambda}}{(1+\eta_1/L)^{\lambda}} \int_0^1 \frac{(1-s)^{\lambda}}{s^q(1 + s\,\eta_1/L)} ds\,. \tag{E.9c}$$

The stress field in the lower half plane ($\eta_2 < 0$) can be obtained by invoking the symmetries associated with mode II deformation.

Appendix F

Solution to the Cauchy Type Singular Integral Equation

The solution procedure for the integral equations in (5.8) is shown here only for the intersonic case. The procedure for the subsonic case is similar and is omitted.

$$\hat{f}(\eta_1)\left\{1+\beta\frac{v^3}{c_s^3}\,\frac{\hat{\alpha}_s}{R_q}\,\cos q\pi\right\}-\left\{\beta\frac{v^3}{c_s^3}\,\frac{\hat{\alpha}_s}{R_q}\,\sin q\pi\right\}\frac{1}{\pi}\,\mathrm{pv}\int_{-L}^{0}\frac{\hat{f}(\xi)}{(\xi+|\eta_1|)}\,d\xi = \frac{1}{|\eta_1|^{1-q}} \qquad c_s<v<c_l\,, \tag{F.1}$$

where

$$\hat{f}(\eta_1)=\frac{\tau(\eta_1/L)}{\tau_o|\eta_1|^{1-q}} \qquad c_s<v<c_l\,. \tag{F.2}$$

Define a Cauchy type integral,

$$\phi(z)=\frac{1}{2\pi i}\int_{-L}^{0}\frac{\hat{f}(\xi)}{\xi-z}d\xi \tag{F.3}$$

If we assume that that $\hat{f}(\eta_1)$ satisfies the Hölder condition, then by Plemelj formulae,

$$(A-iB)\phi^{+}(\eta_1)-(A+iB)\phi^{-}(\eta_1)=\frac{1}{|\eta_1|^{1-q}}\,, \tag{F.4}$$

where

$$A = 1 + \beta \frac{v^3}{c_s^3} \frac{\hat{\alpha}_s}{R_q} \cos q\pi \,, \tag{F.5}$$

$$B = \beta \frac{v^3}{c_s^3} \frac{\hat{\alpha}_s}{R_q} \sin q\pi \,. \tag{F.6}$$

(F.4) can be rewritten as

$$\left(\frac{\phi}{z^\lambda}\right)^+ - \left(\frac{\phi}{z^\lambda}\right)^- = \frac{1}{\sqrt{A^2+B^2}} \frac{1}{|\eta_1|^{1-q}} \,, \tag{F.7}$$

where

$$\lambda = \frac{1}{\pi} \tan^{-1}\left(\frac{B}{A}\right) \,. \tag{F.8}$$

Rearranging (F.7) as

$$\left[\frac{(z+L)^{\lambda_1}\phi}{z^{\lambda+n}}\right]^+ - \left[\frac{(z+L)^{\lambda_1}\phi}{z^{\lambda+n}}\right]^- = \frac{1}{\sqrt{A^2+B^2}} \frac{(\eta_1+L)^{\lambda_1}}{|\eta_1|^{\lambda+n+1-q}} (-1)^n \,, \tag{F.9}$$

where n, an integer and λ_1 are to be determined, we obtain a Riemann-Hilbert problem.

The general solution of the R-H problem above is given by

$$\frac{(z+L)^{\lambda_1}\phi}{z^{n+\lambda}} = P(z) + \frac{1}{2\pi i} \int_{-L}^{0} \frac{1}{\sqrt{A^2+B^2}} \frac{(\eta_1+L)^{\lambda_1}(-1)^n}{|\eta_1|^{\lambda+n+1-q}} \frac{1}{\eta_1 - z} \, d\eta_1 \,. \tag{F.10}$$

$P(z)$ is an entire function (a polynomial). Ensuring that both sides have the same behavior as $|z| \to \infty$, we obtain $\lambda_1 = \lambda + m$, where m is an integer.

$$\hat{f}(\eta_1) = \phi^+(\eta_1) - \phi^-(\eta_1) \tag{F.11}$$

$$\Rightarrow \hat{f}(\eta_1) = \frac{\cos\lambda\pi}{\sqrt{A^2+B^2}}\frac{1}{|\eta_1|^{1-q}} + \frac{|\eta_1|^{n+\lambda}}{(\eta_1+L)^{\lambda+m}}\frac{\sin\lambda\pi}{\sqrt{A^2+B^2}}\left\{P(z) \text{ of order } m-1-n \right.$$
$$\left. + \frac{1}{\pi}\,\mathrm{pv}\int_{-L}^{0}\frac{(\xi+L)^{\lambda+m}}{|\xi|^{1-q+\lambda+m}}\frac{1}{\xi-\eta_1}\,d\xi\right\}. \tag{F.12}$$

Introducing the boundary condition (see (5.11)),

$$\lim_{\eta_1\to 0}\hat{f} = \frac{1}{|\eta_1|^{1-q}}, \tag{F.13}$$

we obtain $n = 0$. Introducing the second boundary condition (see (5.11)),

$$\left[\lim_{\eta_1\to -L}\hat{f}\right](\eta_1+L)^q|\eta_1|^{1-q} \to 0 \tag{F.14}$$

we obtain, $m = 0$ and $P(z) = 0$. Thus all the unknown quantities are determined. After some further simplification, the cohesive traction distribution is obtained as

$$\frac{\tau(-1<\eta_1/L\le 0)}{\tau_o} = 1 + \frac{\sin\lambda\pi}{\pi}\frac{(-\eta_1/L)^{1-q+\lambda}}{(1+\eta_1/L)^{\lambda}}\int_0^1\frac{(1-s)^{\lambda}}{s^q(1+s\,\eta_1/L)}\,ds \qquad c_s<v<c_l\,. \tag{F.15}$$

By a similar procedure the cohesive traction distribution for subsonic speeds can be obtained.

$$\frac{\tau(-1<\eta_1/L\le 0)}{\tau_o} = 1 + \frac{\sin\gamma\pi}{\pi}\frac{(-\eta_1/L)^{\gamma+1/2}}{(1+\eta_1/L)^{\gamma}}\int_0^1\frac{(1-s)^{\gamma}}{\sqrt{s}(1+s\,\eta_1/L)}\,ds \qquad 0\le v<c_R\,, \tag{F.16}$$

where

$$\gamma = \frac{1}{\pi}\tan^{-1}\left\{\beta\frac{v^3}{c_s^3}\frac{\alpha_s}{R(v)}\right\} \qquad 0\le v<c_R\,. \tag{F.17}$$

Appendix G

Intersonic Crack on an Elastic/Rigid Interface with a Detached Contact Zone

The near tip stress field (in the upper half plane $\eta_2 > 0$) around the tip of an intersonic crack with a finite traction free zone behind the tip followed by a finite zone of crack face frictional contact, steadily propagating along an interface adjoining a homogeneous, isotropic, linear elastic solid and a rigid substrate under 2-D plane stress or plane strain conditions, is as follows:

$$\sigma_{ij}(\eta_1, \eta_2) = \mu \sum_{n=0}^{\infty} A_n S_{ij}(\eta_1, \eta_2; q_1 - n, q_2, q_3)\,, \tag{G.1}$$

where

$$\begin{aligned}
S_{11} = \frac{1}{1+\alpha_l^2\hat{\alpha}_s^2}\Bigg[&\frac{(1+2\alpha_l^2+\hat{\alpha}_s^2)}{r_1^{q_1-n}r_2^{q_2}r_3^{q_3}}\Big[\alpha_l\hat{\alpha}_s\cos\{(q_1-n)\theta_1+q_2\theta_2+q_3\theta_3\}\\
&+\sin\{(q_1-n)\theta_1+q_2\theta_2+q_3\theta_3\}\Big]\\
&-\frac{2\alpha_l\hat{\alpha}_s}{|\zeta_1|^{q_1-n}|\zeta_2|^{q_2}|\zeta_3|^{q_3}}H(\zeta_1)\\
&-\frac{(1-\hat{\alpha}_s^2)}{|\zeta_1|^{q_1-n}|\zeta_2|^{q_2}|\zeta_3|^{q_3}}\left[\alpha_l\hat{\alpha}_s\cos(q_1-n)\pi+\sin(q_1-n)\pi\right]\left[H(\zeta_2)-H(\zeta_1)\right]\\
&-\frac{2\alpha_l\hat{\alpha}_s}{|\zeta_1|^{q_1-n}|\zeta_2|^{q_2}|\zeta_3|^{q_3}}\left[\cos(q_1+q_2-n)\pi-\alpha_l\hat{\alpha}_s\sin(q_1+q_2-n)\pi\right]\left[H(\zeta_3)-H(\zeta_2)\right]
\end{aligned}$$

$$- \frac{(1-\hat{\alpha}_s^2)}{|\zeta_1|^{q_1-n}|\zeta_2|^{q_2}|\zeta_3|^{q_3}} \left[\alpha_l\hat{\alpha}_s \cos(q_1-n)\pi + \sin(q_1-n)\pi\right] H(-\zeta_3)\Bigg], \tag{G.2a}$$

$$\begin{aligned} S_{22} = \frac{1}{1+\alpha_l^2\hat{\alpha}_s^2} \Bigg[& \frac{-(1-\hat{\alpha}_s^2)}{r_1^{q_1-n} r_2^{q_2} r_3^{q_3}} \Big[\alpha_l\hat{\alpha}_s \cos\{(q_1-n)\theta_1 + q_2\theta_2 + q_3\theta_3\} \\ & + \sin\{(q_1-n)\theta_1 + q_2\theta_2 + q_3\theta_3\}\Big] \\ & + \frac{2\alpha_l\hat{\alpha}_s}{|\zeta_1|^{q_1-n}|\zeta_2|^{q_2}|\zeta_3|^{q_3}} H(\zeta_1) \\ & + \frac{(1-\hat{\alpha}_s^2)}{|\zeta_1|^{q_1-n}|\zeta_2|^{q_2}|\zeta_3|^{q_3}} \left[\alpha_l\hat{\alpha}_s \cos(q_1-n)\pi + \sin(q_1-n)\pi\right] \left[H(\zeta_2) - H(\zeta_1)\right] \\ & + \frac{2\alpha_l\hat{\alpha}_s}{|\zeta_1|^{q_1-n}|\zeta_2|^{q_2}|\zeta_3|^{q_3}} \left[\cos(q_1+q_2-n)\pi - \alpha_l\hat{\alpha}_s \sin(q_1+q_2-n)\pi\right] \left[H(\zeta_3) - H(\zeta_2)\right] \\ & + \frac{(1-\hat{\alpha}_s^2)}{|\zeta_1|^{q_1-n}|\zeta_2|^{q_2}|\zeta_3|^{q_3}} \left[\alpha_l\hat{\alpha}_s \cos(q_1-n)\pi + \sin(q_1-n)\pi\right] H(-\zeta_3)\Bigg], \end{aligned} \tag{G.2b}$$

$$\begin{aligned} S_{12} = \frac{1}{1+\alpha_l^2\hat{\alpha}_s^2} \Bigg[& \frac{-2\alpha_l}{r_1^{q_1-n} r_2^{q_2} r_3^{q_3}} \Big[\cos\{(q_1-n)\theta_1 + q_2\theta_2 + q_3\theta_3\} \\ & - \alpha_l\hat{\alpha}_s \sin\{(q_1-n)\theta_1 + q_2\theta_2 + q_3\theta_3\}\Big] \\ & + \frac{\alpha_l(1-\hat{\alpha}_s^2)}{|\zeta_1|^{q_1-n}|\zeta_2|^{q_2}|\zeta_3|^{q_3}} H(\zeta_1) \\ & + \frac{(1-\hat{\alpha}_s^2)^2}{2\hat{\alpha}_s} \frac{1}{|\zeta_1|^{q_1-n}|\zeta_2|^{q_2}|\zeta_3|^{q_3}} \left[\alpha_l\hat{\alpha}_s \cos(q_1-n)\pi + \sin(q_1-n)\pi\right] \left[H(\zeta_2) - H(\zeta_1)\right] \\ & + \frac{\alpha_l(1-\hat{\alpha}_s^2)}{|\zeta_1|^{q_1-n}|\zeta_2|^{q_2}|\zeta_3|^{q_3}} \left[\cos(q_1+q_2-n)\pi - \alpha_l\hat{\alpha}_s \sin(q_1+q_2-n)\pi\right] \left[H(\zeta_3) - H(\zeta_2)\right] \\ & + \frac{(1-\hat{\alpha}_s^2)^2}{2\hat{\alpha}_s} \frac{1}{|\zeta_1|^{q_1-n}|\zeta_2|^{q_2}|\zeta_3|^{q_3}} \left[\alpha_l\hat{\alpha}_s \cos(q_1-n)\pi + \sin(q_1-n)\pi\right] H(-\zeta_3)\Bigg]. \end{aligned} \tag{G.2c}$$

where (η_1, η_2) is a coordinate system centered at the moving crack tip with the η_1-axis along the interface perpendicular to the crack front and the η_2-axis perpendicular to the crack plane. $H(\cdot)$ is the unit step function. Further,

$$r_1 = \sqrt{\eta_1^2 + \alpha_l^2\eta_2^2}\,, \qquad \theta_1 = \tan^{-1}\left[\frac{\alpha_l\eta_2}{\eta_1}\right], \tag{G.3a}$$

$$r_2 = \sqrt{(\eta_1 + l_1)^2 + \alpha_l^2 \eta_2^2}\,, \qquad \theta_2 = \tan^{-1}\left[\frac{\alpha_l \eta_2}{\eta_1 + l_1}\right], \tag{G.3b}$$

$$r_3 = \sqrt{(\eta_1 + l_1 + l_2)^2 + \alpha_l^2 \eta_2^2}\,, \qquad \theta_3 = \tan^{-1}\left[\frac{\alpha_l \eta_2}{\eta_1 + l_1 + l_2}\right], \tag{G.3c}$$

$$\alpha_l = \sqrt{1 - \frac{v^2}{c_l^2}}\,, \qquad \hat{\alpha}_s = \sqrt{\frac{v^2}{c_s^2} - 1}\,, \tag{G.3d}$$

the singularity exponents

$$q_1 = \frac{1}{\pi}\tan^{-1}\left\{\frac{\alpha_l \hat{\alpha}_s\,[4 - (1 - \hat{\alpha}_s^2)^2]}{4\alpha_l^2 \hat{\alpha}_s^2 + (1 - \hat{\alpha}_s^2)^2}\right\}, \tag{G.4a}$$

$$q_2 = \frac{1}{\pi}\tan^{-1}\left\{\frac{\alpha_l (1 - \hat{\alpha}_s^4)(1 - \hat{\alpha}_s^2 - 2\lambda\hat{\alpha}_s)}{4\alpha_l^2 \hat{\alpha}_s (1 + \hat{\alpha}_s^2 + 2\lambda\hat{\alpha}_s) + \lambda(1 - \hat{\alpha}_s^2)^3}\right\}, \tag{G.4b}$$

$$q_3 = -q_2 \tag{G.4c}$$

and

$$\zeta_1 = \eta_1 + \hat{\alpha}_s \eta_2\,, \tag{G.5a}$$

$$\zeta_2 = \eta_1 + l_1 + \hat{\alpha}_s \eta_2\,, \tag{G.5b}$$

$$\zeta_3 = \eta_1 + l_1 + l_2 + \hat{\alpha}_s \eta_2\,. \tag{G.5c}$$

μ is the shear modulus of the elastic solid, λ is the Coulomb friction coefficient, l_1 is the length of the traction free zone and l_2 is the length of the frictional contact zone. A_n are undetermined coefficients which measure of the amplitude of the near-tip fields and are related such that the normal displacement vanishes in the frictional contact zone.

The particle velocity field in the upper half plane ($\eta_2 > 0$) is given by

$$\begin{aligned}
\dot{u}_1 = &-\frac{v}{1+\alpha_l^2\hat{\alpha}_s^2}\sum_{n=0}^{\infty} A_n \Bigg[\frac{1}{r_1^{q_1-n} r_2^{q_2} r_3^{q_3}}\Big[\alpha_l\hat{\alpha}_s \cos\{(q_1-n)\theta_1 + q_2\theta_2 + q_3\theta_3\} \\
&+ \sin\{(q_1-n)\theta_1 + q_2\theta_2 + q_3\theta_3\}\Big] \\
&- \frac{\alpha_l\hat{\alpha}_s}{|\zeta_1|^{q_1-n}|\zeta_2|^{q_2}|\zeta_3|^{q_3}} H(\zeta_1) \\
&- \frac{(1-\hat{\alpha}_s^2)}{2|\zeta_1|^{q_1-n}|\zeta_2|^{q_2}|\zeta_3|^{q_3}}\left[\alpha_l\hat{\alpha}_s\cos(q_1-n)\pi + \sin(q_1-n)\pi\right]\left[H(\zeta_2) - H(\zeta_1)\right] \\
&- \frac{\alpha_l\hat{\alpha}_s}{|\zeta_1|^{q_1-n}|\zeta_2|^{q_2}|\zeta_3|^{q_3}}\left[\cos(q_1+q_2-n)\pi - \alpha_l\hat{\alpha}_s\sin(q_1+q_2-n)\pi\right]\left[H(\zeta_3) - H(\zeta_2)\right] \\
&- \frac{(1-\hat{\alpha}_s^2)}{2|\zeta_1|^{q_1-n}|\zeta_2|^{q_2}|\zeta_3|^{q_3}}\left[\alpha_l\hat{\alpha}_s\cos(q_1-n)\pi + \sin(q_1-n)\pi\right]H(-\zeta_3)\Bigg], \qquad \text{(G.6a)}
\end{aligned}$$

$$\begin{aligned}
\dot{u}_2 = &\frac{v}{1+\alpha_l^2\hat{\alpha}_s^2}\sum_{n=0}^{\infty} A_n \Bigg[\frac{\alpha_l}{r_1^{q_1-n} r_2^{q_2} r_3^{q_3}}\Big[\cos\{(q_1-n)\theta_1 + q_2\theta_2 + q_3\theta_3\} \\
&- \alpha_l\hat{\alpha}_s \sin\{(q_1-n)\theta_1 + q_2\theta_2 + q_3\theta_3\}\Big] \\
&- \frac{\alpha_l}{|\zeta_1|^{q_1-n}|\zeta_2|^{q_2}|\zeta_3|^{q_3}} H(\zeta_1) \\
&- \frac{(1-\hat{\alpha}_s^2)}{2\hat{\alpha}_s}\frac{1}{|\zeta_1|^{q_1-n}|\zeta_2|^{q_2}|\zeta_3|^{q_3}}\left[\alpha_l\hat{\alpha}_s\cos(q_1-n)\pi + \sin(q_1-n)\pi\right]\left[H(\zeta_2) - H(\zeta_1)\right] \\
&- \frac{\alpha_l}{|\zeta_1|^{q_1-n}|\zeta_2|^{q_2}|\zeta_3|^{q_3}}\left[\cos(q_1+q_2-n)\pi - \alpha_l\hat{\alpha}_s\sin(q_1+q_2-n)\pi\right]\left[H(\zeta_3) - H(\zeta_2)\right] \\
&- \frac{(1-\hat{\alpha}_s^2)}{2\hat{\alpha}_s}\frac{1}{|\zeta_1|^{q_1-n}|\zeta_2|^{q_2}|\zeta_3|^{q_3}}\left[\alpha_l\hat{\alpha}_s\cos(q_1-n)\pi + \sin(q_1-n)\pi\right]H(-\zeta_3)\Bigg]. \qquad \text{(G.6b)}
\end{aligned}$$